

**An Examination of Relationships among the Energy Balance,
Surface Properties and Climate over Snow Covered Sea Ice during
the Spring Season**

by

Timothy Nicholas Papakryiakou

A thesis
presented to the University of Waterloo
in fulfilment of the
thesis requirement for the degree of
Doctor of Philosophy
in
Geography

Waterloo, Ontario, Canada, 1999

© Timothy Nicholas Papakryiakou 1999



**National Library
of Canada**

**Acquisitions and
Bibliographic Services**

**395 Wellington Street
Ottawa ON K1A 0N4
Canada**

**Bibliothèque nationale
du Canada**

**Acquisitions et
services bibliographiques**

**395, rue Wellington
Ottawa ON K1A 0N4
Canada**

Your file Votre référence

Our file Notre référence

The author has granted a non-exclusive licence allowing the National Library of Canada to reproduce, loan, distribute or sell copies of this thesis in microform, paper or electronic formats.

The author retains ownership of the copyright in this thesis. Neither the thesis nor substantial extracts from it may be printed or otherwise reproduced without the author's permission.

L'auteur a accordé une licence non exclusive permettant à la Bibliothèque nationale du Canada de reproduire, prêter, distribuer ou vendre des copies de cette thèse sous la forme de microfiche/film, de reproduction sur papier ou sur format électronique.

L'auteur conserve la propriété du droit d'auteur qui protège cette thèse. Ni la thèse ni des extraits substantiels de celle-ci ne doivent être imprimés ou autrement reproduits sans son autorisation.

0-612-38261-3

Canada

The University of Waterloo requires the signatures of all persons using or photocopying this thesis.
Please sign below, and give address and date.

ABSTRACT

In this thesis, the form of the springtime energy balance, its linkage to snow and sea ice thermodynamics, and the environmental forcing on the melt process of sea ice in the Canadian Arctic Archipelago (CAA) are examined. I address the following questions:

- How much energy is available to the surface snow cover and when?
- Where does this energy come from and what are the major energy sinks to the system?
- How do characteristics of the surface (sea ice and snow) and the atmosphere influence these relations?

Answers to these questions are necessary so that parameterizations of the energy balance may be developed and properly interpreted for the improvement of climate models. The multiple-year nature of this study permits an examination of energy interactions in a fully coupled surface-atmospheric system, and for the first time, under widely varying springtime atmospheric and surface conditions.

The major findings of the work are summarized in the following points. The available energy to the surface is strongly linked to processes within the snow volume (heat conduction and ice production), but not to net radiation in the early spring. Net radiation in the early spring accounts for, on average, only 18% of the total available energy. In contrast, approximately 95% of the energy available to the system is attributable to the radiation balance in the late spring. Sublimation at the snow surface is the dominant heat loss mechanism while the snow is cold, but the snow volume consumes a larger proportion of the surface's available energy when the snow warms. The presence of salt within the snow is particularly effective at decoupling the snow surface energy balance from oceanic heating. This feature will not be reproduced using a single snow model.

The nature of the difference in the energy balance between first-year (FYI) and multi-year sea ice (MYI) types depends on the characteristics of the ice types being compared. A thick multi-year sea ice floe is shown to be an environment of (i) lower albedo, (ii) higher net radiation, (iii) larger melt rates and (iv) enhanced turbulent heat loss relative to nearby first-year sea ice. Failure

to consider the difference in sea ice properties can cause errors in the prediction of complete *in-situ* sea ice melt by up to 12 days.

Five feedback mechanisms, which involve the surface energy balance, are observed to operate in a fully coupled system. Two negative feedback processes between the surface and atmosphere, and involving the turbulent heat fluxes, are extremely effective at moderating the heating of the snow surface by the atmosphere throughout the spring season. Conductive heat flow into the snow from below tends to warm a cooling snow volume under cooling atmospheric conditions. The surface albedo positive feedback is isolated to periods of clear sky and rising air temperature; however, under such circumstances, the outgoing long-wave flux negative feedback is observed, and acts to offset surface heating.

The net effect of clouds is to warm the snow surface throughout the diurnal cycle in the early spring, and during hours outside of the daytime period during the late spring. Negative feedbacks involving the turbulent heat fluxes act to counter any differences in the net radiation of snow between the cloud regimes when averaged over the diurnal cycle. Overcast conditions are effective at limiting refreezing within the snow during the early spring, but melt rate is 22% larger under clear skies later in the season. Hence the environmental conditions associated with cloud cover promote a more rapid ripening of the snow, but clear skies facilitate a rapid removal of the snow after the onset of melt. Precipitation often accompanies overcast conditions and, in the late spring, it can act to (i) delay melt by maintaining a high surface albedo if the precipitation is solid, or (ii) accelerate melt by reducing the surface albedo, as is the case for rain.

The result of variable environmental forcing on snow covered sea ice of the CAA is a lag of up to 20 days in the timing of accelerated snowmelt within this three-year study. These findings show that the net response of the sea ice zone, in the presence of a warming atmosphere, will depend heavily on the patterns of environmental change associated with warming.

ACKNOWLEDGEMENTS

The seemingly endless number of decisions, questions and sleepless nights, over the course of this degree, were made bearable through the support and encouragement of family and friends. There are many individuals to thank. I would like to acknowledge the assistance of my advisor, Dr. Ellsworth LeDrew, and committee members: Dr. Wayne Rouse, Dr. Ric Soulis, Dr. Doug Dudycha and Dr. Phil Howarth. I would like to take this opportunity to thank them for their support, guidance and patience. Several of my fellow students and close friends also contributed to this thesis, either in the form of field support, and/or insightful discussion. I should like to make particular mention of the contribution by David Barber, Roger De Abreu, Arvids Silis, Dean Flett, Kevin Misurak, Chris Derksen and Mike Wulder. Field activities were made possible by the logistical support extended by the Polar Continental Shelf Project in Resolute NT. Finally, to my father, brothers and sister, and friends, thank-you for your patience and understanding.

DEDICATION

Sadly, my mother died before the completion of this work.

To Gertrude Katharina Papakyriakou (1931 to 1995).

TABLE OF CONTENTS

<i>Abstract</i>	<i>iv</i>
<i>Acknowledgements</i>	<i>vi</i>
<i>Dedication</i>	<i>vii</i>
<i>Table of Contents</i>	<i>xiii</i>
<i>List of Tables</i>	<i>xiv</i>
<i>List of Illustrations</i>	<i>xviii</i>
<i>Chapter 1: Introduction and Statement of Objectives</i>	<i>1</i>
1.1 Motivation.....	1
1.2 Statement of Objectives.....	5
1.3 Thesis Structure.....	6
<i>Chapter 2: Background Material</i>	<i>8</i>
2.1 Introduction.....	8
2.2 Seasonal Evolution of Sea Ice and Snow.....	8
2.2.1 The Annual Cycle of Sea Ice and Its Bulk Physical Properties.....	8
2.2.2 The Physical Properties of Snow.....	13
2.3 The Arctic Climate.....	16
2.3.1 General Characteristics.....	16
2.3.2 Arctic Boundary Layer.....	17
2.4 The Energy Balance of Snow and Sea Ice Surfaces.....	18
2.4.1 Introduction and General Characteristics.....	18
2.4.2 Controls Over the Energy Balance.....	24
2.4.3 Definitions and Descriptions of Energy Balance Terms.....	32
2.5 Summary.....	62

<i>Chapter 3: Experimental Sites and Instrumentation</i>	65
3.1 Introduction	65
3.2 Physical Setting	65
3.3 Experimental Sites	68
3.3.1 Overview of the Snow and Sea Ice Conditions at the Experimental Sites	69
3.3.2 Microclimate Stations and Instrumentation.....	75
3.3.3 Snow Physical Property Sampling Procedures.....	81
<i>Chapter 4: Physical Properties of the Snow and Sea Ice Volume</i>	83
4.1 Introduction	83
4.2 Background	83
4.3 Snow Depth	84
4.4 Characterization of the Snow Salinity and Density	86
4.4.1 Analysis Methods	86
4.4.2 Results.....	87
4.4.3 Discussion	89
4.5 Measured Snow Wetness	93
4.6 Summary	94
<i>Chapter 5: Modeled Snow Albedo, Extinction and Radiation Transmission</i>	100
5.1 Introduction	100
5.2 Computational Methods	100
5.2.1 Radiation Transfer through Snow	100
5.2.2 Absorbed Solar Radiation within the Snow Volume.....	101
5.3 Analysis Methods	101
5.4 Validation of Radiation Transfer Scheme	102
5.5 Spectral Albedo and Extinction Coefficients for Snow	104
5.6 Absorption and Transmission of Solar Radiation within the Snow Cover	109

5.8 Summary	111
Chapter 6: Temporal Dynamics of the Surface Energy Balance.....	114
6.1 Introduction.....	114
6.2 Computational Methods.....	114
6.2.1 Initial Processing.....	114
6.2.2 Radiation Balance	115
6.2.3 Non-Radiative Components of the Energy Balance.....	116
6.3 Analysis Methods	121
6.3.1 General Climatic Conditions	121
6.3.2 Energy Balance Analysis.....	122
6.4 General Climatological Conditions	123
6.4.1 Atmospheric Properties and Precipitation.....	123
6.5 Computational Results	132
6.5.1 Springtime Averages.....	132
6.5.2 Net Radiation and the Components of the Radiation Balance.....	132
6.5.3 Components of the Surface and Volume Energy Balance.....	141
6.6 The Surface and Snow Volume Energy Balance.....	158
6.6.1 Accuracy and Precision of the Energy Balance Model.....	158
6.6.2 Seasonal Episodes	161
6.6.3 Diurnal Variation of the Energy Balance and Meteorological Variables.....	164
6.7 Summary	182
Chapter 7: Spatial Dynamics of the Surface Energy Balance.....	185
7.1 Introduction.....	185
7.2 Methods.....	186
7.3 Results	186
7.3.1 Volume Thermodynamics.....	186
7.3.2 Surface Albedo and Net Radiation.....	192
7.3.4 The Surface Energy Balance.....	195

7.3.5	Testing of Differences between Ice Types	201
7.4	Summary	207
	Chapter 8: Environmental Effects on the Surface Energy Balance.....	209
8.1	Introduction/Background.....	209
8.2	Methods.....	210
8.3	Clouds and the Surface Energy Balance	213
8.4	Statistical Analysis of the Relationship between Environmental and Energy Balance Variables	222
8.4.1	Principal Components Analysis of Energy Balance Components.....	222
8.4.2	Canonical Correlation between Environmental and Energy Balance Variables	228
8.4.3	Heating of the Snow Volume: A Contrast between the 1992 and 1993 Spring Seasons...	248
8.5	Summary	251
	Chapter 9: Concluding Remarks	255
9.1	Introduction.....	255
9.2	Temporal Dynamics	255
9.2.1	Optical and Thermal Properties of Snow and Volume Thermodynamics	255
9.2.2	Surface-Atmosphere Energy Exchange	257
9.3	Spatial Dynamics.....	258
9.4	Environmental Forcing on the Components of the Energy Balance	259
9.5	Recommendations and Concluding Remarks.....	261
	Appendix 1: Day of Year Calendar.....	265
	Appendix 2: Calculation of Spectral Albedo and Extinction.....	266
A2.1	Introduction.....	266
A2.2	Ice Surface Albedo.....	268
A2.3	Mie Scattering Equations and Efficiency Factors	270
	Appendix 3: Site Instrumentation and Layout	276

<i>Appendix 4: Uncertainty Associated with Temperature and Wind Speed Measurements</i>	282
A4.1 Introduction	282
A4.2 Procedure	283
A4.2.1 Laboratory Matching of Sensors	283
A4.2.2 Field Matching of Sensors	283
A4.3) Results and Discussion	284
A4.4 Summary	288
<i>Appendix 5: Statistical Methods</i>	292
A5.1 Introduction	292
A5.2 Mean Bias and Root Mean Square Error	292
A5.3 Pearson’s Product Moment Coefficient of Correlation	293
A5.4 Kruskal-Wallis and Mann-Whitney U-Test	293
A5.5 Principal Components Analysis	294
A5.6 Canonical Correlation	295
<i>Appendix 6: Broadband to Narrowband Irradiance Conversion</i>	298
A6.1 Introduction	298
A6.2 Methods	298
A6.3 Results	300
A6.4 Validation	304
A6.5 Summary	304
<i>Appendix 7: An Assessment of the Direct Measure of Net Radiation during the Simms Experiments</i>	310
A7.1 Introduction	310

A7.2	Methods	311
A7.3	Results	311
A7.4	Summary	317
<i>Appendix 8: Sensitivity of the Individual Flux Terms to Forcing Variables</i>		318
A8.1	Introduction	318
A8.2	Methods	318
A8.2.1	Surface Albedo and Extinction	318
A8.2.1	Long-wave Radiation and Surface Temperature.....	319
A8.2.2	Non-radiative Fluxes	319
A8.2.3	Eddy Correlation Determination of Q_H	321
A8.3	Results	323
A8.3.1	Sensitivity of Absorbed Solar Radiation to Variation in Snow Albedo, Extinction, and Irradiance	323
A8.3.2	Sensitivity Relations Involving Long-wave Radiation and Surface Temperature	329
A8.3.3	Sensitivity Relations for the Non-Radiative Fluxes	331
A8.3.4	A Comparison of Computational Techniques For Q_H	339
<i>Reference List</i>		341

LIST OF TABLES

2.1	Relationship between thermal conductivity and snow density.	45
3.1	Coordinates of microclimate stations and ice thickness ranges over the experimental periods.	68
3.2	Summary of near surface (upper 10 cm) sea ice density (kg m^{-3}) during the SIMMS experiments.	75
3.3	Summary of near surface (upper 10 cm) FYI sea ice salinity (ppt) during the SIMMS experiments.	75
4.1	Average snow properties (\pm one standard deviation) per site, during cold, warm and overall snow temperature conditions.	88
5.1	The mean bias error (MBE) and root mean square error (RMSE) describing the relationship between modeled and measured transmitted radiation in the PAR for three SIMMS experimental periods.	103
5.2	The effective snow grain radii (mm) used for the computation of albedo and the snow extinction coefficient for the experimental periods.	104
6.1	The effective snow grain radii (mm) used for the computation of albedo and the snow extinction coefficient for the experimental periods.	117
6.2	Statistics describing the energetics of the surface volume over the three FYI experiments.	133
6.3	Physical properties corresponding to the curves appearing in Fig. 6.14.	147
6.4	Ranked distribution of the hourly computed Monin-Obukhov stability parameter.	156
6.5	Comparison between melt energy computations using the energy balance approach and ablation measurements of snow during the period of active snow melt at each site.	161
6.6	Summary of energy balance components and select atmospheric and surface properties.	163

7.1	Average energy balance components for first-year and multi-year sea ice sites during SIMMS'93 and SIMMS'95.	196
7.2	P-values (1-tailed) for Mann-Whitney test between multi-year and first-year sites and test interpretation (Res.).	203
7.3	The average turbulent fluxes and Bowen ratio over the seasonal sub-periods, and variation between daytime (between 600 and 1900) and nighttime periods, and over the diurnal cycle.	204
8.1	Summary of energy balance components and environmental properties averaged over four hour intervals for periods of low cloud amount (TCA<3) and high cloud amount (TCA>7) in the a) <i>early</i> spring and b) <i>late</i> spring.	220
8.2	Summary of principal components analysis on energy balance components: a)FYI'92 <i>Early</i> and <i>Transitional</i> Spring.	225
8.3	Summary of canonical correlation analysis.	230
A2.1	The spectral albedo of ice surfaces.	269
A3.1	A description of the instrumentation used at the research stations.	276
A3.2	Sampling rate and duration (Julian Days) of the components of the microclimate and physical property data set. NA indicates that data are not available.	277
A3.3	Manufacturer's specification for sensor accuracy.	277
A3.4	Waveband and sensitivities of radiometers used during the SIMMS spring experiments.	278
A3.5	Measurement height above the snow surface.	278
A3.6	Distance of snow sensor above the snow/ice interface (cm) for sensor arrays in (a) SIMMS'92, (b) SIMMS'93, and (c) SIMMS'95.	277
A3.7	Positioning of Ice temperature sensors during 1992, 1993 and 1995.	280
A3.8	Variables measured during the snow physical property sampling program.	280
A4.1	Calibration of thermistor temperature references.	285

A4.2	Mean bias error and root-mean square error of temperature references (°C).	285
A4.3	Calibration data for sample air thermal couple sensors (°C).	286
A4.4	Mean bias error and root-mean square error of sample thermocouple sensors (°C).	286
A4.5a	Comparison of sample 'blue' thermocouple sensors over a temperature range.	286
A4.5b	Comparison of sample 'red' thermocouple sensors over a temperature range.	287
A4.6	Average of the maximum difference of sample air temperature sensors within calibration bath.	288
A4.7	Field comparison of air temperature sensors with the foam inserts.	289
A4.8	Field comparison of air temperature sensors without the foam inserts.	290
A4.9	Field comparison of wind speed sensors ($\text{m}\cdot\text{s}^{-1}$).	291
A6.1a	Background atmospheric parameters and solar zenith angles (°) used during the STREAMER simulations.	300
A6.1b	Cloud parameters used for the different STREAMER simulations, and modeled solar noon global radiation for the 15 th day of each spring month.	300
A6.2	Proportion of global radiation (fraction) within each waveband centered on wavelength, λ (μm) for each sky condition category.	306
A6.3	Diffuse proportion of global radiation ($\text{W}\cdot\text{m}^{-2}$) within each waveband centered on wavelength, λ (μm) for each sky category.	307
A6.4	The mean bias error (MBE), and root mean square error (RMSE) describing the relationship between modeled and measured irradiance over PAR wavelengths for the respective SIMMS experiments and for each of the spring months.	308
A7.1	MBE and RMSE describing the relationship between hourly $L_{\text{meas}}^{\downarrow}$ and computed $L_{\text{calc}}^{\downarrow}$ for hours designated as cloud-free, and complete overcast, during SIMMS'93.	312
A7.2	MBE and RMSE describing the relationship between hourly $L_{\text{meas}}^{\downarrow}$ and $L_{\text{mol}}^{\downarrow}$, using the empirical expression of Jacobs et al.,(1978) with the clear sky function of Efimova (1961), for hours designated as cloud-free, and complete overcast, during SIMMS'93.	312

A7.3	MBE and RMSE describing the relationship between computed and modeled sky radiation for hours designated as cloud-free and complete overcast, during SIMMS'95.	313
A8.1a	Sensitivity of computed net radiation at a snow level to a unit variation in the spectrally proportioned global radiation ($W \cdot m^{-2}$), spectral albedo (fraction) and spectral extinction coefficient (m^{-1}).	324
A8.1b	The variation in net solar radiation (δK^*_2) expressed in $W \cdot m^{-2}$ and as a percent of the computed flux (bracketed value) at levels 0.01m and 0.1m through snow to estimated levels of uncertainty in albedo, extinction coefficient and global radiation.	325
A8.2	The allowable relative error in (a) albedo, (b) extinction coefficient, and (c) incident solar radiation in order to maintain $K^*(z, \lambda)$ to within $\pm 10\%$ within the visible portion of the electromagnetic spectrum: a) Required Accuracy in α , a) Required Accuracy in κ , c) Required Accuracy in $K^{\downarrow}_{o\lambda}$	327
A8.3	Sensitivity of measured long-wave flux to unit variation in the pyrgeometer case temperature, and sensitivity of the computed surface temperature to up- and down-welling long-wave radiation.	329
A8.4	Estimate of uncertainty associated with the computation of Q_{So} , and Q_{io}	331
A8.5	Elements of the ranked distribution of the absolute value of the hourly finite difference in u , θ , and q between 2 m and 0.1 m from the first-year sea ice experiments.	334
A8.6	Statistics describing the relationship between Q_{Hec} , and Q_{Hacro} , among the stable, unstable and combined regimes.	338

LIST OF ILLUSTRATIONS

2.1	Sea ice nomenclature and relationship to sea ice thickness and environmental forcing.	9
2.2	The evolution of the vertical distribution of sea ice salinity with increasing sea ice age and thickness.	11
2.3	Sample cross section of multi-year ice.	12
2.4	Freezing point of brine as a function of the ratio of dissolved salts to pure water at temperatures greater than -23°C	39
2.5	Liquid volume proportion of snow (volume fraction) as a function of salinity and temperature for snow density $450\text{ kg}\cdot\text{m}^{-3}$, $300\text{ kg}\cdot\text{m}^{-3}$, and $150\text{ kg}\cdot\text{m}^{-3}$	41
2.6	Specific heat of sea ice ($\text{kJ}\cdot\text{kg}^{-1}\cdot^{\circ}\text{C}^{-1}$) as a function of temperature for ice for sea ice salinity of 20 ppt, 10 ppt, and 0 ppt.	42
2.7	The variation of predicted snow thermal conductivity using the nine empirical formulae provided in Table 2.1 over a snow density range.	44
2.8	Thermal Conductivity ($\text{W m}^{\circ}\text{C}^{-1}$) of bubbly sea ice as a function of temperature ($^{\circ}\text{C}$) for sea ice of varying salinity (ppt), as determined using Schwerdtfeger's (1963) physical relation.	48
2.9	Thermal Conductivity ($\text{W m}^{\circ}\text{C}^{-1}$) of bubbly sea ice as a function of ice density (kg m^{-3}) for sea ice of varying temperature as determined using Schwerdtfeger's (1963) physical relation.	48
2.10	Schematic of Pittman and Zuckerman's (1967) ice sphere cubic lattice with representation of a liquid phase according to Crocker (1984).	51
2.11	The thermal conductivity of snow's non-ice components: brine (K_b), and air within the pore space (K_p).	53

2.12	Snow effective thermal conductivity ($W \cdot m^{-1} \cdot ^\circ C$) shown as a function of salinity and temperature for snow density $450 \text{ kg} \cdot m^{-3}$, $300 \text{ kg} \cdot m^{-3}$, and $150 \text{ kg} \cdot m^{-3}$	54
2.13	Snow effective thermal conductivity ($W \cdot m^{-1} \cdot ^\circ C$) shown as a function of salinity and density for snow temperatures of $-5^\circ C$, $-10^\circ C$ and $-15^\circ C$	55
3.1	Location of the study region relative to the water bodies and islands of the Canadian Arctic Archipelago.....	66
3.2	The position of the ice edge in Lancaster Sound-Barrow Strait in winter.....	67
3.3	Location of first-year sea ice research sites in Barrow Strait.....	69
3.4	Image generated by the airborne STAR-2 (January 17, 1992) of the Resolute Passage area.....	70
3.5	Image generated from ERS-1 data (February 14, 1993) of the Resolute Passage area.....	71
3.6	Image generated from ERS-1 data (March 5, 1995) of the SIMMS'95 research area.....	72
3.7	Record of ice thickness at the first-year sea ice sites.....	73
3.8	Aerial photographs chronicling the surface transformation from pre-melt to advanced melt conditions.....	74
3.9	Typical principal energy balance and wind tower used during the SIMMS experiments.....	76
3.10	Typical snow temperature sensor assembly used during the SIMMS experiments.....	77
3.11	Lower three air temperature shields at FYI'92. Also shown in the photo is a one-dimensional sonic anemometer (Campbell Scientific CA27).....	79
3.12	Extension arm and mounting bracket complete with pyrradiometer (centre), down-facing pyrgeometer (left), and pyranometer (right).....	80
4.1a	The record of snow depth at the first-year sea ice sites.....	85
4.1b	The record of snow depth at the multi-year sea ice sites.....	86
4.2	Snow density ($\text{kg} \cdot m^{-3}$) variation with depth during FYI'92, FYI'93 and MYI'93.....	90
4.3	Snow salinity (ppt) distributed over depth during FYI'92 and FYI'93.....	91

4.4	Graphical interpretation of Scheffe's pair-wise means test.....	92
4.5a	Average snow density within each snow layer at the first-year sea ice sites.	95
4.5b	Average snow salinity within each snow layer at the first-year sea ice sites.....	96
4.6	Average snow density within each snow layer at the multi-year sea ice sites.	97
4.7	Measured snow wetness in the upper centimeters of the snow cover at FYI'92.....	98
4.8	Measured snow wetness (% by volume) within snow layers at FYI'92, FYI'93 and MYI'93.	99
5.1	Modeled snow albedo for each ice sphere effective radius used in the study for wavelengths between 0.36 μ m to 4.0 μ m.	105
5.2a	Simulated (grey lines) and measured spectral albedo (black lines) over the visible and near infrared portion of the spectrum for snow over first-year sea ice (FYI'93) for day 135, and day 162.....	106
5.2b	Simulated (grey lines) and measured (black lines) albedo over the visible and near infrared portion of the spectrum for snow with a multi-year sea ice melt pond depression (MYI'93).	106
5.3	Modeled extinction coefficients (m^{-1}) and shown over the wavelength band 0.36 μ m to 4.0 μ m. Values are computed for 12:00 LAT on day 135.....	108
5.4	Profiles of (a) transmitted solar radiation and radiation absorbed per unit volume at FYI'93 for snow properties representative of the early, mid, and late spring.	110
5.5	The percent reduction from surface values of (a) K_{\downarrow} and (b) K^* within the snow volume. The upper 2 cm of the profile is snow in the insets.	112
5.6	Absorption of solar radiation shown as a function of wavelength and depth at solar noon.	113
6.1	The salinity of the sea ice surface for FYI'92, FYI'93 (dashed line) and FYI'95.....	118
6.2a	Daily summary of general meteorological conditions during 1992.	124
6.2b	Daily summary of general meteorological conditions during 1993.	125

6.2c	Daily summary of general meteorological conditions during 1995.	126
6.3	Frequency histogram of wind direction during the 1992, 1993 and 1995 SIMMS experiments.	127
6.4	Autocorrelation coefficients of sea level pressure for time lags between 1 and 14 days (n=93) during the spring of 1992, 1993, and 1995.	129
6.5a	Snowfall measured at the Resolute weather station for the spring seasons of 1992, 1993, and 1995.	130
6.5b	Rain recorded at the Resolute weather station for the spring seasons of 1993, and 1995.	131
6.6	Box and whisker plots showing the spread in the distributions of the daily average energy fluxes and surface properties from each of the research sites.	134
6.7	Daily average net radiation of the snow/ice/ocean volume (Q^*), and the net radiation of the snow volume (Q^*_s), among the experimental sites.	135
6.8	Daily average global radiation (open circles) and reflected solar radiation (open squares) for the first-year sea ice experimental sites.	136
6.9	Daily net solar radiation (open circles) and net longwave radiation (open squares) for the first-year sea ice experimental sites.	137
6.10	Daily surface albedo (open circles) and solar radiation transmitted through the snow cover (open squares; Wm^{-2}) of the first-year sea ice.	138
6.11	Daily average down-welling (open circles) and up-welling (open squares) longwave radiation at the first-year sea ice experimental sites.	140
6.12	Daily average temperature at the snow and sea ice surface over each experiment.	142
6.13	Cross section of snow thermal conductivity (upper plots) and heat capacity (lower plots) for snow over first-year sea ice.	143
6.14	The distance a temperature change propagates through the snow as a function of time (a) over the diurnal cycle and (b) within an hour.	146

6.15	The temperature structure within the snow and upper sea ice volume at FYI'92 for (a) solar midnight and (b) solar noon.	150
6.16	The seasonal evolution of heat conduction through the snow and upper sea ice at (a) solar noon and (b) solar midnight.	151
6.17	Daily average conductive flux at the snow (Q_{s0}), and ice (Q_{i0}) surface at the first-year sea ice sites.	152
6.18	Different forms the temperature gradient within first-year sea ice shows during the spring transition.	153
6.19	Daily average sensible and latent heat flux.	155
6.20	Daily average of atmospheric heating to the snow and heat of fusion.	157
6.21	Hourly average (a) T_a and T_s , (b) VPD, (c) RH, (d) wind speed, (e) median TCA, and (f) hourly average surface albedo for the <i>early</i> and <i>late</i> spring.	165
6.22	Hourly average (a) Q^* and Q^*_{is} , (b) K^* and L^* , (c) $K\downarrow$ and $K\uparrow$, (d) $L\downarrow$ and $L\uparrow$	168
6.23	Hourly average (a) Q_H and Q_E , (b) Monin-Obukhov stability parameter and (c) Bowen ratio for the <i>early</i> and <i>late</i> spring.	170
6.24	Hourly average (a) conductive heat flux at the snow and sea ice surface and (b) change in atmospheric heating of the snow and energy of fusion within the snow cover for the <i>early</i> and <i>late</i> spring.	171
6.25	A summary (at four hour increments) of the diurnal energy balance during the <i>early</i> spring.	174
6.26	A summary (at four hour increments) of the diurnal energy balance during the <i>late</i> spring.	175
6.27	The springtime energy balance of first-year sea ice.	176
6.28	A summary of the seasonal evolution of the energy balance and energy available to the snow surface and volume.	178

6.29	The ratio of conductive to radiative input to the snow cover (the heating ratio) during the first-year sea ice experiments.....	181
7.1	The daily average temperature at the snow surface and sea ice surface of a multi-year melt pond depression.	188
7.2	Temperature structure across the upper metre of FYI'93 and MYI'93.....	189
7.3	Seasonal evolution in the vertical variation in thermal conductivity (upper pair) and heat capacity (lower pair) within a shallow FYI snow cover and deep snow of a melt pond depression.	190
7.4	A cross section of the evolution of conductive heat flow ($W \cdot m^{-2}$) within the snow and upper sea ice of thin first-year sea ice (FYI'93) and the snow within the melt pond of thick multi-year sea ice (MYI'93).	191
7.5	Daily average surface albedo of FYI and MYI during SIMMS93 and SIMMS95.	193
7.6	Daily average net radiation (Q^*) of FYI and MYI during SIMMS93 and SIMMS95.	194
7.7a	The seasonal evolution of the energy balance at FYI'93 and MYI'93.	197
7.7b	The seasonal evolution of the energy balance at FYI'93 and MYI'93.	198
7.8	The seasonal evolution of the average partitioning of available energy at the snow surface and within the snow volume for the FYI and MYI sites.	199
7.9	Cumulative energy totals of Q^* , Q_{io} , Q_E and Q_H at FYI'93 and MYI'93.	207
8.1	The diurnal and daily variation in the net radiation (Q^*), net solar radiation (K^*) net long-wave radiation (L^*), total cloud amount (TCA), wind speed and the Monin-Obukhov stability Parameter at FYI'92.	214
8.2	The diurnal and daily variation in the net radiation (Q^*), net solar radiation (K^*) net long-wave radiation (L^*), total cloud amount (TCA), wind speed and the Monin-Obukhov stability Parameter at FYI'93.	215
8.3a	A contrast in the energy balance components from overcast ($TCA > 7$) and predominately clear sky coverage ($TCA < 2$) at FYI'92 and FYI'93 during the <i>early</i> spring.....	216

8.3b	A contrast in the energy balance components from overcast (TCA>7) and predominately clear sky coverage (TCA<2) at FYI'92 and FYI'93 during the <i>late</i> spring.....	217
8.4	Principal component loadings for the significant principal components of the energy balance components at FYI'92 and FYI'93 during the (a) combined <i>early</i> and <i>transitional</i> spring and (b) the <i>late</i> spring.....	224
8.5a	Bivariate relationship between the significant energy balance principal components and (i) melt energy and (ii) net radiation during the early and transitional spring, FYI'92.....	234
8.5b	Bivariate relationship between the significant energy balance principal components and (i) melt energy and (ii) net radiation during the <i>late</i> spring, FYI'92.....	235
8.5c	Bivariate relationship between the significant energy balance principal components and (i) melt energy and (ii) net radiation during the <i>early</i> and <i>transitional</i> spring, FYI'93.....	236
8.5d	Bivariate relationship between the significant energy balance principal components and (i) melt energy and (ii) net radiation during the <i>late</i> spring, FYI'93.....	237
8.6	Schematic representation of feedback mechanisms which are observed to operate in the spring period over the SIMMS' experiments.....	247
8.7a	Diurnal and seasonal variation in the atmospheric heating of the snow and energy of fusion for FYI'92 and FYI'93.....	249
8.7b	Diurnal and seasonal variation in the sensible and latent heating at FYI'92 and FYI'93.....	250
8.8	A comparison of the diurnal form of the energy balance between FYI'92 and FYI'93 during the transitional spring.....	252
A2.1	The asymmetry factor of ice computed with Choudhury and Chang's (1981) approximation (CC) and by using the numerical methods provided by Bohren and Huff (1983) (Mie).....	273
A2.2	The single scattering albedo of ice of computed with Choudhury and Chang's (1981) approximation and by using the numerical methods provided by Bohren and Huff (1983).....	273

A2.3	Single scattering albedo ω of soot plotted as a function of size parameter, x	274
A2.4	Asymmetry factor g of soot plotted as a function of size parameter, x	274
A2.5	The extinction efficiency Q_{ext} , of soot plotted as a function of size parameter, x	275
A3.1	Plan view schematic of typical microclimatological site.	281
A6.1a	Simulated global radiation partitioned into its direct- and diffuse beam components for solar noon, 15-April.	301
A6.1b	Simulated global radiation partitioned into its direct- and diffuse beam components for solar noon, 15-May.	301
A6.1c	Simulated global radiation partitioned into its direct- and diffuse beam components for solar noon, 15-May.	302
A6.2	The spectral distribution of the diffuse component of global radiation, shown here under clear skies for 15-April, and 15-June.	302
A6.3a	The modeled spectral proportion of global radiation per waveband for clear sky (clr) and heavy stratus cover (h-str) on June 15.....	303
A6.3b	The modeled spectral proportion of global radiation per wavelength at the central wavelength of the respective wavebands for clear sky (clr) and heavy stratus cover (h-str) on June 15.	303
A7.1	Daily average calculated and measured net radiation for the FYI'92, FYI'93 and MYI'93 experiments.....	311
A7.2a	Measured L_{\downarrow} as a function of total cloud amount as observed at the AES weather station at Resolute.	314
A7.2b	The difference between measured and modeled L_{\downarrow} for the various cloud amounts.	314
A7.3a	Diurnal variation in measured L_{\downarrow}	315
A7.3b	The difference between measured and modeled L_{\downarrow} over the diurnal cycle. The error bars denote one standard deviation unit surrounding the mean value.....	315

A8.1 The variation in the estimate of: (a) specific humidity at level 2 (δq_2) and level 1 (δq_1), and in the near surface difference in humidity ($\delta \Delta q$), each as a function of air temperature, and (b) the dependency of both the saturated vapour pressure of air over ice (e_s , expressed in Pa) and the slope of the saturation vapour pressure/temperature relationship ($\partial e_s / \partial T_a$, $\text{Pa}\cdot\text{C}^{-1}$) over ice, as a function of temperature. 332

A8.2 Sensitivity of the turbulent heat fluxes (Q_H and Q_E) to uncertainties (prefix δ) in the measurement of Δq , Δu and $\Delta \theta$ for small, moderate and large values of Δq , Δu and $\Delta \theta$ 335

A8.3 A contrast in the distributions of T_s and RH between FYT'93 and the AES weather station at Resolute over the three spring periods. 336

A8.4 Bivariate plot of Q_{Hec} and Q_{Haero} over the full range in atmospheric stability. 338

CHAPTER 1: INTRODUCTION AND STATEMENT OF OBJECTIVES

1.1 Motivation

There is growing concern about anthropogenic impacts on climate and particularly those associated with increasing concentrations of greenhouse gases. A challenge facing the science community is to provide a basis for assessing the potential magnitude, timing and spatial patterns of environmental change in the event of a warming atmosphere and to isolate an anthropogenic signal from the natural variability in the climate record (IPCC, 1996).

The general circulation model (GCM) is the most comprehensive tool available to assess the mechanisms of a potential climate change. Most of the GCMs show that the zonally averaged warming in the Arctic is two to three times larger than the global mean warming (Kattenberg et al., 1996). The enhanced warming in the Arctic (and high latitudes) is attributed to the retreat of sea ice in response to strong feedback¹ mechanisms between the atmosphere, cryosphere and the surface temperature. Sea ice has a profound effect on climate because it is a tremendous moderator of energy exchange between the ocean and atmosphere. Both snow and sea ice have a high albedo to solar radiation, a high emissivity in the thermal infrared wavelengths, and a relatively small thermal diffusivity. The small heat capacity of the relatively thin ice cover results in the tremendous seasonal variation in sea ice extent, from approximately 14 million km² in the winter to 8.5 million km² in the summer in the northern hemisphere, in response to seasonal climatic forcing (Washington and Parkinson, 1986). Because the seasonal sea ice is thin relative to

¹ Feedback refers to the potential for an effect upon a forcing variable by a change in the response variable initially caused by a perturbation in the forcing variable (LeDrew, 1992). The feedback is considered positive if the response acts to enhance the initial perturbation in the forcing variable, and negative if there is a tendency for the response to act against further change in the forcing variable.

the pack ice of the central Arctic², the ice extent of the seasonal sea ice zone (SSIZ) is susceptible to variation and it is this susceptibility that forms the basis of a powerful positive feedback process; namely, the snow and ice-albedo feedback. As ice extent is reduced in response to a warming atmosphere, less solar radiation is reflected (the sea ice albedo being much greater than ice-free ocean), leading to further warming. Other specific feedback processes that are associated with the polar amplification of simulated near-surface warming include:

- The water vapor feedback. This mechanism operates under the principal that a warmer atmosphere has a larger water holding capacity. A resulting enhancement of downward long-wave radiation by the increased cloudiness and atmospheric moisture in the troposphere will contribute to high latitude warming.
- The cloud radiative feedback. Clouds can absorb and reflect solar radiation and absorb and emit long-wave radiation. Their interaction with solar radiation acts to cool the surface (a negative feedback) while the long-wave effect of clouds is to warm the surface (a positive feedback).

The strong atmospheric stability that is common to the polar regions, especially during winter, inhibits vertical mixing of warm air, thereby augmenting any near surface heating (Walsh and Crane, 1992). These processes link the surface energy balance with the mass balance of sea ice. The detailed nature and strength of these feedbacks are unknown and there may be a variety of negative feedbacks which as of yet are undetermined (LeDrew, 1992).

Experiments with GCMs have shown that the simulated global temperature response to elevated CO₂ levels is highly sensitive to the simulation of high latitude sea ice (Kattenberg et al., 1996). This is because the polar regions, and their associated sea ice cover, occupy a central role in atmospheric and oceanic circulation. The poleward transport of sensible and latent heat in the atmosphere and oceans, attempting to balance a radiative deficit at the poles (Nakamura and Oort, 1988; Schweiger and Key, 1994), drives the global climate system (Barry, 1989). Furthermore, the production of dense water at the ice margins of the polar caps drives the northern terminus of the global “conveyor belt” transport of heat and fresh water between the high latitude Atlantic Ocean and the Pacific Ocean (Broecker, 1991). Of concern then, is the widely varying simulation

² Multi-year sea ice thickness in the central Arctic Basin averages 3 to 4 m (Barry, 1989), while first-year sea ice is usually considered to be between 0.3 and 2.0 m thick (Steffen, 1986).

of present day Arctic climate and the simulated sea ice extent among GCMs (Gates et al., 1996). This variability among GCM simulations results from a crude representation of sea ice and the uncertain parameterization of strong feedback processes. Deficiencies for the most part stem from a limited understanding of the physical processes which operate across the atmosphere-sea ice-ocean interface (ASO), including an appreciation of expected ranges of energy fluxes and feedback processes (IPCC, 1996). Continuing progress in climate modeling will depend on the development of comprehensive data sets and their application to improving and validating important parameterizations (IPCC, 1996). For instance, many GCMs still represent sea ice as a single homogeneous slab and snow, in particular, is not well represented in sea ice models. We know that the ice thickness distribution varies within most sea ice regions (Thorndike et al., 1975), and both field observations (e.g., Makshstas, 1991) and modeling (e.g., Maykut, 1978) have demonstrated that components of the energy balance can differ dramatically with sea ice thickness. The role of snow is to increase the latent heat needed for complete *in situ* melt of the ice cover and snow typically has a higher albedo and emissivity than sea ice, and a substantially lower heat diffusion coefficient. The net affect of snow on sea ice and climate is complex. The properties of snow that warm the sea ice are particularly important in the winter (e.g., its low thermal diffusivity), and they inhibit ice growth. Those properties that cool the surface are active in the summer (e.g., the albedo effect) and tend to encourage ice growth (Ebert and Curry, 1993; Ledley, 1991). Some (Maykut and Untersteiner, 1971; Ledley, 1991; Ebert and Curry 1993) predict that the cooling and warming effect will offset one-another for snow depths near average values ($\pm 50\%$) over multi-year sea ice. For very small, or very large snow coverage, the albedo effect dominates. Owens and Lemke (1990) observed seasonal sea ice extent in the south polar ocean to be reduced slightly in the winter and substantially in the summer with increasing snow cover. The insulation effect on the freezing rates dominated the influence of albedo. They suggest that because the snow thickness is relatively small compared to the multi-year ice thickness, snow has only a small affect on freezing rates of multi-year sea ice. For seasonal sea ice however, the snow thickness may be comparable to the ice thickness and therefore has a greater affect on freezing rates. Ledley (1993) suggested that snow cools the climate system and that the cooling increases with increasing snow thickness.

Once initiated, the melt of snow (and sea ice) in the Arctic is thought to be a rapid process (Ebert and Curry, 1993). The climatic character of the sea ice zone outside of the central Arctic

Basin causes a complete melting of the ice cover almost every year. Observations, however, have documented large interannual and regional variation in the onset and progression of spring in both the central Arctic basin (Robinson et al., 1986; Barry et al., 1989) and in the SSIZ (Barber et al., 1997). The initial stages of snow and sea ice melt occur between May and June in the high Arctic (Robinson et al., 1986). Since this period corresponds to the maximum potential irradiance in the Northern Hemisphere, the extent, timing and rate of snow and ice melt may be a critical variable influencing the sea ice balance and summer climatic regime in the polar regions (Barry and Maslanik 1989, Ebert and Curry 1993). Any substantial change in the regional ice balance would strongly impact a highly specialized biological system, which is extremely sensitive to small variations in photosynthetically active radiation at the ice base and within the ocean mixed layer (Welch et al., 1995). Though these variations have not yet been related to variations in environmental forcing, we do know that the movement of air masses and synoptic disturbances associated with large-scale circulation can affect the energy balance of snow-covered surfaces at any time over the annual cycle (Male and Granger, 1981).

An appreciation of the importance of sea ice on global climate, the inherent variability of the sea ice system, and uncertainties in the range and seasonal form of feedback processes involving the surface energy balance, have prompted renewed interest into *in-situ* investigations of the heat transfer processes over sea ice. There have been relatively few published reports of the measurements of radiation and turbulent air-surface exchange over sea ice surfaces in the Arctic. Since 1990, the Seasonal Sea Ice Monitoring and Modeling Site experiment (SIMMS) has operated in the Barrow Strait region of the Canadian Arctic Archipelago (CAA) during the spring periods between 1990 and 1995 and was continued as the Collaborative Interdisciplinary Cryospheric Experiment (C-ICE) in 1996 and 1997 (LeDrew and Barber, 1994). The purpose of these campaigns is to characterize the temporal variability of the processes at the ASO interface and to parameterize these processes for improved models of atmospheric analysis. A parallel objective is the development of methodologies to extract information regarding the surface state and energetics using remote sensing. The rationale being that the energy regime of the snow volume is linked to the volume's physical, optical and electrical characteristics. Any links among the snow physical, optical and dielectric properties may be exploited such that the optical and electrical characteristics of the snow, as derived using remote sensing, may be used as a means of estimating aspects of

volume energetics and physical properties (Barber et al., 1995a; 1995b). The application of remote sensing is well suited for surface (and volume) monitoring in such vast, inaccessible regions which show strong spatial and temporal variability (Thomas 1986; Carsey, 1989; Barry et al., 1989; LeDrew, 1995).

In summary, the modeling community is faced with the immediate task of assessing the likelihood, magnitude and timing of an anthropogenically induced climate change. The polar regions occupy a central role as a driving force in the global climate system, and the presence of strong positive feedback mechanisms in the polar regions make high latitudes highly sensitive to climate change. Despite this importance, we have a limited understanding of the physical processes that operate across the ASO system and this is a source of great uncertainty in the prediction of Arctic climate and in determining its role in global energetics. There are very few detailed observational studies from which we can formulate a stronger empirical understanding. The extent, morphology and properties of sea ice (and associated snow cover) are highly variable both temporally and spatially, and limited field observation has shown the energy balance to be sensitive to the sea ice characteristics. Remote sensing can potentially provide information regarding surface state, and links between detectable surface properties and energetics may be exploited as a means of monitoring climatic variability and supporting process studies. However, without a firm understanding of target characteristics, an accurate interpretation of remote sensing data is difficult. Confidence in our ability to simulate Arctic climate will improve with the improved representation of processes which link the seasonally varying ASO system in sea ice models for the mosaic of ice types which make-up a large proportion of the polar regions. Both an empirical understanding of the major processes involved in the ASO energy and mass exchange and a strong observational data set are necessary to address the task at hand.

1.2 Statement of Objectives

In this thesis, the form of the springtime energy balance, its linkage to snow and sea ice thermodynamics and the forcing on the melt process of snow-covered sea ice by the atmosphere and surface in the Canadian Arctic Archipelago (CAA) are examined. The intention is to provide a sound understanding of the surface heat fluxes and their linkage to the environment. In doing so I hope to perform the necessary prerequisite for the improved representation of the surface heat

forcing of sea ice in climate models, and for the advancement of forward and inverse remote sensing models of the sea ice environment.

The first objective of this thesis is to provide an explicit description of the evolution of the surface energy balance of sea ice over the winter to summer transition period using a multiple year data set. The purpose is to identify how much energy is available to the surface and when, where is the energy from, and where is it directed. This objective may be loosely termed the *temporal dynamics* of the energy balance of first-year sea ice during the spring season.

The second objective is to determine whether the two predominant mature sea ice types in the CAA (namely first-year and multi-year sea ice) can be treated as identical *icescape* units with respect to energy and momentum exchange with the atmosphere. The concept of *icescape* is introduced (LeDrew and Barber, 1994) as a unit of the surface that behaves in a uniform manner for a variety of processes. Differences in the form of the energy and radiation balance are identified and quantified where possible. The results will provide a basis from which the scientific community may assess the potential shortfalls of simulating sea ice thermodynamics by assuming horizontal uniformity with respect to ice type and properties. This objective may be loosely termed *spatial dynamics* of the surface and volume energy balance within the central Parry Channel region.

The third objective is to identify what environmental forcing agents are most effective at dictating the time and rate of snow melt. Relationships between the major energy balance components, surface properties and atmospheric state are highlighted over the progression toward summer. Any observed interannual variation in the form of the energy balance or in the onset of snow melt between the years of study may be explained in terms of these relationships and some knowledge of the interannual variation in environmental forcing. The latter may be linked to differences in large scale atmospheric forcing between years.

1.3 Thesis Structure

This thesis is divided into nine chapters. In Chapter 1, I define the objectives of the thesis and place the objective in the context of the science issues and constraints facing ASO energy exchange studies and the climate change initiative. Chapter 2 provides an introduction to the physical characteristics of sea ice and its accompanying snow cover, the Arctic climate, and

reviews our theoretical and empirical understanding of the energy balance. Chapter 3 describes the physical setting of the Central Parry Channel region and overviews the experimental sites and methods. The physical properties of the snow and sea ice volume are described in Chapter 4. In Chapter 5 I outline a methodology for the derivation of snow albedo and extinction and I describe their seasonal evolution. Chapter 6 addresses the first objective of this thesis. The focus is the examination of the temporal dynamics of the surface and volume energy balance of snow covered first-year sea ice during the spring season. In Chapter 7, I examine the spatial dynamics of the energy balance. The nature of the surface and volume energy balances is compared between first-year and multi-year sea ice while subjected to similar atmospheric forcing. The results directly address the second objective of this thesis. Chapter 8 is the final analysis chapter. In this chapter, I explore the relationship between the major components of the energy balance and those parameters which describe the state of the atmosphere and surface volume. The purpose is to identify which atmospheric and/or surface properties are most strongly linked to the initiation of the melt process and the maintenance of melt once snow melt is underway. The results of this chapter directly address the third objective of this thesis. Chapter 9 is used to summarize and reinforce the major conclusions of this work. Future research directions are also discussed.

CHAPTER 2: BACKGROUND MATERIAL

2.1 Introduction

This study chronicles the energy transfer between the atmosphere, an active surface and underlying snow and sea ice, and highlights factors which affect this process. Aspects of both the surface and atmosphere should act to influence the nature of energy exchange. In the following sections I provide an outline of the seasonally varying snow and sea ice cover, the Arctic climate, and review the energy balance of snow and sea ice surfaces. The review is intended to provide a basis for the calculation of the energy fluxes and to provide sufficient background information of the system necessary for the interpretation of the results presented in Chapters 6 to 8.

2.2 Seasonal Evolution of Sea Ice and Snow

2.2.1 The Annual Cycle of Sea Ice and Its Bulk Physical Properties

The various stages of sea ice development are classified according to World Meteorological Organization (WMO) nomenclature (Fig. 2.1). This work is concerned with processes operating on first-year and multi-year sea ice.

The growth rate beneath the ice sheet is restricted by the rate at which latent heat is released during the ice formation and the sensible heat from the ocean can be conducted from the sea/ice interface to the overlying atmosphere (Weeks and Ackley, 1986). After frazil consolidates, the initial downward ice growth is rapid, but drops off with increasing ice thickness (Nakawo and Sinha, 1981). Upward growth as superimposed ice can result from surface flooding and snow ice formation, but is considered secondary to the growth of sea ice into the ocean (Lock, 1990). In its first year of growth ice thickness ranges between 30 to 200 cm (Steffen, 1986).

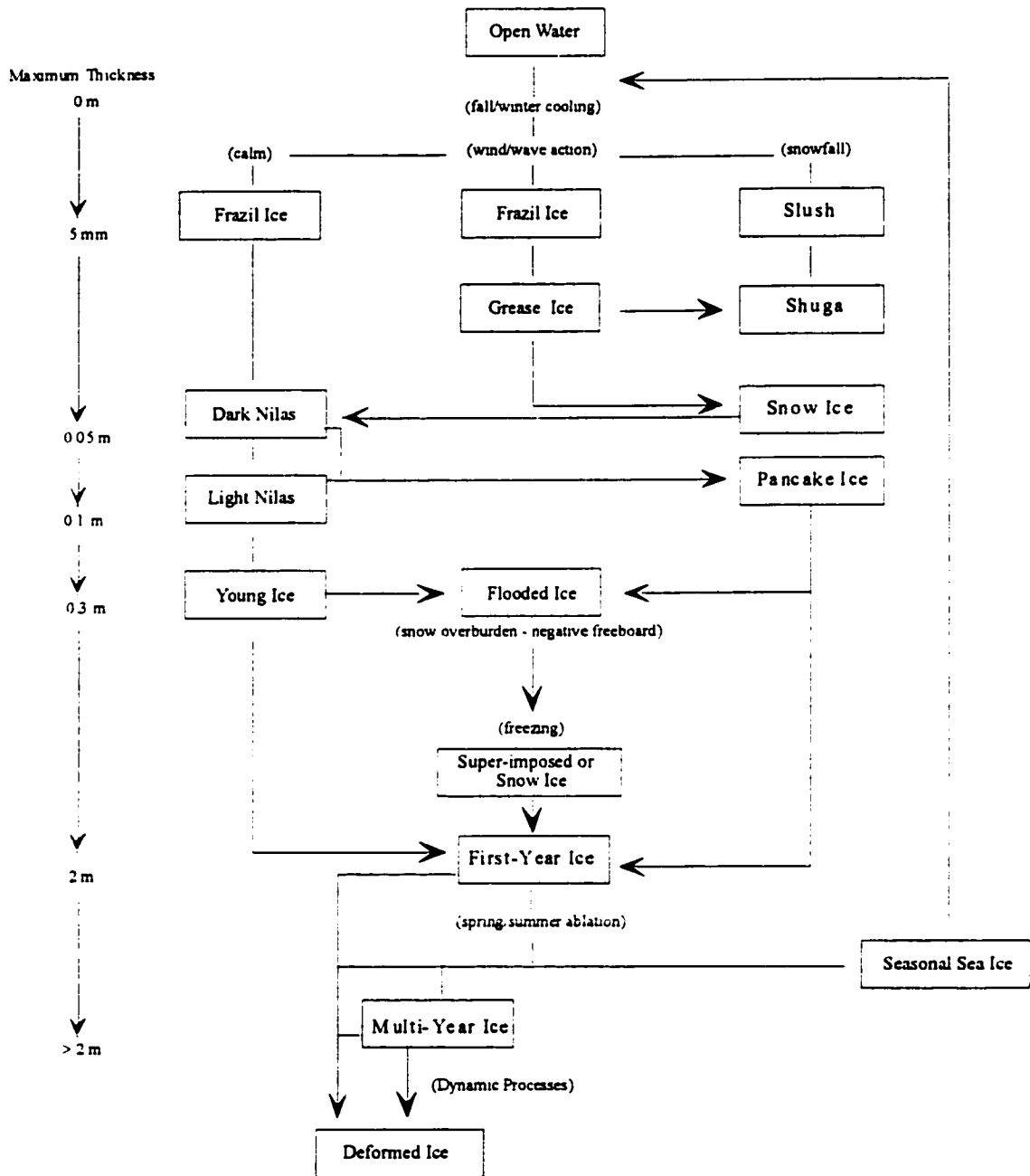


Figure 2.1 Sea ice nomenclature and relationship to sea ice thickness and environmental forcing (bracketed). Adapted from Grenfell et al.,(1992).

Ice will not incorporate impurities within its crystal lattice, however, salts may be trapped between growing crystals during ice sheet consolidation (Lock, 1990). Any trapped salt is in the form of liquid brine or solids trapped between the crystal boundaries, depending on the sea ice's temperature (Lock, 1990). After the initial entrapment of brine pockets during ice consolidation and subsequent growth, there is a gradual decrease in the average salinity, creating a 'C-shaped' salinity distribution in first-year and younger sea ice (Fig. 2.2). The re-distribution of brine occurs through the mechanisms of brine migration, brine expulsion, gravity drainage and brine flushing (Untersteiner, 1966).

In some regions the net ice accumulation will exceed the net ice ablation over the annual cycle. Ice that has survived one summer is termed second-year ice, while ice that has survived more than one summer melt is termed multi-year ice (MYI). Multi-year ice thickness is typically greater than 2.5 m (Weeks and Ackley, 1986). During the summer season the sea ice surface experiences extensive re-crystallization and differential melt creating a rolling hummocky topography interspersed by depression of refrozen water (formerly melt water or 'melt ponds' refer to Fig. 2.3). Melt-pond coverage may encompass 34% of a MYI floe in Parry Channel (Piwowar et al., 1995). Serreze et al., (1993a) and Misurak (1995) report similar areal proportions. The melt pond to hummock ratio may, however, vary with floe age (e.g., Barber et al., 1995a).

A pronounced reduction in sea ice salinity occurs over the summer melt and as a result MYI exhibits salinity substantially lower than FYI (Fig. 2.2). Differences are also observed between salinity profiles through hummocks and melt pond depressions (e.g., contrast curves e and f in Fig. 2.2).

Typically FYI densities range from 880 to 910 kg·m⁻³, with much of the variation attributed to the air and salt content (Fukusako, 1990). Ice density tends to increase with an increase in salinity (provided an air bubble content remains constant) and to decrease with an increase in porosity (Fukusako, 1990). MYI hummock density is typically smaller because it can be highly porous. Densities range between 620 and 933 kg·m⁻³ (Vant et al., 1978). The porous hummock ice merges into a layer of refrozen ice of slightly higher density (refer to Fig. 2.3), and then into a lower clear-ice layer of the refrozen melt pond, of density between 800 and 900 kg·m⁻³ (Vant et al., 1978).

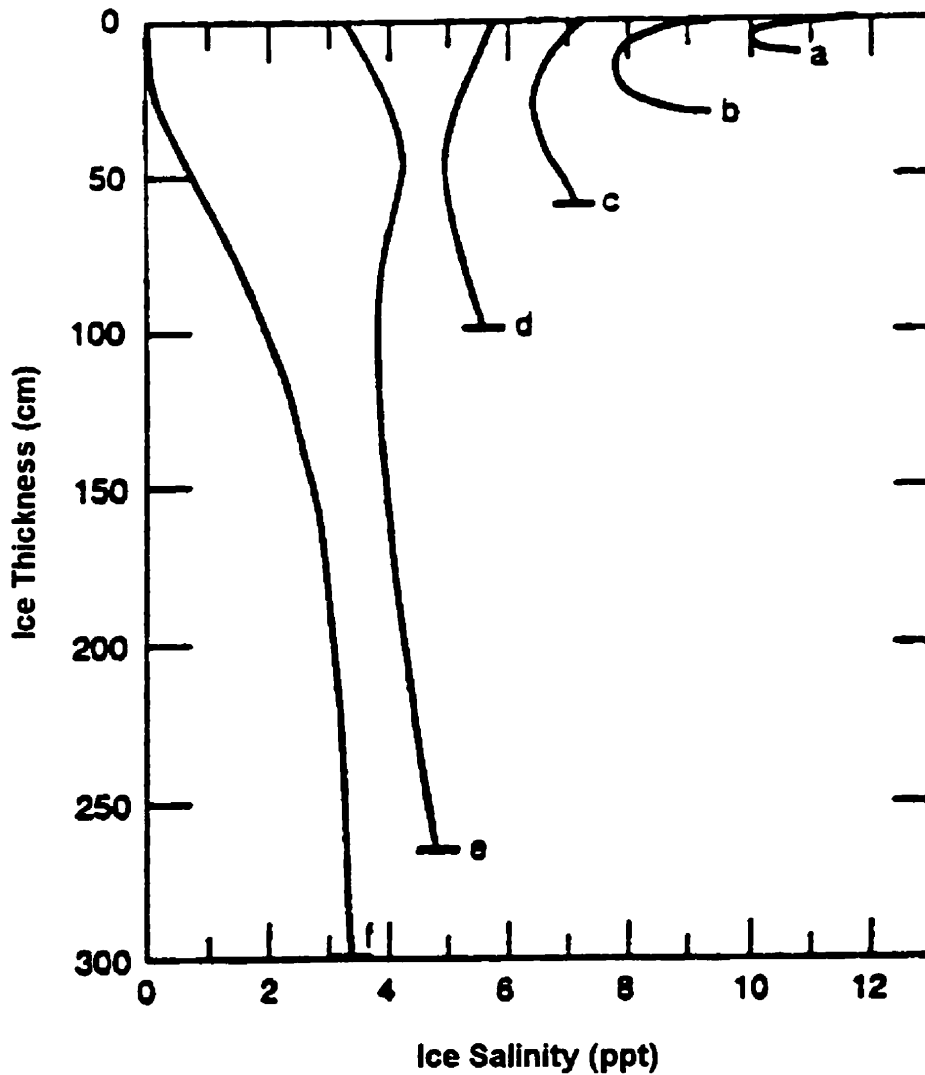


Figure 2.2 The evolution of the vertical distribution of sea ice salinity with increasing sea ice age and thickness (curves a to f). Curves a to d represent salinity profiles within FYI while e and f are MYI melt pond and hummock profiles, respectively. Source: Weeks and Ackley (1986).

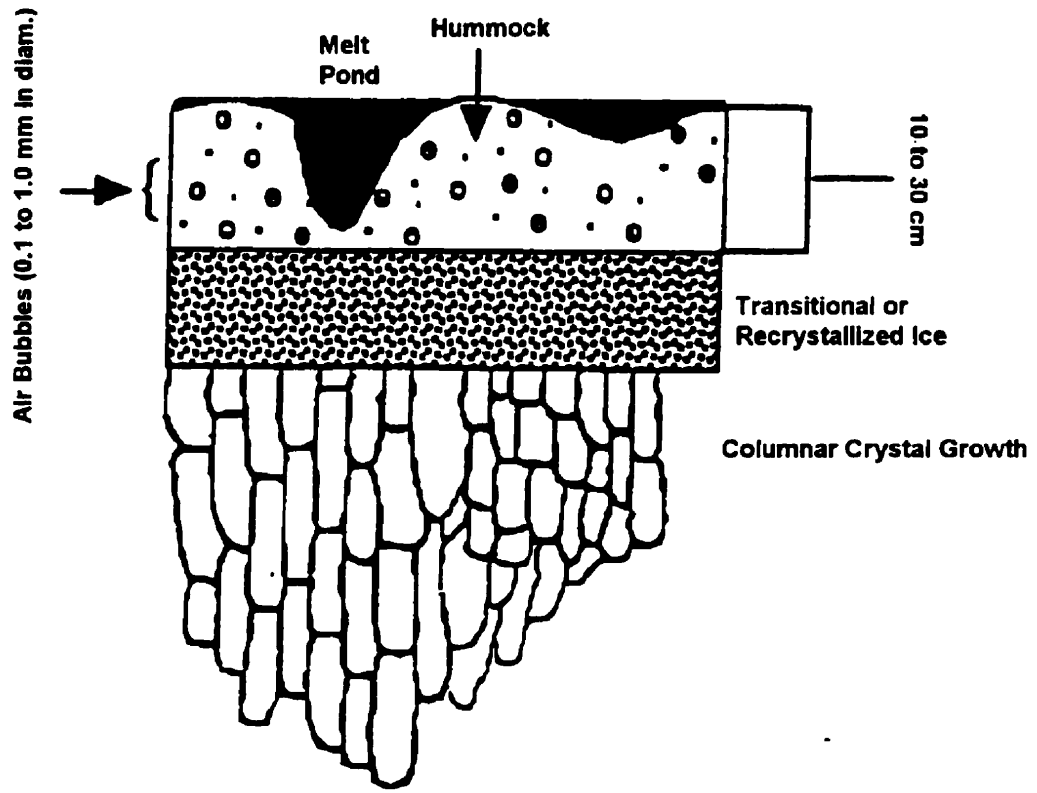


Figure 2.3 Sample cross section of multi-year ice. Adapted from Vant et al. (1978).

The maximum ice thickness expected for each sea ice class is noted in Fig. 2.1. Within a region the ice thickness categories continually change because of *in-situ* ice growth and ice motion (Barry 1989). Ice motion will lead to zones of ice convergence and divergence and the collision of ice floes causes ice rafting, rubble formation, ridging and the amalgamation and consolidation of similar and dissimilar ice types, which are collectively (but loosely) termed *deformed ice* (Tucker et al., 1992). Deformed sea ice constitutes a significant proportion of the Arctic sea ice cover. As much as 50% of the multi-year ice in the Arctic may have been deformed first-year sea ice (Tucker et al., 1992). Undeformed FYI ice is flat and when it is deformed the resultant ridges consist of angular blocks. Multi-year ridges, on the other hand, are highly weathered and, as a consequence, rounded.

2.2.2 The Physical Properties of Snow

2.2.2.1 Overview

Snow is a porous permeable matrix of ice grains that can exist as either single crystals or as crystal clusters (Alford, 1974). The inter-granular pores are filled with air and water vapour and possibly liquid if the snow is wet (Colbeck, 1982). After the snow is deposited, the particle shapes and packing are modified through metamorphic processes. Both the snow cover and its properties are highly variable.

Snow bulk density is highly variable. Densities may range from less than 100 kg m^{-3} for freshly deposited snow to greater than 400 kg m^{-3} for snow deposited after transport by strong winds (Mellor, 1977). Upon deposition, snow density increases rapidly in response to the processes identified above. Density is expected to increase in the vertical dimension with depth, provided there are no appreciable temperature gradients within the snow (Colbeck, 1982; Sturm, 1991). Overburden pressure results in the reduction of snow void space due to the shifting and rotation of individual grains (Langham, 1981).

Our understanding of snow and its internal metamorphism is based largely on the analysis of terrestrial snow data (e.g., Anderson, 1976; Alford 1974; Colbeck 1982). Snow over sea ice may differ from terrestrial snow covers because a salinity gradient is often observed over sea ice (for young ice and FYI), and the snow base is subject to heat forcing from an oceanic source

(Crocker, 1984; Takizawa, 1985; Ono and Kasai, 1985; Drinkwater and Crocker, 1988; Barber et al., 1994, Barber et al., 1995b).

Salt in the snow is observed in situations where the upward brine permeability of sea ice exceeds the downward brine permeability (Ono and Kasai, 1985). Upward brine expulsion during rapid growth of the underlying sea ice is a mechanism responsible for the high surface salinity observed over thin ice (Perovich and Richter-Mentge 1994). Young sea ice of several centimeters thick is commonly overlain by a highly saline (e.g., salinity of up to 100 ppt) skim of brine (Perovich and Richter-Mentge 1994).

2.2.2.2 Snow Metamorphism

Naturally occurring ice exists relatively close to its melting temperature at normal ambient environmental temperatures. On a crystal level this means that the surface molecules are highly mobile (Alford, 1974), and therefore highly susceptible to rapid metamorphism. The metamorphic process differs for dry and wet snow.

a) Dry Snow

Metamorphism in dry snow is a phenomenon of ice crystal growth from vapour (Alford, 1974). The process is one of continual sublimation/evaporation from warmer and/or more curved surfaces, and sublimation/condensation on colder and/or less curved surfaces (Colbeck, 1987). Any snow cover may contain rounded and highly faceted³ crystals. Rounded crystals are slow growing and occur more frequently in warm snow (>-10°C) and in the absence of strong temperature gradients (Colbeck 1987). The equilibrium crystal shape is spheroid and grain growth is governed by phase-equilibrium thermodynamics; thermodynamic processes whereby water molecules migrate to minimize any crystal surface-free energy⁴ (Colbeck, 1982; Colbeck, 1983; Colbeck, 1987). Sintering of snow occurs when adjacent ice grains are welded together by the movement of water molecules to the inter-granular contacts (i.e., the concave surface). The sintering process causes (i) a shift in the particle size distribution of a snow layer toward larger

³ Having flat crystal faces.

⁴ Conceptually, "free-energy" may be thought of as the energy free to do useful work (Langham, 1981).

rounded particles (at the expense of smaller rounded particles), (ii) a reduction in pore space, and (iii) an increase in snow bulk density (Alford, 1974).

Highly faceted crystals are indicative of high crystal growth rates and are associated with strong temperature gradients (15 to 70 $^{\circ}\text{C m}^{-1}$), cold bulk snow temperature ($<-10^{\circ}\text{C}$), and super-saturated pore space air (Colbeck, 1987). The rate of vapor diffusion is increased and crystal growth accelerates in the presence of a strong temperature gradient. This kinetic growth process was first described by Yoshida et al., (1955) as “the hand-to-hand delivery of water vapor”, or the upward flow among a sequence of adjacent ice particles (Colbeck, 1991). Kinetic growth acts to increase the average crystal size, but also to decrease the total number of crystals. The growth rates is proportional to the separation distance between source and sink, and for this reason faceted crystals grow more readily in lower density snow (Colbeck, 1983).

Highly faceted crystals are collectively termed hoar. Hoar layers are prevalent, and highly developed in high-latitude snow covers (e.g., Sturm, 1991; Barber et al., 1994). Depth hoar normally forms near the base of the snow cover, but hoar is also observed close to the surface, and immediately beneath a denser layer within the snow pack (Colbeck, 1991). Its position near the surface and at the snow base is associated with warmer snow temperatures. Hoar growth beneath a density discontinuity is associated with higher vapour supersaturation (Colbeck, 1991).

b) Wet Snow

The porosity of seasonal snow is generally greater than 50% and therefore liquid water can readily move through a snow cover (Colbeck, 1979). Some liquid, however, may be held within a snow matrix against gravity by capillary forces⁵ at temperatures near the freezing mark. A quantity of liquid that is immobile, held as a thin film around the ice grain and around the grain contacts, is termed snow's irreducible water content (Colbeck et al., 1990). The amount of irreducible water within snow at any one time varies with snow texture, but generally its limit is considered to be about 3% by volume. In the *pendular* regime (approximately 3% - 8% liquid content by volume), air occupies a continuous path throughout the pore space, and liquid can migrate along matrix potential gradients (Colbeck, 1974). At a liquid volume fraction of between

⁵ Capillary pressure is defined as the difference in pressure between the air and liquid (Colbeck 1979).

8% - 15% the liquid is continuous throughout the pore space and is freely draining. The moisture regime is termed *funicular* (Colbeck et al., 1990). Very wet snow is called slush and occurs at liquid contents above 15% by volume (Colbeck et al., 1990). At this point the pore space is flooded with liquid and contains relatively small amounts of air.

If a snow pack is saline it may contain liquid at temperatures well below the freezing mark of ice (Perovich and Richter-Mentge, 1994; Crocker, 1984). Brine will percolate to the snow base at liquid water contents within the funicular regime. The coincident warming of the ice surface in the spring activates brine drainage mechanisms within the sea ice, allowing some liquid to drain (Jacobs et al., 1975). A slush layer at the snow base is, however, invariably found over at least part of the winter to summer transition (Garrity, 1992).

Liquid water causes the snow grains to undergo rapid growth (Colbeck, 1982). Grains tend to be round, and larger grains grow at the expense of smaller grains. At low liquid water contents (i.e., the pendular regime) the ice grains cluster together in tightly packed clusters of two or three grains (Colbeck, 1982). Liquid is held as veins between the grains of the clusters (Colbeck, 1982). At higher liquid water contents (funicular regime), the ice grains lack cohesion and are surrounded by liquid. Once dry snow begins to melt, its surface turns into large-grained wet snow usually before the entire snow cover is raised to its melting temperature (Colbeck, 1988).

2.3 The Arctic Climate

2.3.1 General Characteristics

The climatic character of the Arctic is largely determined by the annual cycle of solar radiation, high surface albedo and extended periods of large fractional cloud coverage during the summer months (Barry, 1989). The surface experiences severe radiation losses during the polar night.

The continental airmasses of Arctic Canada and Greenland (continental polar, and continental Arctic, cP and cA, respectively) are characteristically stable, with a small vapour content (Barry and Chorley, 1987). In winter there is virtually complete dominance by the cA air except for rare penetrations of maritime Arctic air (mA) air, particularly in the eastern Baffin Island area (Maxwell, 1980). In the spring and summer the air masses affecting the Arctic are cold maritime Arctic and maritime polar air masses (mP) (Maxwell, 1980). The maritime air is wetter

and slightly warmer than the continental air masses. The flooded ice surface in the summer represents a source of mA (Maxwell, 1980). In general cA and mA air are separated by the *Arctic front* (Hare and Thomas, 1974). Mean summer pressure fields tend to be flat, with a general lack of spatial variation in the mean cyclone and anticyclone pressures (Serreze et al., 1993b). Cyclones are uncommon over the central Arctic in the winter (Serreze et al., 1993b). Cyclone trajectories that would be well south of the central Arctic islands in the winter migrate progressively farther north during the late spring and summer (Serreze et al., 1993b). Because of weak horizontal pressure gradients during the high Arctic summer, it is not uncommon for pressure systems to become blocked, and remain stationary for long periods of time (Maxwell, 1980).

2.3.2 Arctic Boundary Layer

The planetary boundary layer (BL) may be defined as that part of the troposphere that is directly influenced by the presence of the earth's surface and responds to surface forcing on an hourly time scale (Oke, 1987). The surface boundary layer (also termed the internal boundary layer or constant flux layer) occupies the lowest 10% or so of the BL and is characterized by intense turbulence generated by surface wind shear and convection.

The Arctic boundary layer tends to be shallower than in the midlatitudes and inverted temperature profiles (i.e., warmer air overlying cooler air) are frequently observed (Oke, 1987). The inverted temperature structure, or *inversion*, inhibits the vertical mixing of heat, moisture, and momentum coupling between the surface and atmosphere (Oke, 1987). Inversions may be formed through surface cooling associated with long-wave radiation emission, or through surface evaporation (or sublimation), adiabatic warming associated with air subsidence, or by the advection of warmer air over a cooler surface. The classic polar inversion is sustained through surface radiative cooling (Overland and Guest, 1991). In the winter 98% of observed temperature structures may be inverted (Kahl et al., 1992), but inversions tend to be less frequent and weaker in the summer months. Advective inversions account for between 20% and 30% of all Arctic summertime inversions (Kahl et al., 1992). In the central Arctic, Agnew and Silis (1994) associated radiative inversions with calm, light winds and clear to scattered skies while advective inversions were associated with calm to light southerly winds and air temperature above 0°C. Lapse temperature profiles were associated with warm southerly winds and heavy cloud coverage.

2.4 The Energy Balance of Snow and Sea Ice Surfaces

2.4.1 Introduction and General Characteristics

The net radiation of a shallow snow volume, Q^*_s , is represented by Male and Granger (1981) as:

$$Q^*_s = Q^* - Q^*_{is} = K^* + L^* - Q^*_{is} = K\downarrow - K\uparrow + L\downarrow - L\uparrow - Q^*_{is}, \quad (2.1)$$

where Q^* , K^* and L^* are the net all-wave, net solar and net long-wave radiation of the snow/sea ice/ocean volume. $K\downarrow$, $K\uparrow$, $L\downarrow$ and $L\uparrow$ are the incident and reflected solar radiation and down- and up-welling long-wave radiation, respectively. The net radiation at the ice surface Q^*_{is} :

$$Q^*_{is} = K\downarrow_b - K\uparrow_b, \quad (2.2)$$

represents radiant energy not available to the snow (the subscript, b, denotes the snow base), but available to the underlying ice and ocean. The surface albedo is taken as the ratio of reflected to incident solar radiation:

$$\alpha = \frac{K\uparrow}{K\downarrow}. \quad (2.3)$$

The surface and atmosphere exchange energy *via* radiation, sensible (Q_H) and latent (Q_E) heat flow. The energy exchange processes that operate at the surface are linked with the underlying snow volume through,

$$Q^*_s + Q_H + Q_E = dQ_s, \quad (2.4)$$

where dQ_s is the net atmospheric heating of the snow volume. The Bowen ratio,

$$\beta = \left(\frac{Q_H}{Q_E} \right), \quad (2.5)$$

describes the partitioning of the turbulent heat between sensible and latent heat flow and gives some insight into the evaporative regime of surface. Each component of the surface energy (Eq. 2.4) and radiation balance (Eq. 2.1) is considered positive if the energy flux is directed toward the surface-atmosphere interface. This interface is considered the *active* surface, that is, the level where the majority of the radiant energy is absorbed, reflected and emitted; where the main

transformations of energy and mass occur; where precipitation is intercepted and where the major portion of drag on airflow is exerted (Oke, 1987).

The balance of energy within a finite snow volume may be described by:

$$dQ_s + Q_{io} - Q_{so} + Q_{abs} + Q_M + Q_W = 0, \quad (2.6)$$

where, Q_{io} is the conductive heat fluxes at the ice surface; Q_{so} is the conductive heat flux at the snow surface; Q_{abs} is the absorbed solar radiation by the volume; Q_M is energy associated with any phase transition, and Q_W is heat energy associated with percolating water. Eq. 2.6 assumes a horizontally infinite layer and assumes only vertical heat flow. The relation may be reduced to

$$dQ_s + Q_{io} - Q_{so} + Q_M = 0. \quad (2.7)$$

when dQ_s is evaluated as a residual in the surface energy balance (Eq. 2.4) and if Q_W is assumed negligible. The net radiation of the snow cover (Q^*_s) in equations 2.1 and 2.4 includes that solar radiation absorbed by the snow and, therefore, the term Q_{abs} does not appear in Eq. 2.7. Rain on snow and its subsequent percolation has important implications for the water retention and optical characteristics of snow, but is thought to be of minor importance as an energy flux to the snow volume, provided the rain is similar in temperature to the snow (Male and Granger, 1981). A downward heat flux associated with gravity drainage of water can, however, be an effective heat transport process within the snow cover (Ohmura, 1982; Langham, 1981). Equation (2.7) also ignores any contribution to Q_{io} from the transmission and subsequent absorption of solar radiation at the snow/ice interface. Ramifications of these neglected effects on the energy balance are addressed in the discussion surrounding the energy balance results.

Vowinckel and Orvig (1970) published a summary of the large-scale energy balance of the Arctic. The general form of the seasonal evolution in the energy balance of sea ice in the central Arctic Basin has been reviewed by Maykut (1986), Barry (1989), and Makshtas (1991) from Soviet and American drifting stations between 1950 and 1991. Drifting stations are established on large multi-year ice floes or on islands of glacial ice and therefore are only representative of thick ice. The Arctic Ice Dynamics Joint Experiment (AIDJEX) operated over MYI between 1975 and 1976 in the Beaufort Sea (Pritchard, 1980). A number of field studies also have been conducted over seasonal sea ice in the eastern Arctic between 1979 and 1989 (refer to Johannessen et al 1992) in regions outside of the central Arctic. The Arctic Leads Experiment (LEADEX) took place in the

Beaufort Sea during the spring 1992 (Wolfe et al., 1993). The primary focus of these studies (other than LEADDEX) were either ice dynamics or mesoscale interactions between the ASO and not specifically the processes associated with the surface energy balance. The turbulent heating of the atmosphere from leads was a primary focus of the LEADDEX experiment. Steffen and DeMaria (1996) examined the surface energy fluxes of sea ice in the Canadian Arctic Archipelago from observations made between November and February of 1980/81. The Surface Heat and Energy Balance of the Arctic Ocean (SHEBA) operated between 1997-1998 in the Beaufort Sea. Its objective is to examine the physical processes associated with ice albedo feedback over the Arctic Ocean and the response of these processes to clouds (Moritz and Perovich, 1996).

In the central Arctic Basin the annual cycle of solar radiation drives the surface's radiation balance (Maykut, 1986). The region experiences seasonal darkness while peak monthly totals of net solar radiation occur in July. The long-wave energy exchange is active throughout the year and monthly net long-wave losses are fairly consistent over the winter months, but drop off during the course of the summer and fall. Net solar and net long-wave radiation are similar during the spring and fall months, however net radiation increases rapidly with net solar radiation during the summer months.

Results from field studies over snow and ice surfaces indicate that the radiation fluxes are more important at heating the snow/sea ice surface than the turbulent fluxes, at least during the melt period (Rouse et al., 1989; Maykut, 1986, Ohmura, 1982, Male and Granger, 1981). During the fall consolidation, and subsequent early winter growth, the conductive flux supplies up to 80% of the available energy to the surface (Steffen and DeMaria, 1996). During the spring and summer, a seasonal increase in Q^* corresponds to a decline in surface albedo within the SSIZ (Barber et al., 1995b; Crane, 1979; Weaver et al., 1978). Prior to the late season rise in Q^* , the net radiation can vary in response to fluctuations in albedo associated with snowfall (Weaver et al., 1978). Weaver et al.,(1978) reported that higher values of Q^* were associated with cloudy sky conditions in the early spring, however, during the period of advanced and rapid surface melt a higher Q^* was associated with periods of clear sky. In their study, net radiation was observed to covary with K^* but the strength of relationship was dependent on the stage of the melt season. The contribution by L^* toward Q^* on the other hand, was on average, small.

Turbulent flux totals over sea ice in the high Arctic are provided by Leavitt et al.,(1978) for the annual cycle from the AIDJEX experiment. Monthly totals of turbulent energy transfer

were usually an order of magnitude less than the net solar and long-wave totals. During the winter months the sensible flux was usually directed toward the surface and its magnitude diminished during the spring and summer. The latent heat flux totals were virtually always directed toward the atmosphere, and increased during the summer months. In August and September all of the available energy for turbulent transfer was directed into the latent heat flux. During the early spring and fall months, the turbulent flux totals were comparable in magnitude to Q^* .

Rouse et al.,(1989) observed the summer turbulent fluxes to be generally directed into the atmosphere over landfast ice near Cape Churchill MB. The combined sensible and latent heat loss by the surface was equivalent to approximately 18% of Q^* . Ohmura (1982) on the other hand, showed that the combined turbulent loss into the atmosphere can represent up to 80% of Q^* over snow-covered tundra during the spring season. The sensible heat flux was typically directed away from the surface during periods of positive Q^* . Crane (1979) observed springtime latent heating to be directed away from a fast ice surface near Baffin Island, reflecting persistent evaporative and sublimation losses by the surface. The vapor flux was about the twice the magnitude of sensible heat transfer, which itself was usually positive (directed toward the surface). Weaver et al.,(1978) document a distinct change in the pattern of daytime Q_H and Q_E between June and July over sea ice off of Broughton Island, NT. The latent heat flux disposed of 53% of the total available energy to the surface in June, but only 6% of it in July. The remaining energy was directed into the sea ice cover. The change corresponded to an increased tendency for stably stratified atmosphere, a rise in Q^* , and a decline in surface albedo. Granger and Male (1978) report a large variation in the role of Q_H from year to year over a prairie snow cover. The sensible heat flux typically contributed between 5 and 40% of the surface's available energy, depending on the characteristics of the atmosphere. In some instances however, the heat input by atmospheric sensible heat flux could be twice the magnitude of net radiation. By comparison the latent heat flux was usually around 10% of Q^* , although it could be the same magnitude as Q^* .

Little is known about the nature of the turbulent fluxes over growing sea ice in the fall and winter. Steffen and DeMaria (1996) showed that the sensible heat flux is effective at removing heat over thin sea ice, but its role as a heat sink declined relative to longwave emissions as the ice grew in thickness. The sensible heat flux increased by a factor of 10 between November and February (e.g., from on average $-108 \text{ W}\cdot\text{m}^{-2}$ to $-10 \text{ W}\cdot\text{m}^{-2}$) in the CAA. The latent heat flux, on the other hand, was ineffective at either supplying or removing heat from the surface.

In general, the role of the turbulent fluxes is not well defined over snow/ice surfaces. In some instances the turbulent fluxes are significant features of the energy exchange, while in other instances their role is negligibly small relative to the other energy exchange processes.

An annual cycle of surface conductive heating has not been reported. The flux is thought to range between 30 and 40 MJ·m⁻²·mo⁻¹ (i.e., averaging 12 to 15 W·m⁻²) between September and April over the perennial ice in the central Arctic Basin (Maykut, 1986). The heat flux near to the ice surface averaged approximately 9 W·m⁻² and 17 W·m⁻² for the multi-year and first-year sea ice in April (Makshtas, 1991). Over young and growing sea ice the conductive flux to the surface can be appreciable. Steffen and DeMaria (1996) observed the flux to range between 129 W·m⁻² over rapidly growing sea ice in November, to around 40 W·m⁻² for young first-year sea ice in January. Over this period the ice increased in thickness from 40 cm to 115 cm.

With a progression into the summer months, heat flow is directed into the sea ice from the warmer atmosphere (Crane, 1979; Weaver et al., 1978). Crane (1979) reported that 65% of Q* was directed into the ice volume, of which a proportion of this heating occurred *via* conduction. His study encompassed 17 days in June, during which time Q* averaged 86 W·m⁻².

Ruffieux et al.,(1995) showed that the sun drives the diurnal cycle of most of the meteorological parameters during LEADEX, despite the low sun angle in the early spring (March and April) and high surface albedo of the multi-year sea ice. The diurnal amplitude of the sensible heat flux (Q_H) was ±10 W·m⁻² about a mean of -3 W·m⁻², while net radiation (Q*) was ±30 W·m⁻² about a mean of -15 W·m⁻². The surface conductive flux (Q_{so}) was ±20 W·m⁻² about a mean of -12 W·m⁻². Weaver et al.,(1978) reported that atmospheric stability was typically at its maximum near mid-day in the late spring over landfast sea ice. This pattern was the consequence of warm air overlying a surface locked at 0°C. No diurnal cycle was observed in either the radiation or sensible heat fluxes (Q_H and Q_{so}) by Steffen and DeMaria (1996).

The albedo of an ice-covered water body is subject to extreme spatial and temporal variability, ranging between 0.1 for open water (Maykut, 1986) to 0.93 for fresh-dry snow (Grenfell et al., 1994). Wind blown dry snow is typically between 0.80 and 0.85 but drops to about 0.63 with age and increased wetness (Grenfell and Maykut, 1977). Snow-free sea ice exhibits a large range depending on ice thickness, temperature, age, and degree of surface puddling. Typically, the albedo for a 1-2 m thick first-year ice sheet ranges between 0.5-0.6 when the ice is

cold, and 0.3-0.5 at melt onset (Maykut, 1986). The albedo of snow-covered first year sea ice is closer to 0.80 (e.g., Weaver et al., 1978). The albedo of multi-year sea ice ranges between 0.7-0.75 when cold and dry to 0.5-0.7 at melt onset (Maykut, 1986). Melt pond albedo ranges from 0.15 to 0.40 (Maykut, 1986).

Factors affecting snow albedo have been examined theoretically (e.g., Wiscombe and Warren, 1980; Warren and Wiscombe, 1980; Choudhury and Chang 1981) and through *in-situ* observation (De Abreu et al., 1995; Grenfell et al., 1994; Grenfell et al., 1981; Grenfell and Maykut, 1977). In general, the albedo of a snow and ice surface is found to increase as solar zenith angle increases. Pronounced surface roughness tends to decrease albedo because the roughness elements tend to trap radiation (Warren, 1982). The albedo tends to decrease, at all wavelengths, with increasing grain size (Grenfell et al., 1981; Warren, 1982). This is because the scattering of light predominately occurs at the snow crystal and therefore the probability of a photon being scattered increases with decreasing optical path length within a crystal, and *vice versa*. The effect of liquid water is to increase the effective grain size because the contrast in the refractive index of water and ice is very small (Warren, 1982). Weaver et al.,(1978) reported that surface albedo dropped from 0.74 to 0.53 in conjunction with a sharp increase in snow melt and snow wetness. Snow density is shown to have only a small effect on albedo (Warren, 1982).

The solution to the energy balance over snow and ice is complicated by latent heating within the surface volume and by the absorption and transmission of solar radiation within and beyond the snow cover. The transmission of solar radiation into the ocean is necessary for the growth of ice algae, which constitutes the first trophic level of the ice covered marine ecosystem (Welch et al., 1992).

Ebert et al.,(1995) examined the interaction of solar radiation with the central Arctic Ocean. They indicated that 69% of the total annual solar radiation is reflected, 15% is absorbed by the snow cover, 12% is absorbed by the sea ice, and 4% is transmitted to the ocean mixed layer of the perennial sea ice. Jin et al.,(1994) showed, using a radiative transfer model, that snow cover (i) reduced the amount of solar energy absorbed by atmosphere/snow/ice/ocean volume by about 23% and (ii) limited the absorption within the ice and ocean. They indicated that the total absorption by the ASO system was independent of snow depth beyond a depth of 5 cm. In their simulations the snow density was assumed constant at $400 \text{ kg}\cdot\text{m}^{-3}$ with an ice grain radius of 1 mm.

Less is known about the attenuation process relative to our understanding of snow reflection characteristics. We do know that attenuation within the snow and ice is controlled primarily by internal inhomogeneities and in clear ice, the attenuation is mostly attributed to absorption (Warren, 1982). The internal absorption of solar radiation contributes directly to the thermal energy of the snow/ice volume affecting both the heat diffusion and snow/ice metamorphism (Schwerdtfeger, 1963; Maykut and Untersteiner, 1971; Weller, 1968; Alley et al., 1990; Schlatter, 1972; Fukami et al., 1985; Colbeck, 1988). Some believe that the latter initiates a positive feedback process. That is, warming the snow changes the optical properties to favor transmission and absorption, which in turn affects the vertical distribution of absorbed radiation (Colbeck, 1988). Others believe that the solar heating of the snow interior is very small (Brandt and Warren, 1993). The closer the snow pack is to its freezing temperature, the greater the proportion of total available energy will be associated with phase change (Ohmura, 1982). We are still unclear as to where in the snow the bulk of solar radiation is absorbed for a seasonally evolving snow cover. Furthermore, we do not know the effect of the penetration depth of solar radiation on the partitioning of available energy at the surface and within the snow cover.

2.4.2 Controls Over the Energy Balance

Sea ice models have identified linkages between components of the physical system. By doing so they have dictated the focus of field investigations and *in-situ* experimentation. Maykut and Untersteiner (1971) examined the response of equilibrium ice thickness to changes in some environmental conditions. Ebert and Curry (1993) re-examined many of the issues raised by Maykut and Untersteiner (1971), using a more sophisticated thermodynamic model. The sensitivity of predicted equilibrium ice thickness to sea ice parameters and external forcing was examined over an annual cycle. During the course of their analysis they identified six feedback processes associated with the surface energy balance (the direction of the feedback is provided in brackets):

1. *The surface albedo feedback (+)*: A reduction in albedo increases the absorption of solar radiation and therefore the net energy input at the surface, thereby contributing to enhanced melting and a further reduction in albedo.
2. *The conduction feedback (+)*: A thinner ice cover experiences greater conduction of heat from the ocean through the ice, contributing to further surface warming and earlier onset of melting.

3. *The lead solar flux feedback (+)*: Thinner ice allows a greater proportion of the solar flux entering the ocean to be absorbed below the level of the ice where it contributes to warming of the mixed layer and greater basal ablation.
4. *The lead fraction feedback (+)*: A thinner ice cover experiences greater lateral ice ablation and accretion, resulting in a greater lead fraction in summer and a smaller lead fraction in winter. This allows more solar radiation to be absorbed by the ocean in summer, and insulates the ocean more effectively in winter, both of which contribute to a warmer ocean mixed layer and greater basal ablation.
5. *The outgoing long-wave flux feedback (-)*: The increased outgoing long-wave flux from a warmer surface decreases the surface net flux, resulting in surface cooling.
6. *The turbulent flux feedback (-)*: A warmer surface reduces the downward sensible and latent heat fluxes (or increases the upward fluxes), which decreases the energy available to the surface and leads to surface cooling.

Whenever a change was imposed on the system, all of the feedback processes participated in the response of the system, but the relative importance of each feedback depended on the nature of the perturbation (Ebert and Curry, 1993).

Ebert and Curry, (1993) found the equilibrium ice thickness to be extremely sensitive to changes in down-welling long-wave radiation and air temperature, with the complete ablation of the ice for an increase of greater than 2% in L_{\downarrow} , or an increase greater than 1°C in air temperature. The ice thickness was also highly sensitive to the short-wave flux, and atmospheric humidity, and only moderately sensitive to the oceanic heat flux. Thickness was relatively insensitive to small changes in wind velocity, snowfall, and rain.

When interpreting these results, bear in mind that only one forcing variable was permitted to change at a time during each analysis. Any 'real' environmental change would simultaneously impact each forcing variable. Furthermore, (i) the surface was not coupled to the atmosphere, (ii) many aspects of the flux parameterizations were crude and (iii) the sensitivity was determined for annual averages. In an environment where the components of the energy balance may undergo extreme seasonal variation, the long-term response of the system may not reflect a short-term contribution an energy flux may play in initiating morphological changes in the snow and ice, which in turn may impact other energy fluxes.

Energy balance studies over snow and ice have demonstrated forcing on the energy balance by both the atmosphere (Sverdrup 1936; Nyberg 1965; Granger and Male, 1978; McKay and Thurtell, 1978) and surface (De Abreu et al., 1995; Grenfell et al., 1981, Colbeck, 1988; Male and Granger, 1981; Langleben, 1966).

2.4.2.1 Atmospheric Controls

Changes in atmospheric circulation control the movement of air masses and synoptic disturbances, which can affect surface energetics throughout the annual cycle. Male and Granger (1981) review several studies that have identified an association between air mass characteristics and surface heat fluxes. Early studies (e.g., Sverdrup, 1936) related the components of the surface energy balance to synoptic activity and weather types over snow. Sverdrup (1936) showed that upward sensible and latent heat fluxes corresponded to periods of cold dry air, while a warm dry period encouraged downward turbulent fluxes. Positive sensible and latent heat, with frost development usually accompany a warm wet period. Nyberg (1965) observed maximum vapor losses in the presence of cold dry air and maximum latent heat gains while the surface was under the influence of warm maritime air. McKay and Thurtell (1978) confirmed the observations of Sverdrup (1936) and Nyberg (1965), and further suggested that evaporation can be greatly enhanced by heat stored within the snow pack, particularly after the transition from a warm to a cold air mass. The sensible and latent heat fluxes were typically larger than net radiation at these times. This observation has led to the speculation that a large proportion of energy stored in the snow pack is not related to the radiation balance but, rather, is associated with warm air masses driven in response to horizontal atmospheric pressure gradients. Net radiation, on the other hand, was observed to contribute significantly to the energy storage of the snow under a persistent airmass. This last situation is believed to prevail over the perennial sea ice in the central Arctic Basin (Maykut, 1986). The sensible heat flux was shown to be a function of the energy content of the air mass in absence of local advection (Granger and Male 1978). They observed a linear relationship between the sensible heat flux over prairie snow and the air temperature at the 850 mb level.

Examples of both local and macroscale forcing on the energy balance are prevalent. Ohmura (1982) observed the melt rate to increase under periods of strong atmospheric stability. Andreas and Ackley (1982) speculate that the advection of dry air over snow and ice from

katabatic flow, originating over the Antarctic continent, enhanced the evaporative and sublimation losses by the surface. In this situation little energy was available for melt and the process discouraged the formation of melt ponds. Rouse et al.,(1989) observed that the sensible heat flux changed direction from down to up for offshore and onshore winds, respectively, over ice near the coast of Cape Churchill in Hudson Bay. A land-sea breeze sequence was in effect. The temperature difference between snow-free land and sea ice was most pronounced under anticyclonic conditions because the cloud cover associated with cyclonic disturbances reduced the solar heating of the land surface.

The effect of clouds on the energy balance is as of yet uncertain. Summer clouds are typically stratocumulus and stratus (Barry, 1989). Clouds reflect short-wave radiation (with some absorption and transmission) and they are opaque to long-wave radiation. The short-wave effect cools the surface while the long-wave effect warms the surface. These properties make clouds central to several feedback processes that operate at high latitudes. Over most surfaces the presence of clouds will reduce global radiation, however, multiple reflections between the cloud base and the highly reflective surfaces of snow and ice may enhance surface irradiance (Rouse, 1987).

Yamanouchi and Borre Orbaek (1995) associated larger downward long-wave radiation with maritime air masses (i.e., increased cloudiness and warmer) when compared to measured L_{\downarrow} while under the influence of a Continental Arctic air mass. The variability in the long-wave balance was observed to increase in the spring with the increased frequency of maritime air. In the summer the variability may decrease due to the reduced variation in air mass characteristics. Leontyeva and Stamnes (1993) indicate that a positive infrared balance at a snow surface may occur in the event of low cloud cover.

Studies have shown that clouds act to both increase and decrease bulk snow albedo. Clouds selectively absorb radiation in the near-infrared wavelengths, leaving the shorter wavelengths (for which the snow albedo is higher) to interact with the surface (Grenfell and Maykut, 1977; Grenfell and Perovich, 1984). During overcast conditions the integrated albedo was increased by between 5 to 11% relative to that during clear skies (Weller, 1968; Grenfell et al., 1981). Furthermore, clouds alter the distribution of the solar radiation between the direct and diffuse components. This can be important for surface types whose reflection characteristics are

not Lambertian (Warren, 1982). The effective zenith angle of purely diffuse radiation is about 50° (Warren, 1982) and therefore, during periods of low solar elevation (i.e., zenith angles greater than 50°), clouds may act to reduce the effective zenith angle, thereby reducing surface albedo. This phenomenon was observed by Carroll and Fitch (1981) at the South Pole.

Cogley and Henderson-Sellers (1984) determined that clouds of all heights warm the surface and that net radiation is greater under overcast conditions than under clear-skies. In their study the cloud-base height was used as a surrogate for cloud optical depth. They found that the degree of warming decreases with increasing cloud base height. Clouds with low base-heights (i.e., 1.0-1.5 km) were associated with positive net radiation. Wendler and Kelly (1988) and Wendler and Eaton (1990) observed that Q^* under cloudy conditions is larger than under clear skies at Antarctica and Barrow, Alaska. An increase in net radiation with cloud cover was also reported over high latitude glaciers (e.g. Holmgren, 1971; Ambach, 1974). Minnett (1998) observed the effect of clouds on summer sea ice energetics to be primarily determined by the solar zenith angle. The long-wave warming effect of clouds was dominant for zenith angles greater than 80° , while the short-wave cooling effect was greater for lesser angles. Walsh and Chapman (1998) reported that cloud radiative forcing warms a sea ice surface except for a few weeks during the summer. Curry et al. (1993), Shine and Crane (1984) and Schweiger and Key (1994) predicted similar findings with thermodynamic models. Zhang et al. (1996) indicated that, in theory, the effect of clouds on Q^* and melt rate varied with cloud height and thickness. Q^* (and melt rate) was shown to increase for thin clouds and decrease for thick clouds. They concluded that a comprehensive field program is needed to expand on these relations.

2.4.2.2 Surface Controls

The optical and thermal properties of a surface can affect the energy balance both in time and space. The declining albedo of a warming snow cover is well documented (e.g., De Abreu et al., 1995; Grenfell et al., 1981) and is instrumental in triggering a springtime rise in surface net radiation and melt rates (Barber et al., 1995b; Colbeck, 1988; Male and Granger, 1981; Langleben, 1966). Within a diurnal cycle, any freeze-thaw at the surface can cause hysteresis in the diurnal cycle of snow albedo (McGuffie and Henderson-Sellers, 1985) and can affect the depth at which microwave scattering occurs within the snow or sea ice volume (e.g., Barber et al., 1992).

Maykut (1978) has examined the relationship between the surface energy balance and sea ice thickness using a one-dimensional thermodynamic model. Increasing sea ice thickness causes a dramatic decrease in (i) conductive input to the surface, (ii) absorbed solar radiation, (iii) energy lost to the atmosphere by turbulent fluxes and long-wave emission. Net energy exchanged at the surface was a factor of two greater for ice 5 cm thick, than for ice 20 cm thick. During the winter months the available energy is approximately a factor of two less over ice 3 m thick when compared to the energy levels of a 0.8 m thick ice sheet. The discrepancy widens in the spring and early summer, as available energy is nearly a factor of three-times larger over the 0.8 m thick sea ice. This increase is thought related to a lower surface albedo over thin first-year sea ice. These ice thickness (3 m and 0.8 m) are representative of MYI and FYI sea ice, albeit fairly thin FYI.

Results by Steffen and DeMaria (1996) are reported earlier in this section. Recall that they observed a significant decline (tenfold) in the sensible heat loss by the surface and conductive transfer to the surface (a factor of 4) with increasing ice thickness between November (ice thickness of 40 cm) and February (ice thickness of 115 cm) in the CAA. These results demonstrate the effect of ice thickness on the energy balance and lend qualitative support to Maykut's (1978) projections.

Recent field experiments have shown that subtle contrasts in the surface characteristics of snow and ice may modify some components of the energy balance. Barber et al.,(1995a) observed the net solar and net radiation to differ between multi-year and first-year sea ice surfaces during the 1993 SIMMS field experiment. The net long-wave radiation and surface temperature could not, however, be distinguished between ice types. Bintanja and van den Broeke (1995) observed differences in net radiation, the latent heat flux, and surface conductive heating between snow and ice covered surfaces during the Antarctic spring. They observed that Q^* differed by over a factor of 5 between snow and ice covered surfaces in close proximity (i.e., Q^* averaged $7 \text{ W}\cdot\text{m}^{-2}$ over snow and $42 \text{ W}\cdot\text{m}^{-2}$ over ice). The latent heat flux was near a factor of 2 greater over ice than over the snow surfaces. Furthermore, the mean sensible heat flux was directed toward the surface over snow, while it was directed into the atmosphere over the nearby ice. Even though this study was not conducted over sea ice, it does illustrate that both the non-radiative and radiative components of the energy balance can be sensitive to the characteristics of the snow or ice surface. Makshtas

(1991) observed that the sensible heat flux may be directed up over first-year ice while directed down over multi-year ice in the central Arctic basin during the winter and spring period.

The effect of surface heterogeneity on the energy balance has a temporal component. The difference between some components of the energy balance between surfaces with differing characteristics can narrow with the progression toward summer, while the difference in other fluxes may widen (e.g., Makshtas, 1991; Minnett, 1995). Makshtas (1991) observed a discrepancy in conductive heating between FYI and nearby MYI to diminish with the onset of summer. An upward sensible heat flux of $100\text{-}300\text{ W}\cdot\text{m}^{-2}$ is typical during the fall and winter through open sea ice while net radiation is highly negative at this time (Launiainen and Vihma, 1994; den Hartog et al., 1983). During the summer months, on the other hand, most the energy available to water is attributed to Q^* . Minnett (1995) observed that summer Q^* averaged $133.3\text{ W}\cdot\text{m}^{-2}$ during the Northeast Water Polynya study, while the turbulent fluxes accounted for on average only $-7.1\text{ W}\cdot\text{m}^{-2}$.

2.4.2.3 Factors Affecting Melt

The initial stages of snow and sea ice melt occur between May and June in the high Arctic (Robinson et al., 1986). Observations have documented large interannual and regional variation in the onset and progression of spring melt in the central Arctic basin (Robinson et al., 1986; Barry et al., 1989). In the central Arctic, the melt progression was shown to vary by up to three weeks, with corresponding lags in surface albedo. The timing and rate of snow and ice melt may be critical in determining the summer sea ice balance climate regime. This is because (i) the timing of snow and ice melt corresponds to the period of maximum potential irradiance, and (ii) there is a tremendous difference in albedo between an ice-free and ice covered sea (Barry et al., 1989, Ebert and Curry 1993).

The temporal and spatial variations in melt onset have not yet been related to variations in environmental forcing. Barry (1978) found no clear-cut relationship between $K\downarrow$, or Q^* , and ice break-up off of Broughton Island despite the fact that radiation input is thought to be the primary control over sea ice ablation. He found better association between melting degree day totals and ice break-up. This supports the hypothesis that sensible heating by the atmosphere is instrumental in triggering morphological changes in the snow pack (namely: warming the snow, snow grain

growth, increased free water within the snow) necessary for the initiation of melt (Weaver et al., 1978; Male and Granger, 1981; Colbeck, 1988). The role of the sensible heat flux may not be so straightforward in that it may act to support or counteract the effect of net radiation (Granger and Male, 1978), depending on the characteristics of the near surface atmosphere. In the Weddell Sea for instance, the springtime sea ice surface virtually always loses heat *via* turbulent transfer to the atmosphere, thereby, offsetting the effect of Q^* on melt rates (Andreas and Makshtas, 1985). The increase in low and middle level clouds which accompanies the poleward retreat of the Arctic Front in the spring also acts to increase levels of down-welling radiation (Yamanouchi and Orbaek, 1995).

Serreze et al.,(1993c) presented the hypothesis that cloudy conditions may hasten the melt process, partly because of the long-wave warming effect, but also because the cloud cover in the spring and summer is commonly associated with the advection of warm southerly air. They observed that early melt onset and rapid melt progression might have been favored by a combination of limited cloud cover with strong northward air advection; however, a conclusive signal was not found. These observations were derived using a time series of passive microwave imagery (the Scanning Multichannel Microwave Radiometer (SMMR)) for the Arctic Basin.

It is believed that essentially all the energy needed to drive the melt cycle is supplied by global radiation in regions of perennial sea ice (Maykut and Perovich, 1987). The proximity of nearby land in coastal areas may, however, augment the energy available for melt through the advection of warm air over the ice. In such instances the turbulent heat input to the ice can be significant (Langleben, 1966; Rouse et al., 1989).

Periods of high pressure were associated with large Q^* and warm southerly and westerly airflow over shorefast ice near Broughton Island, NT (Crane, 1979). Both features acted to escalate rates of surface melt. Cold south-easterly winds and cloud cover tended to retard ablation, and these were associated with low pressure centres. Crane (1979) grouped the stages of fast ice decay into days of similar net radiation characteristics. Within each stage, the conductive flux was the most important variable of five variables (Q^* , Q_H , Q_{so} , Richardson Number⁶, and Bowen ratio) for defining the energy balance groups. It was concluded that Q^* differed greatly between the

⁶ Refer to Eq. 2.38.

stages of ice decay, but was relatively unimportant in defining shorter variations in the energy balance regimes.

The melt rate within the surface volume is related to the terms of the energy balance as described by Eqs. 2.4 and 2.7. Depending on the role of the turbulent fluxes, snow melt may occur at air temperatures as cold as -10°C or as warm as 10°C , assuming positive surface net radiation (Kuhn, 1987). The direction and magnitude of the turbulent heat fluxes may then be instrumental in determining the timing and rate of snow melt in the sea ice environment. In any event, the environmental mechanisms contributing to the initiation and maintenance of melt are expected to be complex.

2.4.3 Definitions and Descriptions of Energy Balance Terms

2.4.3.1 Radiation Fluxes

Only the 0.1 to 100 μm wavelength portion of the sun's electromagnetic spectrum is usually considered in climate studies. This range is traditionally divided into two categories: *short wave* or *solar radiation* (0.15-3.0 μm), and *long-wave* (3.0-100 μm) radiation (Oke, 1987). The visible portion of the spectrum extends between 0.36 μm and 0.75 μm . Infrared radiation shoulders the visible portion at 0.7 μm to 1.3 μm (near-infrared), 1.3 μm to 3.0 μm (mid-infrared) and beyond 3.0 μm (thermal-infrared). Plant pigments are particularly good absorbers of radiation in the 0.38 μm to 0.71 μm range, and hence this band is termed photosynthetically active radiation (PAR).

Interaction of Solar Radiation with Snow and Ice

When radiant energy is incident on a surface, it is absorbed, reflected and transmitted according to:

$$R + Tr + A = 1 \quad (2.8)$$

where A is the absorptance, R is the reflectance, and Tr is the transmittance (Iqbal, 1983). Each of the measures may be applied to discrete wavelengths, and in such instances the terms are preceded by the prefix, *spectral*. In climate studies, the term albedo is commonly used instead of reflectance. Reflectance often infers a directional component, while albedo simply refers to the

fraction of incident flux that is reflected in all upward directions (Iqbal, 1983). The properties of a surface associated with these three functions are respectively called its absorptivity, reflectivity and transmissivity.

The attenuation process (absorption and scattering along a path within a medium) is related to the total optical depth (dimensionless) by:

$$\tau_{o,\lambda} = -\ln(Tr_{\lambda}), \quad (2.9)$$

(Iqbal, 1983), where Tr_{λ} is the ratio to transmitted to incident radiation. Beer's Law describes the relationship between transmitted radiation and the extinction coefficient:

$$K \downarrow_{z,\lambda} = K \downarrow_{o,\lambda} \exp(-\kappa_{\lambda} z), \quad (2.10)$$

where κ_{λ} is the spectral extinction coefficient (m^{-1}), and z is the vertical distance (Brandt and Warren, 1993).

a) *Spectral Albedo of Snow and Sea Ice*

Fundamental to the description of the albedo is an understanding of the absorption characteristics of ice. Spectral absorption is related to the wavelength dependency of the imaginary part of the complex index of refraction (m_{im}) of ice through:

$$a_{i,\lambda} = \frac{4\pi m_{im}}{\lambda}, \quad (2.11)$$

where λ is the wavelength (m) (Warren, 1984). The absorption coefficient of ice is highly wavelength dependent, varying by orders of magnitude across the solar spectrum. Pure ice is highly transparent at the visible wavelengths and fairly opaque at the near and thermal infrared wavelengths.

Measurements of albedo taken during SIMMS'93 show that early (cold dry snow) albedo is uniformly high (e.g., 0.86) in the visible wavelengths, and decreases marginally with wavelength across the near infrared (De Abreu et al., 1995). These values agree with curves provided by Grenfell and Maykut (1977) over sea ice, but are lower than those observed for other snow surfaces (e.g., Grenfell et al., 1994). Grenfell et al., (1994) report a surface albedo of between 0.96 and 0.98 in the visible portion of the spectrum for snow in the Antarctic. The difference in albedo spectra between the Arctic and the Antarctic study is attributed to snow contaminants (De Abreu et al., 1995).

Seasonally, both an overall reduction in albedo and change in wavelength dependency accompany the various stages of snow melt. Snow-covered sea ice will maintain a high albedo in the visible portion of the electromagnetic spectrum until changes in the volume's depth and microstructure allow incident radiation to interact with the underlying ice surface. The largest changes in the albedo spectra of wet snow occur in the infrared, where the absorption by ice and water are very large and the incident beam is strongly effected by the scattering properties of the individual grains at the surface (De Abreu et al., 1995). The albedo of pooled water is determined primarily by the scattering properties of the underlying ice at wavelengths smaller than 0.5 μm (Grenfell and Maykut, 1977).

b) Transmissivity of Snow and Ice

The maximum transmission through the snow and sea ice volume occurs in the 450 to 550 nm region (Maykut and Grenfell, 1975). Most of the solar radiation absorbed by snow occurs in the near- and mid- infrared portions of the spectrum and this occurs near to the snow surface. As a consequence, a spectral extinction coefficient is more appropriate (i.e., Eq. 2.10) than a bulk or spectrally integrated value (Choudhury and Chang 1981; Brandt and Warren, 1993). Scattering is the dominate attenuation process in the visible wavelengths (Warren, 1982).

Grenfell and Maykut (1977) showed that an attenuation coefficient decreased by a factor of 2 in the visible and near infrared during snow melt as the snow density increased from about 400 to 500 kg m^{-3} . Spectrally integrated extinction coefficients (i.e., between the wavelengths 0.4 μm to 1.1 μm) for dry snow of density between 90 and 470 kg m^{-3} are reported to range between 37 and 97 m^{-1} (Fukami et al., 1985). These coefficients were observed to decrease with snow age and snow compaction. For a given density the coefficient decreased with increasing average grain size with increasing snow wetness. Extinction coefficients ranged between 23 and 58 m^{-1} for wet snow of density 430 to 530 kg m^{-3} .

c) Absorption of Solar Radiation by Snow and Ice

The radiation absorbed at a level within the snow (or ice) can be represented by

$$K^*_z = \int_{\lambda_1}^{\lambda_2} (K \downarrow_{z\lambda} - K \uparrow_{z\lambda}) d\lambda, \quad (2.12)$$

where

$$K \uparrow_{z\lambda} = \alpha_{s\lambda} K \downarrow_{o\lambda} \exp(-\kappa_{\lambda} z), \quad (2.13)$$

and $\alpha_s(z, \lambda)$ and κ_{λ} are the spectral albedo and spectral extinction coefficient (Grenfell and Maykut, 1977; Brandt and Warren, 1993).

d) *Theoretical Representation of Albedo and Radiation Extinction*

Radiative transfer models have been used extensively to investigate the interaction of solar radiation with a snow volume (e.g., Wiscombe and Warren, 1980; Choudhury and Chang, 1981). Warren (1982) provides a comprehensive review of radiative transfer models. Theoretical modeling of light scattering and absorption is usually divided into two parts, single scattering by volume elements and multiple scattering by the entire volume (Hansen and Travis, 1974). Mie scattering⁷ theory is commonly used to describe single scattering (Wiscombe, 1980). Wiscombe and Warren (1980) present an accurate representation of the optical characteristics of snow (Warren, 1982). Their model is described in Appendix 2.

Long-Wave Radiation

The Stefan Boltzman law describes the amount of long-wave radiation emitted by an object:

$$L = \epsilon \sigma T_o^4, \quad (2.14)$$

where L is emitted radiation ($\text{W}\cdot\text{m}^{-2}$), ϵ is the long-wave emissivity of the material, σ is the Stefan Boltzman constant ($5.67 \times 10^{-8} \text{ W}\cdot\text{m}^{-2}\cdot\text{K}^{-4}$) and T_o is the material's radiative temperature ($^{\circ}\text{K}$). Broadband emissivity of sea ice and water is close to 0.97, while a value of 0.99 is usually used for snow (Maykut, 1986). Snow emissivity is fairly insensitive to snow morphology (Warren, 1982).

Down-welling long-wave radiation is determined by the structure of the temperature and humidity profile in the lower atmosphere. Various techniques are available to determine $L\downarrow$ if these profiles are known (e.g. Kneizys, et al., 1988), otherwise Eq. 2.14 may be used with empirical expressions which relate an effective sky emissivity to variables such as near surface vapour pressure, temperature and fractional cloud coverage. The all-sky formulation of Jacobs

⁷ The scattering of light by spherical particales of diameters comparable with the incident wavelength (Illingworth, 1991)

(1978) with the clear sky formulation of Efimova (1961) agreed best with Arctic observation in a study by Key et al.,(1996a). The parameterization is:

$$L \downarrow = L \downarrow_{clr} (1 + 0.26 \cdot TCA), \quad (2.15a)$$

where TCA is the total cloud amount (expressed as a fraction), and

$$L \downarrow_{clr} = \sigma T^4 (0.746 + 0.006 \cdot e), \quad (2.15b)$$

is the clear-sky long-wave radiance, and e is the near surface vapour pressure⁸.

2.4.3.2 Heat Flow through the Snow Volume

Heat Conduction

The vertical heat transfer process may be expressed in terms of Fourier's heat conduction equation:

$$Q_{s_x} = \rho_x C_{p_x} \frac{dT_x}{dt} = -k_x \frac{dT_x}{dz_x} \quad (2.16)$$

where Q_s is the heat transfer rate in the z - direction per unit area perpendicular to the temperature gradient, $\frac{dT_x}{dz_x}$ (Incropera and DeWitt, 1990). The second term in the equation represents the time rate of energy change at a point, where ρ_x and C_{p_x} are the density ($\text{kg}\cdot\text{m}^{-3}$) and specific heat ($\text{Jkg}^{-1} \text{ } ^\circ\text{C}^{-1}$), respectively, for the medium x (e.g. snow or ice). The proportionality constant, k , is a transport property known as the thermal conductivity. Heat transport in both snow and sea ice may occur by processes other than molecular conduction. Therefore an effective thermal conductivity in Eq. 2.16 is used to relate the total heat flow by the various processes to a temperature gradient. Various transport processes include: (i) molecular conduction through ice, air and liquid, (ii) the transfer of latent heat associated with sublimation, (iii) the transport of vapor along a temperature gradient, (iv) thermal convection, (vi) long-wave radiation across the pore spaces and by (vii) the absorption of solar radiation. It is difficult to isolate the relative magnitude of each of the respective heat transfer processes (Fukusako, 1990; Yen, 1981; Yen et al., 1991).

⁸ The expected units of vapor pressure here are mb.

The minus sign in Eq. 2.16 is a consequence of the fact that heat is transferred in the direction of decreasing temperature.

A related term to the thermal conductivity is the thermal diffusivity ($\text{m}^2\cdot\text{s}^{-1}$) and it is a measure of the material's ability to diffuse thermal influences (Oke, 1987):

$$\nu_x = k_x / \rho_x C_{p_x} \quad (2.17)$$

The thermal properties of snow and sea ice are described in the following section.

Recently, researchers (Sturm and Johnson, 1992; Maeno and Kuroda, 1986) have shown that the contribution of the latent heat transfer associated with vapor diffusion can account for between 20% and 75% of total heat flow, depending on snow texture. This process is described in relation to metamorphism in dry snow in Section 2.3.2.

Thermal Properties of Sea Ice and Snow

A study of heat flow through sea ice or snow is complicated by the relationship between ice, salinity and temperature. The salinity of the liquid brine within a sea ice inclusion is temperature dependent (Fig. 2.4). The brine salinity increases with decreasing temperature and vice versa, to maintain phase equilibrium. Each and every temperature change initiates melting/freezing at the ice boundaries of the brine pockets allowing for a variable brine volume. At temperatures above -8.2°C the fraction of precipitated salts is negligible and the brine in sea ice has the same salt composition as that in sea water. At temperatures between -8.2 and -22.9°C , a continuous precipitation of $\text{Na}_2\text{SO}_4 \cdot 10\text{H}_2\text{O}$ occurs (Schwerdtfeger, 1962). Over 90% of all salts in solution are crystallized at temperatures below -22.6°C (Doronin and Kheisin, 1977). The physical properties of the sea ice are strongly effected by the phase equilibrium between ice and brine, giving rise to a substance with strongly temperature-dependent physical properties, particularly at temperatures above -8.2°C . Conversely, the presence of solid salts at the lower temperatures do not appreciably change the thermal properties of the sea ice (Schwerdtfeger, 1962).

The derivation of many of the physical properties of snow and ice often require estimates for the volume proportions of air, brine, and ice. Frankenstein and Garner (1967) developed a relation for the brine volume per salt/ice mixture (v_b):

$$v_b = s \left(\frac{a}{\text{abs}(T_i)} \right) + b, \quad (2.18)$$

where

a=52.56	b=-2.28	-0.5°C ≤ T _i ≤ -2.06°C
a=45.914	b=0.930	-2.06°C < T _i ≤ -8.2°C
a=43.795	b=1.189	-8.2°C > T _i ≥ -22.6

where s is the sea ice (or snow) salinity (grams salt per gram of ice), and T_x is the temperature (°C) of ice (subscript i) or snow (subscript s). The relative volumes of ice (V_i), brine (V_b) and air (V_a) can then be determined by using the weight ratios of ice and brine to total mass, such that:

$$V_b = \left[\frac{v_b \rho_b}{(1-v_b)\rho_i + v_b \rho_b} \right] \left[\frac{\rho_{si}}{\rho_b} \right], \quad (2.19a)$$

$$V_i = \left[\frac{(1-v_b)\rho_i}{(1-v_b)\rho_i + v_b \rho_b} \right] \left[\frac{\rho_s}{\rho_i} \right], \quad (2.19b)$$

and

$$V_a = 1 - (V_b + V_i), \quad (2.19c)$$

where ρ_{si} , ρ_b , and ρ_i are the densities of sea ice, brine and pure ice, respectively (Drinkwater and Crocker, 1988). Eide and Martin (1975) approximate the density of brine with

$$\rho_b = \rho_w (1 + 0.01T_b), \quad (2.20)$$

where ρ_w is the density of water, and T_b is the brine temperature (°C).

The proportional volume of ice within a volume of non-saline snow is determined using:

$$V_i = \frac{\rho_s - M_w}{\rho_i}. \quad (2.21)$$

The mass of liquid water per unit snow volume, M_w , for nonsaline snow is computed as:

$$M_w = fl \cdot \rho_s, \quad (2.22)$$

where,

$$f_l = \left(\frac{1}{1 + (100 \cdot (273.15 - T_k))^2} \right), \quad (2.23)$$

and T_k is the snow temperature ($^{\circ}\text{K}$). The above describes the mass-liquid water fraction of unfrozen water (mass ratio of liquid phase to combined liquid and solid phase) per unit snow volume as a function of temperature (Guryanov, 1985). The volumetric proportion of liquid water per unit snow volume is:

$$V_w = \frac{M_w}{\rho_w}. \quad (2.24)$$

where ρ_w is the water density.

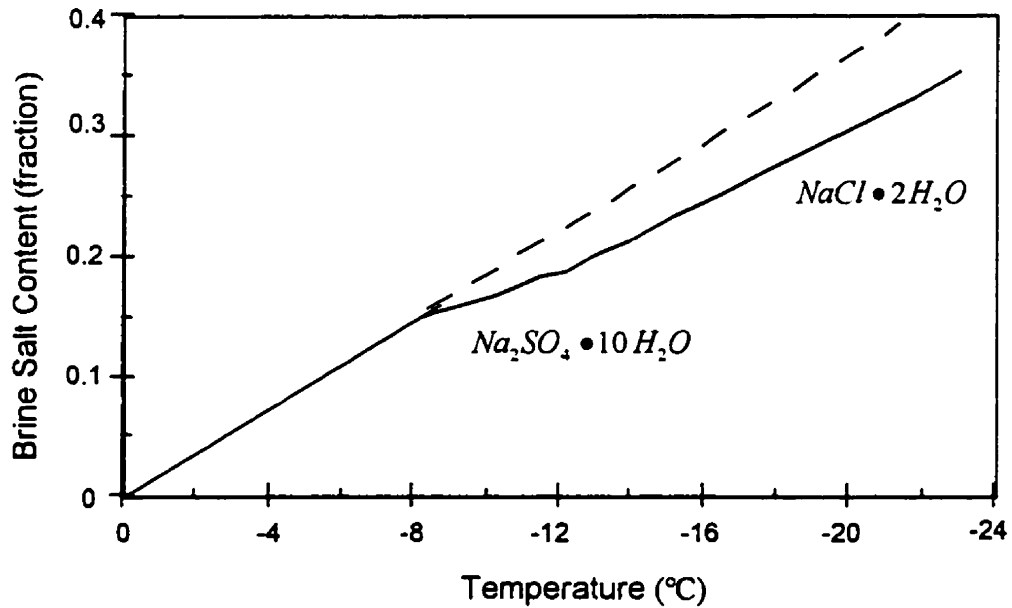


Figure 2.4 Freezing point of brine as a function of the ratio of dissolved salts to pure water at temperatures greater than -23°C (Assur, 1968). Above -8.2°C the slope of the relationship is $-0.0182^{\circ}\text{C}^{-1}$. The hydrate $\text{Na}_2\text{SO}_4 \cdot 10\text{H}_2\text{O}$ first precipitates at -8.2°C and the precipitation of $\text{NaCl} \cdot 2\text{H}_2\text{O}$ initiates -22.9°C .

Equations 2.19 to 2.24 show the volume relationships to be strong functions of salinity, temperature and density. The volumetric proportion of liquid (V_B for saline snow, V_W for non-saline snow) can be substantial in snow, particularly at temperatures above -3°C (Fig. 2.5). The volumetric proportion of liquid for varying snow salinity and temperature is represented in the figure as a contoured surface for densely packed ($\rho_s = 450 \text{ kg}\cdot\text{m}^{-3}$), moderately packed ($\rho_s = 300 \text{ kg}\cdot\text{m}^{-3}$) and loosely packed snow ($\rho_s = 150 \text{ kg}\cdot\text{m}^{-3}$). At a given temperature, the liquid volume fraction is larger for higher snow salinity and, likewise, liquid volume fraction increases with increasing temperature at a given salinity. Both relationships are amplified for increasing snow density. The rate of increase (as denoted by the spacing between contours) increases with increasing temperature/salinity. Because the mass of water (solid and liquid) within a snow volume increases with snow density, it is expected that the mass (and hence volume) of liquid should rise with increasing density at a given brine salinity, as more ice surface area is available for melt. The liquid content for non-saline snow is negligible, except at temperatures very near to the freezing point of pure ice. At this time the liquid contents may approach 25% for high-density snow.

a) *Latent Heat*

The latent heat of fusion of pure ice is defined as the change in enthalpy when a unit mass of ice is converted isothermally and reversibly into liquid water (Incropera and de Witt, 1990). The most commonly reported value at 0°C and standard atmospheric pressure is $333.5 \text{ kJ}\cdot\text{kg}^{-1}$ (Yen et al., 1991). The latent heat of sublimation of ice represents the enthalpy change when a unit mass of ice is transformed isothermally and reversibly into water vapour at the standard atmospheric pressure, and at the ice-liquid-water triple point (Yen et al., 1991). Its value is approximately $2838 \text{ kJ}\cdot\text{kg}^{-1}$.

A latent heat of fusion technically does not exist for saline sea ice, because there is no one distinct melting temperature. The heat required in this process is considered a specific heat (Schwerdtfeger, 1962).

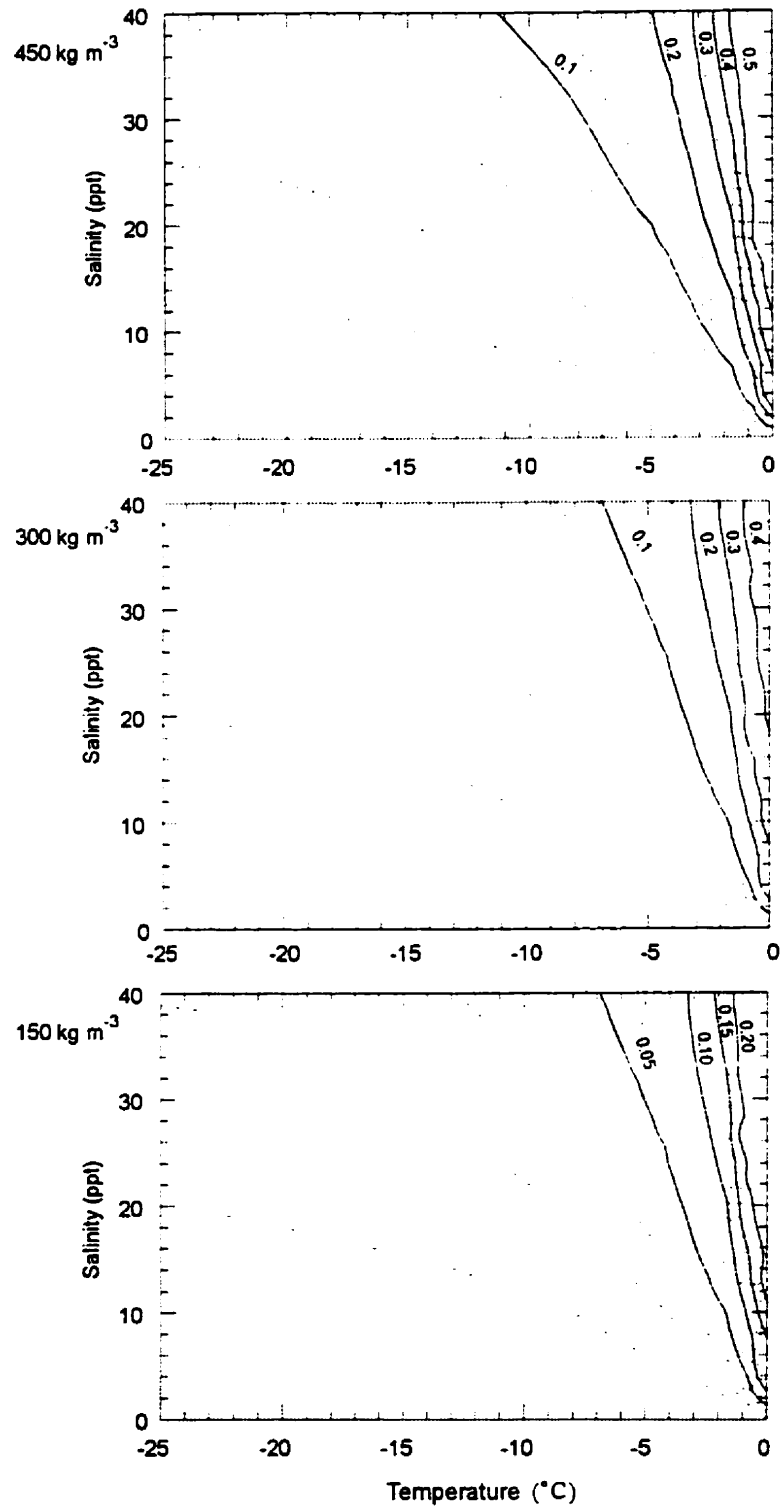


Figure 2.5 Liquid volume proportion of snow (volume fraction) as a function of salinity and temperature for snow density $450 \text{ kg}\cdot\text{m}^{-3}$, $300 \text{ kg}\cdot\text{m}^{-3}$, and $150 \text{ kg}\cdot\text{m}^{-3}$.

b) *Specific Heat*

A specific heat is defined as the heat required to raise a unit mass one degree at constant pressure. A related term, the volumetric heat capacity ($\text{kJ}\cdot\text{m}^{-3}\cdot\text{K}^{-1}$), is defined as the heat required to raise a unit volume one unit of temperature at constant pressure. For a temperature increase in saline sea ice, energy is needed to increase the temperature of the solid ice and brine and to melt a fraction of ice (Schwerdtfeger, 1962). As a consequence, saline ice may have an abnormally large specific heat with respect to that of pure ice (e.g., Fig. 2.6), while at low temperatures ($<-23^\circ\text{C}$), the specific heat is only about 4-6% higher than that of pure ice. The melting of saline sea ice is a major heat absorbing process at temperatures near the freezing point.

The relationship between specific heat of sea ice (or saline snow), temperature and salinity is demonstrated with Ono's (1966) empirical expression (note the units for the expression are $\text{kJ}\cdot\text{kg}^{-1}\cdot^\circ\text{C}$):

$$C_p = 2.114 + 0.0075T_i + 18052\frac{s}{T_i^2} - 3.35s + 0.84sT_i, \quad (2.25)$$

where T_i is the ice temperature ($^\circ\text{C}$). The heat capacity of air and solid salts are small compared to ice and brine and therefore are often ignored (Schwerdtfeger, 1962).

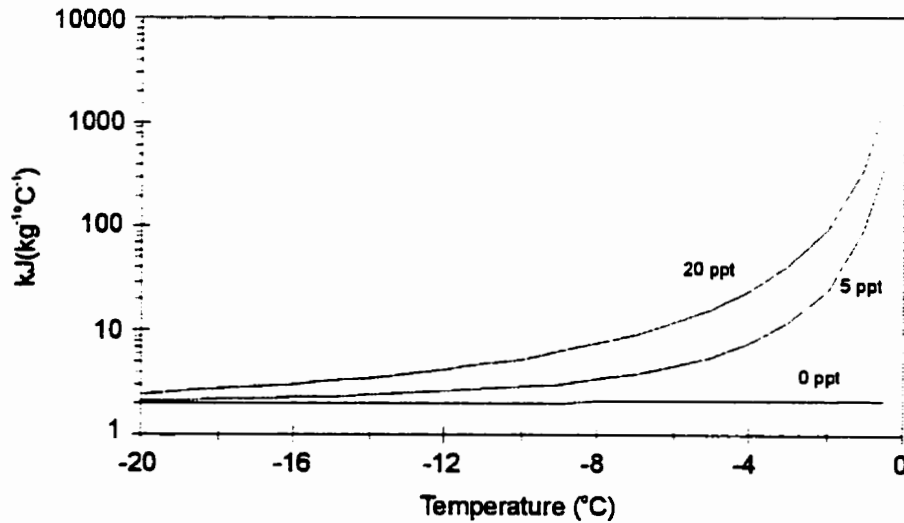


Figure 2.6 Specific heat of sea ice ($\text{kJ}\cdot\text{kg}^{-1}\cdot^\circ\text{C}^{-1}$) as a function of temperature for sea ice salinity of 20 ppt, 10 ppt, and 0 ppt. Source: Ono (1966).

c) *Thermal Conductivity of Sea Ice and Snow*

Sea ice and snow can contain a solid, liquid and vapour phase. The thermal conductivity ($\text{W}\cdot\text{m}^{-1}\cdot\text{°C}^{-1}$) of pure ice is an exponential function of temperature:

$$k_i = 9.828 \cdot \exp(-0.0057 \times (T_i + 273.15)), \quad (2.26)$$

(Yen et al., 1991). Reported values at the freezing point range between 2.09 and 2.23 $\text{W m}^{-1}\text{°C}^{-1}$ (Yen et al., 1991). The presence of brine decreases the thermal conductivity of sea ice relative to that of fresh water ice. Untersteiner (1961) demonstrated this relationship using the empirical relation:

$$k_n = k_o + \frac{(BS)}{T_i}, \quad (2.27)$$

where B is 0.13 $\text{W}\cdot\text{m}^{-1}$, S is salinity (parts per thousand, ppt), and T_i is ice temperature (°C).

Little is known about the thermal conductivity of snow over sea ice. In a terrestrial setting, researchers have related the measurements of the effective thermal conductivity to snow bulk density (e.g. Yen et al., 1991; Fukusako, 1990). Some of the more widely used parameterizations appear in Table 2.1 and are illustrated over a range of snow density in Fig. 2.7. The difference between the relations is related to (i) sampling and measurement error, (ii) by the fact that density itself does not provide a complete representation of snow texture and (iii) because latent heat transfer along a temperature gradient is not well reproduced in a laboratory setting (Fukusako, 1990). Goodrich (1976) suggested that the empirical curves are probably not reliable for snow densities less than about $100 \text{ kg}\cdot\text{m}^{-3}$. Because vapor diffusion and the latent heat flux through the snow increases in response to an increased temperature gradient, a latent heat enhancement may be applied to any empirical formula, as shown by Anderson (1976) and later by Ebert and Curry (1993).

Unfortunately little is known about the effect of other snow parameters on thermal conductivity. The effect of texture, which includes the grain size, shape, bonding and spatial arrangement of grains, on effective thermal conductivity has not been quantified or described in detail. Texture is believed to be particularly important in describing the thermal conductivity of low density snow. Sturm and Johnson (1992) found that the standard relationships of thermal conductivity versus density overestimate the thermal conductivity of depth hoar by a factor of 2 to 7. They measured the effective thermal conductivity to be between 0.026 and $0.105 \text{ W}\cdot\text{m}^{-1} \text{°K}^{-1}$,

with an average of $0.063 \text{ W}\cdot\text{m}^{-1} \cdot\text{K}^{-1}$, for snow densities between 154 and 220 kg m^{-3} . They observed a near linear increase in effective thermal conductivity with temperature in the hoar layer for temperatures greater than -20°C . Their data suggests that most of the temperature dependence is the result of latent heat transfer associated with the movement of water vapor. Pitman and Zuckerman (1967) also observed an increase in snow thermal conductivity with temperature (e.g., Fig. 2.7); however, Sakazume and Seki (1978) observed the effective thermal conductivity to monotonically decrease with increasing temperature. Their rate of decrease was a function of density, being large for high density snow ($> 500 \text{ kg}\cdot\text{m}^{-3}$), and small for low snow densities ($< 200 \text{ kg}\cdot\text{m}^{-3}$).

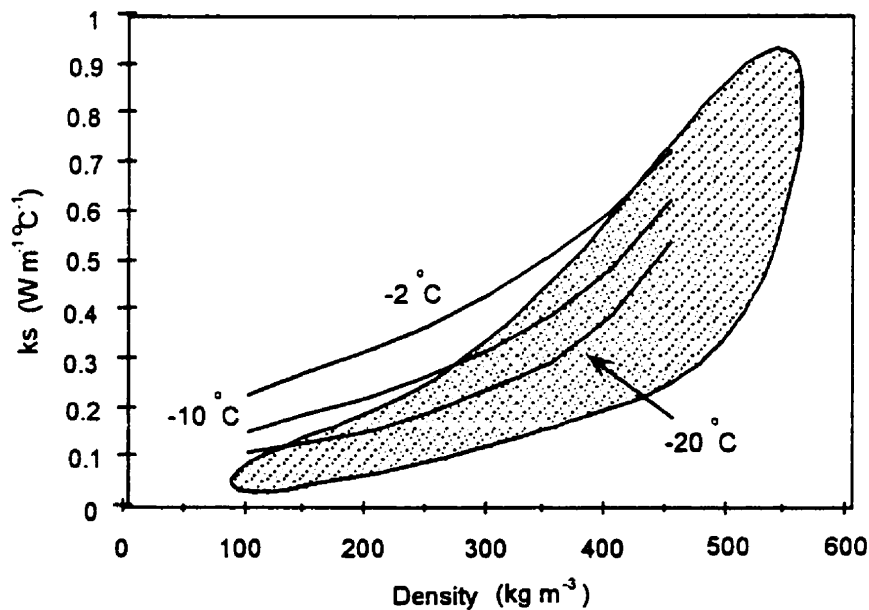


Figure 2.7 The variation of predicted snow thermal conductivity using the nine empirical formulae provided in Table 2.1 over a snow density range. The curves represent snow thermal conductivity as computed using Maeno and Kuroda's (1986) version of Pitman and Zuckerman's (1967) physical model at snow temperatures of -2°C , -10°C , and -20°C . The model is described in the text.

The presence of any liquid beyond its irreducible level introduces the possibility of heat flow associated with liquid migration along gradients of capillary pressure (Langham, 1981). This process is generally considered independent of a thermal conductivity formulation (e.g., Jordan, 1991). Traditionally the thermal conductivity of wet snow is not modeled because melting snow is assumed to be near isothermal at 0°C. If a salinity gradient exists, portions of the snow may be wet (refer to Fig. 2.5) in the presence of appreciable temperature gradients. Papakyriakou and LeDrew (1999) showed that the effect of brine is to lower the thermal conductivity of snow relative to non-saline snow. At snow liquid water contents within the pendular moisture regime, the thermal conductivity of snow may be lowered by up to 10%. Snow thermal conductivity may be lowered by 80% at high liquid volumetric proportions (e.g., 40% by volume). This assumes that the liquid in the snow exists at the expense of the ice volumetric proportion and results because the ice thermal conductivity is much larger than the thermal conductivity of brine. This situation may occur within the shallow, highly saline snow over thin, rapidly growing sea ice. In deeper freely draining snow this situation is unlikely to occur because any water drainage from overlying snow may increase the volume proportion of liquid in the lower reaches of the snow profile without appreciably changing the ice volumetric proportion. In this case we would expect a decline in the volume proportion of air, which should act to raise the snow's overall thermal conductivity. When slush freezes its thermal conductivity can be between 10-75 times that of snow (Weeks and Lee 1958).

Table 2.1 Relationships between thermal conductivity and snow density. Source: Fukusako (1990).

<i>Investigator</i>	<i>Expression ($W \cdot m^{-1} \cdot K^{-1}$)</i>	<i>Density Range ($kg \cdot m^{-3}$)</i>
1) Abels	$k_s = 2.9 \times 10^{-6} \rho^2$	140-340
2) Jansson	$k_s = 2.1 \times 10^{-2} + 8.0 \times 10^{-4} \rho + 2.5 \times 10^{-12} \rho^4$	80-500
3) Van Dusen	$k_s = 2.1 \times 10^{-2} + 4.2 \times 10^{-4} \rho + 2.2 \times 10^{-9} \rho^3$	-
4) Devaux	$k_s = 2.9 \times 10^{-2} + 2.9 \times 10^{-6} \rho^2$	100-600
5) Kondrat'eva	$k_s = 3.6 \times 10^{-6} \rho^2$	> 350
6) Yoshida and Iwai	$\log_{10} k_s = -1.4 + 2 \times 10^{-3} \rho$	70-400
7) Yen	$k_s = 3.2 \times 10^{-6} \rho^2$	-
8) Izumi and Fujioka	$\log_{10} k_s = -1.17 + 2.16 \times 10^{-3} \rho$	80-500
9) Sakazume and Seki	$\log_{10} k_s = -1.25 + 2.12 \times 10^{-3} \rho$	150-700

Air in the snow is assumed to be stationary in each of the thermal conductivity formulations provided above. Airflow in the snow, and an associated flow of heat and moisture may also occur as an independent process to conduction and diffusion. Air motion may also affect snow metamorphism and increase the growth rate of hoar (Sturm and Johnson, 1991). There remains considerable uncertainty regarding the conditions necessary for the occurrence of convection in natural snow covers. Recently, Gray and Morland (1994) postulated that airflow through snow is negligible when surface airflow is slow but convection can make a significant contribution to the heat flow process when pressure variations at the surface are large. Sturm and Johnson (1991) suggested that it is the spatial variation in boundary conditions of a natural snow cover that plays a dominant role in the development of convection. Convection cells arise through differential heating at the snow base. They commented that convection is rarely reproduced in the laboratory because laboratory experiments typically assume homogeneous boundary conditions. Further work is required on this matter.

d) *Physical Models of Thermal Conductivity for Sea Ice and Snow*

Sea Ice

Physical models of sea ice thermal conductivity are based on the relative proportions and the spatial arrangement of the different components of sea ice (i.e., pure ice, trapped air, and brine). A model presented by Schwerdtfeger (1963) considers a short length of sea ice to be a system of parallel connected conductors. This assumption is physically valid because the heat flow through flat sea ice is essentially one dimensional and vertical (Schwerdtfeger, 1963). Schwerdtfeger considers sea ice as two parallel conduits, one of bubbly ice (ice with uniformly distributed spherical air bubbles), and the other of brine. The thermal conductivity of sea ice is represented as the conductivity of brine and bubbly ice, acting in parallel and weighted by their relative cross-sectional areas:

$$k_{si} = k_{bi}A_{bi} + k_bA_b, \tag{2.28}$$

such that

$$k_{si} = k_{bi} - (k_{bi} - k_b) \frac{s\rho_a}{\Xi\rho_w T_i}, \tag{2.29}$$

where k and A are the thermal conductivity and relative cross-sectional area of brine (subscript b), and bubbly ice (subscript bi), respectively, and s is salinity (mass of salt per mass of sea ice), ρ_{si} and ρ_w are the densities of sea ice and water and Ξ defines the relationship between the fractional salt content of brine and temperature (i.e., the slope of curve defined in Fig. 2.4). The thermal conductivity of bubbly-ice is

$$k_{bi} = \frac{2k_i + k_a - 2V_a(k_i - k_a)}{2k_i + k_a + V_a(k_i - k_a)} k_i, \quad (2.30)$$

where k_i and k_a are the thermal conductivity of pure ice and air, and V_a is the volume of air per unit volume of ice. The thermal conductivity of air ranges between 0.02 and 0.03 $\text{W m}^{-1}\text{C}^{-1}$ for temperatures between -30°C and 0°C . Lange and Forker (1952) represent the thermal conductivity of brine as a function of temperature using:

$$k_b = 0.4184 - (1.25 + 0.030 \cdot T_i + 0.00014 \cdot T_i^2). \quad (2.31)$$

The effect of temperature, salinity and density on thermal conductivity (as determined using Schwerdtfeger's physical model) is represented in Figs 2.8 and 2.9. Increasing temperature and salinity act to lower sea ice thermal conductivity (Fig. 2.8), while increasing sea ice density tends to raise ice thermal conductivity (Fig. 2.9). The thermal conductivity of bubbly-ice is marginally less than for pure ice (Fig. 2.9). The effect of salinity on the thermal conductivity of saline ice is amplified for warm ice ($> -8^\circ\text{C}$) because the volume proportion of brine increases rapidly, largely at the expense of the volume proportion of ice. The thermal conductivity of salt precipitates is thought to have only a small effect on the thermal conductivity of bulk sea ice. Also shown (Fig. 2.8) is Untersteiner's (1961) empirical relation for sea ice thermal conductivity (i.e., Eq. 2.27). Even though it is a cruder estimate for the coefficient, it compares well with Schwerdtfeger's model for cold ice. Untersteiner's relation is within 3% of Schwerdtfeger's physical model for low salinity sea ice (e.g., 5 ppt) and within typically 1.5% for high salinity sea ice (e.g., 30 ppt), at temperatures of less than -13°C . The discrepancy between the two increases by up to 35% as the ice warms.

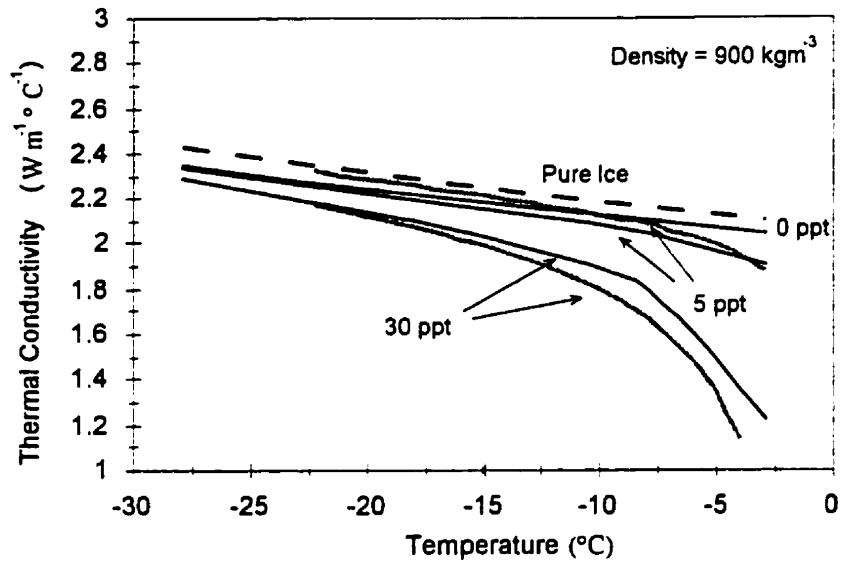


Figure 2.8 Thermal Conductivity ($W m^{-1} \cdot ^\circ C^{-1}$) of bubbly sea ice as a function of temperature ($^\circ C$) for sea ice of varying salinity (ppt), as determined using Schwerdtfeger's (1963) physical relation. Also shown for comparison is the thermal conductivity of pure ice (dashed line, Yen, 1991), and the empirical expression of Untersteiner (1961) (grey lines).

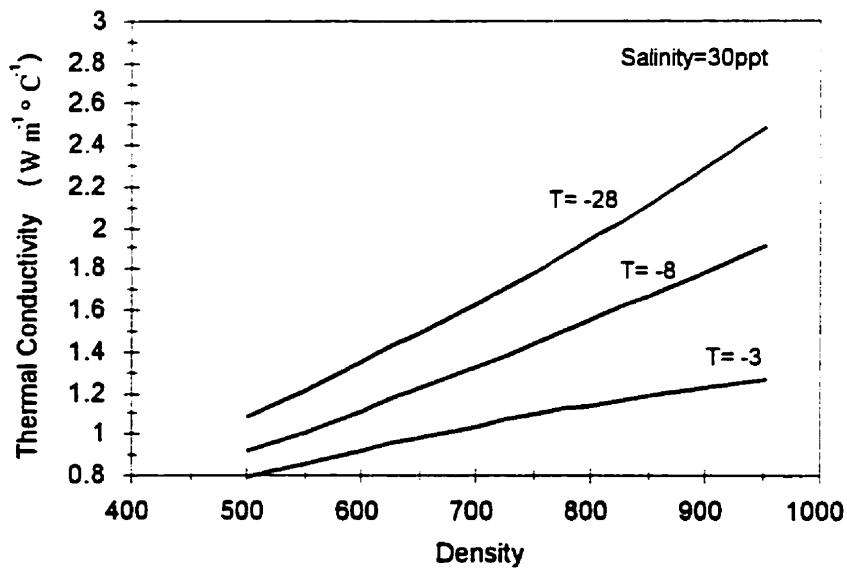


Figure 2.9 Thermal Conductivity ($W m^{-1} \cdot ^\circ C^{-1}$) of bubbly sea ice as a function of ice density ($kg m^{-3}$) for sea ice of varying temperature as determined using Schwerdtfeger's (1963) physical relation.

Dry Snow

Goodrich (1976), and more recently Arons and Colbeck (1995), present excellent reviews on the development of snow physical models. Only models relevant to this work are discussed here.

Woodside (1958) considered snow as non-contacting ice spheres arranged in a cubic lattice. Because the lattice is symmetric, the system could be considered as a unit cell and the heat flow through each component (air and ice) is treated as a system of resistors assembled in series and parallel. The major criticism of the model is that the ice spheres do not touch and consequently the model does not reproduce the widely accepted dependency of snow thermal conductivity on density.

Pitman and Zuckerman (1967) more closely mimic a snow matrix by connecting Woodside's (1958) ice spheres with cylindrical bonds, thereby allowing heat flow through the grain connections, as well as across the pore space (Fig. 2.10). Moist air in the pore space is assumed stationary so that heat transfer by convection is neglected. The ice spheres resemble the equilibrium form of snow (Colbeck, 1982); however, they do not resemble a faceted crystal produced during kinetic growth. The ice spheres are not permitted to touch; hence, the maximum allowable snow density is $480 \text{ kg}\cdot\text{m}^{-3}$. Heat conduction along the horizontal ice cylinders is also ignored. Regardless of these assumptions, the model, as originally presented, does a good job of representing heat transfer through conduction (Goodrich, 1976), however, as pointed out by Arons and Colbeck (1995), the model's treatment of latent heat transfer associated with vapor diffusion is deficient.

The resistance to vertical heat flow of a unit cube of the ice sphere lattice using the Pitman and Zuckerman model is:

$$k_s = \left[\frac{(1-R) \left[\frac{(k_i - k_p)\gamma + k_p}{2a\pi R[k_i - k_p]} + 4 \ln\left(a + \frac{1}{a} - 1\right) \right]}{2a\pi R[k_i - k_p]} \right]^{-1}, \quad (2.32)$$

where

$$a = \left[1 + \frac{4}{\pi \left(\frac{k_i}{k_p} - 1 \right) (R^2)} \right]^{1/2}; \quad (2.33)$$

R is the radius of the ice spheres:

$$R = \left(\frac{6V_i}{\pi} \right)^{1/3}, \quad (2.34)$$

and γ is the cross sectional area of one-quarter of the ice cylinders of radius r :

$$\gamma = \frac{\pi r^2}{4}. \quad (2.35)$$

In these equations, k_i is the thermal conductivity of ice, k_p is the effective thermal conductivity of the pore space, r is the radius of the cylindrical bonds between ice spheres and V_i is the volume of ice per unit volume of snow. The ice cylinder radius was originally selected to match observed thermal conductivity. The selected bond radii agreed well with observed neck radii of sintered ice.

The effective thermal conductivity across the pore space can be described using,

$$k_p = k_a + \left(\frac{\Omega}{g_w \cdot T_k} \right) D_e L_s, \quad (2.36)$$

(Yoshida et al., 1955) and represents the combined thermal conductivity of dry air (k_a) and any latent heat transfer associated with water vapor diffusion (the second term on the right-hand side of the equation). In Eq. 2.36, g_w is the gas constant for water vapor, D_e is the diffusion coefficient in snow, L_s is the latent heat of sublimation and Ω represents the water vapor concentration dependence on temperature over ice. The diffusion coefficient for water vapor in snow should be corrected for temperature and pressure dependency. Anderson (1976) provides the expression:

$$D_e = D_{e0} \frac{1000}{P_a} \left(\frac{T_k}{273.15} \right)^{n_d}, \quad (2.37)$$

where D_{e0} is the effective diffusion coefficient for water vapor in snow at 0°C and 1000 mb pressure, P_a is the atmospheric pressure (mb) and n_d is a temperature exponent. Jordan (1991) assigned D_{e0} at $9.2 \times 10^{-5} \text{ m}^2 \cdot \text{s}^{-1}$ and applied a temperature exponent (n_d) of 6.

Ice Crystal
Lattice

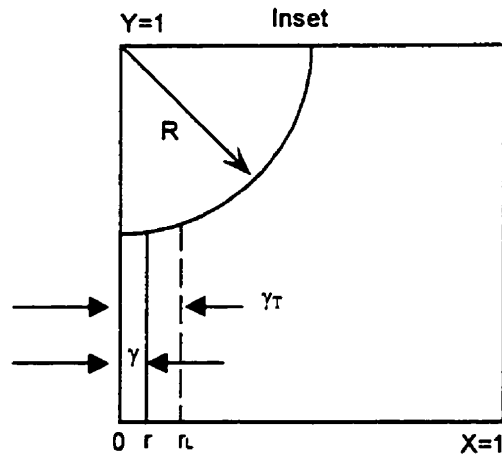


Figure 2.10 Schematic of Pittman and Zuckerman's (1967) ice sphere cubic lattice with representation of a liquid phase according to Crocker (1984). The inset is a unit cell. In the figure: R is the sphere radius, γ is the cross-sectional area of one quarter of the ice cylinder, γ_T is the cross-sectional area of one quarter of the ice cylinder increased by the ice equivalent area of brine, r is the ice cylinder radius and r_L is the radius of a liquid cylinder.

Maeno and Kuroda (1986) examined the effect of enhancing the vapor diffusion on the Pittman and Zuckerman model by enhancing the diffusion coefficient of air within snow (i.e. $D_e = 6.5 \times 10^{-5} \text{ m}^2 \cdot \text{s}^{-1}$ as opposed to $2.1 \times 10^{-5} \text{ m}^2 \cdot \text{s}^{-1}$). The model does not realistically represent mass flow, and hence can not be used to examine the evolution of snow texture. It does however produce effective thermal conductivity within a range of measured thermal conductivity provided by Sakazume and Seki (1978) for snow of density between $100 \text{ kg} \cdot \text{m}^{-3}$ and $480 \text{ kg} \cdot \text{m}^{-3}$. Maeno and

Kuroda's (1986) solution to the Pitman and Zuckerman (1967) model is shown in relation to a range of empirical functions in Fig. 2.7.

Wet Snow

Crocker (1984) examined the case of brine wetted snow by modifying the Pitman and Zuckerman (1967) model to accommodate a liquid phase. In Crocker's work the brine was allowed to wrap around the cylindrical bonds which connect the lattice of ice spheres of the Pitman and Zuckerman (1967) model. An equivalent ice radius of brine (r_L) was obtained by multiplying the radius of a brine cylinder by the ratio of brine thermal conductivity to ice thermal conductivity (k_b/k_i). The equivalent ice radius of brine was added to the ice cylinder radius (refer to Fig. 2.10), from which the total cross-sectional area γ_T was computed and replaced γ in Eq. 2.32.

Papakyriakou and LeDrew (1999) adapted Crocker's model to consider all liquid (brine and water) in the snow matrix and modified Crocker's treatment of heat transfer associated with vapour diffusion. The model was used to assess the relationship between thermal conductivity of snow over sea ice and snow physical parameters, including density, temperature and salinity. The volume proportion of liquid water in the snow cover was described by Eqs. 2.21 to 2.24 for a given snow temperature and density. The radius of the water cylinder was determined in exactly the same fashion as described by Crocker for brine. The model does not literally represent the grain clusters described by Colbeck (1982) for snow within the pendular regime, but the location of a liquid phase at the grain contact is, however, accurate. The model assumes a grain cluster to behave as a single grain.

The thermal conductivity of the non-ice components of snow and sea ice is shown in Fig. 2.11 over a temperature range. The thermal conductivity of the pore space ranges between 0.03 to 0.1 $\text{W}\cdot\text{m}^{-1}\text{C}^{-1}$ and is approximately 20 to 60 times less than k_i over this temperature range. Ice thermal conductivity ranges between 2.4 and 2.1 $\text{W}\cdot\text{m}^{-1}\text{C}^{-1}$, which is between 4 to 8 times greater than k_b (0.29 to 0.51 $\text{W}\cdot\text{m}^{-1}\text{C}^{-1}$). Brine thermal conductivity increases monotonically with temperature, but remains approximately a factor of 5 less than the thermal conductivity of pure ice. The effective thermal conductivity of moist air within the inter-crystal voids is a weak function of temperature and salinity, increasing with increasing temperature and decreasing brine salinity.

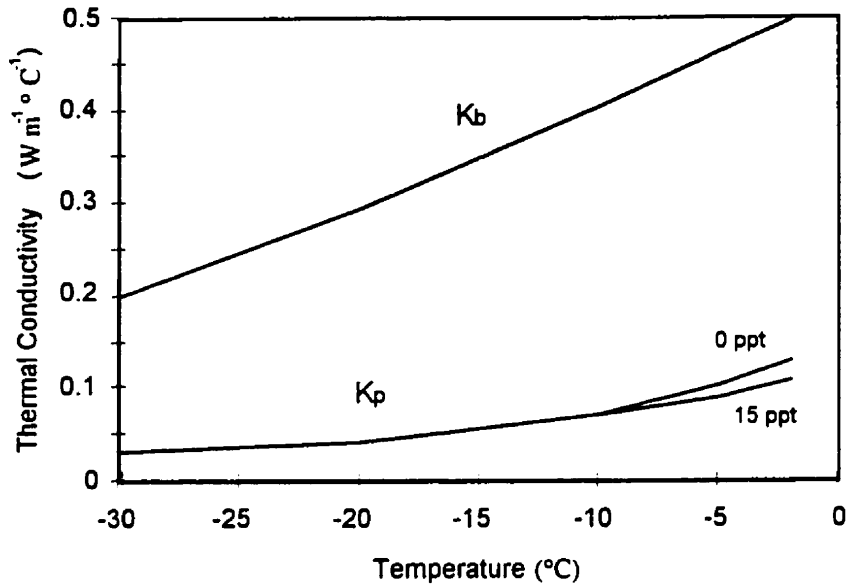


Figure 2.11 The thermal conductivity of snow's non-ice components: brine (K_b), and air within the pore space (K_p). K_p is shown for snow of 0 ppt, and 15 ppt.

The relationship among temperature, salinity, density (independent variables) and k_s (dependent variable) is illustrated in Fig. 2.12 and 2.13. For non-saline snow, modeled thermal conductivity was shown to increase with increasing snow density (Fig. 2.13) and temperature (Fig. 2.12). Increasing salinity within the snow matrix at a given temperature, or increasing snow temperature at a given salinity, acted to decrease k_s (Fig. 2.12), with the steepest rate of change occurring for warm, densely-packed snow at temperatures greater than -5°C . The narrow spacing of the contours in Fig. 2.13 show k_s to decrease for a given density with increasing salinity. The effect is amplified at high snow density and at warm snow temperatures. Both figures show that only a small amount of salt ($S < 10$ ppt) is required to modify k_s in dense snow ($\rho_s > 350 \text{ kg}\cdot\text{m}^{-3}$) for snow temperatures above -10°C . The appropriateness of the model at high liquid water contents is discussed above. Liquid water in salt-free snow had only a negligible effect on snow thermal conductivity at snow temperatures below -0.03°C . This is because the volumetric proportion of liquid is very small in the non-saline case. The authors concluded that there is little to gain by extending Crocker's model to consider water within the snow cover.

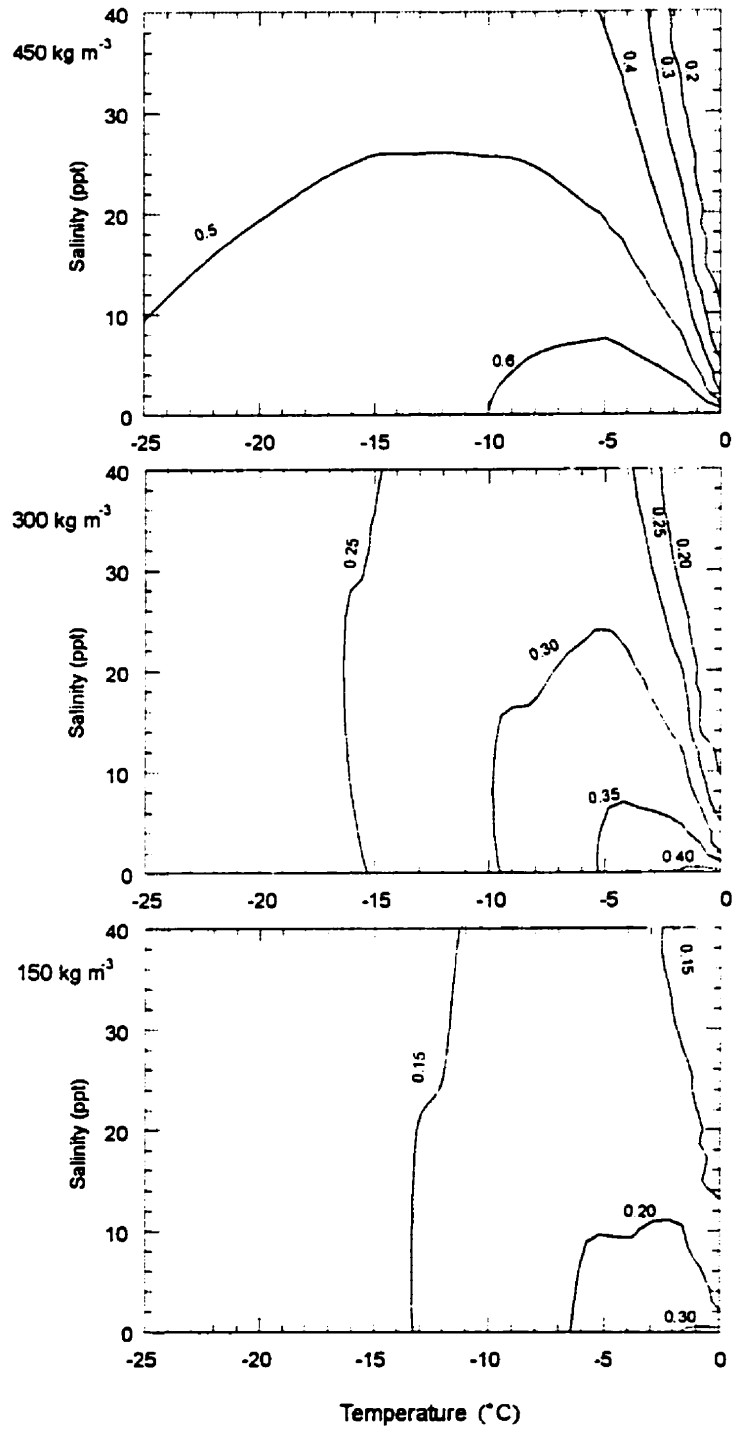


Figure 2.12 Snow effective thermal conductivity ($W \cdot m^{-1} \cdot ^\circ C$) shown as a function of salinity and temperature for snow density 450 kg m^{-3} , 300 kg m^{-3} , and 150 kg m^{-3} .

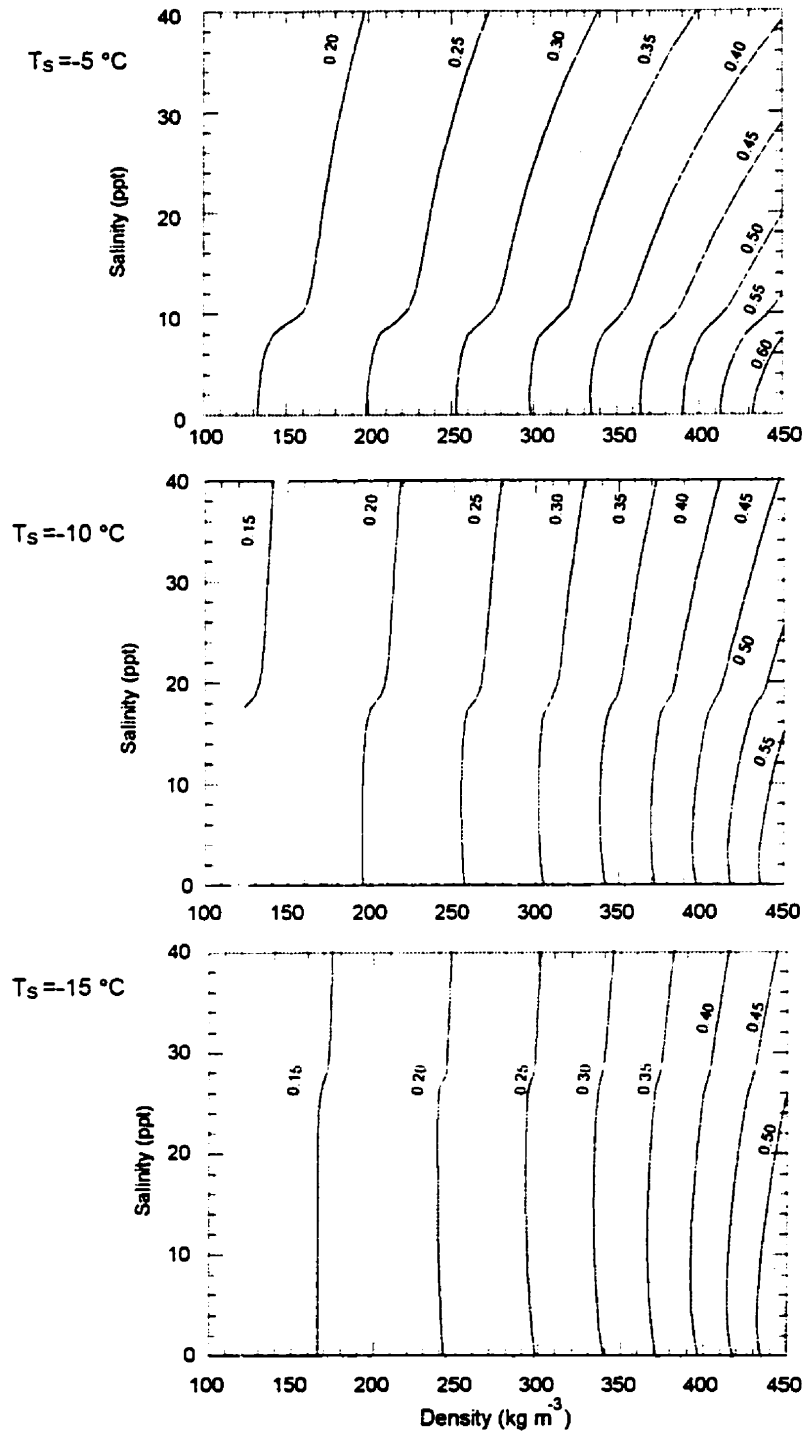


Figure 2.13 Snow effective thermal conductivity ($W \cdot m^{-1} \cdot ^\circ C$) shown as a function of salinity and density for snow temperatures of $-5^\circ C$, $-10^\circ C$ and $-15^\circ C$.

The increase in the effective thermal conductivity of snow with increasing snow bulk density is well documented (refer to Fig. 2.9). The physical model reported here computes snow effective thermal conductivity to also increase with increasing temperature. The direction of the temperature dependence of snow thermal conductivity is surprising considering that ice thermal conductivity decreases with increasing temperature. As reviewed above, observational studies are inconclusive as to the effect of snow temperature on effective thermal conductivity (e.g., Pitman and Zuckerman, 1967; Sakazume and Seki, 1978; and Sturm and Johnson, 1992). The rise in k_s with increasing snow temperature is attributed to the geometric arrangement of the snow matrix in the original Pitman and Zuckerman model. Snow is represented as an assemblage of conductors, which are assembled in both parallel and series. The cylindrical contacts between ice spheres impede heat flow and, because resistance is proportional to the radius of the conducting cylinder, resistance will increase as the ice cylinder radius decreases. Pitman and Zuckerman (1967) observed the ratio of bonding area between snow crystals to the crystal size to decrease with decreasing temperature. Furthermore, the effective thermal conductivity of air in the pore space rises with increasing temperature (Fig. 2.11). These two factors contribute to our observed temperature dependence using the geometric arrangement adopted in the original Pitman and Zuckerman (1967) model.

2.4.3.3 Turbulent Heat Fluxes and Momentum Transfer

Turbulence and Atmospheric Stability

Flow in the surface boundary layer is virtually always turbulent and the turbulence is supported by shear production (forced convection) and/or buoyant production (free-convection) (Arya, 1988). Mass, as well as any other scalar properties of an air parcel (enthalpy, humidity, CO₂, etc.) are transferred *via* turbulent eddies.

The likelihood of buoyancy is described by atmospheric stability⁹ (Oke, 1987). The atmosphere is termed *unstable* if it is conducive to free convection (i.e., in the case of cold air overlying warm air) and *stable* if it inhibits vertical motion (i.e., in the case of warm air overlying

⁹ Atmospheric stability may be viewed as the relative tendency for an air parcel to move vertically (Oke, 1987).

cold air). If the movement of a parcel of air is neither encouraged nor discouraged the atmospheric state is neutral. Neutral stability is rarely observed in the lower atmosphere (Arya, 1988). The Richardson Number (Ri) provides a means of categorizing the atmospheric stability as unstable (Ri<0) or stable (Ri>0), where:

$$Ri = \frac{g}{\theta} \frac{d\theta/dz}{\left(\frac{du}{dz}\right)^2}, \quad (2.38)$$

and g is the acceleration due to gravity, θ is the potential temperature, u is the horizontal wind speed and z is the height above the surface. Neutral stability is assumed when Ri is between ± 0.01 (Oke, 1987).

Turbulence is entirely dependent on shear production in a stably-stratified boundary layer. The flow of sensible heat from the atmosphere to the surface during these periods is expected to be small because vertical eddy transport is suppressed (Arya, 1988). A consequence of suppressed vertical mixing is steep temperature, wind speed and humidity gradients. Radiative cooling over snow and ice enables a stable boundary layer to be maintained at higher wind speeds than would normally be observed for other surfaces (Overland and Guest, 1991). Because the stable BL is less energetic, it responds slower than convective boundary layers to changes in surface characteristics (Overland and Guest, 1991; McBean 1986) and therefore, requires a large fetch before a distinct surface layer develops which is at equilibrium with the underlying surface.

Micrometeorological Techniques

Two commonly adopted methodologies for the derivation of the turbulent fluxes in the surface layer are the eddy fluctuation (or eddy correlation) technique, and the profile or (flux-gradient) technique. In the eddy fluctuation method, the covariance of the instantaneous properties (i.e., temperature, moisture, CO₂, vertical velocity, etc.) of eddies in the air are measured along an atmospheric path and related to an average turbulent flux (i.e., sensible heat, latent heat, CO₂, etc.). In the profile method, fluxes are inferred from the observed profile of atmospheric properties in the surface layer. Any introductory text on microclimate or micrometeorology will

provide a basic description of each approach (e.g., Oke, 1987; Arya, 1988). Only an aerodynamic method, the flux-profile technique, is described here.

Flux-Profile Technique

The turbulent shear stress, sensible heat flux and latent heat flux can be related to the gradients of wind speed, potential temperature and specific humidity, viz.:

$$\tau = \tau_o = \rho K_m \frac{\partial u}{\partial z} \quad (2.39)$$

$$Q_H = Q_{Ho} = -c_p \rho_a K_H \frac{\partial \theta}{\partial z} \quad (2.40)$$

$$Q_E = Q_{Eo} = -\rho L_{e,s} K_E \frac{\partial q}{\partial z} \quad (2.41)$$

where the subscript, o, refers to the respective surface value and K is the turbulent transfer coefficient ($m^2 \cdot s^{-1}$) for momentum, heat and vapour (subscripts m, h, and e). The equations, as written, describe an upward flux as positive. This is the accepted convention adopted by the micrometeorological community, but it does not make intuitive sense when examining the energetics of the near-surface volume. In this section, the 'positive-up' convention is used to be consistent with the reference texts, but during the computation of the fluxes and in the subsequent analyses, a positive turbulent flux is directed toward the snow/ice surface. The equations (Eqs. 2.39 to 2.41) are usually solved using empirical relations that assume similarity between the transfer coefficients under neutral stability. Similarity theory applies within the constant flux layer and assumes a horizontally homogeneous surface and stationary flow conditions. The condition of uniformity means that only vertical transport takes place and the independence of time infers that the vertical flux is constant with height. The requirements of horizontal uniformity and time independence should be reasonably well met over sea ice where changes in roughness remain small (Smith et al., 1983; Andreas and Murphy 1986).

There remains a great deal of uncertainty pertaining to the validity of the similarity assumption. Dyer (1974) suggests the assumption is acceptable, however, there is evidence indicating that K_H/K_M is not equal to one at neutral stability (Businger et al., 1971; King 1990; Granger 1977). Granger (1977) showed the ratio of K_v/K_H to be close to 0.5 during both stable and unstable atmospheric states. Lang et al., (1983) observed the ratio of K_v/K_H to approach 1, but

the ratio decreased to 0.65 with increasing stability. These results are not unexpected considering that moisture will not significantly affect the buoyancy of a parcel of air (Brutsaert, 1982).

The basis for the flux-profile technique is the observation that the gradients of scalar properties in the surface layer are logarithmic functions of height under neutral atmospheric conditions. For example, the increase in mean wind speed at height (z) above a rigid surface is closely approximated by:

$$\frac{du}{d \ln z} = \frac{u^*}{k} \quad (2.42)$$

where u^* is the friction velocity (ms^{-1}), k is von Karman's constant and z_0 is the aerodynamic roughness length (m). von Karman's constant is non-dimensional and has been determined experimentally to fall between 0.35 and 0.47, but is usually assigned a value of 0.41 (Brutsaert, 1982). Equation 2.42 is also referred to as the dimensionless wind speed gradient.

For non-neutral conditions, the wind profile (and the vertical distribution of other scalar properties) departs from a log-linear form as a result of atmospheric stability. The log-linear form can be extended beyond the neutral case by incorporating dimensionless stability functions. Both a gradient and an integrated form of stability correction appear in the literature as functions of either the Richardson number, or the Monin-Obukhov (M-O) stability parameter. Monin and Obukhov (1954) provided a framework whereby, in the surface layer, the dimensionless gradients of atmospheric properties are functions of a stability parameter, ξ (Arya, 1988). If the similarity assumption is applied, the turbulent transfer coefficients in Eqs. 2.39 to 2.41 can be transformed into dimensionless similarity functions of the Monin-Obukhov dimensionless stability parameters, $\Phi_{M,H,E}(\xi)$, where the subscripts, M, H, E, apply to momentum, sensible heat and vapour transfer. These functions are referred to as the gradient forms of Monin-Obukhov 'universal' stability functions and are functions of the dimensionless wind shear, dimensionless temperature gradient and dimensionless humidity gradient:

$$\left(\frac{kz_m}{u^*} \right) \left(\frac{\partial U}{\partial z} \right) = \Phi_m(\xi), \quad (2.44a)$$

$$\left(\frac{kz_m}{\theta^*} \right) \left(\frac{\partial \theta}{\partial z} \right) = \Phi_H(\xi) \quad (2.44b)$$

$$\left(\frac{kz_m}{q^*}\right)\left(\frac{\partial q}{\partial z}\right) = \Phi_V(\xi), \quad (2.44c)$$

where u^* , θ^* , and q^* are scales of velocity (friction velocity, $m \cdot s^{-1}$), temperature ($^{\circ}C$), and humidity ($kg \cdot kg^{-1}$) (Arya, 1988). z_m is the geometric mean height. The stability functions are related to the transfer coefficients of Eqs 2.39 to 2.41:

$$\frac{K_H}{K_M} = \frac{\Phi_M(\xi)}{\Phi_H(\xi)} = \frac{K_E}{K_M} = \frac{\Phi_M(\xi)}{\Phi_E(\xi)}. \quad (2.45)$$

With the similarity assumption, the scales of velocity, temperature and humidity can be used to relate the energy fluxes Q_H , Q_E , and momentum flux, τ , to the mean gradients of wind velocity:

$$\tau = \tau_o = \rho_a u^{*2} = \rho_a k^2 \left(\frac{du}{d \ln z}\right)^2 \Phi_M^{-2} \quad (2.46)$$

$$Q_h = Q_{ho} = -\rho_a c_p u^* \theta^* = -\rho_a c_p k^2 \left(\frac{du}{d \ln z}\right) \left(\frac{d\theta}{d \ln z}\right) (\Phi_H \Phi_M)^{-1} \quad (2.47)$$

$$Q_E = Q_{E0} = -\rho_a L_{e,s} u^* q^* = -\rho_a L_{e,s} k^2 \left(\frac{du}{d \ln z}\right) \left(\frac{dq}{d \ln z}\right) (\Phi_V \Phi_M)^{-1}, \quad (2.48)$$

where:

$$\frac{d}{d \ln z} = z_m \frac{d}{dz}. \quad (2.49)$$

Paulson (1970) presented an integrated form of the gradient stability functions. The reader is referred to Paulson (1970) or Arya (1988) for details.

Monin-Obukhov Similarity Functions

Empirical solutions to the similarity functions (Eq. 3.53 a to c) are available as expressions of Monin-Obukhov's dimensionless stability parameter, ξ :

$$\xi = \frac{z}{L} = -\frac{kz g Q_H}{\rho_a C_a \theta u^{*3}}, \quad (2.50)$$

where the Obukhov scaling length, L (m), is defined as

$$L = -\frac{\rho_a C_a \bar{\theta}_a *^3}{kg Q_H} \quad (2.51)$$

The negative sign is included so that ξ has the same sign as Ri (Recall, Ri is positive for a stable boundary layer and negative an unstable boundary layer). The Obukhov length (its absolute value) represents the thickness of the near-surface layer in which the shear production is dominant.

Different formulations for the stability functions appear in the literature. The most commonly used coefficients are those presented by Dyer and Hicks (1970) for an unstable atmosphere and Hicks (1976) for a stable atmosphere:

unstable ($\xi < 0$)

$$\Phi_M = (1 - 16\xi)^{-\frac{1}{4}}, \quad (2.52a)$$

$$\Phi_H = (1 - 16\xi)^{-\frac{1}{2}}, \quad (2.52b)$$

stable ($\xi \geq 0$)

$$\Phi_M = (1 + 5\xi), \quad (2.52c)$$

$$\Phi_H = (1 + 5\xi), \quad (2.52d)$$

The functions have been more thoroughly tested under unstable conditions, but are probably adequate for moderately stable, and unstable atmospheres ($-2 < \xi < 1.5$) (Brutsaert, 1982).

The heat transfer process under stable conditions is still rather poorly understood. Under extreme stability, turbulence may cease altogether so that any vertical heat transfer is accomplished by molecular transport process, or accomplished during periods of intermittent turbulence (Carson and Richards, 1971). Under periods of strong stability, the stability functions ($\Phi_{M,H,V}$) are thought to range between 6 and 12 (King, 1990). Hicks (1976) observed the functions to asymptote near 10. Under these conditions the turbulent exchange is small and the exact value is of little consequence.

The M-O theory does not consider intermittent turbulence, nor does it address radiative transfer within the near surface air. This last point may be a source of some error over snow and ice. Several authors have observed temperature profile anomalies that can be associated with the radiative heating of the air in close proximity to the snow surface. Yen (1993) reviews this

phenomenon. The anomalies include reversals in the temperature profile within the lower 50 cm of the atmosphere, regardless of whether the snow is above or below 0°C. The temperature structure may be affected by the near surface humidity profile. Under intense insolation, water vapor subliming from the snow surface enhances the vapour concentrating in the near-surface air beyond that of the air aloft. The lower layer both absorbs more solar radiation, and emits more terrestrial radiation than the overlying air. Finally, the flux-profile technique assumes a rigid surface. Mass flow of snow may occur downstream of the airflow. Because of these issues, specific to snow surfaces, empirically-derived stability formulations that have been developed for terrestrial surfaces, may not apply over snow and ice.

2.5 Summary

The macro-scale climate of the Arctic region is largely controlled by the annual cycle of solar radiation. Properties of the ice (and snow) surface act to maintain the region in a state of net energy deficit over the annual cycle. Surface-based cooling encourages the formation of cold, dry and predominately stable air mass over the winter period, with perpetual northerly airflow. In the spring and summer the region is affected by warmer maritime air. The northward retreat of the *Arctic Front* is marked by an increase in cloud cover and more frequent incursions of southerly air. Cyclones rarely enter the Arctic Basin but frequently affect the southern extent of the CAA in the spring and summer.

The snow and sea ice undergoes a seasonal evolution in response to the seasonally changing climate. Sea ice evolves through several distinct forms over the annual cycle and each form can differ in thickness and physical make-up. Snow distribution is highly variable in the Arctic. Once deposited, snow undergoes rapid metamorphism.

In some climatic zones sea ice may survive a summer melt. This multi-year ice is typically thicker and less saline than first year sea ice. It possesses an undulating surface topography as a consequence of differential melt during the summer season. Both snow and sea ice is horizontally non-uniform, but also exhibit varying morphology and properties in the vertical dimension.

Radiation and heat exchange processes at the surface are linked with processes that operate within the snow volume and the ice surface. The snow and sea ice are both translucent to solar radiation and the proportions of incident solar radiation transmitted and reflected are

determined by the volume's albedo and extinction coefficient. Both can be highly variable over the course of the spring season. A debate is ongoing regarding the role of solar radiation as a heat source for the snow interior. Radiation absorbed at depth will contribute to the enthalpy of the volume, but will not be readily available for heat exchange at the surface.

The thermal properties of snow and sea ice (k and C_p) are strongly affected by salt content and temperature; particularly at temperatures above -8.2°C . In both snow and sea ice the thermal conductivity in Fourier's heat conduction equation is replaced by an effective thermal conductivity to consider the potential for heat flow through processes other than strictly thermal conduction.

The magnitude of the turbulent fluxes in energy balance studies over snow and ice is traditionally considered secondary to the radiation balance. Their role depends on both the nature of the surface and the atmosphere. The fluxes are highly dependent upon ice thickness during the cold seasons. An aerodynamic technique is presented. There remains a degree of uncertainty regarding the applicability of the technique over snow and ice. The uncertainty relates to the appropriateness of empirically derived stability corrections and with assumptions regarding the absence of heat transfer *via* the absorption and emission of radiation between levels of the near surface atmosphere.

The role of the energy flux terms is fairly well understood over the perennial sea ice of the central Arctic Basin. Our understanding, however, is limited to measurements on drifting stations which are representative of only a small proportion of the *icescapes* of the Arctic Ocean and surrounding seas.

Studies over snow and ice surfaces have shown that the characteristics of the surface and atmospheric affect both the available energy to the surface and the manner in which this energy is partitioned among the terms of the energy balance. Our understanding the relationship between sea ice age and the heat transfer processes is largely based on analyses with simple thermodynamic models. Some radiation and heat transfer processes are shown to differ between the two mature sea ice types (FYI and MYI) of landfast sea ice, however, the extent of the difference and a temporal component to any difference is not well defined.

Recent sensitivity analyses with a sea ice model have indicated linkages between atmospheric forcing, the surface energy balance and the surface state. The air temperature, downwelling long-wave radiation and the surface morphology during the spring period are the major

factors affecting the annual sea ice balance. These sensitivities were determined from an uncoupled ASO system, and pertain to annual averages, and therefore may not be accurate.

Large interannual variations have been observed at the onset of melt within any region but the mechanism(s) triggering the melt onset are not known with any certainty. Researchers have speculated that: (i) the heat influx from southerly latitudes, or from warmer terrestrial surfaces, (ii) long-wave warming effect of clouds, and (iii) increased global radiation under clear-sky conditions, are potentially effective processes for initiating snow melt. These processes occur in tandem during the spring period. A challenge remains to identify which (or which combination) of these is most effective at triggering the melt process. Such information would allow us to anticipate the response of the ice balance in the SSIZ to a changing environment.

Two broad themes of investigation are associated with the major sources of uncertainty identified above. They include an analysis into the nature of the seasonally evolving energy balance over sea ice types outside of the perennial ice zone of the central Arctic basin, and an analysis into the environmental controls over the energy balance components. These research themes are consistent with the objectives identified in Chapter 1 and form the basis of Chapters 6 to 8.

CHAPTER 3: EXPERIMENTAL SITES AND INSTRUMENTATION

3.1 Introduction

In this chapter I introduce the study region and the experimental sites, complete with a description of the instrumentation and experimental methods.

3.2 Physical Setting

This study is performed at sites on sea ice within a 100 km radius of Resolute NT (74° 45'N, 94° 59'W). Resolute is situated on the south coast of Cornwallis Island near the geographic centre of the Queen Elizabeth Islands of the CAA (Fig. 3.1). To the east and north of the settlement are rolling hills rising to approximately 250 m from sea level. The surface deposits are of alluvial and coastal origin. The settlement serves as a transportation centre for air traffic in the CAA. Refuse is burned at a dump situated several kilometres northwest of the community, and electricity is generated by diesel-powered generators. Neither the airstrip nor roads are paved; consequently, when not snow or ice-covered, plane and automobile traffic create considerable amounts of dust.

There is a general flow of water from the Arctic Ocean eastward to Baffin Bay through the CAA (Gorman, 1988). Only the upper layer of the water (approximately the upper 150 m) enters Barrow Strait, and it is characteristic of Arctic Ocean water, i.e., cold (-1.9 to 0°C) and of low salinity (32 parts per thousand, ppt) (Gorman, 1988). Bathymetry of Barrow Strait ranges between 100 to 300 m in depth, falling steeply off the coast of Cornwallis Island. Waters within Resolute Passage are less than 200 m deep (Gorman, 1988). The current velocities do not exceed 14 nautical miles per day (Gorman, 1988).

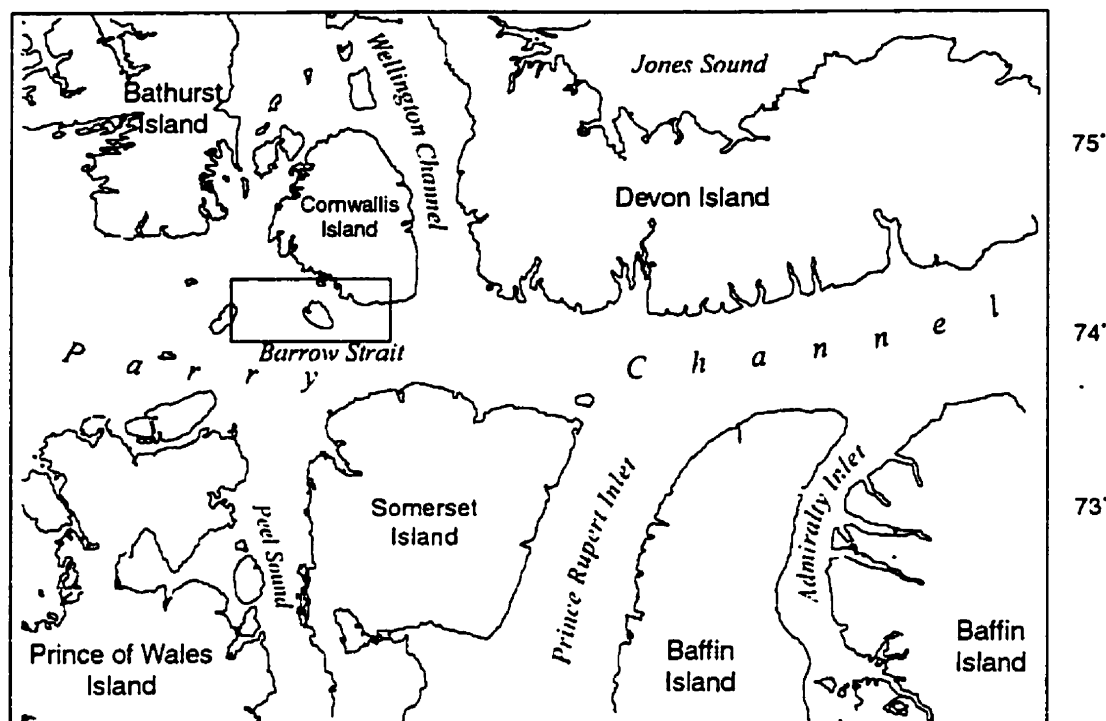


Figure 3.1 Location of the study region relative to the water bodies and islands of the Canadian Arctic Archipelago.

The sea ice regime of Resolute Passage, McDougall Sound and Western Barrow Strait fall under Gorman's (1988) McDougall Sound and Central Barrow regime. He used 'regime' to define a region where ice has definable characteristics related to pattern of break-up, movement and pattern of freeze-up. These regimes are characterized by smooth, level first-year ice, with small areal proportions of multi-year ice (less than 3%). As the ice moves into Barrow Strait from McDougall Sound and Resolute Passage, it becomes heavily ridged. FYI ice thickness at Resolute Bay is typically 1.6 to 1.8 m by May, however ice keels and ridging are prevalent in the channels because of strong ocean currents and high winds during consolidation (Gorman, 1988).

Freeze-up begins in mid-September in the bays and narrow channels, and proceeds seaward (eastward) throughout the winter forming an ice edge (A to F in Fig. 3.2) across Barrow Strait or Lancaster Sound. Formation of the Griffith Island ice bridge ("B" in Fig. 3.2) occurs between late October to late February (Gorman, 1988). Depending on the winter, the final

consolidation in February or March may leave the ice edge as far west as Resolute, or as far east as Bylot Island. The final consolidation in February-March occurs at "C" about 50% of the time (of a 22 year period) and around 20% of the time at "B" (Dickens, 1990). Only in 4% of the observations did spring consolidation extend to Bylot Island, "F". Typically, the ice west of the edge is relatively uniform, with the occasional lead, and increases in thickness throughout the winter with a general east-west thickness gradient.

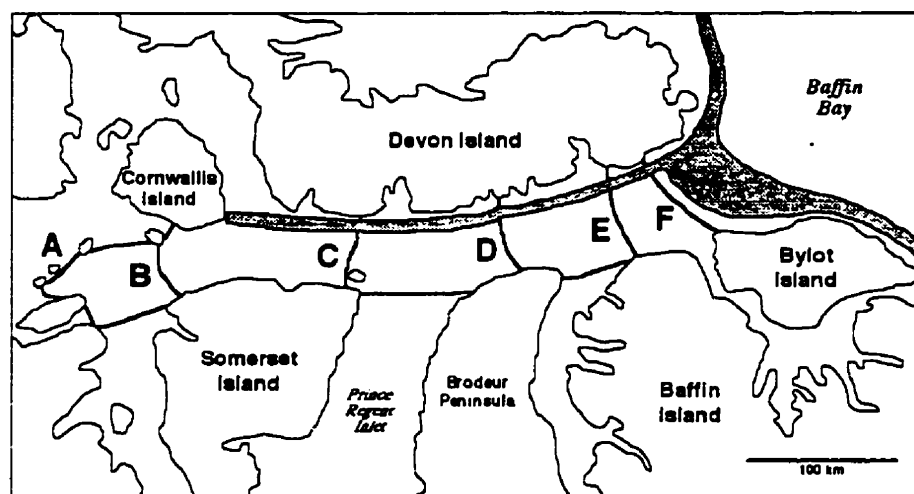


Figure 3.2 The position of the ice edge in Lancaster Sound-Barrow Strait in winter. Letters define the observed extent of the ice edge and shaded areas denote polynya and shore leads. Adapted from Gorman (1988) and Welch et al. (1992).

The ice breaks away sequentially from its eastern terminus in the spring (Gorman, 1988). Break-up occurs at Resolute around 20-July; however, this date can vary depending on the location of the winter ice edge (Welch et al., 1992). Ice reduction in the Barrow Strait region is largely through *in-situ* melt, but is subject to a slow eastward drift (Gorman, 1988).

The general climate (i.e., synoptic activity, precipitation, temperature, etc.) of Resolute Bay and the central Barrow Strait region is representative of the region surrounding Cornwallis, Bathurst and Prince of Wales Islands (Maxwell, 1980).

At 74° N latitude sun is continually below the horizon between 9-November and 3-February, and continually above the horizon between 27-April and 17-August. In the winter there

is an almost complete dominance of cA air, except for rare penetrations of mA air (cold and moist) from the eastern Baffin Bay region (Maxwell, 1980). Winter conditions are typically cold, dry, and clear. In the summer the air masses affecting the central islands are more maritime than continental.

3.3 Experimental Sites

Data used in this investigation were collected as part of the SIMMS experiments during the 1992, 1993, and 1995 spring field campaigns. Detailed measurements of the physical characteristics of the snow and sea ice were made in conjunction with measurements of the surface's microclimate. Measurements were taken in the vicinity of research sites (microclimate stations), which were distributed in the Resolute Passage region during SIMMS'92 and SIMMS'93, and in Barrow Strait (approximately 8 km east of Lowther Island) during SIMMS'95 (refer to Fig. 3.3). Experimental sites (Table 3.1) were established on both first-year and multi-year sea ice: FYI'92, FYI'93, MYI'93, FYI'95 and MYI'95. Both hummock ice (hk), and melt pond (mp) ice surfaces were instrumented on the sample multi-year ice floes.

Table 3.1 Coordinates of microclimate stations and ice thickness ranges over the experimental periods. A day of year calendar is provided as Appendix 1.

	<i>FYI'92</i>	<i>FYI'93</i>	<i>MYI'93</i>	<i>FYI'95</i>	<i>MYI'95</i>
Latitude (°N)	74.68	74.59	74.58	74.57	74.57
Longitude (°W)	95.58	94.71	94.78	96.94	97.05
Experiment Length ^a (day ^b)	107 to 175	111 to 171	111 to 171	108 to 169	108 to 169
Ice Thickness (m)	1.4 - 1.6	1.3 - 1.4	4 - 6	1.7 - 1.9	2.5 - 3.5

^a approximate start/stop dates;

^b day denotes Julian Day

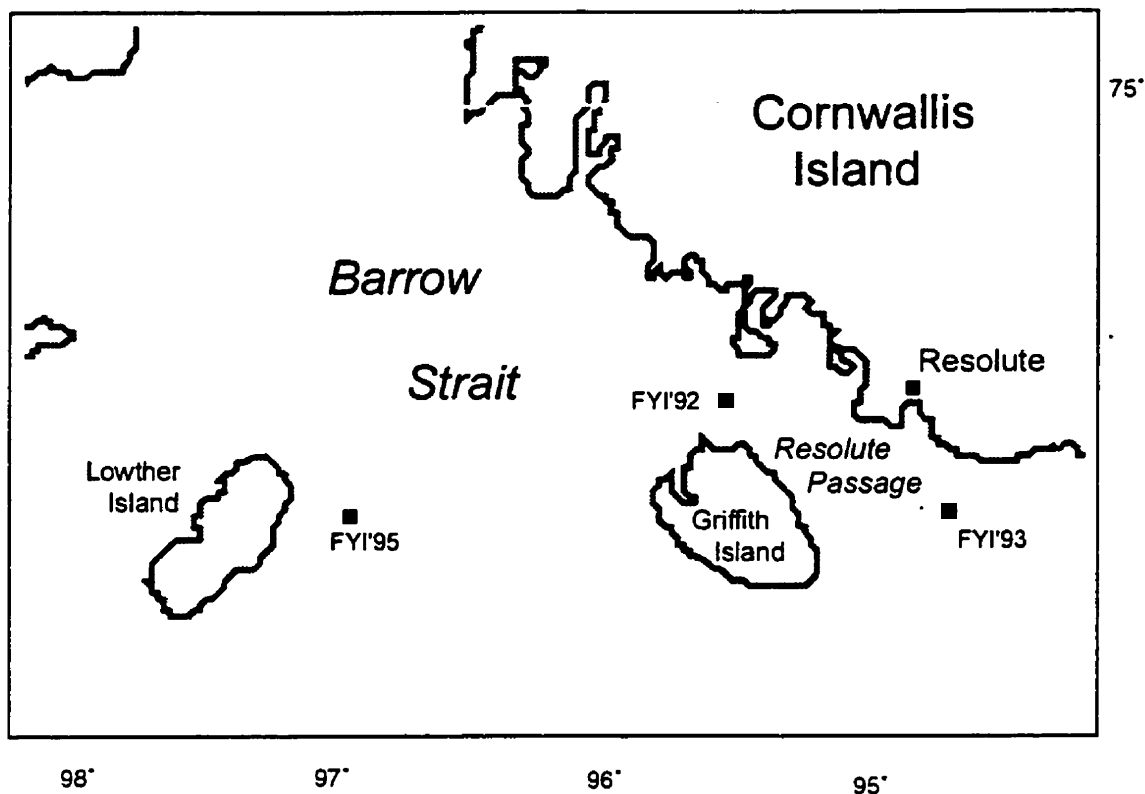


Figure 3.3 Location of first-year sea ice research sites in Barrow Strait.

3.3.1 Overview of the Snow and Sea Ice Conditions at the Experimental Sites

Resolute Passage consolidates in a step-like fashion with the northern part of the passage consolidating first (Gorman, 1988). The Lancaster Sound ice edge formed at Prince Leopold Island (i.e., position 'C' in Fig. 3.2) during each of the three spring seasons. The ice conditions in Resolute Passage during the winters of 1992, 1993, and 1995 may be interpreted from radar images of the study regions which are provided as Figs. 3.4 to 3.6. Fig. 3.4 (SIMMS'92) was acquired by the airborne STAR-2¹⁰ and represents ice conditions on January 17, 1992. The image

¹⁰ An X-Band (9.8 Ghz), horizontal transmit-horizontal receive polarization, HH, synthetic aperture radar installed on a Challenger aircraft.

shown by Fig. 3.5a (SIMMS'93) was acquired by the active Synthetic Aperture Radar¹¹ (SAR) onboard the European Resource Satellite (ERS-1) and represents sea ice conditions as of February 14, 1993. Fig. 3.6 (SIMMS'95) was acquired on March 5 by the SAR on board the ERS-1. Dark tones in the radar images represent flat first year sea ice, while rough ice, multi-year floes and rubble ice appear as varying shades of textured grey tones.



Figure 3.4 Image generated by the airborne STAR-2 (January 17, 1992) of the Resolute Passage area.

¹¹ C-Band (5.3 Ghz), vertical transmit-vertical receive polarization, VV, with 25-30 m resolution.

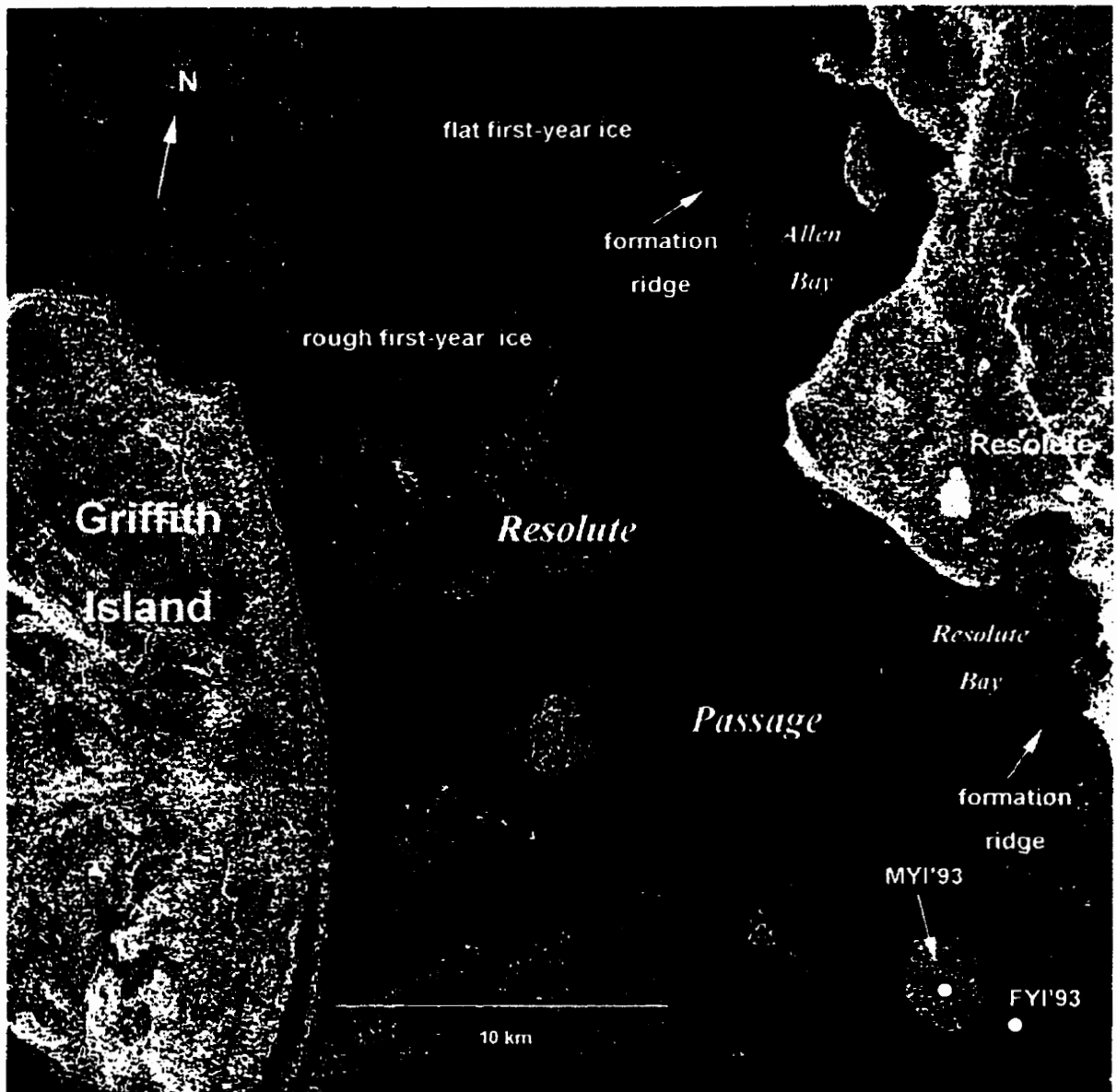


Figure 3.5 Image generated from ERS-1 data (February 14, 1993) of the Resolute Passage area.

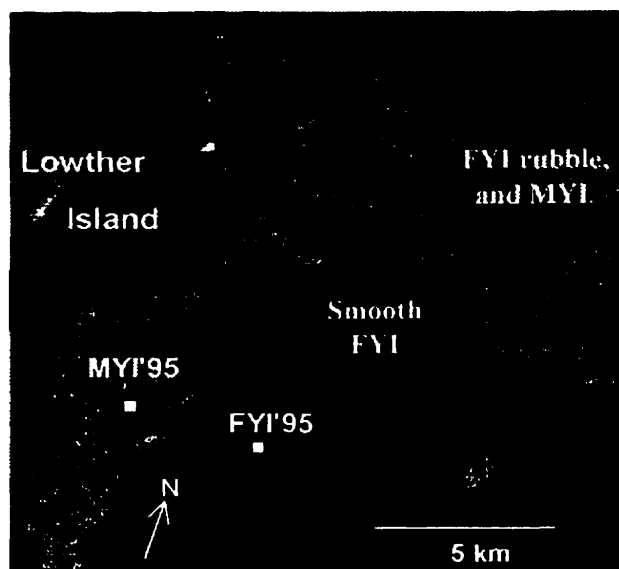


Figure 3.6 Image generated from ERS-1 data (March 5, 1995) of the SIMMS'95 research area.

In 1992 the ice in the passage was mainly smooth first-year ice which consolidated some time in late December of 1991. In 1993 the sample MYI floe and FYI site were situated in close proximity on a consolidation zone that formed on the southern side of the Griffith Island ice bridge (Fig. 3.5). FYI'95 was situated on uniform sea ice that had consolidated by mid January 1995. The region was bordered to the west, north and east by a rough conglomerate sea ice consisting of both FYI and MYI floes (Fig. 3.6). MYI'95 was located on a multi-year ice floe situated within a much larger field of conglomerate ice floes.

The first-year ice differed in thickness among the three FYI experiments (Fig. 3.7). Ice was thickest at FYI'95 (ice thickness ranged between approximately 1.7 to 1.9m) and thinnest during FYI'93 (ice thickness ranged between approximately 1.3 and 1.4m). The two sample MYI floes incorporated into this study also differed with respect to ice thickness and hummock development. In 1993 the youngest multi-year ice of the conglomerate floe averaged 2.7 m thick and typically had a small amplitude and large frequency of hummocks and inter-hummock depressions. The next oldest component of the floe averaged 4.7 m in thickness, with pronounced

hummock, inter-hummock depressions. The research site was situated on the oldest portion of the sample floe. The sea ice was greater than 6 m in thickness and had well defined hummock and inter-hummock depressions. The hummock crests were flattened and the snow cover over the crests was generally thin (0 to 5 cm). The sample floe during the 1995 experiment, on the other hand, ranged between 2.5 and 3.5 m in thickness. The thinner ice thickness corresponded to the melt pond depressions. Hummocks occupied approximately 65% of the MYI surface area during both SIMMS'93 and SIMMS'95 (Piwowar et al., 1995; Serreze et al., 1993a; Misurak, 1995).

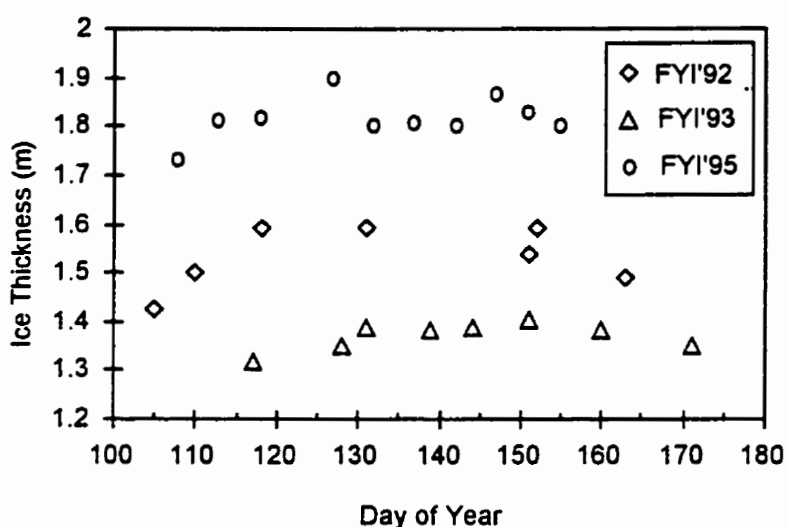
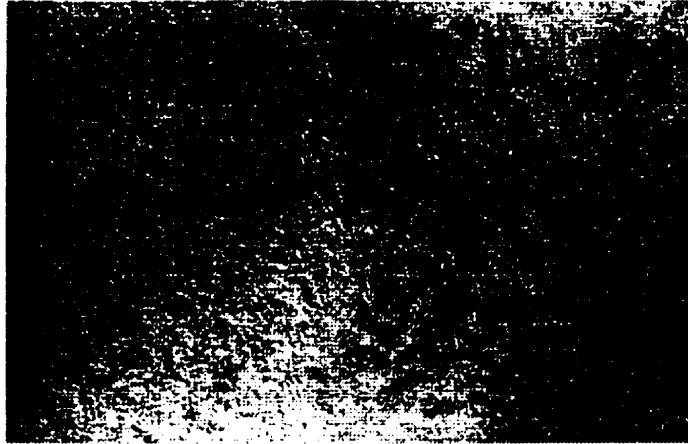


Figure 3.7 Record of ice thickness at the first-year sea ice sites.

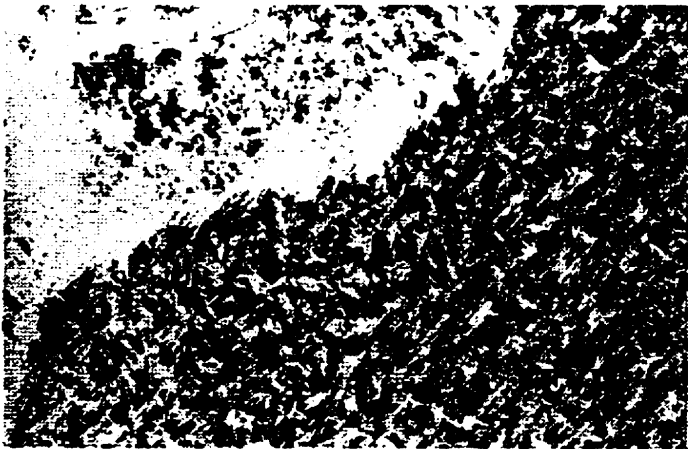
The transformation of the surface morphology from its winter state (i.e., cold dry snow over cold sea ice and air temperatures less than -5°C) to the final stages of advanced melt is shown in Fig. 3.8. Approximately 50% of the first-year sea ice surface was flooded by the end of the 1993 and 1995 experiments, while puddles covered between 30% and 35% of the surface area over multi-year sea ice. By way of contrast, the degree of surface flooding was only between 10 and 20% by the end of FYI'92, which ironically was the only experiment to extend into the summer season.



Day 158
Time 1745
Alt. 300 m



Day 161
Time 0800
Alt. 100 m



Day 167
Time 1230
Alt. 300 m

Figure 3.8 Aerial photographs chronicling the surface transformation from pre-melt to advanced melt conditions. Photos were taken during SIMMS'95.

The physical properties of the snow are described in Chapter 4. The sea ice bulk density and salinity for the upper 10 cm of the sea ice at the respective sites are provided in Tables 3.2 and 3.3. Salinity was near zero for both the MYI meltpond and hummock ice.

Table 3.2 Summary of near surface (upper 10 cm) sea ice density (kg m^{-3}) during the SIMMS experiments. Statistics were performed on data provided by Shokr and Sinha (1993, 1995a,b).

	FYI'92	FYI'93	MP'93	HK'93	FYI'95	MP'95	HK'95
Average	898.2	887.8	892.9	815.4	914.8	916.0	824.0
St. Dev.	11.3	16.2	19.9	18.8	7.2	6.5	6.2
No. Cores	5	1	3	1	2	1	1
No. Sample	15	5	15	5	10	5	5

Table 3.3 Summary of near surface (upper 10 cm) FYI sea ice salinity (ppt) during the SIMMS experiments. Statistics were performed on data provided by Shokr and Sinha (1993, 1995a, and b).

	FYI'92	FYI'93	FYI'95
Average	8.48	9.42	9.8
St. Dev.	3.10	2.4	1.1
No. Cores	5	3	2
No. Sample	15	15	10

3.3.2 Microclimate Stations and Instrumentation

3.3.2.1 Overview

A summary of the microclimate data set is provided in Appendix 3. Temperatures of the snow cover, upper sea ice, and lower atmosphere were measured in profile at locations within each site. Four to five sensors for wind speed and temperature were arranged in profile on towers¹² devoted to the measurement of temperature and wind speed (Fig. 3.9). These towers were approximately 10 m in height during SIMMS'92 and SIMMS'93, and approximately 5m in height during SIMMS'95. Air temperature towers were made up of triangular scaffold tower, 12 inches across (TV antennae towering), while wind towers consisted of guyed sections of aluminum tubing (three inches in diameter). The mast was hinged at its base so it could be lowered to allow periodic

¹² Anemometers and air temperature sensors were placed on the same tower during FYI'93.

access to the anemometers. The TV antennae tower allowed direct access to the sensors. The day to day height of the lowest sensor in profile from the snow surface was recorded.

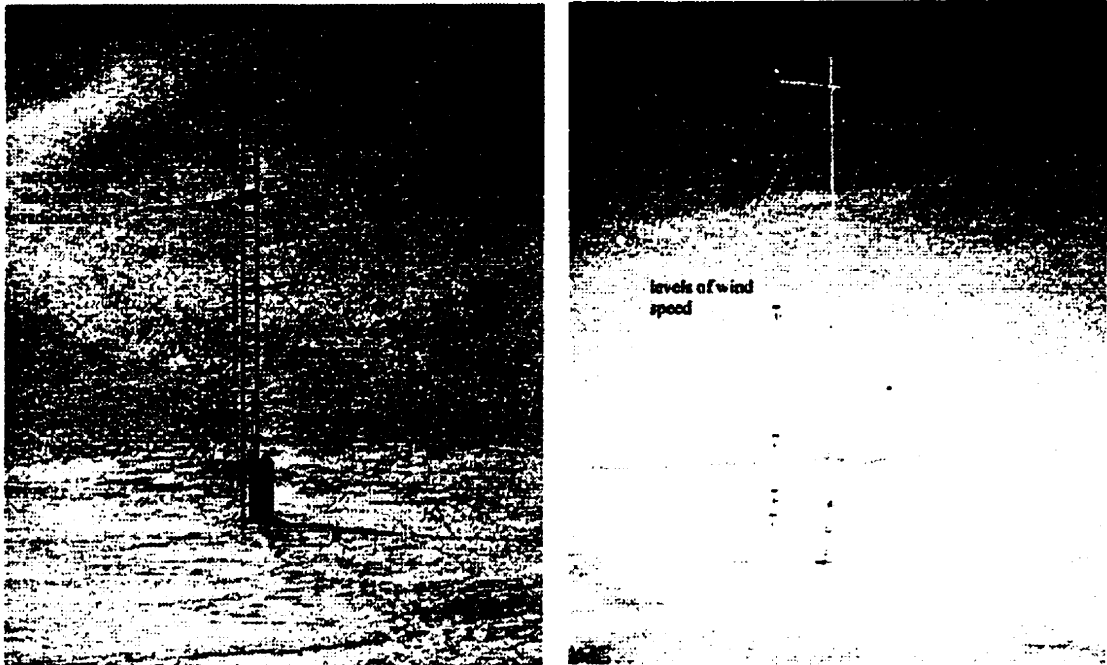


Figure 3.9 Typical principal energy balance and wind tower used during the SIMMS experiments. Tower heights are approximately 10 m.

All measurements were logged by Campbell Scientific dataloggers (models CR21X and CR10). The data loggers were housed in thermally insulated enclosures ('doghouses'). Signals from the snow and sea ice thermocouples were either logged directly by CR21X datalogger (using panel temperature as thermocouple reference) or were channeled through a multiplexer (Campbell Scientific model AM30 and AM416). Thermistors (Fenwall UUA 41J1) were attached flush to the multiplexer wiring panel to provide a temperature reference for the multiplexer panel. A multiplexer was either stored in the 'doghouse' at each site or was housed in an independent insulated enclosure near to the snow sensor arrays. All air temperatures were recorded directly by a CR21X. Sensor specifications are provided in Appendix 3. An estimate of the precision and

accuracy associated with the temperature and wind speed measurements are reviewed in Appendix 4.

3.3.2.2 Snow Temperature

Snow temperature was measured at increments extending from the snow/ice interface to the snow surface at the experimental sites during each of the three years. The number and positioning of sensors are provided in Appendix 3. Each sensor consisted of a thermocouple junction that was epoxied into the tip of a brass tube. Sensors were fixed at predetermined levels to a 2.5 cm x 3.8 cm wooden stakes (Fig. 3.10). Both the leads and sensor assemblies (termed sensor arrays) were painted white. The sensor arrays were installed into the northerly exposure of the exposed face of a snow pit excavated in the vicinity of the instrument towers at each research site. An effort was made to pack the snow evenly during the backfilling process and the sensor leads were buried to minimize thermal gradients along the cables. The length of each sensor lead was typically less than 10 m. Snow temperature was measured within both the deep snow of the melt pond depression and within the shallower snow of the hummock shoulder at the MYI sites.



Figure 3.10 Typical snow temperature sensor assembly used during the SIMMS experiments.

3.3.2.3 Ice Temperature

Ice temperature was measured in profile at levels extending from the snow/ice interface to the sea ice interior (levels are provided in Appendix 3). The measurement apparatus consisted of a series of thermocouple sensors imbedded into holes drilled at increments of a 4.12 cm diameter wooden dowel. The sensor leads lay along a groove that extended the length of the dowel. Each apparatus was immersed in fiberglass resin, then painted white. The sensor rod was inserted into a slightly oversized hole in the sea ice. The fit was snug and shortly after installation the hole's inside diameter constricted, freezing the sensor firmly in place. Snow was backfilled over the sensor immediately after installation. An ice temperature dowel was installed into both a melt pond ice and hummock ice volume at the MYI sites. At the first-year sea ice sites the sensor length never exceeded beyond the upper 70% to 80% of the ice cover to prevent the flooding of the ice surface and snow with sea water. This was not an issue at the MYI sites where ice thickness was substantially greater than the ice temperature dowel.

3.3.2.4 Air Temperature, Wind Speed and Direction

A micro-vane was installed on the air temperature tower at each site. Each air temperature sensor was shaded and ventilated in housings similar in design to those described by Lindroth and Halldin (1990) (Fig. 3.11). Air temperature sensors extended 0.5 m out from the support tower and had a northerly orientation. Anemometers extended 1.4 m from their tower toward the northwest.

The degree to which the sensors within a profile were matched was determined by comparing their output while at the same level. The average difference between the sensor recording the warmest and coldest temperature of the sensors within a profile was $0.105^{\circ}\text{C} \pm 0.05^{\circ}\text{C}$ over a 25-hour calibration period (Appendix 4). Similarly, the average difference between the anemometer recording the slowest and fastest wind speed for anemometers within a profile was $0.242 \text{ m s}^{-1} \pm 0.077 \text{ m s}^{-1}$ over the same 25 hour period.

3.3.2.5 Humidity

Relative humidity (RH) was monitored using CSI temperature and relative humidity probes (model 207) at each experimental. A Vasaila (Model HMP35CF) humidity probe was also used at MYI'95. Each sensor was housed in a Gill (model 41004) radiation shield and mounted

directly on the *mini-tower* at each site, with a northerly orientation. At FYI'92 the lone humidity probe was installed on day 156. Prior to this date no reliable humidity measurement was available.

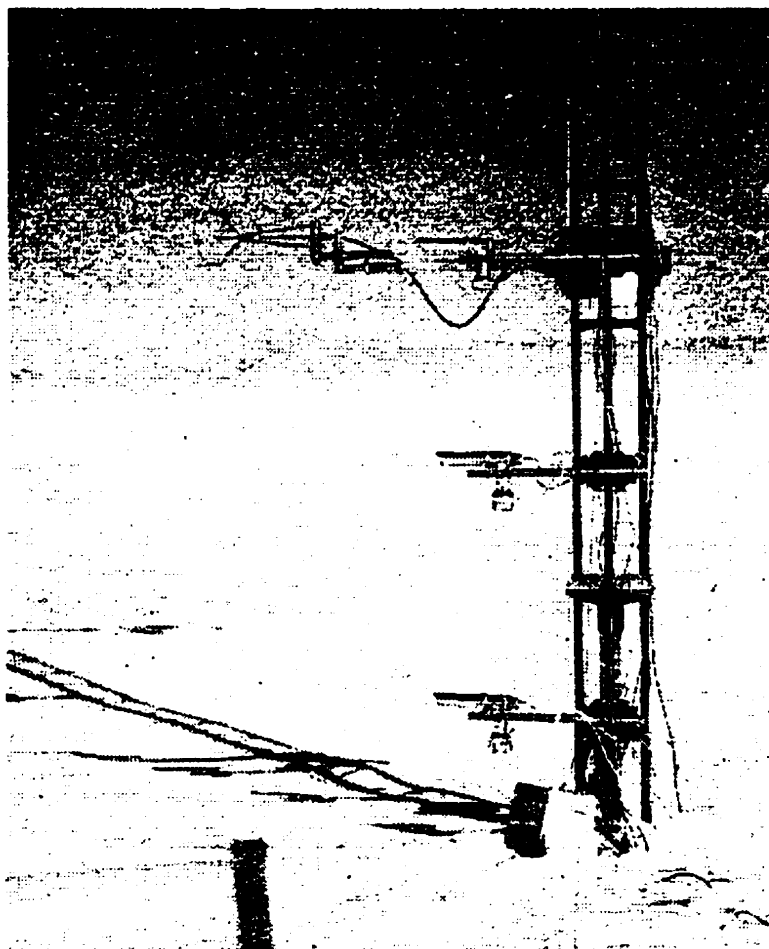


Figure 3.11 Lower three air temperature shields at FYI'92. Also shown in the photo is a one-dimensional sonic anemometer (Campbell Scientific CA27). The sonic anemometer is 2.5 m from snow surface. The box at the base of the tower housed a pump used to aspirate the pyrriometer located at the top of the tower (not shown) during SIMMS'92. Photo was taken in May.

3.3.2.6 Sonic Anemometer and Fine Wire Thermocouple

Sensible heat was sampled periodically using a one-dimensional sonic anemometer with fine-wire thermocouple (Campbell Scientific, model CA27-T, Fig. 3.11) at FYI'92. The midpoint of the sonic path was 2.56 m from the snow surface and the sensor was orientated toward the north-west. Signals were logged by a CR21X using a sampling rate of 10 Hz with sub-interval averaging every 10 minutes. The final 30 minute output represented the weighted average of the three ten-minute sub-intervals.

3.3.2.7 Radiation Measurement

Radiometer heights are provided in Appendix 3. Each radiometer was calibrated prior to the field experiments at the Air Quality Research Branch, Experimental Studies Division (ARQX) of Canada's Atmosphere Environment Service (Downsview, Ontario). The level of the radiometer and the cleanliness of its dome was inspected at least once daily. Radiometers were orientated toward the south.

The Middleton & Co.'s version of Funk's pyrriadiometer (model CN-1) used in the experiments was purged with dry gas (dry air in 1992 and nitrogen in 1993 and 1995). The thin polyethylene domes were replaced every three to four weeks. The sensor was attached to a retractable extension arm and held out approximately 2 m from the principal energy balance tower. (see Fig. 3.12). The calibration multiplier for each pyrriadiometer represented the average calibration of the thermopiles to short-wave and long-wave radiation.



Figure 3.12 Extension arm and mounting bracket, complete with pyrriadiometer (centre), down-facing pyrgeometer (left), and pyranometer (right). Photo was taken in June at FYI'95.

The inverted pyranometer and pyrgeometer were mounted adjacent to the site's pyrradiometer on the air temperature tower during FYT'92. During each of the other experiments both of the inverted radiometers ($L\uparrow$ and $K\uparrow$) were mounted on the smaller secondary tower. The sky-facing pyranometer and pyrgeometer were placed on a platform (1.5 m above the surface), well away from the support towers. The temperature of the instrument housing and its dome were also recorded. A polar bear severely damaged $L\downarrow$ shortly after installation at FYT'95. Consequently, no $L\downarrow$ measure was available for the 1995 experiment.

Quantum sensors (Li Cor model LI-190SA) were installed next to the sky-facing pyranometers at MYT'93 and FYT'95. That radiation in the 0.4 - 0.7 μm wavelength band transmitted through the snow cover was measured by a quantum sensor (Li Cor model LI-192SA) installed at the snow/ice interface at FYT'92, FYT'93, MYT'93 (melt pond) and FYT'95. The process of installing the sensors was similar to the procedure described for the snow temperature sensors. A block of snow was removed, exposing a snow wall. Enough sea ice underlying the exposed face of a snow pit was chiseled away so that the quantum sensor could be inserted beneath undisturbed snow. The snow block was returned to the pit after installation.

3.3.3 Snow Physical Property Sampling Procedures

The snow samples used for the determination of snow density and salinity were extracted from an area adjacent to the snow and ice temperature arrays. Sampling was performed every third day near local solar noon. Samples were extracted from an excavation of approximately 0.5 m^2 during SIMMS'92 and SIMMS'93. Sampling within the pits is performed vertically, without replacement on an exposed pit face at 3 cm increments during FYT'92 and MYT'93 and every 2 cm during FYT'93. Physical property data are also available from sampling grids (approximately 300 m^2 in area) which were established beyond the confines of the experimental sites. The grid sampling involved only the measurement of snow depth, near surface snow density and salinity. Information regarding the snow physical property data set is taken from Reddan (1992) and Misurak (1993, 1995). Six areas were sampled at five day intervals during SIMMS'95. Sampling was conducted at each microclimate station and four locations were distributed over adjacent first-year and multi-year sea ice. Within a pit, samples were extracted from the snow base, mid-depth region and upper region of the snow profiles. Snow depth was measured against a graduated stake

that was frozen at locations within each research site. The extent of the snow profile occupied by hoar crystals is also recorded during the snow pit sampling. The hoar layer was defined on the basis of an abrupt tonal and textural difference between the faceted crystals at the snow base and the overlying snow.

The snow physical properties sampled are summarized in Appendix 3. Snow bulk density was measured using the gravimetric approach¹³ with samples of known snow volume (i.e., 100 cm³ at FYI'92, FYI'95, MYI'93 and MYI'95 and 66 cm³ during FYI'93). The salinity (parts per thousand, ppt) of the melted snow samples was measured using an optical salinometer (Atago). *In-situ* snow wetness (% water by volume) was measured at each level using a capacitance plate (Institute for Experimental Physics, University of Innsbruck, Austria). The accuracy of water volume measurements is considered acceptable for brine-free snow and compared well against other techniques (Barber et al., 1995b). The uncertainty associated with density and salinity measurements is approximately $\pm 30 \text{ kg m}^{-3}$ and ± 0.5 ppt (Barber et al., 1995b).

Replicate sampling was performed in 1993 to assess the variation in density, salinity and wetness within a layer among 5 pits over a 25 m transect. A sample was taken/measured at 2 cm intervals from the snow base. Wetness measurements were limited to the upper 4 cm of the snow volume. The standard deviation of bulk density, salinity and wetness within a layer averaged 23.5 kg m⁻³, 0.88 ppt and 0.64%, respectively. The variation in density is within the uncertainty of the technique, while the variation in salinity, though small, is slightly higher than the resolution of the optical salinometer. Barber et al.,(1995b) contrasted properties among the pit and grid sampling data set and concluded that the pit sampling observations were typical of the snow deposition and thermodynamic conditions experienced over first-year sea ice during SIMMS'92. These results support our belief that the physical property estimates from a pit are consistent and representative of the surrounding snow, at least over a uniform sea ice consolidation. Further details regarding the snow physical property sampling methodology are available from Reddan (1992) and Misurak (1993, 1995).

¹³ Snow density and wetness were measured with a snow dielectric device (Shivola and Tiuri, 1986) at FYI'92 between days 107 and 137.

CHAPTER 4: PHYSICAL PROPERTIES OF THE SNOW AND SEA ICE VOLUME

4.1 Introduction

In this chapter I assess the vertical variation in snow salinity and density among sites to identify distinct groupings, within which the properties are shown not to significantly vary. Temporally, we are interested in the seasonal evolution of any vertical variation. A layered snow model will be used for the computation of the heat flow through the snow if the snow cover is vertically heterogeneous. A vertical characterization of these properties is particularly important for the simulation of heat diffusion because, like a system of series-connected conductors, heat flow through the snow is most strongly influenced by the least conducting layer (Goodrich, 1976). Snow's effective thermal conductivity ranges over an order of magnitude for a snow density range between $100 \text{ kg}\cdot\text{m}^{-3}$ and $400 \text{ kg}\cdot\text{m}^{-3}$ (e.g., Fig. 2.7) and the specific heat of saline snow can exhibit a tremendous range with increasing temperature (e.g., Fig. 2.6).

4.2 Background

Variations in morphological characteristics of the snow cover during SIMMS'92 and SIMMS'93 have been reviewed over first-year sea ice (Barber et al., 1995b; Barber et al., 1995a) and over multi-year ice (Barber et al., 1995a; Misurak, 1995). In these works, the size and shape characteristics of the snow grains were observed to be functions of depth and time for FYI and MYI. The statistical characterization of the snow grain morphology in the vertical dimension at FYI'92 indicated two distinct layers (0 to 6 cm, and 6 to 25 cm) under cold atmospheric temperatures ($< -20^\circ\text{C}$) with a third appearing (27 to 36 cm) during warm ($> -5^\circ\text{C}$) conditions. The three zones are termed 'basal', 'original' and 'new' snow (Barber et al., 1995b). The basal layer accounted for on average 25% of the snow depth.

Snow-cover within the melt pond depressions at MYI'93 was thick and presented a more complex density distribution with depth than observed for the thinner snow over FYI. Misurak (1995) observed three distinct zones within the inter-hummock depression when air temperature was less than approximately -15°C (i.e., cold atmosphere), namely:

- the snow extending from the snow base to the lower 40% of the snow cover,
- within the middle 40% and 60% of the snow cover, and
- the upper 40% of the snow.

He observed four distinct layers (transition at 25%, 55%, 80% of the snow pack from the snow base) when the air temperature was greater than -5°C (i.e., warm atmosphere). The fourth and upper layer during the warm season is attributed to increases in crystal size associated with repeated melt-freeze processes. A general increase in snow grain area was observed at any point within the snow pack as the season progressed for both FYI and MYI snow covers.

The underlying objective of the previous works was to characterize the snow morphology, and morphological changes of snow at stages approaching snow melt and to relate the geophysical properties of the snow pack to the snow's electrical characteristics. The time series of both density and salinity were qualitatively reviewed, but variations in the vertical dimension were assumed relative to the indices of snow shape and size parameters. This assumption may or may not be valid since density is a complex function of both snow texture (grain size distribution) and structure (grain packing).

4.3 Snow Depth

The snow depth records from each of the sites are provided in Fig. 4.1a and b. The fluctuations in depth illustrate the transient nature of the snow cover over sea ice. Step increases in depth correspond to dry precipitation and subsequent drifting of snowfall. The lowering of the snow surface at each site is associated with either *in-situ* melt or wind erosion. Rapid melt was observed by day 171 at FYI'92, day 163 at FYI'93 and after day 155 at FYI'95. The record of minimum snow depth at MYI'93 and MYI'95 represents the snow cover adjacent to a snow temperature array on a hummock shoulder. In the early spring the entire hummock was snow-covered. Late in the spring the hummock crest was typically snow-free while the hummock shoulder remained snow covered. The maximum snow depth record for the multi-year sites

corresponds to snow within the melt pond depressions. The hummock-shoulder snow depth by the temperature array is greater at MYI'93 relative to MYI'93, however measurements by Misurak (1995) show the hummock snow depth across our sample floe to be greater during SIMMS'95 relative to SIMMS'93.

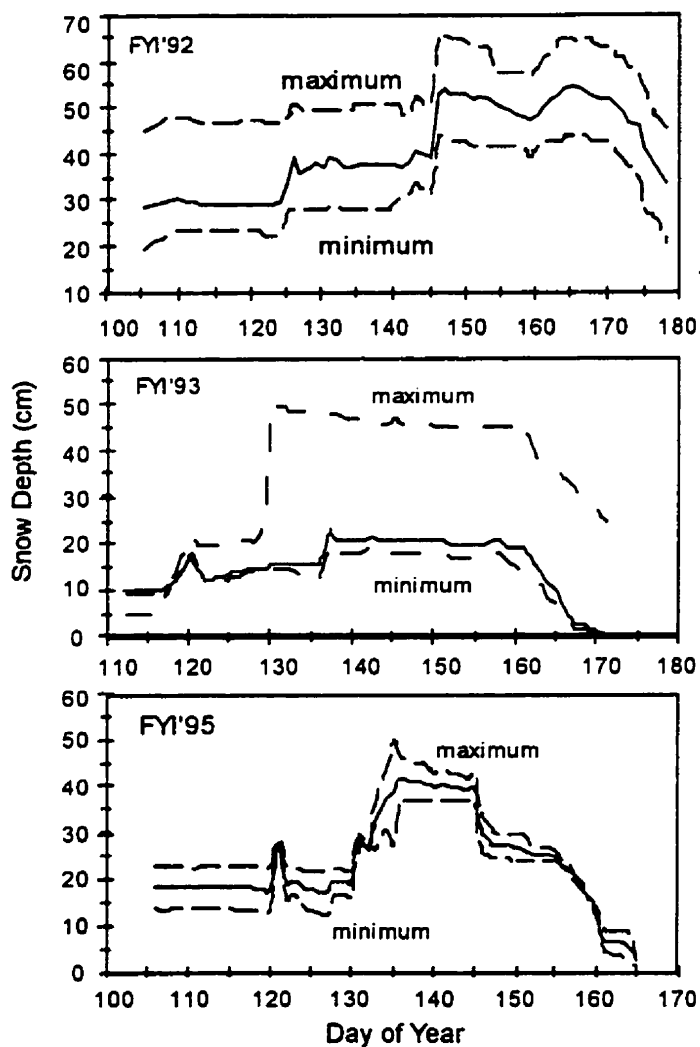


Figure 4.1a The record of snow depth at the first-year sea ice sites.

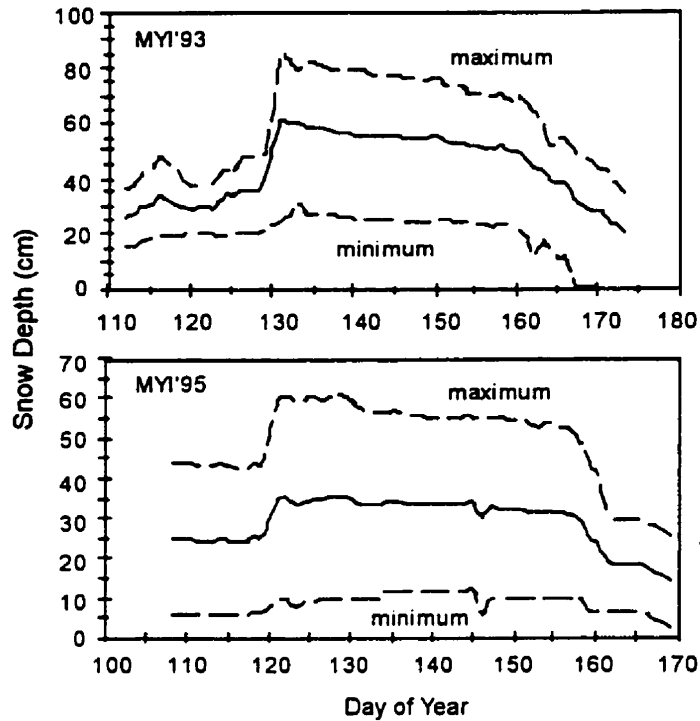


Figure 4.1b The record of snow depth at the multi-year sea ice sites.

4.4 Characterization of the Snow Salinity and Density

4.4.1 Analysis Methods

The data are divided into 2 samples for each site, based on the daily average air temperature. One sample contains the physical properties corresponding to a daily average air temperature of less than or equal to -10°C , while the other sample contains measurements corresponding to warmer air temperatures (i.e., greater than -10°C). A delineating temperature of -10°C was not completely arbitrary. Below a daily average air temperature of -10°C the temperature of the snow base is on average less than -8.2°C and recall from Section 3.2.2 that below this temperature the fraction of salts in solution of saline snow (or ice) is very small.

The snow density and salinity are examined as functions of relative distance from the ice surface. The data are grouped into relative depths categories: 0.2, 0.4, ... 1.0. For example, the 0.2 category represents snow observations from between the snow base and the bottom 20% of the

snow profile. The poor vertical resolution of sampling during SIMMS'95 discounts a detailed examination of the vertical structure of density and salinity.

A one-sample Analysis of Variance (ANOVA) is used to determine whether the snow property differed among relative depth intervals within each seasonal period. A Scheffe's *post hoc* analysis (Miller, 1985) follows the ANOVA to identify statistically viable ($P\text{-value} < 0.05$) pairwise differences. The ANOVA is a robust parametric test (Norcliffe, 1982; page 162).

4.4.2 Results

Average properties of the snow pack during cold and warm atmospheric temperatures are provided as Table 4.1. Only trace salinity was found in the MYI snow samples and salinity was not sampled above the snow base at FYI'95. Prior to day 137 at FYI'92 the snow bulk density was measured with a snow dielectric sensor. The presence of salt at the snow base may have adversely affected the measurement of snow density and, therefore, densities near to the snow base over this period are not incorporated into the analysis.

Of note from the table are:

1. the decrease in salinity between warm and cold periods over first-year sea ice,
2. the increase in relative depth occupied by hoar between seasons during FYI'93 and MYI'95 and
3. the relatively large proportion of the snow cover occupied by hoar at these sites.

The hoar layer occupied from between 30% to 32% of the snow pack during FYI'93, and between 30% and 42% of the snow pack during MYI'95. The hoar development constituted on average 39% of the hummock snow coverage.

The distribution of density and salinity as functions of depth, and seasonal episode are graphically displayed for FYI'92, FYI'93 and MYI'93 in Figs. 4.2 and 4.3. Typically, density is smallest and most variability near the upper and lower of the snow boundaries. There exists a sharp salinity gradient up-ward from the snow base.

Table 4.1 Average snow properties (\pm one standard deviation) per site, during cold, warm and overall snow temperature conditions.

Site	Period	Depth	Hoar	Salinity	Density
FYT'92	Cold	28.2 \pm 4.2	5.4 \pm 0.6	4.2 \pm 6.5	348.9 \pm 63.4
FYT'92	Warm	37.8 \pm 5.1	4.3 \pm 2.2	2.4 \pm 4.8	324.0 \pm 80.8
FYT'92	Total	33.7 \pm 6.3	5.1 \pm 1.4	3.2 \pm 5.8	340.8 \pm 72.7
FYT'93	Cold	10.1 \pm 1.9	3.2 \pm 0.7	6.3 \pm 7.5	309.0 \pm 61.6
FYT'93	Warm	9.3 \pm 3.1	2.8 \pm 2.1	3.4 \pm 4.6	329.7 \pm 77.2
FYT'93	Total	9.8 \pm 2.3	3.2 \pm 1.3	5.2 \pm 6.3	310.9 \pm 68.1
FYT'95	Cold	34.1 \pm 11.8	5.0 \pm 0.9	7.0 \pm 7.5	334.6 \pm 85.1
FYT'95	Warm	30.7 \pm 6.2	5.3 \pm 0.6	5.4 \pm 5.0	335.3 \pm 107.9
FYT'95	Total	32.4 \pm 9.4	5.1 \pm 0.8	6.15 \pm 6.2	335.0 \pm 96.8
MYI'93	Cold	45.6 \pm 16.9	2.7 \pm 0.7	0.0	329.8 \pm 49.3
MYI'93	Warm	63.7 \pm 8.4	4.6 \pm 1.2	0.0	367.9 \pm 65.3
MYI'93	Total	58.4 \pm 15.5	3.4 \pm 1.2	0.0	343.5 \pm 60.2
MYI'95	Cold	50.7 \pm 14.2	16.2 \pm 7.7	0.0	329.3 \pm 72.2
MYI'95	Warm	58.6 \pm 17.8	25.7 \pm 10.4	0.0	322.4 \pm 69.5
MYI'95	Total	54.9 \pm 16.6	21.2 \pm 10.3	0.0	325.6 \pm 70.5

The *post hoc* analysis into the vertical groupings of density and salinity is limited to the FYT'92 and the MYI'93 data set. The snow depth during FYT'93 was too shallow to permit any analysis based on more than two levels, and recall the sampling resolution during FYT'95 and MYI'95 was poor. Instead, the FYT'93, FYT'95 and MYI'95 data are grouped into two zones, basal and upper, with the hoar depth representing the transition. Any difference between the groups is tested using an ANOVA.

Results of the analysis into the vertical groupings indicate that density is statistically different (P -value < 0.05) in the early and late seasonal category between: (i) the hoar level and overlying snow for FYT'93, (ii) at both first-year and multi-year sites during SIMMS'95, and (iii) among at least two of the relative depth increments during FYT'92 and MYI'93. Results of the Scheffe's *post hoc* test (P -value < 0.05) are summarized in Fig. 4.4. All results are significant at a 95% confidence level. The analysis indicates that three distinct layers of density are apparent within the deep snow pack of FYT'92 and MYI'93 during both the early and late periods. The distinct zones are termed basal (lower 0.2 of the snow cover) middle (between 0.2 and 0.8 of the snow cover) and upper (0.8 to 1.0 of the snow cover). We assume that the 0.2 zone of FYT'92 does differ from the overlying snow during the early spring (when the dielectric snow sensor was

used). This assumption is reasonable considering that the hoar layer is shown to differ from the overlying snow in each of the other sites and the hoar layer occupies between 12% and 20% of the snow cover at FYI'92 (Table 4.1). We did not consider the density data from the lower 40% of the FYI'92 snow cover during the early spring. This region is shaded black in Fig. 4.4.

4.4.3 Discussion

Based on the preceding analysis the snow cover may be partitioned into levels of homogeneous density. Three snow layers were observed for the deep snow covers, like those at FYI'92 and within the melt pond depression of MYI'93. Even though the data are not available to perform a detailed investigation into the vertical variation for the snow of FYI'95 and MYI'95, the covers are deep and the three-layer snow model is assumed to apply. At FYI'92, FYI'95 and MYI'93 (mp) the layers are taken between: (a) the snow base and the lower 20% of the snow cover; (b) the middle 60% of the snow cover; (c) the upper 20% of the snow. The lower zone is assumed between the snow base and the lower 40% of the snow at the MYI'95 melt pond, because of the thick hoar development at this site. Two snow levels are assumed for shallow snow covers like those observed during FYI'93 and over the MYI hummocks. The top of the average hoar layer delineated the boundary between the basal and upper zone. Hoar is observed to occupy on average the lower 40% of the hummock snow profile. The hoar layer occupied approximately 30% of the FYI'93 snow cover.

Snow density and salinity are assumed homogeneous within each snow layer and are represented by the average of either density, or salinity, within the layer boundaries (Fig. 4.5a, b and Fig. 4.6). In the case of the hummock snow covers, where repeated physical property sampling was not performed, snow density is assumed to be the average density of the FYI'93 hoar (approximately $240 \text{ kg}\cdot\text{m}^{-3}$) and overlying snow (approximately $340 \text{ kg}\cdot\text{m}^{-3}$), respectively. The FYI'93 experiment provided the only physical property data set for shallow snow. The average basal zone density from FYI'93 is also used for FYI'92 prior to day 137. The last day of physical properties sampling during SIMMS'95 is day 156. The snow density at the sites was linearly extrapolated from the last day of observation to a maximum value of $470 \text{ kg}\cdot\text{m}^{-3}$ on day 169.

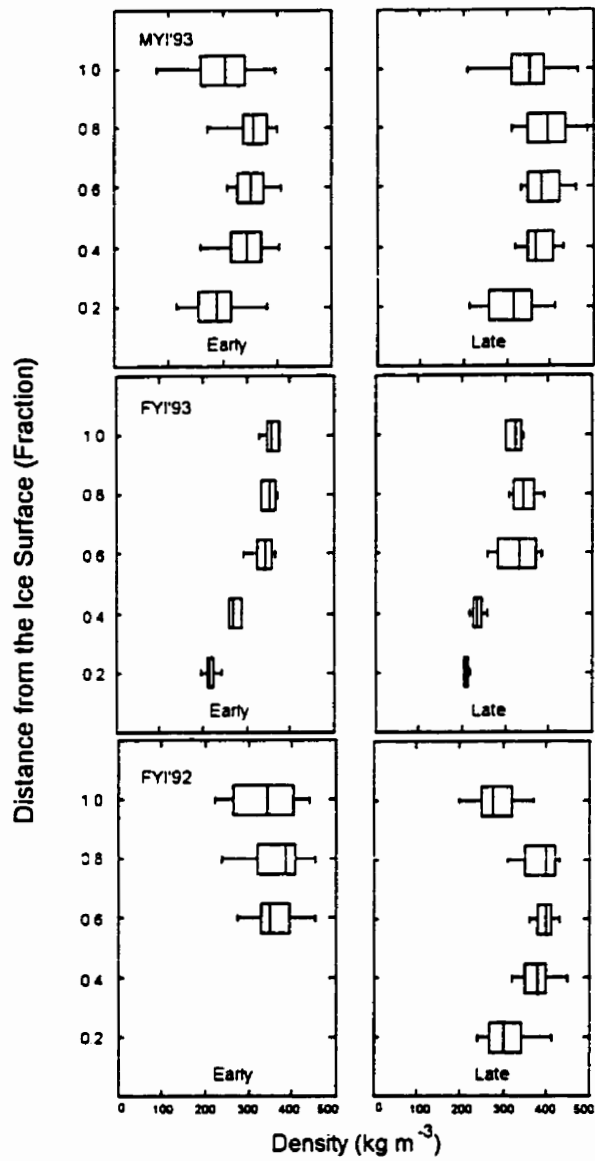


Figure 4.2 Snow density ($\text{kg}\cdot\text{m}^{-3}$) variation with depth during FYI'92, FYI'93 and MYI'93.

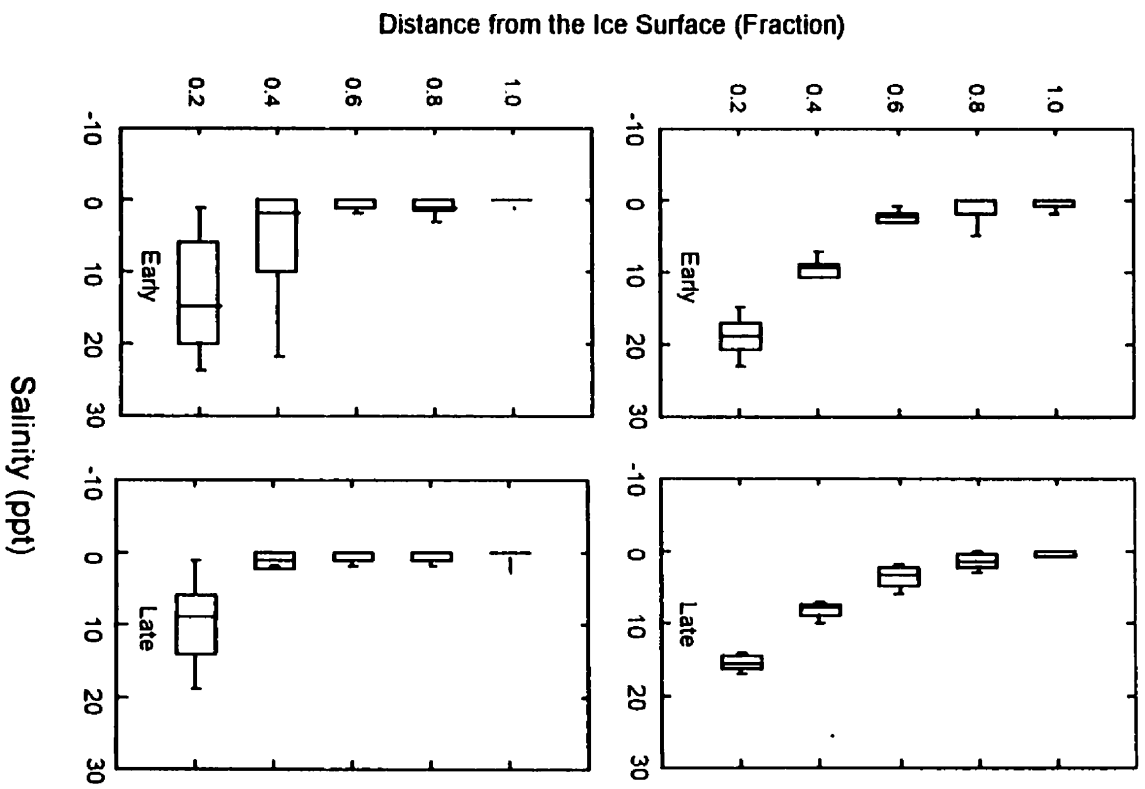


Figure 4.3 Snow salinity (ppt) distributed over depth during FYT'92 and FYT'93.

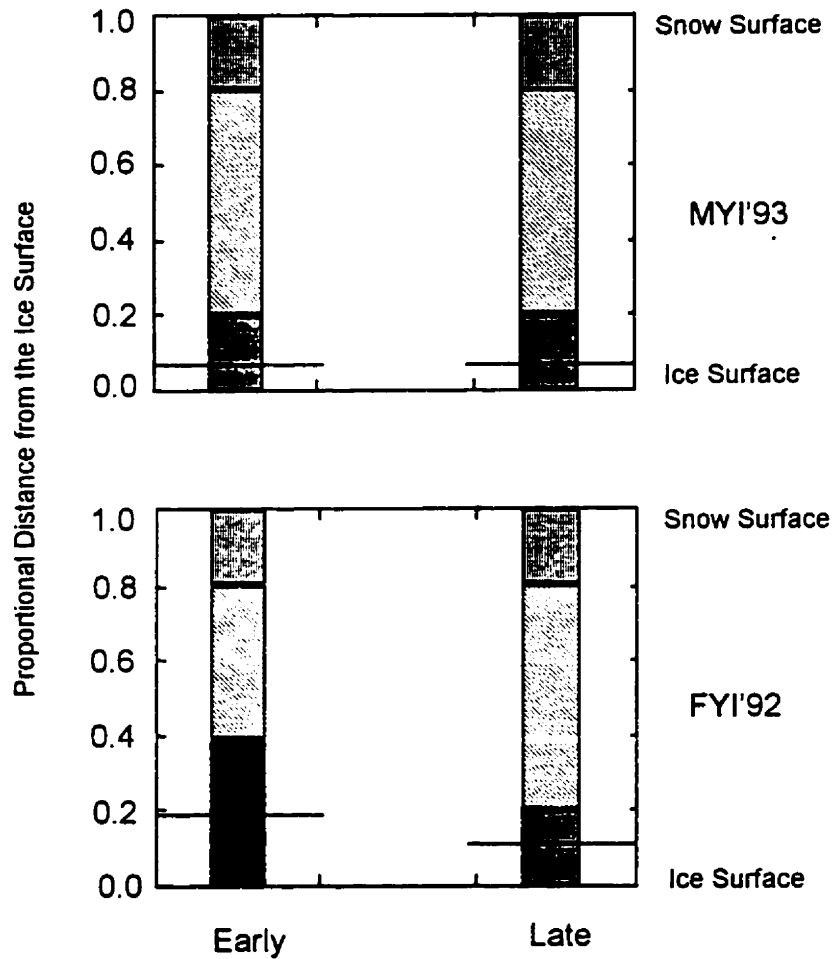


Figure 4.4 Graphical interpretation of Scheffe's pair-wise means test. The relative depth zones encompassed by the bar pattern did not statistically differ with respect to density at greater than 95% level of significance. Horizontal lines denote average observed hoar extent relative to total average depth. Black shading denotes the zone within the snow cover that was excluded from the analysis (refer to text).

A snow density of $470 \text{ kg}\cdot\text{m}^{-3}$ lies within the range of snow density for seasonal snow for temperatures between 0 and -10°C (Mellor, 1977) and is close to the final observations of snow bulk density at the melt pond of MYI'95 (Fig. 4.6b). Interpolated values are used for days with missing data.

The major features identified by Barber et al.,(1995a, b) appear in the time series' of snow physical properties. Snow density is usually smallest in the basal layer, over much of the experimental periods regardless of the underlying sea ice type (Figs. 4.6a, b), and salinity is greatest in the basal layer of snow over first-year sea ice. The snow density at the surface fluctuates more than within the underlying layers, particularly at FYI'92 and MYI'93. A fairly substantial reduction in snow density is observed with time at both of these sites. The reduction in snow density during the late spring is attributed to subsurface sublimation and the formation of *firnspeigel*¹⁴, which was first observed on day 167 at FYI'92 and around day 150 during SIMMS'93. *Firnspeigel* was observed over a greater proportion of the surface volume as the season progressed. Its presence was documented during the other SIMMS experiments, but it is not recognizable in the layer density data. The proximity of the near surface snow to atmospheric processes (e.g. snowfall, rain, sunshine and aeolian processes) contributes to the high variability in surface bulk density throughout most of the spring periods.

4.5 Measured Snow Wetness

Without liquid retention curves one cannot assign exact liquid content limits for the various snow density and moisture regimes. However, using the record of measured snow wetness in the upper centimeters of the snow, we can roughly determine the irreducible liquid content, the capillary water capacity and the evolution of the liquid contents into the pendular regime for snow over first-year sea ice (Fig. 4.7). The lowest observed snow wetness hovers around 3% by volume, which may be representative of the snow's irreducible water limit. After day 130, in 1992, we observe a rise in liquid contents into the pendular regime. The capillary liquid holding capacity occurs at approximately 6%. The drop in wetness after day 160 is attributed to a reduction in capillary suction (and hence the capillary liquid holding capacity) and is associated with increasing

ice grain radius in the upper snow. Therefore, our 0.05 isoline of liquid volume proportion (Fig. 2.5) roughly represents the amount of water the snow matrix could hold against gravity for varying snow temperature, density and salinity. Our computed brine volumes indicate that saturation is realized at fairly low snow salinity ($S < 10$ ppt) at temperatures of approximately -2°C for dense snow, but at temperatures above -1°C for only moderately dense and loosely packed snow.

Measured snow wetness shows that the snow remained within the pendular moisture regime throughout much of the experimental period (Fig. 4.8). These conditions are conducive to the application of the snow thermal conductivity model described by Papakyriakou and LeDrew (1999) and reviewed in Section 3.3.2.

4.6 Summary

Snow depth is highly variable at a point over the seasonal transition. Snow density and salinity are shown to vary in the vertical dimension and to vary with the progression of the spring season at each site. The degree of variation in the vertical dimension discounts the use of volume averaged properties for the computation of the heat fluxes. Instead, the properties were partitioned into layers, within which the properties were shown not to statistically differ. Treating the snow as layers during the computation of the volume fluxes permits some semblance of heterogeneity to be represented in an ensuing analysis. The three layers in deep snow covers represent the hoar, or basal layer (i.e., zone of faceted crystal growth with typically a low bulk density and high bulk salinity for first year sea ice), mid-snow zone (i.e., dense snow associated with the process of pressure metamorphism) and upper snow (i.e. low density snow associated with either fresh snow deposition or by near surface mass loss through sublimation). Snow moisture remains within (or below) the pendular moisture regime for much of the measurement period.

¹⁴ The transformation of snow into friable 'skeleton-like' plates of ice associated with sub-surface sublimation in the presence of strong surface insolation at sub-zero air temperature (Colbeck et al., 1990).

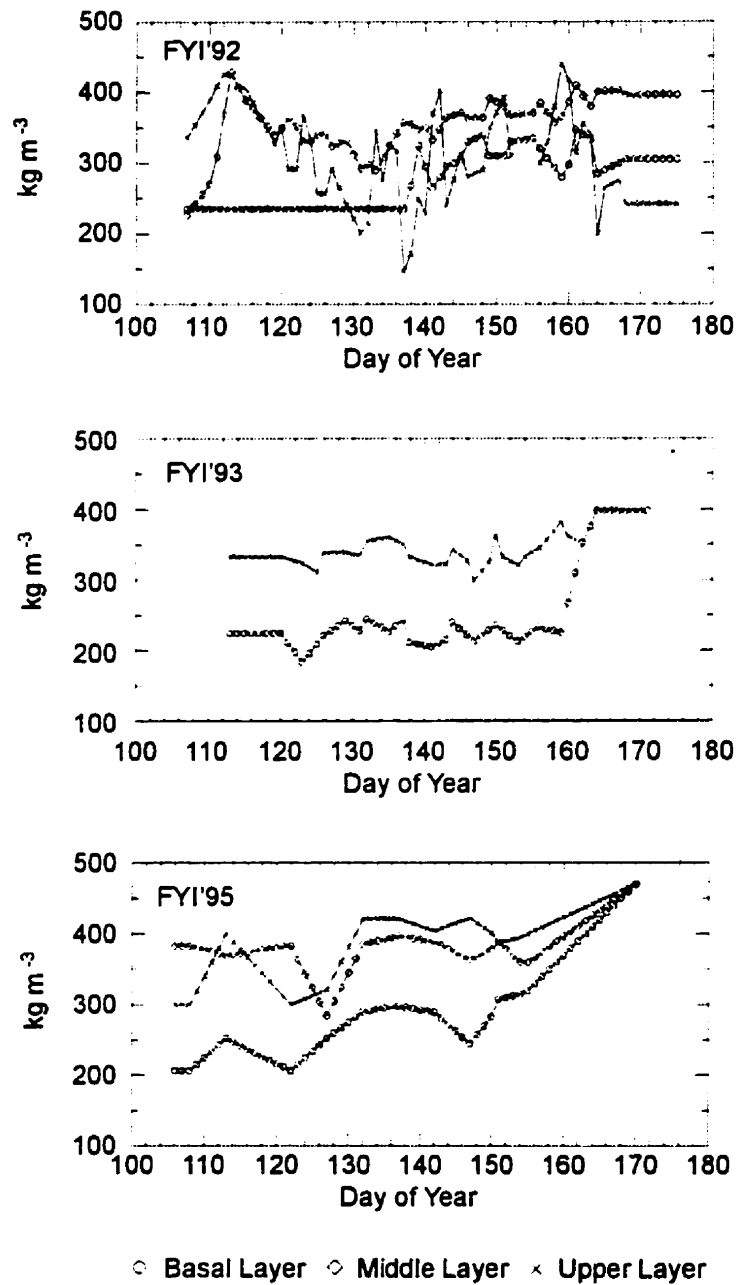


Figure 4.5a Average snow density within each snow layer at the first-year sea ice sites.

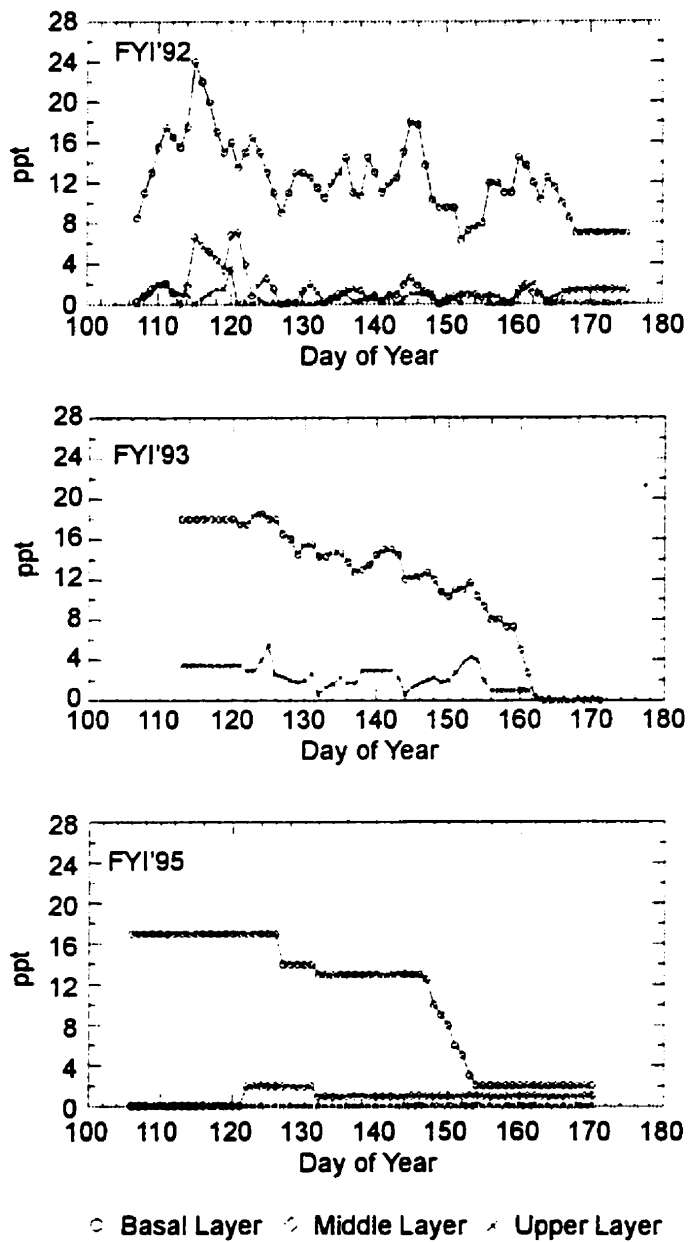


Figure 4.5b Average snow salinity within each snow layer at the first-year sea ice sites.

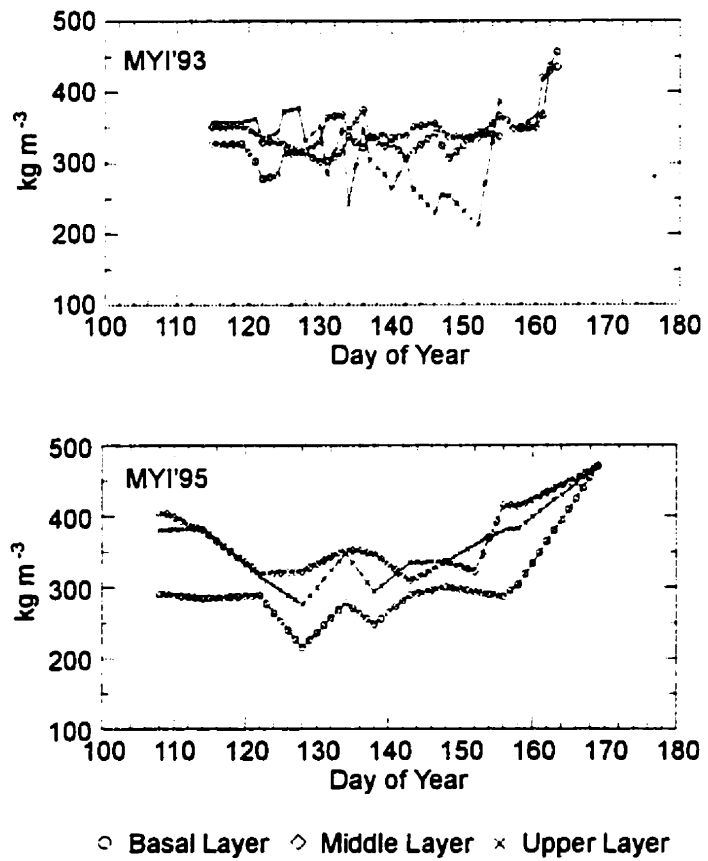


Figure 4.6 Average snow density within each snow layer at the multi-year sea ice sites.

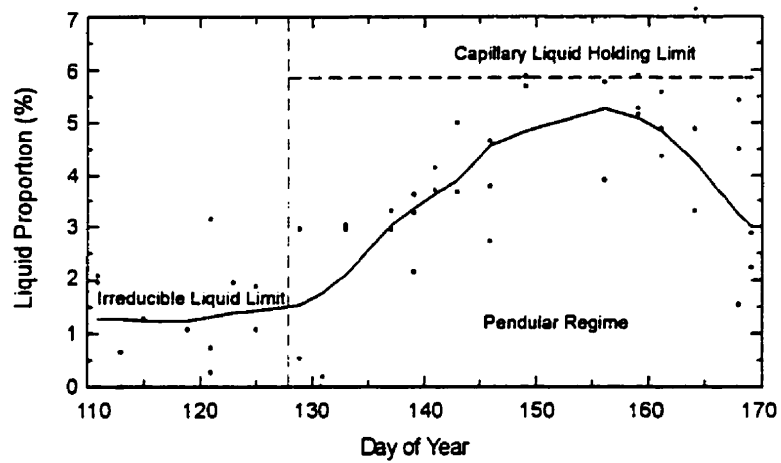


Figure 4.7 Measured snow wetness in the upper centimeters of the snow cover at FYT'92. The solid line represents a locally weighted regression scatter plot smoothing (LOWESS) to the sample values (solid squares).

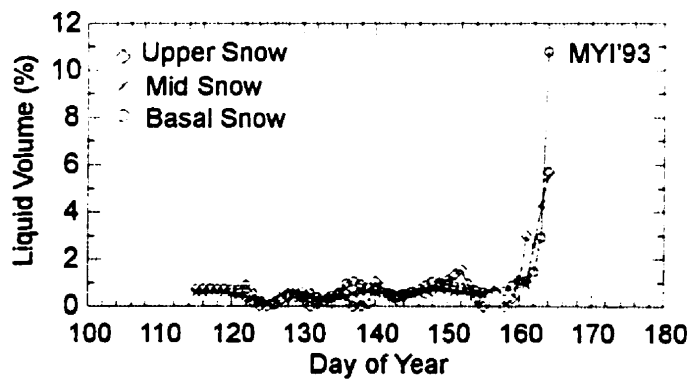
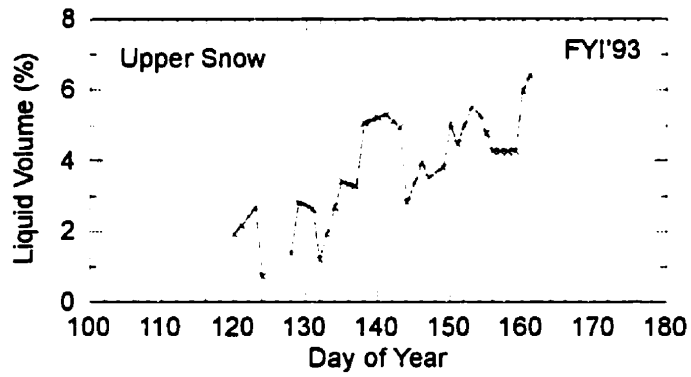
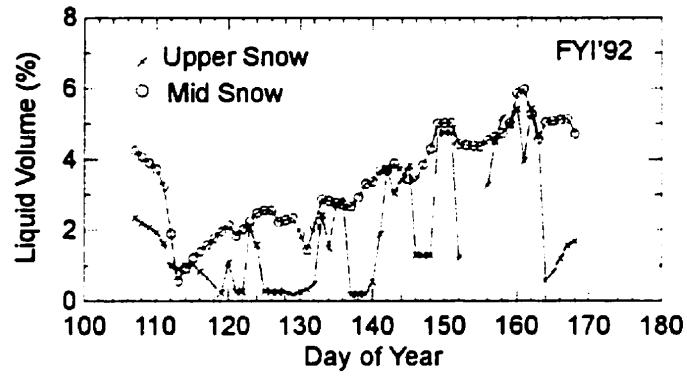


Figure 4.8 Measured snow wetness (% by volume) within snow layers at FYI'92, FYI'93 and MYI'93.

CHAPTER 5: MODELED SNOW ALBEDO, EXTINCTION AND RADIATION TRANSMISSION

5.1 Introduction

In this chapter I describe the spectral albedo and extinction coefficient for the SIMMS' snow cover. The model of Wiscombe and Warren (1980) and Warren and Wiscombe (1980) are used and outlined in Appendix 2. Estimates of these optical properties are required so that the transmission of solar radiation through the snow can be modeled to evaluate, (i) net radiation beneath the snow cover (Eq. 2.1), and (ii) to determine where in the snow pack the bulk of solar radiation is absorbed. The second point may be useful in interpreting the role of solar radiation in the energy balance. The radiation transfer scheme is validated against measured radiation in the PAR region of the spectrum.

5.2 Computational Methods

5.2.1 Radiation Transfer through Snow

The radiation transmitted beyond the snow volume ($K\downarrow_s$) is modeled using Beer's Law (Eq. 2.10). Narrowband irradiance is estimated using measured hourly global radiation and proportionality coefficients for 22 wavelength bands between 0.36 and 4.0 μm . The coefficients are derived using STREAMER¹⁵ (Key, 1996b) for six different sky categories¹⁶ (clear, 5/10th As, 5/10th St, 10/10th As, 10/10th thin St, and 10/10th thick St) for solar noon on April 15, May 15 and June 15. Similarly, coefficients describing the diffuse proportion of global radiation, per waveband were generated, as required for the estimate of net albedo. The broadband to narrowband conversion of global radiation is described in Appendix 6.

¹⁵ STREAMER is described in Appendix 6.

¹⁶ St and As refer to stratus and alto-stratus cloud cover.

The spectral albedo is modeled as the combination of the albedo for the diffuse [$\alpha_s(\lambda)_{diff}$] and direct-beam components [$\alpha_s(\mu_o, \lambda)$] of irradiance:

$$\alpha_s(\lambda)_{net} = C\alpha_s(\lambda)_{diff} + (1 - C)\alpha_s(\mu_o, \lambda), \quad (5.1)$$

where C is the diffuse fraction of incident radiation and μ_o is the cosine of the zenith angle. The solutions to $\alpha_s(\lambda)_{diff}$ and $\alpha_s(\mu_o, \lambda)$ appear in Appendix 2.

5.2.2 Absorbed Solar Radiation within the Snow Volume

Absorbed solar radiation is calculated at 1 mm increments through the snow cover, over 22 spectral intervals between the wavelengths 0.36 μm and 4 μm using Eq. 2.12. Net solar radiation absorbed within a layer of snow (or ice) is equal to the difference in spectrally integrated net solar radiation at levels delineating the layer's boundaries:

$$K^*_{z_1-z_2} = K^*_{z_1} - K^*_{z_2}, \quad (5.2)$$

where $Z_1 < Z_2$ are any two levels within the snow. The total amount of solar radiation absorbed by the entire snow volume is therefore:

$$K^*_{tot} = K^*_o - K^*_{z=b}, \quad (5.3)$$

where K^*_o is equivalent to K^* in Eq. 2.1 and $K^*_{z=b}$ is equivalent to Q^*_{is} , and $z=b$ denotes the snow base (or ice surface). $K^*_{z=b}(\lambda)$ was modeled using Beer's Law with our predicted $K^*_{\downarrow}(o, \lambda)$ and κ_λ .

5.3 Analysis Methods

The appropriateness of the computed optical terms is evaluated by comparing the modeled radiation transmission through the snow cover at each site in the photosynthetically active portion of the spectrum (PAR) and measured PAR at the snow/ice interface at FYT'92, FYT'93, MYT'93 (melt pond only) and FYT'95. The validation procedure consisted of: (i) partitioning hourly measured global radiation into spectral wavebands, (ii) modeling the transfer of radiation within each spectral band through the snow cover using Beer's Law, (iii) summing the transmitted solar radiation ($\text{W}\cdot\text{m}^{-2}$) over the 0.4 to 0.7 μm wavelength range, (iv) comparing the modeled transmission in the PAR region to measured values.

5.4 Validation of Radiation Transfer Scheme

Results of the comparison between measured and modeled radiation (0.4 μm to 0.7 μm) appear in Table 5.1. The maximum RMSE between the modeled and measured transmission at a site is $3.81 \text{ W}\cdot\text{m}^{-2}$. The largest variation occurred during the month of June in 1995. The corresponding RMSE ($7.91 \text{ W}\cdot\text{m}^{-2}$) represents approximately 30% of the average transmitted flux. Over the same month, a relative RMSE of 23% ($2.74 \text{ W}\cdot\text{m}^{-2}$) is observed at FYI'93. Root-mean square differences are less than $3 \text{ W}\cdot\text{m}^{-2}$ at the other sites over the spring months. The MBEs of the comparison are small (less than $1.7 \text{ W}\cdot\text{m}^{-2}$). Both error terms are small throughout the experiments of FYI'92 and MYI'93. Because these sites have a thicker snow cover, we may assume that the effects of inadequacies in the model terms are reduced for deep snow. The relative errors in the modeled transmitted flux are misleading for April and May since the measured flux is small to begin with. The large relative RMSE computed for June at the first-year sites in both 1993 and 1995 is attributed to inability of the model to capture a rapidly changing snow morphology associated with the onset of melt. Furthermore, the spectral irradiance is imperfectly modeled. The RMSE associated with modeled PAR at the snow surface (against the measured term) ranged between $12.1 \text{ W}\cdot\text{m}^{-2}$ and $7.9 \text{ W}\cdot\text{m}^{-2}$ in June of 1993 and 1995 (Appendix 6). Any errors in the spectral distribution of the incident flux may contribute to the observed discrepancy between the measured and modeled transmitted terms.

The effective grain radii (mm) used for the computation of albedo and snow extinction is shown in Table 5.2. The derived effective ice grain radii (Table 5.2) are similar to the snow grain dimensions reported by Barber et al.,(1995a, b), Misurak (1995), and De Abreu et al.,(1995) for the SIMMS snow covers. There is little difference in the effective grain sizes among the sites during the earliest two periods at each site. The required effective grain sizes at FYI'95 and MYI'93 for periods 3 and 4 are however a factor of 2 larger than required at FYI'92 and FYI'93. The small effective grain sizes required at FYI'92 and FYI'93 is attributed to the frequent occurrence of snowfall during the respective seasons. Snowfall is described in Section 6.3.1. Fresh snow acts to raise albedo, thereby diminishing transmission. There is a difference between the derived late season effective grain sizes at the first-year and multi-year sea ice site in 1993. During the third period we require an effective grain radius of 1.20 mm at the multi-year sea ice melt pond and a 0.5 mm grain radius over the same period at FYI'93. The difference may be

attributed to water beneath the snow surface within the inter-hummock depression of the multi-year ice. Melt water is more apt to drain through cracks in the thinner first-year ice. Recall that the effect of water is to increase the 'within ice' optical path length, thereby acting also to increase the effective ice grain radius.

Table 5.1 The mean bias error (MBE) and root mean square error (RMSE) describing the relationship between modeled and measured transmitted radiation in the PAR for three SIMMS experimental periods. The average measured flux, the number of hours in the analysis and the average snow thickness over the quantum sensor are also provided. All fluxes are expressed in $W \cdot m^{-2}$.

Period	Statistic	FY192	FY193	FY195	mp93
SIMMS	Average	0.29	5.39	6.68	0.54
SIMMS	MBE	0.00	0.07	-0.05	0.10
SIMMS	RMSE	0.31	2.66	3.81	0.47
SIMMS	N	1679	1032	1344	1104
SIMMS	Depth	50.26	17.25	27.16	65.45
April	Average	0.05	0.34	0.43	
April	MBE	-0.02	1.36	0.85	
April	RMSE	0.05	1.76	1.51	
April	N	336	48	312	
April	Depth	47.57	14.80	23.35	42.40
May	Average	0.08	2.80	0.60	0.02
May	MBE	0.07	-0.28	0.18	-0.01
May	RMSE	0.11	2.68	1.01	0.08
May	N	720	696	744	672
May	Depth	51.23	19.37	33.85	69.47
June	Average	0.65	11.65	27.42	1.32
June	MBE	-0.06	0.69	-1.64	0.26
June	RMSE	0.49	2.74	7.91	0.75
June	N	623	288	72	432
June	Depth	50.59	14.06	17.18	58.91

Table 5.2 The effective snow grain radii (mm) used for the computation of albedo and the snow extinction coefficient for the experimental periods.

Site	Variable	Period 1	Period 2	Period 3	Period 4
FYT'92	ending day	121	161	177	-
FYT'92	radii (mm)	0.15	0.25	0.35	-
FYT'93	ending day	131	161	165	-
FYT'93	radii (mm)	0.10	0.22	0.5	-
MYT'93	ending day	121	161	166	171
MYT'93	radii (mm)	0.15	0.25	1.20	1.60
FYT'95	ending day	129	155	159	170
FYT'95	radii (mm)	0.15	0.25	0.80	1.20

* note that the effective snow grain radii computed for the first-year sea ice sites are used for the multi-year hummock covers.

5.5 Spectral Albedo and Extinction Coefficients for Snow

The albedo for the ice grain radii of Table 5.2 are illustrated as a function of wavelength in Fig. 5.1. These curves are computed for a 20 cm snow pack, with solar zenith angle of 56° (i.e., solar noon on May 15, 1993). The form of the curves (i.e. position of local maximum and minimum) correspond to albedo spectra provided by Warren and Wiscombe (1980). Albedo is fairly flat across the visible portion of the spectrum and decreases with increasing grain effective radius. Albedo rapidly drops for all grain sizes in the near infrared.

The decrease in visible albedo with increasing effective grain radii mimics the evolution of spectral albedo for a maturing snow pack demonstrated by De Abreu et al.,(1995). Computed albedo is compared to measured albedo spectra¹⁷ for shallow snow over first-year sea ice (Fig. 5.2a) and for deeper snow within a melt pond depression (Fig. 5.2b). Modeled albedo was computed assuming a complete A_s coverage, and the prescribed ice sphere radii are provided in Table 5.2. Modeled albedo marginally overestimates measured values by about 3.5 % in the visible portion of the spectrum for conditions representative of early (day 135) and late (day 162) spring over the shallow snow at FYT'93. This level of agreement is very near to the necessary accuracy for a $\pm 10\%$ level of uncertainty in Q^*_s as reported in Appendix 8. The rapid decline in

¹⁷ Note that all measured albedo spectra are taken under ten-tenths cloud coverage. A cosine response error with the instrument prevented the use of clear-sky albedo.

measured albedo with wavelength beyond $0.7 \mu\text{m}$ on day 162, is more pronounced than shown by the simulated curve. De Abreu et al.,(1995) attribute the drop in albedo to increased absorption associated with grain enlargement and increased moisture at the snow surface, a process not well represented using a single layer snow model. The local peak in measured albedo around the $0.94 \mu\text{m}$ wavelength for day 162 is spurious, and is attributed to sensor noise (De Abreu et al., 1995).

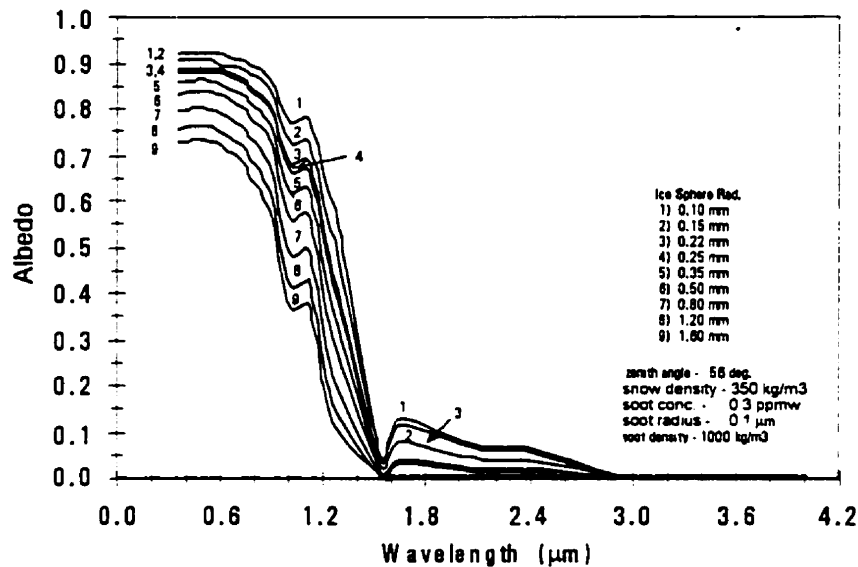


Figure 5.1 Modeled snow albedo for each ice sphere effective radius used in the study for wavelengths between $0.36 \mu\text{m}$ to $4.0 \mu\text{m}$. Values are computed for a 20 cm thick snow cover at 12:00 LAT on day 135 (1993) over first-year sea ice.

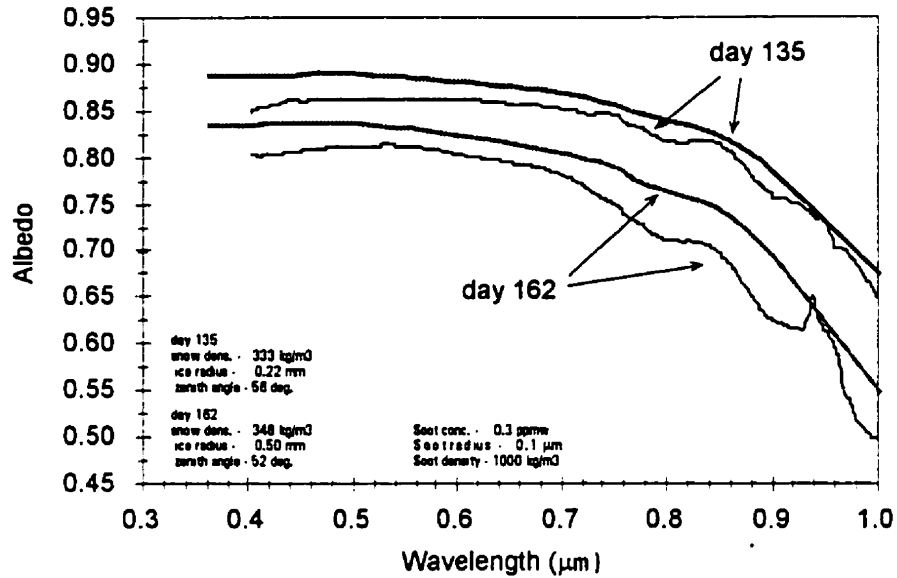


Figure 5.2a Simulated (grey lines) and measured spectral albedo (black lines) over the visible and near infrared portion of the spectrum for snow over first-year sea ice (FYI'93) for day 135, and day 162. Curves represent near noon values. Measured albedo is taken from De Abreu et al. (1995).

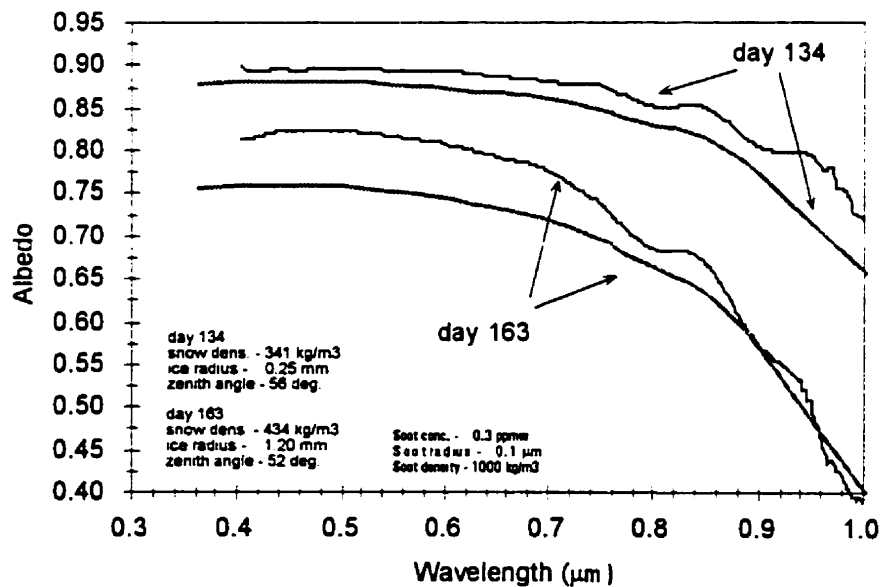


Figure 5.2b Simulated (grey lines) and measured (black lines) albedo over the visible and near infrared portion of the spectrum for snow with a multi-year sea ice melt pond depression (MYI'93). Snow depth is 48 cm on day 134 and 61 cm on day 163.

Excellent agreement is observed between measured and modeled albedo for the deep snow (greater than 40 cm) within a melt pond depression on day 134 (Fig. 5.2b). Maximum discrepancy (approximately 7.0%) occurs for wavelengths beyond 0.9 μm . Computed albedo underestimates measured values by about 12% over most of the visible portion of spectrum later in the spring season (e.g., day 163). The poor late season performance of the model may be related to melt water within the snow cover by day 163. Despite the presence of a saturated zone, the surface crust of snow maintained a fairly high albedo in the visible wavelengths. Consequently, the simulated albedo, using a large effective grain radius, underestimated albedo in the visible wavelengths relative to measured values. In retrospect, a layered model would be better able to simulate the seasonal evolution of the reflective properties of the heterogeneous snow volume over both first-year and multi-year sea ice. By treating the snow as a homogeneous volume, modeled albedo spectra is typically within 7% for dry snow, and within about 12% for deep snow during the advanced stages of melt.

The computed snow spectral extinction varied by two orders of magnitude between the visible (i.e., $\kappa_s = 10^1 \text{ s}^{-1}$) and the infrared portions of the spectrum (i.e., $\kappa_s = 1000^1 \text{ s}^{-1}$) (Fig. 5.3). The seasonal decrease in radiation extinction at all wavelengths by the snow is demonstrated by the decrease in the simulated extinction coefficient with increasing ice grain radii over the nine ice grain categories. The computed coefficients remained relatively constant in the PAR for each ice grain category, ranging from approximately 25 m^{-1} to 6 m^{-1} for effective grain radii between 0.10 mm and 1.60 mm, respectively. This range is slightly wider than the range provided by Grenfell and Maykut (1977) for the spectral extinction coefficients between dry compact snow ($\kappa_{\text{PAR}} \approx 19 \text{ m}^{-1}$), and melting snow ($\kappa_{\text{PAR}} \approx 10 \text{ m}^{-1}$), for wavelengths between 0.4 μm and 0.65 μm . Unfortunately grain size is not provided by Grenfell and Maykut, but their measured extinction for dry compact snow agrees well with modeled extinction coefficients having effective grain radii between 0.22 mm and 0.5 mm (i.e., curves 3 to 5 in Fig. 5.3). The extinction coefficient is between 17 and 18 m^{-1} in the visible portion of the spectrum for these grain radii. These effective grain radii resemble measured grain radii reported by Barber et al., (1995a, b) for cold dry snow over first-year sea ice during both SIMMS'92 and SIMMS'93.

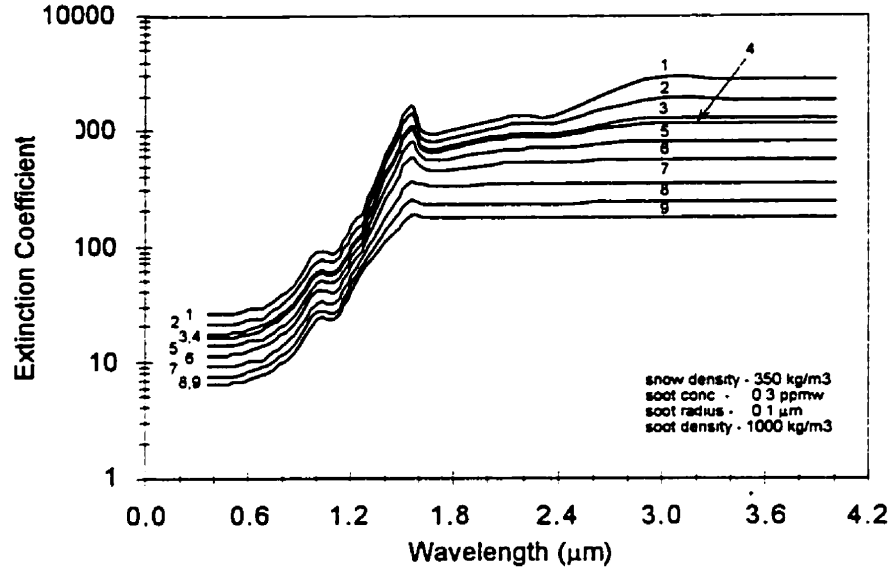


Figure 5.3 Modeled extinction coefficients (m^{-1}) and shown over the wavelength band $0.36\mu m$ to $4.0\mu m$. Values are computed for 12:00 LAT on day 135.

Results from a sensitivity analysis (Appendix 8) indicate that the net radiation at any level within the snow volume is highly sensitive to the seasonal evolution of the snow spectral albedo and spectral extinction coefficient. Albedo has the greatest impact on computed net radiation for dry snow. The results highlight the danger of prescribing the snow optical properties in radiative transfer schemes without making allowances for the seasonal evolution of the terms. Albedo spectra should be estimated to between 1% and 3% over the visible wavelengths for fine grain and coarse grain snow, respectively, to maintain a $\pm 10\%$ limit on Q^*_{\downarrow} . κ_s must be estimated to within approximately 5% over the visible wavelengths for deep snow. In shallow snow (1 cm), the absorbed solar radiation is less sensitive to the parameterization of κ_s because the flux is more sensitive to variations in snow albedo. The necessary accuracy should be between 30% to 75% over the range in snow conditions, from cold and dry, to warm and wet.

5.6 Absorption and Transmission of Solar Radiation within the Snow Cover

The availability of absorbed solar radiation to the surface depends on where in the snow volume the bulk of the energy is absorbed. The reduction in transmitted solar radiation (Wm^{-2}), and the solar radiation absorbed per unit volume ($\partial K^*/\partial z$, $\text{W}\cdot\text{m}^{-3}$) through a snow profile during the early, mid and late period of an experiment is illustrated in Fig. 5.4 (a and b). The transfer and absorption profiles are computed for solar noon on days 127, 135 and 165, at FYI'93. These dates are selected to correspond to available albedo spectra measurements and to illustrate the evolution of the transmission and absorption characteristics for cold fine-grained snow (e.g., day 127) and wet snow near its melting temperature (e.g., day 165). Snow optical properties (spectral albedo and extinction coefficient) on these dates are represented by curves 1, 3 and 6 in Figs. 5.1 and 5.4, which are computed using effective snow grain radii of 0.1, 0.22 and 0.5 mm, respectively. The upper-most values in Fig. 5.4 correspond to the surface value of $K\downarrow$ and $\partial K^*/\partial z$ respectively. The integration of the radiation absorbed per unit volume ($\text{W}\cdot\text{m}^{-3}$) between levels in Fig. (5.4b) represents the absorbed solar radiation ($\text{W}\cdot\text{m}^{-2}$), summed for all discrete layers between the levels and is equal to the difference in the spectrally integrated net solar radiation (K^*_z) between the upper and lower level in the snow. The steepest rate of change in the energy relations occurs within millimetres of the snow surface.

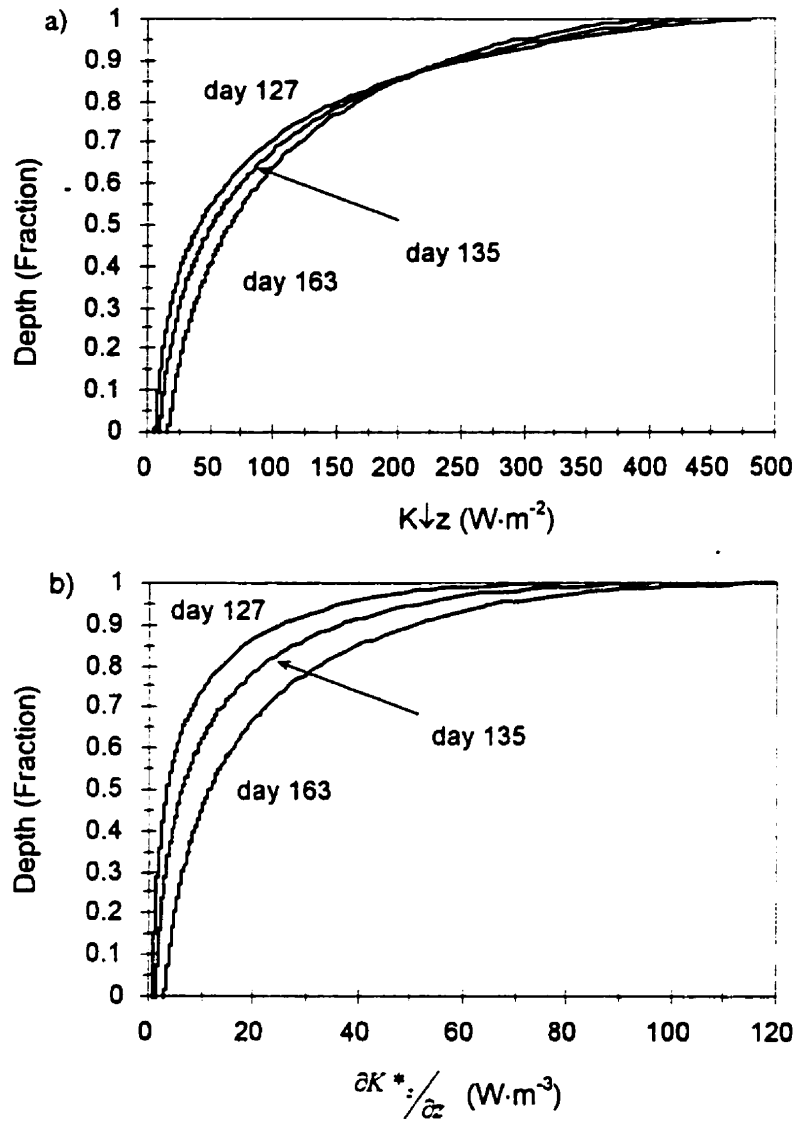


Figure 5.4 Profiles of (a) transmitted solar radiation and radiation absorbed per unit volume at FYI'93 for snow properties representative of the early, mid, and late spring.

The rate at which the transmitted solar flux and the absorbed solar flux per unit volume are reduced, relative to their surface values is shown in Fig. 5.5a and b. Depth in the figure is expressed relative to the total snow depth to allow the comparison between the sample dates. The form of the reduction in the upper 2 cm of the snow is magnified in the inset of each figure. The

transmitted flux is reduced to approximately 50% of its surface value within the upper 2 cm of the snow volume on both days 135 and 163, while over the same depth on day 127, the flux was lowered to less than 40% of its surface value. Only a small proportion of incident solar radiation made its way through the snow pack (<5%) in each of the three examples.

The absorbed radiation was reduced to 55% of its surface value across the upper-most millimetre of snow near its melting temperature (e.g., day 163 in Fig. 5.5b), and to less than 30% of its surface value (i.e., a 70% reduction) for cold dry snow (e.g., day 127 in Fig. 5.5b). Absorbed radiation was reduced to 10% of its surface value (i.e., a 90% reduction in surface values) within: (i) 3 mm from the surface on day 127, (ii) 4 mm from the surface on day 135, and (iii) 6 mm of the surface on day 163. Absorption predominately occurred in the longer wavelengths ($\lambda > 0.75 \mu\text{m}$, Fig. 5.6), which are generally attenuated within the upper 5 mm. The lowest rate of absorption with depth occurred for wavelengths shorter than about $0.48 \mu\text{m}$. The wavelength dependency on absorption is consistent with simulations presented by Jin et al. (1994) using a 4-stream radiative transfer model.

5.8 Summary

In this chapter, modeled snow albedo and extinction coefficients are presented using the model of Wiscombe and Warren (1980) with the modifications suggested by Warren and Wiscombe (1980) for soot contaminated snow. The model reproduces major features of the snow spectral albedo and extinction coefficient. Modeled albedo closely matches measured spectra for cold, dry snow, regardless of snow depth. Wet snow is well represented for a shallow snow cover, however, the model may underestimate albedo by up to 12% in the visible portion of the spectrum for wet deep snow. Simulated spectral extinction coefficient is a strong function of grain size and showed strong wavelength dependency. Modeled radiative transmission at the snow base showed reasonable agreement with measured values when integrated over the PAR region of the spectrum. The transmission term is small, so a critical comparison was difficult in light of sensor limitations.

Incident solar radiation is attenuated in the upper snow volume. Only a small proportion of the incident flux will reach the ice surface (usually less than 5%), except during the final days of the snow cover. The bulk (90%) of radiation absorbed by snow-covered sea ice occurs within the upper centimeter of the snow.

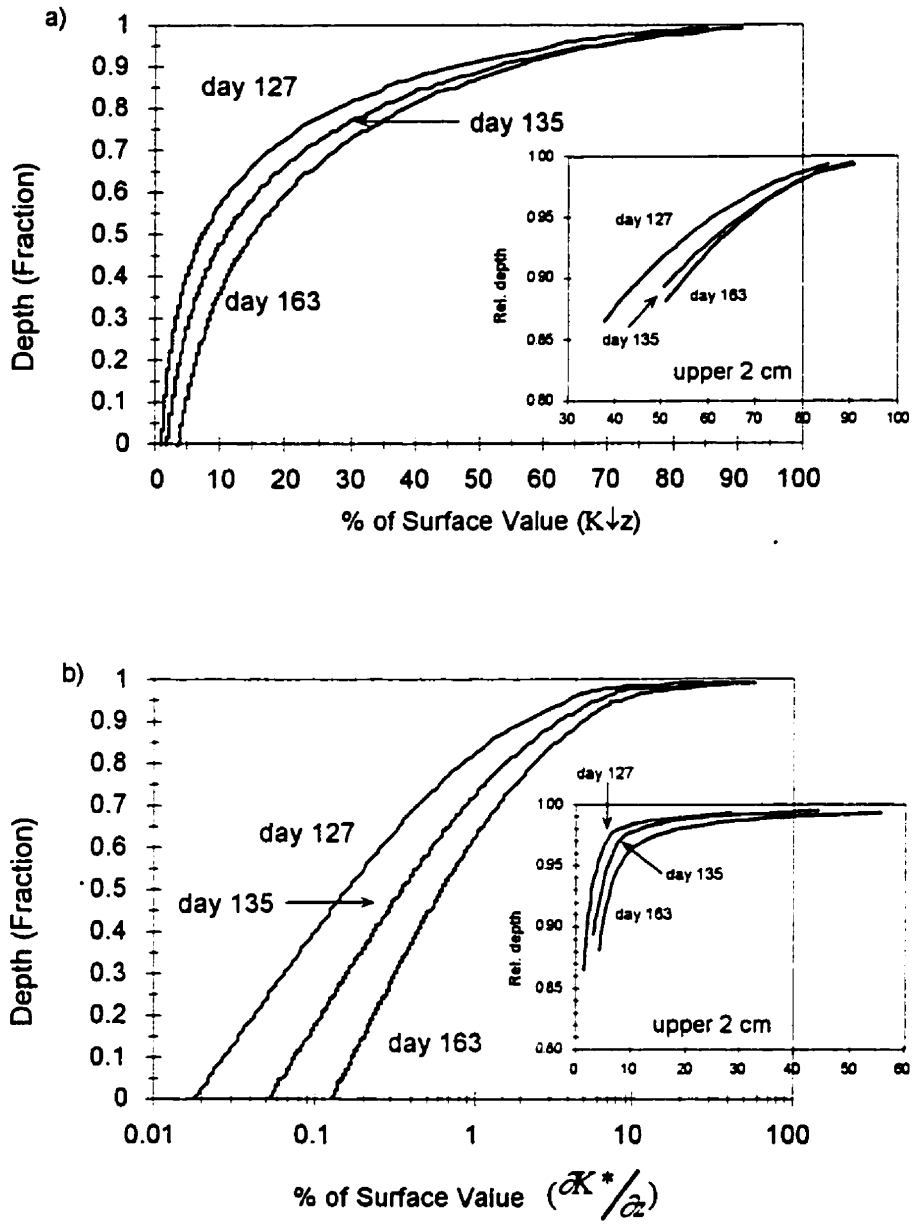


Figure 5.5 The percent reduction from surface values of (a) K_{\downarrow} and (b) K^* within the snow volume. The upper 2 cm of the profile is snow in the insets.

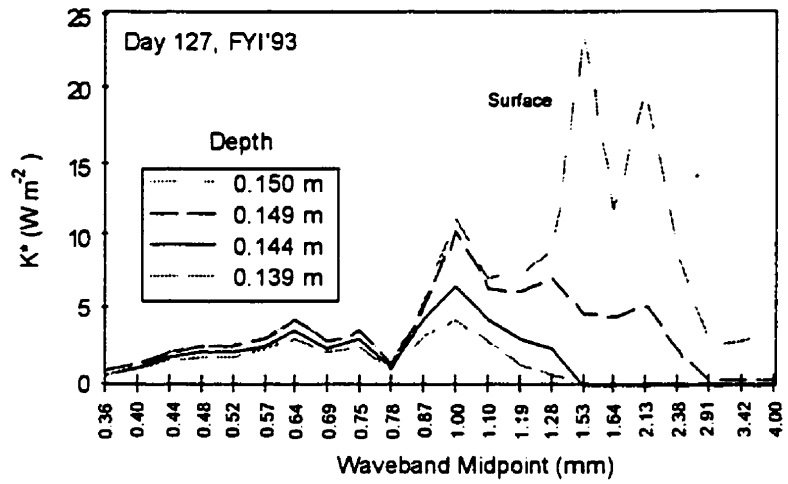


Figure 5.6 Absorption of solar radiation shown as a function of wavelength and depth at solar noon.

CHAPTER 6: TEMPORAL DYNAMICS OF THE SURFACE ENERGY BALANCE

6.1 Introduction

The objective of this chapter is to provide an explicit description of the temporal dynamics of the surface and volume energy balance of snow-covered sea ice during the spring transition. The purpose is to identify which energy fluxes are the key contributors/consumers of the available energy to the surface and upper sea ice volume and under what circumstances. Variation is examined on time scales ranging from minutes to years, thus addressing research issues associated with the first objective of this thesis.

The chapter begins with a description of the computational methods for deriving the individual energy balance components, followed by a review of the ambient climate during each of the three spring experiments. A description of the general meteorology places the energy balance in the context of broader climatic features. The focus then shifts to the energy exchange processes described by the surface and volume energy balance and highlights the importance of the individual energy balance components for heating and cooling the snow volume. All analysis pertains to the environment presented by first-year sea ice within the scope of the SIMMS experiments.

6.2 Computational Methods

6.2.1 Initial Processing

The initial processing of the microclimate data consists of converting the average readings (30 and 15 minute averages) to hourly averages and computing the equivalent local solar apparent time (LAT) to each local standard time of measurement. Low air temperature, blowing snow, frost and low solar elevations stressed the measurement program. Data are screened and flagged for the cases of reported or suspected instrument misalignment, damage, or malfunction.

6.2.2 Radiation Balance

6.2.2.1 Solar Radiation

The global and reflected solar radiation are measured directly and converted to $W \cdot m^{-2}$ within the datalogger programming. PAR measurements were converted from $\mu mol \ s^{-1} m^{-2}$ to $W \cdot m^{-2}$ using a proportionality constant of 0.2174 (McCree, 1972). An immersion effect error is typically $\pm 2\%$ or less in the case of flooding of the quantum sensor at the snow base (Li-Cor, Inc., 1992).

6.2.2.2 Infrared Radiation and Surface Temperature

The Eppley (PIR) is equipped with a thermistor-battery-resistance circuit to compensate for the effect of infrared radiation emitted from the thermopile on the measured infrared flux. The infrared radiation is derived using:

$$L \downarrow \text{ or } \uparrow = L_{in} - L_{out} = L_{in} - \sigma T^4 \quad (6.1)$$

where L is a long-wave flux (the arrows refer the direction of the flux); *in* and *out* denotes energy directed toward and away from the sensing thermopile; σ is the Stefan Boltzman constant and T (in Kelvin) is a measure of the thermopile temperature. We measured and archived the *emf* produced by the thermopile and the temperature (Kelvin) of the sensor housing and the rim of the silicon dome using the available factory installed thermistors. The housing temperature is substituted into Eq. 6.1. The dome temperature is available to assess the extent to which the dome and the case temperature vary. Our derivation of L assumes that any solar heating of the instrument dome and subsequent re-radiation to the thermopile is negligible and that the case temperature closely approximates the thermopile temperature. There is the potential for the measured long-wave flux to be augmented by long-wave radiation transfer between the thermopile and dome. This issue has been addressed by Albrecht and Cox (1977), Alados-Arboledas et al., (1988) and Philipona et al., (1995), among others. The net effect of solar heating of the dome is to increase the measured flux relative to the true flux (Albrecht and Cox, 1977).

A damaged sensor cable prevented the use of the case temperature for the blackbody correction for $L \uparrow$ during FYI'95. Out of necessity, the dome temperature was used for the correction and any undue bias to the computed flux which resulted from the substitution may be examined by replacing the case temperature by the dome temperature (T_{dome}) in Eq. 6.1.

The surface thermodynamic temperature (°C) is computed using the infrared radiation emitted by the surface with:

$$T_s = \left(\frac{L \uparrow - (1 - \varepsilon)L \downarrow}{\sigma \varepsilon} \right)^{\frac{1}{4}} - 273.15, \quad (6.2)$$

where σ is the Boltzman constant, and ε is the snow surface emissivity. Broad-band emissivity is assigned as 0.99. The spectral emissivity of snow over the 4 μm and 50 μm wavelength sensitivity range of the pyrgeometer fluctuates with 0.01 of this value for snow grain radii between 200 and 1000 μm (Warren, 1982).

Down-welling long-wave radiation was modeled using the all-sky formulation of Jacobs (1978) with the clear sky formulation of Efimova (1961) (refer to Eqs. 2.5) during SIMMS'95. Vapor pressure was derived from hourly measurements of relative humidity and air temperature and TCA was recorded at site. Cloud amount, as observed at the Resolute weather station, was substituted when no cloud observations were available at the site.

6.2.3 Non-Radiative Components of the Energy Balance

6.2.3.1 Energy of Fusion and Conductive Heat Flow within the Sea Ice and Snow

The snow volume energy balance is shown by Eq. 2.7. The conductive heat flux at the sea ice and snow surface is computed using,

$$Q_{x,z} \approx k_x \frac{\Delta T_{x,z}}{\Delta z}, \quad (6.3)$$

where x denotes the medium (s or i, representing snow or ice). A cubic spline is applied to the temperature profiles and temperature is interpolated at 1 cm increments within the snow and ice. Any snow temperature sensor within 3 cm of the surface is not incorporated into the interpolation routine to minimize a potential heating bias associated with the absorption of solar radiation by the snow sensor. The surface values of the flux are computed using the temperature change with depth within the upper 3 cm of the snow and sea ice. The thermal conductivity of snow is modeled using a physical model (Papakyriakou and LeDrew 1999) and sea ice thermal conductivity is computed using Schwerdtfeger's (1962) physical model (Section 2.4.3.1). Variables that are assumed constant in the computation of snow thermal conductivity are shown in Table 6.1. The model

requires independent estimates for the thermal conductivity of pure ice (Eq. 2.26), pore space air (Eq. 2.36) and an estimate of snow density and salinity. Sea ice density is assumed constant over the measurement period within each of three sea ice layers, namely 0 to 10 cm, 10 to 20 cm, and below 20 cm. For the first-year ice and the multi-year ice melt pond, the densities are held constant at 900 kgm^{-3} . Ice density was prescribed as 800 kgm^{-3} , 850 kgm^{-3} , and 900 kgm^{-3} for ice levels one to three, respectively for the multi-year hummock ice. These values are consistent with density measurements shown in Table 3.2. Average salinity for the three levels (i.e., 9.0 ppt, 6.3 ppt, 5.5 ppt) were computed from the ice core samples (Table 3.3) and held constant for the duration of the experiment for first year ice. An exception was made for the upper-most node (i.e., the first 3 cm of the ice volume), for which the daily average ice surface salinity is applied (Fig. 6.1). The upper melt-pond and hummock sea ice is considered non-saline.

Table 6.1 Variables assumed constant in the computation of snow effective thermal conductivity.

<i>Variable</i>	<i>Symbol</i>	<i>Value</i>	<i>Unit</i>
water density (0°C)	ρ_w	999.10	kg m^{-3}
air thermal conductivity (-10°C)	k_a	0.0233	W (m K)^{-1}
water thermal conductivity (0°C)	k_w	0.5526	W (m K)^{-1}
gas constant (dry air)	g_c	287.04	J (kg K)^{-1}
gas constant (water vapor)	g_w	461.50	J (kg K)^{-1}
air pressure	P_a	100.00	k Pa
effective diffusion coef. of water vapor in snow at 0°C and under an ambient atmospheric pressure of 100.0 kPa*	Deo	0.92E-4	m^2s^{-1}

* From Jordan (1991). All others from List (1966).

Because snow is translucent to solar radiation and because the optical and thermal properties of a temperature sensor differ from those of snow, it is probable that the near surface snow sensors experienced solar heating. Brandt and Warren (1993) speculate that under clear skies, absorbed solar radiation by the temperature sensors may bias measured temperatures by up to 0.3°C at 6 cm depth beneath the snow surface, while measured temperatures at 2 cm depth can be biased by up to 0.8°C . Their experiment consisted of monitoring the temperature change after the sensors were shaded. However, because shading also cools the snow surrounding the sensor, it is difficult to isolate the effect of solar heating on the sensor and their values may overstate the

heating bias. We attempted to minimize the solar heating of a sensor by: (a) painting the sensor white, (b) orienting the sensors toward the north, and (c) incorporating only those sensors deeper than 4 cm from the snow surface into any analysis. The temperature at the snow surface was estimated with Eq. 7.3, using the long-wave radiation balance. The snow depth in the vicinity of each of the snow sensor arrays is known on a daily basis. The depth of the upper-most sensor within the sea ice that is incorporated into the study is 0.05 m at FYI'92 and FYI'95 and 0.03 m at FYI'93.

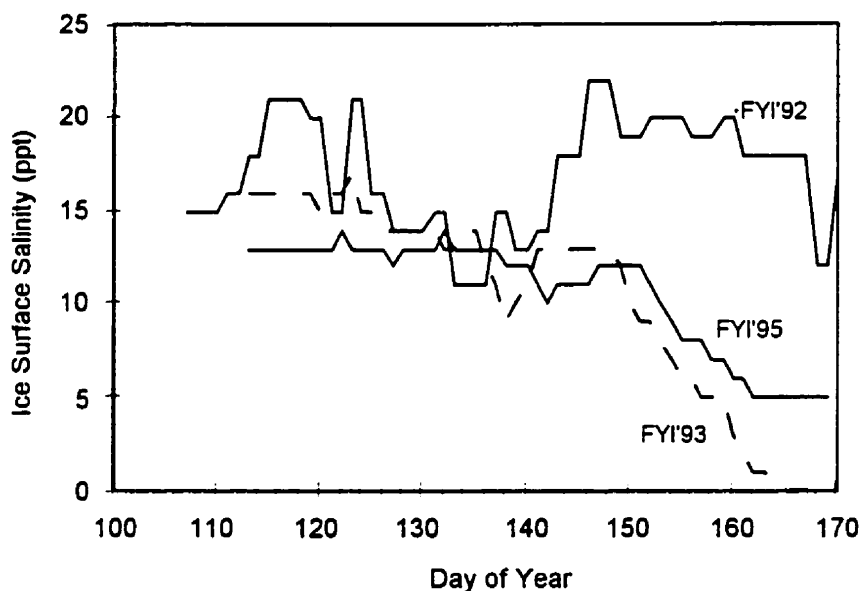


Figure 6.1 The salinity of the sea ice surface for FYI'92, FYI'93 (dashed line) and FYI'95.

6.2.3.2 Sensible Heat Flux

The estimation of sensible heat and evaporation is cited as one of the most difficult aspects of snow modeling (Morris, 1989). The flux-profile technique is adopted in this work (see Section 2.4.3.3).

The sensible heat flux and the momentum flux are computed using Eqs. 2.47 and 2.48 with measured gradients of temperature and wind speed. The log-linear gradients of wind and potential temperature are estimated using a linear regression of u and θ versus the natural logarithm of

sensor height. The concentration of sensors in logarithmic fashion acted to minimize the effect of non-neutral stability on the measured profiles, while at the same time sampling within the region which should contain the highest temperature and wind speed change with height. A custom graphics program is used to view the temperature and wind speed profiles for each time interval to ensure that the profiles are near-linear with log height, free of environmental measurement biases and within the constant flux layer prior to the flux calculation. Measurements that did not conform to the above criteria were removed prior to the analysis. The entire profile is rejected if for any reason the data are in doubt. The proportion of air temperature data rejected ranged from 11.2% during FYI'95 to 24.6% during FYI'92. The proportion of wind data rejected ranged from 3.6% during FYI'95, 7.7% during FYI'92 to 27.3% during FYI'93. We suspect that the high proportion of wind data rejected during FYI'93 is related to our decision to mount the anemometers onto the principal energy balance tower and not on a separate tower as was the case during FYI'92 and FYI'93. Because of the large number of wind data rejected during FYI'93 we opted to calculate the wind speed gradient as the change in wind speed between the upper-most anemometer and the velocity ($u=0 \text{ m}\cdot\text{s}^{-1}$) at the average aerodynamic roughness length, z_0 , which was computed during FYI'92. The upper-most anemometer was mounted at the top of the energy balance tower and therefore was free from any obstruction.

We assume that the von Karman constant, k , is equal to 0.41 (following Dyer and Hicks, 1970). Air density of moist air ($\text{kg}\cdot\text{m}^{-3}$) is computed following Brutsaert (1982):

$$\rho_a = \frac{p}{R_d(273.15 + \bar{\theta})} \left(1 - \frac{0.38e}{p} \right), \quad (6.4)$$

where R_d is the universal gas constant of dry air ($287.04 \text{ J}\cdot\text{kg}^{-1}\cdot\text{K}^{-1}$), p is the atmospheric pressure (Pa), e is the vapour pressure (Pa), and $\bar{\theta}$ is the profile-average of the potential air temperatures, and:

$$\theta_z \approx T_{a_z} + (0.0098 \cdot z). \quad (6.5)$$

T_{a_z} is the measured air temperature at height, z , above the surface. Hourly measurements of atmospheric pressure are available from Atmosphere Environment Service (AES) weather station at Resolute. The saturated vapor pressure is estimated using the polynomial expression of Lowe (1976) and is converted to a vapor pressure using measured relative humidity at the site.

The specific heat of moist air at constant pressure is calculated as the weighted sum of the specific heats of the dry air and the water vapor (Brutsaert, 1982):

$$C_p = C_{pd}(1 + 0.84q), \quad (6.6)$$

where q is the specific humidity:

$$q = \frac{0.622 \cdot e}{p - 0.378 \cdot e}. \quad (6.7)$$

The specific heat of dry air (c_{pd}) is $1005 \text{ Jkg}^{-1}\text{K}^{-1}$ (List, 1966).

The empirical stability functions (Eq. 2.52) are computed as functions of the Monin-Obukhov stability parameter (Eq. 2.50), using the coefficients presented by Hicks (1976). The derivation of the Monin-Obukhov Length closely follows the procedure outlined by Berkowicz and Prahm (1982). The procedure is iterative and the steps are outlined below:

step A. The fictional velocity u^* and temperature scale θ^* were computed using Eqs. 2.44 (a and b) with the measured wind and temperature profiles, and assuming neutral atmospheric conditions (i.e., L approaches infinity and therefore Φ_M , and Φ_H approach 1).

step B. The Monin-Obukhov length is computed using:

$$L = \frac{\overline{\theta u_*^2}}{gk\theta_*}, \quad (6.8)$$

with the initial estimates of u^* , and θ^* from *step A*. ξ is calculated (Eq. 2.50) using the geometric mean height of sensors in the profile.

step C. The stability functions, $\Phi_{H \text{ and } M}$, are computed as functions of ξ using Eq. 2.52. These estimates are used in the recalculation of u^* , and θ^* in *step A*.

step D. The cycle *a* to *c* is repeated until the successive values of L do not change by more than 10%. If the number of iterations exceeds 20, the time period is skipped, as it is doubtful that L will converge (as is the case during periods of strong atmospheric stability).

6.2.3.3 Latent Heat Flux

The turbulent exchange of latent heat with the atmosphere is also expressed in terms of the Monin-Obukhov similarity functions and the log-linear gradients of wind speed and humidity (Eq. 2.48). Similarity is assumed between the stability functions for sensible and latent heat. The latent

heats ($\text{J}\cdot\text{kg}^{-1}$) of vaporization (subscript e), and sublimation (subscript v) are estimated as functions of temperature from values provided by List (1966).

The log linear gradients for specific humidity are taken between a height of 10 cm above the snow surface and the height of a relative humidity probe (approximately 2 m) at each site. The air at 10 cm is assumed saturated with respect to the air temperature at 10 cm above the snow surface. Others adopt a similar assumption for snow and ice surfaces (e.g., Leavitt et al., 1978, King and Anderson, 1994). The vapour pressure at the upper level is estimated by scaling the saturated vapour pressure (e_s ; Pa) by the measured relative humidity fraction ($e_2 = e_{s2} \cdot rh$). Specific humidity is subsequently computed using Eq. 6.7. The air temperature at levels 2 and 1 is derived using the temperature-height relations established during the computation of Q_H . The relative humidity measured at the AES weather station prior to day 156 was used at FYI'92 for the calculation of e_2 . Possible ramifications of this are discussed below.

6.3 Analysis Methods

6.3.1 General Climatic Conditions

Previous work has commented on the variability in the spring season climate in the central Canadian Islands (Agnew and Silis, 1995). The spring of 1992 was extremely cold: being the second coldest year on record at Resolute. The spring of 1993, on the other hand, was unusually warm and, in fact, was the sixth warmest spring on record. The spring of 1995 was also unseasonably warm (Silis, 1995). Weather information (i.e., air temperature, relative humidity, cloud amount and opacity, sea level pressure, hours of bright sunshine, wind speed and direction) from the Atmospheric Environment Service (AES) weather station in Resolute, is used to describe the general thermal and kinetic state of the atmosphere. The daily averages of most climatic variables are computed in order to assess day-to-day variation in magnitude. For certain variables (i.e., wind direction, total cloud amount and opacity), a daily mode represents a more meaningful index, and is calculated instead of a daily average. I adopt a methodology for analysis similar to others (e.g., Ohmura, 1982; Crane, 1979) and stratify the analysis into the seasonal episodes. A K-means Cluster Analysis (Johnson and Wichern, 1982) is used to partition each day of the total sample of days into categories: cold, transitional, and warm, using the temperature at the sea ice/snow interface as the discriminating variable. These groups are used to define three seasonal

episodes: *early*, *transitional* and *late* spring. The choice of the interface temperature as the discriminating variable is justified below.

Mean patterns in sea level pressure are useful for the interpretation of discontinuities in temperature, relative humidity, wind direction cloud coverage and other physical phenomena at a site (Barry and Chorley, 1987). The autocorrelation function of daily average sea level pressure may help to identify cycles in the time series of sea level pressure at Resolute. The function can provide an index in the persistence of weather patterns. The persistence of cyclone and anticyclone systems over several days is known as coherence (Barry and Perry, 1973). Most climatological time series are non-stationary because regimes of weather and climate exist. For instance, values that are close together in the time sequence tend to be similar in magnitude. Therefore, the time series are first transformed using a first order difference transformation ($\text{lag}=1$) in order to remove any trend in the series prior to the correlation analyses (Chatfield, 1984). In this way, local fluctuations in atmospheric pressure may be assessed and not the trend. The confidence limits surrounding the correlation coefficients were evaluated after Haan (1977).

6.3.2 Energy Balance Analysis

6.3.2.1 Energy Balance

During the course of the analysis I describe the role the respective energy balance components play by examining the evolving contribution of each variable to the total heat gain/loss by the snow volume. Each component of Eq. 2.4 and 2.7 is presented as a percent of the total heat available for partitioning, between the atmosphere and surface and within the snow cover. The total energy available at the surface is the total amount of energy contributed through each positive component of Eq. 2.4. Q_{vol} represents any energy that is supplied to the snow surface by the snow volume and is simply the negative of dQ_s . The total energy available to the snow volume is the sum of each positive component of Eq. 2.7. Bear in mind that a positive conductive flux at the snow surface is heat gained by the surface, but heat lost by the snow volume.

6.3.2.2 Within Snow Thermal and Radiative Coupling Distances

An analytical relationship is used to relate the depth within the seasonally evolving snow that is thermally coupled to the surface over an atmospheric time scale (Guest and Davidson 1994):

$$z_1 = 2 \left(\frac{t_s \nu}{\pi} \right)^{1/2}, \quad (6.9)$$

where the depth scale, z_1 , represents the depth within an ice volume which thermally interacts with the surface over a time scale, t_s , of atmospheric forcing, and ν is the material's thermal diffusivity (m^2s^{-1}). The coupling distance is used in support of a discussion on the role of absorbed solar radiation and snow cover itself on the partitioning of available energy between the atmosphere and underlying snow and sea ice volume.

6.4 General Climatological Conditions

6.4.1 Atmospheric Properties and Precipitation

The air temperature and relative humidity increased with the progression toward summer (Fig. 6.2 a to c). In each graph a LOWESS curve (locally weighted regression scatter plot smoothing) is fit to the daily averages. The daily average air temperature ranged over 22°C during each field experiment. Both the 1992 and 1993 experiments are underway prior to a rapid increase in air temperature, while the start of the 1995 experiment is coincident with elevated springtime temperatures. The rise in air temperature in 1995 appears to be associated with intense high pressure during the early season. The form of the increase in relative humidity mimics the seasonal increase in air temperature. Both the seasonal increase in solar zenith angle and the day-to-day variation in total cloud amount influence the daily total of bright sunshine. As one would expect there appears an inverse relationship between sunshine hours and TCA. The time series of daily modal TCO (total cloud opacity) corresponds in most instances to the temporal distribution of TCA.

Wind speed fluctuates around a fairly stationary mean during each of the spring seasons (Fig. 6.2 a to c). Wind direction is described at each site according to the direction in which the wind blows and data are categorized into the four primary compass directions for presentation purposes. The frequency distribution of the daily modal direction shows the prevailing winds during each spring period to be from the north (Fig. 6.3). Northerly winds accounted for between 48% and 58% of the daily modal wind direction. Southerly winds are the next most frequent, but never accounted for more than 27% of the springtime total.

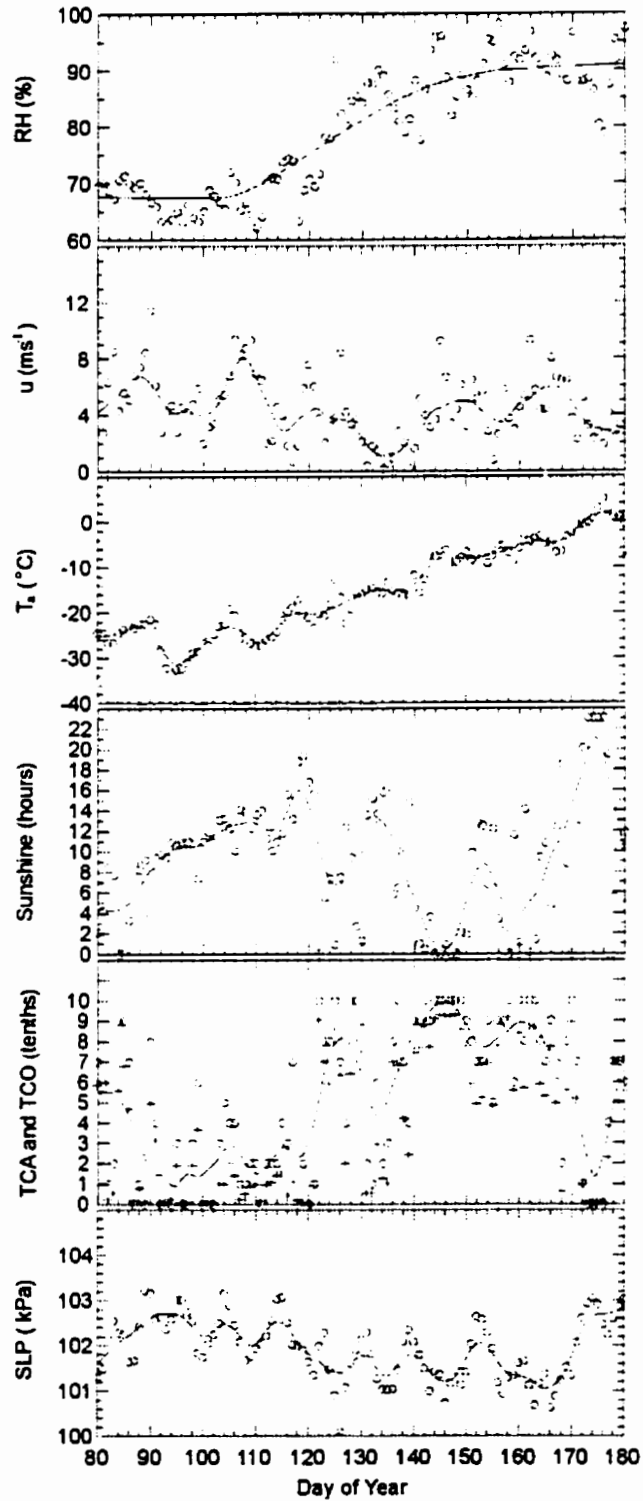


Figure 6.2a Daily summary of general meteorological conditions during 1992. LOWESS curve is drawn through the daily average slp, T_a , sh, u, RH and through the daily mode of TCA. Also provided is the TCO.

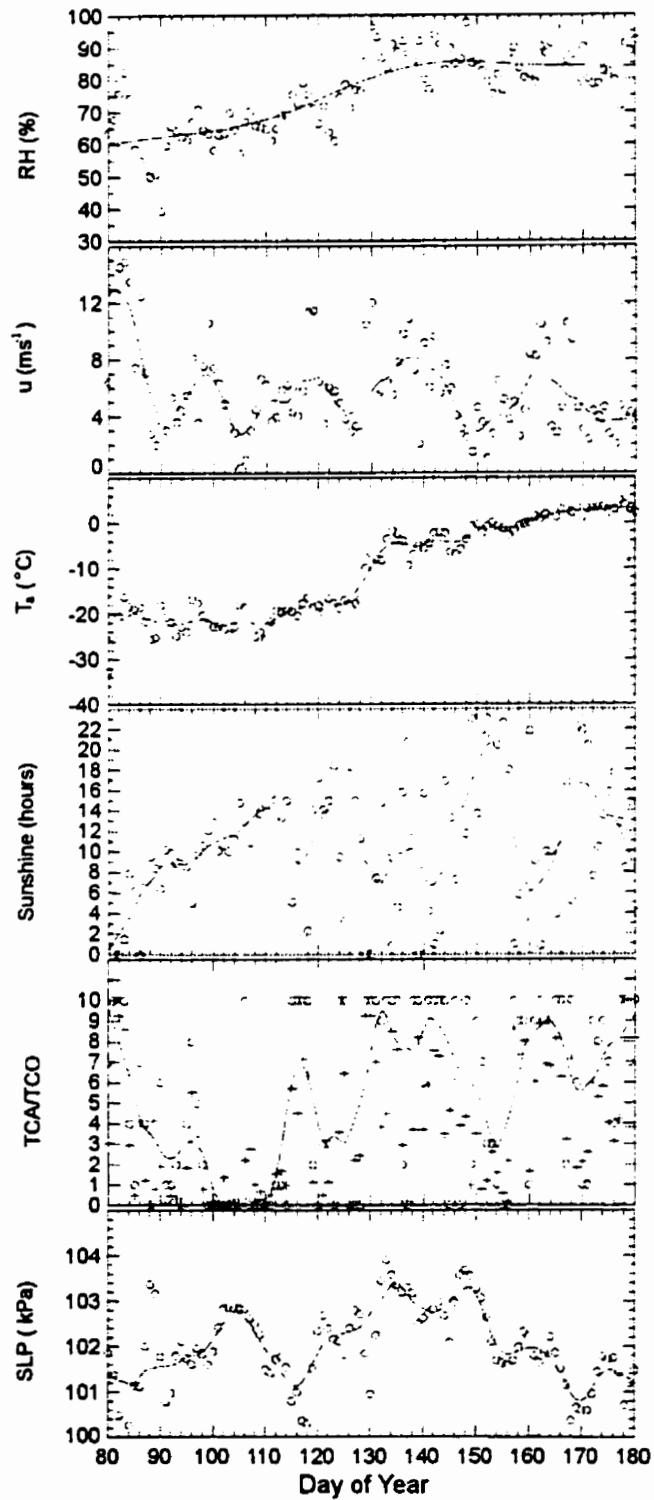


Figure 6.2b Daily summary of general meteorological conditions during 1993. Refer to Fig. 6.2a for details.

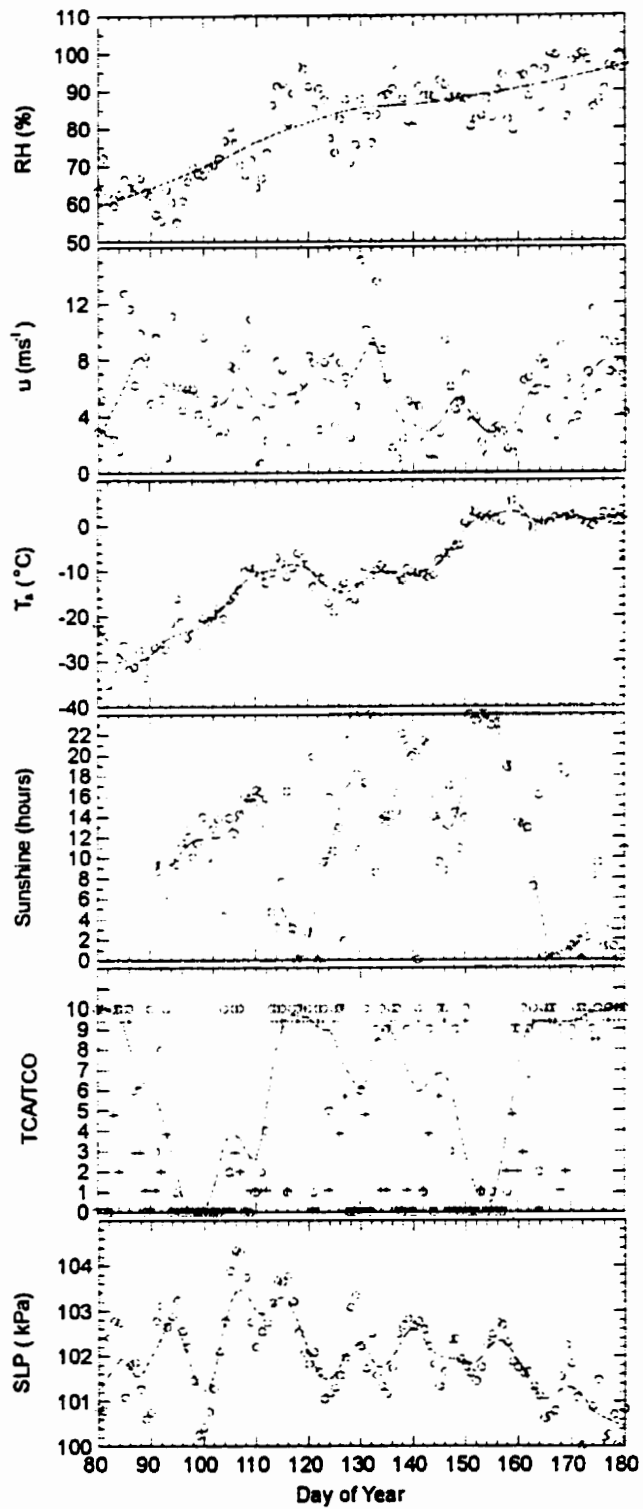


Figure 6.2c Daily summary of general meteorological conditions during 1995. Refer to Fig. 6.2a for details.

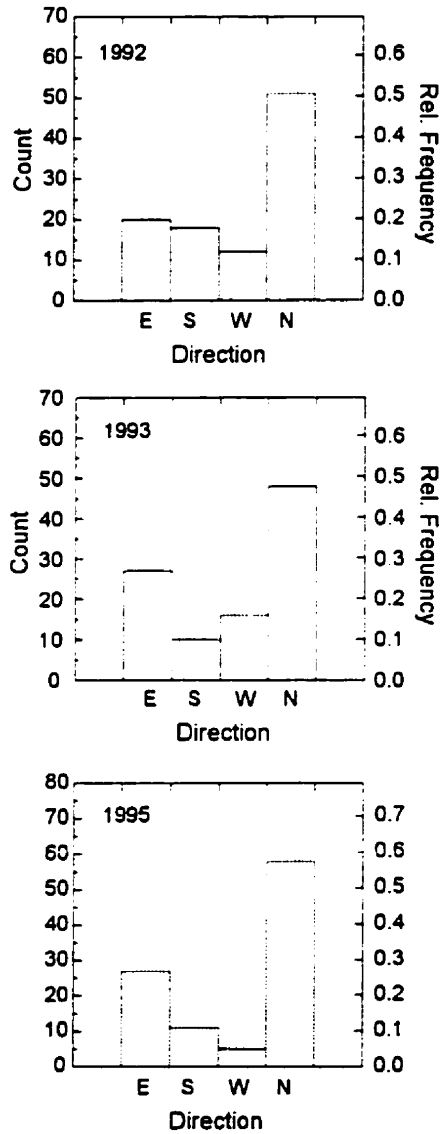


Figure 6.3 Frequency histogram of wind direction during the 1992, 1993 and 1995 SIMMS experiments.

The sinusoidal pattern exhibited by the time series of daily average sea level pressure at Resolute (Fig. 6.2 a to c) provides an indication of the frequency of the cyclone-anticyclone sequence and the persistence of the cyclone or anticyclone systems. An analysis in the time domain shows (refer to Fig. 6.4) that:

- periodic cycling is observed between 7 and 8 days (half period every 2 to 5 days) in 1992,
- the pattern exhibited during 1993 is poorly defined relative to 1992 and 1995, and
- periodic cycle is observed between 8 and 11 days (half period between 5 to 6 days) in 1995.

The cycling of pressure systems shown for 1992 and 1995 is in line with published observations (Maxwell, 1980). The region was dominated for extended periods by surface high pressure in 1993 and 1995, but not in 1992. The area was dominated by high pressure for much of the period between day 130 (May 10) and day 150 (May 30) in 1993, while Resolute was situated under intense high pressure during the first weeks of the 1995 spring season.

Total snowfall (refer to Fig. 6.5) was more than the long-term average at Resolute in both 1992 (47 cm) and 1993 (46.2 cm), while the spring of 1995 received an amount of snow (20.2 cm) comparable in magnitude to the region's long-term average between April and June (21.3 cm). The bulk of the snow in each year was deposited in association with storm events. The spring of 1995 received more than double the rainfall (6 mm – refer to Fig. 6.5b) than received in either 1992 or 1993. Only trace accumulations were recorded in 1992.

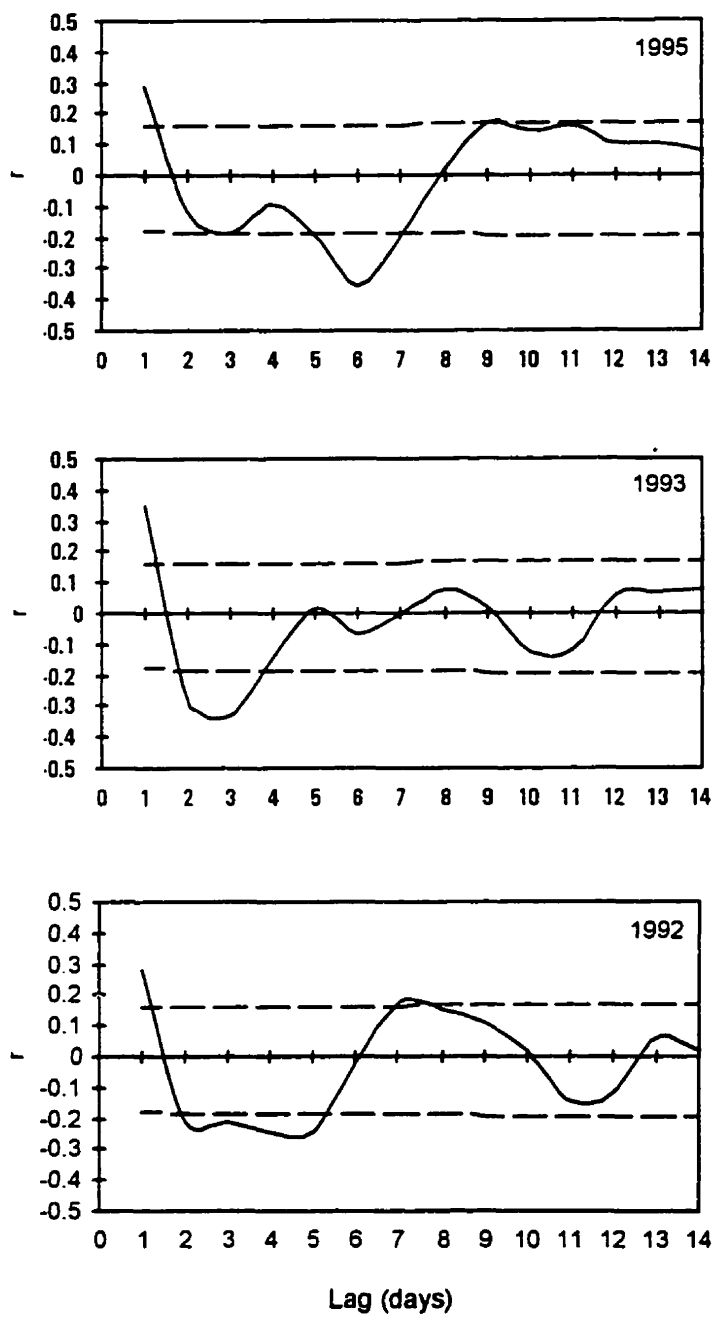


Figure 6.4 Autocorrelation coefficients of sea level pressure for time lags between 1 and 14 days ($n=93$) during the spring of 1992, 1993, and 1995. The dashed lines represent the upper and lower 90% confidence limits (after Haan, 1977).

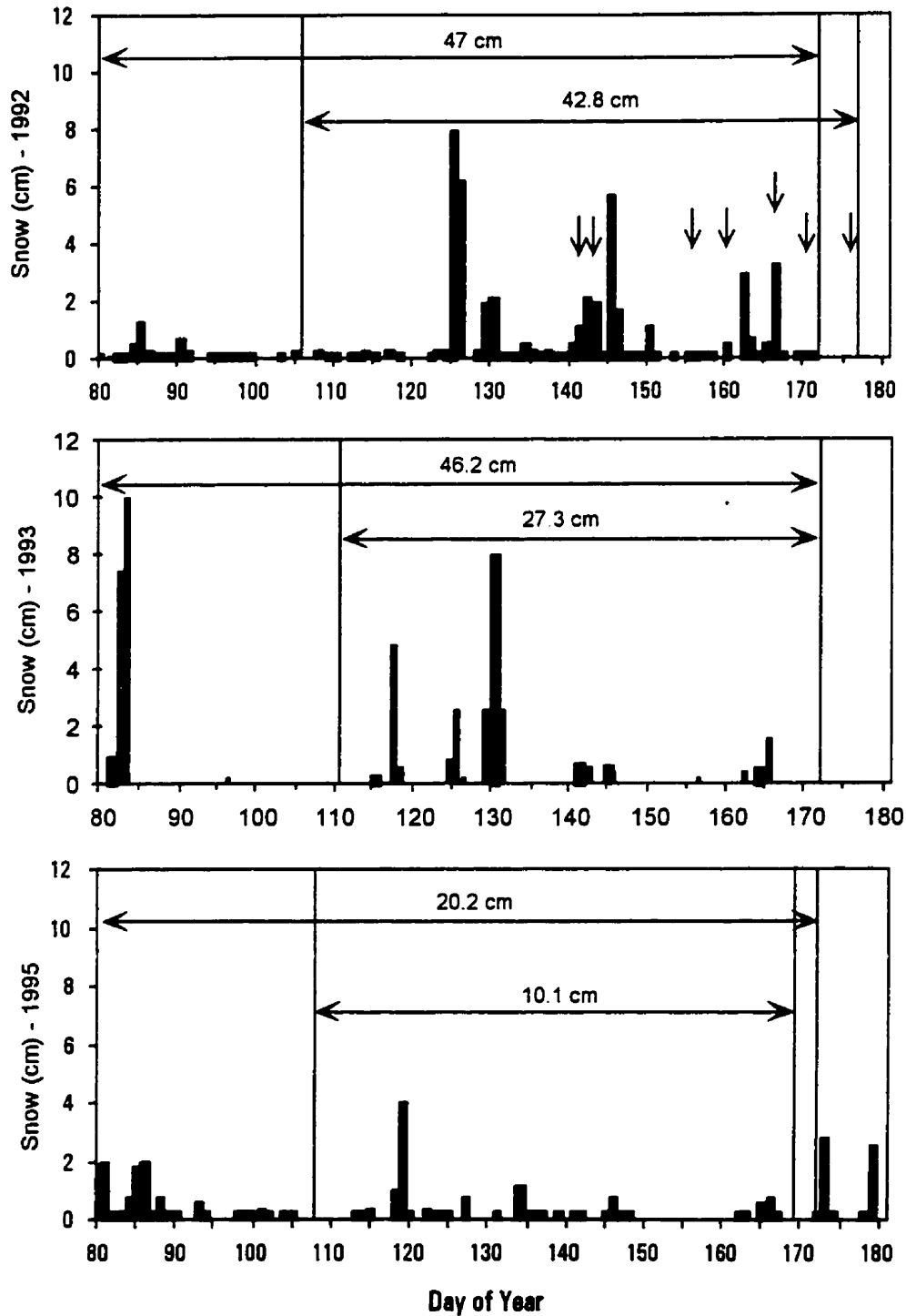


Figure 6.5a Snowfall measured at the Resolute weather station for the spring seasons of 1992, 1993, and 1995. The arrows indicate days on which trace rainfall were observed, while the vertical lines delineate the SIMMS field experiments. Day 172 represents the last day of spring (also marked with a vertical line).

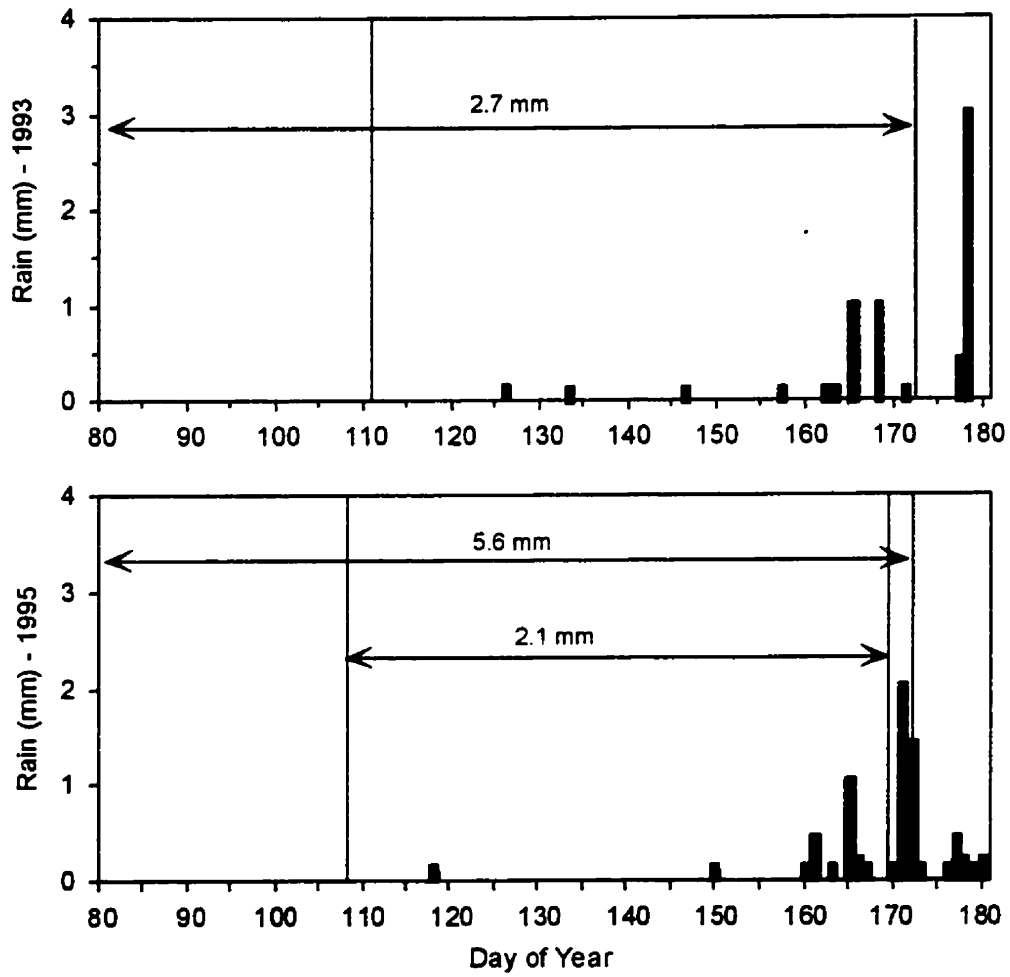


Figure 6.5b Rain recorded at the Resolute weather station for the spring seasons of 1993, and 1995. Lines and numbers are described in Fig. 6.5a.

6.5 Computational Results

6.5.1 Springtime Averages

The distribution of the major energy and radiation balance components and surface properties are presented in Fig. 6.6 and described in Table 6.2. The first, second and third quartile of each distribution are shown as vertical lines in each box. The whiskers denote the 10th and 90th percentile. The central value of both L^* and K^* are quite large relative to the energy balance terms, however the central value of Q^* is not substantially larger than the absolute value of the median of the other energy balance components. A large spread is exhibited by many of the energy balance components over the duration of the respective experiments. Many of the energy terms range (when averaged over the diurnal cycle) from highly negative, to strongly positive, and in most instances the range in flux magnitudes is several factors larger than their median value. The variation of each term is described in the context of seasonal change in the following sections.

6.5.2 Net Radiation and the Components of the Radiation Balance

Net radiation reported in this work is taken as the sum of the measured net solar and net long-wave radiation components. Appendix 7 outlines reasons for not using the measured flux. Net long-wave radiation loss exceeds or balances solar radiation gains by the surface (Fig. 6.7) resulting in a negative, or only slightly positive, radiation balance over much of the spring period. A seasonal rise in net radiation occurs shortly after day 150 at FYI'95, but isn't observed until after day 170 at FYI'92. The onset to rising Q^* reflects the seasonal increase in global and net solar radiation (Fig. 6.8 and 6.9), the late season decline in surface albedo and an associated increase in solar radiation transmitted through the snow cover (both shown in Fig. 6.10). The rate and timing of the seasonal drop in surface albedo and rise in radiative transmission varies among stations, the earliest occurring at FYI'95 (around day 150) and the latest at FYI'92 (around day 171). Note the factor of 10 difference in radiation transmitted to the sea ice surface between FYI'92 and the other sites. The 20 to 22 day lag in the onset to rising net radiation is a testament to the effect of a late spring snowfall and a persistent snow cover at FYI'92 on the radiation balance of sea ice, through its control over surface albedo. Daily average surface albedo remained above 0.7 for the entire FYI'92 experiment, while the late season values approached 0.45 during both FYI'93 and FYI'95.

Table 6.2 Statistics describing the energetics of the surface volume over the three FYI experiments. Statistics pertain to daily averages and units are $W \cdot m^{-2}$.

<i>Site</i>	<i>Statistic</i>	<i>Cases</i>	<i>Min.</i>	<i>Max.</i>	<i>Range</i>	<i>Mean</i>	<i>St. Dev.</i>	<i>Med.</i>
FYI'92	Q*	54	-13.63	45.23	58.86	18.29	15.02	20.61
FYI'92	Q*s	54	-13.67	44.65	58.33	18.20	15.21	19.97
FYI'92	K*	54	23.70	102.18	78.48	51.82	19.39	46.81
FYI'92	L*	54	-62.57	-0.85	61.72	-33.53	18.79	-36.60
FYI'92	Q*is	55	0.02	0.49	0.47	0.09	0.09	0.07
FYI'92	K↓b	58	0.02	3.10	3.08	0.25	0.47	0.11
FYI'92	dQs	47	-22.83	49.15	71.98	-0.63	18.02	-0.59
FYI'92	Q _M	47	-48.39	18.23	66.62	-5.97	19.72	-8.26
FYI'92	Q _{obs}	57	0.78	3.82	3.04	2.15	0.87	2.04
FYI'92	Q _{io}	57	-7.53	19.29	26.81	2.50	6.89	0.27
FYI'92	Q _{so}	57	-16.12	49.79	65.90	11.25	11.13	12.43
FYI'92	Q _H	46	-24.55	11.45	36.00	-5.56	8.84	-3.46
FYI'92	Q _E	46	-29.77	-1.50	28.26	-13.28	8.18	-11.84
FYI'93	Q*	44	-13.81	173.98	187.80	29.85	38.78	19.12
FYI'93	Q*s	44	-14.03	161.20	175.23	27.08	32.53	18.67
FYI'93	K*	47	31.24	237.61	206.37	72.01	40.64	64.36
FYI'93	L*	44	-77.29	-9.64	67.64	-42.17	20.15	-41.66
FYI'93	Q*is	50	0.07	42.75	42.68	2.76	8.09	0.29
FYI'93	K↓b	51	0.32	72.54	72.21	10.66	17.97	3.55
FYI'93	dQs	42	-31.26	109.91	141.17	20.95	24.53	10.50
FYI'93	Q _M	42	-80.95	30.03	110.99	-19.14	23.92	-6.51
FYI'93	Q _{obs}	48	0.35	2.49	2.14	1.28	0.53	1.39
FYI'93	Q _{io}	58	-20.60	18.90	39.50	0.97	8.69	0.62
FYI'93	Q _{so}	47	-9.36	14.18	23.54	0.44	7.22	-2.01
FYI'93	Q _H	43	-20.40	19.83	40.23	-0.41	6.83	-0.39
FYI'93	Q _E	42	-23.40	6.94	30.34	-5.72	6.45	-3.73
FYI'95	Q*	53	-13.44	110.44	123.88	18.21	32.56	9.00
FYI'95	Q*s	53	-14.00	61.40	75.40	12.83	20.27	5.70
FYI'95	K*	58	18.00	156.03	138.03	64.71	30.79	56.56
FYI'95	L*	53	-69.23	-15.21	54.02	-46.51	12.93	-47.56
FYI'95	Q*is	57	0.01	65.80	65.78	5.38	13.70	0.37
FYI'95	K↓b	55	0.23	65.96	65.73	6.90	16.52	0.72
FYI'95	dQs	50	-34.80	64.74	99.55	6.16	20.33	2.41
FYI'95	Q _M	50	-99.05	33.77	132.83	-8.55	28.68	-0.11
FYI'95	Q _{obs}	57	0.50	4.78	4.29	1.51	0.94	1.38
FYI'95	Q _{io}	57	-63.55	13.49	77.03	-2.51	14.15	2.04
FYI'95	Q _{so}	50	-12.36	12.94	25.30	1.40	6.47	1.78
FYI'95	Q _H	54	-18.28	12.90	31.18	2.20	6.06	3.30
FYI'95	Q _E	55	-27.57	-0.31	27.26	-8.87	6.43	-7.92

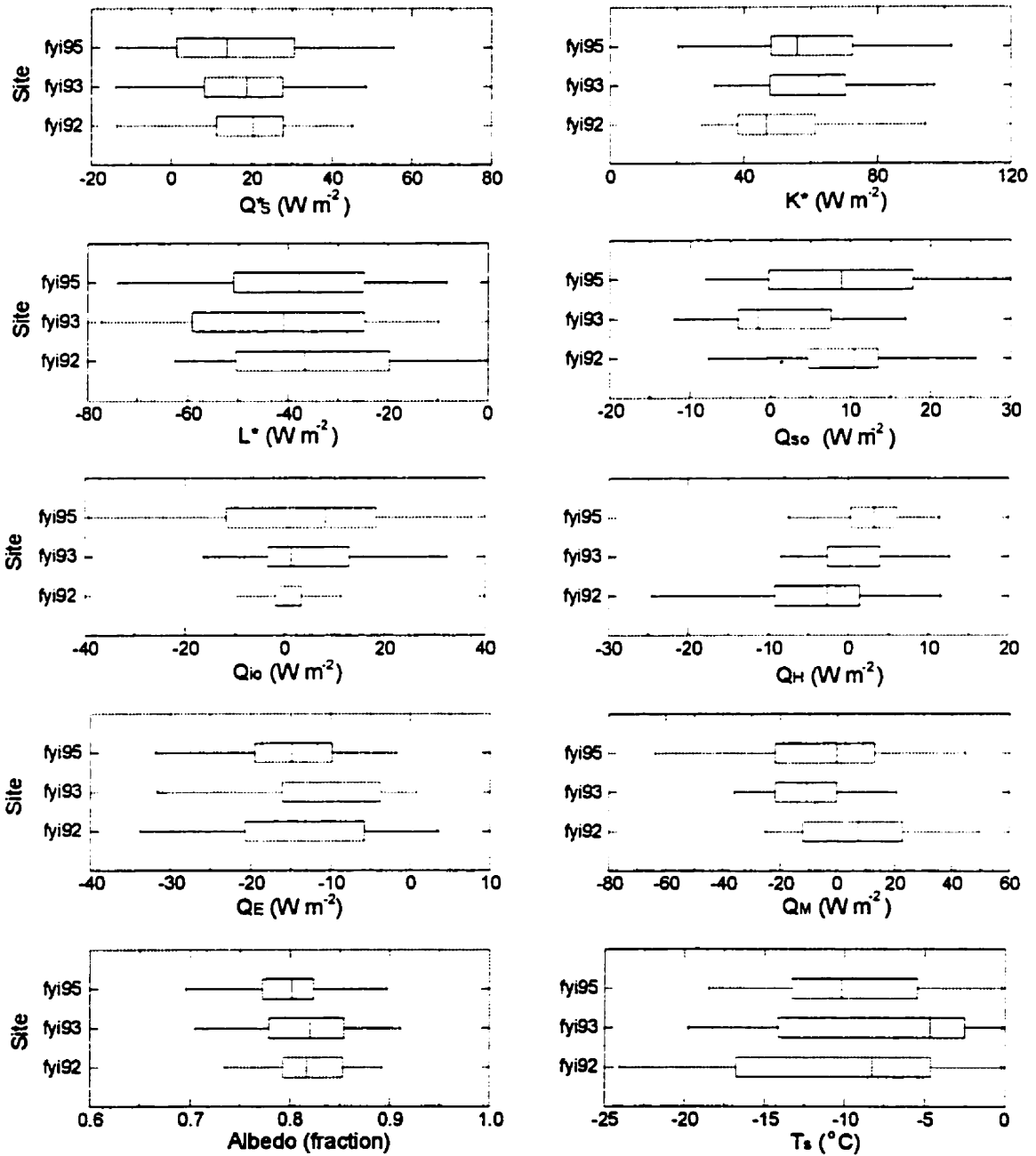


Figure 6.6 Box and whisker plots showing the spread in the distributions of the daily average energy fluxes and surface properties from each of the research sites.

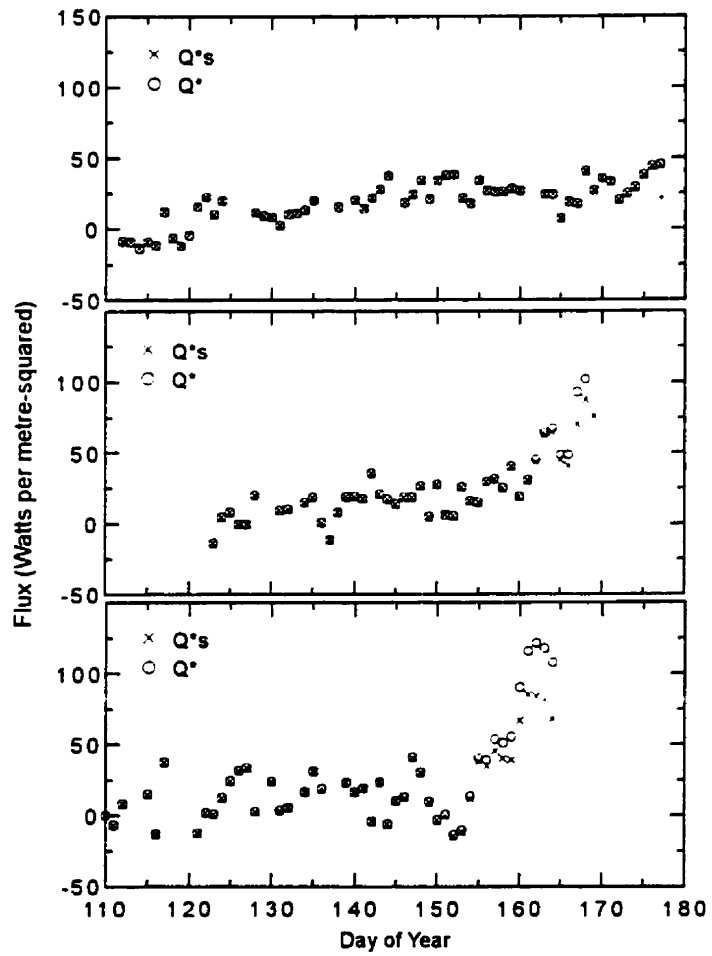


Figure 6.7 Daily average net radiation of the snow/ice/ocean volume (Q^*), and the net radiation of the snow volume (Q^*s), among the experimental sites.

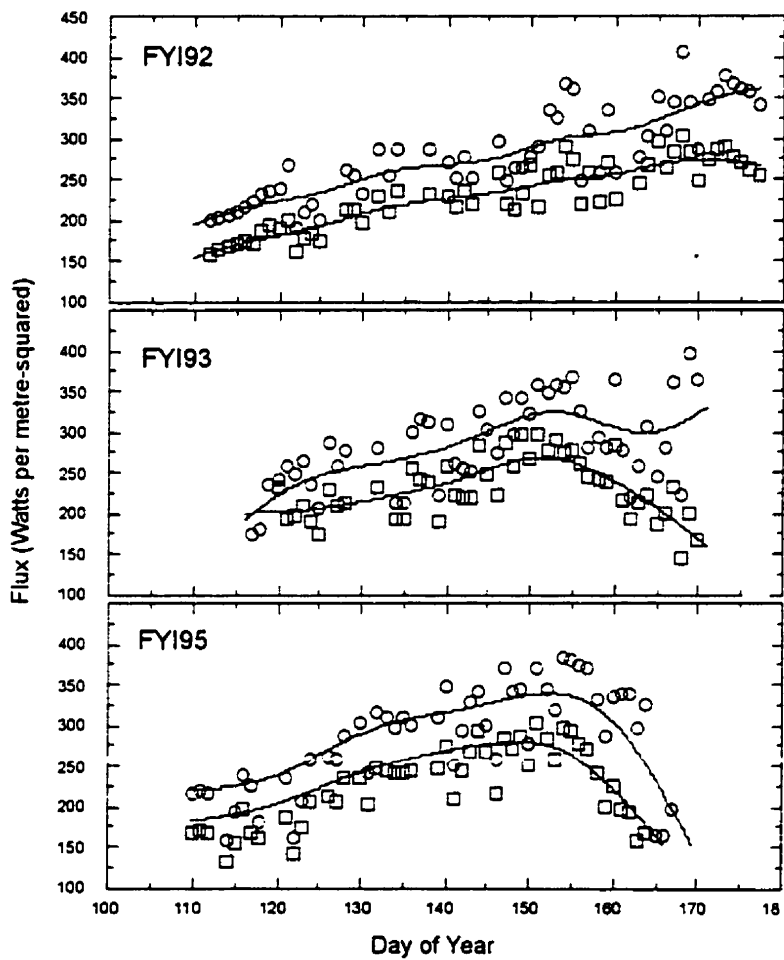


Figure 6.8 Daily average global radiation (open circles) and reflected solar radiation (open squares) for the first-year sea ice experimental sites. A LOWESS curve is fit through the daily average flux values.

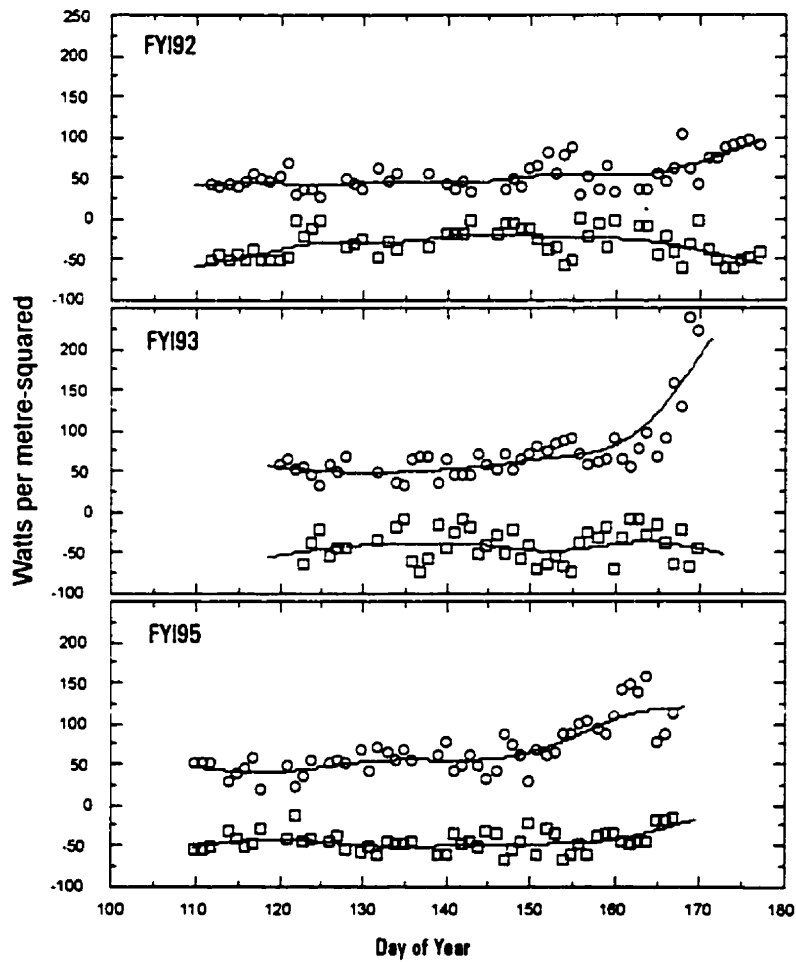


Figure 6.9 Daily net solar radiation (open circles) and net longwave radiation (open squares) for the first-year sea ice experimental sites. A LOWESS curve is fit through the daily average flux values.

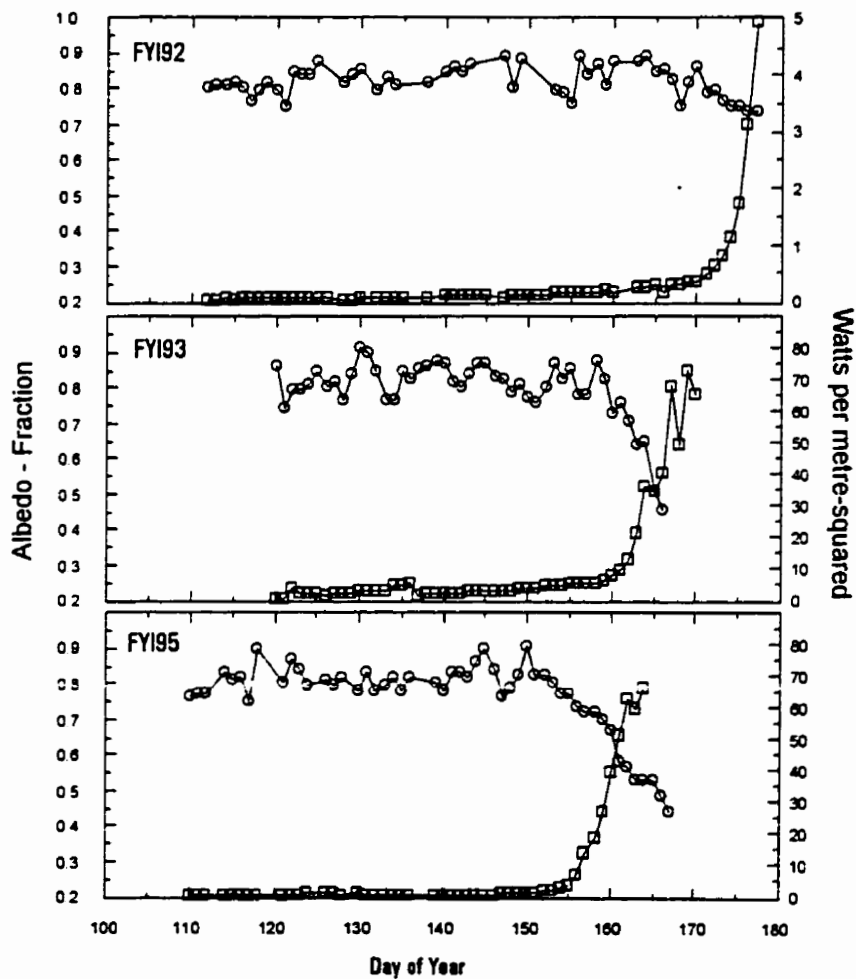


Figure 6.10 Daily surface albedo (open circles) and solar radiation transmitted through the snow cover (open squares; $W \cdot m^{-2}$) of the first-year sea ice.

Each surface maintains a net long-wave radiation deficit throughout the spring (Fig. 6.9). The daily average of both $L\downarrow$ and $L\uparrow$ increase as the seasons progress (Fig. 6.11), however, no seasonal rise in L^* is observed. The increased scatter in measured global radiation that is observed shortly after day 120 during SIMMS'92 is the consequence of a variable atmospheric optical depth, owing largely to increases in both cloud amount and opacity (Fig. 6.2 a). Much of the day to day variation in $L\downarrow$ and $L\uparrow$ is likewise attributed to variations in the cloud coverage and cloud base height. These linkages are discussed in Chapter 8. Minimum $L\downarrow$ under clear skies is typically around $160 \text{ W}\cdot\text{m}^{-2}$ and the flux maximum approaches $330 \text{ W}\cdot\text{m}^{-2}$ under full overcast conditions. The clear-sky minimum is approximately $50 \text{ W}\cdot\text{m}^{-2}$ less than measured over an Arctic polynya in the summer (Minnett, 1995), but is representative of average Arctic winter clear sky conditions (Ruffieux et al., 1995; Overland and Guest, 1991). On the other hand, our cloudy-sky maximum is greater than reported over sea ice in the Arctic Basin during the winter, but does correspond with the measurements from the polynya study.

The close association between Q^* and Q^*_s over most of the experiments (Fig. 6.7) indicates that the majority of the solar radiation interaction of the sea ice volume occurs on or within the snow in support of the modeling results of Chapter 5. The relatively high albedo of the underlying sea ice surface acts to reduce the net radiation at the ice surface by scattering back into the snow volume much of the transmitted flux, even during periods in which the snow is highly transmissive to solar radiation. The solar flux which is transmitted into the sea ice is negligible over much of the season, but did exceed $100 \text{ W}\cdot\text{m}^{-2}$ within the last days of the FYI'93 and FYI'95 experiments (Fig. 6.10). The solar radiation absorbed beneath the snow cover is equal to the difference between Q^* and Q^*_s , in Fig. 6.7. The term is negligible during the entire FYI'92 experiment and negligible for all but the final 4 to 8 days of a snow cover at each of the sites. At its maximum, Q^*_s represented between 35% and 55% of Q^*_s when averaged over the diurnal cycle between days 162 and 164 at FYI'93.

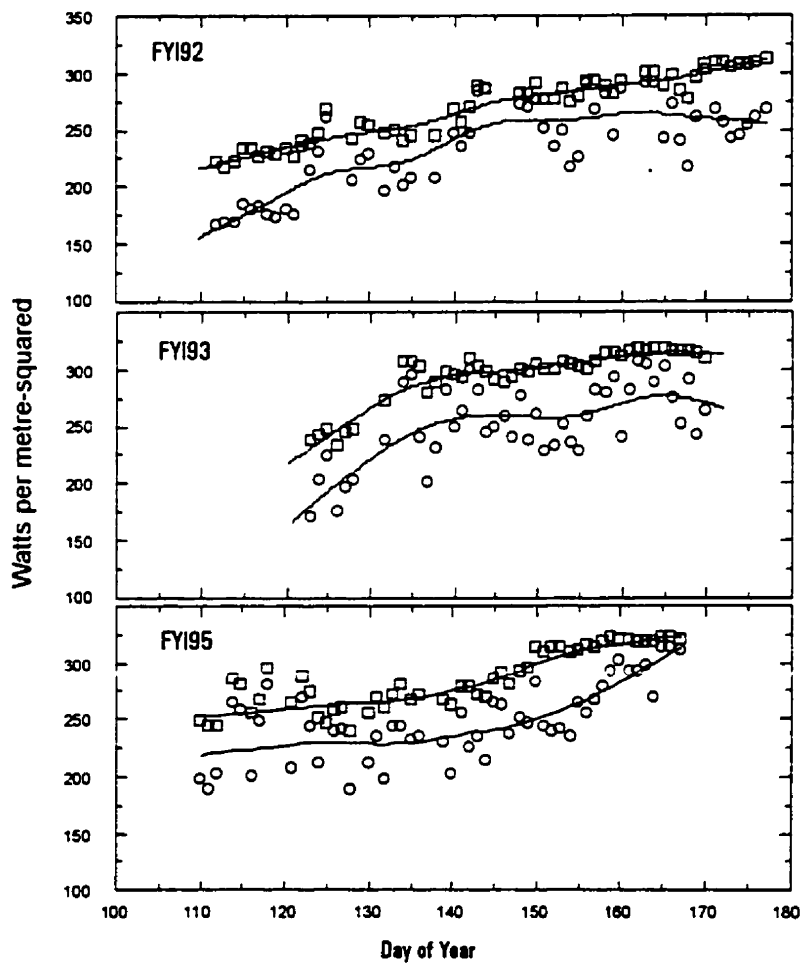


Figure 6.11 Daily average down-welling (open circles) and up-welling (open squares) longwave radiation at the first-year sea ice experimental sites. A LOWESS curve is fit through the daily average flux values.

6.5.3. Components of the Surface and Volume Energy Balance

6.5.3.1 Snow and Sea Ice Temperature

The temperature at the snow surface and base (Fig. 6.12) each increase with the progression toward summer. The snow surface temperature is initially less than the temperature of the ice surface at all sites, indicating that the snow thermally insulates the atmosphere from the ice/ocean volume in the early spring. Conversely, the snow acts to thermally insulate the ice/ocean volume from the atmosphere when the ice surface is colder than the snow surface. The daily average temperature at the snow and ice surface converge between days 164 and 166 at FYI'93 and by day 162 at FYI'95. A similar feature is not observed at the end of the 1992 field experiment, simply because the experiment did not continue long enough for the fairly thick snow cover to achieve an isothermal state.

The surface temperature responds rapidly to changes in the radiation balance and hence shows a substantial degree of day-to-day variation. The low thermal conductivity of the snow and its large optical depth limits most temperature exchange at the snow base to the slow process of conduction. The form of the temperature increase at the snow base reflects the response of the surface volume to the warming atmosphere without displaying the pronounced day-to-day variation observed at the snow surface, or within the near surface atmosphere. The respective temperatures converge toward the end of the spring period.

6.5.3.2 Thermal Properties of Naturally Occurring Snow and Sea Ice

The nature of the vertical variation in those thermal properties associated with Fourier's heat conduction equation (Eq. 2.16) is illustrated in Fig. 6.13 for snow over first-year sea ice. The ordinates of the figures represent the distance toward the snow surface from the snow base. Snow thermal conductivity is highly variable across the snow profile. Thermal conductivity in the mid-snow layer can be more than twice as large as in the upper- or basal layer at times during the spring transition. An increase in k_s occurs at all layers with the advancing season. k_s increases by about 100% in the basal layer (e.g., approximately $0.2 \text{ W}\cdot\text{m}^{-1}\cdot\text{C}^{-1}$ to $0.4 \text{ W}\cdot\text{m}^{-1}\cdot\text{C}^{-1}$) and by close to 70% in the mid-snow layer (i.e., from $0.34 \text{ W}\cdot\text{m}^{-1}\cdot\text{C}^{-1}$ to approximately $0.57 \text{ W}\cdot\text{m}^{-1}\cdot\text{C}^{-1}$) with the season's progression. The seasonal rise in k_s is a consequence of increasing snow density and temperature and decreasing snow salinity.

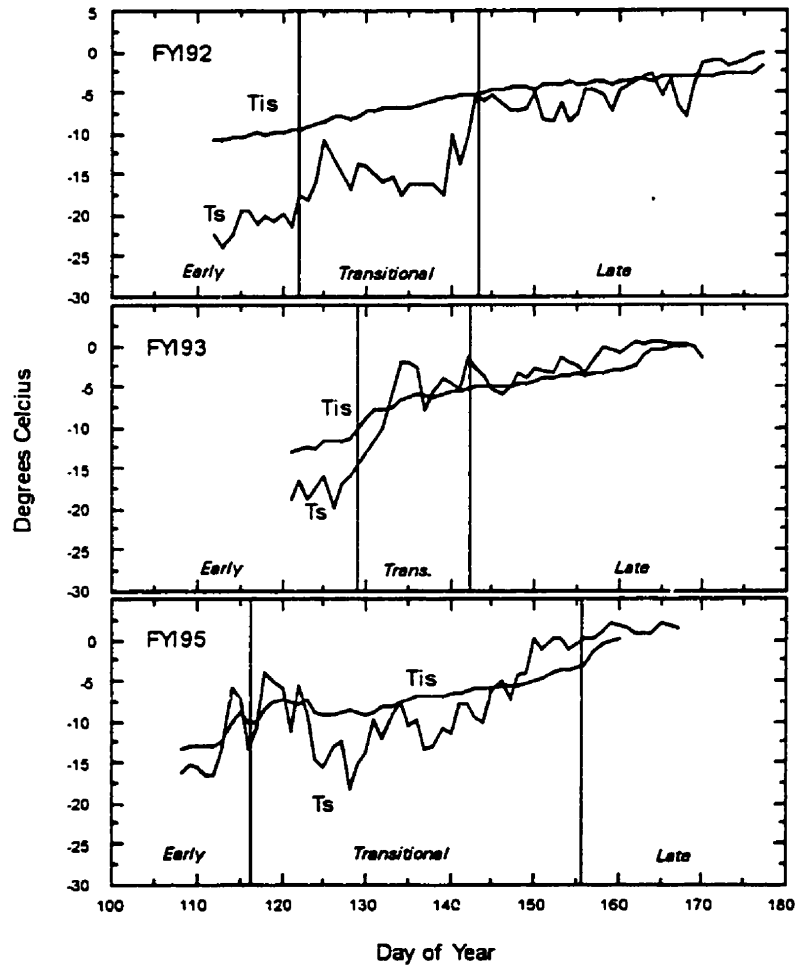


Figure 6.12 Daily average temperature at the snow and sea ice surface over each experiment. Seasonal categories, Early, Transitional and Late are described in the text.

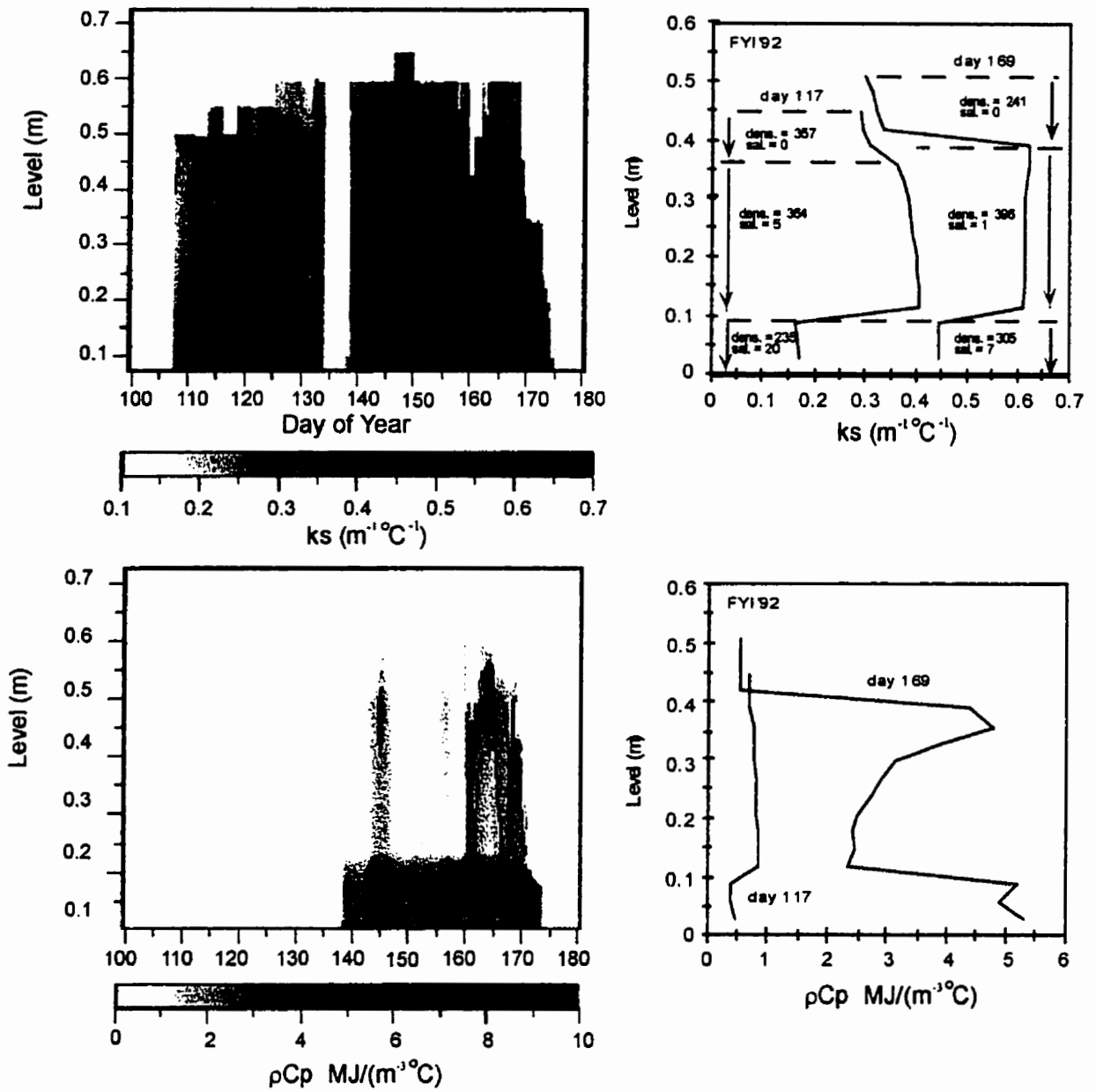


Figure 6.13 Cross section of snow thermal conductivity (upper plots) and heat capacity (lower plots) for snow over first-year sea ice.

The poorly conducting layers within the snow profile are mainly the consequence of low snow density. Low bulk density at the snow base during the early spring (e.g., day 117) is associated with depth hoar. Low density within the upper snow in the late spring (e.g., day 169) is believed the consequence of sub-surface sublimation, which leads to the formation of *firnspiegel*. On day 117 the snow temperature within the basal layer averaged -10.3°C , which is too cold for the development of large liquid contents. The relationship shown in Fig. 2.5 indicates that liquid water content is only around 2% by volume for the temperature, density and salinity combination observed over the first-year sea ice. The liquid contents in the upper snow on day 169 is limited to the snow's capillary-holding capacity at the onset of summer, which according to Fig. 4.7, is approximately 6% by volume. By day 169 we expect the percent liquid by volume in the snow basal layer to be at least between 5% and 6% (Fig. 2.5) for a snow density/salinity/temperature of $300\text{ kg}\cdot\text{m}^{-3}/7\text{ ppt}/-2.5^{\circ}\text{C}$, respectively. This estimate does not consider the possibility for liquid pooling at the snow base. Our estimate of k_s may underestimate the actual thermal conductivity of the layer in late spring if the percent liquid volume at the snow base exceeds the pendular limit (approximately 11% to 15% liquid by volume). Any underestimation in k_s at this time is of little consequence on the heat flux, because the temperature gradient at the snow base is small in the late spring.

The heat capacity also varies across the snow profile over first-year sea ice. Heat capacity increased at all levels within the snow with increasing snow temperature and density. The vertical variation of heat capacity increased with a warming snow volume. In the late spring (e.g., day 169) the heat capacity within the saline basal layer (lower 9 cm of the snow), averaged approximately $5.0\text{ MJ}\cdot\text{kg}^{-1}\cdot^{\circ}\text{C}^{-1}$, which is approximately two to three times larger than the average computed for the mid- and upper portions of the snow. By way of comparison the heat capacity varied by a mere 0.5 to $1\text{ MJ}\cdot\text{kg}^{-1}\cdot^{\circ}\text{C}^{-1}$ throughout the profile on days prior to day 120. The large increase in heat capacity, which is observed in the snow basal layer during the late spring, is a consequence of the rapid rise in saline ice specific heat with increasing temperature (refer back to Fig. 2.6). The heat capacity increased by a factor of ten in the snow basal layer and by a factor of 4 to 5 within the mid-snow layer over the measurement period. The term remained fairly constant within the upper-snow throughout the season. The reduction in snow density in the upper snow

layer offsets any increase in specific heat which otherwise should be attributed to increased snow temperature.

The depth within the seasonally evolving snow, which is thermally coupled to a surface over an atmospheric time scale (hereafter referred to as coupling distance), is a function of the material's thermal diffusivity. The thermal diffusivity of the snow responds to variations in the thermal conductivity and specific heat, in accordance with Eq. 2.17. The coupling distance will increase with increasing thermal conductivity and will decrease with increasing specific heat. Salt content will dramatically reduce the coupling distance by raising the specific heat (Fig. 2.6), regardless of snow density. The rate of heat diffusion, in response to a thermal forcing, is very different for saline and non-saline snow (Fig. 6.14). The ordinate is provided as negative distance, assuming the propagation of heat from the snow's upper boundary. If the depth scale were inverted, the relationship would describe the coupling distance into the snow volume from the snow base. The depth/time scale relationships are shown over a 60 minute period and over a 24 h period for the snow physical properties provided in Table 6.3. Temperature is prescribed at -3°C and -10°C , for snow salinity of 0 ppt and 15 ppt, and snow density is held constant at $300\text{ kg}\cdot\text{m}^{-3}$. The prescribed salinity and density are within the range experienced within a snow profile over first-year sea ice. The corresponding snow liquid volumetric proportion ($\rho_s=300\text{ kg}\cdot\text{m}^{-3}$) at -3°C and snow salinity of 15 ppt is 7.8% (refer to Fig. 2.5), which is well within the pendular moisture regime. All liquid contents during the other scenarios are within the irreducible liquid content range (i.e., less than approximately 2% by volume).

The coupling distance is greater in non-saline snow, relative to saline snow and the discrepancy between the two increases with increasing snow temperature. For example, at -3°C , a non-saline snow depth of 33.5 cm (or roughly the depth of snow cover over first-year sea ice) is coupled to the forcing boundary over the diurnal period. In contrast, only 6 cm of saline snow is coupled to the boundary over a 24 h period. The presence of salts, in our example, reduces k_s by 8.4% at -3°C , but more importantly, raises the specific heat by over a factor of 15 (i.e., from $2091.5\text{ kJ}\cdot\text{kg}^{-1}\cdot^{\circ}\text{C}^{-1}$ to $32090.1\text{ kJ}\cdot\text{kg}^{-1}\cdot^{\circ}\text{C}^{-1}$). Consequently, the available heat energy is largely consumed by latent heat associated with changing brine volume in saline snow and does not contribute to an enthalpy flux.

The difference in thermal properties between the saline and non-saline snow is much smaller at cold temperatures and the difference in the thermal diffusion coefficient and the coupling depth are likewise reduced. A larger coupling distance is observed for saline snow at colder temperatures, while a shorter coupling distance is computed for non-saline snow relative to the warm snow scenario. Approximately 15 cm of saline snow from a boundary will be affected by thermal forcing over a diurnal cycle.

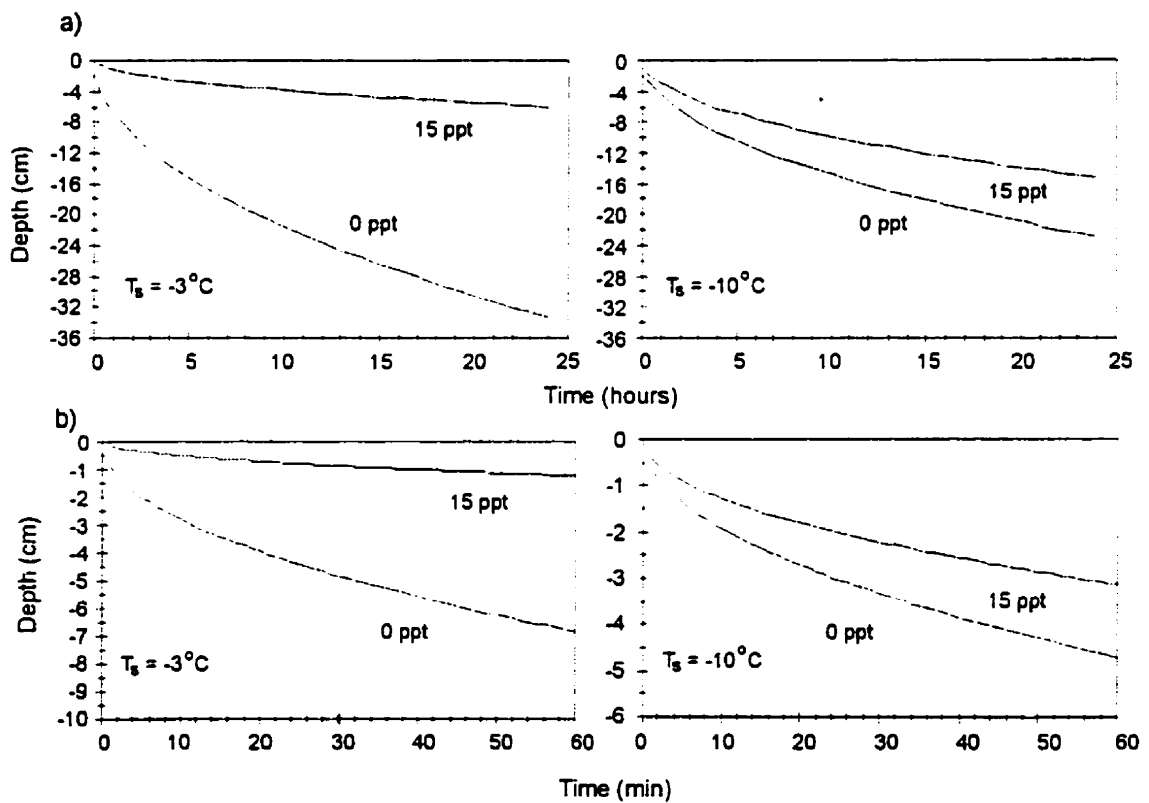


Figure 6.14 The distance a temperature change propagates through the snow as a function of time (a) over the diurnal cycle and (b) within an hour. Distance relationships are shown for both warm ($T_s = -3^\circ\text{C}$) and cold ($T_s = -10^\circ\text{C}$) snow.

The major ramifications of these observations are that:

- oceanic heating will not likely participate in atmospheric energy interactions at the snow surface over the course of a 24 hour period in the presence of a saline snow layer,
- the sea ice surface is more thoroughly insulated from atmospheric heating under saline snow, relative to non-saline snow,
- solar energy absorbed by the snow volume is potentially available to the surface energy balance on time scales less than one minute for non-saline snow.

The first point indicates that the bulk of oceanic heating will be confined to the snow base, because salinity typically increases toward the ice surface. The second point acts to delay melt during the spring and summer, while the first point acts to warm the sea ice volume, thus reducing sea ice growth during the fall and winter. The third point indicates that solar energy is readily available for transfer to the atmosphere and will not likely contribute to the volume energetics over time scales greater than about one minute in non-saline snow. This estimate is based on our observation that over 90% of the radiation absorbed by the snow cover occurs within the upper cm of the snow (refer to Section 5.6). Solar radiation will contribute to melt at the brine/ice contacts for saline snow and the time lag necessary for absorbed solar radiation to diffuse to surface will increase with increasing snow salinity. The presence of a saline layer also has ramifications on the overlying snow morphology. The temperature gradients above the saline layer should steepen in response to heat loss by the snow surface and warming at the snow base, thereby encouraging the growth of faceted snow crystals.

Table 6.3 Physical properties corresponding to the curves appearing in Fig. 6.14.

Property	Non-Saline Snow	Non-Saline Snow	Saline Snow	Saline Snow
S (ppt)	0	0	15	15
ρ_s ($\text{kg}\cdot\text{m}^{-3}$)	300	300	300	300
T_s ($^{\circ}\text{C}$)	-3	-10	-3	-10
k_s ($\text{W}\cdot\text{m}^{-1}\cdot^{\circ}\text{C}^{-1}$)	0.64	0.29	0.32	0.29
c_p ($\text{kJ}\cdot\text{kg}^{-1}\cdot^{\circ}\text{C}$)	2.091	2.0	32.1	4.6
ν ($\text{m}^2\cdot\text{s}^{-1}$) $\times 10^{-7}$	10.0	4.8	0.33	2.1

The physical properties of the sea ice are not extensively documented in this work, hence a detailed examination of the vertical variation of the thermal properties is not performed. Over the

experiments, the hourly averages of the effective thermal conductivity for the first-year ice ranges between 1.5 and 2.5 $\text{W}\cdot\text{m}^{-1}\text{C}$, averaging 1.9 $\text{W}\cdot\text{m}^{-1}\text{C}$.

6.5.3.3 Conductive Heating

The temperature structure within the snow and upper sea ice volume drives the conductive heat flux. The nature of the temperature structure is shown for deep snow over thick FYI (e.g., FYI'92 see Fig. 6.15). The temperature gradient appears to be highly non-linear. It weakens as the volume warms and is stronger near to the snow surface, relative to snow base and sea ice surface. At midnight, temperature gradients in excess of $60^{\circ}\text{C m}^{-1}$ are observed during the first days of the FYI'92 experiment, which is more than seven times greater than the temperature gradient observed over the same period in the upper ice volume (i.e., between 7.5 to 8°C m^{-1}). The temperature isolines within the sea ice are evenly spaced during the first 20 to 30 days of the experiment, indicating a near linear temperature gradient.

Within the snow volume, and over the spring transition, the conductive heat flux within the first-year sea ice snow cover is generally less than $30 \text{ W}\cdot\text{m}^{-2}$ and much smaller at solar noon relative to solar midnight (Figure 6.16 a and b). A positive flux in the figure is directed toward the atmosphere. In this example the form of the heat flow through the upper volume of first-year sea ice and snow is in an extremely non-steady state. It is essentially capped by the poorly conducting snow basal layer during the first 20-days of the experiment and prone to reversals in flux direction within the profile during the final weeks of the experiment. The combination of high snow heat capacity and low thermal conductivity combine to reduce the material's thermal diffusivity, thereby decoupling the snow surface from the sea ice. Despite the presence of this poorly conducting snow base, a strong heat flux of greater than $25 \text{ W}\cdot\text{m}^{-2}$ is maintained at the snow surface at night. This flux is driven by radiative cooling at the surface and operates independently of ocean heat. The heat loss by the volume is solely offset by heat stored within the snow cover.

The general trend is for the conductive heat flux at the snow and sea ice surface of each site to decrease with the spring progression (Fig. 6.17). Conductive heating at the ice surface (Q_{io}) is highly positive during the initial days at each first-year sea ice station. The maximum 24 hour average ranges between 20 and $40 \text{ W}\cdot\text{m}^{-2}$ and averaged between 10 to $20 \text{ W}\cdot\text{m}^{-2}$ over the first 10-days of each of the experiments. This value is comparable in magnitude to the average flux of 17.4

$\text{W}\cdot\text{m}^{-2}$ as reported by Makshtas (1991) for first-year ice in the central Arctic Ocean for the month of April. No measurements of the conductive heating at snow surface (i.e., Q_{so}) over sea ice are available for comparison with our study. The maximum Q_{so} can be potentially quite large, and may approach $50 \text{ W}\cdot\text{m}^{-2}$ (as a daily average).

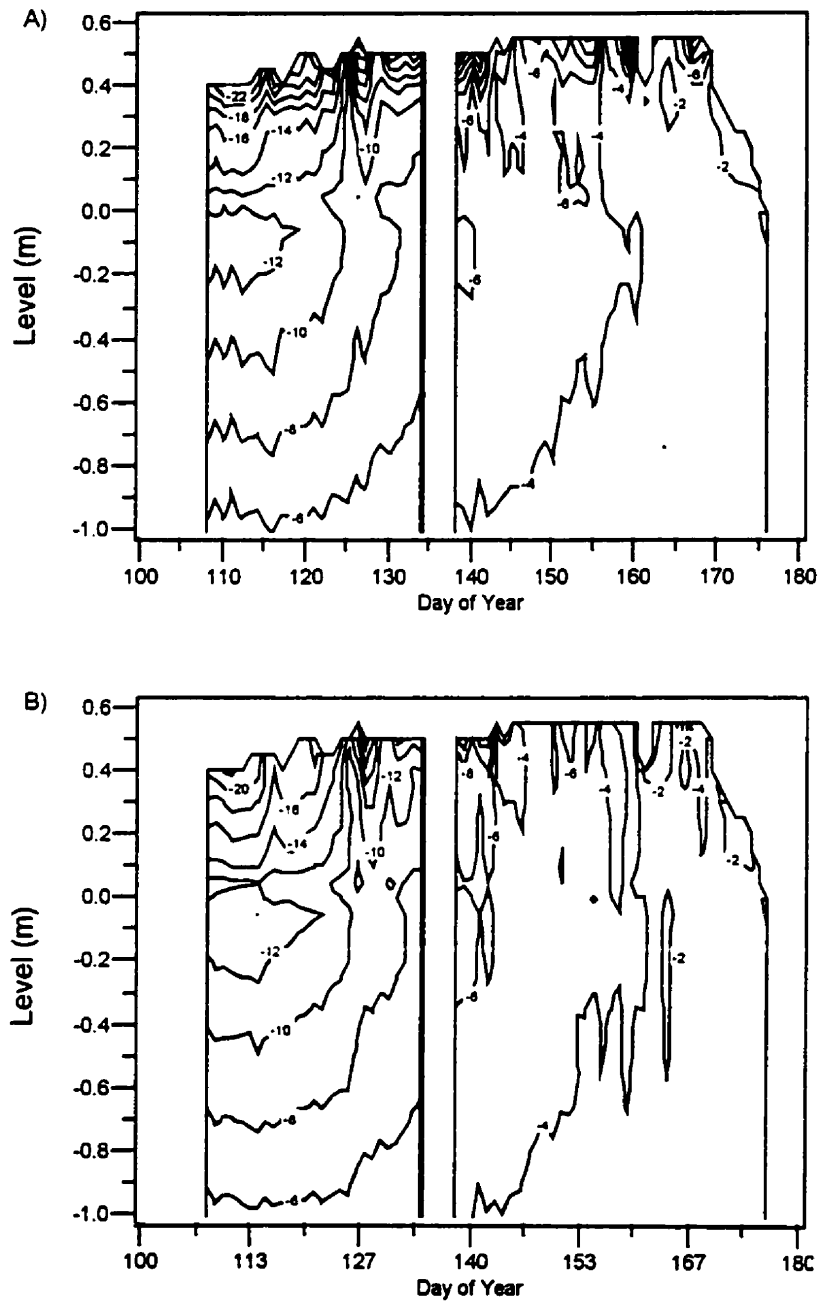


Figure 6.15 The temperature structure within the snow and upper sea ice volume at FYI'92 for (a) solar midnight and (b) solar noon.

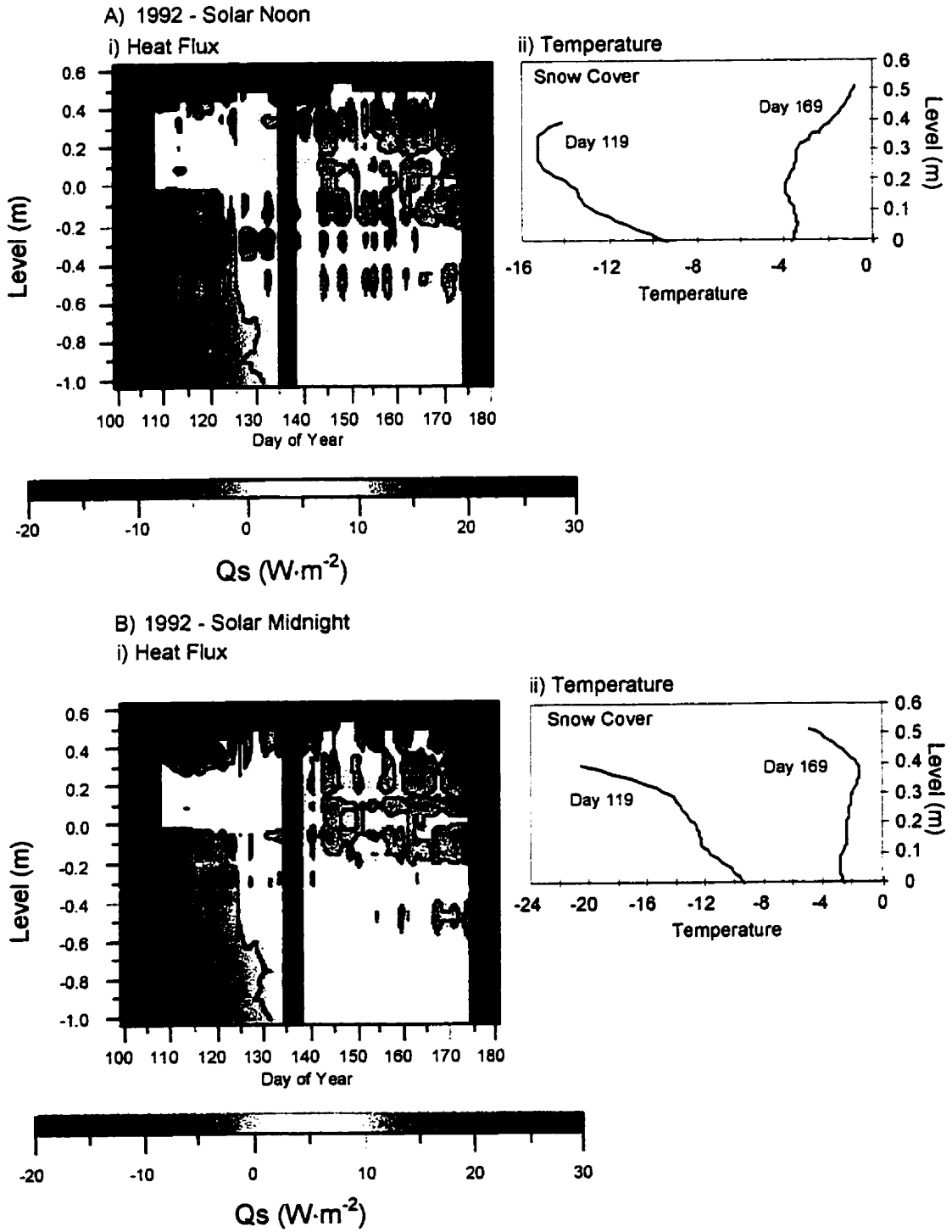


Figure 6.16 The seasonal evolution of heat conduction through the snow and upper sea ice at (a) solar noon and (b) solar midnight.

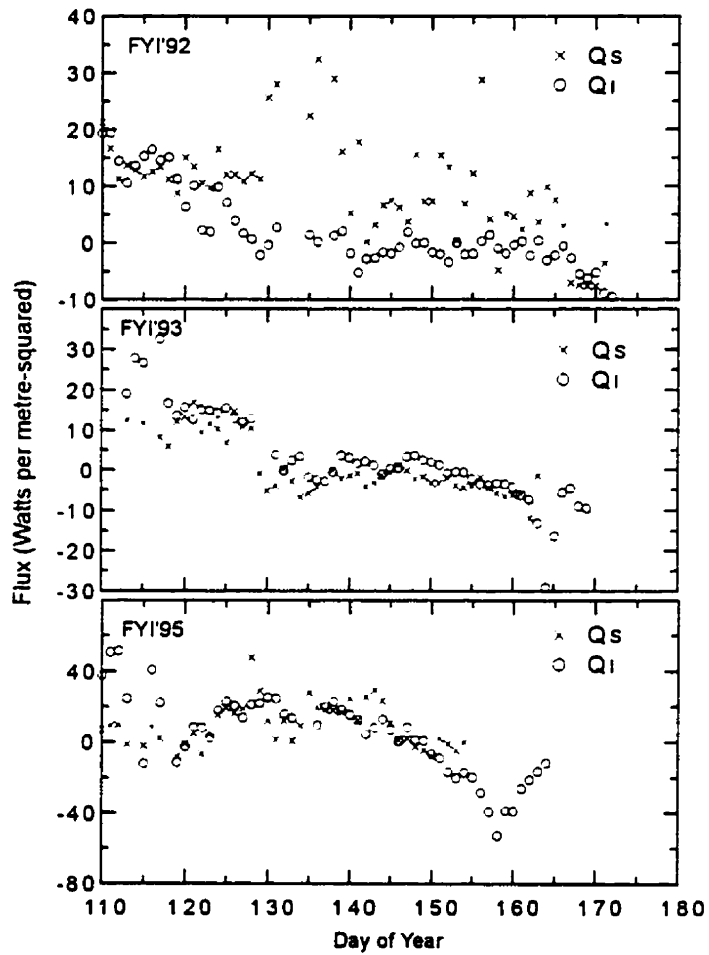


Figure 6.17 Daily average conductive flux at the snow (Q_{s0}), and ice (Q_{i0}) surface at the first-year sea ice sites.

The downward conductive flux (i.e., negative values) observed toward the end of each experiment correspond to the rapid rise in the temperature of the snow/ice interface (Fig. 6.12) and a reversal in the near ice surface temperature gradient (e.g., see day 164 in Fig. 6.18). The heat flux represents the net of the downward heat flow through conduction and heat associated with the mass transport of water. Net radiation at the ice surface is considered secondary as a forcing agent on Q_{i0} because $K_{\downarrow b}$ is only appreciable when the surface is warm (refer to Fig. 6.9). At this time the bulk of any absorbed solar radiation should be directed into melt, particularly over saline first-year sea ice. The intensity of the downward conductive flux at the ice surface is reduced, in response to a slackening of the temperature gradient (e.g., refer to day 170 in Fig. 6.18).

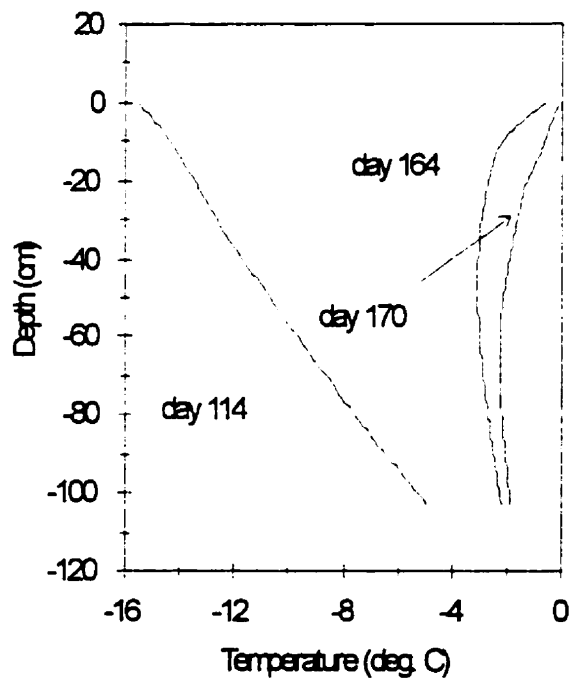


Figure 6.18 Different forms the temperature gradient within first-year sea ice shows during the spring transition. Examples are taken during FYT'93.

The intensity of the downward conductive heat flux at the ice surface is larger during the latter portion of FYI'95 relative to FYI'93 and FYI'92 (Fig. 6.17). This flux may be related to heat associated with water drainage. Over twice as much rainfall was received during the spring of 1995 relative to the other seasons (Fig. 6.5b), and we observed high liquid contents at the snow base by day 156 in 1995. Since an enthalpy flux associated with rain is not considered in the Q_M computation, the energy equivalent melt rate computed during and after rain is probably in error.

The conductive flux at the snow surface is not computed during the period in which the snow volume is highly transmissive to solar radiation because of the potential for solar heating of the temperature sensors. This occurs shortly after melt onset at FYI'93 and FYI'95. At these times the snow profile is near isothermal and the conductive flux should not substantially depart from zero over the diurnal cycle.

6.5.3.4 The Turbulent Heat Exchange

The turbulent heat fluxes (i.e., Q_H , Q_E) show pronounced short-term fluctuations relative to their local means (Fig. 6.19a and b). The daily average sensible heat flux fluctuates between removing and supplying heat to/from the surface on a day to day basis, while the daily average latent heat flux is usually directed away from the snow surface. Rarely is the daily average sensible heat flux greater than $\pm 20 \text{ W}\cdot\text{m}^{-2}$, while the daily average Q_E loss can approach $40 \text{ W}\cdot\text{m}^{-2}$. A daily average loss of $40 \text{ W}\cdot\text{m}^{-2}$ is equivalent to a loss of approximately 3 mm of snow over a 24 hour period at -10°C , assuming a snow density of $350 \text{ kg}\cdot\text{m}^{-3}$. Therefore, the mass loss associated with sublimation can be appreciable over a prolonged period.

The sign and magnitude of the sensible heat flux reported here is consistent with other studies over sea ice (e.g., Makshtas 1991, Leavitt et al., 1978, Ruffieux et al., 1995) during the spring season. Our latent heat flux however can be substantially larger than reported elsewhere. For example, the latent heat loss over the Beaufort Sea during the AIDJEX experiment only averaged about $3.5 \text{ W}\cdot\text{m}^{-2}$ during May and early June (Leavitt et al., 1978). This is comparable in size to our median flux during FYI'93, but their vapour loss is smaller than observed at FYI'92 ($-11.84 \text{ W}\cdot\text{m}^{-2}$) and FYI'95 ($-7.92 \text{ W}\cdot\text{m}^{-2}$) (Table 6.2). Steffen and DeMaria (1996) also reported the latent heat flux to be on average less than $7 \text{ W}\cdot\text{m}^{-2}$ under winter conditions in Barrow Strait.

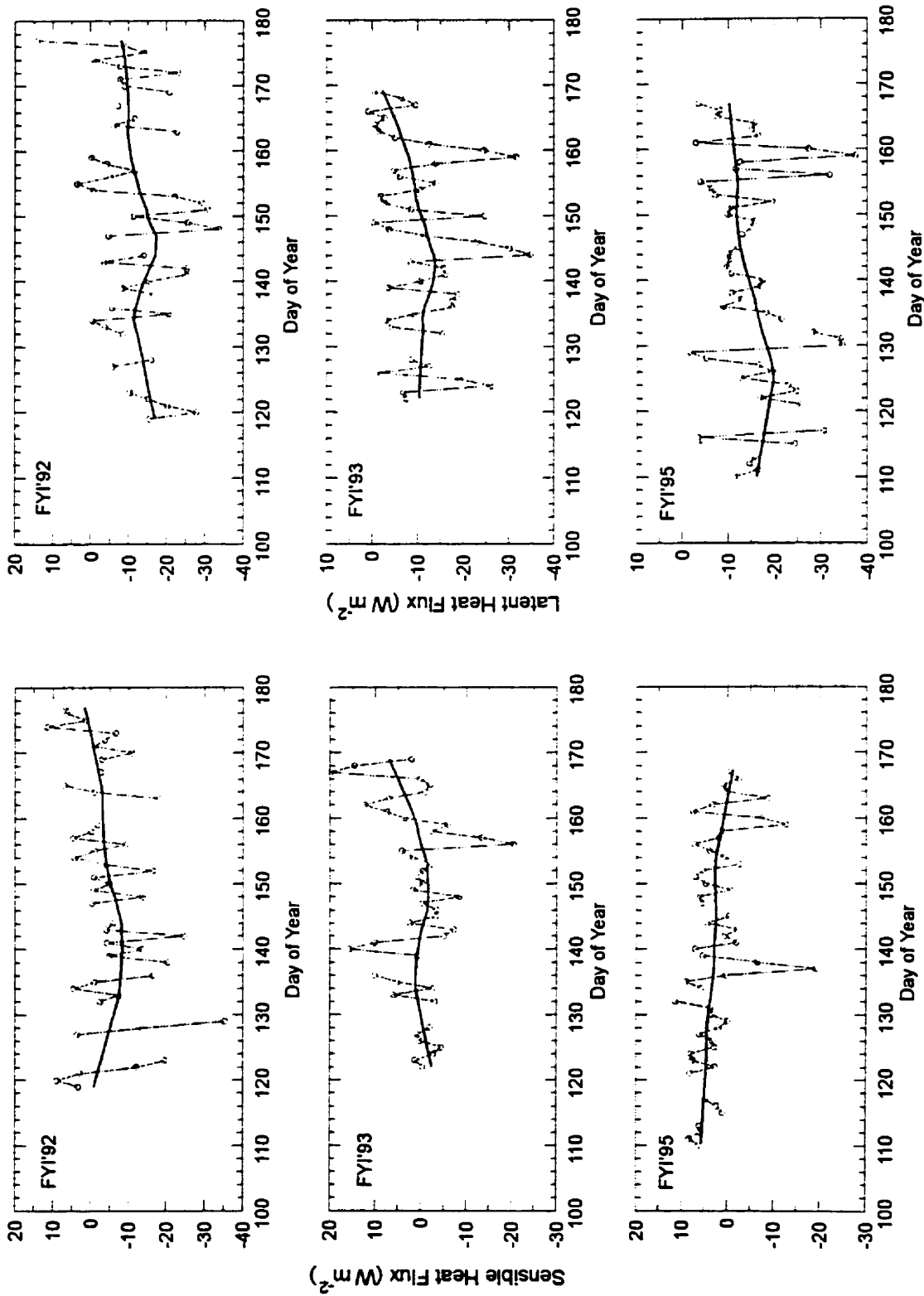


Figure 6.19 Daily average sensible and latent heat flux. Bolded line denotes the LOWESS fit through the daily average values.

An examination of the stability parameter distribution indicates that an unstable boundary layer is rare during the spring season (Table 6.4). Boundary layer instability is most frequent in 1992, and even then, the tenth percentile of the stability function is only -0.649. By comparison, the tenth percentile of the stability function in both 1993 and 1995 is near zero, indicating near neutral stability.

Table 6.4 Ranked distribution of the hourly computed Monin-Obukhov stability parameter.

Percentile	FYI'92	FYI'93	FYI'95
90 th	2.00	2.00	2.00
75 th	0.19	1.05	0.20
50 th	0.00	0.03	0.05
25 th	-0.11	0.00	0.01
10 th	-0.659	-0.02	-0.02
N	1003	1069	1179

The 90th percentile in each of the three experiments is the same ($\xi=2$). This is an artifact of our programming. Hicks (1976) shows that $\Phi_{(H,L,M,V)}$ asymptotes near 10 for ξ of greater than one. Therefore the stability function is assigned as two whenever $\Phi_{(H,L,M,V)}$ was observed to be greater than 10. There is still no agreement on the values of the universal stability functions under very stable conditions (Brutsaert 1982), but small variations in the stability parameter are inconsequential at these times.

6.5.3.5 Changing Heat Storage within the Snow and the Energy of Fusion

Atmospheric heat storage within the snow volume evolves through three stages over the spring, namely, a period of net heat deficit, no net change in heat storage and a period of net heat surplus (Fig. 6.20a). The rise from the transitional (no net change in heat storage) to the period of heat surplus is rapid at all sites, but the timing varies between seasons. The transition occurs approximately 10 days later at FYI'92, relative to FYI'93, and almost 20 days later than experienced in 1995. This lag is consistent with the time lag observed between experiments for α and Q^* . The maximum atmospheric heating of the snow can exceed $80 \text{ W}\cdot\text{m}^{-2}$ when averaged over the diurnal cycle.

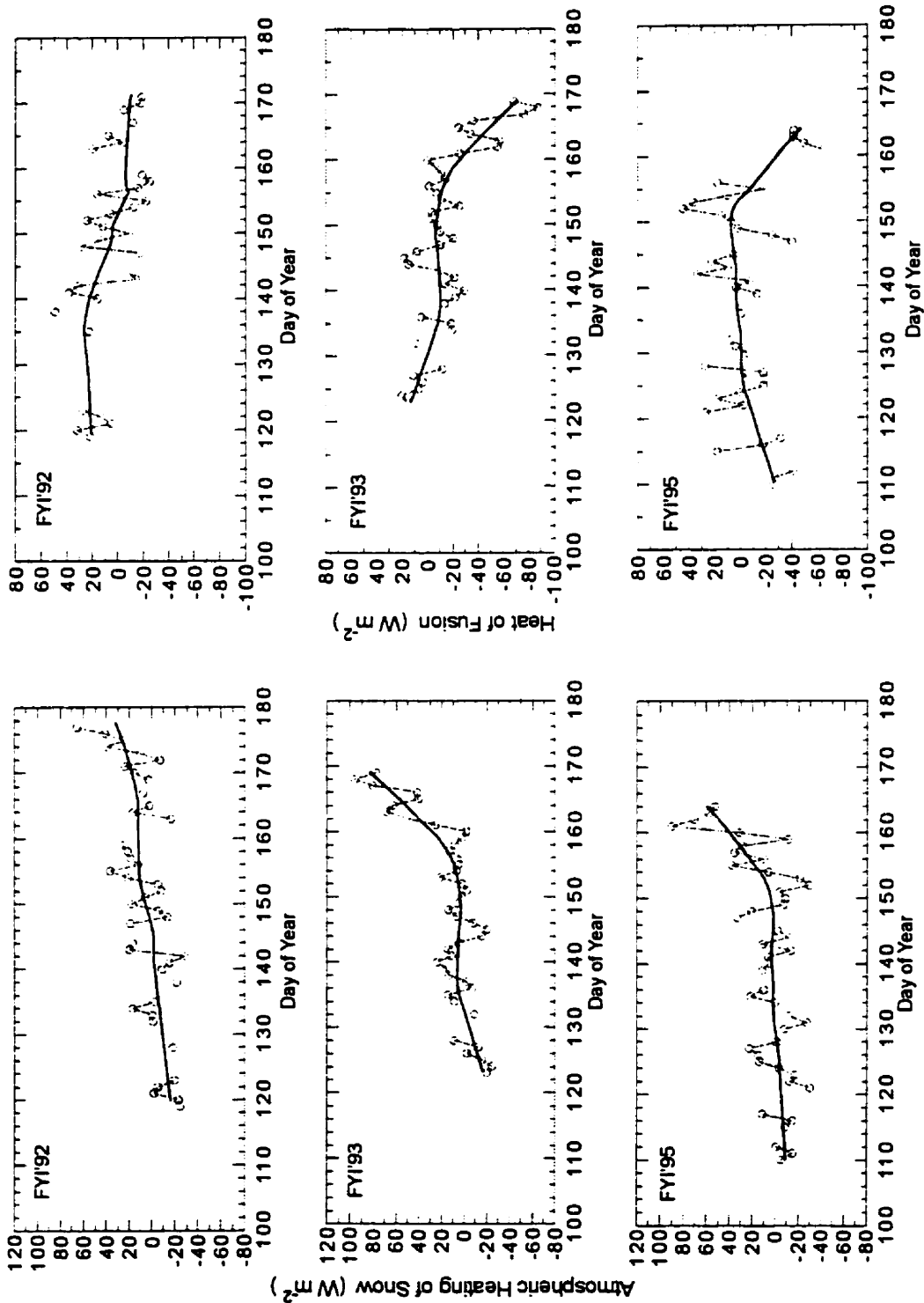


Figure 6.20 Daily average of atmospheric heating to the snow and heat of fusion. Bolded line denotes the LOWESS fit.

A rapid transition from net ice production to net melt over a 24 hour period occurs with the progression into the period of snow heat surplus (Fig. 6.20b). Maximum 24 hour melt rates can exceed $-80 \text{ W}\cdot\text{m}^{-2}$ when averaged over the diurnal cycle. Such rates are the equivalent of approximately 6 cm of non-saline snow ($\rho_s=350 \text{ kg}\cdot\text{m}^{-3}$), or approximately 2.3 cm of non-saline sea ice ($\rho_i=900 \text{ kg}\cdot\text{m}^{-3}$). Melt rate during the period of rapid *in-situ* melt ranges between $-17 \text{ W}\cdot\text{m}^{-2}$ at FYI'92 for days between day 170 and 175, and $-36 \text{ W}\cdot\text{m}^{-2}$ for days between day 156 and 164 at FYI'95 and averages approximately $-28 \text{ W}\cdot\text{m}^{-2}$ among the first-year sea ice research sites. This average rate is approximately one-half of the average summer melt rates reported for a high altitude snow field (e.g. Munro 1990) or for melting snow-covered tundra in the sub-Arctic (e.g., Ohmura 1982).

6.6 The Surface and Snow Volume Energy Balance

6.6.1 Accuracy and Precision of the Energy Balance Model

An assessment of our direct measure for Q^* is outlined in Appendix 7. The sensitivity of energy fluxes to forcing variables is described in Appendix 8. Halldin and Lindroth (1992) suggest the total accuracy for a net radiation calculation, based on the component sum approach, to be the largest of 3.5% of the flux, or $\pm 10 \text{ W}\cdot\text{m}^{-2}$. The largest source of measurement error is attributed to the long-wave flux. The Eppley pyranometers used in the study (i.e. Eppley model PSP and 848) perform well in both laboratory and field settings (Fritschen and Fritschen, 1991). The Eppley infrared radiometer (model PIR) used in the SIMMS experiments is considered the industry standard in long-wave radiometry. Under laboratory conditions, a measurement should be within 3 to 5% of the measured flux (Latimer, 1972). Studies have indicated that the Eppley pyrgeometer is prone to measurement error associated with long-wave radiation transfer between the thermopile surface and dome (Appendix 8). It is doubtful that heating of the pyrgeometer domes overly biased the $L\downarrow$ measurements during the SIMMS experiments. During May of 1992 the dome was observed to be on average only $0.089\pm 0.27^\circ\text{C}$ ($N = 3360$ cases) warmer than the case, with a maximum deviation of 1°C for the sky-facing sensor. The sensitivity of T_s to any uncertainty in ϵ , or any variation in $L\downarrow$ or $L\uparrow$, is described in Appendix 8. The bias in the surface temperature related to the accuracy of the pyrgeometer thermistor reference measurement is approximately 0.22°C at -10°C , or about as accurate as the thermistor reference measurement itself. The surface

temperature appears fairly insensitive to the accuracy of the down-welling flux, but it is highly sensitive to the assigned thermal emissivity. Fortunately the expected uncertainty in emissivity is small. A ± 0.01 variation in thermal emissivity provided by Warren (1982) for snow with grain radii between 200 and 1000 μm , translates into a variation in derived surface kinetic temperature of $\pm 0.11^\circ\text{C}$ at -10°C . A positive variation in emissivity diminishes the calculated surface temperature, relative to a true value.

The uncertainty surrounding our computation of the conductive heat flux within the snow and sea ice is estimated to be approximately 20% and 60%, respectively, during the early spring, when the fluxes are strongly positive (Appendix 8). The temperature gradients in the snow and sea ice slacken in the late spring causing the relative uncertainty surrounding the computation of the snow and ice conductive fluxes to increase to approximately 42% and close to 100%, respectively. The measurement errors associated with the snow and ice temperatures contribute the most to the overall flux uncertainty. The fluxes are typically small in the late spring (for example refer to Fig. 6.16) and, therefore, the ramifications of the large relative errors in terms on the energy balance are not overly damaging.

The sensitivity of the turbulent heat fluxes to variations in measured temperature, humidity and wind speed differences are shown to be strong functions of atmospheric stability; decreasing with increasing stability (Appendix 8). The uncertainty in the determination of $\Delta\theta$ and Δq causes a variation in Q_H and Q_E of between $58 \text{ W}\cdot\text{m}^{-2}$ (for Q_H) and $16 \text{ W}\cdot\text{m}^{-2}$ (for Q_E) for large wind speed differences during highly unstable conditions (i.e., $\xi=-1$), to less than $7.5 \text{ W}\cdot\text{m}^{-2}$ (for Q_H) and $2 \text{ W}\cdot\text{m}^{-2}$ (for Q_E) under stable atmospheres ($\xi>0$). Both heat fluxes are quite sensitive to variations in wind speed differences under unstable atmospheres. Fortunately, a stable boundary layer is the more common state (refer to Table 6.4). As an independent check on the accuracy of the aerodynamic technique, I compared the sensible heat flux against an eddy correlation estimate (Appendix 8). The aerodynamic and eddy correlation techniques are highly correlated, but the aerodynamic technique overestimated the flux, relative to the eddy correlation approach by between 10 to 14%. These results are preliminary and represent only a small sample over a limited stability range. However, they do show that the aerodynamic technique, in conjunction with our profile measurements of air temperature and wind speed, can provide reasonably accurate estimates of the

sensible heat flux, despite the sensitivity of the flux to measurement error in temperature and wind speed difference.

There is the concern that these relatively large errors in the solution to the non-radiative fluxes will contribute to large uncertainties in the estimate of dQ_s and Q_M . Calculations in Appendix 8 show that, in theory, the uncertainty surrounding dQ_s ranges from approximately $\pm 40\%$ to $\pm 50\%$ in the early and late periods of spring. The uncertainty for Q_M is somewhere between $\pm 60\%$ in the early spring, to well over 100% by the end of the experiments. As an independent check on the energy balance, the energy balance estimate of melt is compared against the melt energy equivalent of snow loss through *in-situ* ablation (Table 6.5). For the multi-year floes Q_{Ma} is provided for the hummock shoulder (hk), melt pond center (mp) and area-weighted floe average. Area averaging is described in Chapter 7 (refer to Eq. 7.1). The percent difference between melt estimates ranged between 9 and 66% among the research stations (not including the independent mp or hk estimates). The worst case was observed during FYI'95. We suspect that the energy balance estimate is somehow biased. The bias may be related to uncertainties in the computation of Q_{io} . Recall that the downward conductive flux at the ice surface in the final week of the experiment is extremely large, relative to the other sites and I speculate earlier in the text that the flux most likely is the result of heat flow associated with draining water. The energy balance flux estimate improves to within 13.6% of Q_{Ma} if days 157 to 160 are excluded from the FYI'95 energy balance estimate. If FYI'95 is not considered, the level of agreement between the energy balance and ablation estimates of melt is quite good; within, on average, $10.7 \text{ W}\cdot\text{m}^{-2}$ or 9% of each other. If just FYI'92 and FYI'93 are considered, the agreement is within $1.6 \text{ W}\cdot\text{m}^{-2}$ or 3.2%. The closeness of the two approaches is remarkable. Munro (1990), for instance, reported a difference between Q_{Ma} and Q_M of 28% for an alpine snow cover.

Table 6.5 Comparison between melt energy computations using the energy balance approach and ablation measurements of snow during the period of active snow melt at each site.

Site	Period	dt (days)	dH _s	density (kgm ⁻³)	salinity (ppt)	Total Ablation (kJ)	Q _{M_a} (Wm ⁻²)	Q _M (Wm ⁻²)	Difference (Wm ⁻²)	Difference (%)
FY192	170-175	5	0.09	350	7	9176.67	21.24	17.17	4.07	19.1
FY193	159-166	7	0.13	380	0	16482.28	27.25	29.74	-2.49	-9.1
FY195	156-164	8	0.19	400	2	21736.37	31.45	10.57	20.88	66.39
FY195 ¹	156-164	8	0.19	400	2	21736.37	31.45	35.73	-4.28	-13.6
mp93	158-167	9	0.21	400	0	28056.00	36.08	44.69	-8.61	-23.9
hk93	158-167	9	0.22	400	0	29392.00	37.79	44.69	-6.90	-18.3
MY193 ⁵	158-167	9	-	-	-	-	36.68	44.69	-8.01	-21.8
mp95	158-166	8	0.24	400	0	32064.00	46.38	33.07	13.31	28.7
hk95	158-166	8	0.10	400	0	13360.00	19.33	33.07	-13.74	71.1
MY195 ⁵	158-166	8	-	-	-	-	28.79	33.07	-4.28	14.9

¹ This estimate excludes days 157 to 160.

⁵ Weighted average of the hk and mp estimate.

6.6.2 Seasonal Episodes

Only the ice surface temperature reflects the response of the energy balance on the surface volume without exhibiting the strong degree of day to day variation that is exhibited by the energy balance components and surface temperature. Day to day variation would complicate a delineation of seasonal stages through the affect of short-term variation in the atmosphere. Consequently, the ice surface temperature is used to partition the time series' into phases during the spring progression. A K-means Cluster Analysis on the sea ice surface temperatures identifies three clusters at a 95% level of confidence. The central group temperatures are -11°C, -7°C and -3°C. The groups correspond respectively to cold, transitional and warm sea ice. The energy balance and climate parameter data are grouped according to these divisions. The categories are considered to represent *early*, *transitional* and *late* spring stages. The timing of the progression from one stage to the next varied among the years (refer back to Fig. 6.12). The transition from *early* to *transitional* occurs on days 122, 129 and 117 during 1992, 1993 and 1995. The transition into the *late* seasonal sub-episode occurs on days 143, 142, and 156 for the three years, respectively.

A summary of the atmospheric and surface parameters during the three seasonal stages is provided as Table 6.6. The snow cover during the *early* spring stage is cold and dry and air temperatures are less than -14°C at each station. Average air temperatures in the *late* spring range

from -4.5°C in 1992 to 0.32°C at FYI'95. The *early* spring of each year typically has a lower percent occurrence of overcast hours (arbitrarily defined as hours with a total cloud amount of greater than or equal to 7) than the later seasonal episodes. With the transition from the *early* stage, the percent frequency of overcast hours rises sharply in 1992 and 1993, accompanied by a large reduction in hours of bright sunshine. In contrast, substantially more sunshine is received during the transitional stage of 1995 when compared to the *early* spring period. In the *late* spring the total sunshine remains low in 1992, drops slightly in 1995, but rises sharply in 1993.

Table 6.6 Summary of energy balance components and selected atmospheric and surface properties.

Variable	Year	early	trans	late	Variable	Year	early	trans	late
Q^* (Wm^{-2})	1992	-3.20	12.28	27.73	Q_{st} (Wm^{-2})	1992	0.80	-11.08	-2.46
	1993	10.16	12.97	38.21		1993	-1.05	8.12	0.28
	1995	6.95	13.16	83.70		1995	4.90	2.74	-0.75
	Ave	4.63	12.80	49.88		Ave	1.55	-0.07	-0.98
Q_{ns}^* (Wm^{-2})	1992	0.06	0.09	0.10	Q_{Ez} (Wm^{-2})	1992	-19.67	-12.46	-11.44
	1993	0.18	0.29	5.59		1993	-11.82	-11.98	-10.87
	1995	0.25	0.54	23.01		1995	-16.69	-15.26	-15.86
	Ave	0.16	0.31	9.57		Ave	-16.06	-13.23	-12.72
Q_{s}^* (Wm^{-2})	1992	-3.26	12.20	27.63	T_s ($^{\circ}C$)	1992	-21.34	-16.14	-4.48
	1993	9.97	12.68	32.62		1993	-16.73	-4.97	-1.54
	1995	6.70	12.62	60.69		1995	-14.36	-10.12	0.32
	Ave	4.47	12.50	40.31		Ave	-17.48	-10.41	-1.90
K^* (Wm^{-2})	1992	44.25	43.51	57.74	T_s ($^{\circ}C$)	1992	-20.69	-15.21	-4.50
	1993	32.92	49.31	81.26		1993	-16.38	-4.99	-1.82
	1995	47.74	53.97	112.17		1995	-13.85	-8.87	0.57
	Ave	41.64	48.93	83.72		Ave	-17.21	-9.69	-1.88
L^* (Wm^{-2})	1992	-47.46	-31.22	-30.01	VPD (daPa)	1992	2.99	2.31	3.30
	1993	-22.76	-36.35	-43.05		1993	3.75	5.38	5.72
	1995	-40.79	-40.81	-28.47		1995	3.62	3.78	4.86
	Ave	-37.00	-36.13	-33.85		Ave	3.45	3.82	4.63
K_{\downarrow} (Wm^{-2})	1992	219.28	257.73	315.09	U (ms^{-1})	1992	4.86	3.30	4.53
	1993	237.14	265.79	308.36		1993	4.48	2.78	1.91
	1995	216.86	293.67	292.36		1995	3.06	3.64	2.46
	Ave	224.42	272.40	305.27		Ave	4.13	3.24	2.97
K_{\uparrow} (Wm^{-2})	1992	175.03	214.22	257.35	RH (fraction)	1992	0.70	0.84	0.92
	1993	204.22	216.48	227.10		1993	0.76	0.87	0.89
	1995	169.12	239.70	180.19		1995	0.79	0.85	0.92
	Ave	182.79	223.47	221.55		Ave	0.75	0.85	0.91
L_{\downarrow} (Wm^{-2})	1992	180.58	217.42	261.83	α (fraction)	1992	0.80	0.83	0.82
	1993	218.95	257.65	263.60		1993	0.80	0.84	0.79
	1995	215.35	237.75	290.04		1995	0.78	0.82	0.60
	Ave	204.96	237.61	271.82		Ave	0.79	0.83	0.74
L_{\uparrow} (Wm^{-2})	1992	228.04	248.64	291.84	Stable B.L. % occurrence	1992	53	46	48
	1993	241.71	294.00	306.65		1993	69	82	71
	1995	256.15	278.56	318.52		1995	90	80	79
	Ave	241.97	273.73	305.67		Ave	71	69	66
Q_{σ} (Wm^{-2})	1992	12.96	1.30	-2.08	Overcast (% of total)	1992	29	64	69
	1993	17.50	1.04	-4.02		1993	42	73	55
	1995	30.85	7.37	-15.75		1995	35	49	52
	Ave	20.44	3.24	-8.95		Ave	35	62	59
Q_{sa} (Wm^{-2})	1992	13.21	16.30	5.00	Sunshine (hours)	1992	176	165	305
	1993	10.27	-3.05	-3.44		1993	229	106	472
	1995	4.77	10.81	-		1995	83.9	548	210
	Ave	9.42	8.02	0.78		Ave	161	273	329
dQ_s (Wm^{-2})	1992	-22.13	-11.34	13.73	Snowfall (cm)	1992	1.1	24.7	17.1
	1993	-2.90	8.82	22.02		1993	12.0	11.9	3.5
	1995	-5.08	0.09	44.08		1995	0.5	8.4	4.1
	Ave	-10.04	-0.81	26.61		Ave	5	15.0	8
Q_{dt} (Wm^{-2})	1992	21.88	-3.66	-20.81	Rain (mm)	1992	0	Trace	Trace
	1993	10.13	-4.73	-22.60		1993	0	Trace	3
	1995	31.17	-3.53	-59.83		1995	0	Trace	6
	Ave	21.06	-3.97	-36.08		Ave	0	Trace	4

6.6.3 Diurnal Variation of the Energy Balance and Meteorological Variables

Both the surface and air temperature follow a similar 24 hour form, albeit slightly out of phase (Fig. 6.21a). Air temperature peaks approximately one hour after the surface temperature during the *early* spring, but lags the surface temperature by two hours in the *late* spring. The maximum surface temperature shifts closer to solar noon with the progression toward summer. The surface temperature responds rapidly to the radiation balance, while the lag in air temperature represents the time necessary for the transfer of heat from the surface *via* turbulence. Peak T_s occurs around 14:00 in the *early* spring and around 13:00 in the *late* spring. The surface temperature undergoes larger diurnal variation than the air temperature throughout both spring stages and both temperature amplitudes dampen with the progression toward summer. The surface is typically colder than the atmosphere during the low sun hours, while the opposite is observed during the mid-afternoon. The snow surface temperature is, on average, 0.37°C warmer than the air temperature, with a RMSE of 1.51°C over the three experimental periods ($N=3844$).

The vapor pressure deficit (VPD) follows a diurnal form similar to the air temperature (Fig. 6.21b). Peak VPDs occur in the mid-afternoon (i.e., 14:00 LAT) during the *early* spring but shift closer to solar noon later in the season. Typically larger VPDs are observed in the afternoon throughout the spring period. Maximum afternoon temperatures are larger in *late* spring, as is the variation surrounding each hourly mean. Relative humidity is fairly constant over the diurnal cycle in the *early* spring, but is generally lower during the high sun hours of the *late* spring (Fig. 6.21c).

Wind speed, is on average fairly consistent throughout the spring period. Values range, on average, between 2.5 ms^{-1} and 4 ms^{-1} in the *early* spring and hover between 2.6 ms^{-1} and 3 ms^{-1} later in the season (Fig. 6.21d). The diurnal variation in horizontal wind speed is dampened in the *late* spring relative to the *early* season. *Early* spring maxima occur around 14:00 LAT.

Median cloud amount over the diurnal cycle (surrounded by the first and third quartile) is generally larger in the afternoon, relative to the morning, in the *early* spring while the opposite is observed in the *late* spring (Fig. 6.21e). The central values are typically greater than 7 throughout the diurnal cycle, during the *late* spring and less than 4 during the *early* spring.

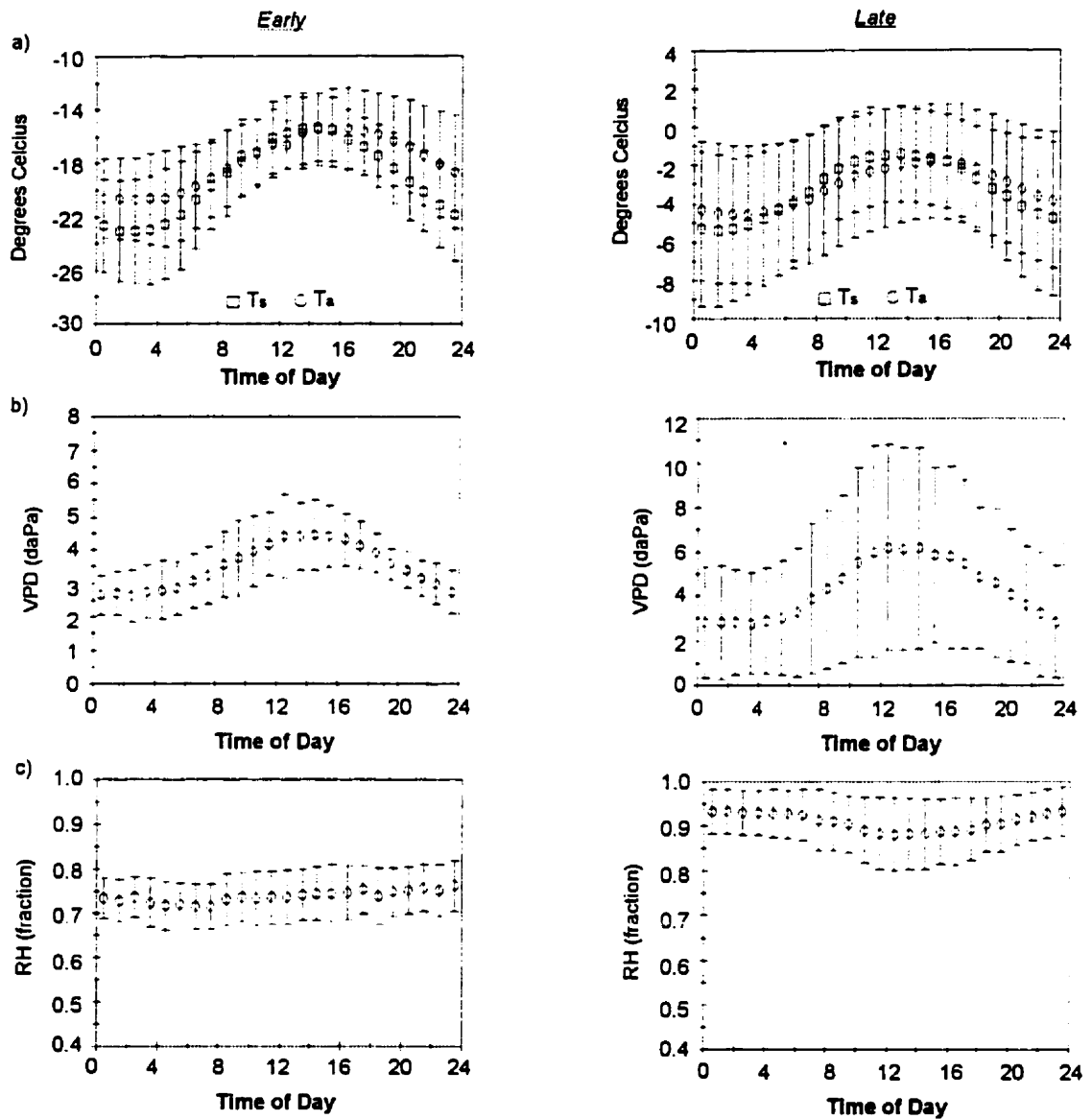


Figure 6.21 Hourly average (a) T_s and T_a , (b) VPD, (c) RH, (d) wind speed (see next page), (e) median TCA and (f) hourly average surface albedo, for the *early* and *late* spring. Error bars represent plus or minus one standard deviation unit (or first and third quartile, as is the case for TCA).

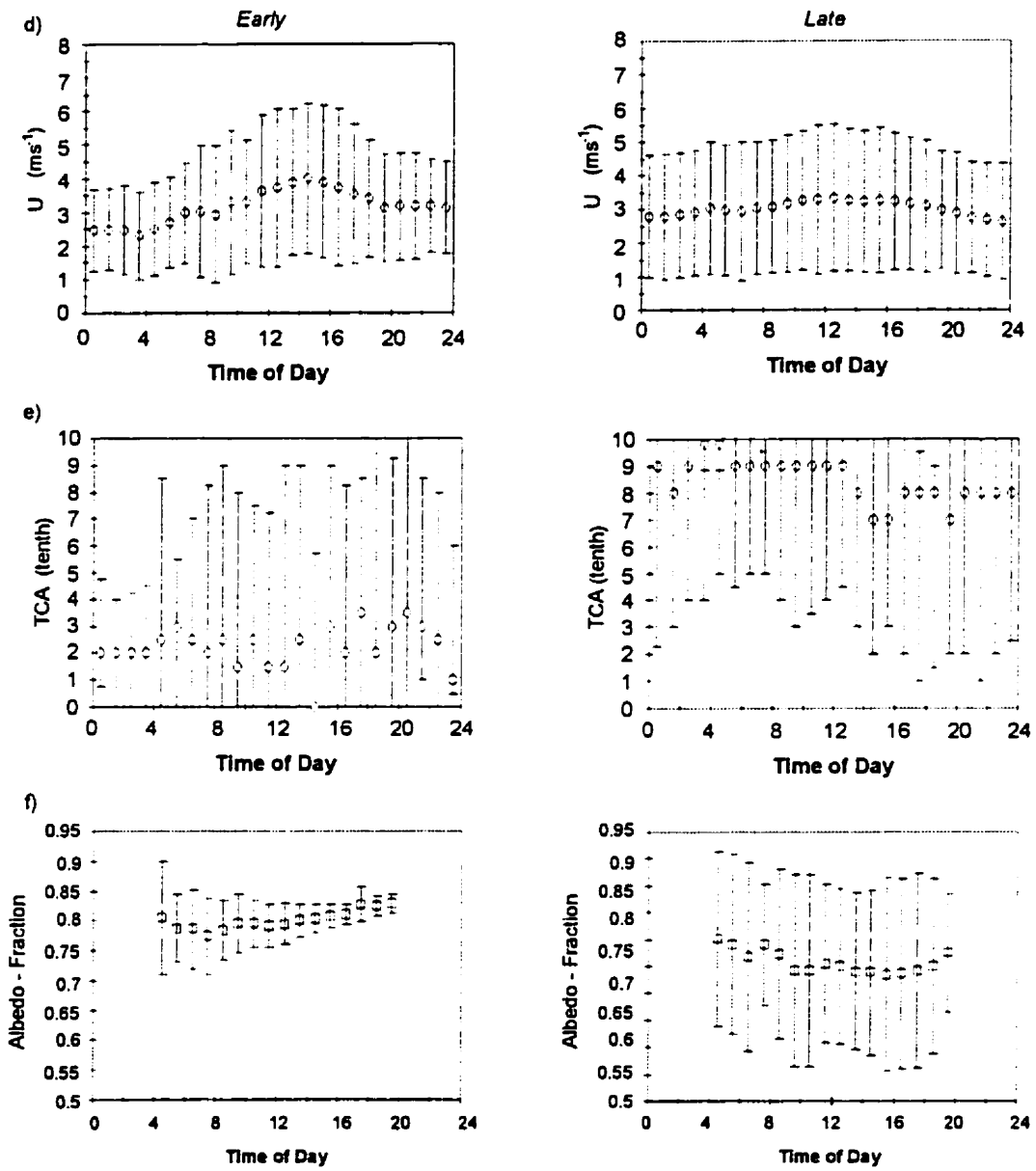


Figure 6.21 Continued.

The form of the surface albedo follows the same diurnal trend identified for the cloud amount in both seasonal episodes. That is, both increase over the diurnal cycle in the *early* spring and decrease over the course of the day in the *late* spring (Fig. 6.21f). This association is physically sound because the spectral albedo of snow is lowest in the longer wavelengths, which are filtered from the incident beam by cloud cover (Warren, 1982). The potential for increased wetness at the snow surface, associated with elevated afternoon air and surface temperatures, may effect a lowering in afternoon albedo during *late* spring. Variation in the diurnal cycle of snow albedo is also shown by McGuffie and Henderson-Sellers (1985) and was related to diurnal variations in surface snow properties. The scatter surrounding the hourly averages tends to decrease with increasing albedo in the *early* spring. This observation may be related to the finding that scattered and broken skies (here considered between fractional cloud coverage of 3 to 7) occur more often between 4:00 and 9:00 LAT (40% of the total hours) than between 13:00 and 20:00 LAT (29% of the total hours). The scatter surrounding the hourly mean albedo is consistently large over the diurnal cycle during the *late* spring. Some of this scatter may be attributed to the changing cloud coverage, but a proportion of the variation is associated with the changing optical properties of the evolving seasonal snow cover.

The seasonal rise in daily average Q^* and K^* responds to a broadening and amplification of the peak radiation flux intensities within the diurnal cycle (Fig. 6.22 a and b). The diurnal cycle of the net radiation of a snow volume is driven by the diurnal cycle of global radiation ($K\downarrow$) and modified by the surface's control over reflected solar radiation (Fig. 6.22 c) and long-wave radiation exchange (Fig. 6.22 b and d). Peak $K\downarrow$ occurs at solar noon, however, the diurnal maximum of the other radiation fluxes may lag several hours to either side of zenith. The time lag evolves with the transition from *early* to *late* spring. For instance, Q^*_s and K^* peak one hour prior to solar noon during the *early* spring, but their 24 hour maximum corresponds to solar noon in the later stages of spring. An *early* season peak in $L\downarrow$ is weakly developed and occurs around 9:00 LAT. It shifts with the season's progression to occur at about 11:00 LAT in the *late* spring. Maximum $L\uparrow$ also shifts closer to solar noon in the *late* spring. The timing is coincident with the diurnal maximum previously identified for T_s .

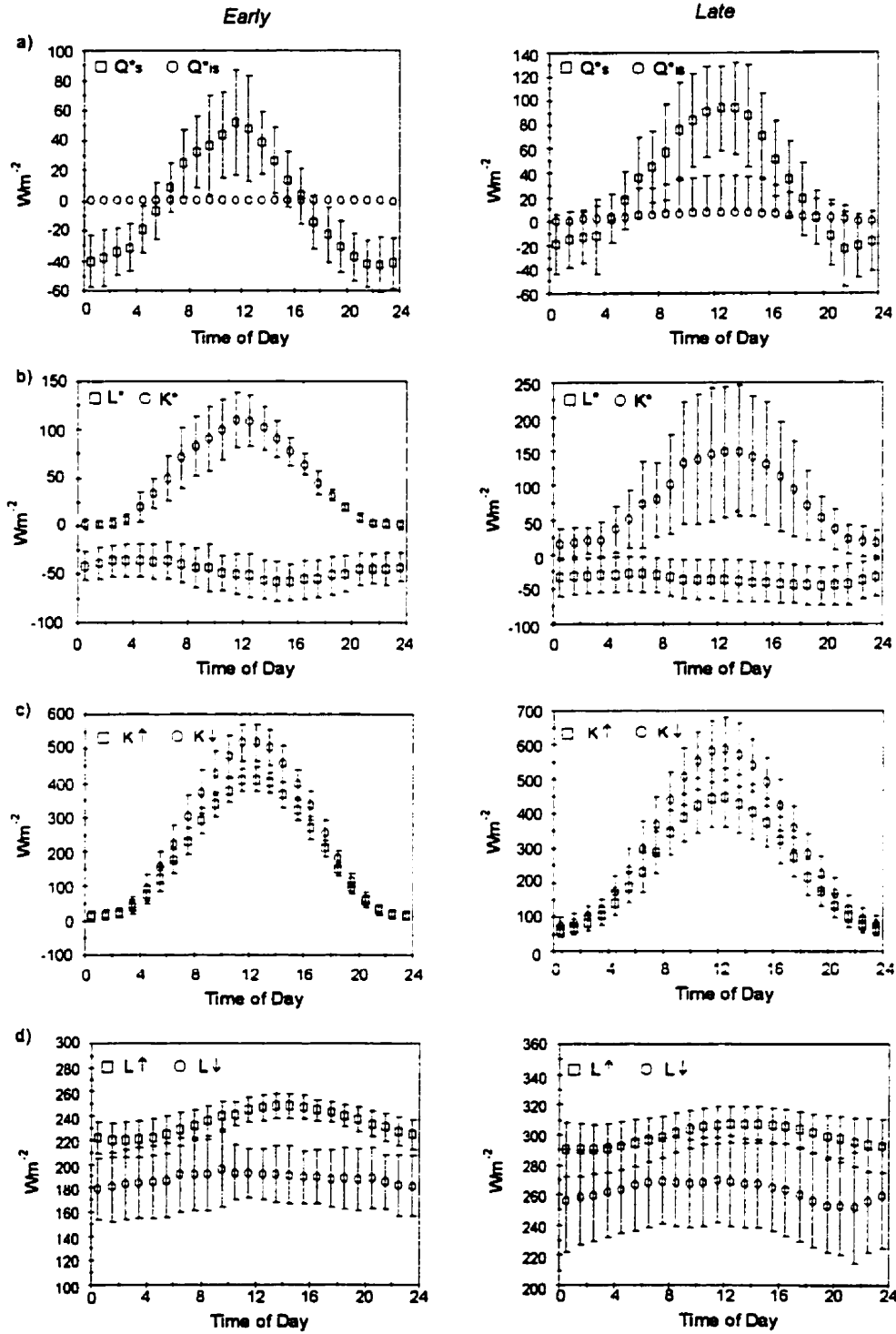


Figure 6.22 Hourly average (a) Q^* and Q^*_{is} , (b) K^* and L^* , (c) K_{\downarrow} and K_{\uparrow} , (d) L_{\downarrow} and L_{\uparrow} .

Both K^* and Q^*_s are asymmetric around their central peaks, even though $K\downarrow$ is fairly symmetric about solar noon. K^* is higher in morning than in the afternoon during the *early* spring. The diurnal pattern corresponds both to the lower morning average surface albedo and lower morning median cloud coverage. In the *late* spring the opposite occurs. Net solar radiation is larger in the morning, while albedo is generally lower. Net radiation follows the same general trend as K^* . Depressed afternoon Q^* values respond to elevated net long-wave losses, particularly in the *early* spring.

The role of Q_H reverses, from heating the surface during the low sun hours, to heating the atmosphere during the mid-day (Fig. 6.23 a). Q_E on the other hand transfers vapour into the near surface atmosphere (on average) throughout the diurnal cycle (Fig. 6.23 a). The occurrence of a down-directed vapour flux is more common during the late spring in response to higher levels of near surface relative humidity. Maximum surface Q_H and Q_E losses occur between 11:00 and 12:00 LAT during the *early* spring; however, the timing of maximum Q_H loss shifts toward mid-morning (i.e., between 8:00 and 10:00 LAT) during the *late* spring. Hourly values of the absolute value of the Bowen ratio (i.e., $|\beta|$) rarely exceed unity (Fig. 6.23c). This indicates that Q_E is the dominant form of turbulent heat exchange over most of the day. However, sensible heat gains by the surface do on average exceed latent heat losses (i.e., $|\beta|$ exceeds unity) during the periods of minimum Q^*_s , and maximum atmospheric stability (Fig. 6.23 b). This happens on average before 6:00 and after 20:00 LAT, particularly in the *late* spring. The nocturnal net radiation deficit shown in Fig. 6.22a is instrumental in maintaining the stable nighttime boundary layer in both the early and late spring season (Fig. 6.23b). The occurrence of a stable boundary layer during periods of surplus net radiation in the *late* spring is probably maintained by warm air aloft.

The enthalpy fluxes at the snow and ice surface (Q_{io} and Q_{so}) each exhibit a ‘U-shaped’ distribution within the diurnal cycle and the hourly minimum occurs sometime in the mid-afternoon (Fig. 6.24a). Minimum Q_{so} corresponds to peak Q^*_s and occurs around 11:00 LAT in the *early* spring, but shifts to around 12:00 LAT later in the season. The trace of Q_{io} lags Q_{so} by approximately 8 h during the *early* spring. A subtle drop in Q_{io} is observed approximately 7 hours after the Q_{so} minimum during the late spring. The lag demonstrates the low thermal diffusivity of the snow cover to heat diffusion. Our earlier hypothesis that the radiation balance does not directly contribute to the conductive heating of the sea ice interior (in the presence of a snow cover), is

supported by the observation that minimum Q_{10} does not correspond to peak Q^* in the *late* spring. Rather, Q_{10} is directed into the ice volume, throughout the diurnal cycle.

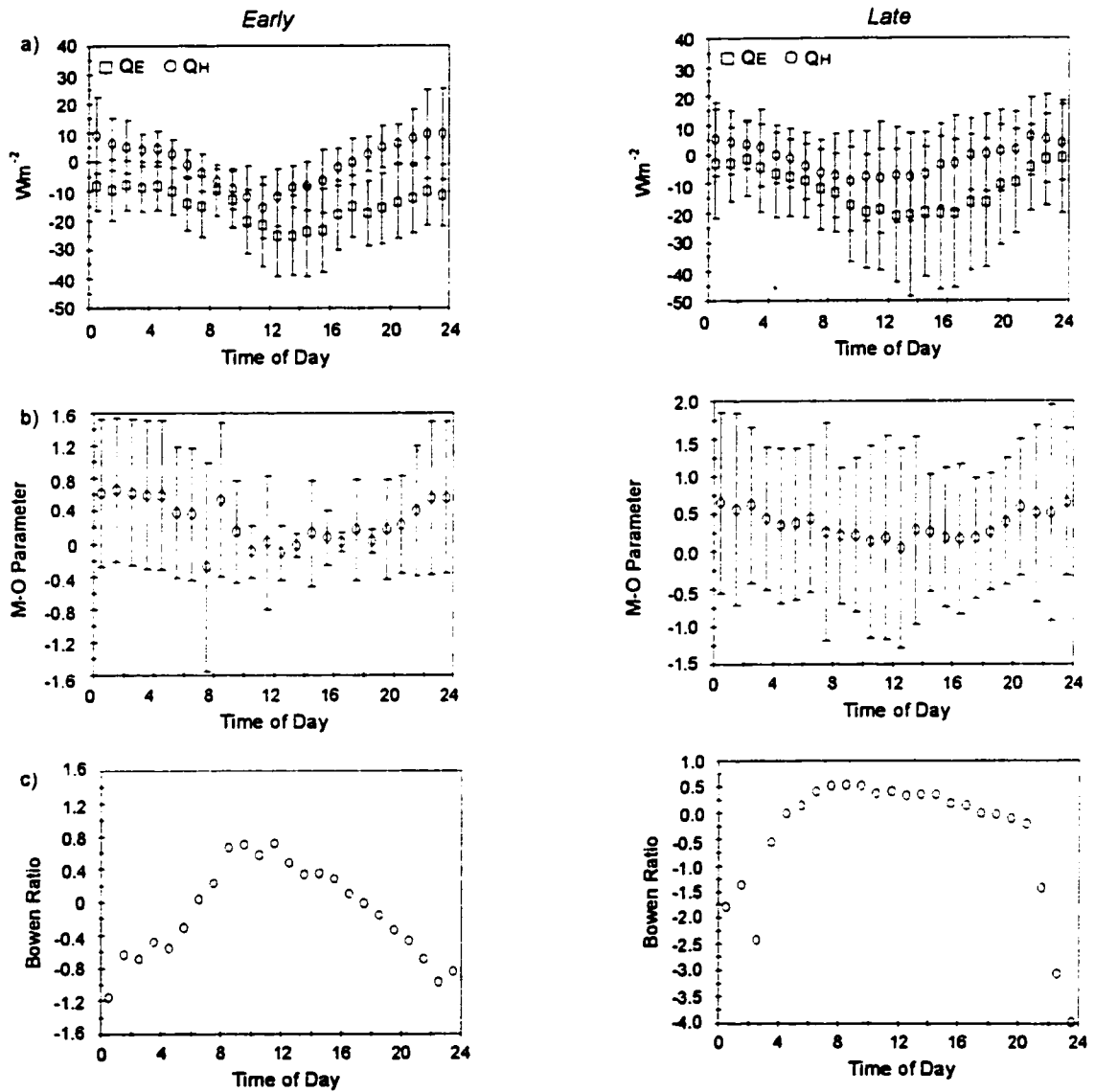


Figure 6.23 Hourly average (a) Q_H and Q_E , (b) Monin-Obukhov stability parameter and (c) Bowen ratio for the *early* and *late* spring.

The snow volume operates on a heat surplus between the mid-morning and mid-afternoon and undergoes a heat deficit during the low sun hours (Fig. 6.24b). Periods of heat deficit occur over a smaller proportion of the day during the *late* spring. Peak heating occurs shortly between 8:00 and 9:00 LAT in the *early* spring, but shifted to occur around solar noon, later in the season. Peak melt rates correspond to periods of maximum atmospheric heating of the snow volume (also shown in Fig. 6.24b). Nighttime ice production is appreciable, particularly in the *early* spring (in excess of $40 \text{ W}\cdot\text{m}^{-2}$). The rates of re-freezing within the snow volume in the *late* spring is still quite large (i.e., in excess of $20 \text{ W}\cdot\text{m}^{-2}$), however the process typically operates over a smaller proportion of the day (before 5:00 and after 19:00 LAT) relative to the *early* spring.

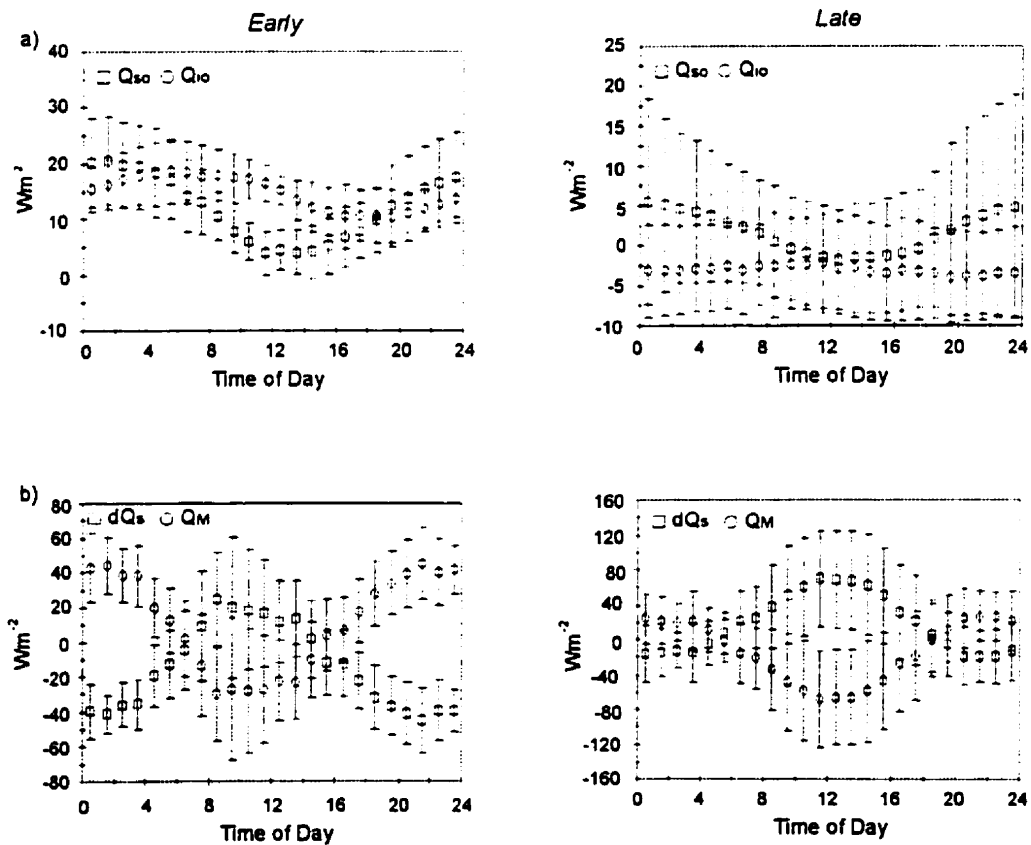


Figure 6.24 Hourly average (a) conductive heat flux at the snow and sea ice surface and (b) change in atmospheric heating of the snow and energy of fusion within the snow cover for the *early* and *late* spring.

The diurnal energy balance is summarized in Fig. 6.25 and 6.26. In the *early* spring the available energy to the surface is preferentially directed into the turbulent heating of the atmosphere, rather than raising the enthalpy level of the snow volume, particularly in the mid- to late afternoon (Fig. 6.25 a). The maximum heating of the snow volume occurs in the mid-morning (between 9:00 and 12:00 LAT), but still only constitutes 32% of the available energy to the surface (Fig. 6.25 c). The remaining heat is transferred to the atmosphere. In the morning and night (i.e. before 9:00 and after 17:00 LAT) the snow volume supplies over 80% of the available energy to the surface (Fig. 6.25 c). The bulk of the volume heat loss at night is offset by ice production (Fig. 6.25 f) and sensible heating from the atmosphere (Fig. 6.25 c). Conductive heating constitutes a progressively larger proportion of the volume's available energy during the mid-day hours. Net radiation supplies virtually all of the available energy between 9:00 and 14:00 (Fig. 6.25 c). It is interesting to note that the surface and volume energy balances consume more energy at night, than during the mid-day (Fig. 6.25 b and e), which indicates that the energy balance is not strongly coupled to global radiation during the *early* spring. The diurnal cycle in the energy balance components that is observed during the early spring is not observed during the winter season (e.g., Steffen and DeMaria, 1996) and the difference is attributed to the influence of the 24 hour cycle of incident solar radiation during the spring season on the energy content of the lower atmosphere and surface.

Later in the season, the available energy to the surface is determined solely by Q^*_s for two-thirds of the diurnal cycle (Fig. 6.26 c). Over the remaining hours, the available energy is small ($< 20 \text{ W}\cdot\text{m}^{-2}$) and is made up predominately (i.e., 80%) through contributions by the snow volume. Most of the available energy to the surface (approximately 70%) is directed into the snow volume between the hours of 9:00 and 14:00 LAT (Fig. 6.26 c), which encompasses the hours of maximum surface heating (Fig. 6.26 b). The combined turbulent loss consumes the remaining 30%. Virtually all of the energy directed into the snow during the midday supports snow melt while proportionally less energy is directed into the conductive heating of the underlying sea ice (Fig. 6.26 f). Proportionally more energy is devoted to conductive heating of the ice interior and to the snow surface outside of the 9:00 to 14:00 LAT window (Fig. 6.26 f). The timing of the distribution of energy within the snow volume indicates that the energy that is directed toward the ice interior is largely from latent heat released from re-freezing of melt water within the snow

during the morning and night. Surplus Q^*_s during the midday immediately contributes to snow melt. This observation may be explained using our earlier findings that the vast majority of solar radiation is absorbed very near to the snow surface and that the rate of temperature propagation through snow over first-year sea ice is extremely small.

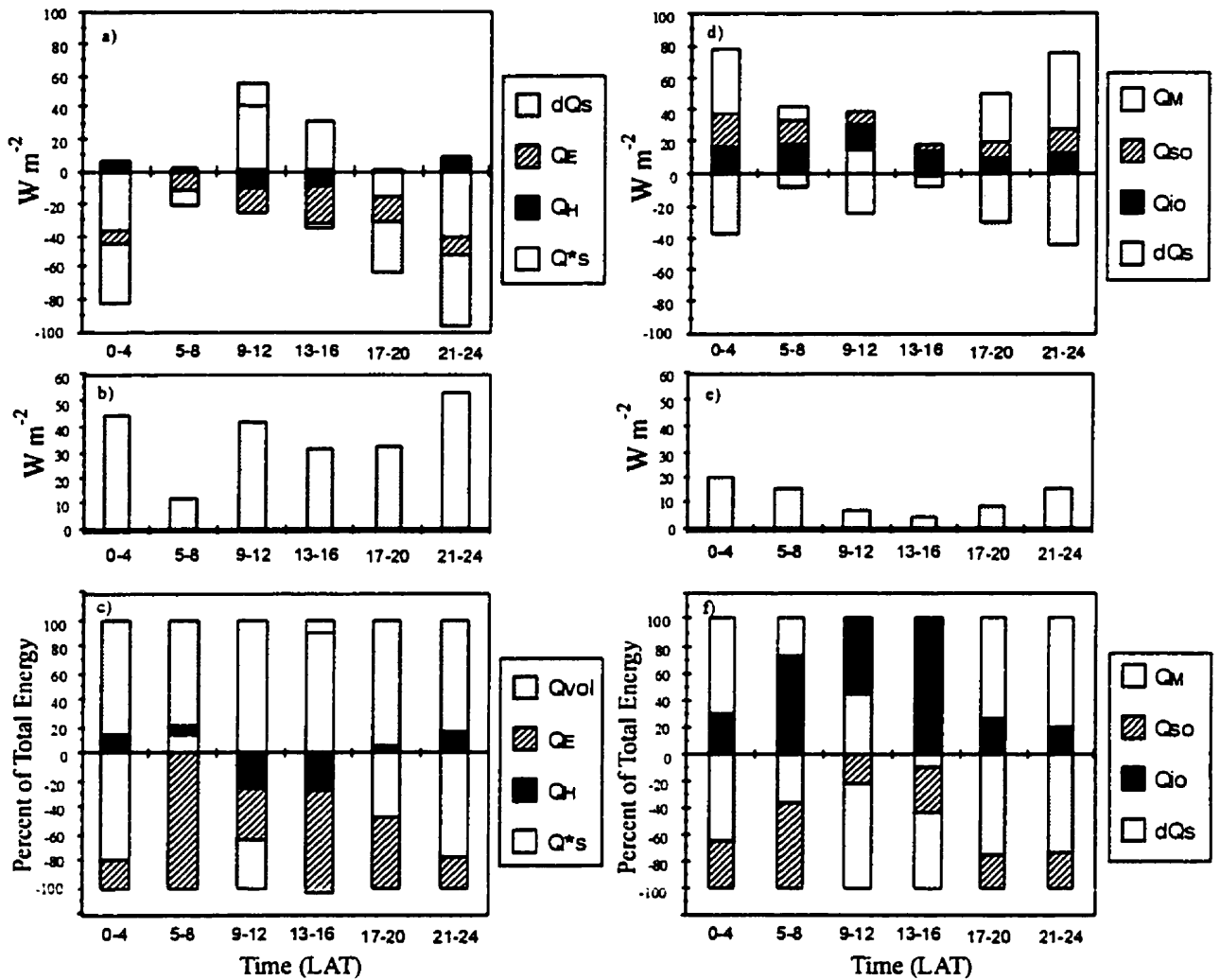


Figure 6.25 A summary (at four hour increments of the diurnal energy balance during the *early* spring: (a) the average energy balance components over the diurnal cycle, (b) the total average energy to the surface, (c) the role of the individual energy balance terms in terms of their proportional contribution for warming/cooling the surface, (d) the average energy balance components of the snow volume, (e) the total average energy to the snow volume and (f) the role of the individual energy balance terms in terms of their proportional contribution for warming/cooling the volume.

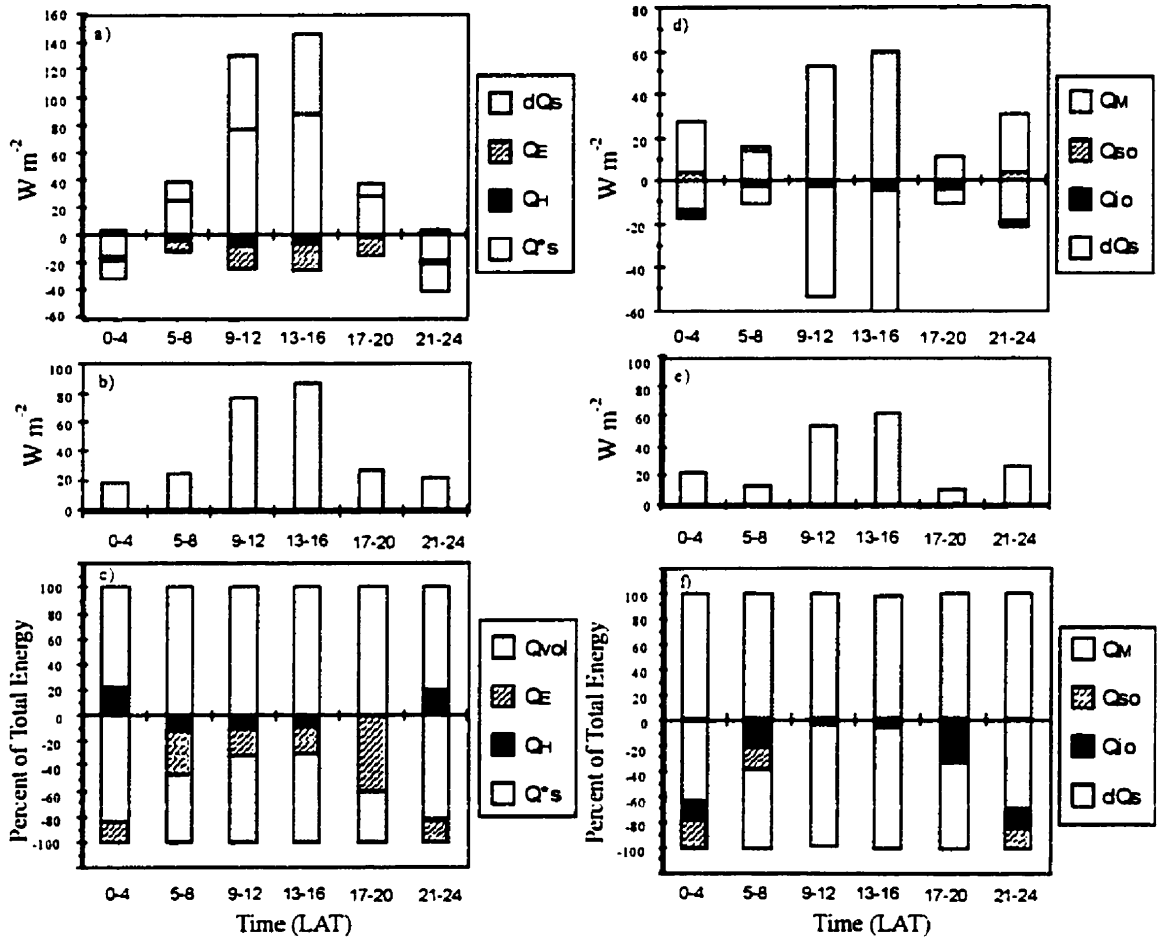


Figure 6.26 A summary (at four hour increments) of the diurnal energy balance during the *late* spring: (a) average energy balance components over the diurnal cycle, (b) total average energy to the surface, (c) the role of the individual energy balance terms at the surface in terms of their proportional contribution for warming or cooling the surface, (d) the average energy balance components of the snow volume and (f) the role of the individual volume energy balance components for warming/cooling the snow volume.

6.6.4 Day to Day Variation of the Energy Balance

The relationship between the components of the energy balance for the surface and snow volume (Equations 2.4 and 2.7) are shown in relationship to each other over the three seasonal stages (Fig. 6.27). The error bars in the figure denote the range in average terms among the experiments; thus illustrating a degree of inter-annual variation in the energy balance components.

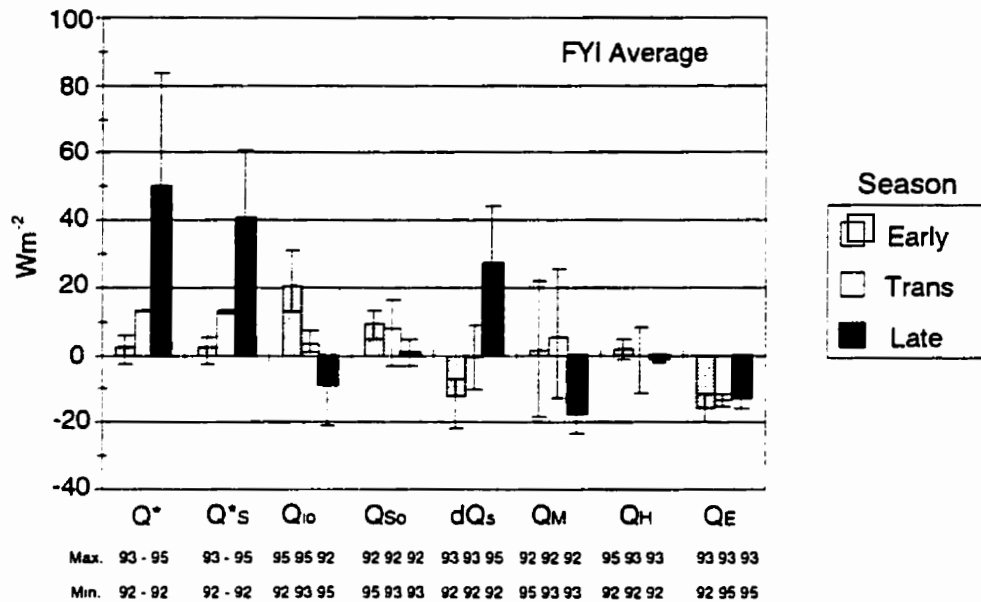


Figure 6.27 The springtime energy balance of first-year sea ice. The error bars denote the range among the spring seasons, FYI'92, FYI'93 and FYI'95. The spring season corresponding to the minimum and maximum flux is also provided.

Those previously identified characteristic features of the energy balance are conspicuous in the figure. Note, with the season's progression that we observe a rise in net radiation, a reversal in the direction of the conductive flux at the snow and ice surfaces and a reversal in the direction of phase change from net ice production within the snow volume, to net ice melt. The change in heat storage fluctuates around a mean of near zero during the *transitional* stage. The snow volume operates on a heat deficit during periods of negative net radiation; however, a net heat loss by the snow volume can also occur when the surface's net turbulent heat loss exceeds net radiation gains by the snow. This is observed during the *early* and *transitional* spring. The *late* spring

encompasses the period of energy surplus for the snow volume (positive dQ_s). The average sensible heat flux is typically small within any of the seasonal episodes. The average latent heat loss is consistently large during the *early* and *transitional* spring, but declines during the *late* seasonal episode. The long-term Bowen ratios are typically small (i.e., $1 \geq |\beta|$), indicating that the latent heat flux is the dominant form of turbulent heat exchange over extended periods of time. Ohmura (1982) also documented a reduction in turbulent heat exchange during the periods of advanced snowmelt. This feature was (and is) attributed to increasing atmospheric stability resulting from warm air overlying the snow at its melting temperature.

The evolving role of each component of the energy balance is evident when the fluxes are scaled to represent a proportion of the total energy for partitioning at the surface and within the snow volume itself (Fig. 6.28). A graph showing the total energy available to the surface and volume is shown adjacent the relative contribution of each of the energy transfer processes in Fig. 6.28 a and c. The error bars surrounding the mean values in the plots denote the range in the role of the fluxes among the three first-year sea ice experiments. The experiments with the largest and smallest average of available energy are labeled, as are the extremes in the proportional breakdown of the total available energy per energy flux.

The total available energy for partitioning at the surface increased by on average over a factor of 2 between the *early* and *late* stages of spring (Figs. 6.28a). The increase can be as large as a factor of three, as is the case at FYI'95. The difference in total available energy for partitioning at the surface among years is largest during the *late* spring. For example, there exists over 100% difference in surface heating between the *late* stages of 1992 and 1995. The energy available for partitioning within the snow volume actually drops during the *transitional* stage (Fig. 6.28c), despite the small rise in surface energy levels. The decline is related to a reduction in the conductive heat contribution to the snow volume from the ice surface during the *transitional* spring stage (refer back to Fig. 6.27).

The net of the radiation fluxes make up an increasing proportion of the total energy available to the surface with the progression toward summer (Fig. 6.28b). The contribution of Q^* toward surface heating increases from about 18% in the *early* spring, to represent virtually 100% of the available energy at all stations during the *late* spring. Thus, the snow melt appears to be driven almost exclusively by the radiation balance at our study sites, consistent with observations from the sea ice regime within the central Arctic Basin (i.e., the zone of perennial sea ice cover).

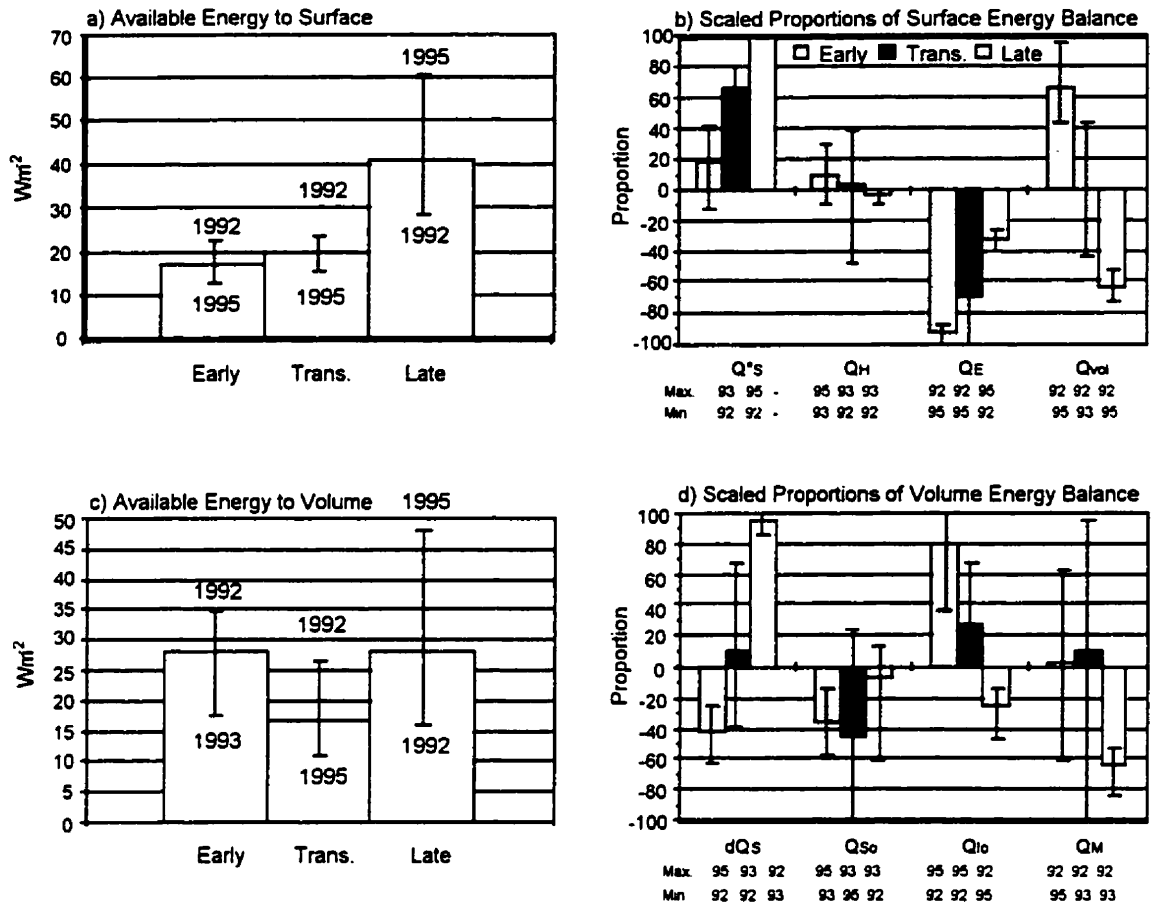


Figure 6.28 The evolution of the average energy available to the (a) the snow surface and (c) the snow volume of first-year sea ice and the role of the individual energy balance components (in terms of proportional contribution) toward supplying (positive) or removing (negative) available energy at the (b) surface and (d) within the volume. The error bars represent the range among first-year sea ice experiments.

The snow volume supplies on average 66% of the available energy to the surface in the *early* spring, but its contribution may be as high as 96%, as is the case in 1992. Much of this energy is supplied by conduction from the underlying sea ice, which acts to minimize ice production within the snow pack (Fig. 7.28d). Ice production is particularly high in 1992 (refer to the upper limb of the error bar). This finding is thought to be related to the previous observation

that the snow surface energy balance is decoupled from the ice surface because of the poorly conducting snow base. In the *late* spring, the volume consumes between 51% and 73% of the available energy to the surface. Thus the role of the snow volume changes, from a strong heat source for surface energy loss during the early spring, to a major heat sink later in the season.

Net radiation accounts for, on average, 95% of the total energy available to the surface when averaged over the entire experimental period, and therefore the radiation balance is the dominant source of energy when long term totals are considered. Sublimation at the surface is the major heat loss mechanism while the snow volume is cold; however, the volume consumes a progressively larger proportion of the available energy as the snow cover warms. The proportion of the total energy consumed by Q_E drops from almost 100% of the available energy during the *early* and *transitional* periods to, on average, between 26% to 40% (for an average of 33%) of the energy lost by the system during the *late* seasonal episode. In total, more energy is lost to the atmosphere through sublimation than is consumed by the snow volume for either melt or conduction to the underlying sea ice during both the 1992 and 1995 experiments. The latent heat transfer to the atmosphere consumes between 40% (as in 1993) and 66% (as in 1992) of the available energy to the snow surface, when averaged over the entire spring period. In the discussion surrounding Fig. 6.19, I indicate that the latent heat losses by the surface are larger than reported in other Arctic studies. Clearly, in this study, the vapour transport from snow in the early spring is an important component of the energy balance and warrants further investigation.

The role of the sensible heat flux varies widely among years. It represents only a minor heat source, or sink, to the first-year surface during the *late* spring, however, the flux may represent either a substantial heat source or sink during the earlier spring periods, depending on the characteristics of the near surface atmosphere. For example, in the transitional spring, Q_H contributes up to 40% of the energy available to the system at FYI'93, but represents close to 50% of the energy lost by the system at FYI'92. These observations should not be surprising considering that a stable boundary layer was 36% more likely to occur during the *transitional* stage in 1993 than in 1992. The sensible heat flux can therefore be a significant component of the energy balance during the *transitional* spring, but its ability to heat or cool the surface appears to be variable from year to year.

The role of the energy exchange processes operating within the snow volume differs, depending on whether the volume loses or gains heat to or from the atmosphere (i.e., positive or

negative dQ_s). The bulk of the heat available for loss to the atmosphere *via* radiation and turbulence during the *early* spring is offset by upward heat flow at the ice surface from oceanic sources. This process represents between 38% and 100% of the volume's available energy at this time (Fig. 6.28d). A remaining deficit is offset by ice production within the snow. Between 52% (as in FYI'95) and 84% (as in FYI'93) of the energy available to the snow is consumed by melt during periods of heat surplus. The over-all first-year sea ice average is 62%. Anywhere between 16% (as in FYI'93) and 48% (as in FYI'95) of the remaining heat surplus is directed into the heating of the underlying ice interior through conduction. The large discrepancy in these proportions is related to differences in temperature between the sea ice interior and the sea ice surface between years. A larger temperature gradient is measured near the FYI'95 surface during the *late* spring, which may be the consequence of a thicker ice cover in 1995. We have already established that the sea ice surface temperature increased rapidly toward the end of the FYI'95 experiment. The melt process consumes 25% of the total available energy to the snow volume of first-year sea ice when averaged over the three spring periods, even though accelerated melt is confined to the *late* spring. The proportion may be as high as 94%, as is the case in 1993. Both the snow cover and the first-year sea ice are thinner in 1993, relative to the other years, and the combined snow and ice cover warmed faster than the other years (refer back to Fig. 6.12). As a consequence, a large amount of the available energy is directed into melt, which otherwise would be required to raise the temperature of the snow and ice.

The *transitional* stage is a period of tremendous inter-annual variation in the disposition of available energy among the fluxes operating within the snow volume. This is because the snow can either gain or lose heat. The evolution between the conductive and radiative regimes of the *early* and *late* spring can be described using the ratio of Q_{io} to Q^*_s (Fig. 6.29). The transition is complete when the ratio approaches zero. The sign of the ratio is frequently negative prior to about day 123 at FYI'92, a function of fact that the surface frequently experiences net radiative loss and positive conductive heat input. The magnitude of the ratio varies between years depending on the size of the conductive flux relative to net radiation. The large ratios observed during 1995 demonstrate the relative importance of conductive heating as a heat source to the snow volume at this time.

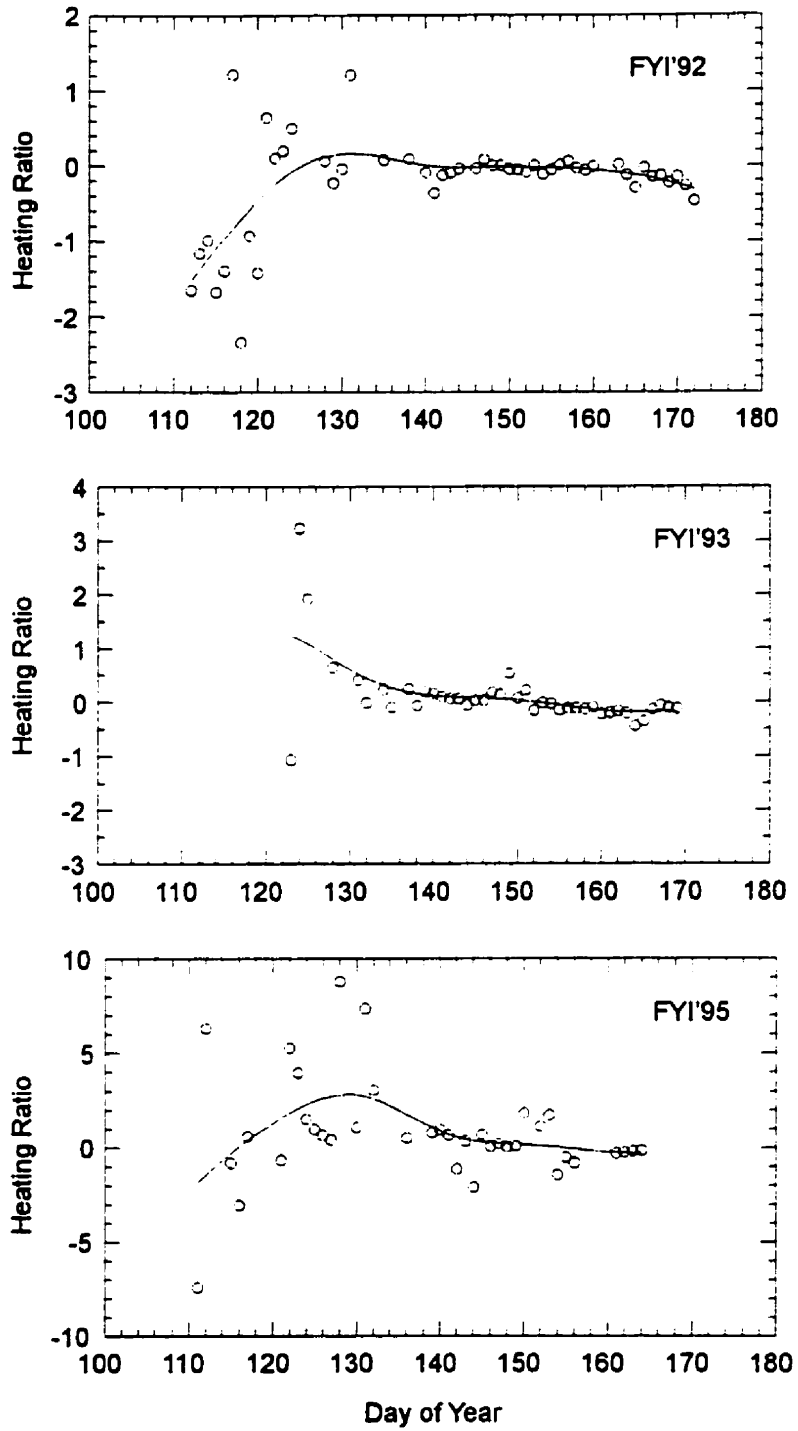


Figure 6.29 The ratio of conductive to radiative input to the snow cover (the heating ratio) during the first-year sea ice experiments.

6.7 Summary

The energy transfer processes operating on and within a snow cover are described over the winter to summer transition of years exhibiting different atmospheric and surface characteristics. The evolution of the energy balance is described through three stages: *early*, *transitional*, and *late*, using the temperature at the snow base as the delineating criterion.

The modeled thermal properties (k_s , ρ_c) for the spring snow cover over first-year sea ice are highly variable in both the vertical dimension and with the spring progression. The variation in the thermal properties is associated with variation in the snow's physical properties. Snow thermal conductivity decreases away from the mid-snow zone and may vary by a factor of two over the snow profile throughout the spring period. Extreme variation in the snow's heat capacity across the snow profile results in association with a salinity gradient within the snow; particularly when the snow is warm ($T_s > -8^\circ\text{C}$). The heat capacity in a saline basal layer may be larger than in the overlying snow by a factor of two to three in the *late* spring.

A depth-time relationship applied to the first-year sea ice snow properties shows that salt content significantly reduces the distance through a snow cover that a temperature change can propagate over a period of time. Approximately 30 cm of the snow cover is coupled to the snow boundary over a 24 hour period in non-saline snow, which is approximately the depth of a typical springtime snow cover. The coupling distance can be reduced by a factor of between 2 to 5 for snow with salinity levels typically observed at the snow base over the spring season. The effect of a saline layer is to insulate the ice cover from atmospheric heating in the late spring, but it acts to reduce sea ice growth in fall and winter by impeding the upward transfer of heat. The depth and time scale relationships are, however, sufficiently large to make the bulk of absorbed solar radiation readily available to the snow surface, thereby reducing the potential for solar heating to contribute to the heat storage of the snow volume interior.

The vertical variation in a snow cover's thermal properties causes a non-steady state conductive heat flow through the snow. The presence of a poorly conducting layer at the snow base of a first-year sea ice surface during the early spring de-couples the atmosphere from underlying sea ice and ocean volumes, confining any conductive contribution to the surface to the lower portion of the snow volume. The conductive flux is directed toward the surface at all levels within the snow volume during the early spring, but the upward flux rapidly weakens and reverses to direct heat toward the snow and ice interior. The timing of the reversal coincides with a rise in

snow moisture content above snow's irreducible liquid content and the rate at which the downward flux propagates over the snow volume. This association suggests that gravity drainage of melt water (or rain) is key to the thermal coupling of the snow and sea ice volume.

Both the radiation fluxes and non-radiation heat exchange processes are instrumental in heating and cooling the surface, although the relative magnitude of their contribution varies strongly across the seasonal transition and within the diurnal cycle and between years. In the *early* spring a larger proportion of the energy available to the snow volume and surface is supplied by conduction at the sea ice surface and by heat released during ice production within the snow volume relative to the total contribution by the net amount of the radiation fluxes. The heating of the snow volume is not strongly coupled to solar radiation because the surface albedo is high (between 0.78 and 0.80) and the mid-day atmospheric structure is typically unstable, allowing for the bulk of radiation absorbed at the surface to be transferred back to the atmosphere *via* turbulence. In fact, the maximum heat input to the snow volume occurs in the early morning, during the *early* spring, and at this time the net solar radiation is typically very small. The radiation balance accounts for only about 18% of the available energy to the snow, while heat conduction can contribute between 38% and 100% of the available energy. The conductive input to the system may or may not be associated with oceanic heating. In one year the conductive heat input into the snow was significant relative to the other fluxes, while in another year the ice production within the snow was a larger heat source than conduction from below. In this instance, the surface energy balance was not strongly coupled to the underlying ice and ocean heat flux.

During the *late* spring, the heat available to the snow surface and volume is several factors larger than during the *early* spring and both the surface and volume energy balances operate on a heat surplus. Virtually all of the energy available to the system is related to the radiation balance. The increase in net radiation corresponds to the lowering of the surface albedo, which in turn is responding to morphological changes in the thinning snow cover. These changes include increased snow wetness and snow grain growth. At its minimum, the surface albedo dropped to between 0.48 and 0.44 over the first-year ice. The majority of the available heat to the snow upper boundary is directed into the volume instead of into the turbulent heat fluxes, however, the proportion of energy which is directed into the volume varies considerably between years (i.e., between 51% to 73% of available energy). Once within the snow volume, the proportion of the available energy which supports melt ranges between 50% and 84%. The remaining heat warms

the underlying (colder) sea ice through conduction. Snow melt appears to be almost exclusively maintained by the radiation balance during the *late* spring and, in this respect, the forcing on the melt process is consistent with observations from the central Arctic Basin.

Sublimation at the snow surface is the dominate heat loss mechanism, while the snow is cold, but generally the snow volume consumes a larger proportion of the surface's available energy when the snow warms. Because water vapor transfer to the near surface atmosphere is active throughout the spring period, more energy in total may be lost by the surface to the atmosphere through sublimation than is directed into raising the enthalpy of the snow volume. The proportion of energy consumed by sublimation ranged between 40% and 66% over the experimental periods.

During the *transitional* spring the available energy to the surface and snow cover is small. This is because (i) the conductive heat flow to the surface is reduced relative to the *early* spring, and (ii) frequent snowfall events maintain a high surface albedo which in turn, prevents large net radiation gains by the surface. Sensible heat can represent a substantial heat source, or sink to the surface during this stage, depending on the characteristics of the near surface atmosphere. In the years examined, Q_H contributed up to 40% of the energy available to the system (e.g., at FYI'93) or represented close to 50% of the energy lost by the system (e.g., FYI'92) during the *transitional* spring. Hence, the atmospheric sensible heat flux can play a role in progressing the snow cover into the initial stages of snow melt, or it can be effective at cooling the surface, thereby discouraging and delaying the melt process.

The timing of the late season rise in Q^* and dQ_S is observed to vary by up to 22 days between experimental years. This variation is a testament to the inherent variation in the climate system. This observation is in line with comments by Male and Granger (1981) to the effect that the components of the energy balance within a snow-covered region are highly variable from year to year. Aspects of the both the snow volume and atmosphere play a role in determining the amount of energy available to the surface and in affecting the manner in which the energy is partitioned among the energy balance components. A challenge remains to identify the environmental conditions most apt to discourage or encourage the warming of the snow cover and to examine the effect of different surfaces on the energy balance, when exposed to similar environmental forcing.

CHAPTER 7: SPATIAL DYNAMICS OF THE SURFACE ENERGY BALANCE

7.1 Introduction

In this chapter the energy balance of the two predominate mature sea ice types in the CAA (first-year and multi-year sea ice) are examined to determine if these surfaces can be treated as identical *icescape* units with respect to energy and momentum exchange with the atmosphere. Differences in the form of the energy and radiation balance are identified and quantified where possible.

Previous studies have shown that snow or ice surfaces in close proximity with different optical and thermal properties may show differences in the radiative and non-radiative transfer of energy with the atmosphere (e.g., Maykut 1978; Makshtas, 1991; Bintanja and van den Broeke 1995; Barber et al., 1995a). The two mature (non-deformed) sea ice types in the Archipelago are FYI and MYI. FYI occupies the vast majority (on average 97%) of surface coverage (Gorman, 1988). Regionally however, MYI can represent a large proportion; particularly in narrow passages. Multi-year sea ice presents an obstacle to ship navigation and is instrumental in clogging passages, thereby allowing young ice to form.

I show in the previous chapter that the snow volume supports heat exchange with the atmosphere during the early spring, but represents a heat sink for atmospheric heating during the late spring. The amount of energy available to the snow surface varies widely among years and the role of the individual energy balance components is highly variable and appears strongly dependent on both the characteristics of the snow and the nature of the near surface atmosphere. MYI is thicker than FYI and the upper sea ice contains very low salt content relative to the FYI. The rolling topography of the MYI floe encourages a horizontally non-uniform snow cover. Because of these differences, I expect the radiative and conductive fluxes to differ between sea ice types. Any difference in melt rates between sea ice types will depend on the amount of energy available to

either surface and on the manner in which the energy is partitioned. We extend previous work (i.e., Barber et al., 1995a) and examine for differences in each of the energy balance components and surface properties and seek to demonstrate any seasonal variation to these differences. The morphology of the sample multi-year floes during the SIMMS experiments is described in Chapter 3. The 1993 sample MYI floe was in places three times thicker than the flow in 1995.

7.2 Methods

The horizontal scale of the hummock and melt pond sequence of the multi-year ice floes is sufficiently fine such that the surface presented to the radiometers and air temperature and wind speed sensors provides a spatial amalgamation of each feature. Our site instrumentation allows an investigation into the energetics of the shallow snow over the hummock ice and the deep snow that collects within the melt-pond depressions. We spatially average the flux terms specific to the snow volume (i.e., Q_{is}^* , Q_{so} , and Q_{io}) to reflect an average multi-year ice value. The heat fluxes associated with the hummock (hmmkflux) and the melt pond (mpflux) snow covers are linearly weighted based on the estimated proportional areal coverage of hummock surfaces and melt pond depressions of floes during the SIMMS experiments:

$$\text{myiflux} = 0.35 \cdot \text{mpflux} + 0.65 \cdot \text{hmmkflux} . \quad (7.1)$$

The proportionality coefficients in Eq. 7.1 represent the compilation of both transect sampling (Misurak, 1995; Serreze et al., 1993a) and low-level aerial photography (Piwowar et al., 1995).

The surface and snow volume energetics between the FYI and MYI sites are examined over the three previously defined seasonal sub-episodes using the SIMMS'93 and SIMMS'95 data sets. A comparison of the daily energy balance terms between the ice types is performed using a one-tailed Mann-Whitney test. The experimental hypothesis for the Mann-Whitney test is that a directional difference (i.e., > or <) in rank location exists between the fluxes of the respective ice type. The null hypothesis is that no specified difference exists.

7.3 Results

7.3.1 Volume Thermodynamics

The temperature and temperature structure of the snow and ice volume are fundamental in dictating the thermal properties and heat conduction. The temperature at the snow base of the melt

pond depression increases in a fairly uniform manner with the spring not overly different than observed at the first-year sea ice sites (Fig. 7.1). An example of the evolution of the temperature structure within the snow and upper metre of sea ice between the two ice types (FYI and MYI) appears in Fig. 7.2. The same general characteristics pertaining to the temperature gradients as outlined in Section 6.5.3.3 are evident, namely:

- the gradient weakens as the volume warms,
- the gradient is stronger in the snow volume relative to sea ice.

The temperature decreases toward the ice interior of the thick multi-year flow while it rapidly increases with distance into the interior of the first-year ice cover. The temperature gradient at the snow base of the multi-year floe is smaller than observed over the first year sea ice during the initial weeks of the experiment. Not only is the snow base of the melt pond depression and the upper multi-year sea ice volume effectively insulated from oceanic heating, but the ice surface is also insulated from a warming atmosphere by an ample snow cover.

The properties (k_s and ρC_p) within the multi-year snow cover lack the distinct variation observed over first-year sea ice (Fig. 7.3). The form of the variation within the thin snow of FYI'93 shown in the figure differs slightly from the thicker snow of FYI'92 (Fig. 6.13), however the major features are intact. They include:

- the presence of a poorly conducting snow base,
- an increase in snow thermal conductivity throughout the snow volume with the season's progression
- a large increase in snow heat capacity, with a rise in snow temperature, particularly in a saline basal layer.

During the late spring the heat capacity at the snow base is almost an order of magnitude greater over the first-year sea ice relative to multi-year ice and the discrepancy is attributed to the presence of salt within the first-year sea ice snow cover. Because salt within the snow is extremely effective at suppressing thermal diffusion within snow (refer to Fig. 6.13), a greater proportion of energy should be directed into the fusion process over first-year sea ice, instead of contributing to the enthalpy flux.

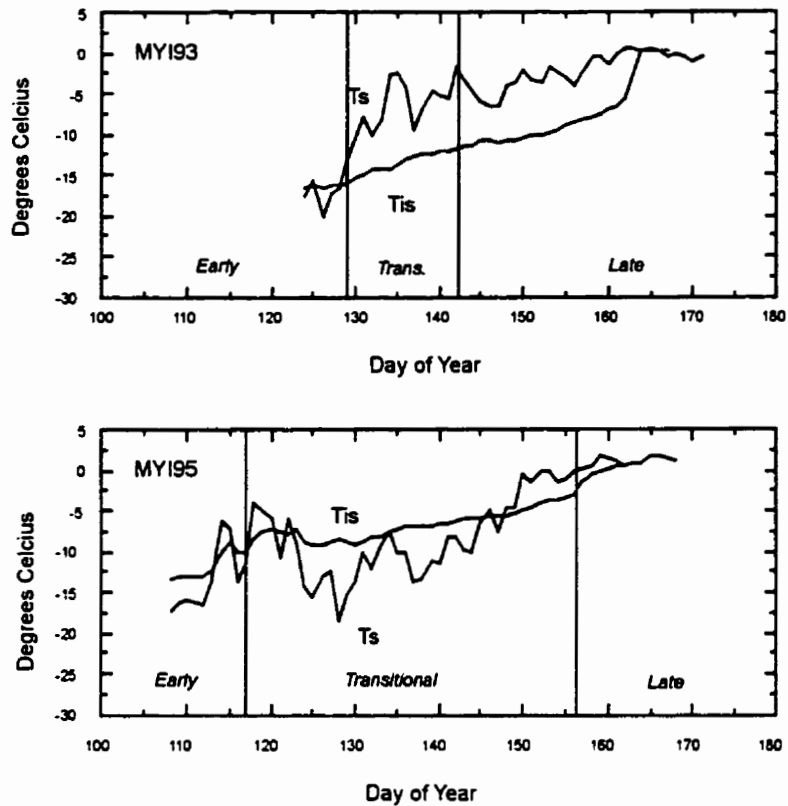


Figure 7.1 The average temperature at the snow and sea ice surface a multi-year melt pond depression during MYI'93 and MYI'95.

The form of conductive heat flow within the two different sea ice volumes (and associated snow cover) is vastly different (Fig. 7.4). On day 129 we observe a reversal in the heat flux direction from up to down over the first-year sea ice. At the multi-year site on the other hand, the heating of the underlying (colder) sea ice interior from the snow volume occurs throughout the experimental period, even though an upward flux may be maintained at the snow surface.

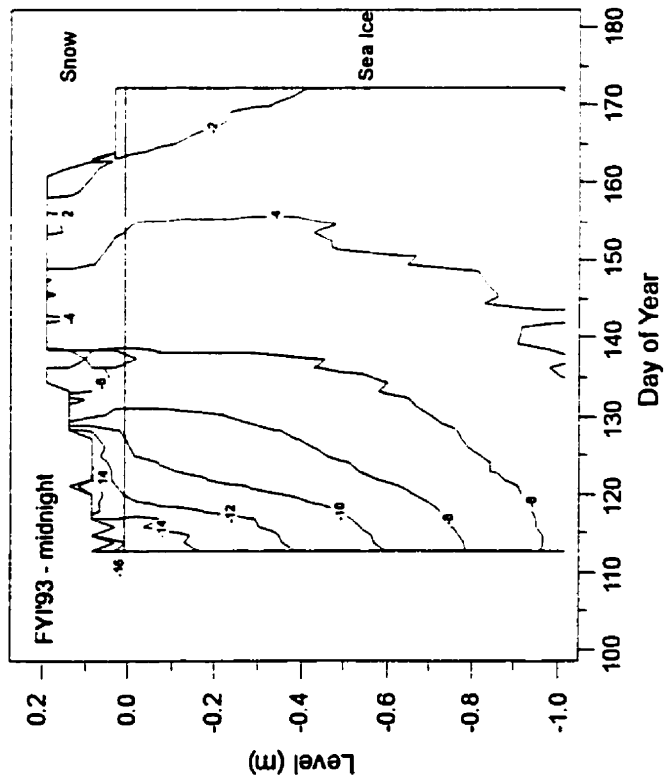
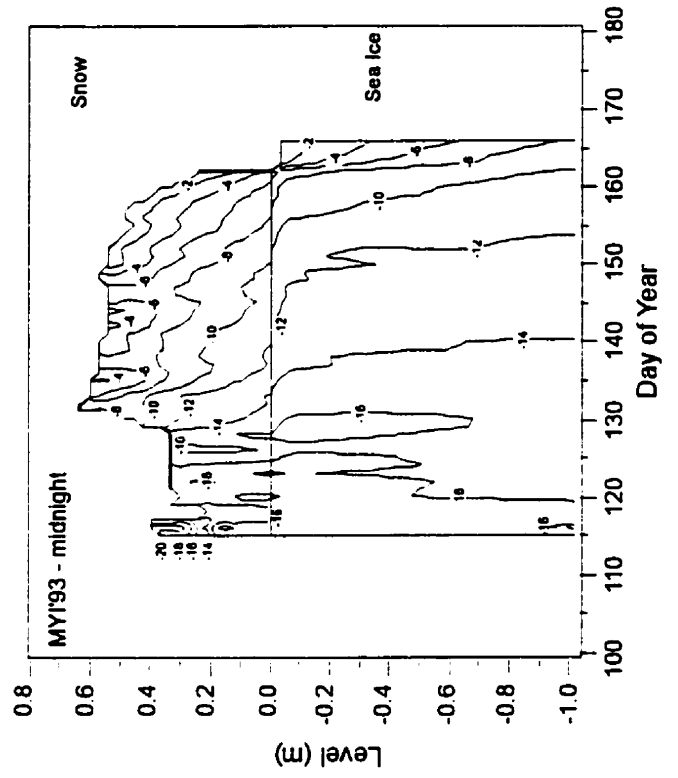


Figure 7.2 Temperature structure across the upper metre of FYI'93 and MYI'93.

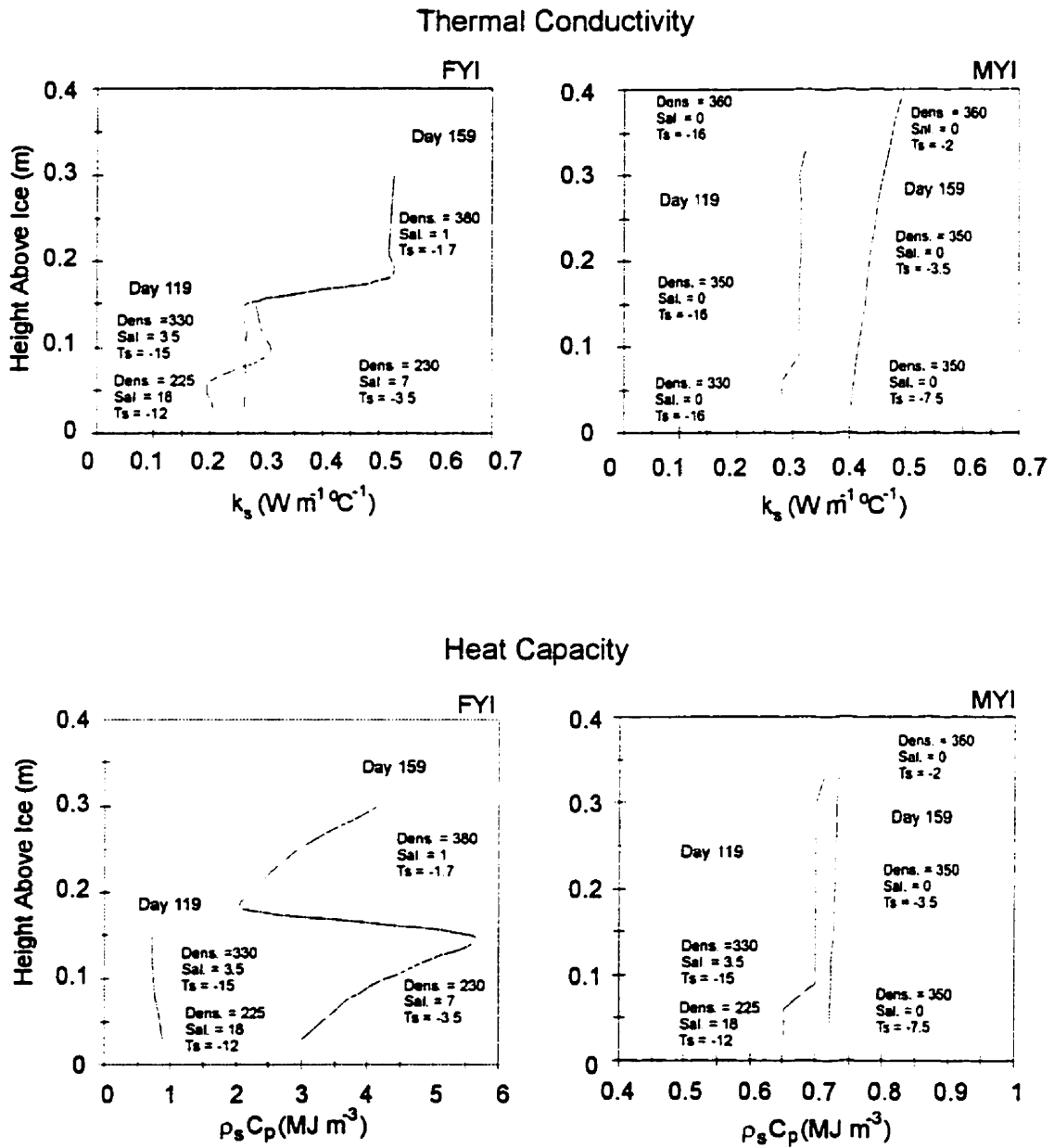


Figure 7.3 Seasonal evolution in the vertical variation of snow thermal conductivity (upper pair) and heat capacity (lower pair) across a shallow FYI snow cover and deep snow within a melt pond depression. Snow density, salinity and temperature for the comparison are provided in kg·m⁻³, ppt and °C, respectively.

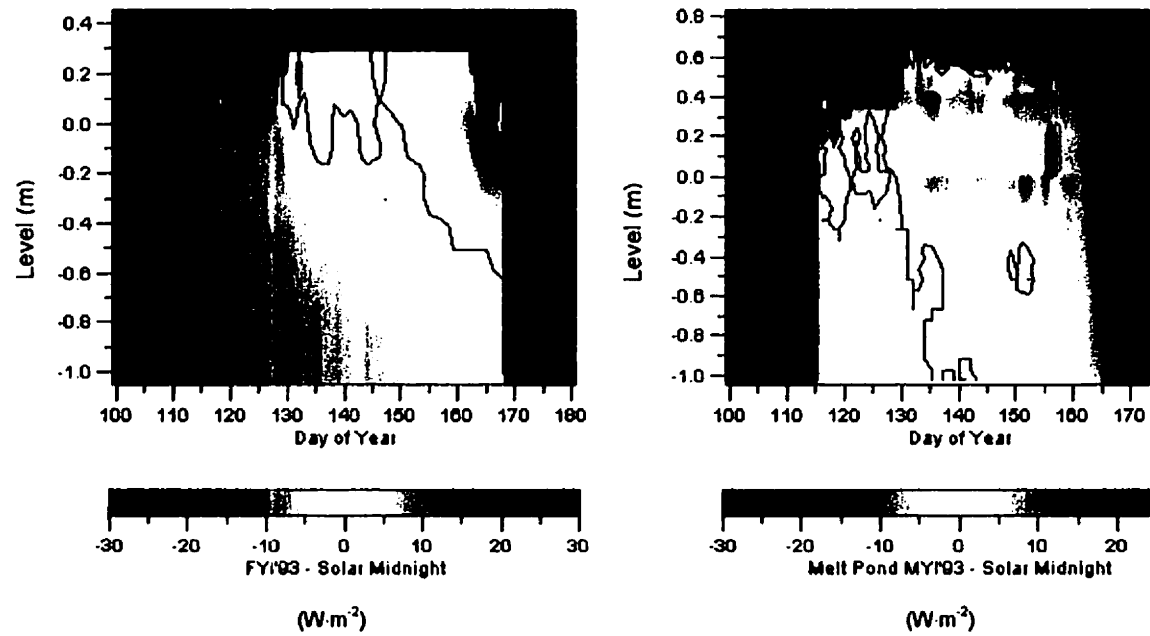


Figure 7.4 A cross section of the evolution of conductive heat flow ($\text{W}\cdot\text{m}^{-2}$) within the snow and upper sea ice of thin first-year sea ice (FYI'93) and the snow within the melt pond of thick multi-year sea ice (MYI'93).

7.3.2 Surface Albedo and Net Radiation

The time series of albedo may or may not vary between ice categories (Fig. 7.5). In 1995 there is very little difference in the surface albedo until around day 157, after which the albedo at FYI'95 drops at a faster rate than at MYI'95. The daily average albedo drops to between 0.44 over the first-year sea ice and to 0.54 over the multi-year surface. The albedo at MYI'93, on the other hand, is distinctly lower relative to the first-year site over the period beyond day 130. The albedos of the respective surfaces diverge after the storm event between days 129 and 130 in 1993. High winds and a large increase in melt pond snow depth accompanied the storm. The snow on the hummock surface was windswept. Warm air entered the region on day 130. The early drop in albedo at the MYI station appears to be the consequence of snow removal from the hummock surface and the result of elevated temperatures on the optical properties of the shallow snow over the hummock shoulders. The albedos of both surfaces decline rapidly on day 157, reflecting the rapid increase in snow liquid volume and grain size associated with the onset of melt. The albedo of the first-year sea ice becomes lower than measured at the multi-year station in both years during the final period of snow cover. The albedo minimum is lower over first-year sea ice. An exposed hummock surface can present a higher albedo than flooded first-year sea ice (De Abreu et al., 1995).

The net radiation of the snow/sea ice/ocean volume remains distinctly higher at MYI'93 relative to FYI'93 after the storm of day 129 (Fig. 7.6). A rapid rise in the flux occurs for both ice types within a day of one-another during both years. The net radiation at the first-year sites is larger than at the multi-year sites during the final days of the experiment.

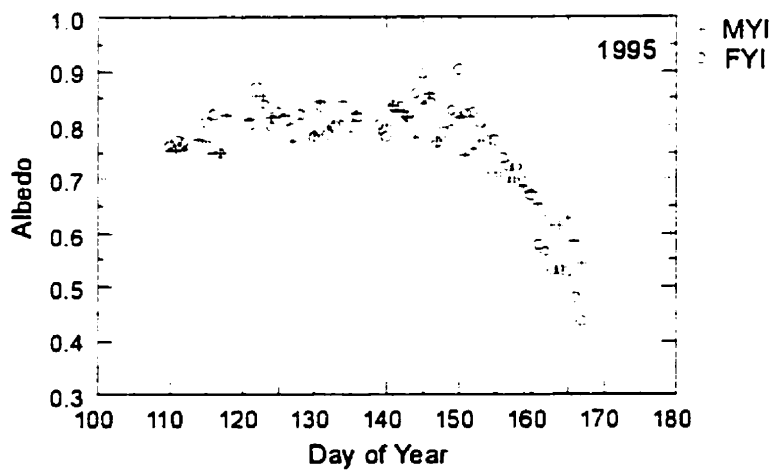
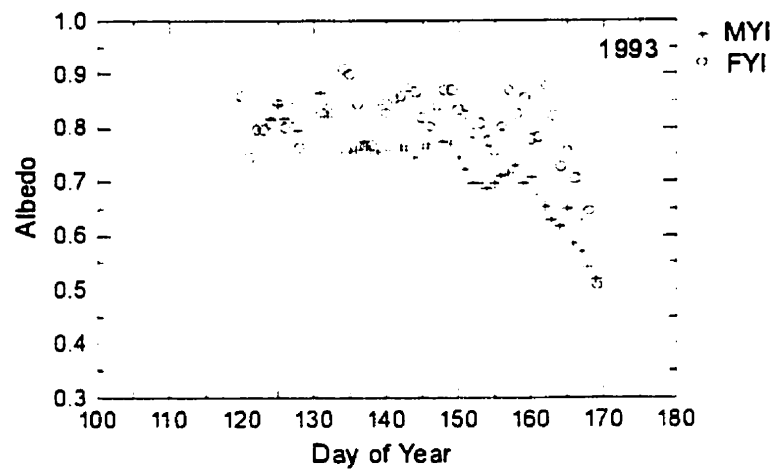


Figure 7.5 Daily average surface albedo of FYI and MYI during SIMMS93 and SIMMS95.

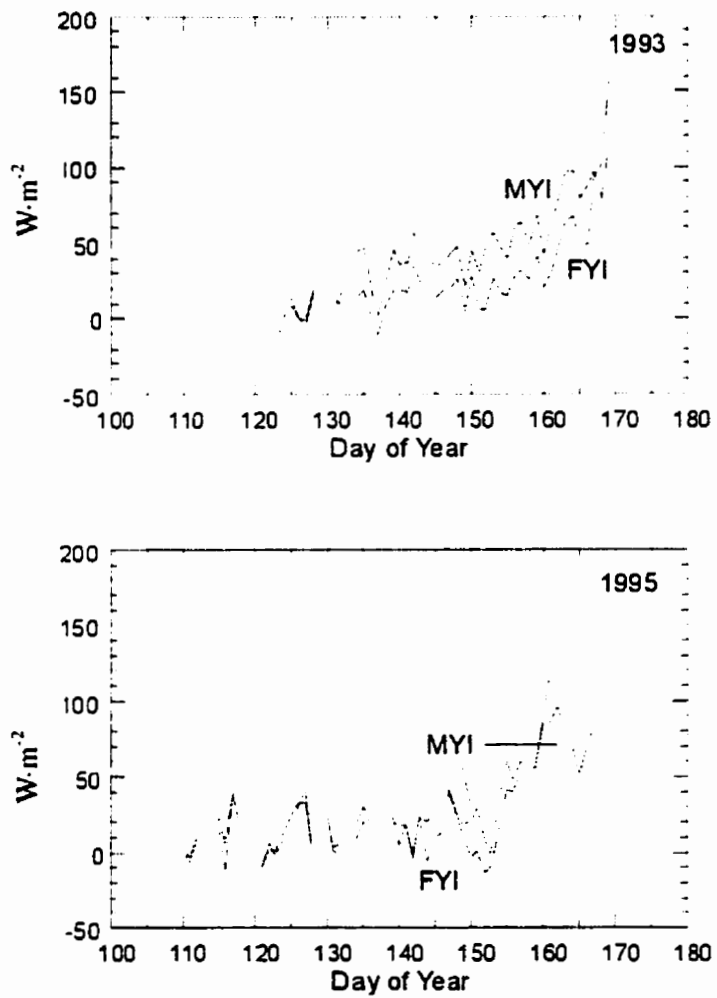


Figure 7.6 Daily average net radiation (Q^*) of FYI and MYI during SIMMS93 and SIMMS95.

7.3.4 The Surface Energy Balance

The time evolution of the energy balance for the sea ice types is summarized for each seasonal episode (i.e., *early*, *transitional*, *late*) in Fig. 7.7 (a and b) and in Table 7.1. Values for the first-year sea ice surfaces (FYI'93 and FYI'95) are reproduced for comparison¹⁸. The error bars in the figures represent plus or minus one standard deviation unit from the mean. At the MYI floes we observe:

- a seasonal rise in Q^*_s and dQ_s ,
- a reversal in the role of fusion energy from net ice production within the snow volume to net melt and
- a strong latent heat loss by the surface to the atmosphere in the *early* and *transitional* spring with subdued turbulent exchange in the *late* spring.

Each point is consistent with observations from the FYI sites. A notable difference between the two ice types relates to the direction of the average conductive heat flux, as previously discussed

The total energy available to the respective surfaces increases with the progression toward summer (Fig. 7.8) and the rate of increase is greater over the multi-year surfaces. It is interesting to note that the variation among the multi-year sites decreases into the *late* stage, while variation over first-year sea ice is greatest in the *late* spring. Because the net radiation of the snow cover represents virtually 100% of the available energy to the surface during the *late* spring, it is not unreasonable to suggest that the net radiation of melting snow over a multi-year floe is less variable between years than that of melting snow over first-year sea ice. Q^*_s accounts for a marginally larger proportion of the available energy to the multi-year surfaces relative to the first-year sea (i.e., 99% versus 92%) when averaged over the entire experimental period.

¹⁸ The variable set is standardized to include only those times common to both FYI and MYI sites.

Table 7.1 Average energy balance components for first-year and multi-year sea ice sites during SIMMS '93 and SIMMS '95.

Variable	Year	FYI early	FYI trans	FYI late	MYI early	MYI trans	MYI late
Q*s	1993	2.17	12.97	32.62	6.78	30.71	56.45
(W·m ⁻²)	1995	6.95	13.16	60.69	12.74	16.05	52.23
K*	1993	48.89	49.31	81.26	49.23	64.01	101.56
(W·m ⁻²)	1995	47.74	53.97	114.77	50.08	57.02	99.53
L*	1993	-46.72	-36.35	-43.05	-42.45	-33.30	-42.04
(W·m ⁻²)	1995	-40.79	-40.81	-32.91	-37.33	-40.98	-31.96
K↓	1993	253.11	265.79	308.36	275.26	285.22	324.28
(W·m ⁻²)	1995	216.86	293.67	314.92	206.25	280.81	295.85
K↑	1993	204.22	216.48	227.10	226.02	221.21	222.72
(W·m ⁻²)	1995	169.12	239.70	200.15	156.18	223.79	196.32
L↓	1993	194.99	257.65	263.60	200.05	257.62	263.60
(W·m ⁻²)	1995	215.35	237.75	285.61	222.43	237.75	284.91
L↑	1993	241.71	294.00	306.65	242.50	290.92	305.63
(W·m ⁻²)	1995	256.15	278.56	318.52	259.76	278.73	316.87
Q _{io}	1993	13.74	1.04	-4.02	-4.38	-15.06	-14.85
(W·m ⁻²)	1995	30.85	7.37	-20.75	-3.18	-2.62	-12.17
Q _{so}	1993	9.14	-3.05	-3.44	-0.50	-4.17	-5.79
(W·m ⁻²)	1995	4.77	10.81	-	-3.24	2.40	-
dQ _s	1993	-11.52	9.11	22.02	-3.12	12.18	40.56
(W·m ⁻²)	1995	-4.84	0.63	42.15	-5.21	-5.91	38.75
Q _M	1993	6.92	-13.20	-21.45	7.00	-1.29	-31.50
(W·m ⁻²)	1995	-21.24	2.80	-21.40	5.15	10.93	-26.58
Q _H	1993	-1.17	8.12	0.28	0.33	0.93	-1.78
(W·m ⁻²)	1995	4.90	2.74	-0.66	3.12	-0.88	4.25
Q _E	1993	-12.52	-11.98	-10.87	-10.24	-19.47	-14.11
(W·m ⁻²)	1995	-16.69	-15.26	-17.88	-21.08	-21.08	-17.73
α	1993	0.81	0.82	0.72	0.82	0.78	0.68
(fraction)	1995	0.78	0.82	0.62	0.76	0.80	0.66
T _s	1993	-16.28	-4.89	-1.80	-16.29	-5.66	-2.14
(°C)	1995	-13.86	-8.87	0.61	-13.14	-8.95	0.33
T _a	1993	-16.29	-4.97	-1.54	-16.17	-5.10	-1.85
(°C)	1995	-14.36	-10.12	0.29	-13.59	-9.84	0.55
VPD	1993	3.75	5.38	5.72	3.57	5.23	5.63
(Pa)	1995	3.62	3.78	5.40	3.64	4.39	8.01

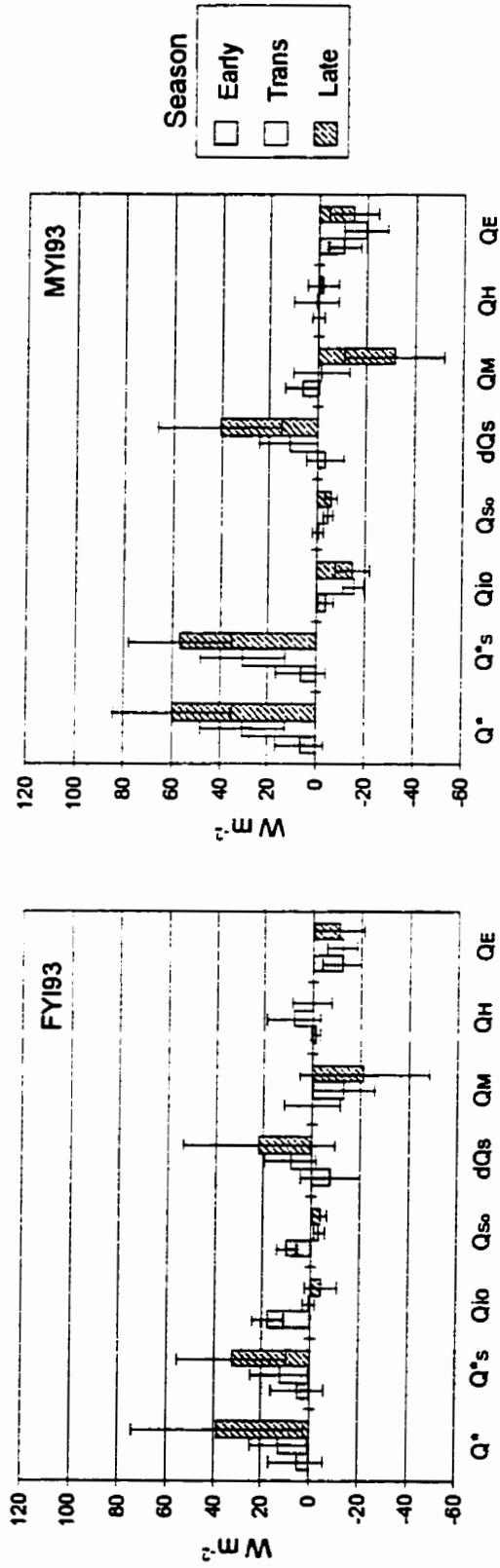


Figure 7.7a The seasonal evolution of the energy balance at FY1'93 and MY1'93. Error bars denote plus or minus one standard deviation unit from the mean.

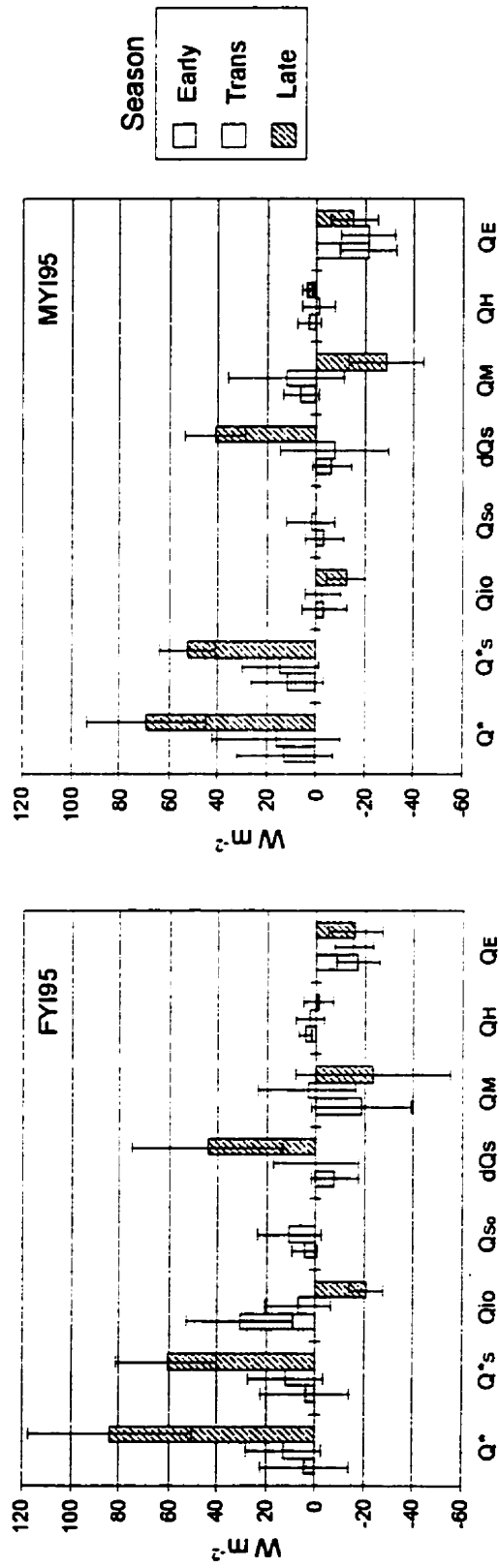


Figure 7.7b The seasonal evolution of the energy balance at FY1'95 and MY1'95. Error bars denote plus or minus one standard deviation unit from the mean.

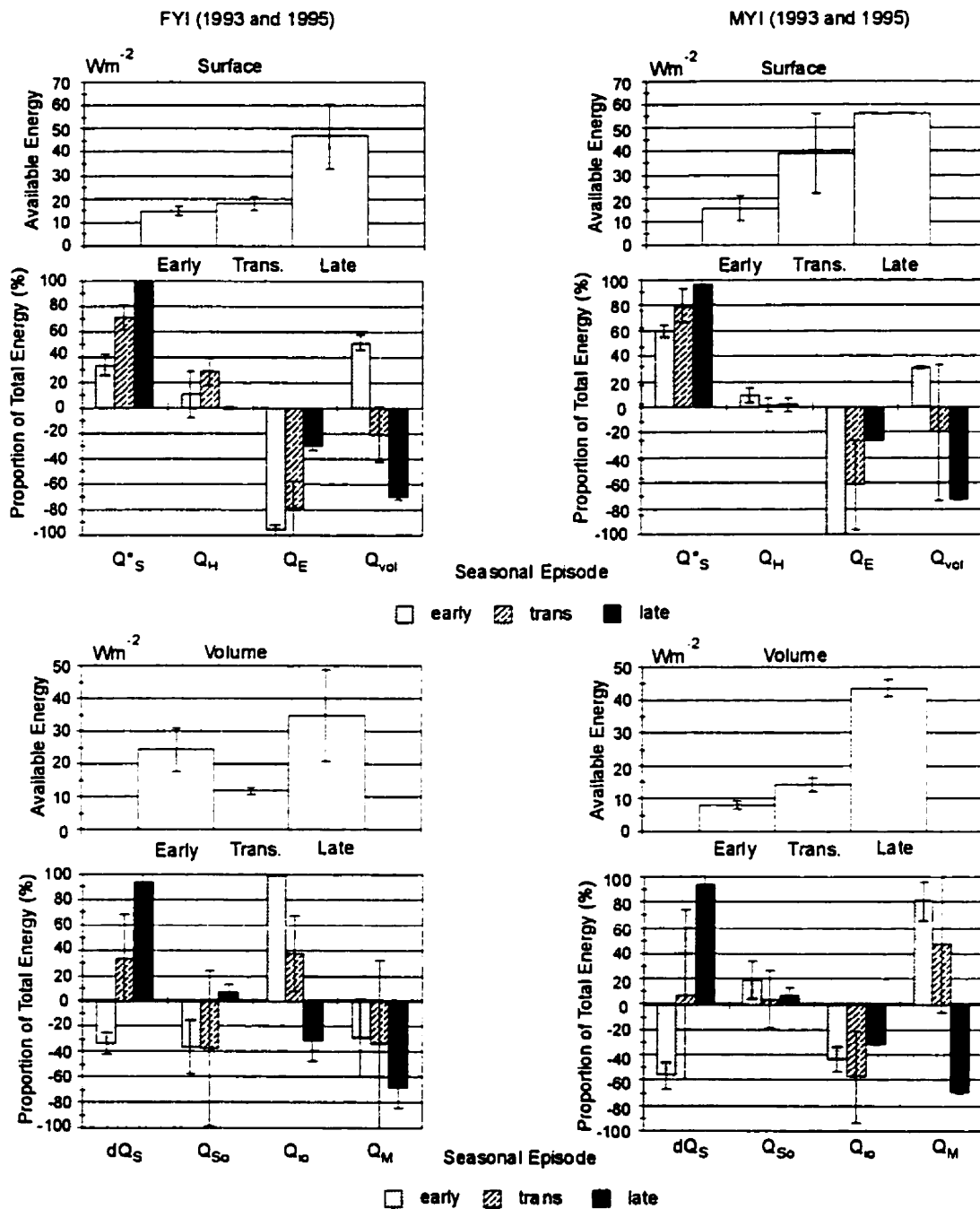


Figure 7.8 The seasonal evolution of the average partitioning of available energy at the snow surface and within the snow volume over FYI and MYI. The error bars represent the range between the SIMMS'93 and SIMMS'95 experiment.

On the whole, the role of the individual energy balance components appears similar between ice types (Fig. 7.8). The proportion of energy consumed by the latent heat flux declines with the advancing spring over multi-year sea ice while the energy consumed by the snow volume increases, consistent with observations from first-year sea ice over several years. A similar proportion of available energy is lost to the atmosphere via latent heat over MYI relative to FYI. The upward vapor transport consumed about 58% of the available energy to the multi-year surfaces, while over the same period latent heating accounted for 53% of the total energy lost by first-year sea ice. The remaining energy is directed into the snow volume, which consumed between 42% and 48% of the available energy to multi-year and first-year sea ice, respectively.

On average, the snow volume over first-year sea ice contributes more to surface energetics during the *early* spring (i.e., the volume contributes between 45 and 57% of the available energy to the surface) relative to the multi-year stations. The role of the snow volume changes from a heat source to a heat sink at the surface for both ice types during the *transitional* spring and represents a heat sink of comparable magnitude between sea ice types through to the *late* spring stage. The tremendous range in the role of the volume within the multi-year category during the *transitional* spring highlights the difference in behavior of sample floes between years. During the *transitional* spring of 1995 the thinner multi-year snow volume actually contributes a significant proportion (i.e., 33%) of available energy to the surface. At MYI, on the other hand, the flux consumes about 70% of the available energy.

Sensible heat acts to supply a greater proportion of the available energy to the first-year sea ice surface during the *early* and *transitional* stages of spring when compared to the role of the flux over multi-year sea ice. Its contribution is approximately 10% (versus 9% for multi-year sea ice) and 28% (versus 1.5% for multi-year sea ice) of available energy respectively for the two spring intervals when averaged over the sample years. Over the entire season its percent of total contribution averages 8% to first-year sea ice, while over MYI the sensible heat flux represents less than 1% of the total available energy.

The available energy to the multi-year snow cover increases with each seasonal episode. At the first-year sea ice sites, the available energy to the snow volume is less during the *transitional* spring than in the *early* spring. The difference is related to the observation that conductive heat from below is a major *early* spring heat source for the first-year sea ice snow cover and its magnitude declines during the *transitional* spring. In the *early* spring the term

accounts for virtually 100% of the available energy to the snow over first-year sea ice, whereas the flux over multi-year sea ice removes between 33% and 55% of snow's available energy to the ice interior. Instead, heat is made available for transport to the MYI snow surface from ice production. The snow volume is decoupled from oceanic heating by the huge volumetric heat capacity of the sea ice cover. During the period of heat surplus, approximately 70% of the available energy to the volume is directed into snow melt for each sea ice category. However, over the experimental periods, more than three times as much of the available energy is directed into snow melt at first-year sea ice (e.g., 70%), relative to multi-year sea ice (e.g., 17%). At the multi-year sites, 57% of the available energy to the volume is on average directed into heating the underlying ice interior.

Over the entire measurement periods, the percent ratio of $Q^*/K\downarrow$ is virtually identical between first-year sea ice sites (i.e., between 9.6% and 9.2%), while for the multi-year surfaces the percent ratio ranges between 14.9% at MYI'93 and 10.6% at MYI'95. The average percent ratio is larger at the multi-year site relative to the first-year sea ice average; however, the interaction of solar radiation at the surface of MYI'95 more closely resembles observations from first-year sea ice sites than with MYI'93. We attribute this to the combination of weakly defined hummocks during the 1995 experiment and to the fact that snow covered the hummock crest longer into the season relative to the 1993 experiment. These observations show that we should not expect clear-cut differences in the manner in which energy is supplied and partitioned between sea ice types. Rather we should expect a large degree of variation surrounding the form of the energy balance within sea ice class between years and perhaps regionally for a particular sea ice type within a season.

7.3.5 Testing of Differences between Ice Types

A comparison among the energy balance components between sea ice types, using a Mann-Whitney test, indicates that both the radiative and non-radiative energy fluxes can differ between the mature sea ice categories (Table 7.2). There is, however, a seasonal and spatial component in the nature of the differences. Spatially, any difference between sea ice categories is dependent on the characteristics of the FYI and MYI.

7.3.5.1 SIMMS'93: Thin FYI Versus Thick MYI

In 1993 the number of energy balance components which differ (at 95% level of confidence) increases with the spring progression. Only the conductive heat fluxes are different between ice classes in the *early* spring. The flux direction is directed upward within the FYI and directed down within the MYI (e.g., Fig. 7.4).

By the *transitional* spring the albedo is lower at MYI and consequently both Q^*_s and K^* are greater at MYI relative to FYI. The conductive flux at the ice surface remains lower at MYI, however the flux at the snow surface can no longer be considered different. The sensible heat flux acts to warm the surface at FYI'93 while the flux is negligible at MYI'93. Despite the differences in Q^*_s , the atmospheric heating of the snow cover (dQ_s) and energy associated with melt can not be considered different between sites. Any discrepancy in radiation balance between sites is offset by differences in (a) sensible heat input from the atmosphere, (b) sensible heat from the underlying ice cover at FYI'93 and (c) enhanced Q_E loss over the MYI (P-value=0.053).

All of the energy balance components differ during the late spring, except for L^* and the turbulent heat fluxes. The albedo is, on average, less at MYI'93 and the net radiative and net solar gains are therefore greater. More energy is available to the MYI'93 surface and volume, which supports greater rates of snow melt, heating of the underlying sea ice volume and vapour transfer to the atmosphere.

Despite the difference in Q^*_s between ice classes, the surface temperature can not be considered different at a reasonable level of confidence, nor can the components of the long-wave exchange. The latent heat loss is marginally larger at the MYI sites during the *transitional* and *late* spring (P-values = 0.053 and 0.065, respectively). All atmospheric properties (T_a , VPD, and RH) can not be considered different at a reasonable level of confidence, except for boundary layer stability (ξ), which is more apt to be unstable (negative) over the MYI'93 surface.

7.3.5.2 SIMMS'95: Thick FYI Versus Thin MYI

Over all, the energy balance components are less apt to differ when the energy balance of a thick FYI surface is contrasted with the energy balance of a thin MYI floe, as is the case in 1995. The components of the radiation balance are similar throughout the spring period, while the conductive fluxes are shown to differ.

During the *transitional* stage, the atmospheric sensible heating of the FYI'95 surface is greater, while latent heat losses are larger at MYI'95. The enhanced latent heat flux at the MYI surface responds to the sites larger VPD. The consequence of the larger vapor flux is a reduced heating (dQ_s) of the MYI snow volume and larger rates of ice production within the MYI snow cover.

During the *late* spring, only Q_{io} and Q_H can be considered different at a 95% confidence level. There is a tendency for Q_{io} at the FYI surface to be lower, while the sensible heat gains to the MYI surface are larger. The large downward conductive flux at the FYI'95 sea ice surface is probably related to percolating water (Section 6.5.3.3) and is instrumental at warming the sea ice surface. A deeper snow cover within the MYI floe would allow heat associated with draining water to be dissipated over a larger volume before reaching the sea ice surface. Therefore the effect of water drainage is expected to contribute more to the downward flux at the first-year sea ice surface, relative to the multi-year sea ice surface. All atmospheric properties can not be considered different between ice types in the *late* spring, except for ξ , which can be considered different (P-value=0.082). There is the tendency for the near surface atmosphere to be more stable at MYI relative to FYI.

Table 7.2 P-values (1-tailed) for Mann-Whitney test between multi-year and first-year sites and test interpretation (Res.). Test results at a 95% level of confidence are bolded.

	1993	1993	1993	1993	1993	1993	1993	1993	1995	1995	1995	1995	1995	1995	1995	1995
Var.	all	Res.	Early	Res.	Trans	Res.	Late	Res.	all	Res.	Early	Res.	Trans	Res.	Late	Res.
Q^*s	0.000	F<M	0.358	F=M	0.010	F<M	0.000	F<M	0.267	F=M	0.196	F=M	0.302	F=M	0.257	F=M
Kn	0.001	F<M	0.428	F=M	0.023	F<M	0.000	F<M	0.449	F=M	0.090	F<M	0.475	F=M	0.203	F=M
Ln	0.308	F=M	0.292	F=M	0.311	F=M	0.388	F=M	0.283	F=M	0.388	F=M	0.320	F=M	0.325	F=M
Qi	0.000	F>M	0.002	F>M	0.000	F>M	0.000	F>M	0.000	F<M	0.006	F>M	0.000	F>M	0.043	F=M
Qs	0.003	F>M	0.007	F>M	0.127	F>M	0.003	F>M	0.002	F<M	0.019	F>M	0.007	F>M	-	-
dQs	0.002	F<M	0.101	F=M	0.299	F=M	0.003	F<M	0.145	F=M	0.443	F=M	0.037	F>M	0.468	F=M
Qm	0.276	F=M	0.292	F=M	0.061	F<M	0.034	F>M	0.036	F<M	0.023	F<M	0.046	F<M	0.181	F=M
Qh	0.096	F>M	0.137	F=M	0.046	F>M	0.211	F=M	0.064	F>M	0.282	F=M	0.005	F>M	0.041	F<M
Qe	0.034	F>M	0.428	F=M	0.053	F>M	0.065	F>M	0.013	F>M	0.149	F=M	0.012	F<M	0.470	F=M
$Tbar$	0.403	F=M	0.443	F=M	0.389	F=M	0.281	F=M	0.351	F=M	0.364	F=M	0.313	F=M	0.182	F=M
vpd	0.454	F=M	0.500	F=M	0.490	F=M	0.408	F=M	0.012	F<M	0.454	F=M	0.031	F<M	0.066	F<M
rh	0.432	F=M	0.159	F=M	0.351	F=M	0.317	F=M	0.073	F>M	0.209	F=M	0.066	F>M	0.076	F>M
alb	0.000	F>M	0.233	F=M	0.002	F>M	0.000	F>M	0.137	F=M	0.077	F>M	0.148	F=M	0.299	F=M
T_s	0.317	F=M	0.443	F=M	0.275	F=M	0.281	F=M	0.438	F=M	0.209	F=M	0.449	F=M	0.163	F=M
T_s^*	0.420	F=M	0.415	F=M	0.315	F=M	0.363	F=M	0.187	F=M	0.281	F=M	0.121	F=M	0.001	F<M
Kd	0.110	F=M	0.101	F=M	0.125	F=M	0.120	F=M	0.082	F>M	0.158	F=M	0.127	F=M	0.100	F=M
Ku	0.433	F=M	0.100	F=M	0.267	F=M	0.231	F=M	0.055	F>M	0.077	F>M	0.038	F>M	0.470	F=M
Lu	0.383	F=M	0.428	F=M	0.289	F=M	0.349	F=M	0.454	F=M	0.334	F=M	0.485	F=M	0.163	F=M
Ld	0.429	F=M	0.322	F=M	0.487	F=M	0.500	F=M	0.466	F=M	0.333	F=M	0.500	F=M	0.500	F=M
zL	0.004	F>M	0.443	F=M	0.199	F=M	0.004	F>M	0.323	F=M	0.337	F=M	0.353	F=M	0.041	F<M

Table 7.3 The average turbulent fluxes and Bowen ratio over the seasonal sub-periods, and variation between daytime (between 600 and 1900) and nighttime periods, and over the diurnal cycle.

Period	Time	1993	1993	1993	1993	1993	1993	1995	1995	1995	1995	1995	1995
		FYI	FYI	FYI	MYI	MYI	MYI	FYI	FYI	FYI	MYI	MYI	MYI
		Q_H	Q_E	β									
early.	day	-4.3	-3.8	1.1	-4.0	-10.1	0.4	2.1	-7.1	-0.3	1.3	-12.1	-0.1
early	night	3.5	-0.8	-4.3	4.9	-3.9	-1.3	8.1	-1.9	-6.3	8.2	-2.3	-3.5
trans.	day	-2.1	-11.4	0.2	-10.7	-25.5	0.4	-1.5	-13.8	-0.1	-4.7	-17.8	0.3
trans.	night	5.3	-4.4	-1.2	4.5	-9.6	-0.5	7.0	-3.9	-1.8	5.3	-5.0	-1.0
late.	day	3.3	-2.1	-1.6	0.2	-12.1	-0.0	-8.4	-16.2	0.5	5.0	-4.4	-1.1
late.	night	6.4	-1.3	-4.9	1.9	-8.9	-0.2	3.4	-4.9	-0.7	-3.5	-1.5	-3.2

7.3.5.3 Discussion

Thick MYI floes represent an environment of lower albedo, higher net radiation and melt rates, with elevated surface vapour loss to the atmosphere. Conductive heat flow during the spring usually warms a colder MYI interior instead of heating the surface, as observed at FYI. A thin MYI flow on the other hand, may have a similar radiation balance and each non-radiative flux may differ between ice classes, but not in a consistent fashion. In fact, FYI'95 behaves like a thick MYI floe during the *transitional* and *late* spring, because a large proportion of available energy to the snow cover is directed into the underlying sea ice. The contrast in differences between the ice types between years is because: (i) the ice interior at MYI'93 remains colder, relative to the snow cover, longer into the spring period (a consequence of the large heat capacity of the thick MYI floe) and (ii) because the hummock surfaces are snow-free earlier in the 1993 experiment (around day 130). This second point acts to depress the albedo at MYI'93, relative to FYI'93.

Observations from both years show that Q_E loss is larger over MYI, while the surface temperature and $L\uparrow$ can not be considered different between the sea ice types, even though net radiation may be different between sea ice categories. The larger latent heat flux at MYI'93, relative to FYI'93, can be attributed to a larger Q^*_s at the multi-year site (i.e., more energy readily at the surface for sublimation). At MYI'95 on the other hand, the enhanced latent heat flux is not related to differences in Q^*_s . The difference in Q_E between ice types is apparently driven by a

larger VPD at the multi-year site. There is the possibility that a small systematic difference existed in the RH probes between sites during the 1995 experiment. Another possibility is related to the fact that the saturation vapour pressure - temperature relationship is non-linear and that only small differences in air temperature can result in large variations in saturation vapour pressure at a site.

The difference in long-wave emissivity between snow ($\epsilon \approx 0.99$) and hummock ice ($\epsilon \approx 0.97$) may contribute to our observation of similarity in L^* and T_s between sites. Maykut (1986) provided these emissivities as representative of snow and sea ice, respectively. The presence of exposed ice on the multi-year floe may depress L^* for a given thermodynamic temperature, relative to snow covered sea ice at the same temperature, assuming an emissivity of 0.99. According to Eq. 7.1, a weighted emissivity should be 0.977. A sensitivity analysis (Appendix 8) indicates that an overestimation in emissivity by 0.013 will lead to an underestimation in computed T_s by between approximately 0.22° to 0.08°C for clear sky and full cloud cover conditions, respectively. The emissivity effect acts to elevate L^* for the multi-year ice relative to snow-covered first-year sea ice. The variable, T_s^* , in Table 7.2 represents the comparison of surface temperatures between sites using estimates of surface temperature computed with an emissivity of 0.977 for the multi-year floes. Calculating the surface temperature, using a lower surface emissivity for multi-year sea ice, acts to widen the difference between the surface temperature of the two sea ice types during the spring of 1995, but not in 1993. We can reject the hypothesis of similarity in the surface temperature between the sea ice types during the late spring of 1995 using the weighted emissivity, but the temperature can not be considered to differ between ice types in any of the other periods. Small uncertainties in surface emissivity are therefore unlikely to be the reason why we do not detect a difference in the distribution of surface temperature between sea ice types.

Another explanation is that Q^*_s is preferentially directed into latent heating at the surface, and not the sensible heating of the adjacent atmosphere or snow. If Q^*_s is preferentially directed into latent heating we should see an inverse relationship between β (Eq. 2.5) and Q^*_s . Support for these comments maybe taken from Table 7.3. We see from the table that:

- small β are observed during the daytime and larger β are observed at night (i.e., typically periods of high and low Q^*_s , respectively),
- larger β are observed during the winter state (i.e., typically a period of lower Q^*_s), and
- larger β are observed over FYI ice surfaces (i.e., the ice type showing lower Q^*_s levels).

At night, when Q^*_s is typically small (for both ice types), the re-freezing of the surface layer will release latent heat, which should partially offset any discrepancy in the surface temperature that could be related to differences in conductive heat flow between the ice types. In other words, phase change activity at the immediate surface buffers the radiative and conductive impact on the surface temperature, thereby acting to minimize differences between the ice types during the spring transition, regardless of differences in surface heating.

The findings show that all MYI floes can not be considered different *icescape* units from FYI, on the basis of their thermal and radiative coupling to the atmosphere at all times. However, a thick MYI floe can differ in regard to most components of the energy balance; particularly in the *transitional* and *late* spring. Many of the non-radiative energy balance components are small in magnitude and therefore a temptation may be to ignore statistically viable differences in energy transfer processes between mature sea ice types in sea ice models. The cumulative effect of differences in the energy balance between sea ice types can be important from the perspective of an ice balance. The cumulative differences in Q^* , Q_{io} , Q_H and Q_E between FYI'93 and MYI'93 are shown in Fig. 7.9. During the 1993 experiment 66.7 MJ more net radiation was received over MYI, while 48.6 MJ more energy was directed into the underlying sea ice cover. These energy values are equivalent to the melting of 22 cm of ice ($\rho_s=900 \text{ kg}\cdot\text{m}^{-3}$) and 16 cm of ice, respectively. A downward heat conduction into the ice interior in the presence of a snow cover is typically not considered in sea ice models (e.g., Ebert and Curry, 1993). The cumulative difference in turbulent heating is approximately 10 MJ for both Q_H and Q_E , which is the melt equivalent of approximately 3.5 cm of ice. This value is only about 2% of the thickness of a typical FYI in the Parry Channel, assuming an ice thickness of 150 cm. On the other hand, the melt equivalent of differences in Q^* and Q_{io} between ice types represents between 10% and 15% of a typical FYI cover. Therefore, the consequences of treating sea ice as horizontally homogeneous with respect to the radiative exchange with the atmosphere and of neglecting downward heat conduction in the presence of a snow cover, particularly for thick multi-year sea ice, are non-trivial. Failure to consider the unique properties of sea ice types in models can cause errors in predicted *in-situ* melt of between 8 to 12 days, assuming the energy equivalent of melt rate to average $80 \text{ W}\cdot\text{m}^{-2}$.

7.4 Summary

The temperature structure, physical properties, thermal properties and conductive flux within the snow and sea ice cover can be vastly different between snow-covered FYI and MYI. Over FYI, a saline layer at the snow base insulates the upper snow cover for ocean heat in much the same way as the large heat capacity of the thick multi-year sea ice. Snow-covered FYI warms faster and possesses a near steady-state temperature gradient with increasing temperature toward the ice interior. In contrast, the temperature gradient is non-steady state within the snow and sea ice of MYI and the snow and upper sea ice are warmer than the ice interior.

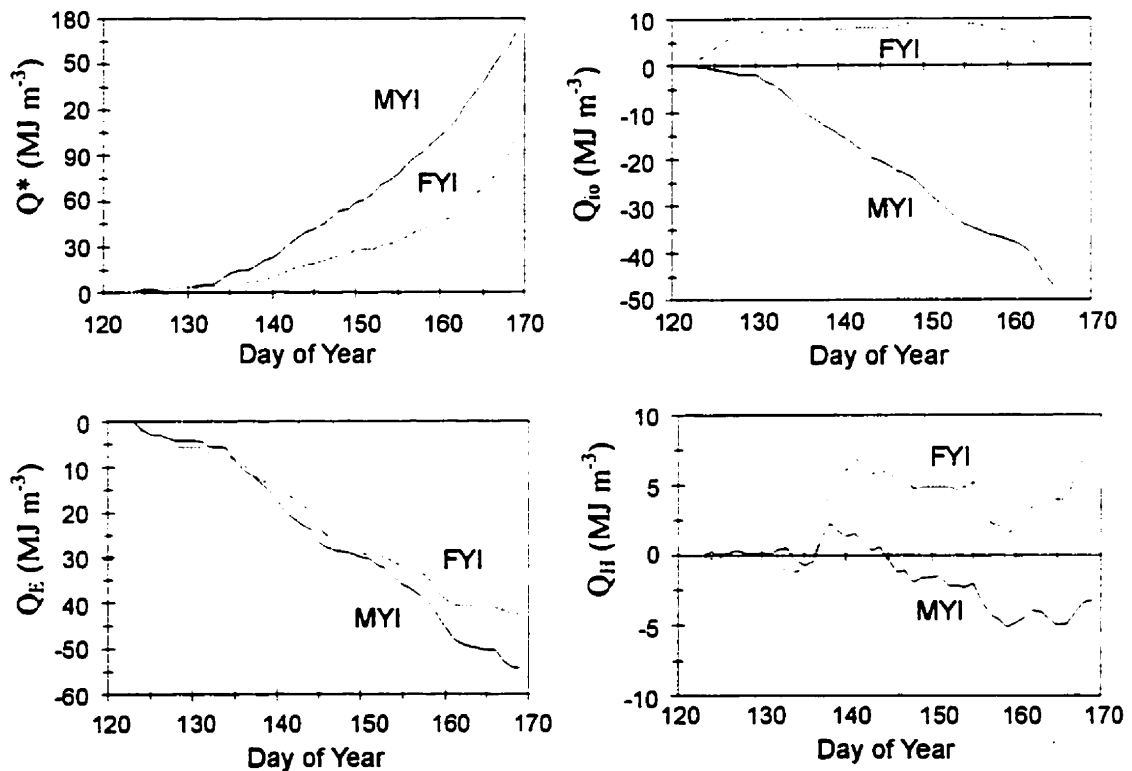


Figure 7.9 Cumulative energy totals of Q^* , Q_{10} , Q_E and Q_H at FYI'93 and MYI'93.

Both snow covers are vertically heterogeneous with respect to physical properties but the presence of a salinity gradient within the FYI snow causes extreme variation in specific heat across

the snow profile as the snow temperature rises. The strong upward flux observed during the *early* spring at the FYI site is absent within the MYI floe where, instead, a heat flux is directed into the snow and ice volume over much of the experiment. The nature of the difference between the energy balance varies depending on the characteristics of the MYI and FYI being compared. A thick MYI floe is shown to be an environment of (i) lower albedo, (ii) higher net radiation, (iii) larger melt rates and (iv) enhanced turbulent heat loss relative to nearby FYI. A thin MYI floe, on the other hand, need not significantly differ from a thick FYI with respect to the radiation balance and most non-radiative energy transfer processes. The albedo of the flooded first-year sea ice is low, relative to the multi-year surface during the final days of a snow cover in both years. As a consequence, K^* and Q^* becomes larger over the FYI surface. In 1993 we observed a drop in surface albedo and a rise in Q^* approximately 27 days earlier over the multi-year than over the nearby first-year sea ice. In contrast, the timing of changes in albedo and net radiation are similar between sites in 1995. The findings show that all MYI floes can not be considered different *icescape* units from FYI on the basis of their thermal and radiative coupling to the atmosphere at all times. In some situations, significant differences exist and the failure to consider these differences can impact springtime ice balance estimates and predicted timing of ice break-up.

Irrespective of the potential difference in net radiation between sea ice classes over periods of the spring transition, the surface temperature remains similar between sea ice types. Any difference in radiation loading onto the MYI surface is apparently offset by enhanced turbulent heat loss by the MYI surface. This finding discounts the use of the surface temperature as a reliable means of classifying mature ice types over the spring period.

CHAPTER 8: ENVIRONMENTAL EFFECTS ON THE SURFACE ENERGY BALANCE

8.1 Introduction/Background

In this chapter I identify the environmental forcing agents and conditions which are most effective at determining whether the energy balance acts to warm or cool the surface volume within the CAA. Relationships among the major energy balance components, surface properties and the atmospheric states are highlighted over the progression toward summer. These linkages are used to interpret the observed variation in the onset of melt from year to year within the spring season.

The environmental mechanism(s) responsible for the initial lowering of the surface albedo, which is considered to be a first stage of melt, are not immediately obvious from the preceding analysis and, in general, are not well defined (Robinson et al., 1986; Serreze et al., 1993b). Studies have identified rising air temperature and increased levels of global radiation as variables that initiate the melt process (refer to Section 2.4.2.3). There is, however, no reason to believe that air temperature and solar radiation should be strongly correlated. Other environmental factors, and processes which accompany an increase in either variable may act to support, or counter-act the melt process. As discussed in Chapters 1 and 2, clouds in the early spring are often associated with surface warming, but the feedbacks between cloud cover and the surface energy balance are complex and their parameterization represents a significant source of potential error in climate simulations. An investigation into these mechanisms, using observational data, has advantages over one-dimensional modeling because each component of the ASO system is coupled. Patterns among the elements of the energy balance may be detected using our observational data set. These patterns should be reproduced in GCM output and, therefore, the information presented here may be used to assess whether the surface fluxes, and linkages among the surface fluxes, are realistically

represented by modelers. An investigation into the factors that affect the components of the energy balance, including melt, is the third objective of this thesis (Section 1.3).

The spring seasons of 1992 and 1993 sharply contrast with respect to atmospheric and surface forcing of the energy balance components. Recall that the spring of 1992 was unusually cold and received a large amount of snow during the *transitional* spring stage. A large proportion of snowfall was associated with the passage of cyclones through the Resolute area. The spring of 1993, on the other hand, was warmer than average and received a much larger amount of sunshine relative to the 1992 spring season. In 1993, much of the spring period was dominated by surface high pressure. High pressure was situated over the Resolute area for much of May and was a manifestation of a persistent 50 kPa ridge across the central Arctic (Agnew and Silis, 1995). Agnew and Silis (1995) describe the transition from cA to mP dominance toward the end of May in 1993. These two years form the basis of our analysis, partly because of the contrasting surface and atmospheric characteristics between seasons, and partly because both stations were in close proximity to the Resolute weather station.

8.2 Methods

The analysis is divided into three sections: (i) an assessment of the role of clouds on the energy balance, (ii) a statistical analysis of the relationship between environmental and energy balance variables, and (iii) a contrast in the melt evolution between the spring seasons of 1992 and 1993. The statistical tools used in the second stage of the analysis are described below.

In Chapter 6 we indicate that several energy budget components contribute to heat the snow cover, while several processes at the surface and within the volume act to dissipate this energy. The investigation is therefore multi-variate, where each process may itself be both an independent (or forcing) variable and a dependent (or forced variable) variable. Principal Components Analysis (PCA, Appendix 5) is well suited to this type of investigation. The procedure decomposes a data set into a number of components (principal components) which are the linear weights of the original variables. The weighting or contribution of each variable to a principal component gives insight into the relative importance of that variable within the over-all data set. The technique groups variables that are highly correlated with one another but are largely

independent of other subsets of variables. Therefore, the technique maybe useful for finding order in a complex system of interrelated variables.

There are few examples of the PCA in energy balance studies. Crane (1979) summarized several aspects of the energy budget over landfast sea ice, using the first two principal components of the energy balance. The components were then used in a cluster analysis to identify energy budget groupings that tended to support or retard the melt process. The conductive flux was the most important term in defining the energy balance groupings and the highest within group correlation was between the conductive flux and sensible heat flux. The use of PCA is more widespread in areas of synoptic climatology (Barry and Perry, 1973). LeDrew (1980) used PCA on a time series of total vorticity fields to classify major synoptic systems. As with the Crane (1979) study, a PCA was used as an intermediate step by LeDrew (1980). He subsequently related the eigenvectors of the components of total vorticity (i.e., thickness advection, surface enthalpy effects, latent heat release, frictional and orographic effects) to the total vorticity fields by canonical correlation. The purpose was to identify which eigenvector of the component fields were highly correlated with one or more of the eigenvectors of the total vorticity fields. More recently, Jones et al.,(1995) observed a high correlation between atmospheric circulation types based on a PCA grouping of sea level pressure and precipitation chemistry, and used the correlation structure to derive atmospheric circulation pattern-pollution relationships.

In this work, a PCA is used to identify groups of inter-correlated variables within an energy balance variable set consisting of daily averages from the *early*, *transitional* spring and *late* spring for each year. The data from the *early* and *transitional* spring periods are pooled to maintain a minimum of at least ten data values for each variable. Eight individual energy fluxes that impinge on the snow volume are included in the analysis: K_{\downarrow} , K_{\uparrow} , L_{\downarrow} , L_{\uparrow} , Q_{So} , Q_{io} , Q_{Hs} , and Q_E . Net radiation of the snow-sea ice-ocean volume is partitioned into its four components to highlight the relative importance of each in the context of these eight variables. The albedo data from the *late* spring in 1993 was squared to alleviate a negative skew in the original data. No other transformations were necessary.

The eigenvectors, eigenvalues and component loadings (see Appendix 5 for definitions) are extracted from a correlation matrix of the variables within each group using the SYSTAT statistical package (Wilkinson et al., 1992). Typically (e.g., Johnson and Wichern, 1992 and

Tabachnick and Fidell 1989), a principal component is considered to have explanatory significance if either:

- the eigenvalues are greater than unity, or
 - the percent of total variance that is explained by a principal component exceeds 12.5%.
- If neither of these conditions is satisfied, I still consider the component to have interpretive value if it is reasonably well correlated with at least one variable and the component explains at least 10% of the total variance of the original variable set.

A subsequent analysis involves an examination of the relationship between the energy balance principal components and environmental variables, using a canonical correlation analysis (Appendix 5). Canonical correlation is a multivariate technique that reduces the full array of relationships between two sets of variables to a few pairs of correlated canonical variates (Tabachnick and Fidell, 1989). Each variate is made up of linear combinations of the original variables (or principal components). Canonical correlation is similar to a multiple regression analysis, except that multiple dependent variables are considered (Tabachnick and Fidell, 1989). Input data consist of the significant principal components from the PCA and the daily average of the environmental variables: T_a , VPD, u , α , ξ and daily total hours of bright sunshine (sh). These variables summarize the thermodynamic and dynamic state of the atmosphere and provide a measure of the enthalpy and optical state of the snow. The use of principal components, instead of the original energy balance variables, eliminates the potential biasing effects of multicollinearity among variables of the energy budget data set and reduces the number of variables in the analysis. The statistical significance of the canonical correlation ($r_c \leq 1$) is verified by using a χ^2 -test with a selection criteria at the 95% level of significance.

The objective is to find which, if any, of the principal components are highly correlated with the environmental variable. The analysis should identify formal relationships between the energy budget and environmental parameters, gauge the strength of each relationship, and confirm the persistence of the relationship over the spring season. I am unaware of the use of canonical correlation in the analysis of an energy balance data set, even though it seems well suited for this application. Canonical correlation, however, has been adopted in other areas of the geographical and biological sciences. I have already cited its use by LeDrew (1980) for determining the physical processes responsible for vertical velocity in the Eastern Canadian Arctic atmosphere. Ebisemiju

(1988) describe the use of the technique in relating morphometric characteristics of watersheds (e.g., basin area, total stream length, total drainage density, etc.) to environmental parameters of the drainage basin (e.g., soil permeability, tree density, relief, etc.) to identify patterns in the development of Nigerian drainage networks. Ratha and Sahu (1993) studied the effect of sediment size parameters on the concentration of trace elements using canonical correlation. They found that the type and level of geochemical pollution in soils could be predicted by physical parameters of the medium. Jakubauskas (1996) examined the relationship between Thematic Mapper bands and forest structural variables for lodgepole pine stands. He found that tree height, live basal area, leaf area index and size diversity are highly inter-correlated and act in combination to affect the overall stand reflectance.

8.3 Clouds and the Surface Energy Balance

The evolution of the diurnal form of TCA, Q^*_s , L^* , K^* , u and ξ are displayed in Figs. 8.1 and 8.2. The images relate a colour gradient to flux (or atmospheric property) intensity over the time of day (abscissa) and the day of year (ordinate). In both years we observe synchronous banding in the plots of TCA, L^* and u . Periods of high L^* are associated with full cloud cover and correspond to local troughs in the time series of daily average sea level pressure (Fig. 6.2 a and b), peaks in wind speed and a tendency for weakened atmospheric stability, or atmospheric instability. The banding is more prevalent in 1992 than in 1993; a consequence of the regular and frequent migration of cyclones over the research site in 1992 (refer to the discussion surrounding Fig. 6.4). The effect of cloud cover is to reduce nighttime long-wave radiation loss and peak mid-day K^* . In response, Q^*_s exhibits smaller diurnal variation relative to clear-sky periods. Clouds therefore directly impact the radiation balance, but environmental conditions associated with cloud cover will also indirectly influence non-radiative heat fluxes through the effects of wind speed and atmospheric stability. These relationships are not captured in investigations on the role of cloud cover over sea ice through modeling initiatives (e.g., Zhang et al., 1996).

The effect of environmental conditions that accompany cloud cover on the energy balance is summarized in Table 8.1 (and Fig. 8.3a and b) for the *early* and *late* spring periods of the FYI'92 and FYI'93. Overcast skies are associated with (relative to clear-sky conditions):

- higher daily average Q^* , predominately through a reduction in L^* loss across the diurnal cycle,
- lower upward conductive heating; particularly at the snow surface,

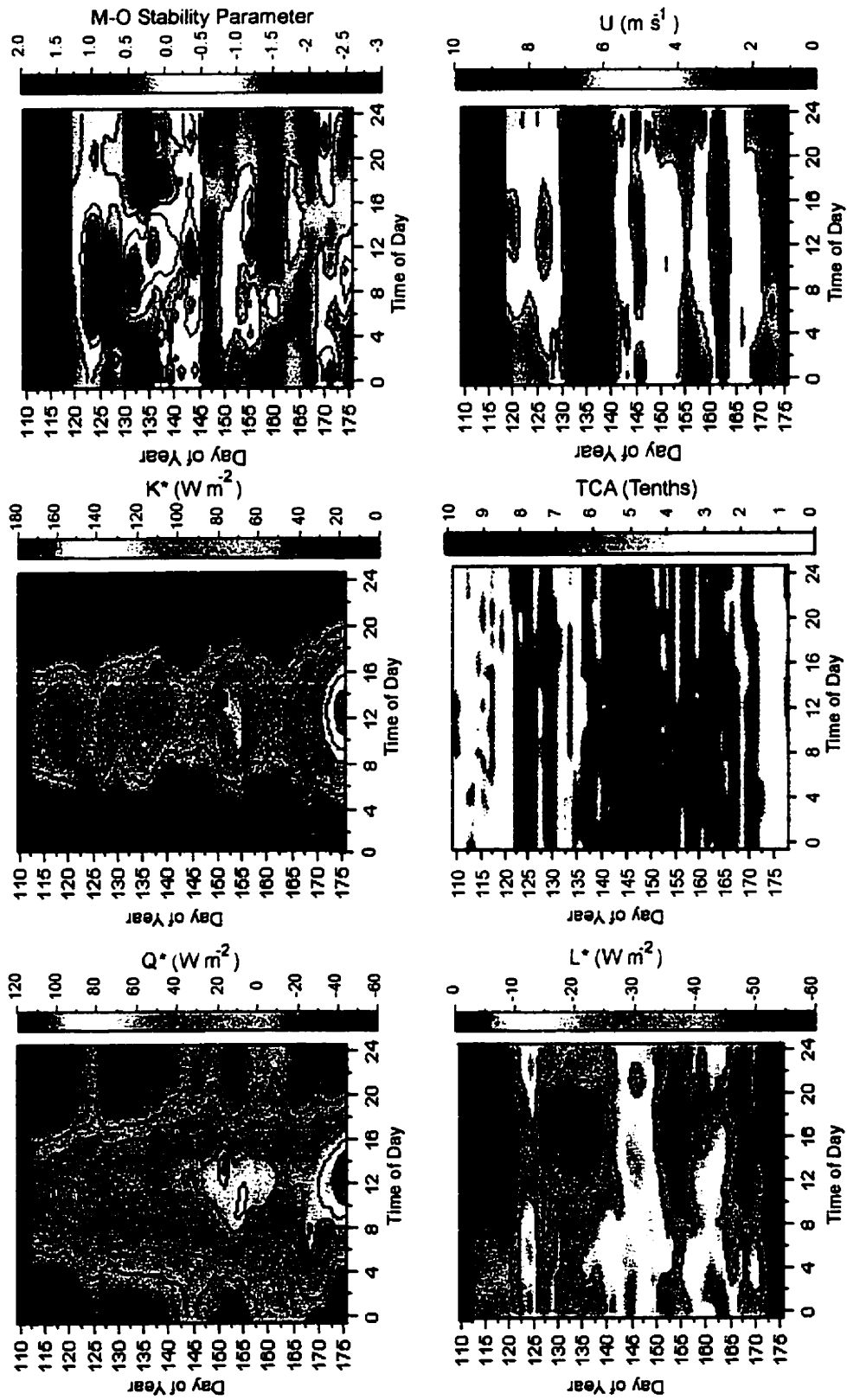


Figure 8.1 The diurnal and daily variation in the net radiation (Q^*), net solar radiation (K^*), net long-wave radiation (L^*), total cloud amount (TCA), wind speed and the Monin-Obukhov stability Parameter at FYI'92.

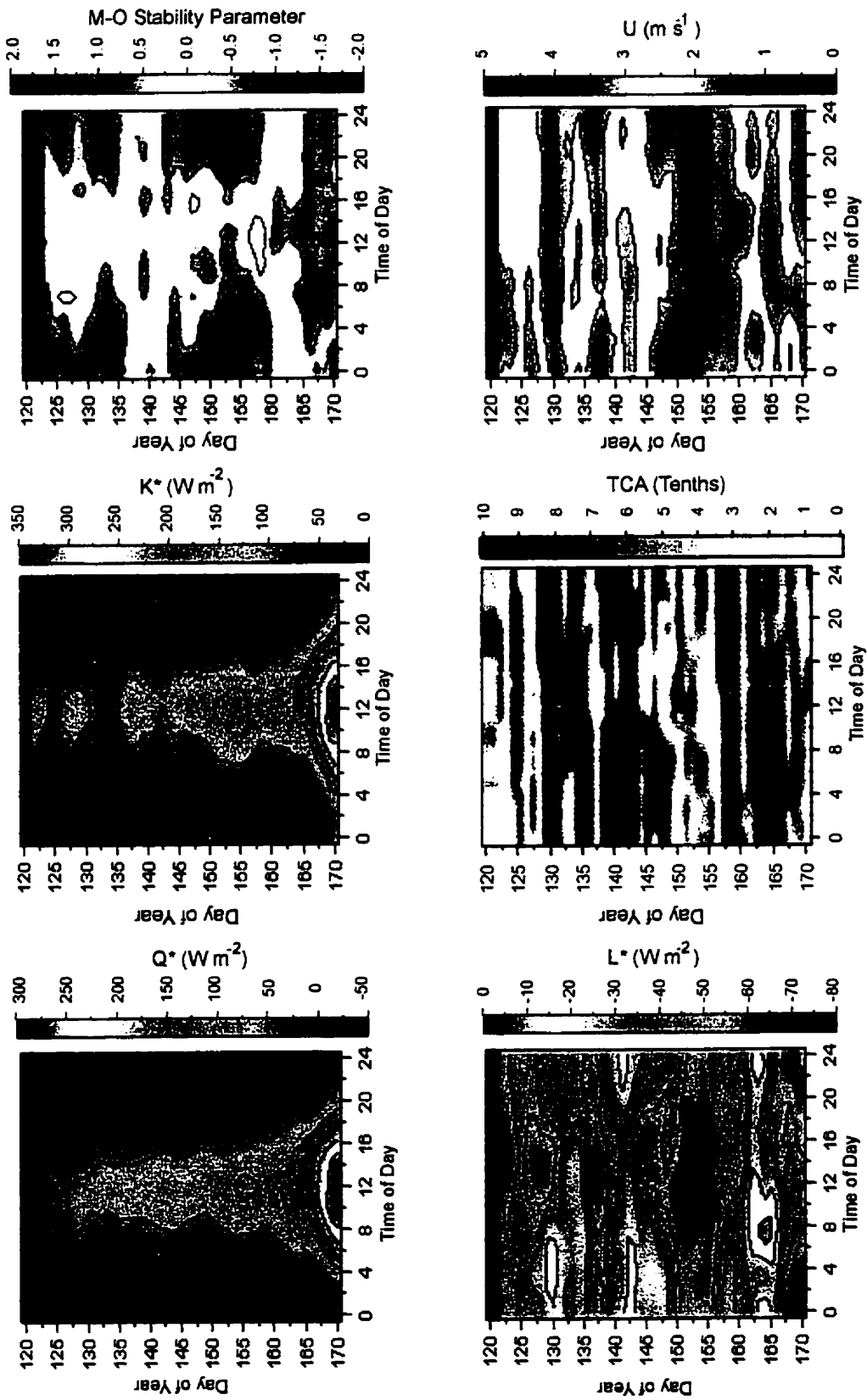


Figure 8.2 The diurnal and daily variation in the net radiation (Q^*), net solar radiation (K^*), net long-wave radiation (L^*), total cloud amount (TCA), wind speed and the Monin-Obukhov stability Parameter at FYI'93.

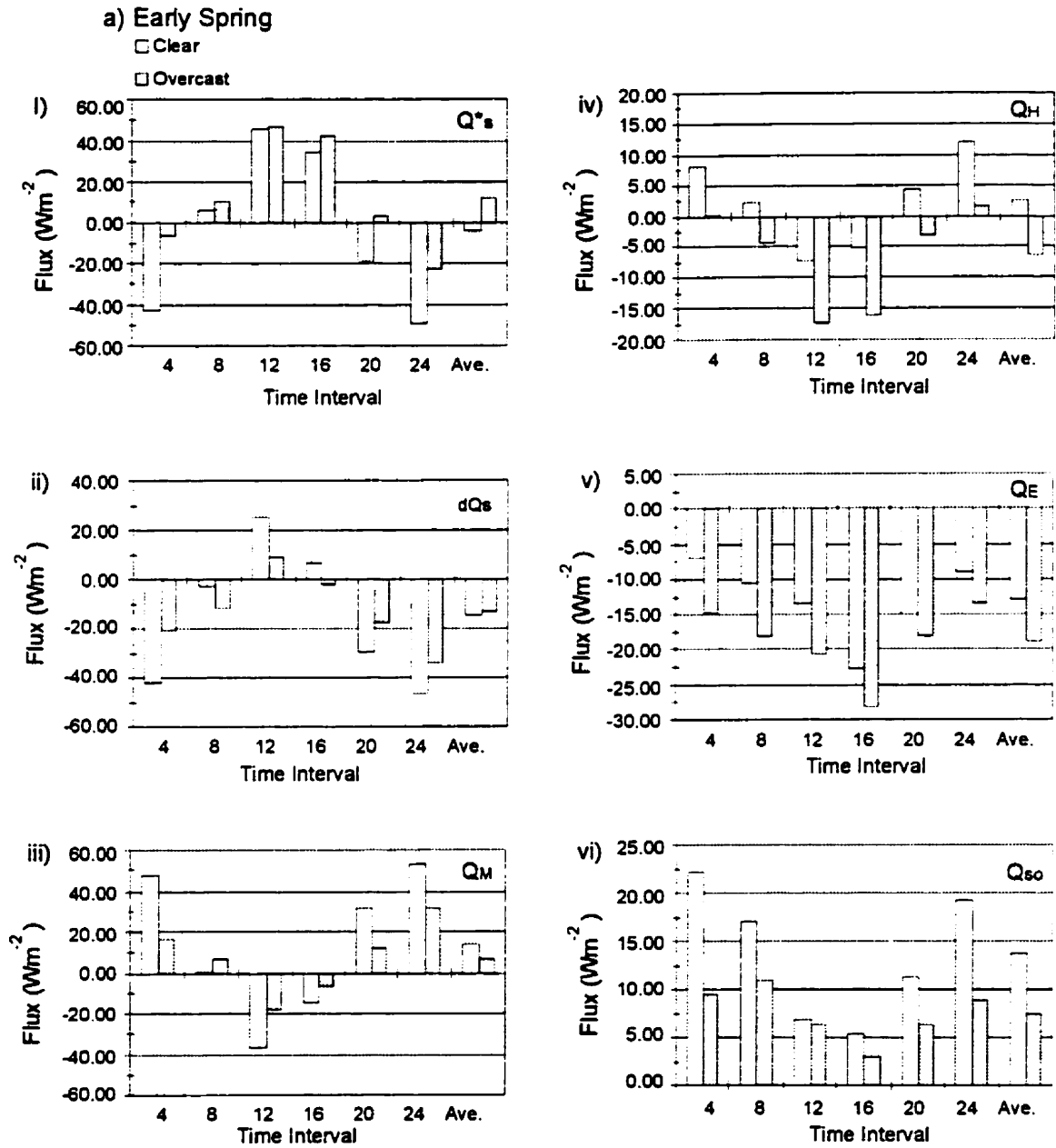


Figure 8.3a A contrast in the energy balance components from overcast (TCA>7) and predominately clear sky coverage (TCA<2) at FYI'92 and FYI'93 during the *early* spring.

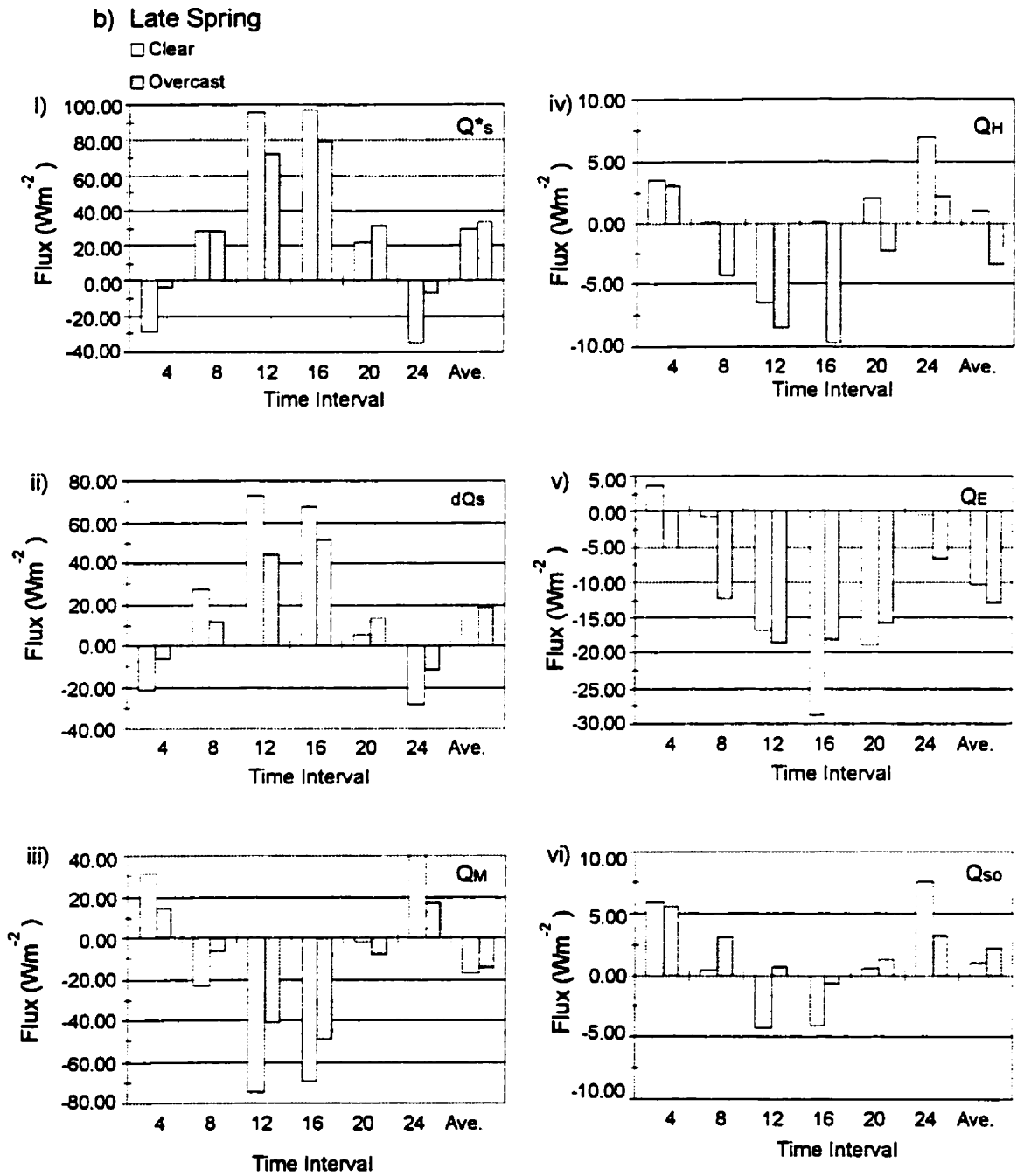


Figure 8.3b A contrast in the energy balance components from overcast ($TCA > 7$) and predominately clear sky coverage ($TCA < 2$) at FYI'92 and FYI'93 during the *late* spring.

- a tendency for weakened boundary layer stability near to the snow surface,
- a higher surface albedo,
- larger combined daily average turbulent heat loss,
- almost 50% less ice production within the snow volume,
- warmer snow surface and atmosphere,
- higher wind speed.

Net radiation is consistently higher, relative to clear-sky values over a 24 hour period, which indicates that the long-wave warming effect of clouds dominates throughout the day (Fig. 8.3a i). Only a marginal difference is observed in the daily average atmospheric heating of the snow volume (dQ_s , Fig. 8.3a ii), despite the large difference in radiative heating of the surface between the two sky regimes. The difference in radiative heating between the cloudy and clear sky regimes is offset by enhanced surface heat loss *via* turbulence to the lower atmosphere under overcast conditions (Fig. 8.3a iv and v). Maximum sensible heat loss by the surface under cloudy skies is coincident to maximum Q^* and maximum near surface atmospheric instability within the diurnal cycle (Table 8.1). The atmosphere is less stable throughout the diurnal cycle under overcast conditions and, as a result, the sensible heat flux is directed into the atmosphere over virtually the entire 24 hour period. An unstable atmosphere during the overcast regime may be the result of the combined effects of higher wind speed and long-wave heating of the surface, which accompany the overcast regime. Under clear skies, Q_H is only directed into the atmosphere during the period of maximum net radiation (e.g., between 8:00 and 16:00 LAT). The latent heat flux is highly negative throughout the 24 hour period during the cloudy regime, while under clear skies the latent heat loss may be a factor of 3 to 4 less at night than during the mid-day.

The daytime (i.e., 12:00 and 16:00 LAT averaging periods) heating of the snow volume by the atmosphere is greater during the clear-sky regime; however, large nighttime radiative heat loss by the snow cover acts to depress the daily heat totals relative to the overcast regime (Fig. 8.3a ii). Both cloud regimes show a diurnal cycle consisting of mid-day melt and nighttime ice production. Mid-day snow melt is a factor of two larger under clear skies relative to the cloudy sky regime (Fig. 8.3a iii), however, the rate of nighttime ice production is much lower under overcast conditions. Nighttime conduction through the snow to the surface partially offsets surface

radiative loss (Fig. 8.3a vi) and provides the impetus for ice production. The daily average ice production under overcast conditions is approximately one-half the rate computed for clear-skies, despite the small difference in the average heating of the snow volume between the two cloud regimes. A higher surface albedo during overcast conditions is attributed to the combination of the spectral thinning of the infrared wavelengths by the cloud cover and snowfall associated with frontal activity.

In the *late* spring, overcast periods are associated with:

- only marginally higher net radiation,
- only marginally higher conductive heating to the snow and sea ice surface,
- higher wind speed,
- a tendency for reduced atmospheric stability,
- a higher surface albedo,
- higher turbulent heat loss,
- approximately 17% lower heating of the snow volume,
- approximately 22% lower melt rate within the snow volume,
- warmer air temperature.

Within the diurnal cycle the net radiation is larger under overcast skies for all hours except the mid-day averaging periods (12:00 and 16:00 LAT in Fig. 8.3b i). The long-wave heating effect dominates over the short-wave cooling effect of clouds for the remaining two thirds of the 24-h cycle. The daily average heating rate of the snow cover by the atmosphere is virtually identical between cloud regimes, despite the larger net radiation under clear skies (Fig. 8.3b ii). A larger proportion of the available energy to the snow is lost to the atmosphere *via* turbulence under overcast conditions (Fig. 8.3b iv and v), thereby reducing the energy available to the snow volume for melt.

The surface temperature experiences larger diurnal amplitude and higher 24h maximum during the clear sky regime (Table 8.1). The combination of a high mid-day surface temperature (mid-day surface temperature approaches 0°C) and a large range in temperature at the snow surface raises the snow liquid water content and encourages morphological changes in the upper snow, including equilibrium crystal growth and grain clustering through freeze-thaw activity. The effect of these morphological changes is to lower snow albedo and raise the snow's transmissivity

to solar radiation. For these reasons, the frequency of clear-sky days in the *late* spring may be more effective at reducing surface albedo than the long-wave warming effect associated with cloud cover. Hence, the environmental conditions associated with cloud cover promote a more rapid ripening of the snow, but clear skies facilitate a more rapid removal of the snow after the onset of melt.

Table 8.1 Summary of energy balance components and environmental properties averaged over four hour intervals for periods of low cloud amount (TCA<3) and high cloud amount (TCA>7) in the a) *early* spring and b) *late* spring. Results are based on pooled FYT'92 and FYT'93 hourly data. Energy fluxes, temperatures, wind speed are reported in $W \cdot m^{-2}$, $^{\circ}C$ and $m \cdot s^{-1}$, while the albedo and stability parameter are dimensionless.

		Averaging Period						
Early	Var.	4.00	8.00	12.00	16.00	20.00	24.00	day
clear	Q^*_s	-43.38	5.46	45.98	34.39	-19.27	-49.69	-4.42
cloudy	Q^*_s	-6.38	10.32	47.00	41.78	3.18	-22.49	12.23
clear	K^*	2.86	53.03	103.55	99.74	43.38	2.72	50.88
cloudy	K^*	5.14	25.36	68.03	74.51	33.67	5.12	35.31
clear	L^*	-46.24	-47.50	-57.39	-65.16	-62.57	-52.40	-55.21
cloudy	L^*	-11.52	-14.94	-20.74	-32.42	-30.35	-27.61	-22.93
clear	Q_{io}	16.40	19.16	18.26	13.37	10.14	12.76	15.02
cloudy	Q_{io}	13.96	16.56	15.89	12.19	11.94	11.37	13.65
clear	Q_{so}	22.15	17.07	6.90	5.42	11.39	19.28	13.70
cloudy	Q_{so}	9.48	10.86	6.36	3.01	6.24	8.94	7.48
clear	dQ_s	-41.95	-2.83	25.37	6.39	-29.88	-46.73	-14.94
cloudy	dQ_s	-20.77	-12.01	8.98	-2.58	-18.09	-34.19	-13.11
clear	Q_M	47.69	0.74	-36.73	-14.34	31.13	53.25	13.63
cloudy	Q_M	16.29	6.30	-18.51	-6.60	12.38	31.76	6.94
clear	Q_H	8.29	2.16	-7.32	-5.17	4.32	11.94	2.37
cloudy	Q_H	0.21	-4.20	-17.32	-16.24	-3.07	1.76	-6.48
clear	Q_E	-6.85	-10.45	-13.29	-22.84	-14.94	-8.99	-12.89
cloudy	Q_E	-14.59	-18.13	-20.70	-28.13	-18.19	-13.46	-18.86
clear	T_a	-21.86	-21.54	-18.26	-16.70	-17.22	-19.45	-19.17
cloudy	T_a	-17.82	-17.25	-16.01	-14.51	-14.40	-15.43	-15.90
clear	u	2.78	2.98	3.94	4.82	4.25	3.77	3.76
cloudy	u	5.05	6.26	6.28	6.74	5.18	5.69	5.87
clear	T_s	-24.39	-22.78	-17.94	-16.11	-18.13	-21.88	-20.20
cloudy	T_s	-17.41	-17.80	-15.96	-14.28	-15.50	-18.08	-16.50
clear	α		0.76	0.78	0.80	0.82		0.79
cloudy	α		0.85	0.82	0.82	0.83		0.83
clear	ξ	0.82	0.46	0.31	0.11	0.16	0.67	0.42
cloudy	ξ	0.19	-0.02	-0.26	-0.16	0.06	0.22	0.01

Table 8.1 continued

b)

Late	Var.	Averaging Period						Day
		4.00	8.00	12.00	16.00	20.00	24.00	
clear	Q^*_S	-28.59	28.20	95.91	96.55	22.56	-34.65	30.00
cloudy	Q^*_S	-4.07	28.19	72.09	78.79	31.12	-6.61	33.25
clear	K^*	28.07	95.62	167.20	162.70	97.25	32.47	97.22
cloudy	K^*	12.60	44.92	97.65	106.89	56.95	16.18	55.87
clear	L^*	-54.33	-57.74	-59.63	-63.47	-65.00	-63.45	-60.60
cloudy	L^*	-16.41	-14.28	-22.73	-21.19	-23.79	-22.58	-20.17
clear	Q_{∞}	-3.62	-3.67	-2.06	-2.82	-3.75	-4.64	-3.43
cloudy	Q_{∞}	-2.44	-2.72	-2.94	-2.70	-3.54	-2.92	-2.88
clear	$Q_{S\infty}$	5.92	0.30	-4.25	-4.01	0.51	7.47	0.99
cloudy	$Q_{S\infty}$	5.53	3.01	0.74	-0.69	1.24	3.15	2.16
clear	dQ_S	-21.50	27.44	72.77	67.91	5.74	-28.14	20.70
cloudy	dQ_S	-6.09	11.60	44.88	51.12	12.98	-11.21	17.21
clear	Q_M	31.05	-23.48	-74.96	-69.10	-1.48	40.25	-16.29
cloudy	Q_M	14.07	-5.87	-41.21	-49.10	-8.20	17.28	-12.17
clear	Q_H	3.42	0.05	-6.42	0.10	2.00	6.93	1.01
cloudy	Q_H	3.01	-4.20	-8.54	-9.69	-2.35	2.15	-3.27
clear	Q_E	3.66	-0.81	-16.72	-28.75	-18.82	-0.42	-10.31
cloudy	Q_E	-5.04	-12.39	-18.67	-17.98	-15.79	-6.75	-12.77
clear	T_a	-4.61	-3.41	-0.90	-0.83	-1.61	-3.21	-2.43
cloudy	T_a	-4.82	-4.30	-3.50	-2.52	-2.87	-3.68	-3.61
clear	u	1.99	2.80	3.54	3.71	3.74	2.58	3.06
cloudy	u	4.25	4.39	4.49	4.46	4.42	4.15	4.36
clear	T_S	-6.45	-3.82	-1.01	-0.83	-2.47	-5.01	-3.26
cloudy	T_S	-4.99	-3.91	-2.58	-2.04	-2.90	-3.91	-3.39
clear	α		0.74	0.70	0.73	0.71		0.72
cloudy	α		0.80	0.78	0.77	0.78		0.78
clear	ξ	1.25	0.58	0.09	-0.02	0.13	1.02	0.51
cloudy	ξ	0.24	0.13	0.16	0.29	0.22	0.22	0.21

8.4 Statistical Analysis of the Relationship between Environmental and Energy Balance Variables

8.4.1 Principal Components Analysis of Energy Balance Components

The purpose of the PCA is two fold: firstly, to identify patterns within the energy budget variable set; secondly, to reduce the number of variables in subsequent analysis, while retaining the information provided by the original 7 or 8 energy budget variables (depending on whether Q_{so} is included or not in the *late* category). The original variables are organized into 7 or 8 principal components for each site and seasonal grouping (Table 8.2), of which the analysis has identified 2 or 3 weighted linear combinations of the original sets which capture much of the variance of the original variables. The first three principal components account for between 81% (*late* spring of 1992) and 93% (*early/transitional* spring of 1993) of the total variation in the variables sets. The component loadings for each principal component appear in Table 8.2 and the significant principal components are contrasted in Fig. 8.4 for FYI'92 and FYI'93. The principal components for the energy balance variable set are termed PCEB and numbered in sequence from 1 to m , where m is the number of variables in the correlation matrix.

A principal component is interpreted by the variables that are highly correlated to it (Tabachnick and Fidell, 1989) and the sign of the component loadings is determined by the correlation between the variables under study and the principal component. The sign of the loading is therefore dependent upon which variables are included in the data set. Variables with similar and large weights are highly correlated with each other and opposite signs mean a negative correlation.

Three patterns are significant in the *early* and *transitional* spring of 1992. The first pattern (i.e., PCEB1) is dominated by the long-wave exchange, conduction from below (Q_{so}) and influenced to a lesser extent by Q_H . It represents 45% of the total variation and is most heavily loaded by $L\uparrow$ ($r_{L\uparrow} = -0.97$), however, there is very little difference in the loadings of the top three contributing variables (i.e., $L\uparrow$, $L\downarrow$ and Q_{so} , refer to Fig. 8.4). The sign of the component loadings shows that the long-wave fluxes are diametrically opposed to the conductive flux. $K\uparrow$ makes a secondary contribution to the principal component. Incident radiation, $K\downarrow$ explains a very small proportion of the total variance (i.e., $r_{K\downarrow}^2 = 0.156$) of the component. The second pattern (i.e.,

PCEB2) describes the exchange of energy at the surface through net solar radiation ($K\uparrow$ and $K\downarrow$) and conduction at the snow surface (Q_{so}). In this instance, $K\downarrow$ has a slightly higher loading than $K\uparrow$. The third pattern (i.e., PCEB3) clearly describes Q_E .

The first principal component during the *late* spring of FYI'92 describes the solar radiation exchange and a pattern of surface or volume heating through down-welling long-wave radiation, sensible heat exchange and conductive heat flow. The component is most heavily influenced by the solar radiation fluxes. The influence of $K\downarrow$, $K\uparrow$ and Q_H are inverse to $L\downarrow$ and the conductive fluxes. PCEB2 describes the long-wave exchange and heat loss through conduction while PCEB3 describes the heat exchange with the atmosphere *via* turbulence.

The first principle component for the *early* and *transitional* spring of FYI'93 resembles PCEB1 from 1992. Common to each of the first principal components are loadings by the long-wave fluxes ($L\uparrow$ and $L\downarrow$), Q_{io} and Q_H . In 1993, however, Q_{so} also strongly contributes. $L\uparrow$ has the highest correlation to the principal component, but there is very little difference between the loadings for $L\uparrow$, Q_{so} and Q_{io} . The variable grouping for the second and third principal component also resemble the patterns identified during FYI'92 (refer to Fig. 8.4). The first principal component during the *late* spring of 1993 is strongly determined by $K\uparrow$, $L\downarrow$, and $L\uparrow$ (in decreasing order of influence). The conductive flux at the ice surface and $K\downarrow$ are also highly correlated to it. The influence of the long-wave and solar fluxes is opposite. The second principal component is heavily weighted by $K\downarrow$, which is correlated with a proportion of the sensible heat population. The third principal component represents the turbulent heat fluxes. Both Q_H and Q_E are similar in loading magnitude, but opposite in direction.

A) *Early and Transitional Spring*

B) *Late Spring*

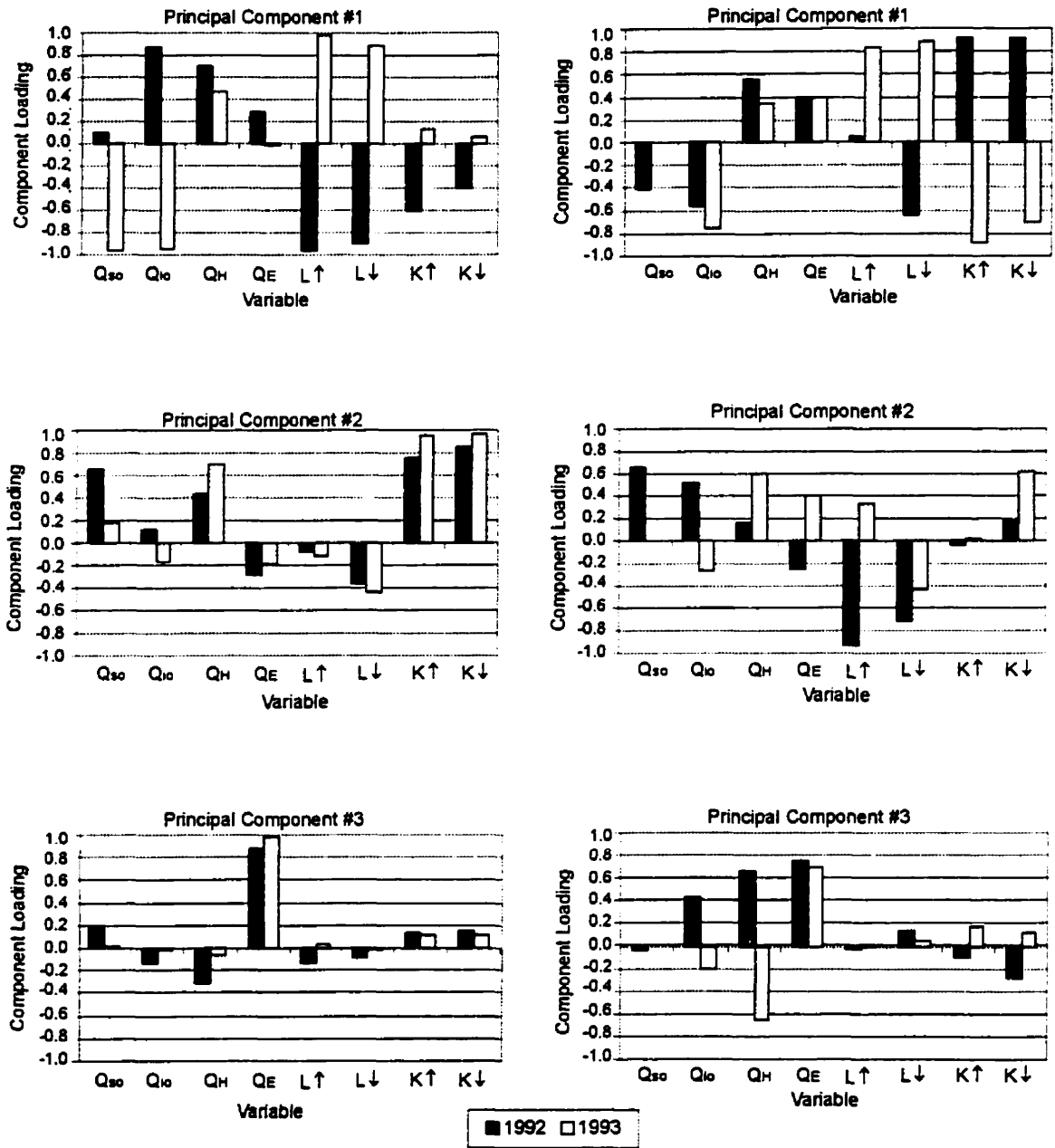


Figure 8.4 Principal component loadings for the significant principal components of the energy balance components at FYI'92 and FYI'93 during the (a) combined *early and transitional* spring and (b) the *late* spring.

Table 8.2 Summary of principal components analysis on energy balance components
a) FYT'92 *Early and Transitional Spring*.

Eigenvalues								
	1	2	3	4	5	6	7	8
	3.58	2.14	1	0.75	0.36	0.12	0.02	0.01

Component Loadings								
Variable	1	2	3	4	5	6	7	8
Q _{So}	0.098	0.645	0.195	-0.729	0.001	0.067	0.020	0.005
Q _{io}	0.869	0.113	-0.133	0.149	0.393	0.194	0.006	-0.001
Q _H	0.701	0.427	-0.314	0.164	-0.429	0.127	0.001	0.006
Q _E	0.283	-0.289	0.887	0.163	-0.116	0.098	0.001	0.004
L↑	-0.969	-0.089	-0.131	0.099	-0.006	0.115	0.112	0.019
L↓	-0.892	-0.363	-0.090	-0.126	-0.037	0.198	-0.090	0.005
K↑	-0.595	0.757	0.137	0.217	0.022	0.030	-0.005	-0.072
K↓	-0.396	0.857	0.152	0.267	0.086	-0.036	-0.035	0.062

Percent of Total Variance Explained								
	1	2	3	4	5	6	7	8
	44.78	26.78	12.60	9.39	4.52	1.53	0.28	0.19

Cumulative Percent of Total Variance by Component								
	1	2	3	4	5	6	7	8
	44.78	71.56	84.17	93.56	98.07	99.60	99.88	100

b) FYT'92 *Late Spring*

Eigenvalues								
	1	2	3	4	5	6	7	8
	3.04	2.20	1.27	0.58	0.41	0.39	0.08	0.02

Component Loadings								
Variable	1	2	3	4	5	6	7	8
Q _{So}	-0.408	0.645	-0.043	0.602	0.221	0.066	0.003	-0.004
Q _{io}	-0.564	0.517	0.417	-0.141	-0.249	0.393	0.064	0.008
Q _H	0.553	0.170	0.657	-0.193	0.439	0.064	0.001	0.006
Q _E	0.390	-0.252	0.747	0.325	-0.276	-0.210	0.010	0.004
L↑	0.053	-0.937	-0.034	0.164	0.101	0.238	0.149	-0.047
L↓	-0.647	-0.717	0.130	0.082	0.080	0.129	-0.112	0.091
K↑	0.912	-0.032	-0.102	0.124	-0.103	0.321	-0.166	-0.034
K↓	0.921	0.189	-0.280	0.085	-0.049	0.080	0.112	0.098

Percent of Total Variance Explained								
	1	2	3	4	5	6	7	8
	38.02	27.55	15.91	7.26	5.12	4.87	0.99	0.27

Cumulative Percent of Total Variance by Component								
	1	2	3	4	5	6	7	8
	38.02	65.58	81.49	88.75	93.87	98.74	99.73	100

c) FYI'93 *Early and Transitional Spring*

Eigenvalues								
	1	2	3	4	5	6	7	8
	3.82	2.65	0.99	0.39	0.09	0.03	0.01	0.00

Component Loadings								
Variable	1	2	3	4	5	6	7	8
Q _{So}	-0.973	0.186	0.021	-0.036	0.011	0.119	-0.053	0.019
Q _{io}	-0.952	-0.171	-0.011	-0.094	0.229	-0.050	0.027	0.004
Q _H	0.460	0.703	-0.058	-0.538	0.016	0.019	0.009	-0.002
Q _E	-0.012	-0.187	0.979	-0.079	-0.010	0.001	0.003	-0.002
L _↑	0.984	-0.123	0.036	0.017	0.093	-0.047	-0.049	0.037
L _↓	0.876	-0.440	-0.012	0.071	0.139	0.118	0.015	-0.017
K _↑	0.141	0.953	0.113	0.230	0.015	0.019	0.009	-0.002
K _↓	0.067	0.970	0.113	0.174	0.085	-0.031	-0.049	-0.030

Percent of Total Variance Explained							
1	2	3	4	5	6	7	8
47.81	33.16	12.37	4.92	1.10	0.44	0.15	0.05

Cumulative Percent of Total Variance by Component							
1	2	3	4	5	6	7	8
47.81	80.97	93.33	98.26	99.36	99.80	99.95	100

d) FYI'93 *Late Spring*

Eigenvalues							
	1	2	3	4	5	6	7
	3.59	1.28	1.00	0.59	0.28	0.22	0.03

Component Loadings							
Variable	1	2	3	4	5	6	7
Q _{io}	-0.756	-0.267	-0.199	-0.472	0.259	-0.165	0.008
Q _H	0.340	0.605	-0.656	-0.240	0.001	0.172	0.025
Q _E	0.393	0.402	0.697	-0.441	0.001	0.062	0.002
L _↑	0.836	0.332	0.003	0.212	0.255	-0.130	-0.061
L _↓	0.878	-0.428	0.039	0.022	0.146	0.064	0.133
K _↑	-0.880	0.024	0.173	0.168	0.253	0.321	-0.004
K _↓	-0.713	0.625	0.120	0.210	0.011	-0.177	0.102

Percent of Total Variance Explained						
1	2	3	4	5	6	7
51.36	18.35	14.30	8.46	3.97	3.09	0.47

Cumulative Percent of Total Variance by Component						
1	2	3	4	5	6	7
51.36	69.70	84.01	92.47	96.44	99.53	100.00

e) FYT'95 *Early and Transitional Spring*

Eigenvalues							
1	2	3	4	5	6	7	8
3.65	1.91	1.19	0.63	0.33	0.23	0.04	0.01

Component Loadings								
Variable	1	2	3	4	5	6	7	8
Q _{So}	-0.351	0.725	-0.303	-0.421	0.277	-0.051	0.052	0.015
Q _{io}	-0.877	0.177	-0.183	0.176	-0.166	0.318	0.076	0.016
Q _H	-0.513	0.073	0.739	0.252	0.343	0.057	0.002	0.001
Q _E	0.454	0.350	-0.584	0.539	0.194	-0.005	-0.028	-0.002
L↑	0.942	-0.238	0.128	0.106	0.025	-0.067	0.149	0.032
L↓	0.670	-0.567	-0.156	-0.240	0.226	0.310	-0.032	0.005
K↑	0.724	0.626	0.233	-0.047	-0.068	0.127	0.032	-0.074
K↓	0.652	0.673	0.296	-0.022	-0.131	0.086	-0.067	0.065

Percent of Total Variance Explained							
45.60	23.85	14.96	7.92	4.16	2.89	0.47	0.14

Cumulative Percent of Total Variance by Component							
45.60	69.45	84.41	92.33	96.49	99.39	99.86	100

f) FYT'95 *Late Spring*

Eigenvalues						
1	2	3	4	5	6	7
3.63	2.05	0.83	0.29	0.17	0.03	0.01

Component Loadings							
Variable	1	2	3	4	5	6	7
Q _{io}	-0.024	0.898	-0.41	0.11	0.103	0.043	0.037
Q _H	0.833	0.348	0.203	0.369	-0.016	-0.082	-0.01
Q _E	0.246	0.766	0.53	-0.213	-0.164	0.013	0.014
L↑	-0.872	-0.261	0.211	0.301	-0.177	0.07	0.017
L↓	-0.817	0.092	0.488	0.025	0.289	-0.023	0.006
K↑	0.733	-0.667	0.108	-0.029	0.029	-0.026	0.058
K↓	0.952	-0.127	0.205	0.054	0.122	0.133	-0.017

Percent of Total Variance Explained						
51.83	29.29	11.81	4.12	2.41	0.46	0.08

Cumulative Percent of Total Variance by Component						
51.83	81.12	92.93	97.05	99.46	99.92	100

8.4.2 Canonical Correlation between Environmental and Energy Balance Variables

The association, or linkage, between variable sets (environmental and energy balance) is examined using canonical correlation between the significant principal components from the energy balance data set, which serve as the dependent variables, and the original environmental variables (i.e., the independent variables). The variables that constitute the environmental variable set are listed in Section 8.2. The air and surface temperature should be highly correlated, as should the number of hours of bright sunshine and total cloud amount. The Pearson's correlation between T_s and T_a is greater than 0.95 throughout the seasonal episodes of 1992 and 1993. The correlation between sunshine hours and total cloud amount ranges between -0.89 and -0.96 in 1992 and around -0.75 in 1993. Therefore, including T_s and TCA into the analysis is redundant and weakens the test, through loss of degrees of freedom, and through the potential for multicollinearity among the independent variables. The surface albedo is sensitive to the quality of incident solar radiation and to the physical properties of the snow cover and therefore provides a measure of surface morphology.

A Pearson's correlation coefficient is computed between the pair of canonical variates from each variable set to determine the direction of the linear association. This information allows us to identify the direction of the relationships between the parameters of the original environmental variables and those heavily loaded principal components that represent the energy budget variable set. A negative association involving either the conductive or turbulent fluxes may infer an increase in surface heat loss or a decrease in surface heating (and *vice versa* for positive associations). The average direction/magnitude of the fluxes over the season is reviewed in the discussion surrounding Figs. 6.27 and 6.28. We can identify the direction and infer the strength of the relationship between the original energy budget and environmental variables using the component loadings of Table 8.2. The analysis will identify association, but the linkage is not necessarily causal. Independent variables may respond in like fashion to external forcing.

The correlation coefficients and canonical loadings for significant variate pairs of the analysis are shaded in Table 8.3. Significance of the canonical correlation between variate pairs is assessed by comparing the computed χ^2 statistic against tabulated values at a 95% level of confidence (0.05 level of significance). The loading of the original energy budget variables onto the principal component is termed *component loading* (r_{cL}), while the loading of a variable or

principal component onto a canonical variate is referred to as *canonical loading* (r_{ccl}). The canonical correlation (r_c) and Pearson's correlation (r_p) are identified as such. The principal components are identified as PCEB (1 to p) for the first p significant principal components from the energy budget sets respectively (refer to Table 8.2). The variables are listed in order of decreasing influence on the principal component. The canonical variates are sequentially termed CCEB (1 to k) and CCEN (1 to p) for the energy budget and environmental variables sets, respectively.

To avoid misinterpretation of the analysis, only those principal components with large canonical loadings (i.e., ≥ 0.40) are considered. This cut-off is arbitrary, but the intent of the analysis is to identify the strongest and, therefore, the most frequently occurring process linkages. A principal component with a canonical loading of greater than 0.40 explains greater than 16% of the variation contained by the canonical variate. The cut-off for the environmental variables within a canonical variate may be slightly lower and still considered noteworthy. This is simply because the environmental variables are either measured terms, or terms derived directly from measurements, and not weighted composites of other terms. An environmental variable with a canonical loading greater than (or less than) ± 0.30 explains close to (or over) 10% of the total variance contained by the variate. Most texts suggest that a loading of less than ± 0.30 have little interpretative value (e.g., Tabachnick and Fidell, 1989).

Table 8.3 Summary of canonical correlation analysis.
A) 1992 *Early and Transitional Spring*

Chi-Square Results		
Variate Pair	χ^2	DF
1	48.074	18
2	24.959	10
3	4.635	4

Canonical Loadings				
Loading Variables on PCEB	Energy Budget Principal Component	1	2	3
-L↑, -L↓, Q _{io} , Q _H , -K↑	PCEB1	0.935	-0.242	0.261
K↓, K↑, Q _{so} , Q _H , -L↓	PCEB2	0.378	0.383	-0.843
Q _E	PCEB3	0.136	0.946	0.293
Environmental Variable				
	T _a	-0.932	-0.156	0.321
	VPD	-0.214	0.548	0.009
	u	0.038	0.692	-0.288
	α	-0.790	-0.003	-0.100
	ξ	0.536	-0.182	-0.213
	sh	0.865	-0.039	0.442
Statistic				
	r _c	0.995	0.991	0.777
	r _p	0.995	-0.991	-0.777
	r _d	0.425	0.137	0.044

B) 1992 *Late Spring*

Chi-Square Results		
Variate Pair	χ^2	DF
1	43.893	18
2	20.970	10
3	5.425	4

Canonical Loadings				
Loading Variables on PCEB	Energy Budget Principal Component	1	2	3
K↓, K↑, -L↓, -Q _{io} , Q _H , Q _{so} , Q _E	PCEB1	0.240	-0.337	0.911
-L↑, -L↓, Q _{so} , Q _{io}	PCEB2	0.882	0.471	-0.004
Q _E , Q _H , Q _{io}	PCEB3	-0.484	0.745	0.459
Environmental Variable				
	T _a	0.838	0.469	-0.185
	VPD	-0.161	-0.230	0.114
	u	-0.356	0.143	0.291
	α	0.849	-0.286	0.056
	ξ	-0.044	-0.729	-0.392
	sh	-0.624	0.383	-0.629
Statistic				
	r _c	0.928	0.870	0.624
	r _p	-0.928	-0.870	-0.624
	r _d	0.328	0.176	0.114

C) 1993 *Early and Transitional Spring*

Chi-Square Results

Variate Pair	χ^2	DF
1	93.850	18
2	47.615	10
3	18.671	4

Canonical Loadings

Loading Variables on PCEB	Energy Budget Principal Component	1	2	3
$L\uparrow, -Q_{io}, -Q_{so}, L\downarrow, Q_H$	PCEB1	0.914	0.404	-0.046
$K\downarrow, K\uparrow, Q_H, L\downarrow$	PCEB2	-0.320	0.785	0.531
Q_E	PCEB3	0.251	-0.470	0.846
	Environmental Variable			
	T_a	-0.947	0.314	0.038
	VPD	-0.416	0.534	-0.224
	u	-0.059	0.774	0.542
	α	-0.760	-0.333	0.350
	ξ	0.160	-0.544	-0.586
	sh	0.612	0.351	-0.598
	Statistic			
	r_c	0.997	0.980	0.935
	r_p	-0.997	0.980	-0.935
	r_d	0.450	0.232	0.095

D) 1993 *Late Spring*

Chi-Square Results

Variate Pair	χ^2	DF
1	112.863	18
2	59.205	10
3	19.700	4

Canonical Loadings

Loading Variables on PCEB	Energy Budget Principal Component	1	2	3
$-K\uparrow, L\downarrow, L\uparrow, -Q_{io}, -K\downarrow, Q_E, Q_H$	PCEB1	-0.993	0.114	0.043
$K\downarrow, Q_H, -L\downarrow, Q_E, L\uparrow$	PCEB2	0.112	0.993	-0.042
$Q_E, -Q_H$	PCEB3	0.047	0.037	0.998
	Environmental Variable			
	T_a	-0.700	-0.618	-0.183
	VPD	0.48	-0.280	-0.633
	u	-0.457	0.151	-0.515
	α	0.230	0.745	0.071
	ξ	0.245	-0.311	0.302
	sh	0.787	-0.607	0.045
	Statistic			
	r_c	0.960	0.921	0.780
	r_p	0.960	-0.921	0.780
	r_d	0.255	0.213	0.081

8.4.2.1 Spring of 1992

Two canonical pairs are significant at a 95% level of confidence in the *early* and *transitional* spring of 1992. The Pearson's correlation coefficients indicate that the first canonical relationship is positive, while the second is negative (Table 8.3).

The environmental variate (CCEN1) is heavily influenced by T_a , sh, α , and ξ . Air temperature and α are correlated and inversely related to both sh and ξ , which are also weakly associated with one another. The lone energy budget principal component that significantly contributes to CCEB1 is PCEB1. The relationship between the environmental and energy budget variables are schematically represented as:

$$\begin{array}{l} L \uparrow - \\ L \downarrow - \\ Q_{io} + \\ Q_H + \\ K \uparrow - \end{array} \left| \begin{array}{l} \\ \\ PCEB1 + CCEB1 + CCEN1 \\ \\ \end{array} \right. \begin{array}{l} -T_a \\ +sh \\ -\alpha \\ +\xi \end{array} .$$

In this example (and others to follow), the direction of the loadings (both the component loading of the original variable on the principal component and canonical loading of the variables onto the canonical variates) and correlation is described by either + or -. The relative strength of the association between the original elements is gauged by the strength of

- the canonical correlation between canonical variates (refer to Table 8.3);
- the canonical loading between a significant energy budget principal component and the canonical variate (refer to Table 8.3);
- the component loading between the original energy budget variable and the significant PCEB (refer to Table 8.2).

In the schematic, the original environmental and energy balance variables are listed in order (top to bottom) of decreasing association with either the canonical variate (as is the case with the environmental variables) or with the energy balance principal components (as is the case with the energy fluxes).

An increase in CCEN1 (i.e., an increase in sunshine hours and atmospheric stability with a corresponding decrease in air temperature and albedo) encourages an increase in PCEB1. In terms of the original variables, this entails a decrease in the elements of the long-wave exchange, an increase in conductive heating to the snow volume and either an increase in sensible heating to the

surface, or a decrease in sensible heat loss by the surface to the atmosphere. $K\uparrow$ also decreases. Each relationship is physically sound. Sunshine hours rise with declining cloud coverage and it has already been established that there is a tendency for air temperature, albedo and the long-wave fluxes to increase with increasing cloud coverage (refer to the discussion surrounding Table 8.1). Increasing atmospheric stability appears to be associated with a clearing sky, which in turn depresses any sensible heat loss at the surface. $K\uparrow$ declines with a lowering of albedo. This is the first indication of the presence of an albedo feedback mechanism. An increase in PCEB1 is strongly associated with declining Q^* and Q_M (Fig. 8.5a). The latter indicates a reduction in ice production within the snow volume. Net radiation declines in association with decreasing $L\downarrow$ and $L\uparrow$, but the rate of ice production and the radiative deficit is partially offset by the combination of heat input at the ice surface from conductive heat flow and sensible heating from the atmosphere (or at least reduced sensible heat loss). It appears that the energy of fusion is more closely aligned with conductive heat flow than with Q^* at this time. The converse of this pattern relates decreasing sunshine hours and increasing air temperature and albedo to increasing elements of the long-wave exchange, a decline in conductive heating and an increase in $K\uparrow$.

The environmental parameters, u and VPD, form the second environmental canonical variate (CCEN2) and are inversely related to an energy budget variate that is loaded heavily by the principal component, PCEB3. The principal component, PCEB3, is itself highly correlated with Q_E ($r_{cL}=0.887$). The sign of the canonical correlation and the component loading indicate that elements of VPD and u are themselves correlated, and an increase in both is associated with a decrease in Q_E (i.e., elevated surface latent heat losses):

$$Q_E + |PCEB3 + CCEB1 - CCEN1| \begin{matrix} +u \\ +VPD \end{matrix}$$

An elevated Q_E loss is associated (through PCEB3) with large isolated periods of ice production, although no conclusive trend with Q_M exists (Fig. 8.5a). PCEB3 also appears independent of Q^* .

In summary, the first canonical pair describes the heating of the snow volume by conduction and sensible heat under clearing skies, increasing stability and declining air temperature. The process is independent of Q^*_s and is accompanied by reduced ice production within the snow cover. The second strongest pattern describes the cooling of the surface through an upward vapor flux and this process is also independent of Q^* . The processes are driven by the

energy and vapour content of the atmosphere, and the energy content of the underlying sea ice, and related to the boundary layer temperature structure. They are not directly related to the solar radiation exchange.

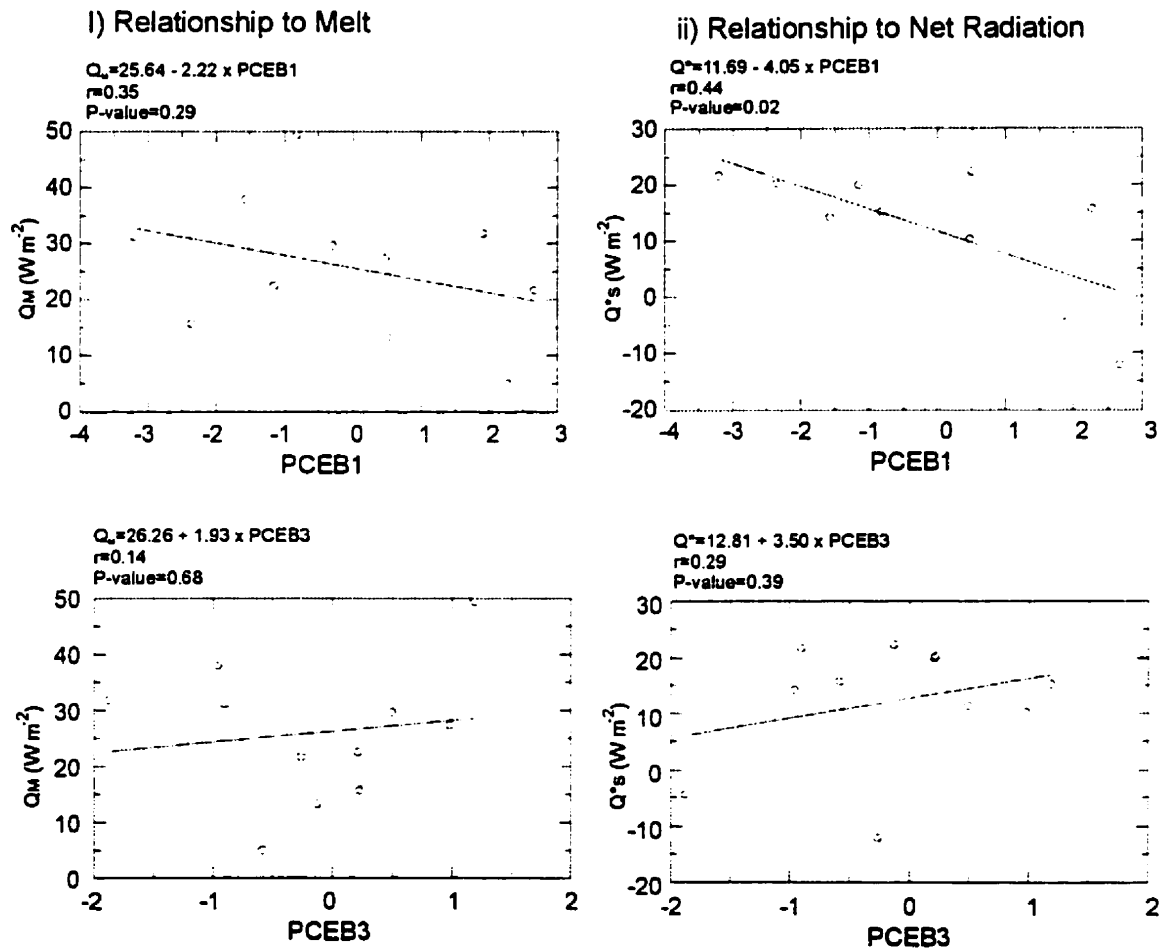


Figure 8.5a Bivariate relationship between the significant energy balance principal components and (i) melt energy and (ii) net radiation during the early and transitional spring, FYI '92.

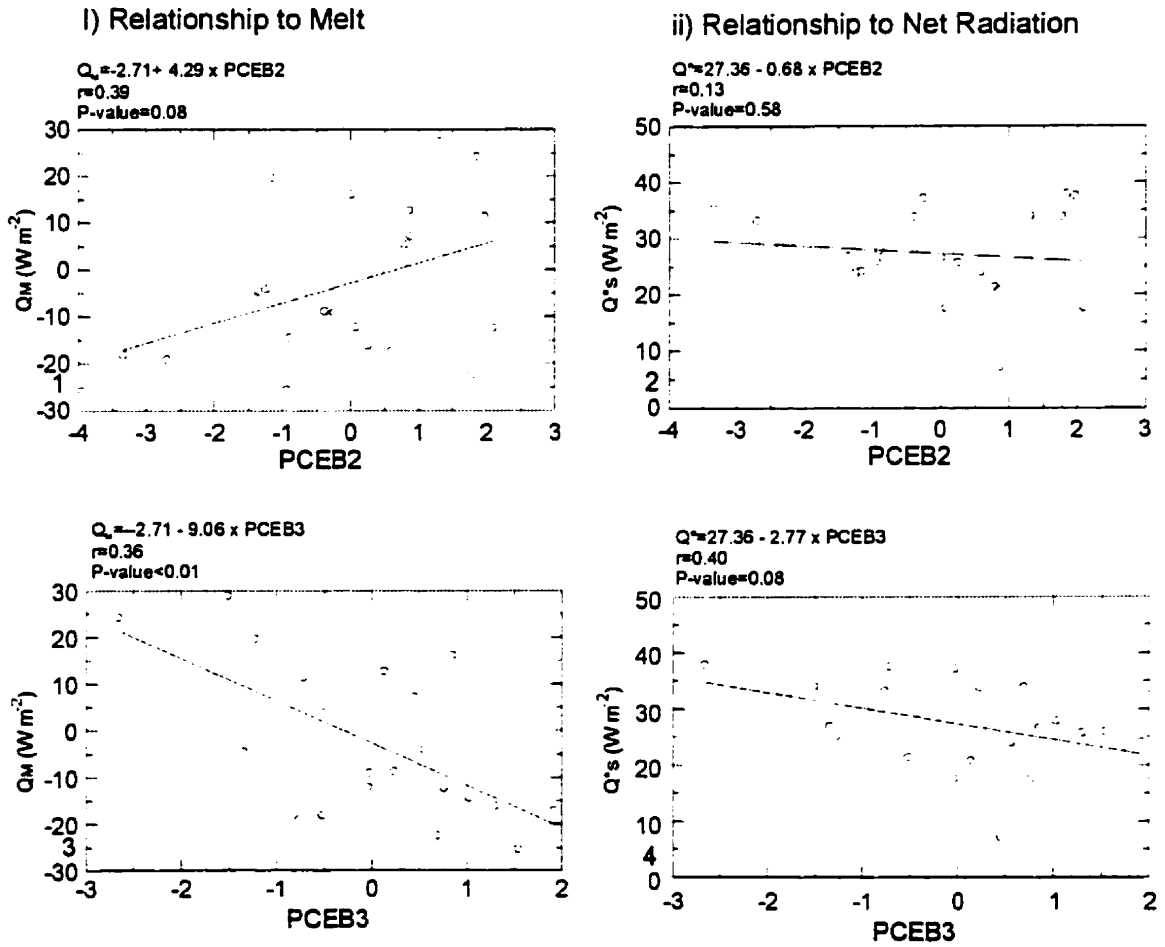


Figure 8.5b Bivariate relationship between the significant energy balance principal components and (i) melt energy and (ii) net radiation during the *late* spring, FYI'92.

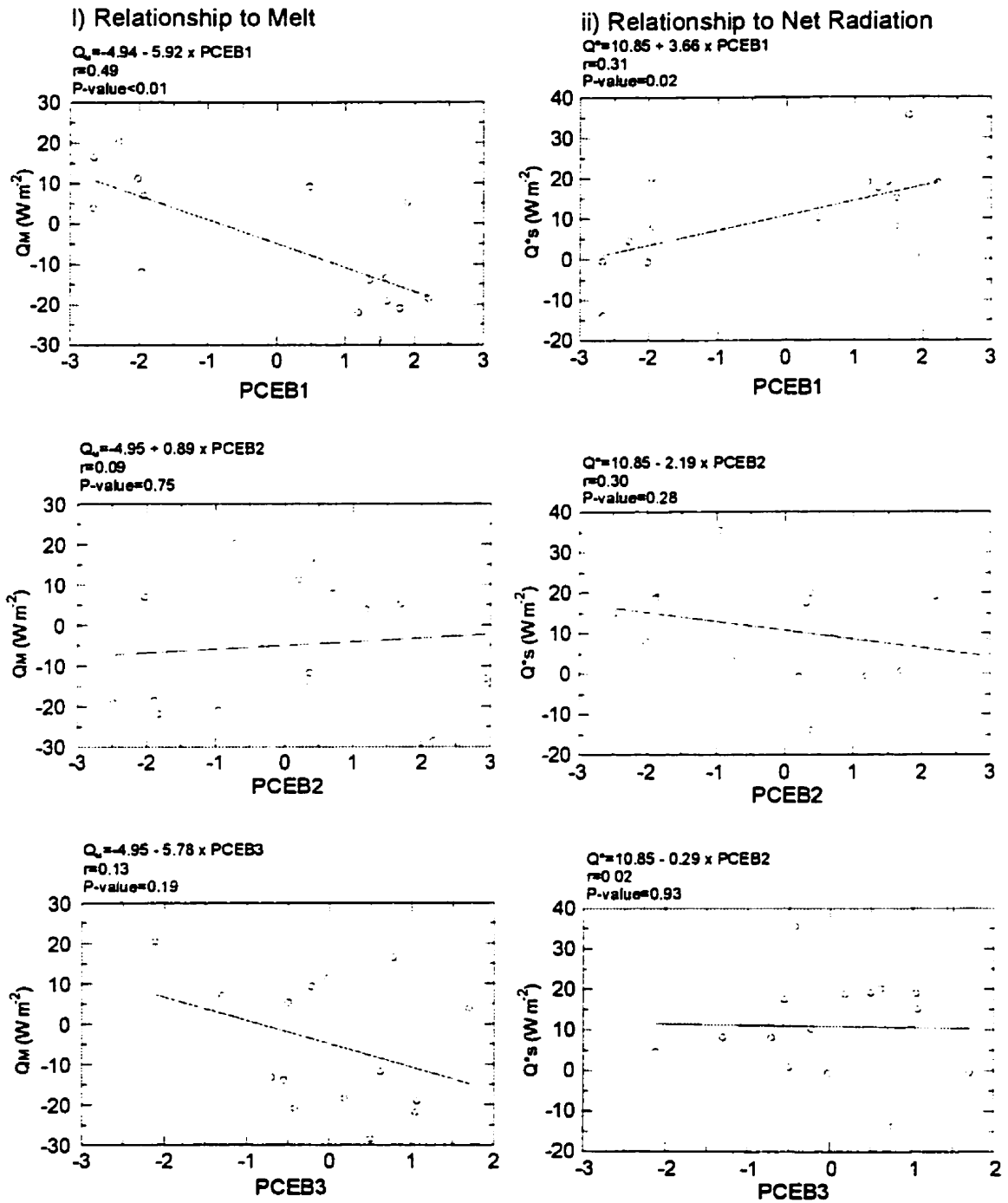


Figure 8.5c Bivariate relationship between the significant energy balance principal components and (i) melt energy and (ii) net radiation during the *early* and *transitional* spring, FY1'93.

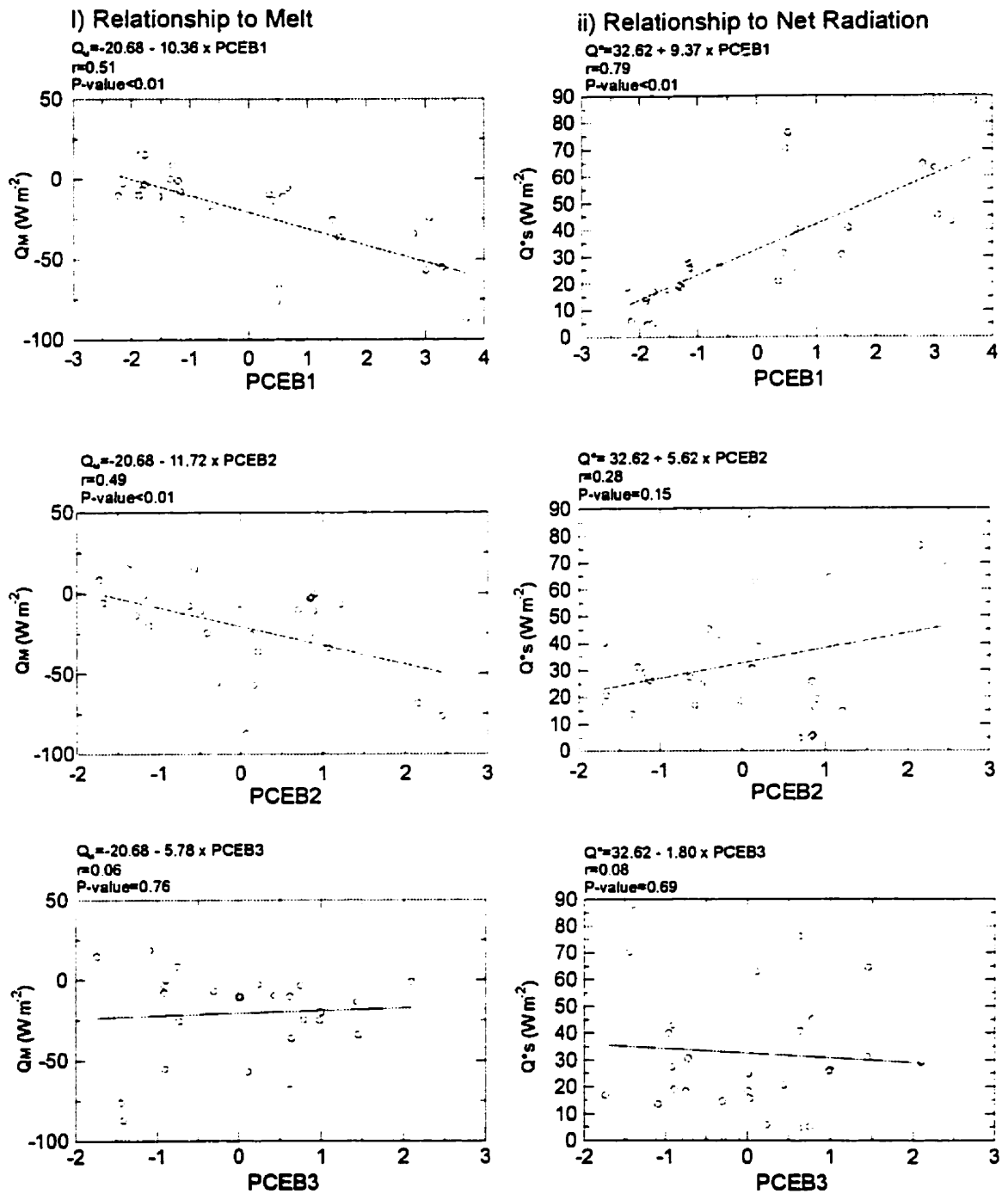


Figure 8.5d Bivariate relationship between the significant energy balance principal components and (i) melt energy and (ii) net radiation during the *late* spring, FYI'93.

Two of the three canonical correlations are significant in the *late* spring of 1992. Both canonical correlation coefficients are smaller than observed during the *early* and *transitional* spring (i.e., $r_{ccL}=0.928$ and 0.870) and Pearson's correlations between both pairs of canonical variates are negative. A complicated pattern of process linkages is identified within the first canonical pair (see below):

$$\begin{array}{c}
 L \uparrow - \\
 L \downarrow - \\
 Q_{so} + \\
 Q_{io} + \\
 Q_E + \\
 Q_H + \\
 Q_{io} +
 \end{array}
 \left| \begin{array}{c}
 \\
 PCEB2 + \\
 \\
 \\
 PCEB3 - \\
 \\
 \end{array} \right|
 \begin{array}{c}
 \\
 \\
 CCEB1 - CCEN1 \\
 \\
 \\
 \end{array}
 \left| \begin{array}{c}
 +\alpha \\
 +T_a \\
 -sh \\
 -u
 \end{array} \right.$$

The first and strongest process linkage relates the canonical variate (CCEN1) loaded by α , T_a , and sh with PCEB2 ($r_{ccL}=0.882$) while a secondary (and weaker) pattern relates CCEN1 with PCEB3 ($r_{ccL}=-0.484$). Recall that PCEB2 contains the long-wave budget and surface or volume cooling through conduction. PCEB3 predominately describes the turbulent heat exchange. An increase in the environmental variate (CCEN1) is associated with increasing temperature and albedo and decreasing sunshine hours (i.e., increasing cloud coverage). There is a tendency for wind speed to also decline. The environmental variate is inversely related to CCEB1 and, therefore, a rise in CCEN1 encourages a reduction in the processes described by CCEB1 (decreasing PCEB2 and increasing PCEB3). The mechanisms responsible for raising air temperature and albedo, while decreasing sunshine hours, act to increase the elements of the long-wave exchange and decrease conductive heating to the snow and ice surface. A reduction in PCEB2 is associated with reduced Q_M (increasing snow melt) and appears independent of Q^* (Fig. 8.5b). An increase in PCEB3 supports increased melt within the snow cover (Fig. 8.5b). Net radiation on the other hand should drop. The pattern associated with PCEB3 involves an increase in turbulent heating to the surface (or a reduction in turbulent heat loss) and an increase in Q_{io} with rising CCEN1. Q_{io} is associated with both PCEB2 and PCEB3. The sign of the association to CCEB1 within each principal component differs. A reduction in Q_{io} is more apt to occur in

association with an increase in CCEN1 because Q_{io} is more closely associated with PCEB2 ($r_{cL}=0.517$) than with PCEB3 ($r_{cL}=0.417$), and the canonical loading of PCEB2 is larger ($r_{cL}=0.882$) than the canonical loading of PCEB3 ($r_{cL}=-0.484$). The converse of this pattern relates increasing PCEB3 with increased ice production within the snow cover. That is, decreasing long-wave fluxes and increasing conductive heat flow to the surface, in association with a drop in air temperature and a rise in sunshine hours. Both features are associated with clearing skies.

The second canonical correlation relates a canonical variate loaded heavily by PCEB3 with the environmental variate loaded primarily by ξ , with secondary contributions by T_a and sh . PCEB2 also contributes to CCEB2, albeit to a lesser extent than PCEB3, as shown by:

$$\begin{array}{c}
 Q_E + \\
 Q_H + \\
 Q_{io} + \\
 L \uparrow - \\
 L \downarrow - \\
 Q_{so} + \\
 Q_{io} +
 \end{array}
 \left|
 \begin{array}{c}
 \\
 PCEB3 + \\
 \\
 \\
 PCEB2 + \\
 \\
 \\
 \end{array}
 \right.
 \begin{array}{c}
 \\
 \\
 CCEB2 - CCEN2 \\
 \\
 \\
 \\
 \end{array}
 \left|
 \begin{array}{c}
 -\xi \\
 +T_a \\
 +sh
 \end{array}
 \right.
 .$$

In the pattern defined by CCEN2, a rise in air temperature is associated with increasing sunshine hours (i.e., a clearing sky) and supports an unstable atmosphere, or at least a decline in atmospheric stability. Pearson's correlation between the canonical variates is negative and therefore, a rise in CCEN2 affects a drop in both PCEB3 and PCEB2. This results in enhanced Q_E and Q_H losses by the surface, increased $L \uparrow$ and $L \downarrow$ and decreased conductive heating to the snow and ice surfaces. Decreasing PCEB3 acts to reduce melt, but encourage ice production. However, a lowering of PCEB2 encourages melt within the snow. These patterns contradict one-another. The process described by PCEB3 is more strongly loaded onto CCEB2 ($r_{cL}=0.74$ versus 0.471 for PCEB2) and is, therefore, the more frequent response to a rise in CCEB2. The converse of this pattern relates increasing atmospheric stability, with decreasing T_a and hours of bright sunshine, to a rise in turbulent heat fluxes (an increase in PCEB3). PCEB3 is associated with increasing melt rate (Fig. 8.5b). This pattern is likely to occur under increasing cloud cover.

By way of review, an increase in Q^* and melt rate during the *late* spring of 1992 is associated with:

1. increasing air temperature and decreasing sunshine hour totals through a long-wave warming effect,
2. a reduction in the turbulent heat loss at the surface in conjunction with decreasing wind speed and rising air temperature, both under increasingly overcast skies,
3. a reduction in turbulent heat transfer to the atmosphere in conjunction with increased atmospheric stability and decreasing air temperature, again under increasingly overcast skies,
4. a long-wave warming effect associated with increasing air temperature under clearing skies.

Melt under clearing skies is infrequent and is isolated to periods described by point number four above. The warming effect of clouds, presumably associated with the influx of warm maritime air, is most effective at promoting and maintaining snow melt in 1992.

8.4.2.2 Spring of 1993

Three canonical correlations are significant during the *early* and *transitional* spring of 1993. Canonical correlations range from 0.99 for the first canonical pair to 0.93 for the third canonical pair. Pearson's correlation between the first and third canonical pairs is negative, while the correlation between the second pair is positive.

The first canonical correlation measures the linear association between the linear combination of T_a , α , sh , and VPD (CCEN1) and a canonical variate loaded heavily by PCEB1:

$$\begin{array}{l}
 L \uparrow + \\
 Q_{10} - \\
 Q_{s0} - \\
 L \downarrow + \\
 Q_H +
 \end{array}
 \left|
 \begin{array}{l}
 \\
 \\
 PCEB1 + CCEB1 - CCEN1 \\
 \\
 \\
 \end{array}
 \right.
 \left|
 \begin{array}{l}
 -T_a \\
 -\alpha \\
 +sh \\
 -VPD
 \end{array}
 \right.
 .$$

The signs of the correlation and loadings support the inference that increasing CCEN1 is associated with decreasing air temperature, albedo, VPD and increasing sunshine hours (i.e., a clearing sky), which collectively act to decrease PCEB1. Declining PCEB1 is associated with: a reduction in long-wave emission by the surface and sky, increased conductive heat to the snow and ice surfaces, and increased sensible heat loss by the surface, or a reduction in sensible heating to the surface. Decreasing PCEB1 results in increased Q_M (ice production) and a lowering in Q^*

(Fig. 8.5 c). The converse of this pattern shows that increasing melt and Q^* (rising PCEB1) is related to increasing air temperature under increasingly overcast skies. These features act to enhance the long-wave warming of the surface and to increase the sensible heat transfer to the surface.

The second canonical correlation relates the linear combination of each of the environmental variables ($u, \xi, VPD, sh, \alpha, T_a$) to a linear combination of the principal components PCEB2 ($r_{ccL}=0.785$), PCEB3 ($r_{ccL}=-0.47$) and PCEB1 ($r_{ccL}=0.404$) (in decreasing order of influence):

$$\begin{array}{l}
 K \downarrow + \\
 K \uparrow + \\
 Q_H + \\
 L \downarrow - \\
 \\
 Q_E + \\
 L \uparrow + \\
 Q_{io} - \\
 Q_{so} - \\
 L \downarrow + \\
 Q_H +
 \end{array}
 \left|
 \begin{array}{l}
 PCEB2 + \\
 \\
 PCEB3 - \\
 \\
 PCEB1 +
 \end{array}
 \right.
 \begin{array}{l}
 CCEB2 + CCEN2
 \end{array}
 \left.
 \begin{array}{l}
 +u \\
 -\xi \\
 +VPD \\
 +sh \\
 -\alpha \\
 +T_a
 \end{array}
 \right.$$

The canonical loadings of PCEB3 and PCEB1 are similar, but opposite. A rise in CCEN2 is associated with an increase in wind speed and is accompanied by a decrease in atmospheric stability and rise in VPD. There is also a tendency for sunshine hours to rise, albedo to drop, and air temperature to increase. These associations are most likely to occur under clearing skies. Rising CCEN2 is associated with increasing CCEB2, which is associated with an increase in PCEB2 and PCEB1 and a decrease in PCEB3. In terms of the original variables, $K \downarrow$, $K \uparrow$, Q_H , and $L \uparrow$ are expected to increase, while Q_E , Q_{io} and Q_{so} will drop with increasing CCEN2. The pattern shows $L \downarrow$ to decrease, through its association with PCEB2, and to increase, through its association with PCEB1. The strongest linkages, however, indicate that $L \downarrow$ will most often decrease with increasing CCEN2. The relationship among the environmental variables does suggest clear, or

through rising atmospheric stability and declining wind speed. Both are associated with clearing sky conditions.

By way of review, an increase in Q^* and melt rate during the *early* and *transitional* spring of 1993 is associated with:

1. enhanced long-wave warming and increased Q_H to the surface, in conjunction with increasing air temperature and increasingly overcast skies,
2. increasing Q_E (or dampened Q_E loss) in conjunction with decreasing wind speed and VPD and increasing ξ under either increasingly overcast or clearing skies,
3. an increase in the elements of the long-wave exchange and sensible heat transfer to the surface under clearing skies with an increase in T_a .

The association between overcast skies, rising air temperature and increased melt rates is more frequent than the clearing-sky scenarios.

Three canonical correlations are statistically significant during the *late* spring of 1993. Pearson's correlation for the first and third canonical pairs is positive, while the correlation for the second pair is negative. Correlations range between 0.96 and 0.78 for the three canonical pairs. The first canonical correlation relates PCEB1 to an environmental variate loaded heavily by the hours of bright sunshine and air temperature, with a secondary contribution by VPD and wind speed:

$$\begin{array}{l}
 K \uparrow - \\
 L \downarrow + \\
 L \uparrow + \\
 Q_{io} - \\
 K \downarrow - \\
 Q_E + \\
 Q_H +
 \end{array}
 \left|
 \begin{array}{l}
 PCEB1 - CCEB1 + CCEN1
 \end{array}
 \right.
 \begin{array}{l}
 +sh \\
 -T_a \\
 +VPD \\
 -u
 \end{array}
 .$$

Based on the direction of the canonical loadings, a rise in CCEN1 is associated with increasing sunshine hours and VPD and decreasing air temperature and wind velocity. The relationship among the environmental variables indicates an atmosphere tending towards clearing sky, with decreasing air temperature and VPD and declining wind speeds. The progression toward

this state is associated with a decrease in PCEB1, which corresponds to increased $K\uparrow$, Q_{io} , and $K\downarrow$, and decreased $L\downarrow$, $L\uparrow$, Q_E and Q_H . The strongest linkages are between the radiation terms ($K\downarrow$, $L\downarrow$ and $L\uparrow$) and the environmental variables, sh and T_a . A decrease in PCEB1 discourages melt and is associated with low net radiation (Fig. 8.5 d). This occurs, despite increasing elements of the short-wave exchange. Any radiative surplus is removed *via* turbulence. Net radiation appears to respond more closely to the long-wave exchange than to the solar radiation exchange in this instance. The converse of this scenario relates increasing melt and Q^* to elevated elements of the long-wave exchange and increasing Q_H and Q_E . These relationships are associated with rising air temperature under increasingly overcast skies.

The second canonical correlation measures the association between the linear composite of α , T_a and sh , and the canonical variate weighted almost exclusively by PCEB2 (i.e., $r_{ccl}=0.993$):

$$\begin{array}{l} K\downarrow + \\ Q_H + \\ L\downarrow - \\ Q_E + \\ L\uparrow + \end{array} \left| \begin{array}{l} PCEB2 + CCEB2 - CCEN2 \end{array} \right. \begin{array}{l} +\alpha \\ -T_a \\ -sh \end{array}$$

A rise in CCEN2 is associated with increasing surface albedo and decreasing air temperature and sunshine hours (i.e., increasing cloud coverage). In response, CCEB2 declines, which in turn is associated with a reduction in PCEB2 and each of $K\downarrow$, Q_H , Q_E and possibly $L\uparrow$ ($L\uparrow$ is very weakly correlated to PCEB2 ($r_{cl}=0.332$)). The long-wave heating of the surface is increased. Each of the loaded environmental variables is similarly weighted and forms the strongest association with $K\downarrow$ and Q_H . Both Q^* and the melt rate decline with decreasing PCEB2 (Fig. 8.5 d). In this instance, Q^* responds to $K\downarrow$ and decreases, despite the tendency for $L\downarrow$ to rise. The melt rate also declines as latent heat and, possibly, sensible heat remove any small amount of radiation surplus. On the other hand, rising air temperature and sunshine hours (decreasing CCEN2) are associated with increased $K\downarrow$, Q_H and Q_E , and a reduction in the elements of the long-wave exchange. The result is a reduction in Q^* and melt.

The third canonical correlation measures the association between PCEB3 (i.e., Q_E and Q_H) and the linear combination of VPD, u and, to a lesser degree, ξ :

$$\begin{array}{l} Q_E + \\ Q_H - \end{array} \left| \begin{array}{l} PCEB3 + CCEB3 + CCEN3 \\ -VPD \\ -u \\ +\xi \end{array} \right. .$$

Both Q_E and Q_H are evenly loaded onto PCEB3, but opposite in sign. A rise in CCEN3 is associated with declining VPD and wind speed, and the tendency for increased atmospheric stability. In turn, the latent heat loss by the surface is suppressed and sensible heating of the surface is reduced. There is no clear response by Q_M or Q^* to varying PCEB3, however, extremely high melt rates may be associated with this pattern (Fig. 8.5 d).

By way of review, increased melt and rising Q^* during the *late* spring of 1993, is associated with:

1. an increase in the elements of the long-wave exchange, in association with rising air temperature under increasingly overcast skies,
2. an increase in the absorption of solar radiation and increasing Q_H and Q_E (or dampened turbulent heat loss), in association with rising air temperature and reduced albedo under increasingly clearing skies.

The cloudy sky scenario is more frequent. A third pattern relates the combination of increasing atmospheric stability, reduced wind speed and VPD to a dampened turbulent heat exchange. Large melt rates can respond to this pattern, but no consistent relationship is observed.

8.4.2.3 Summary and Discussion of Statistical Analysis

This analysis shows that environmental conditions which involve increasing air temperature tend to be associated with increasing Q^* and melt through elevated elements of the long-wave exchange. The long-wave warming effect is more frequent under increasing cloud cover, but it can occur under clearing skies, and it is particularly strong during the *early* and *transitional* spring. This mechanism may demonstrate the effectiveness of the water vapour positive feedback that is introduced in Chapter 1, but differs from the outgoing long-wave flux feedback¹⁹. This is because the analysis shows an increase in $L\uparrow$ to be associated with an increase in $L\downarrow$ during the spring period. The effect of increasing elements of the long-wave exchange is usually to warm the surface and encourage melt. Only in one pattern was the surface cooled

¹⁹ A warming surface cools through enhanced long-wave loss.

through an enhanced outgoing long-wave flux and that occurred during the *late* spring of 1993, under clearing skies.

Environmental conditions which support increased atmospheric stability and a lowering in wind speed tend to: (i) suppress the removal of heat at the surface by turbulence, thereby allowing any radiation surplus to be directed into the snow volume for melt or for raising the volume temperature, or, (ii) allow the surface to be directly heated by the atmosphere *via* turbulence. These processes can occur during both clearing (associated with cooling air temperature) or increasingly overcast conditions (associated with either warming or cooling air temperature). The overcast pattern is most often observed during the late spring, while the clear sky pattern generally occurs during the *early and transitional* spring. The mechanism takes the form of a negative feedback under conditions conducive to cooling air temperature (and presumably cooling surface temperature) because surface cooling is offset by atmospheric heat. An increase in air temperature was only observed to correspond with increasing atmospheric stability in one pattern and this occurred during the *early and transitional* spring of 1993. This suggests that inversions are typically related to surface radiative cooling, which is prevalent under clear sky conditions.

Ice production is observed to increase in response to surface cooling by upward vapor and sensible heat flux during conditions of atmospheric instability and high wind speeds. This mechanism is similar to the turbulent heat flux feedback identified in Section 2.4.2. We may amend the description of the process and state that a warming surface (i.e., positive net radiation) overlain by an unstable atmosphere will cool *via* turbulent heat loss (both Q_H and Q_E). As described, the process is a negative feedback in that surface heating supports convection, which in turn cools the surface. The process can occur under clear or cloudy sky regimes. The two negative turbulent heat flux-atmospheric stability negative feedback patterns are schematically represented (Fig. 8.6 i and ii) for conditions favouring (i) a surface base radiative inversion and (ii) a lapse temperature structure. The environmental conditions favouring the linkage are provided in the figure.

In the event that air temperature drops during the *early and transitional* spring, a resultant increase in conductive heat input from the ice surface may act to offset ice production and may even support limited melt. This mechanism resembles the positive conduction feedback (Section 2.4.2). The effect of dropping air temperature is to increase the temperature gradient within the sea ice, in much the same manner as reducing the ice thickness will increase the temperature

gradient. This mechanism (termed the heat conduction-temperature feedback) is a negative feedback (Fig. 8.6 iii) and is observed to occur in conjunction with the turbulent heat flux-atmospheric stability negative feedback.

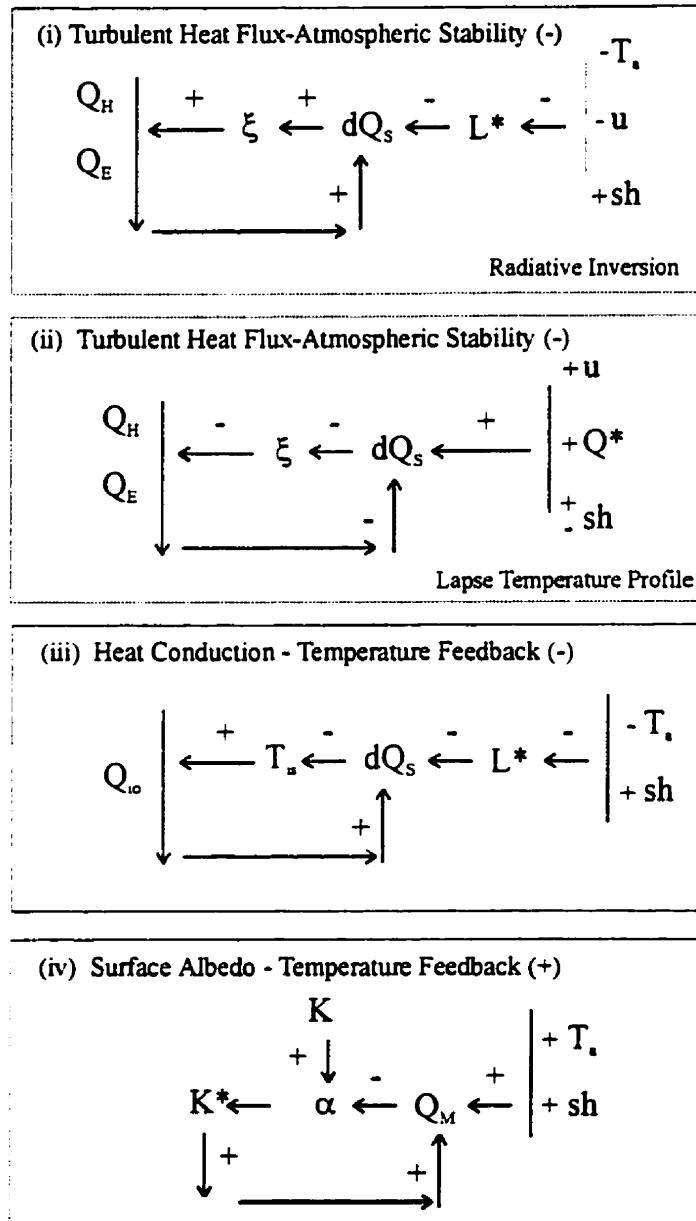


Figure 8.6 Schematic representation of feedback mechanisms which are observed to operate in the spring period over the SIMMS' experiments. The sign of the feedback is bracketed. The symbols + and - represent increasing and decreasing, respectively.

The surface-albedo feedback only occurs during the *late* spring and occurs less frequently than the long-wave warming effect, or the turbulent heat flux-stability feedbacks. This process operates under clear skies and in conditions favouring rising air temperature. In the previous section, I show that melt under clear skies is, on average, 22% greater than melt under overcast conditions during the *late* spring. Therefore, even though the pattern is seldom observed during the spring period, it is highly effective at accelerating snow melt rates. The mechanism is self-perpetuating in that the diurnal temperature cycle associated with clear-sky in the *late* spring supports morphological changes in the snow which act to further reduce the surface albedo (Fig. 8.6 iv).

8.4.3 Heating of the Snow Volume: A Contrast between the 1992 and 1993 Spring Seasons.

There are substantial differences in the evolution of the melt process between years. This is immediately obvious after viewing the seasonal evolution of the non-radiative heat fluxes that are depicted in Fig. 8.7 a and b. Persistent high pressure in 1993 acted to reduce the frequency of snowfall (Fig. 6.5b), maintain a large number of sunshine hours (Table 6.2) and reduce the frequency of overcast conditions (Table 6.2). Both factors are instrumental in maintaining a high mid-day net radiation (Fig. 8.1) and snow melt (Fig. 8.7 a). Boundary layer stability follows a regular cycle of nighttime stability, giving way to mid-day weak instability. The turbulent heat fluxes generally supply the surface with heat at night and remove heat from the surface during the daytime (Fig. 8.7 b). In contrast, significant shifts in the volume thermodynamics are closely coupled to low pressure systems in 1992. Cases in point are the heating episodes centred on day 145 and between days 155 and 172. Melt occurs over much of the diurnal cycle during these periods.

The statistical analysis of the previous section shows that the turbulent heat flux-atmospheric stability feedback acts to both warm and cool the surface in both years. In 1992, however, an unstable boundary layer was as likely to occur as a stable boundary layer within any of the seasonal categories while the ratio of stable to unstable boundary layers ranged between 8:2 and 7:3 during the *transitional* and *late* spring in 1993 (refer to Table 6.6). Long-wave radiation and forced mixing of air at the surface during 1992 discouraged the maintenance of a stable boundary layer. The difference in the form of the surface energy balance during the *transitional*

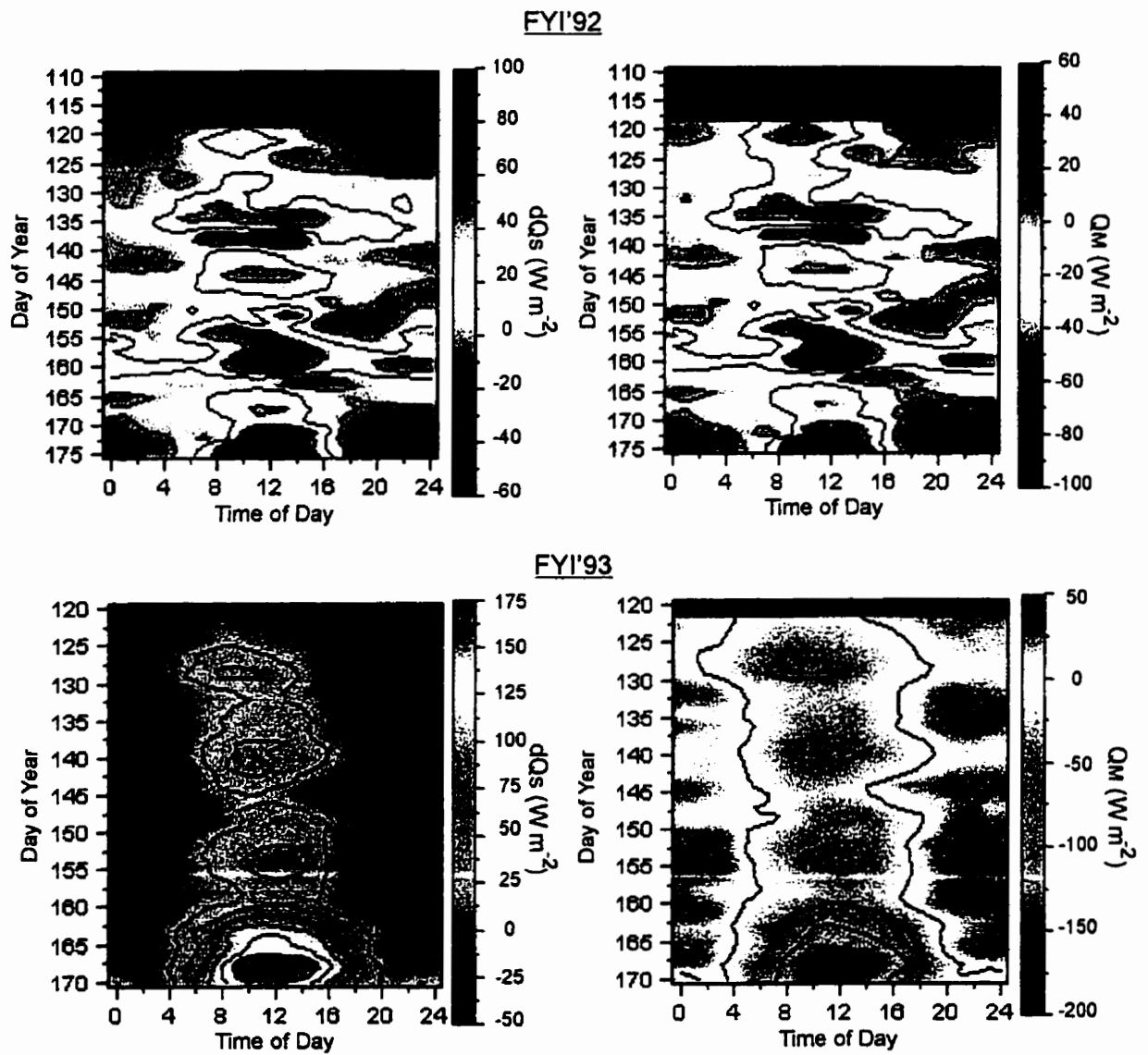


Figure 8.7a Diurnal and seasonal variation in the atmospheric heating of the snow and energy of fusion for FYI'92 and FYI'93.

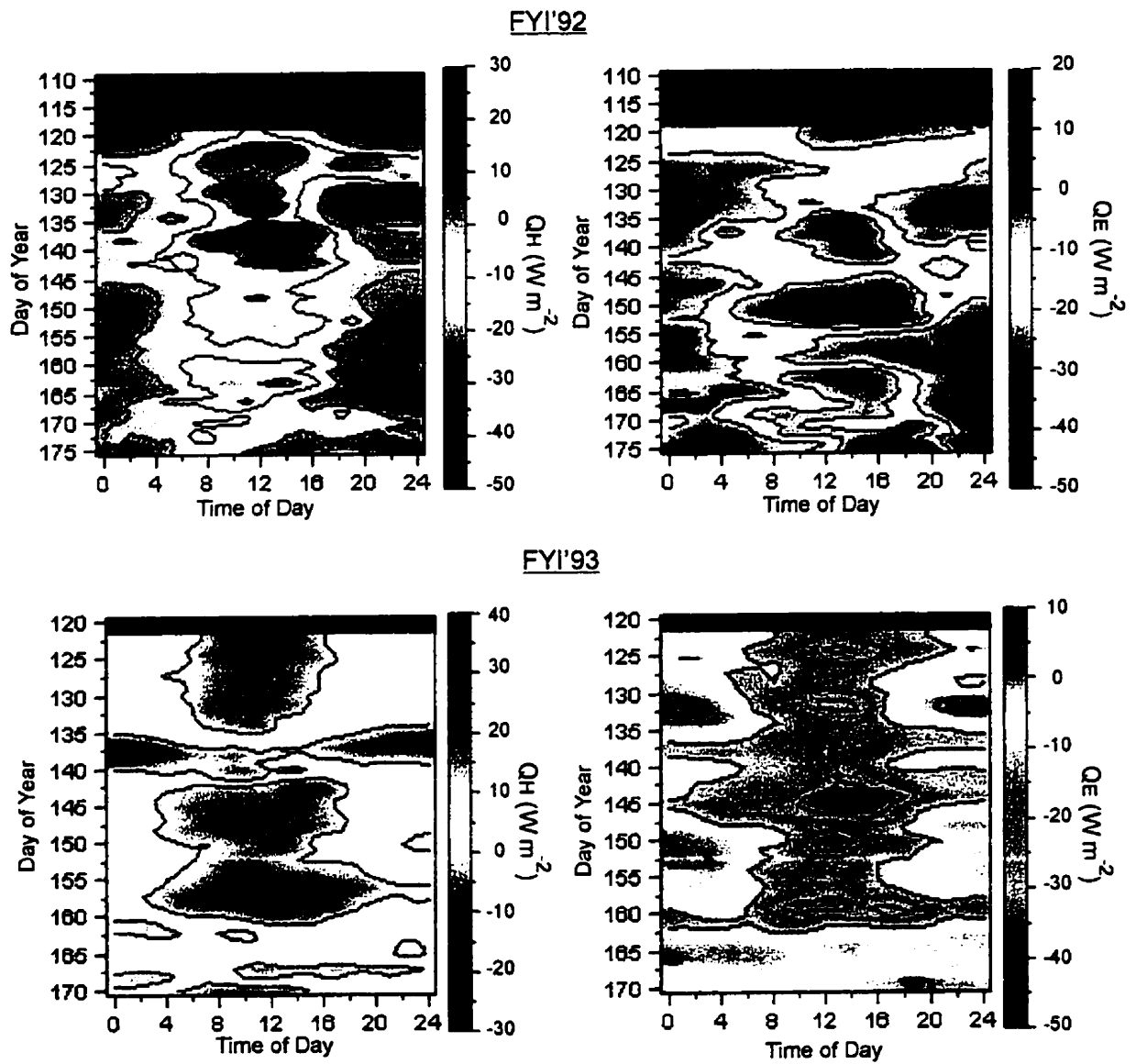


Figure 8.7b Diurnal and seasonal variation in the sensible and latent heat flux at FYI'92 and FYI'93.

spring reflects the difference in the role of the turbulent heat fluxes as the result of near surface atmospheric stability. This becomes evident after viewing Fig. 8.8. The average diurnal distribution of net radiation and available energy to the snow volume is remarkably similar between 1992 and 1993 during the *transitional* spring periods (Fig. 8.8 a and b). However, there is a tremendous difference in the disposition of this energy. Almost 80% of the available energy between 9:00 and 16:00 LAT is transferred to the (colder) atmosphere at FYI'92. In contrast, between 60% and 70% of the available energy is directed into the snow volume at FYI'93. Furthermore, the average nighttime contribution by Q_H to the surface at FYI'93 helped offset radiative loss, thereby reducing ice production within the snow. The average role of the turbulent fluxes in 1992 acted to reduce the enthalpy of the snow volume during both the daytime and nighttime period through the turbulent flux-atmospheric stability negative feedback.

The main difference between the melt process during the late spring seasons is that the surface albedo was allowed to drop in 1993 (Fig. 6.8), thereby allowing for larger net radiation gains by the surface. Snowfall associated with late season cyclones in 1992 acts to maintain the high surface albedo despite warm air temperatures. A reduction in albedo is not realized until the region is under the influence of a high pressure system in association with positive daytime air temperatures. This occurred on and around day 172 (Fig. 6.2a). The accelerated melt in 1993 is also largely an overcast sky phenomena as is evident by viewing TCA in Fig. 8.1b and Fig. 8.7a. However, one millimetre of rain (in combination with snow) was recorded at Resolute on day 165. The effect of the small rainfall is to lower the surface albedo. A second rain event on day 168 acted to further lower albedo and increase snow transmissivity to solar radiation (Fig. 6.8).

8.5 Summary

This chapter examined the extent to which environmental factors affect the components of the energy balance and chronicles the events associated with the heating of the FYI'92 and FYI'93 snow cover.

The effects, on the energy balance, of the environmental conditions that accompany cloud cover vary over the course of the spring transition. The overcast environments have, in general, higher surface net radiation, are warmer and are associated with higher wind speeds, weaker atmospheric stability, and enhanced turbulent heat loss by the surface. The differences between the cloud regimes tend to be larger during the early spring. On average, the long-wave warming effect

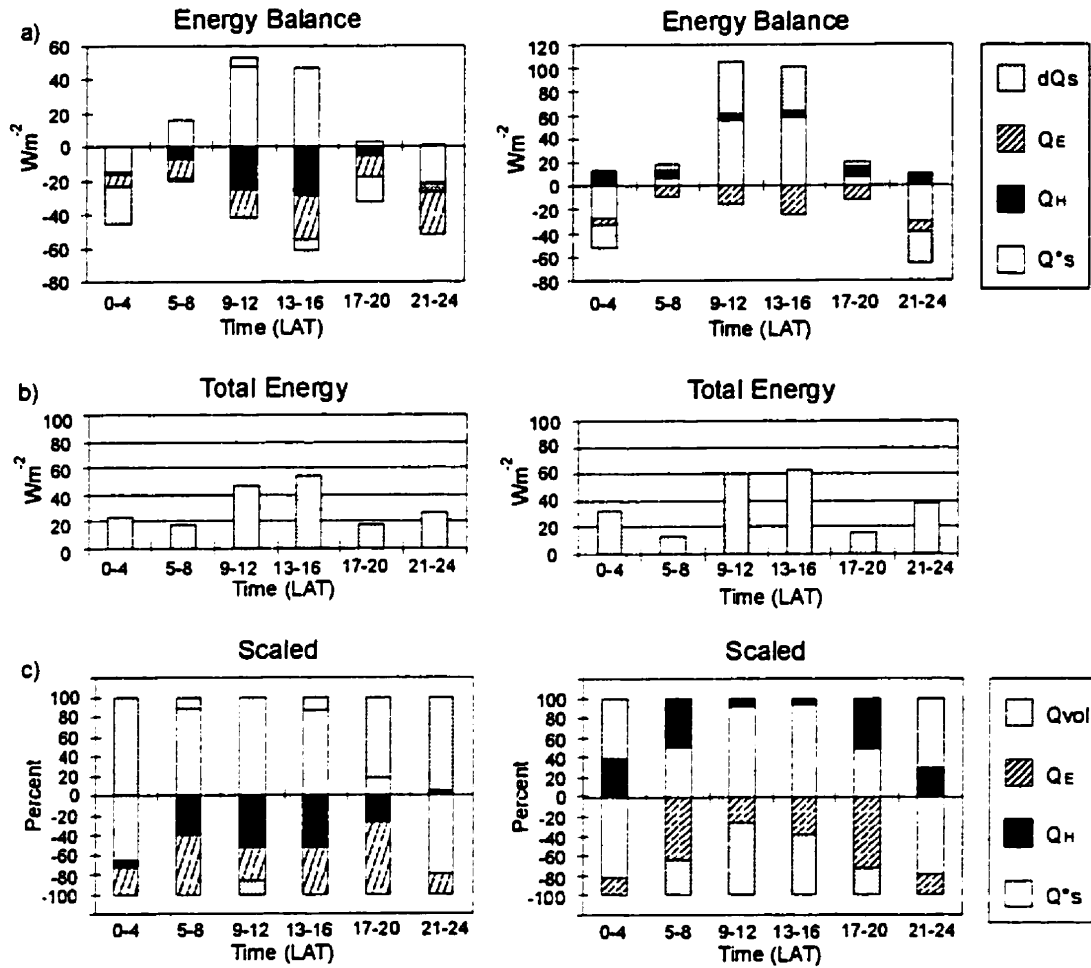


Figure 8.8 A comparison of the diurnal form of the energy balance between FYI'92 and FYI'93 during the *transitional* spring: (a) surface energy balance, (b) the available energy to the surface, (c) proportional contribution of the energy balance components for heating or cooling the surface.

of clouds tends to dominate the short-wave cooling effect throughout the diurnal cycle in the *early* spring and during the hours outside of the daytime (i.e., before 8:00 and after 16:00 LAT) period in the *late* spring. Regardless of the potential for differences in the net radiation between cloud regimes, the difference in net atmospheric heating of the snow is usually small because the turbulent heat flux tends to offset differences in radiative heating of the surface. Even though net radiation is marginally larger under overcast conditions during the *late* spring, the melt rate is typically larger during clear skies. The difference is attributed again to enhanced turbulent heat loss by the surface under overcast skies.

A canonical correlation analysis between energy balance and environmental variable sets identifies some interesting relationships that should exist in GCM simulations of the sea ice zone, if the surface is properly coupled to the atmosphere and, if the surface energy fluxes are adequately parameterized. In this way, these patterns fingerprint correct model performance. We find:

1. Environmental conditions associated with increasing air temperature tend to be associated with increasing net radiation and melt because of a long-wave warming effect. The effect is more frequent under increasingly overcast skies, but does occur under clearing skies, particularly early in the spring period. An increase in up-welling long-wave radiation is usually accompanied by an increase in down-welling long-wave radiation.
2. Environmental conditions which support increased atmospheric stability tend to heat the snow volume by either suppressing turbulent loss by the surface or by allowing the atmosphere to directly heat the surface by turbulent exchange. The pattern may act as both a positive (further heating a warming surface) and negative (the heating of a cooling surface) feedback mechanism. Its role as a positive feedback is infrequent because boundary layer instability is usually associated with a warming surface. Over a warming surface, a turbulent heat flux negative feedback is more common, namely: a warming surface overlain by an unstable atmosphere will cool through turbulent heat loss.
3. In the early spring, a heat conduction-temperature negative feedback may occur under situations of dropping air temperature. That is, an increased conductive heat input into the surface volume associated with an increase in the near surface temperature gradient can act to offset dropping surface temperature.
4. The surface albedo positive feedback is only observed in the late spring under conditions favouring a clear sky and rising air temperature. Environmental conditions that favour a

clear sky in the late spring support large melt rates and are effective at lowering the surface albedo. These conditions are associated with high atmospheric pressure and, therefore, the frequency and duration of high pressure systems in the late spring is instrumental for the rapid removal of a snow cover. The outgoing long-wave flux negative feedback operates in conjunction with the albedo effect, thereby limiting a rise in Q^* associated with a decline in albedo.

The major differences in melt evolution between the two spring seasons pertain to the effectiveness of the turbulent flux-atmospheric stability negative feedback to cool the surface in 1992 and for frequent snow deposition in 1992 to maintain a high surface albedo late into the season. Both features are related to the regular migration of cyclones into the study region in 1992. The analysis also shows that melt within the snow cover can be appreciable prior to the late season reduction in surface albedo.

CHAPTER 9: CONCLUDING REMARKS

9.1 Introduction

At the onset of this work, I identify deficiencies in our understanding of the energy balance over sea ice surfaces and the ramifications of our uncertainty on the climate change initiative. Our situation is that, if we are to gain confidence in our ability to simulate Arctic climate and to determine its role in modifying global climate, we must incorporate improved models of the energy balance components for sea ice surfaces (and associated snow cover) into GCMs. But, the lack of adequate observational data over sea ice is an impediment to our improved empirical understanding of the energy balance and prevents the improvement of climate models. These issues are pertinent because the global effect of the polar regions is considerably greater than for other regions of comparable size. An empirical understanding is necessary so that representations of the energy exchange processes may be developed and properly interpreted.

This work adds to our empirical understanding of surface-atmosphere interactions over sea ice by detailing the form of the energy balance and melt process of snow-covered sea ice and by providing a quantitative account of the interrelationship between the surface energy balance, surface properties and the atmosphere within the Canadian Arctic Archipelago. The multiple year nature of the study allows an examination of the response of the energy balance to widely varying atmospheric forcing. Significant findings within each research theme are summarized below.

9.2 Temporal Dynamics

9.2.1 Optical and Thermal Properties of Snow and Volume Thermodynamics

Wiscombe's and Warren (1980) model for spectral albedo is shown to produce albedo within approximately 3% of *in-situ* measurements in the visible portion of light for cold dry snow, regardless of snow depth, and for wet shallow snow over sea ice. It was observed however, that the model might underestimate albedo by up to 12% in the visible portion of the spectrum for deep

wet snow. This discrepancy is attributed to a wetness gradient within the snow volume. In such instances, a layered albedo model would be more appropriate. A sensitivity analysis shows that albedo calculations are required to within 1% to 3% to maintain a $\pm 10\%$ uncertainty limit in calculations of net solar radiation within and beyond the snow pack. A formal assessment of spectral extinction was not undertaken, however, I did estimate that κ_s must be estimated to within approximately 5% over the visible wavelengths to ensure a $\pm 10\%$ level of uncertainty in net solar radiation calculations. Modeled radiation transmission through snow is shown to agree well with measured values, using the albedo and extinction formulation, and Beer's Law. Much of the observed variation between measured and observed radiation transmission is attributed to a broadband to narrowband conversion of global radiation, and not to the estimate of the snow's optical properties. The confirmation that the Wiscombe and Warren model performs well over a variety of naturally occurring snow over sea ice is pertinent because the model is relatively simple, and it requires only an estimate of effective grain radius, snow bulk density, snow depth, albedo of the underlying sea ice and a soot concentration. The first three properties are easily obtained. Various sources for snow-free sea ice albedo are available and a soot concentration of 0.3 ppm by weight (Warren, 1982) for snow in the CAA appears to be appropriate.

The modeled thermal properties (k_s , ρc_p) for the spring snow cover over first-year sea ice are highly variable, in both the vertical dimension and with the spring progression. Snow thermal conductivity decreases away from the mid-snow zone and may vary by a factor of two over the snow profile throughout the spring period. Extreme variation in the snow's heat capacity across the snow profile is caused by a salinity gradient within the snow, particularly when the snow is warm ($T_s > -8^\circ\text{C}$). The heat capacity in a saline basal layer may be larger than in the overlying snow by a factor of two, to three in the late spring. The ramifications of vertical variation in salinity are demonstrated using a depth-time relationship for thermal diffusion. I show that approximately 30 cm of non-saline snow is coupled to the snow boundary (either the upper or lower boundary) over a 24 hour period. This means that the snow surface energy balance is coupled to the ice surface and oceanic heating within a diurnal cycle for a representative snow cover. The coupling distance can be reduced by a factor of between 2 to 5 for snow with salinity levels typically observed at the snow base of first-year sea ice over the spring season. The effect of a saline snow layer is to decouple the snow surface energy balance from the ice surface, thereby (i)

confining any heat conductive contribution to the surface to the upper snow volume, (ii) steepening near surface temperature gradients, and (iii) promoting ice production within the snow. Saline snow insulates the ice cover from atmospheric heating in the late spring, but acts to reduce sea ice growth in fall and winter by impeding the upward transfer of heat. These findings can not be reproduced using a single-layer snow model and demonstrates, using *in-situ* observations, the relationship between snow morphology, metamorphism and snow energetics.

The bulk (over 90%) of radiation absorbed by snow-covered sea ice occurs within the upper centimeter of the snow. This energy is readily available to the snow surface for transfer to the atmosphere at short time scales and therefore will not contribute to the heat storage of the snow. This observation lends support to others who had discounted the role of solar radiation in contributing to the heat storage of snow.

9.2.2 Surface-Atmosphere Energy Exchange

A major contribution of this work is the description of the evolution of the energy balance over a wide range of springtime atmospheric conditions. Each of the three spring seasons which are incorporated into this work were forced by an atmosphere which differed with respect to frequency of cyclone and anticyclone cycling, precipitation and the number of hours of bright sunshine. I show a high degree of variation in the form of the energy balance between years and the variability appears to be related to vastly different environmental forcing between years. Generalities are as follows. The form of the energy balance can be characterized through three distinct forms: early, transitional and late. The available energy to the surface in the early spring is strongly linked to processes within the snow volume (heat conduction and ice production) and not net radiation. Furthermore, the mid-day boundary layer structure is conducive to convection and therefore, much of the solar radiation absorbed by the surface at this time is preferentially directed into warming the near surface atmosphere and not into heating the snow volume. In fact, the maximum heat input to the snow volume occurs in the morning, while net solar radiation is very small.

During the late spring, the heat available to the snow surface and volume is several factors larger than during the early spring and both the surface and volume energy balances operate on a heat surplus. Approximately 95% of the energy available to the system is related to the radiation balance, consistent with observations from the central Arctic Ocean, a prairie snow cover and

snow-covered tundra during the summer season. The majority (between 51% to 73%) of the available heat to the snow upper boundary is directed into the volume instead of into the turbulent heat fluxes. Between 50% and 84% of this energy will support melt, while the remainder warms the underlying (colder) sea ice through conduction.

Sublimation at the snow surface is the dominant heat loss mechanism while the snow is cold, but the snow volume consumes a larger proportion of the surface's available energy when the snow warms. Water vapor transfer to the near surface atmosphere is active throughout the spring, and more energy may be lost by the surface to the atmosphere through sublimation than is directed into raising the enthalpy of the snow volume over the spring period. Atmospheric stability dictates the proportion of available energy which is directed into the snow, but the temperature difference between the sea ice and snow dictates how much of this energy is directed into melt. The role of the sensible heat flux varies widely between years. It represents only a minor heat source or sink during the late spring; however, the flux may represent either a substantial heat source or sink during the early or transitional stages of the season. In one year the flux contributed close to 40% of the available energy to the surface in the early spring, while in another the flux accounted for approximately 50% of the energy lost by the system.

9.3 Spatial Dynamics

The two major sea ice forms in the Canadian Arctic Archipelago are first-year and multi-year sea ice. The springtime energy balance of these surfaces is contrasted using data collected over multiple seasons. In general, snow-covered first-year ice warms faster relative to multi-year ice in close proximity. The presence of a salinity gradient within the FYI snow causes extreme variation in specific heat across the snow cover as the snow temperature rises. The saline snow layer insulates the upper snow from oceanic heat in much the same way as the thick underlying sea ice of the multi-year floe. The nature of the energy balance difference between ice types depends on the characteristics of the ice types being compared. A thick MYI floe is shown to be an environment of (i) lower albedo, (ii) higher net radiation, (iii) larger melt rates and (iv) enhanced turbulent heat loss relative to nearby FYI. A thin MYI floe, on the other hand, need not significantly differ from a thick FYI with respect to the radiation balance and most non-radiative energy transfer processes. The albedo of the flooded first-year sea ice is typically lower than flooded multi-year sea ice, regardless of floe thickness. Despite the potential difference in net

radiation between sea ice classes over periods of the spring transition, the surface temperature remains similar between sea ice types. The turbulent flux negative feedback tends to offset any difference in radiation loading to the ice surface. This finding discounts the use of the surface temperature as a reliable means of classifying mature ice types over the spring period.

The total difference in heat input between the two sea ice classes associated with differences in net radiation and downward conductive heat flow can represent the energy equivalent of melting between 16 cm and 22 cm of sea ice. This energy difference is non-trivial and demonstrates the need to consider horizontal variation in ice type (and therefore properties) in sea ice models for regions where varying sea ice types are expected. Failure to consider the differences in sea ice properties can cause errors in the prediction of *in-situ* melt by approximately 10 days. Errors of this order may affect the region's summertime energy regime and fall ice balance, with corresponding ramifications on the marine biosphere.

9.4 Environmental Forcing on the Components of the Energy Balance

In Chapter 8, I demonstrate the utility of canonical correlation for identifying patterns of association between the components of the energy balance and characteristics of the environment. This is an innovative application of the technique and the results provide insight into the relative importance of environmental conditions that act to promote and sustain snow melt. The analysis identifies association between fluxes and environmental properties and, therefore, the results provide a basis for anticipating the response of the energy balance (therefore, snow and ice melt) to potential changes in the Arctic environment. These results may be used to ensure that the surface processes, that produce climate feedbacks in numerical models, are realistic in sign and magnitude within climate change scenarios.

Five feedback mechanisms that involve the surface energy balance are observed to operate in a fully coupled system. Two negative feedback processes between the surface and atmosphere, and involving the turbulent heat fluxes, are extremely effective throughout the spring season. Turbulent heat will tend to warm a cooling surface under conditions of stable atmospheric boundary layer and cool a warming surface under conditions of increasing atmospheric instability. Conductive heat flow into the snow from below tends to warm a cooling snow volume, under cooling conditions. The surface albedo positive feedback is isolated to periods of clear sky and

rising air temperature, however, under such circumstances, the outgoing long-wave flux negative feedback is observed, and it acts to offset surface heating. The long-wave warming effect of clouds tends to dominate the short-wave cooling effect throughout the diurnal cycle in the early spring, and during hours outside of the 08:00 to 16:00 daytime window during the late spring. Despite differences in the radiative regime between sky states, the differences in net atmospheric heating of the snow between cloud regimes are small because of negative feedbacks involving the turbulent heat fluxes. Throughout the spring period warm air and cloud cover associated with migrating low pressure systems is instrumental in raising the enthalpy of the snow. Clear sky conditions on the other hand are typically associated with lower net radiation and melt rates in the early spring, but larger melt rates later in the season. Precipitation in the late spring can act to (i) protract melt by maintaining a high surface albedo if the precipitation is solid and (ii) accelerate melt by reducing albedo, as is the case for rain. The result of variable environmental forcing on the snow covered sea ice of the CAA is a lag of up to 20 days in the timing of accelerated snowmelt within the three year study.

In general, the snow cover over first-year sea ice in the central Parry Channel region is warmed by the heat content of non-Arctic airmasses which enter the region in association with migrating cyclones. Warmer and cloudier boundary layers heat the surface through enhanced long-wave emission by the atmosphere, which raises net radiation throughout the spring period. The long-wave radiation warming effect is greatest at night. Other processes associated with the environmental conditions surrounding cloud cover can act to cool the surface during the spring period. These mechanisms include: (i) a tendency for snowfall in the spring and (ii) the tendency for atmospheric stability to weaken and wind speed to increase. The first point is effective at maintaining a high surface albedo late into the spring period, thereby reducing the heating potential of the seasonally increasing global radiation. The second point cools the surface through the turbulent heat flux negative feedback.

The surface albedo undergoes a rapid decline under clear sky conditions in the late spring. The effect of clear skies in the late spring is to increase the daily maximum air temperature and the diurnal range in temperature. The cycle of daytime melt and nighttime refreezing associated with the temperature cycle encourages an increase in the snow transmissivity to solar radiation through a combination of snow grain and snow grain cluster growth, thereby lowering snow albedo and increasing net solar radiation. Furthermore, boundary layer stability is strengthened under clear

skies, thereby reducing the amount of heat transferred away from the snow surface. Clear skies are associated with high pressure systems in the Arctic and, therefore, the frequency and duration of high pressure cells in the late spring may be instrumental in expediting the rapid removal of a snow cover.

Collectively, these results show that synoptic climate forcing plays a pivotal role in determining the progression of the spring energy balance from its early to late spring state and in triggering the rapid rise in net radiation and melt observed during each spring period. The direct net response of the sea ice zone, in the presence of a warming atmosphere, will therefore depend heavily on the associated patterns of environmental change associated with a change in temperature.

9.5 Recommendations and Concluding Remarks

Variation (both temporal and spatial) is the underlying thread of each aspect of the energy balance during the spring season. Because the Arctic sea ice is believed to be a sensitive indicator of climate change, which also actively acts to maintain the present climate state, it is imperative that we monitor this variation at scales sufficiently fine to detect regional and seasonal shifts. The vast and remote nature of the Arctic discounts the use of *in situ* observation for this task. Remote sensing and sea ice modeling are viable alternatives. Neither is discussed at any length within this text, but advancement in both disciplines depends strongly on an improved understanding of the energy balance and its relationship to the physical properties of the snow and sea ice.

Using models, a system may be studied over a range of conditions that can not be feasibly experienced through field experimentation and, therefore, they are an indispensable exploratory tool. Existing sea ice models may be broadly classified according to the processes they include: namely, dynamic or thermodynamic. Ebert and Curry (1993) provide the most elaborate treatment of sea ice thermodynamics and surface energy forcing. Bulk parameterizations describe many of the energy balance components, while snow and sea ice physical and optical properties are taken as functions of time, with several simplifying assumptions. Snow is considered to be a uniform slab, with no representation of the internal thermodynamics which act to produce the vertical variation in the physical properties that occur in natural snow covers (Chapter 6). Currently, we are not sure

how accurate the simulation of processes is in sophisticated one dimensional models and, of further importance, we do not know how sensitive sea ice forecasts are to these uncertainties.

Remote sensing is defined as the acquisition of information about the condition and/or state of a target by a sensor that is not in direct physical contact with it (Asrar, 1989). The synoptic coverage of many spaceborne platforms can provide surface information on scales amenable to regional and larger-scale models. Remote sensing in the microwave region of the electromagnetic spectrum is particularly well suited for polar applications. Seasonal darkness and persistent clouds discount the regular use of remote sensing in optical and thermal infrared wavelengths. Clouds, on the other hand, are relatively transparent to electromagnetic radiation in the microwave wavelengths and microwave remote sensing is not dependent on solar illumination. Scattering of electromagnetic radiation and thermal emission are important in the microwave interaction mechanisms with the surface. The emitted energy by the surface volume in the microwave wavelengths is a function of the surface's kinetic temperature, emissivity, wavelength, surface roughness and dielectric properties (Carlton, 1990). The scattering intensity to incident microwave radiation from active microwave sensors is determined by snow and ice parameters (e.g., wetness, grain size and orientation, brine volume and salinity and the size and distribution of air bubbles), most of which change in response to temperature (Vant et al., 1978). In theory, microwave scattering and emission should be related to the components of the energy balance through their mutual dependence on the volume's physical properties. Preliminary findings (e.g., Barber et al., 1997; and Carlstrom and Ulander, 1995) show that research along these lines may be fruitful.

Traditionally, remote sensing of the surface state can be considered an inverse problem. The objective is to reconstruct physical parameters from remotely sensed scattering and emission information (Asrar, 1989). The process entails the use of physical relations or statistical correlation between the scattering and emission information received by the sensor and surface properties, or energy fluxes, operating at the surface or surface volume (Asrar, 1989). Alternatively, a direct approach (forward model) attempts to simulate the electromagnetic response at (or within) the surface (volume) based on observed or simulated surface conditions. Hence there is a natural synergy between modeling and remote sensing and the application of both requires some understanding of the surface's microclimate, which brings us back to this work. How can the results of this work be used to direct research in these areas?

Based on the results from Chapter 6, a fundamental deficiency is, in my opinion, our understanding and representation of vapour transport from cold surfaces. The aerodynamic formulation used here is limited by assumptions regarding stability correction. The similarity assumption does not consider latent heating within the atmospheric column which may be associated with radiation absorption and re-emission. Similar comments apply to the representation of the sensible heat flux. A comprehensive field study with eddy correlation systems is necessary to resolve some of these uncertainties.

Results from Chapter 6 indicate that the energy balance follows distinct seasonal forms. Can the evolution of the surface state through these episodes be detected using remote sensing technology to aid in the assessment of the form of the surface energy balance?

Recall that, on average, 66% of the energy available to the early spring sea ice surface is attributable to the snow and sea ice volume. As pointed out by Arons and Colbeck (1995), the relationship between the vertical variation of snow microstructure and the energy balance at the snow boundary is poorly understood and this thesis does little to expand our understanding in this area. Clearly, research should be directed into the relationship between the snow physical properties, volume thermodynamics and electromagnetic scattering and emission in the microwave wavelengths early in the spring season. Heat flow modeling applications would be improved if we could predict or detect the presence of a poorly conducting basal snow layer which may be observed over first-year sea ice (Chapter 6). Is it possible to establish a relationship between aspects of snow morphology, sea ice type and snow thickness? The identification of partial sea ice concentration of different sea ice types is necessary because the volume thermodynamics differ substantially between the mature sea ice categories (Chapter 7). Research in these areas would aid in the application of remote sensing for heat flow studies.

As the snow warms, the assessment and detection of those morphological properties that affect snow albedo is more critical, as net radiation becomes the dominant source of available energy to the surface at this time. Clouds also have a profound effect at moderating net radiation. The effect of the environmental conditions associated with clouds (other than effects on the radiation balance) also moderate the amount of surplus radiation available to the surface for melt, through a turbulent heat flux feedback. These processes are difficult to investigate with 'non-coupled' surface-atmosphere models, yet they are fundamental in explaining the role of clouds in the spring season melt rate. I echo Zhang et al.'s (1996) conclusion, that dedicated research is

necessary to expand on our understanding of the cloud related surface energy feedbacks. We need to build on our understanding of the seasonally evolving relationship between clouds and the energy balance and to establish linkages among cloud cover, the energy balance and snow morphology. Is it possible to exploit a relationship between atmospheric stability, surface roughness and cloud cover for the evaluation of turbulent heat exchange at the snow surface?

In conclusion, the evolution of snow-covered mature sea ice during the spring transition is a manifestation of the response of the energy balance to atmospheric forcing and the linkage between the components of the energy balance and the changing physical properties of the snow volume. The nature of this inter-relationship is highly variable in time and space, and will dictate the response of the system to any environmental change. The monitoring of the sea ice atmosphere system is necessary for the detection of change. The information provided above should aid in this endeavor.

APPENDIX 1: DAY OF YEAR CALENDAR

Day of Year Calendar

(note: for leap year add one to day of year totals)

APRIL								MAY						JUNE								
							91		121	122	123	124	125	126						152	153	154
							1		1	2	3	4	5	6						1	2	3
265	92	93	94	95	96	97	98	127	128	129	130	131	132	133	155	156	157	158	159	160	161	
	2	3	4	5	6	7	8	7	8	9	10	11	12	13	4	5	6	7	8	9	10	
	99	100	101	102	103	104	105	134	135	136	137	138	139	140	162	163	164	165	166	167	168	
	9	10	11	12	13	14	15	14	15	16	17	18	19	20	11	12	13	14	15	16	17	
	106	107	108	109	110	111	112	141	142	143	144	145	146	147	169	170	171	172	173	174	175	
	16	17	18	19	20	21	22	21	22	23	24	25	26	27	18	19	20	21	22	23	24	
	113	114	115	116	117	118	119	148	149	150	151				176	177	178	179	180	181		
	23	24	25	26	27	28	29	28	29	30	31				25	26	27	28	29	30		
	120																					
	30																					

APPENDIX 2: CALCULATION OF SPECTRAL ALBEDO AND EXTINCTION

A2.1 Introduction

Wiscombe and Warren (1980) provided a theoretical solution for the spectral albedo of a flat snow surface for: (a) direct beam radiation incident to a shallow (optically thin) snow pack over a diffusely-reflecting surface, (b) direct beam radiation incident to a thick (optically semi-infinite, $\tau \rightarrow \infty$) snow pack, (c) diffuse radiation incident to an optically thin snow pack, and (d) diffuse radiation to a thick snow pack. The transition between optically thin (i.e., albedo is effected by the underlying surface), and optically semi-infinite (i.e., albedo is independent of underlying surface) is a strong function of wavelength. The transition ranges from a snow optical depth of about 10 for the infrared wavelengths to a snow optical depth of about 1000 for the visible wavelengths (from Fig. 5 in Warren, 1982). The volume is considered here as being optically thick if its albedo at all wavelengths is within $\pm 1\%$ on an optically thick snow cover (Wiscombe and Warren 1980).

Snow is modeled as ice spheres and the scattering and absorption of light by a single sphere is described by Mie theory²⁰. Mie scattering provides a useful framework to partition out extinction by a single grain into its scattered and absorbed components, using the relationships²¹:

$$\sigma_{ext} = \sigma_{sc} + \sigma_{ab} , \quad (A2.1a)$$

$$Q_{ext} = Q_{sc} + Q_{ab} , \quad (A2.1b)$$

where σ refers to the element's ability to attenuate (subscript, ext), scatter (subscript, sc), and absorb (subscript, ab) a proportion of incident radiation. These are expressed in terms of an

²⁰ The scattering of light by spherical particales of diameters comparable to the incident wavelength (Illingworth, 1991)

²¹ The dependence of these terms on wavelength and effective sphere radius is impied for each of the Mie scattering quantities.

effective cross-sectional area. Q_{ex} , Q_{sc} , and Q_{ab} are referred to as the efficiency factors for each of the three optical processes (extinction, scattering and absorption). The terms relate the sphere's physical to optical properties. Two other single-scattering terms include the single-scattering albedo and asymmetry factor. The single scattering albedo ($0 \leq \omega \leq 1$) represents the fraction scattered of the total energy removed from the incident beam:

$$\omega = \frac{\sigma_{\text{sc}}}{\sigma_{\text{ab}}} = \frac{Q_{\text{sc}}}{Q_{\text{ex}}} \quad (\text{A2.2})$$

The average value of the cosine of the scattering angle is characterized by the asymmetry factor, g . The asymmetry factor ranges between -1 and 1, where -1 is a perfect backscatter and 1 is a perfect forward scatterer.

Soot contamination in snow is treated as an external mixture (i.e., the soot is assumed to be outside of the snow grain) by Warren and Wiscombe (1980). Soot concentration is assumed to be 0.3 parts per million by weight concentration of soot evenly distributed throughout the snow (Warren and Wiscombe, 1980). Soot radius and density were held constant at 0.1 μm (Warren and Wiscombe, 1980) and 100 $\text{kg}\cdot\text{m}^{-3}$ (Warren, 1982), respectively.

The albedo to direct-beam radiation for optically thin snow over a diffusely-reflecting surface of albedo α_{s} , is a function of the cosine of the zenith angle (μ_0) such that:

$$\begin{aligned} Q\alpha_{\text{s}}(\mu_0) = & 2 \left[P(1 - \gamma + \omega^* b^*) + \omega^* (1 + b^*) \frac{\gamma \xi \mu_0 - P}{1 - \xi^2 \mu_0^2} \right] \\ & \times \exp\left(-\tau_0^* / \mu_0\right) - \omega^* b^* (Q^+ - Q^-) \\ & + \omega(1 + b^*) \left(\frac{Q^+}{1 + \xi \mu_0} - \frac{Q^-}{1 - \xi \mu_0} \right) \end{aligned} \quad (\text{A2.3})$$

where each of the terms are wavelength dependent. The delta-Eddington approximation is used to obtain the transformations of single-scattering parameters: g , ω , and τ_0 :

$$g^* = \left(\frac{g_\lambda}{1 + g_\lambda} \right)_\lambda \quad (\text{A2.4a})$$

$$\omega^* = \left(\frac{(1 - g_\lambda^2) \omega_\lambda}{1 - g_\lambda^2 \omega_\lambda} \right)_\lambda \quad (\text{A2.4b})$$

$$\tau_o^* = \left((1 - \varpi_\lambda g_\lambda^2) \tau_{o\lambda} \right)_\lambda, \quad (\text{A2.4c})$$

and the remaining terms are:

$$a^* = 1 - \varpi^* g^*; \quad (\text{A2.4a})$$

$$b^* = g^* / a^*; \quad (\text{A2.4b})$$

$$\xi = [3a^*(1 - \varpi^*)]^{1/2}; \quad (\text{A2.4c})$$

$$P = 2\xi / (3a^*); \quad (\text{A2.4d})$$

$$\gamma = \frac{(1 - \alpha_{i\lambda})}{(1 + \alpha_{i\lambda})}; \quad (\text{A2.4e})$$

$$Q^\pm = (\gamma \pm P) \exp(\pm \xi \tau_o^*); \quad (\text{A2.4f})$$

$$Q = (1 + P)Q^+ - (1 - P)Q^-; \quad (\text{A2.4g})$$

and α_i is the albedo of the underlying surface (Table A2.1). Q describes the net scattering intensity between the up-welling (+), and down-welling (-) flux.

For optically thick snow packs, the direct-beam reflectance is:

$$\alpha_s(\mu_o, \lambda) = \left(\frac{\varpi^*}{1 - P} \right) \left(\frac{1 - b^* \xi \mu_o}{1 + \xi \mu_o} \right). \quad (\text{A2.5})$$

For diffuse radiation incident to shallow snow packs the albedo is approximated by $\alpha_s(\mu_o, \lambda)$ for solar zenith angles between 45° and 53° (Wiscombe and Warren, 1980). For thick, optically 'semi-infinite' snow packs, diffuse albedo is represented as:

$$\alpha_s(\lambda)_{\text{diff}} = \left(\frac{2\varpi^*}{1 + P} \right) \left\{ \frac{1 + b^*}{\xi^2} (\xi - \ln(1 + \xi)) - b^* / 2 \right\}. \quad (\text{A2.6})$$

A2.2 Ice Surface Albedo

Albedo of the underlying ice surface is taken (Table A2.1) from spectra published by Grenfell and Perovich (1984) and Morrassutti and LeDrew (1995) to correspond with the 22 wavelength bands used in this study. Sea ice albedo is assigned for three sea ice types (FYI, MYI melt pond and MYI hummock) during their early (cold) and late (melting) state. For each surface (first-year ice, melt pond and hummock) the albedo corresponding to the source's description of the surface, which best agreed with the ice surfaces at the respective sites is used.

Table A2.1 The spectral albedo of ice surfaces. All spectra, unless otherwise noted, are taken from Grenfell and Perovich (1984).

	<i>early</i>	<i>late</i>	<i>early</i>	<i>late</i>	<i>early</i>	<i>late</i>
λ (μm)	fyi ¹	fyi ²	melt pond ³	melt pond ⁴	hummock ⁵	hummock ⁶
0.36	0.6	0.61	0.48	0.28	0.75	0.61
0.4	0.62	0.64	49	0.3	0.78	0.64
0.44	0.63	0.64	0.51	0.3	0.76	0.64
0.48	0.65	0.65	0.54	0.28	0.76	0.65
0.52	0.63	0.63	0.56	0.25	0.77	0.63
0.57	0.59	0.61	0.5	0.2	0.75	0.61
0.64	0.57	0.63	0.48	0.17	0.72	0.63
0.69	0.53	0.6	0.38	0.15	0.68	0.6
0.75	0.5	0.58	0.25	0.07	0.62	0.58
0.78	0.47	0.57	0.1	0.02	0.58	0.57
0.87	0.38	0.51	0.08	0.01	0.43	0.51
1	0.26	0.31	0.05	0.01	0.25	0.31
1.1	0.24	0.3	0.05	0.01	0.25	0.3
1.19	0.19	0.18	0.05	0.01	0.18	0.18
1.28	0.17	0.15	0.03	0.01	0.12	0.15
1.53	0.05	0.007	0.03	0.01	0.07	0.007
1.64	0.05	0.007	0.03	0.01	0.05	0.007
2.13	0.02	0.007	0.01	0.01	0.01	0.007
2.38	0.01	0.007	0.01	0.01	0.02	0.007
2.91	0.01	0.007	0.03	0.01	0.02	0.007
3.42	0.007	0.007	0.03	0.01	0.02	0.007
4	0.005	0.007	0.01	0.01	0.02	0.007

- 1) First-year ice with crumbly surface layer
- 2) Melting first-year ice
- 3) Frozen melt pond.
- 4) Black melt pond ice (Morrassutti and LeDrew, 1995)
- 5) Scraped, milky ice surface.
- 6) Same as melting first-year ice surface.

A2.3 Mie Scattering Equations and Efficiency Factors

The Mie scattering terms of soot contaminated snow consists of weighted averages of the single-scattering terms for soot and ice. They are scaled according to the cross-sectional areas of each. The single scattering albedo, and asymmetry factor of the SIMMS' snow are computed as a weighted average of those for pure ice (subscript, ice) and soot (subscript, soot), viz.,

$$\varpi_{\lambda,ave} = A_{soot} \times \varpi_{\lambda,soot} + A_{ice} \times \varpi_{\lambda,ice}, \quad (A2.7)$$

$$g_{\lambda,ave} = A_{soot} \cdot g_{\lambda,soot} + A_{ice} \cdot g_{\lambda,ice}, \quad (A2.8)$$

where A is the proportional area occupied by soot and ice in the snow cover:

$$A_j = \frac{TCSA_j}{TCSA_{soot} + TCSA_{snow}}, \quad (A2.9)$$

and TCSA is the total cross-sectional area per unit volume for the medium j, where j represents either soot or snow. Total cross-sectional area is:

$$TCSA_j = N_j \times GCS_j, \quad (A2.10)$$

and GCS is the geometric cross sectional area of a sphere:

$$GCS_j = \pi r_{eff,j}^2, \quad (A2.11)$$

of effective radius, r_{eff} . The weighted average of the extinction cross section per unit volume of the snow and soot medium is expressed as:

$$\sigma'_{e(ave)} = A_{soot} \cdot \sigma_{e(soot)} + A_{ice} \cdot \sigma_{e(ice)}, \quad (A2.12)$$

where

$$\sigma'_{e(j)} = N_j \cdot r_{eff,j} \cdot \pi^2 \cdot Q_{ex(j)}, \quad (A2.13)$$

and j represents either soot or ice.

The single scattering albedo (ϖ_{λ}) for ice spheres was approximated following Choudhury and Chang (1981):

$$\varpi_{\lambda} = 0.5 + 0.5 \exp(-1.67 \times a_{i,\lambda} r_{eff}), \quad (A2.14)$$

where $a_{i,\lambda}$ is the spectral absorption coefficient of ice. Choudhury and Chang (1981) also provide a parameterization to the solution of the asymmetry factor (g) for large spherical particles with a complex refractive index comparable to that for ice:

$$g_{\lambda} = 0.87 \exp(-2\kappa_{i,\lambda} r_{eff}) + 0.97 [1 - \exp(-2\kappa_{i,\lambda} r_{eff})]. \quad (\text{A2.15})$$

The effective sphere radius in the above equations describes the mean radius for scattering. It is related to the average sphere radii in the medium, but is also a function of the particle size distribution (Hansen and Travis, 1974). The parameterizations for the single-scattering albedo and asymmetry factor for ice is shown (in Figs. A2.1 and A2.2) against formal derivations using the numerical methods of Bohren and Huff (1983). The abscissa, x , in the figures is the size parameter:

$$x = \frac{2\pi r_{eff}}{\lambda}. \quad (\text{A2.16})$$

The spectral extinction coefficient can be computed for a snow cover *viz.*,

$$\kappa_{\lambda} = N\sigma_{ext} [(1 - \omega)(1 - \omega g)]^{1/2}, \quad (\text{A2.17})$$

while the optical depth of the snow cover is,

$$\tau_{o,\lambda} = N\sigma_{ext} d, \quad (\text{A2.18})$$

where N is the number of grains per unit volume:

$$N = \left[\frac{3\rho_s}{4\pi r_{eff}^3 \rho_i} \right]. \quad (\text{A2.19})$$

The weighted average of snow density for each snow layer is used for the calculation of the number of snow grain per unit volume. The ice sphere effective radii is assumed constant within the snow volume and is calibrated per site based on a comparison between modeled and measured radiation transmission between 0.4 and 0.7 μm . The effective radii of the sphere is adjusted over the season's progression to mimic the seasonal increase in snow grain size through the various metamorphic processes which are outlined in Chapter 2

The Mie parameters for soot were computed using the numerical methods outlined by Bohren and Huff (1983). The parameters were evaluated at 0.1 μm wavelength intervals between 0.36 μm and 4 μm , for soot particles of radius 0.07 μm , 0.1 μm , and 0.14 μm , and assuming a complex refractive index of 1.8-i0.5 (Twitty and Weinman, 1971). The single scattering albedo, asymmetry factor and efficiency factor for soot are expressed below as functions of the size parameter, x , and are shown in Figs. A2.3 to A2.5. Expressions are:

$$\varpi_{\text{soot}} = 0.0817 - 0.179667 \cdot x + 0.864331 \cdot x^2 - 0.369672 \cdot x^3 \quad (\text{A2.20a})$$

$$\begin{cases} 0.0942 \leq x \leq 1.250 \\ r^2 = 0.998 \end{cases}$$

$$\varpi_{\text{soot}} = 0.0817 \cdot \ln(x) + 0.403 \quad (\text{A2.20b})$$

$$\begin{cases} 1.250 < x \leq 2.93 \\ r^2 = 0.708 \end{cases}$$

$$g_{\text{soot}} = 0.002390 + \frac{(1 - 0.002390)}{[1 + \exp(1.086734 - 2.567500 \cdot \ln(x))]} \quad (\text{A2.21})$$

$$\begin{cases} 0.0942 \leq x \leq 2.93 \\ r^2 = 0.996 \end{cases}$$

$$Q_{\text{ex}(\text{soot})} = \frac{3.641}{[1 + \exp\{0.1767 - 2.208 \cdot \ln(x)\}]} \quad (\text{A2.22})$$

$$\begin{cases} 0.0942 \leq x \leq 2.93 \\ r^2 = 0.992 \end{cases}$$

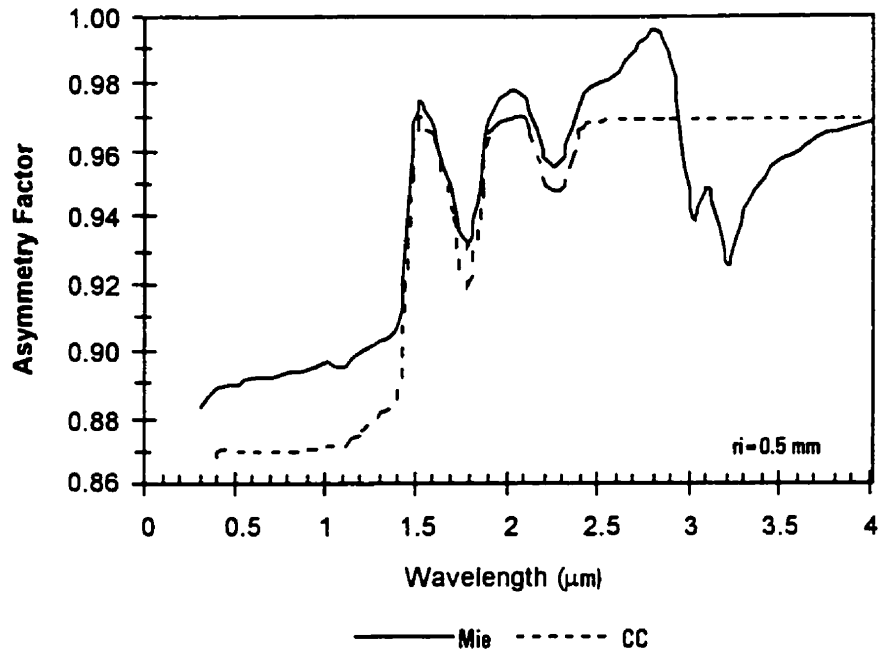


Figure A2.1 The asymmetry factor of ice computed with Choudhury and Chang's (1981) approximation (CC) and by using the numerical methods provided by Bohren and Huff (1983) (Mie). Ice grain effective radius is 0.5 mm.

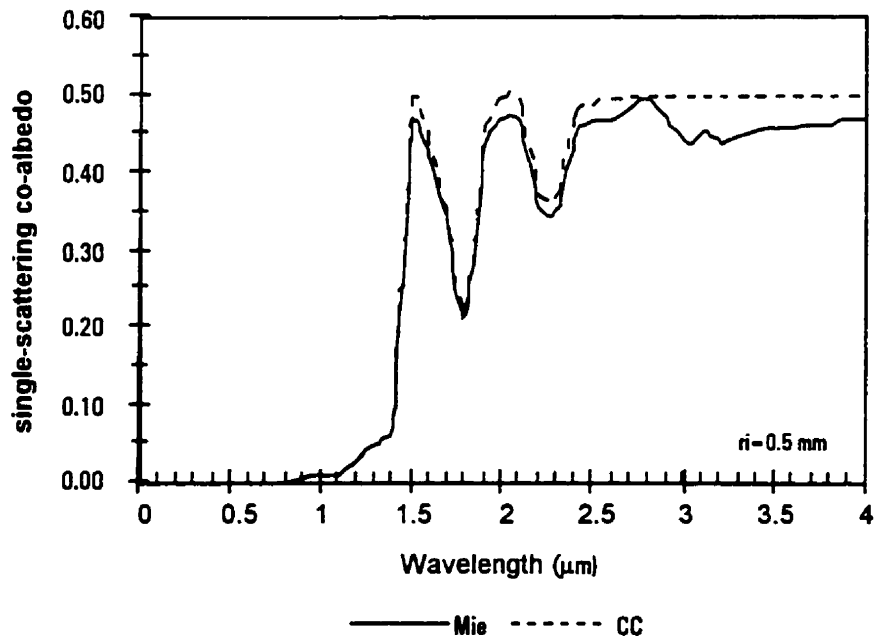


Figure A2.2 The single scattering albedo of ice of computed with Choudhury and Chang's (1981) approximation (CC) and by using the numerical methods provided by Bohren and Huff (1983) (Mie). Ice grain effective radius is 0.5 mm.

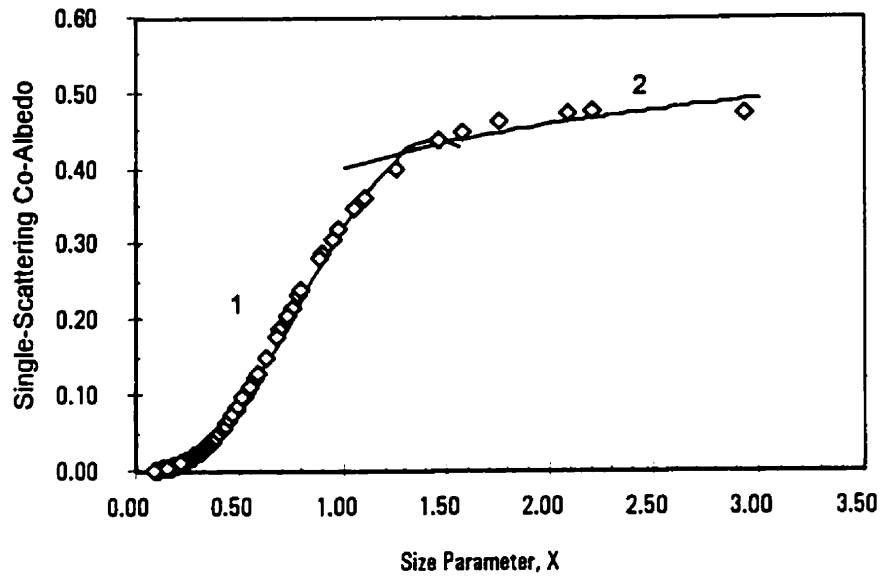


Figure A2.3 Single scattering albedo ω of soot plotted as a function of size parameter, x . Open symbols are values computed with Mie scattering equations. Curves 1 and 2 are Eqs. A2.20a and b, respectively.

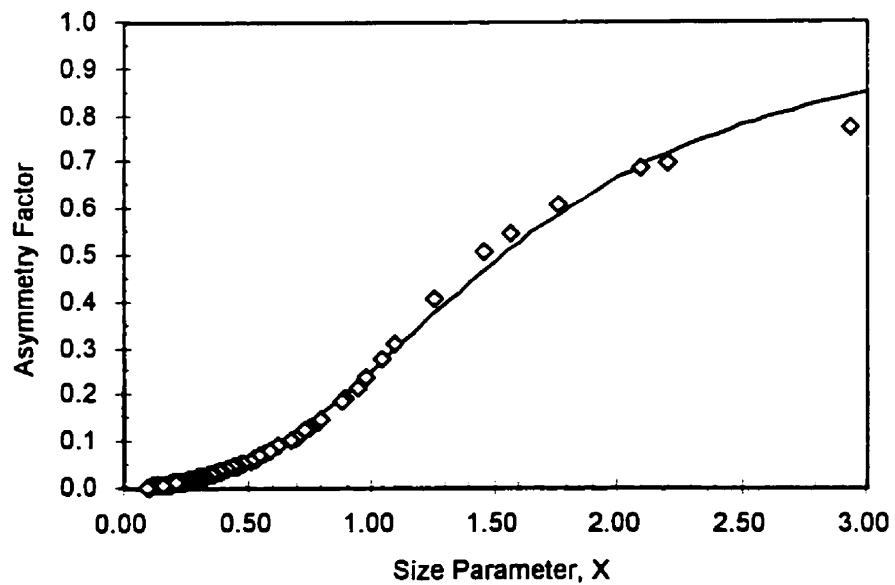


Figure A2.4 Asymmetry factor g of soot plotted as a function of size parameter, x . Open symbols are values computed with Mie scattering equations. The curve represents Eq. A2.21.

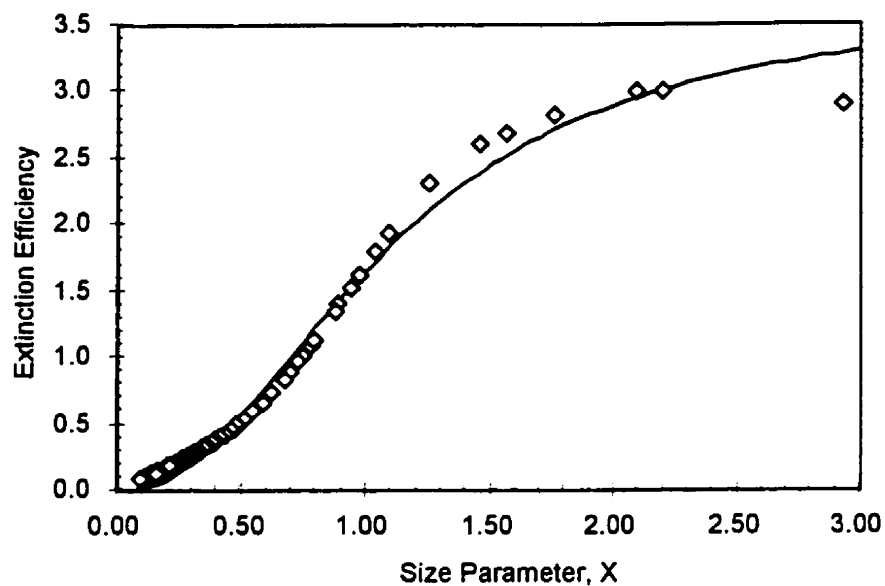


Figure A2.5 The extinction efficiency Q_{ext} , of soot plotted as a function of size parameter, x . Open symbols are values computed with Mie scattering equations. The curve represents Eq. A2.22.

APPENDIX 3: SITE INSTRUMENTATION AND LAYOUT

A plan-view schematic of a typical site layout is provided as Fig. A3.1. Table A3.1 describes the instrumentation used at the research sites while the sampling rate and averaging period for each of the meteorological variables is outlined in Table A3.2. The manufacturer's specification for sensor accuracy is provided in Table A3.3 and the wavelength sensitivity of radiometers used during the SIMMS experiments is shown in Table A3.4. Tables A3.5, A3.6 and A3.7 contain the measurement heights of sensors above the snow surface, the number and depth of each snow temperature sensor, and the number and depth of ice temperature sensors used in each of the experiments, respectively. The variables measured during the snow physical properties sampling program appears in Table A3.8.

Table A3.1 A description of the instrumentation used at the research stations.

Symbol	Unit	Sensor	Description
Q*	Wm ⁻²	pyrradiometer	Middleton (model CN-1) [®]
K↓	Wm ⁻²	pyranometer	Eppley (model PSP and B&W) [®]
K↑	Wm ⁻²	pyranometer	Eppley (model PSP and B&W) [®]
L↓	Wm ⁻²	pyrgeometer	Eppley (model PIR) [®]
L↑	Wm ⁻²	pyrgeometer	Eppley (model PIR) [®]
K↓(o,par)	μmols ⁻¹ m ⁻²	quantum sensor	Li-Cor (Li-190SB) [§]
K↓(z,par)	μmols ⁻¹ m ⁻²	quantum sensor	Li-Cor (Li-192SA) [§]
T _a , T _s , T _i	°C	thermocouple	Cu-Co (24 AWG)
U	ms ⁻¹	3-cup anemometer	Gill (model 12102) ^{**}
Azm.	°	micro-vane	Gill (model 12302) ^{**} and RMYoung Wind Monitor (model 05305-AQ)
RH	%	relative humidity probe	Campbell Scientific (Model 207) [‡] and Vaisala (Model HMP35CF) [*]

[†] only at FYI'92 and MYI'93

[®] McVan Instruments Pty Ltd, Mulgrave, Victoria, Australia

[®] The Eppley Laboratory, Inc., 12 Sheffield Ave., Newport, R.I., USA

[§] Li-Cor Instruments, 4421 Superior Street, Lincoln, Ne, USA

^{**} R.M. Young Co., 2801 Aero-Park Drive, Traverse City, Mi, USA

[‡] Campbell Scientific Canada Corp., 9525 41st Ave., Edmonton. At., Canada

^{*} Vaisala, Inc., Woburn, MA., USA

Table A3.2 Sampling rate and duration (Julian Days) of the components of the microclimate and physical property data set. NA indicates that data are not available.

Category	Var.	Rate	FYI'92	FYI'93	MYI'93	FYI'95	MYI'95
Microclimate	Q*	3/15	107-177	121-170	124-169	106-168	107-168
Microclimate	K↓	3/15	107-177	115-170	124-169	106-168	107-168
Microclimate	K↑	3/15	107-177	121-170	124-169	106-168	107-168
Microclimate	L↓	3/15	107-177	NA	124-169	106-168	107-168
Microclimate	L↑	3/15	112-177	117-170	124-169	106-168	107-168
Microclimate	Ta	1/15	107-177	121-170	123-169	106-168	108-168
Microclimate	Ts	5/15	107-177	113-170	115-169	106-168	108-168
Microclimate	Ti	5/15	107-177	112-170	115-169	106-168	108-168
Microclimate	u	1/15	117-177	121-170	124-169	106-168	107-168
Microclimate	azm	1/15	112-177	121-170	124-169	113-168	NA
Microclimate	K↓ _{z,per}	3/15	107-177	119-170	124-169	106-168	NA
Microclimate	RH	3/15	156-177	121-170	124-169	106-168	107-168
Microclimate	K↓ _{o,per}	3/15	NA	NA	124-169	107-168	NA
Phys. Prop.	Hs	daily	105-177	112-170	112-170	108-162	108-169
Phys. Prop.	snow property	days ^a	105-169	120-165	119-164	108-155	109-156
Phys. Prop.	sea ice property	days ^a	105-169	120-165	119-164	108-155	109-156

[§] Rate is given as sampling rate and averaging period (seconds/minutes) for the microclimate variables.

Note that 30 minute averages were used during FYI'92.

^a The sampling frequency for snow and sea ice physical properties is described in the text.

Table A3.3 Manufacturer's specification for sensor accuracy.

Sensor	Specification
microvane	±5°
relative humidity probe (CSI Model 207) ¹	±5%
relative humidity probe (Vasaila Model HMP35CF) ²	±3%
3-cup anemometer	±2%
Type T thermocouple	±0.4%

¹ Over a 12% to 100% humidity range.

² Manufacturer's specification at 20°C. Temperature dependence is ±0.4% RH/°C

Table A3.4 Waveband and sensitivities of radiometers used during the SIMMS spring experiments. Source: Latimer (1972).

Radiometer	Wavelength Band (μm)	RMSE Measurement Error(%)
Eppley (PSP)	0.285-2.80	2.3
Eppley (B&W)	0.280-2.800	3.6
Eppley (PIR)	4.00-50.00	3.7
Middleton Pyrradiometer (CN1)	0.300-60.00'	3.4
Li-Cor (LI-190SA)	0.400-0.700	8.4 ¹
Li-Cor (LI-192SA)	0.400-0.700	8.4 ¹

¹ Source: Li-Cor (1991).

Table A3.5 Measurement height above the snow surface.

Variable	FYI'92	MYI'93	FYI'93	MYI'95	FYI'95
T _{a1}	0.86	1.05	1.76	0.44	0.79
T _{a2}	1.56	1.68	2.56	0.85	1.65
T _{a3}	2.56	2.93	5.08	1.71	2.51
T _{a4}	5.06	5.43	10.06	2.46	5.15
T _{a5}	10.06	10.43	-	5.05	
RH1	1.5	1.0	2.0	1.0	1.3
RH2	-	2.3	-	2.0	2.0
U ₁	2.07	0.92	1.81	0.54	0.55
U ₂	2.82	1.42	2.56	1.43	1.52
U ₃	5.32	2.47	5.07	2.17	2.49
U ₄	10.32	5.01	10.35	5.11	4.98
U ₅	-	10.02	-	-	-
Azm	10.00	10.70	10.35	-	5.5
Q*	8.9	7.9	7.9	4.90	4.92
K \downarrow	1.5	1.5	1.5	1.33	1.35
K \uparrow	8.9	7.9/2.3	7.9/2.0	4.9	4.92
L \downarrow	1.5	1.5	1.5	-	-
L \uparrow	8.9	2.3	2.0	4.9	4.92
K \downarrow_{par}	-	1.5	-	-	1.35

Table A3.6 Distance of snow sensor above the snow/ice interface (cm) for sensor arrays in (a) SIMMS'92, (b) SIMMS'93, and (c) SIMMS'95.

a) 1992

	Sensor	FYIA	FYIB	FYIC	FYID
Surface					
	9	40.0	41.0		
	8	35.0	36.0		
	7	30.0	31.0		
	6	25.0	26.0	26.0	26.0
	5	18.0	21.0	21.0	21.0
	4	12.0	16.0	16.0	16.0
	3	9.0	11.0	11.0	11.0
	2	6.0	5.0	6.0	6.0
Snow/Ice					
	1	1.0	1.0	1.0	1.0

b) 1993

	Sensor	FYIA	FYIB	Melt Pond MYI	Hummock MYI
Surface					
	22			65.9	
	21			62.7	
	20			59.7	
	19			56.7	
	18			53.3	
	17			49.8	
	16			46.8	
	15			44.1	
	14			40.6	
	13			37.9	
	12			34.5	
	11	33.0	32.4	31.5	
	10	29.5	29.4	28.5	
	9	26.5	26.2	25.5	
	8	23.5	23.2	22.3	
	7	20.5	19.7	19.1	
	6	17.5	16.5	16.5	
	5	14.3	13.5	13.5	
	4	11.1	10.5	10.5	10.7
	3	5.6	7	7.1	7.2
	2	3.8	3.8	3.5	4
Snow/Ice					
	1	1	1	1	1

c) 1995

	Sensor	FYI	Melt Pond MYI	Hummock MYI
Surface				
	11		50.2	
	10		45.6	
	9		40.6	
	8	37.9	35.6	
	7	32.1	30.6	
	6	27.6	25.6	
	5	22.8	20.8	
	4	17.3	15.6	
	3	12.3	11.8	
	2	7.0	7.6	5.9
Snow/Ice				
	1	1.7	0.9	1.1

Table A3.7 Positioning of Ice temperature sensors during 1992, 1993 and 1995.

Sensor	1992	1993 FYI	1993 MYI		1995 FYI	1995 MYI	
			MP	HK		MP	HK
1	5	3	3	3	5	5	5
2	10	8	8	8	10	10	10
3	15	13	13	13	25	15	25
4	20	18	28	28	50	25	50
5	30	28	53	53	100	50	100
6	55	53	103	103		100	150
7	80	78	203	153		150	
8	105	103	253	203			
9	130			253			

Table A3.8 Variables measured during the snow physical property sampling program.

Variable	Unit	Method
depth	cm	graduated stake
profile description	nominal data	photographic
density	kgm ⁻³	gravimetric
salinity	ppt	optical salinometer
wetness	% liquid by volume	dielectric
grain size	mm	photography
grain shape	nominal data	photography

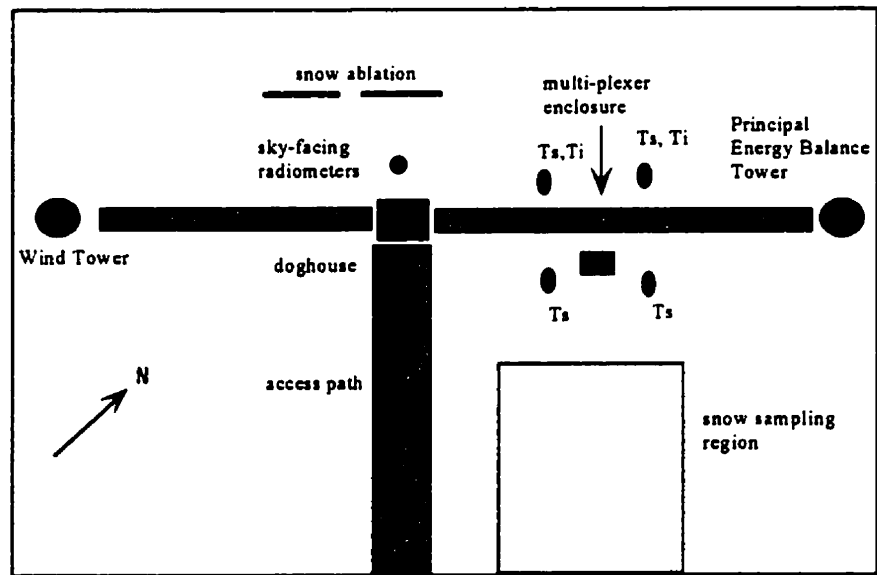


Figure A3.1 Plan view schematic of typical microclimatological site. Note that the sketch is not drawn to scale but the distance between the principal energy balance tower and the doghouse represented approximately 30 m.

APPENDIX 4: UNCERTAINTY ASSOCIATED WITH TEMPERATURE AND WIND SPEED MEASUREMENTS

A4.1 Introduction

During the SIMMS experiments, the signals from the air temperature thermocouples were logged directly by CR21X dataloggers (using panel temperature as thermocouple reference) while the snow/ice temperature thermocouples were channeled through multiplexers (Campbell Scientific model AM30 and AM416). Thermistors (Fenwall UUA 41J1) were attached flush to the multiplexer wiring panel to serve as the multiplexer temperature reference. The CR21X data loggers recorded wind speeds.

The error in a temperature measurement using a thermocouple is the sum of the errors in the reference temperature, the thermocouple output, the recording of the thermocouple voltage output, and the polynomial approximation for the voltage/temperature conversion. The first two components contribute to most of the total measurement error (Campbell Scientific Ltd., 1994). Premium thermocouple cable (Type-T) is specified to within 0.5°C or 0.4% over the specified temperature range. In the case where the reference junction temperature is close to the junction temperature, the thermocouple accuracy should be closer to the percentage error than to the fixed error. Campbell Scientific Inc. (1992) suggest adding 0.25% to the percentage error as a reasonable estimate for thermocouple accuracy. The internal temperature reference of the CR21X is typically within $\pm 0.2^\circ\text{C}$ (Campbell Scientific Inc.). The manufacturer specifies the accuracy of the Gill 3-Cup anemometers used in the studies to be within 2%. Both laboratory and field assessment of the temperature sensors were performed, while only a field calibration of anemometers was performed.

A4.2 Procedure

A4.2.1 Laboratory Matching of Sensors

Prior to SIMMS '92, the precision and accuracy of the thermistors which served as the temperature reference for the multiplexers, and a sample of the thermocouple sensors were assessed. The objective of the analysis process was to assess (1) the accuracy of the resistance-temperature polynomial transformation of the thermistor beads, (2) the accuracy of thermocouple sensor when logged to a CR21X data logger, and (3) the degree to which the thermocouple sensors were matched. In cases one and two, the accuracy is assessed relative to a platinum resistance thermometer (Guildline, model 9540) within a refrigerated bath of circulated glycol. According to the manufacturer's specification, the resolution of the platinum resistance thermometer (hereafter, PRT) is 0.001°C , with a time constant of 5-s. The manufacturer's standardized resistance temperature curve was used to define the polynomial transformation necessary to convert the resistance across our reference thermistors to temperature. The resistance across each thermistor in the bath was measured using a Keithly 4.5 digit multimeter (model 177), with a resolution of 0.04% in the 200 k Ω range. Campbell Scientific Inc. (model 107 probe) manufactured the third type of temperature reference used in the SIMMS experiments. The temperature of the 107 probe, and of each thermocouple was recorded by a CR21X datalogger.

Temperature and resistance measurements were taken at bath temperatures of -12, -6, -4, -2, and 3 $^{\circ}\text{C}$. The bath was allowed to equilibrate between four to five hours after the bath temperature was adjusted. The bath temperature ranged between -12 and 26 $^{\circ}\text{C}$ during the assessment of our thermocouple sensors, however the bulk of the measurements were made at temperatures above 0 $^{\circ}\text{C}$. The fact that the bulk of the calibration data for the thermocouple sensors was collected under relative warm conditions should not bias the assessment of the sensors because the relationship between temperature and voltage for a Type T thermocouple is nearly linear over an environmental temperature range.

A4.2.2 Field Matching of Sensors

The air temperature sensors, within their respective ventilated radiation shields, were matched outdoors over a snow-covered field north of the University of Waterloo. The experiment

was performed under a clear to scattered sky, between the mid-morning and mid-afternoon. The sensor housings were mounted side-by-side on a wooden beam (4"x4"), held horizontal at a height of 1.2 m from the ground surface. The sensors were spaced 30 cm apart. Two types of similar radiation shields were used during the SIMMS experiments. One type of shields contained an inner lining of foam, while the other type did not. Only shields of similar design were used for any air temperature profile.

A similar procedure was following for the Gill 3-Cup anemometers used in the SIMMS experiments. The anemometers were spaced 50 cm apart, and the horizontal beam was oriented perpendicular to the prevalent wind direction. Both the air temperature and wind speed sensors were logged to CR21X data loggers, and the data were recorded as five minute averages.

A4.3) Results and Discussion

It was difficult to maintain a stable bath temperature over the time necessary to record the resistance and temperature measurements. The problem was so severe that the calibration data of the thermistors corresponding to bath temperatures of -12 and -4°C were removed from the analysis. The remaining calibration data is provided as Table 4A2.1 and is summarized in Table A4.2. Two minutes separated each series of measurements at a specific temperature. The mean biases of the thermistors are very small and the root mean square errors are typically within 0.1°C.

The temperature of the calibration bath, as measured using the PRTs and thermocouple sensors, is summarized in Table A4.3. The thermocouple response was assessed relative to the average of two PRTs that were situated at opposite ends of the calibration bath. The analysis shows the thermocouple temperatures to contain very little systematic bias (i.e., within $\pm 0.03^\circ\text{C}$), while the random, or root mean square errors, are within 0.07 °C.

Tables A4.5a and b contain the response of a sample of the thermocouple sensors over a temperature range between -12°C and 27°C. The sensors incorporated into each table were made from one of two rolls of premium thermocouple cable and are termed *red*, and *blue*, respectively. The data are summarized in Table A4.6.

Table A4.1 Calibration of thermistor temperature references, Tr1 to Tr3. R1 and R2 are the resistances associated with Tr1 and Tr2, and Tr3 is the temperature of the 107 probe. diff1 to diff3 is the difference between the temperature measurement using the thermistor, and the temperature of the PRT. All temperatures are in °C.

Bath	PRT	R1 (kΩ)	R2 (kΩ)	Tr1	Tr2	Tr3	diff1	diff2	diff3
-6	-6.380	45.40	45.70	-6.292	-6.417	-6.520	0.0876	-0.0368	-0.1400
-6	-6.561	46.30	46.10	-6.663	-6.581	-6.531	-0.1018	-0.0202	0.0302
-6	-6.782	46.90	46.70	-6.905	-6.825	-6.964	-0.1233	-0.0428	-0.1815
-6	-6.802	46.40	46.41	-6.703	-6.708	-6.980	0.0985	0.0945	-0.1779
-6	-6.598	46.20	46.50	-6.622	-6.744	-6.606	-0.0241	-0.1460	-0.0079
-2	-2.092	36.79	36.50	-2.268	-2.115	-2.052	-0.1763	-0.0228	0.0400
-2	-2.450	36.97	36.85	-2.363	-2.300	-2.541	0.0871	0.1501	-0.0910
-2	-1.855	36.25	36.14	-1.981	-1.922	-1.791	-0.1264	-0.0674	0.0640
-2	-2.260	36.78	37.07	-2.263	-2.415	-2.379	-0.0030	-0.1552	-0.1190
-2	-2.120	36.35	36.43	-2.035	-2.078	-2.076	0.0851	0.0424	0.0440
3	2.959	28.17	28.28	2.992	2.914	2.989	0.0333	-0.0447	0.0300
3	2.887	28.23	28.02	2.950	3.099	2.789	0.0627	0.2123	-0.0980
3	2.815	28.24	28.32	2.943	2.886	2.790	0.1276	0.0710	-0.0250
3	3.062	28.07	28.02	3.064	3.099	3.022	0.0016	0.0373	-0.0400
3	3.005	28.19	28.36	2.978	2.858	2.886	-0.0269	-0.1473	-0.1190

Table A4.2 Mean biased error and root-mean square error of temperature references (°C).

stat	T1	T2	T3
rmse	0.092	0.104	0.097
mbe	0.000	-0.005	-0.053

Table A4.3 Calibration data for sample air thermal couple sensors (°C). Note, Ave, is the average of the PRT responses.

Interval	PRT1	PRT2	Ave	T1	T3	T5	T7	diff1	diff3	diff5	diff7
1	1.455	1.998	1.727	1.742	1.689	1.644	1.668	0.015	-0.038	-0.083	-0.059
2	1.499	2.054	1.777	1.756	1.711	1.658	1.683	-0.021	-0.065	-0.119	-0.093
3	4.988	5.293	5.141	5.140	5.059	5.181	5.175	-0.001	-0.082	0.040	0.034
4	5.079	5.409	5.244	5.251	5.168	5.272	5.272	0.007	-0.076	0.028	0.028
5	9.829	10.067	9.948	9.989	9.907	10.018	9.995	0.041	-0.041	0.070	0.047
6	9.921	10.157	10.039	10.086	10.025	10.101	10.107	0.047	-0.014	0.062	0.068
7	14.875	15.067	14.971	15.001	14.968	15.022	15.013	0.030	-0.003	0.051	0.042
8	14.889	15.089	14.989	15.035	14.995	15.050	15.054	0.046	0.006	0.061	0.065
9	19.805	19.967	19.886	19.971	19.950	19.989	19.992	0.085	0.064	0.103	0.106
10	19.981	19.981	19.981	19.978	19.956	19.989	19.987	-0.003	-0.025	0.008	0.006

Table A4.4 Mean biased error and root-mean square error of sample thermocouple sensors (°C).

<i>stat</i>	<i>T1</i>	<i>T3</i>	<i>T5</i>	<i>T7</i>
rmse	0.039	0.050	0.070	0.062
mbe	0.025	-0.027	0.022	0.024

Table A4.5a Comparison of sample 'blue' thermocouple sensors (°C) over a temperature range.

<i>Interval</i>	<i>Roll.</i>	<i>T1</i>	<i>T2</i>	<i>T3</i>	<i>T4</i>	<i>T5</i>	<i>max diff</i>
1	Blue	-11.86	-11.85	-11.86	-11.9	-11.81	0.09
2	Blue	-12.14	-12.13	-12.17	-12.19	-12.11	0.08
3	Blue	-10.6	-10.59	-10.64	-10.63	-10.62	0.05
4	Blue	-7.88	-7.87	-7.88	-7.87	-7.87	0.01
5	Blue	-6.862	-6.834	-6.818	-6.821	-6.792	0.07
6	Blue	6.629	6.636	6.63	6.613	6.615	0.023
7	Blue	6.41	6.42	6.416	6.392	6.416	0.028
8	Blue	6.7	6.707	6.702	6.678	6.7	0.029
9	Blue	9.38	9.38	9.38	9.35	9.36	0.03
10	Blue	9.36	9.36	9.36	9.33	9.3	0.06
11	Blue	10.8	10.79	10.77	10.75	10.72	0.08
12	Blue	12.41	12.42	12.42	12.39	12.38	0.04
13	Blue	12.75	12.76	12.75	12.71	12.68	0.08
14	Blue	14.63	14.63	14.62	14.59	14.55	0.08
15	Blue	18.73	18.74	18.74	18.73	18.7	0.04
16	Blue	20.48	20.49	20.5	20.49	20.47	0.03
17	Blue	23.13	23.14	23.16	23.14	23.09	0.07
18	Blue	26.57	26.58	26.59	26.58	26.56	0.03
19	Blue	26.56	26.57	26.61	26.6	26.58	0.05
20	Blue	26.59	26.6	26.63	26.62	26.6	0.04
21	Blue	26.76	26.77	26.78	26.78	26.77	0.02
22	Blue	26.75	26.76	26.77	26.76	26.75	0.02
23	Blue	26.73	26.74	26.74	26.73	26.72	0.02
24	Blue	26.44	26.44	26.43	26.43	26.41	0.03
25	Blue	26.38	26.37	26.36	26.36	26.34	0.04
26	Blue	26.39	26.38	26.37	26.37	26.35	0.04
27	Blue	26.38	26.38	26.36	26.35	26.34	0.04

Table A4.5b Comparison of sample 'red' thermocouple sensors (°C) over a temperature range.

<i>Interval</i>	<i>Roll</i>	<i>Ta1</i>	<i>Ta2</i>	<i>Ta3</i>	<i>Ta4</i>	<i>max. diff</i>
1	Red	-11.84	-11.82	-11.82	-11.85	0.03
2	Red	-12.16	-12.16	-12.16	-12.18	0.02
3	Red	-12.1	-12.12	-12.12	-12.14	0.04
4	Red	-11.65	-11.66	-11.66	-11.68	0.03
5	Red	-10.64	-10.66	-10.64	-10.66	0.02
6	Red	-7.82	-7.83	-7.85	-7.86	0.04
7	Red	-6.117	-6.128	-6.155	-6.11	0.045
8	Red	1.097	1.096	1.12	1.092	0.028
90	Red	1.605	1.625	1.624	1.588	0.037
10	Red	2.129	2.124	2.133	2.118	0.015
11	Red	6.593	6.586	6.587	6.576	0.017
12	Red	6.371	6.359	6.358	6.344	0.027
13	Red	6.65	6.641	6.641	6.628	0.022
14	Red	9.33	9.32	9.32	9.31	0.02
15	Red	9.31	9.3	9.29	9.27	0.04
16	Red	10.72	10.69	10.7	10.7	0.03
17	Red	12.36	12.35	12.35	12.33	0.03
18	Red	12.69	12.7	12.69	12.67	0.03
19	Red	14.59	14.62	14.63	14.63	0.04
20	Red	18.74	18.75	18.75	18.74	0.01
21	Red	20.49	20.52	20.54	20.54	0.05
22	Red	23.17	23.18	23.19	23.19	0.02
23	Red	26.58	26.57	26.57	26.56	0.02
24	Red	26.61	26.6	26.59	26.58	0.03
25	Red	26.64	26.63	26.64	26.63	0.01
26	Red	26.78	26.79	26.79	26.79	0.01
27	Red	26.76	26.76	26.77	26.76	0.01
28	Red	26.73	26.74	26.75	26.74	0.02
29	Red	26.42	26.42	26.43	26.43	0.01
30	Red	26.34	26.34	26.35	26.35	0.01
31	Red	26.35	26.35	26.36	26.36	0.01
32	Red	26.35	26.34	26.35	26.35	0.01

Table A4.6 Average of the maximum difference of sample air temperature sensors within calibration bath (°C).

<i>Roll</i>	<i>Average of max. diff.</i>
blue	0.045
red	0.024

The analysis indicates that the sensors manufactured from a roll of thermocouple cable are matched to within $\pm 0.045^\circ\text{C}$.

The results of the field assessment of the thermocouple sensors within the two types of ventilated radiation shields are provided in Table A4.7 and A4.8, respectively. The average (and standard deviation) of the maximum difference between the sensors within the radiation shield with foam inserts are 0.102°C , and 0.050°C respectively, while those sensors within the shields without foam inserts were matched to within 0.113°C and 0.069°C , respectively.

The results of the field assessment of the anemometers are provided in Table A4.9. The average of the maximum difference between sensors within the 5 minute averaging periods is $0.24\text{ m}\cdot\text{s}^{-1}$ ($\pm 0.08\text{ m}\cdot\text{s}^{-1}$).

A4.4 Summary

The thermistors, which acted as the temperature references for the snow and ice thermocouple sensors are accurate to within approximately $\pm 0.1^\circ\text{C}$. The thermocouple couple sensors themselves are shown to be accurate to within $\pm 0.07^\circ\text{C}$, when logged to a CR21X datalogger, and well matched (i.e., within $\pm 0.045^\circ\text{C}$) relative to other sensors manufactured from the same spool of cable. The RMSE associated with a multiplexed snow or ice temperature may be estimated as $\pm 0.122^\circ\text{C}$, which was obtained using:

$$\delta T_{s,i} \approx \left[\delta T_r^2 + \delta T_{TC}^2 \right]^{0.5}, \quad (\text{A1})$$

where δ denotes the uncertainty of the temperature reference ($\delta T_r \approx 0.1^\circ\text{C}$), and the thermocouple sensor ($T_{TC} \approx 0.07^\circ\text{C}$), respectively.

The air temperature sensors within ‘like’ types of ventilated radiation shields are shown to be matched to within 0.11°C while mounted at the same height, while the Gill 3-cup anemometers are typically within $0.24\text{ m}\cdot\text{s}^{-1}$.

Table A4.7 Field comparison of air temperature sensors (°C) with the foam inserts.

<i>Time</i>	<i>T1</i>	<i>T2</i>	<i>T5</i>	<i>T6</i>	<i>T9</i>	<i>min</i>	<i>max</i>	<i>diff</i>
1035	-5.536	-5.742	-5.803	-5.731	-5.557	-5.803	-5.536	0.267
1040	-5.77	-5.875	-5.827	-5.734	-5.679	-5.875	-5.734	0.141
1045	-5.739	-5.737	-5.737	-5.663	-5.582	-5.739	-5.663	0.076
1050	-5.88	-5.877	-5.84	-5.777	-5.731	-5.88	-5.777	0.103
1055	-5.873	-5.898	-5.791	-5.715	-5.606	-5.898	-5.715	0.183
1100	-5.724	-5.679	-5.689	-5.634	-5.533	-5.724	-5.634	0.09
1105	-5.789	-5.813	-5.736	-5.657	-5.622	-5.813	-5.657	0.156
1110	-5.783	-5.784	-5.727	-5.665	-5.625	-5.784	-5.665	0.119
1115	-5.68	-5.67	-5.632	-5.591	-5.528	-5.68	-5.591	0.089
1120	-5.563	-5.554	-5.479	-5.46	-5.329	-5.563	-5.46	0.103
1125	-5.494	-5.464	-5.458	-5.433	-5.191	-5.494	-5.433	0.061
1130	-5.325	-5.319	-5.268	-5.271	-5.071	-5.325	-5.268	0.057
1135	-5.376	-5.378	-5.345	-5.312	-5.074	-5.378	-5.312	0.066
1140	-5.256	-5.232	-5.208	-5.17	-5.004	-5.256	-5.17	0.086
1145	-5.35	-5.346	-5.288	-5.26	-5.182	-5.35	-5.26	0.09
1150	-5.38	-5.385	-5.323	-5.304	-5.173	-5.385	-5.304	0.081
1155	-5.244	-5.255	-5.203	-5.193	-5.113	-5.255	-5.193	0.062
1200	-5.16	-5.129	-5.126	-5.103	-4.984	-5.16	-5.103	0.057
1205	-5.039	-4.934	-4.933	-4.964	-4.671	-5.039	-4.933	0.106
1210	-5.209	-5.214	-5.119	-5.099	-4.92	-5.214	-5.099	0.115
1215	-5.12	-5.125	-5.087	-5.049	-4.976	-5.125	-5.049	0.076
1220	-5.027	-4.961	-4.914	-4.932	-4.673	-5.027	-4.914	0.113
1225	-4.976	-4.8	-4.723	-4.802	-4.286	-4.976	-4.723	0.253
1230	-4.817	-4.739	-4.744	-4.741	-4.563	-4.817	-4.739	0.078
1235	-4.681	-4.543	-4.486	-4.552	-4.251	-4.681	-4.486	0.195
1240	-4.849	-4.856	-4.784	-4.761	-4.696	-4.856	-4.761	0.095
1245	-4.785	-4.704	-4.647	-4.669	-4.4	-4.785	-4.647	0.138
1250	-4.937	-4.966	-4.933	-4.884	-4.662	-4.966	-4.884	0.082
1255	-4.517	-4.436	-4.424	-4.439	-4.165	-4.517	-4.424	0.093
1300	-4.583	-4.444	-4.412	-4.471	-4.163	-4.583	-4.412	0.171
1305	-4.569	-4.524	-4.472	-4.465	-4.249	-4.569	-4.465	0.104
1310	-4.658	-4.594	-4.539	-4.538	-4.32	-4.658	-4.538	0.12
1315	-4.632	-4.601	-4.508	-4.491	-4.332	-4.632	-4.491	0.141
1320	-4.451	-4.408	-4.387	-4.351	-4.245	-4.451	-4.351	0.1
1325	-4.519	-4.513	-4.556	-4.505	-4.347	-4.556	-4.505	0.051
1330	-4.676	-4.706	-4.648	-4.581	-4.326	-4.706	-4.581	0.125
1335	-4.514	-4.444	-4.36	-4.346	-4.211	-4.514	-4.346	0.168
1340	-4.385	-4.345	-4.317	-4.294	-4.105	-4.385	-4.294	0.091
1345	-4.473	-4.451	-4.439	-4.407	-4.23	-4.473	-4.407	0.066
1350	-4.424	-4.417	-4.426	-4.378	-4.167	-4.426	-4.378	0.048
1355	-4.438	-4.455	-4.453	-4.4	-4.22	-4.455	-4.4	0.055
1400	-4.469	-4.519	-4.51	-4.434	-4.361	-4.519	-4.434	0.085
1405	-4.456	-4.489	-4.452	-4.381	-4.309	-4.489	-4.381	0.108
1410	-4.418	-4.344	-4.286	-4.282	-4.049	-4.418	-4.282	0.136
1415	-4.266	-4.243	-4.263	-4.227	-4.061	-4.266	-4.227	0.039
1420	-4.381	-4.359	-4.326	-4.313	-4.191	-4.381	-4.313	0.068
1425	-4.307	-4.302	-4.33	-4.29	-4.163	-4.33	-4.29	0.04
1430	-4.445	-4.439	-4.429	-4.395	-4.374	-4.445	-4.395	0.05
1435	-4.54	-4.531	-4.553	-4.521	-4.36	-4.553	-4.521	0.032
1440	-4.423	-4.389	-4.342	-4.325	-4.255	-4.423	-4.325	0.098

Table A4.8 Field comparison of air temperature sensors (°C) without the foam inserts.

<i>Time</i>	<i>T3</i>	<i>T4</i>	<i>T7</i>	<i>T8</i>	<i>min.</i>	<i>max.</i>	<i>diff.</i>
1035	-5.556	-5.968	-5.662	-5.509	-5.968	-5.556	0.412
1040	-5.679	-5.849	-5.611	-5.510	-5.849	-5.611	0.238
1045	-5.583	-5.730	-5.556	-5.419	-5.730	-5.556	0.174
1050	-5.741	-5.857	-5.650	-5.578	-5.857	-5.650	0.207
1055	-5.736	-5.831	-5.610	-5.561	-5.831	-5.610	0.221
1100	-5.572	-5.658	-5.507	-5.418	-5.658	-5.507	0.151
1105	-5.655	-5.752	-5.562	-5.491	-5.752	-5.562	0.190
1110	-5.646	-5.735	-5.542	-5.486	-5.735	-5.542	0.193
1115	-5.531	-5.629	-5.462	-5.403	-5.629	-5.462	0.167
1120	-5.410	-5.493	-5.320	-5.287	-5.493	-5.320	0.173
1125	-5.347	-5.441	-5.297	-5.253	-5.441	-5.297	0.144
1130	-5.198	-5.275	-5.139	-5.113	-5.275	-5.139	0.136
1135	-5.247	-5.325	-5.197	-5.138	-5.325	-5.197	0.128
1140	-5.094	-5.180	-5.051	-4.994	-5.180	-5.051	0.129
1145	-5.197	-5.290	-5.138	-5.124	-5.290	-5.138	0.152
1150	-5.240	-5.331	-5.175	-5.145	-5.331	-5.175	0.156
1155	-5.109	-5.195	-5.062	-5.023	-5.195	-5.062	0.133
1200	-5.006	-5.085	-4.978	-4.929	-5.085	-4.978	0.107
1205	-4.851	-4.913	-4.848	-4.789	-4.913	-4.848	0.065
1210	-5.075	-5.138	-4.979	-4.995	-5.138	-4.979	0.159
1215	-4.995	-5.077	-4.945	-4.915	-5.077	-4.945	0.132
1220	-4.866	-4.898	-4.833	-4.802	-4.898	-4.833	0.065
1225	-4.770	-4.750	-4.744	-4.694	-4.770	-4.744	0.026
1230	-4.681	-4.674	-4.614	-4.610	-4.681	-4.614	0.067
1235	-4.535	-4.454	-4.439	-4.440	-4.535	-4.439	0.096
1240	-4.740	-4.776	-4.631	-4.651	-4.776	-4.631	0.145
1245	-4.630	-4.638	-4.551	-4.549	-4.638	-4.551	0.087
1250	-4.848	-4.890	-4.820	-4.771	-4.890	-4.820	0.070
1255	-4.371	-4.375	-4.362	-4.285	-4.375	-4.362	0.013
1300	-4.398	-4.369	-4.347	-4.356	-4.398	-4.347	0.051
1305	-4.434	-4.446	-4.365	-4.361	-4.446	-4.365	0.081
1310	-4.532	-4.493	-4.432	-4.447	-4.532	-4.432	0.100
1315	-4.510	-4.492	-4.396	-4.428	-4.510	-4.396	0.114
1320	-4.333	-4.338	-4.264	-4.237	-4.338	-4.264	0.074
1325	-4.425	-4.461	-4.415	-4.356	-4.461	-4.415	0.046
1330	-4.586	-4.627	-4.503	-4.491	-4.627	-4.503	0.124
1335	-4.364	-4.344	-4.270	-4.270	-4.364	-4.270	0.094
1340	-4.279	-4.280	-4.222	-4.194	-4.280	-4.222	0.058
1345	-4.374	-4.380	-4.328	-4.282	-4.380	-4.328	0.052
1350	-4.334	-4.363	-4.307	-4.249	-4.363	-4.307	0.056
1355	-4.351	-4.376	-4.338	-4.259	-4.376	-4.338	0.038
1400	-4.421	-4.461	-4.373	-4.321	-4.461	-4.373	0.088
1405	-4.401	-4.439	-4.318	-4.280	-4.439	-4.318	0.121
1410	-4.309	-4.286	-4.228	-4.197	-4.309	-4.228	0.081
1415	-4.187	-4.191	-4.160	-4.083	-4.191	-4.160	0.031
1420	-4.299	-4.313	-4.235	-4.189	-4.313	-4.235	0.078
1425	-4.251	-4.277	-4.233	-4.142	-4.277	-4.233	0.044
1430	-4.383	-4.403	-4.338	-4.276	-4.403	-4.338	0.065
1435	-4.503	-4.546	-4.512	-4.396	-4.546	-4.503	0.043
1440	-4.346	-4.358	-4.265	-4.230	-4.358	-4.265	0.093

Table A4.9 Field comparison of wind speed sensors ($m \cdot s^{-1}$).

Time	u2	u3	u4	u5	u6	u7	Ave	min	max	diff
1105	3.67	3.52	3.57	3.34	3.35	3.27	3.45	3.27	3.67	0.40
1110	4.40	4.23	4.27	4.21	4.13	4.26	4.25	4.13	4.40	0.27
1115	3.05	2.94	2.99	2.95	2.89	2.97	2.96	2.89	3.05	0.16
1120	4.14	4.03	4.12	4.07	4.08	4.17	4.10	4.03	4.17	0.14
1125	3.47	3.34	3.35	3.28	3.29	3.34	3.34	3.28	3.47	0.19
1130	3.53	3.41	3.43	3.37	3.35	3.40	3.42	3.35	3.53	0.19
1135	3.52	3.39	3.44	3.41	3.43	3.47	3.44	3.39	3.52	0.12
1140	3.72	3.58	3.66	3.64	3.63	3.69	3.65	3.58	3.72	0.14
1145	4.12	4.01	4.07	3.93	3.91	4.02	4.01	3.91	4.12	0.21
1150	3.64	3.55	3.61	3.55	3.54	3.64	3.59	3.54	3.64	0.11
1155	4.33	4.20	4.26	4.19	4.18	4.27	4.24	4.18	4.33	0.15
1200	4.45	4.32	4.36	4.24	4.18	4.29	4.31	4.18	4.45	0.27
1205	5.69	5.49	5.59	5.46	5.51	5.64	5.56	5.46	5.69	0.22
1210	5.04	4.87	4.93	4.83	4.84	4.98	4.91	4.83	5.04	0.21
1215	5.55	5.36	5.47	5.37	5.35	5.49	5.43	5.35	5.55	0.20
1220	5.83	5.61	5.67	5.58	5.45	5.69	5.64	5.45	5.83	0.39
1225	4.96	4.85	4.93	4.87	4.84	4.97	4.90	4.84	4.97	0.12
1230	6.11	5.90	5.94	5.87	5.86	6.02	5.95	5.86	6.11	0.26
1235	5.05	4.90	5.03	4.97	4.89	5.04	4.98	4.89	5.05	0.17
1240	6.03	5.77	5.88	5.84	5.84	6.02	5.90	5.77	6.03	0.26
1245	5.69	5.49	5.59	5.50	5.48	5.68	5.57	5.48	5.69	0.21
1250	5.58	5.37	5.46	5.31	5.30	5.47	5.42	5.30	5.58	0.28
1255	6.37	6.16	6.28	6.09	6.19	6.30	6.23	6.09	6.37	0.28
1300	5.71	5.50	5.62	5.50	5.46	5.65	5.58	5.46	5.71	0.25
1305	4.78	4.62	4.64	4.57	4.52	4.67	4.63	4.52	4.78	0.26
1310	4.86	4.68	4.77	4.66	4.58	4.72	4.71	4.58	4.86	0.28
1315	4.94	4.76	4.87	4.80	4.77	4.88	4.84	4.76	4.94	0.18
1320	5.32	5.19	5.29	5.20	5.18	5.31	5.25	5.18	5.32	0.14
1325	5.28	5.12	5.21	5.15	5.14	5.24	5.19	5.12	5.28	0.16
1330	5.82	5.59	5.68	5.56	5.57	5.71	5.65	5.56	5.82	0.26
1335	5.59	5.39	5.49	5.32	5.25	5.38	5.40	5.25	5.59	0.34
1340	5.46	5.24	5.36	5.26	5.22	5.37	5.32	5.22	5.46	0.25
1345	5.55	5.35	5.45	5.31	5.30	5.44	5.40	5.30	5.55	0.25
1350	5.99	5.74	5.81	5.69	5.61	5.75	5.77	5.61	5.99	0.38
1355	6.04	5.85	5.98	5.89	5.86	6.02	5.94	5.85	6.04	0.19
1400	5.13	4.97	5.07	4.97	4.96	5.06	5.03	4.96	5.13	0.18
1405	5.48	5.32	5.30	5.43	5.36	5.52	5.44	5.32	5.52	0.21
1410	5.31	5.12	5.23	5.13	5.10	5.23	5.19	5.10	5.31	0.21
1415	6.52	6.33	6.47	6.42	6.31	6.52	6.43	6.31	6.52	0.21
1420	5.53	5.35	5.45	5.37	5.33	5.47	5.42	5.33	5.53	0.20
1425	6.16	5.90	5.97	5.83	5.90	6.02	5.96	5.83	6.16	0.33
1430	6.24	6.05	6.15	6.03	5.93	6.08	6.08	5.93	6.24	0.31
1435	5.57	5.36	5.43	5.34	5.35	5.47	5.42	5.34	5.57	0.23
1440	6.17	5.98	6.10	5.96	5.95	6.08	6.04	5.95	6.17	0.23
1445	6.17	5.86	5.94	5.82	5.80	5.98	5.93	5.80	6.17	0.36
1450	6.65	6.43	6.63	6.42	6.35	6.54	6.50	6.35	6.65	0.30
1455	7.38	7.13	7.27	7.05	7.09	7.24	7.19	7.05	7.38	0.33
1500	5.67	5.46	5.54	5.42	5.34	5.50	5.49	5.34	5.67	0.33
1505	6.91	6.74	6.85	6.75	6.61	6.85	6.78	6.61	6.91	0.29
1510	6.26	6.05	6.13	6.03	5.99	6.19	6.11	5.99	6.26	0.27
1515	5.59	5.38	5.44	5.31	5.15	5.32	5.37	5.15	5.59	0.44
1520	5.77	5.57	5.67	5.61	5.58	5.71	5.65	5.57	5.77	0.21
1525	5.45	5.22	5.31	5.18	5.12	5.25	5.25	5.12	5.45	0.33

APPENDIX 5: STATISTICAL METHODS

A5.1 Introduction

In this Appendix I briefly review the statistical procedures and expressions which appear in Chapters 8 and 9 of the thesis body. I also provide a description of the Mean Bias Error and Root-Mean Square Error. Reference texts are referred to where appropriate.

A5.2 Mean Bias and Root Mean Square Error

The measure of variation between predicted and measured variables may be expressed using the Root-Mean Square Error (RMSE), and Mean Bias Error (MBE). The MBE is a measure of the average difference between the variables being compared:

$$MBE = \frac{\sum (y_i - x_i)}{N}, \quad (A5.1)$$

where y is the predicted variable and x is the modeled variable and N is the number of cases.

The RMSE describes the nonsystematic or random variation in the comparison:

$$RMSE = \left\{ \frac{\sum (y_i - x_i)^2}{N} \right\}^{\frac{1}{2}}. \quad (A5.2)$$

The RMSE is always positive and is susceptible to outliers (Iqbal, 1983). The two measures are related to the variance of the comparison through:

$$Var = (RMSE)^2 - (MBE)^2. \quad (A5.3)$$

A5.3 Pearson's Product Moment Coefficient of Correlation

Pearson's r is a 'standardized measure of linear covariance':

$$r = \frac{\text{cov}(XY)}{S_X S_Y} \quad (\text{A5.4})$$

where S_X and S_Y are the standard deviations of the variable sets X and Y , respectively (Sokal and Rolf, 1995). Any inferences regarding the relationship between populations require that the sample sets be normally distributed. The correlation coefficient ranges between ± 1 and may be computed no matter what the underlying distribution of X or Y is (Sokal and Rolf, 1995). The square of the correlation coefficient is the 'coefficient of determination' and is a direct measure of the proportion of the variance in a bivariate distribution explained by a linear correlation coefficient (Sokal and Rolf, 1995). The two variables in this case must be bivariate normal.

A5.4 Kruskal-Wallis and Mann-Whitney U-Test

The nonparametric²² analogue to the One-Way Analysis of Variance is the Kruskal-Wallis test. The test statistic is the expected value of the variance of the sums of ranks of each group (Sokal and Rolf, 1995). The premise of the test is that if populations are similar to each other, then we would expect their rank sums to be approximately the same (allowing for differences in sample size). The null hypothesis is that the groups do not differ in location. If it is true, the test statistic is distributed approximately as $\chi^2_{(k-1)}$. The alternate hypothesis is that ranks differ among groups. Location here refers to the rank-ordered positions of the individual elements of the samples along the measurement axis. Derivation of the test statistic is provided in most texts which overview nonparametric methods (e.g., Sokal and Rolf 1995; Conover, 1971). A Mann-Whitney U-test may be used if the test is between only two samples. The null hypothesis is that the two samples come from populations having the same location. The U statistic may be compared to the t-distribution for hypothesis testing (refer to Sokal and Rolf, 1995).

²² Nonparametric procedures are distribution-free, since they are not dependent on a given distribution. Their null hypothesis is not concerned with specific parameters of theoretical distributions.

A5.5 Principal Components Analysis

Principal Components Analysis (PCA) is a statistical technique which can be applied to a single set of variables when the researcher is interested in determining which variables in the set form subsets that are relatively correlated with one another, but independent of others (Tabachnick and Fidell, 1989). Variables that are correlated with one are combined into components. Mathematically, the components are linear combinations of observed variables. Several multivariate statistical textbooks provide excellent descriptions of the technique (e.g. Johnston, 1984; Johnson and Wichern, 1992; Tabachnick and Fidell, 1989).

The fundamental equation for PCA is:

$$\mathbf{R} = \mathbf{A}\mathbf{A}', \quad (\text{A5.5})$$

where:

$$\mathbf{A} = \mathbf{V}\sqrt{\mathbf{L}} \quad (\text{A5.6})$$

and the prime denotes its transpose and bolded letters denote matrices. In the above, \mathbf{L} and \mathbf{V} are the eigenvalue and eigenvector matrix ($m \times m$ and $p \times m$, respectively²³) of a correlation matrix, \mathbf{R} , between the original variables ($p \times p$ variables). \mathbf{A} is referred to as the component loading matrix ($p \times m$) and contains the correlations between the principal component and the original variables. A principal component is interpreted from the variables that are highly correlated with it, or in other words, have high loadings on it (Tabachnick and Fidell, 1989). The square of each loading indicates the percentage of the variation in the component accounted for by the respective variable. The sum of the squared loading for a principal component is equal to the eigenvalue. If the eigenvalue is large, the principal component closely resembles the original data. If the value is negative and large, the pattern of the principal component is similar to the original data, but opposite in sign. The effect or weight of the variable is considered trivial if a loading is less than 0.3 (Johnson and Wichern, 1992). The component loading matrix can subsequently be rotated to improve the interpretability of the result. There are a number of rotation methods available and in general each act to maximize high correlations and minimize low correlations (Tabachnick and Fidell, 1989).

The important point in Eq A5.5 is that all of the variance contained within the correlation matrix is condensed into eigenvalues. There can be as many principal components as there are

variables in the original variable set. Generally only those components whose eigenvalues are greater than unity, or, only those components which individually explain at least a proportion $1/p$ of the total variance provide information on the original data set (Johnson and Wichern, 1992). The goal of PCA is to extract maximum variance from the data set with each component. The principal component with the largest eigenvalue contains the most variance. The first principal component is the linear combination of observed variables that maximally separates subjects by maximizing the variance. The second component is the linear combination of observed variables that extracts maximum variability uncorrelated with the previous component, and so on to the m^{th} component.

Principal components may also be obtained by extracting eigenvectors and eigenvalues from the covariance matrix instead of the correlation matrix. In this case of the correlation matrix, the original variables are standardized (means of zero and standard deviations of one) prior to analysis. The standardized case (i.e., correlation matrix) is recommended if the variables contain vastly different ranges, or if the measurement units are not commensurate (Johnson and Wichern, 1992).

PCA is sensitive to the correlation matrix and therefore is important that reliable correlations are derived. Tabachnick and Fidell (1989) suggest that at least 5 cases are available for each observed variable. The technique is independent of assumptions regarding the distributions of the variables. Multicollinearity among the observed variables is also not a problem. They (Tabachnick and Fidell 1989) caution however that if substantial skewness and kurtosis are present, variable transformations should be considered. The analysis is not appropriate when non-linear relationships are suspected between variables.

A5.6 Canonical Correlation

Canonical correlation is a multivariate technique that seeks to reduce associations between two sets of variables (e.g., $X_1, X_2 \dots X_p$ and Y_1, Y_2, \dots, Y_q) to a few pairs of maximally correlated canonical variates, where each variate is made up of linear combinations of the original variables (Johnson and Wichern, 1992). The correlation between the variates is called canonical correlation (r_{cc}). Several authors (e.g. Johnson and Wichern, 1992; Tabachnick and Fidell, 1989) compare a

²³ m and p are the number of principal components and number of variables, respectively.

canonical correlation analysis to a multiple regression involving a number of dependent variables considered collectively. Canonical analysis extracts orthogonal vectors (canonical variates) from within each set of variables, such that the resultant linear combinations of the X set of variables is maximally correlated with the linear combination of the Y set of variables. When the influence of the first canonical pair is removed, the procedure is repeated until the number of vector pairs equals the number of variables in the smaller data set (i.e., p or q). Consequently the number of canonical correlation coefficients will be the smaller of p or q.

Canonical correlation solves for the eigenvalues and eigenvectors of the canonical correlation matrix:

$$\mathbf{R} = \mathbf{R}_{yy}^{-1} \mathbf{R}_{yx} \mathbf{R}_{xx}^{-1} \mathbf{R}_{xy}, \quad (\text{A5.7})$$

where \mathbf{R}_{yy} and \mathbf{R}_{xx} are the correlation matrices for the X and Y variable sets and \mathbf{R}_{xy} and \mathbf{R}_{yx} are the cross-correlations between the variable sets (Tabachnick and Fidell, 1989). The eigenvector that corresponds to the eigenvalue is transformed into the canonical coefficients that are used to transform the original variables into the canonical variates. Each eigenvalue is equal to the squared canonical correlation (r_c^2) between the pair of canonical variates. The canonical correlation is interpreted as a Pearson product-moment correlation coefficient. Its square (or the eigenvalue) represents the overlapping variance between the two canonical variates. Researchers usually disregard canonical pairs with canonical correlations less than 0.30 (i.e., less than 10% overlap in variance) (Tabachnick and Fidell, 1989).

Canonical coefficients are computed for the X and Y variable sets. The correlations between the variables, within a variable set, and a canonical variate are termed canonical loadings. The matrices of correlations between the variables and the canonical coefficients are called the loading matrices:

$$\mathbf{A}_x = \mathbf{R}_{xx} \mathbf{B}_x, \quad (\text{A5.8a})$$

and

$$\mathbf{A}_y = \mathbf{R}_{yy} \mathbf{B}_y, \quad (\text{A5.8b})$$

where \mathbf{B} are the canonical coefficients. As is the case in PCA, a variate is interpreted by considering the pattern of variables highly correlated (loaded) with it. Again, variables with loadings of 0.30 and above are usually interpreted (Tabachnick and Fidell, 1989).

A χ^2 -test can be used to test whether each canonical correlation differs from zero. The variance a canonical variate extracts from its own set of variables is described by the sum of squared loadings on a variate divided by the number of variables in the set. Another consideration is the variance a variate from one set extracts from the variables in the other set. This is called the redundancy (Tabachnick and Fidell, 1989) and is equal to the percent of variance the variate extracts from its own set of variables times the eigenvalue for the pair.

Tabachnick and Fidell (1989) outline limitations to the procedure. A canonical correlation examines linear relationship between the two sets of variables. If the relationship is curvilinear, the analysis will miss some or all of the relationship. The test of significance, cited above, assumes multivariate normality. That is, all variables, and all linear combination of variables are normally distributed. The procedure also assumes that the relationships among the pairs of variables are homoscedastic. Pearson's correlation coefficient assumes homoscedastic relationships. It is also important that variables within each variable set and across sets are not too highly correlated with each other. Incorporating variables that are highly correlated weaken the analysis by reducing the degrees of freedom for the χ^2 -test. Furthermore, the determinate of a correlation matrix showing multicollinearity is near zero, which will result in very large and unstable numbers in the inverted matrix. Matrix inversion is required for the derivation of the canonical coefficients (refer to Tabachnick and Fidell (1989), or any text which describe multivariate statistics).

APPENDIX 6: BROADBAND TO NARROWBAND IRRADIANCE CONVERSION

A6.1 Introduction

Proportionality coefficients are used to partition the measured global radiation into 22 wavebands. Spectral irradiance is necessary to model solar transmission through the snow layer at each site using the spectral analogue to Beers Law and to validate modeled spectral albedo and extinction coefficients.

A6.2 Methods

Average global radiation is available on an hourly basis at each site. The measured term is partitioned into 22 spectral wavebands between 0.36 μm and 4.0 μm using a set of proportionality coefficients. Each coefficient per waveband is estimated as the ratio of modeled global radiation (i.e. diffuse and direct beam) per waveband to a spectrally integrated (0.36 μm to 4 μm) estimate using the atmospheric radiative transfer model, STREAMER (Key, 1996b). Similarly, coefficients describing the diffuse proportion of global radiation, per waveband were generated, as required for the estimate of net albedo.

STREAMER is a radiative transfer model that can be used for computing fluxes (Wm^{-2}) or radiative intensities over a wide variety of atmospheric and surface conditions. Cloud forcing and gaseous absorption can be parameterized for 24 short-wave and 105 long-wave bands for up to 48 atmospheric levels. STREAMER incorporates various built-in atmospheric models, including summer and winter Arctic Haze, and various surface types, including snow. Each computation is performed for a *scene*, where the scene can be a mixture of up to 8 individual cloud types, and up to 4 overlapping cloud pairs or clear sky.

Categories of coefficients representing six different sky types are computed and the category that most closely resembled the observed and recorded sky condition for each day during the mid-afternoon was used and applied over the entire diurnal cycle. In the event that observed sky conditions are unavailable, a sky category was selected base on the comparison of measured global radiation (12:00 LAT) and STREAMER's modeled global radiation. That is, the category of spectral proportion coefficients for which simulated global radiation most closely corresponds to measured midday K_{\downarrow} . This is a crude approach, but bear in mind that the purpose is not to model global radiation, rather to generate a set of coefficients from which measured global radiation can be partitioned into finer spectral intervals.

The proportionality coefficients are generated as follows. STREAMER is initialized to its default arctic winter atmospheric temperature and humidity profile with a background tropospheric and stratospheric aerosol loading typical of arctic haze conditions (Key, 1996b). The model is run for six different sky climatologies, and six different categories of coefficients are generated to describe the spectral proportion of global radiation, and diffuse component of global radiation over the 22 wavebands for Resolute (74° 45' N, 94° 59' W), at solar noon, for the dates: 15-April (day 107), 15-May (day 135), and 15-June (day 166). STREAMER's four-stream short-wave option for irradiance fluxes rather than intensities are used. Key (1996b) notes that little gain in accuracy is obtained by using more than four streams for the evaluation of the short-wave fluxes. Iterative runs of the program were performed using the sky climatology: (i) clear sky, (ii) five-tenths high alto-stratus, (iii) five-tenths low stratus, (iv) full alto-stratus cover, (v) full thin stratus cover, and (vi) full thick stratus cover. Background atmospheric parameters that are used during the STREAMER simulations are provided in Table A6.1a. Cloud parameters and modeled global radiation are provided in Table A6.1b.

Table A6.1a Background atmospheric parameters and solar zenith angles (°) used during the STREAMER simulations.

Variable	Value
background water - column total (g m^{-2})	2008.98
background ozone - column total (g m^{-2})	7.57
Aerosol Optical Depth	0.08
Zenith Angle - April 15	62.3
Zenith Angle - May 15	56.1
Zenith Angle - June 15	51.5

Table A6.1b Cloud parameters used for the different STREAMER simulations, and modeled solar noon global radiation for the 15th day of each spring month. In the table; clr = clear-sky, as-part = 5/10ths altostratus, str-part = 5/10ths thin stratus, as = altostratus, t-str = thin stratus, h-str = thick stratus.

Variable	clr	as-part	str-part	as	t-str	h-str
Cloud Thickness (m)	-	184.	250	184	250	250
Cloud Optical Depth	-	2.2	3.2	2.2	3.2	9.2
Cloud liquid water content (g m^{-3})	-	0.06	0.09	0.06	0.09	0.21
Drop diameter (μm)	-	8.0	11.	8.0	11	9.0
Base height (km)	-	3.7	0.10	3.7	250	0.06
Sky-fraction	1	0.5	0.5	1	1	1
Modeled Global Rad. ($\text{W}\cdot\text{m}^{-2}$) - Apr	464.2	362.8	349.7	263.5	237.3	148.1
Modeled Global Rad. ($\text{W}\cdot\text{m}^{-2}$) - May	647.7	526.3	506.9	404.8	366.0	227.5
Modeled Global Rad. ($\text{W}\cdot\text{m}^{-2}$) - June	729.5	589.7	565.2	449.9	400.9	240.2

A6.3 Results

The simulated global radiation from each of the modeled runs is illustrated in Fig. A6.1a, b, and c. An example of the narrowband diffuse fraction of global radiation and the spectral proportion of global radiation over the waveband $0.3 \mu\text{m}$ to $4.0 \mu\text{m}$ is presented in Figs. A6.2 and A6.3 (a and b), respectively. The 22 wavebands are not of equal width, therefore there exist a difference in the form of the relations between the spectral proportion per waveband (Fig. A6.3a), and the normalized spectral proportion per μm at the waveband midpoints (Fig. A6.3b). For our application the proportionality coefficients per waveband are more convenient to work with (Fig. A6.3a).

The spectral dependence of the distribution of the diffuse component of global radiation exhibited in Fig. A6.2 agrees in form to curves presented by Grenfell et al.,(1994) for a clear sky

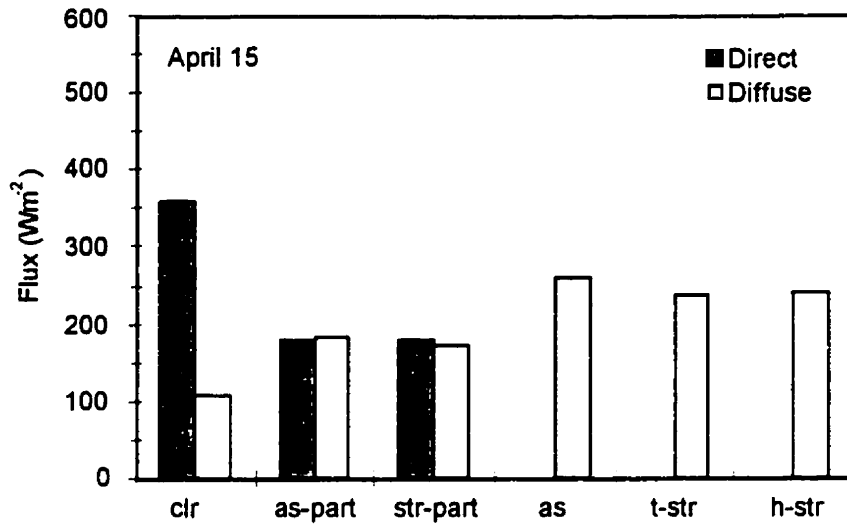


Figure A6.1a Simulated global radiation partitioned into its direct- and diffuse beam components for solar noon, 15-April. The category heading are the same as those used in Table A6.1b.

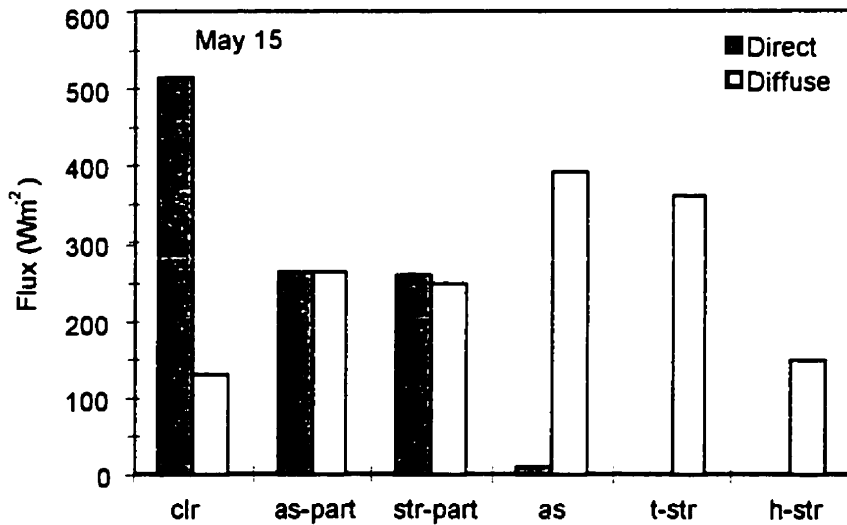


Figure A6.1b Simulated global radiation partitioned into its direct- and diffuse beam components for solar noon, 15-May. The category heading are the same as those used in Table A6.1b.

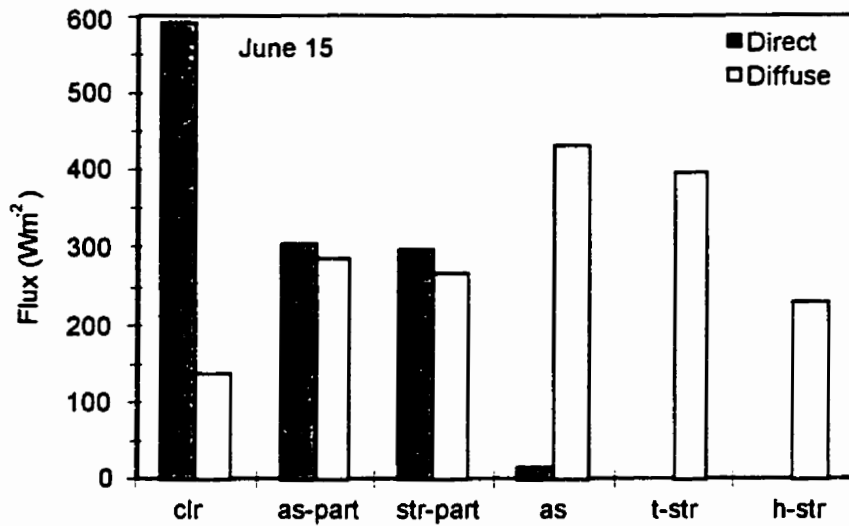


Figure A6.1c Simulated global radiation partitioned into its direct- and diffuse beam components for solar noon, 15-May. The category heading are the same as those used in Table A6.1b.

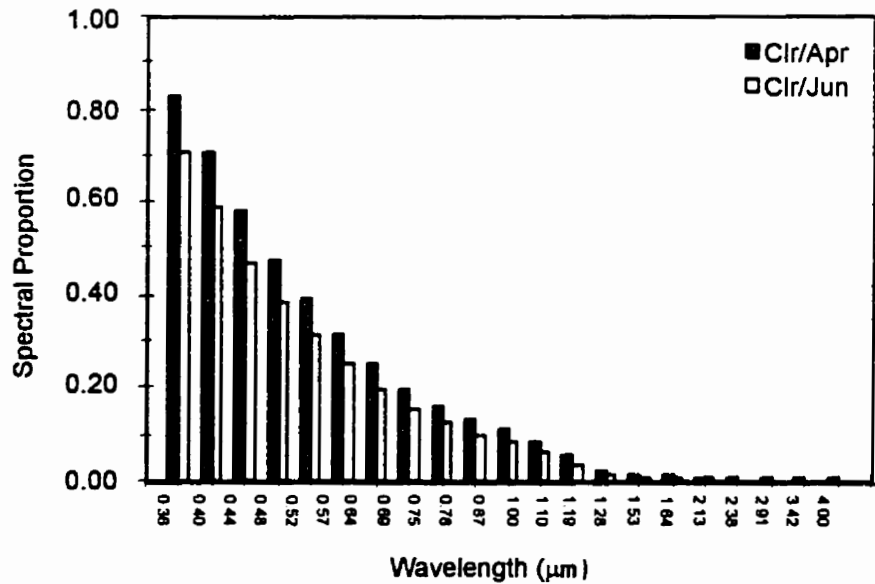


Figure A6.2 The spectral distribution of the diffuse component of global radiation, shown here under clear skies for 15-April, and 15-June.

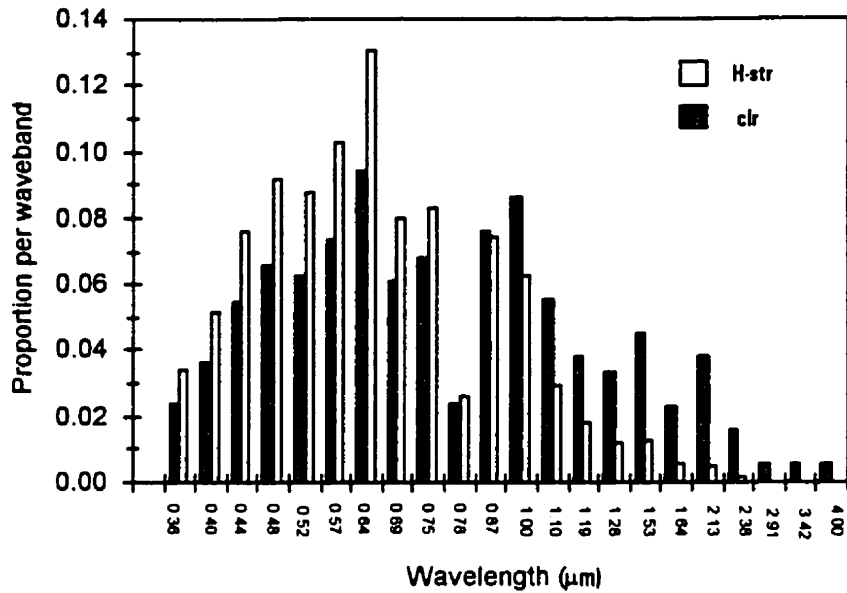


Figure A6.3a The modeled spectral proportion of global radiation per waveband for clear sky (clr) and heavy stratus cover (h-str) on June 15.

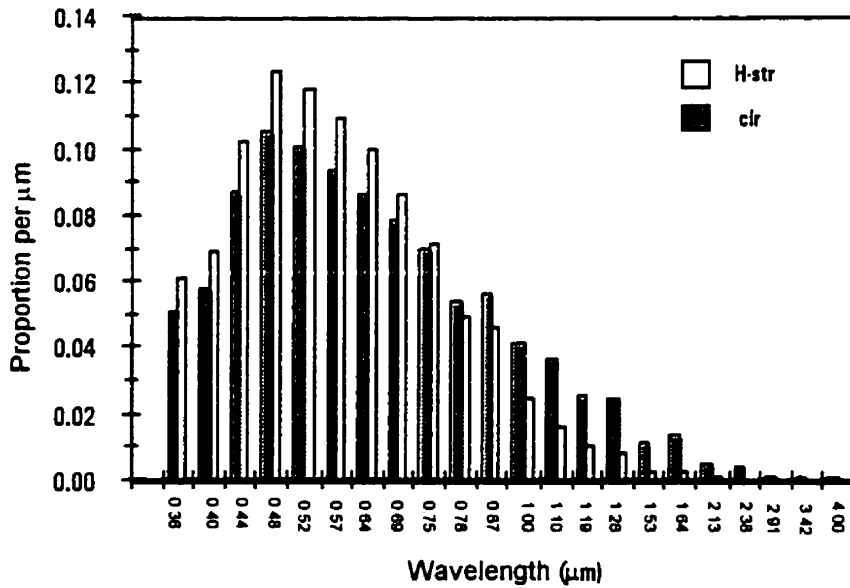


Figure A6.3b The modeled spectral proportion of global radiation per wavelength at the central wavelength of the respective wavebands for clear sky (clr) and heavy stratus cover (h-str) on June 15.

Antarctic atmosphere (their Fig. 8). In their study, atmospheric optical depth was 0.01 (compared to 0.08 here); consequently the diffuse component of global radiation for the shorter wavelengths in Fig. A6.2 are expected to be larger than those peak values reported by Grenfell et al.,(1994). For example, diffuse radiation constitutes greater than 70% of global radiation for the wavebands centred on 0.36 μm and 0.4 μm , whereas Grenfell et al.,(1994) report that approximately 45% of global radiation is diffuse over these wavelengths. The direct beam irradiance constitutes very little of global radiation during overcast conditions (Fig. A6.1a to c).

The spectral proportion of global radiation, normalized per μm at the central wavelength of each waveband (Fig. A6.3b), corresponds in form to published spectral irradiance curves by Grenfell and Perovich (1984) from Point Barrow, Alaska. The peak in global radiation occurs on the spectral interval centred at 0.47 μm . Clouds will skew the spectral proportions toward the shorter wavelengths. The changes are strongest in the infrared because the absorption of radiation by water vapor is largest in this region (Fig. A6.3). The coefficients are supplied in Table A6.2.

A6.4 Validation

The appropriateness of the coefficients is assessed by comparing the modeled radiation (coefficients applied to measured global radiation) in the 0.4 to 0.7 μm band against measured values of incident PAR (Table A6.4). PAR was continuously measured above the snow surface during SIMMS'93 and SIMMS'95.

Modeled irradiance in the PAR slightly overestimates measured incident PAR with average biases being within 3% of the average measured flux. Random errors are within approximately 10% of the measured flux and were generally less during SIMMS'95 (rmse=13.19 $\text{W}\cdot\text{m}^{-2}$ or 9.9% of the average flux) than in SIMMS'93 (rmse=9.11 $\text{W}\cdot\text{m}^{-2}$ or 7.3% of the average flux). The highest rmse corresponds to May of 1993 and represents 10.8% of the average of the measured flux.

A6.5 Summary

Spectral irradiance at the snow surface is derived for 22 wavelength intervals using a suite of coefficients applied to measured global radiation. The coefficients are determined using an atmospheric radiative transfer model for six different sky types and for atmospheres characteristic

of each of the three spring months. The resultant spectral distribution of global radiation agrees in form to published curves and the modeled flux with the 0.4 to 0.7 μm region is in most instances within 10% of a measured flux. The match between measured and modeled PAR is surprisingly good considering the crude methods involved in its computation. Modeled irradiance in the PAR slightly overestimated measured incident PAR by approximately 3%. Random errors are within approximately 10% of the measured flux

Table A6.2 Proportion of global radiation (fraction) within each waveband centered on wavelength, λ (μm) for each sky condition:
 clr=clear, h-part=high alto stratus (5/10 coverage), t-part=thin stratus (5/10 coverage), as=alto stratus, t-str=thin stratus, h-str=heavy stratus.

λ	clr			h-part			t-part			as			t-str			h-str		
	April	May	June															
0.33	0.0000	0.0000	0.0000	0.0000	0.0000	0.0000	0.0000	0.0000	0.0000	0.0000	0.0000	0.0000	0.0000	0.0000	0.0000	0.0000	0.0000	0.0000
0.36	0.0468	0.0428	0.0507	0.0503	0.0523	0.0533	0.0503	0.0523	0.0535	0.0560	0.0559	0.0571	0.0564	0.0563	0.0579	0.0589	0.0588	0.0612
0.40	0.0544	0.0574	0.0578	0.0577	0.0593	0.0604	0.0576	0.0594	0.0606	0.0630	0.0628	0.0643	0.0633	0.0631	0.0651	0.0659	0.0656	0.0687
0.44	0.0832	0.0864	0.0866	0.0870	0.0887	0.0902	0.0871	0.0888	0.0905	0.0932	0.0930	0.0954	0.0939	0.0935	0.0966	0.0974	0.0970	0.1017
0.48	0.1027	0.1052	0.1051	0.1065	0.1076	0.1093	0.1066	0.1078	0.1097	0.1125	0.1122	0.1154	0.1135	0.1130	0.1171	0.1178	0.1173	0.1234
0.52	0.0989	0.1008	0.1004	0.1018	0.1027	0.1043	0.1021	0.1030	0.1048	0.1064	0.1067	0.1099	0.1076	0.1078	0.1118	0.1117	0.1119	0.1179
0.57	0.0932	0.0937	0.0931	0.0954	0.0955	0.0966	0.0958	0.0958	0.0971	0.0991	0.0991	0.1018	0.1003	0.1002	0.1036	0.1044	0.1043	0.1092
0.64	0.0885	0.0866	0.0859	0.0882	0.0882	0.0890	0.0886	0.0886	0.0894	0.0909	0.0914	0.0935	0.0923	0.0926	0.0951	0.0961	0.0966	0.0996
0.69	0.0799	0.0791	0.0780	0.0811	0.0804	0.0803	0.0814	0.0806	0.0804	0.0831	0.0832	0.0835	0.0841	0.0840	0.0843	0.0871	0.0871	0.0863
0.75	0.0719	0.0707	0.0696	0.0723	0.0713	0.0704	0.0728	0.0716	0.0706	0.0730	0.0728	0.0716	0.0742	0.0740	0.0722	0.0758	0.0756	0.0715
0.78	0.0548	0.0543	0.0537	0.0541	0.0537	0.0527	0.0545	0.0543	0.0531	0.0532	0.0534	0.0514	0.0543	0.0550	0.0522	0.0539	0.0545	0.0491
0.87	0.0584	0.0570	0.0559	0.0574	0.0563	0.0544	0.0574	0.0562	0.0540	0.0560	0.0558	0.0523	0.0558	0.0557	0.0510	0.0538	0.0536	0.0461
1.00	0.0427	0.0421	0.0414	0.0401	0.0393	0.0376	0.0401	0.0394	0.0374	0.0358	0.0358	0.0322	0.0354	0.0357	0.0310	0.0306	0.0308	0.0249
1.10	0.0385	0.0372	0.0363	0.0346	0.0334	0.0316	0.0340	0.0327	0.0309	0.0284	0.0283	0.0247	0.0261	0.0259	0.0221	0.0200	0.0200	0.0162
1.19	0.0262	0.0259	0.0255	0.0231	0.0226	0.0218	0.0228	0.0224	0.0215	0.0181	0.0181	0.0162	0.0170	0.0173	0.0150	0.0124	0.0126	0.0104
1.28	0.0263	0.0253	0.0247	0.0221	0.0211	0.0204	0.0216	0.0205	0.0198	0.0154	0.0153	0.0140	0.0133	0.0132	0.0120	0.0085	0.0085	0.0076
1.53	0.0110	0.0111	0.0111	0.0089	0.0089	0.0089	0.0087	0.0086	0.0087	0.0057	0.0057	0.0057	0.0047	0.0049	0.0048	0.0025	0.0026	0.0026
1.64	0.0139	0.0134	0.0131	0.0109	0.0104	0.0104	0.0106	0.0101	0.0101	0.0062	0.0062	0.0065	0.0050	0.0050	0.0053	0.0025	0.0024	0.0027
2.13	0.0050	0.0050	0.0050	0.0039	0.0038	0.0039	0.0038	0.0037	0.0037	0.0022	0.0022	0.0023	0.0016	0.0016	0.0017	0.0005	0.0005	0.0005
2.38	0.0042	0.0040	0.0039	0.0032	0.0030	0.0030	0.0030	0.0029	0.0029	0.0016	0.0016	0.0017	0.0011	0.0011	0.0012	0.0003	0.0003	0.0003
2.91	0.0006	0.0006	0.0006	0.0004	0.0004	0.0004	0.0004	0.0004	0.0004	0.0001	0.0001	0.0001	0.0000	0.0000	0.0000	0.0000	0.0000	0.0000
3.42	0.0006	0.0007	0.0007	0.0004	0.0004	0.0004	0.0004	0.0004	0.0004	0.0001	0.0001	0.0001	0.0000	0.0000	0.0000	0.0000	0.0000	0.0000
4.00	0.0007	0.0006	0.0006	0.0005	0.0004	0.0004	0.0004	0.0004	0.0004	0.0002	0.0002	0.0002	0.0001	0.0001	0.0001	0.0000	0.0000	0.0000

Table A6.3 Diffuse proportion of global radiation ($W \cdot m^{-2}$) within each waveband centered on wavelength, λ (μm) for each sky condition: clr=clear, h-part=high alto stratus (5/10 coverage), t-part=thin stratus (5/10 coverage), as=alto stratus, t-str=thin stratus, h-str=heavy stratus.

	clr		clr	h-part			t-part			as			t-str			h-str		
λ	April	May	June															
0.3	1.0000	1.0000	1.0000	1.0000	1.0000	1.0000	1.0000	1.0000	1.0000	1.0000	1.0000	1.0000	1.0000	1.0000	1.0000	1.0000	1.0000	1.0000
0.33	1.0000	1.0000	1.0000	1.0000	1.0000	1.0000	1.0000	1.0000	1.0000	1.0000	1.0000	1.0000	1.0000	1.0000	1.0000	1.0000	1.0000	1.0000
0.36	0.8241	0.8674	0.7050	0.8993	0.8494	0.8279	0.8971	0.8473	0.8264	0.9987	0.9923	0.9881	1.0000	0.9991	0.9976	1.0000	1.0000	1.0000
0.4	0.7057	0.6181	0.5853	0.8295	0.7777	0.7570	0.8252	0.7743	0.7545	0.9974	0.9891	0.9827	1.0000	0.9981	0.9962	1.0000	1.0000	1.0000
0.44	0.5808	0.5006	0.4717	0.7537	0.7076	0.6895	0.7471	0.7031	0.6862	0.9965	0.9858	0.9780	0.9994	0.9975	0.9953	1.0000	1.0000	1.0000
0.48	0.4752	0.4060	0.3818	0.6887	0.6511	0.6363	0.6805	0.6458	0.6326	0.9956	0.9833	0.9744	0.9995	0.9969	0.9946	1.0000	1.0000	1.0000
0.52	0.3902	0.3316	0.3113	0.6353	0.6063	0.5943	0.6263	0.6008	0.5908	0.9948	0.9811	0.9718	0.9994	0.9967	0.9940	1.0000	1.0000	1.0000
0.57	0.3174	0.2690	0.2523	0.5897	0.5692	0.5596	0.5798	0.5635	0.5556	0.9943	0.9796	0.9697	0.9995	0.9963	0.9935	1.0000	1.0000	1.0000
0.64	0.2509	0.2123	0.1985	0.5477	0.5355	0.5269	0.5370	0.5295	0.5227	0.9938	0.9783	0.9679	0.9993	0.9962	0.9931	1.0000	1.0000	1.0000
0.69	0.1989	0.1666	0.1546	0.5130	0.5081	0.4978	0.5009	0.5011	0.4915	0.9936	0.9773	0.9660	0.9994	0.9959	0.9926	1.0000	1.0000	1.0000
0.75	0.1584	0.1336	0.1229	0.4847	0.4843	0.4705	0.4730	0.4783	0.4640	0.9932	0.9763	0.9636	0.9995	0.9959	0.9922	1.0000	1.0000	1.0000
0.78	0.1324	0.1110	0.1000	0.4602	0.4602	0.4406	0.4501	0.4573	0.4359	0.9926	0.9742	0.9603	1.0000	0.9960	0.9914	1.0000	1.0000	1.0000
0.87	0.1143	0.0960	0.0856	0.4458	0.4509	0.4267	0.4300	0.4408	0.4135	0.9927	0.9745	0.9591	0.9995	0.9955	0.9911	1.0000	1.0000	1.0000
1	0.0864	0.0710	0.0603	0.3997	0.4041	0.3701	0.3822	0.3944	0.3554	0.9917	0.9705	0.9510	0.9990	0.9948	0.9891	1.0000	1.0000	1.0000
1.1	0.0552	0.0448	0.0359	0.3527	0.3633	0.3245	0.3210	0.3361	0.2968	0.9904	0.9669	0.9439	0.9990	0.9938	0.9868	1.0000	1.0000	1.0000
1.19	0.0225	0.0180	0.0142	0.3166	0.3269	0.2950	0.2890	0.3091	0.2737	0.9897	0.9638	0.9398	0.9985	0.9933	0.9860	1.0000	1.0000	1.0000
1.28	0.0167	0.0134	0.0104	0.2786	0.2930	0.2677	0.2392	0.2580	0.2356	0.9882	0.9593	0.9325	0.9979	0.9917	0.9835	1.0000	1.0000	1.0000
1.53	0.0108	0.0080	0.0064	0.2520	0.2568	0.2454	0.2057	0.2221	0.2146	0.9880	0.9534	0.9285	0.9980	0.9901	0.9820	1.0000	1.0000	1.0000
1.64	0.0072	0.0054	0.0042	0.2225	0.2358	0.2377	0.1779	0.1946	0.2006	0.9841	0.9482	0.9255	1.0000	0.9888	0.9809	1.0000	1.0000	1.0000
2.13	0.0051	0.0037	0.0033	0.2144	0.2227	0.2222	0.1565	0.1717	0.1754	0.9852	0.9484	0.9232	0.9968	0.9880	0.9797	1.0000	1.0000	1.0000
2.38	0.0039	0.0029	0.0026	0.1987	0.2112	0.2119	0.1350	0.1509	0.1549	0.9840	0.9448	0.9204	1.0000	0.9890	0.9811	1.0000	1.0000	1.0000
2.91	0.0044	0.0030	0.0026	0.0667	0.0726	0.0721	0.0261	0.0351	0.0355	0.9412	0.8621	0.7895	1.0000	0.9091	0.8667	1.0000	1.0000	1.0000
3.42	0.0043	0.0029	0.0025	0.0496	0.0492	0.0512	0.0172	0.0170	0.0196	0.9167	0.7826	0.7241	1.0000	0.8571	0.8889	1.0000	1.0000	1.0000
4	0.0000	0.0000	0.0000	0.1266	0.1416	0.1457	0.0616	0.0700	0.0756	0.9756	0.9385	0.8987	1.0000	0.9667	0.9714	1.0000	1.0000	1.0000
3-4	0.2296	0.2017	0.1897	0.5072	0.4995	0.4846	0.4910	0.4884	0.4742	0.9934	0.9759	0.9628	0.9994	0.9957	0.9919	1.0000	1.0000	1.0000

Table A6.4 The mean bias error (mbe), and root mean square error (rmse) describing the relationship between modeled and measured irradiance over PAR wavelengths for the respective SIMMS experiments and for each of the spring months. The average measured flux, the number of hours in the analysis are also provided. All flux units in $W \cdot m^{-2}$. Note that incident PAR was not measured during SIMMS'92, and is unavailable for the early portion of SIMMS'93.

Period	Statistic	PAR-irrad93	PAR-irrad95
SIMMS	Average	133.63	124.84
SIMMS	mbe	3.16	1.69
SIMMS	rmse	13.19	9.11
SIMMS	N	1128	1368
SIMMS	Depth	-	-
April	Average		88.73
April	mbe		0.49
April	rmse		8.75
April	N		312
April	Depth	-	-
May	Average	125.83	128.71
May	mbe	3.61	2.61
May	rmse	13.64	9.48
May	N	672	744
May	Depth	-	-
June	Average	145.11	151.74
June	mbe	2.14	0.41
June	rmse	12.11	7.89
June	N	264	240
June	Depth	-	-

APPENDIX 7: AN ASSESSMENT OF THE DIRECT MEASURE OF NET RADIATION DURING THE SIMMS EXPERIMENTS

A7.1 Introduction

In field studies, Q^* can be measured directly using a pyrradiometer or computed using a measurement of each of its constituent fluxes. With respect to the measured term, Halldin and Lindroth (1992) showed discrepancies between a reference measurement and measurements by a variety of different sensors to range between 6% and 20%. They attributed the variation to deficiencies relating to the calibration of the sensor, the sensitivity of the upper and lower thermopiles to long-wave and short-wave radiation, the transmission characteristics of the domes, the cosine response and temperature dependency of the sensors, and to the occasional formation of dew and frost on the sensor domes. Field et al.,(1992) observed differences between sensors from the same manufacturer of between 5% and 7% during the first ISLSCP (International Satellite Land Surface Climatology Project). Other studies comment on a systematic underestimation of Q^* as measured using a pyrradiometer of up to 25% (Bintanja and van den Broeke, 1992; Field et al., 1992). In these studies a discrepancy was observed both during the day and night and was thought related to the measurement of sky radiation through inconsistencies in the long-wave responsivity and/or solar heating of the sensor. Frost development on the radiometer domes is a major source of measurement error during winter conditions and contributed to errors of between 70% and 90% in the measurement of the long-wave component (Halldin and Lindroth, 1992).

The component flux approach is also affected by measurement error in the net short-wave and long-wave exchange. Halldin and Lindroth (1992) suggest the total accuracy for a net radiation calculation using its component sum to be the larger of 3.5%, or $\pm 10 \text{ W}\cdot\text{m}^{-2}$ of the measured flux. The largest source of measurement error is attributed to the long-wave flux. The

Eppley pyranometers used in the study (i.e. Eppley model PSP and B&W) perform well under laboratory conditions and Fritschen and Fritschen (1991) showed the pyranometer (Eppley PSP) to be only mildly affected by wind speed. The Eppley infrared radiometer (model PIR) used in the SIMMS experiments is considered the industry standard in long-wave radiometry. Under laboratory conditions a measurement should be within 3 to 5% of the measured flux (Latimer, 1978). The question remains, which estimate of Q^* is more accurate?

A7.2 Methods

Net radiation was measured by a Middleton pyrrometer (model CN-1). Typically the Funk-type radiometer has shown to possess a strong dependency on wind speed and temperature (Halldin and Lindroth, 1992). Both parameters modify by long-wave emission from the sensor itself. We test the hypothesis that the underestimation in the measured flux is related to the sensor's measurement of $L\downarrow$. We compare three estimates of $L\downarrow$ at each site, namely:

- measured by the pyrgeometer (termed $L\downarrow_{\text{meas}}$),
- solved as a residual in the radiation balance in combination with measured Q^* , $L\uparrow$, and K^* (termed $L\downarrow_{\text{resid}}$),
- modeled using the expression of Jacobs (1978) with the clear sky formulation of Efimova (1961) (i.e., Eqs. 3.22a and b) using measured vapor pressure and observed cloud fraction (termed $L\downarrow_{\text{mod}}$).

Detailed cloud observations were taken during 1995 at the research site, while only intermittent observations were made in 1993. Cloud climatology was poorly documented 1992. We examine the techniques from the third point for cloud-free periods and periods with full cloud coverage.

A7.3 Results

A comparison between measured Q^* and net radiation as derived from its component sums (Q^*_{calc}) shows an underestimation by the measured flux relative to the computed flux (Fig. A7.1). The measured flux underestimates the computed value by $17.9 \text{ W}\cdot\text{m}^{-2}$ at FYI'92, $15.8 \text{ W}\cdot\text{m}^{-2}$ at FYI'93 and $5 \text{ W}\cdot\text{m}^{-2}$ at MYI'93. The root-mean square errors are much larger, being $30.0 \text{ W}\cdot\text{m}^{-2}$ at FYI'92, $32.1 \text{ W}\cdot\text{m}^{-2}$ at FYI'93 and $14 \text{ W}\cdot\text{m}^{-2}$ at MYI'93.

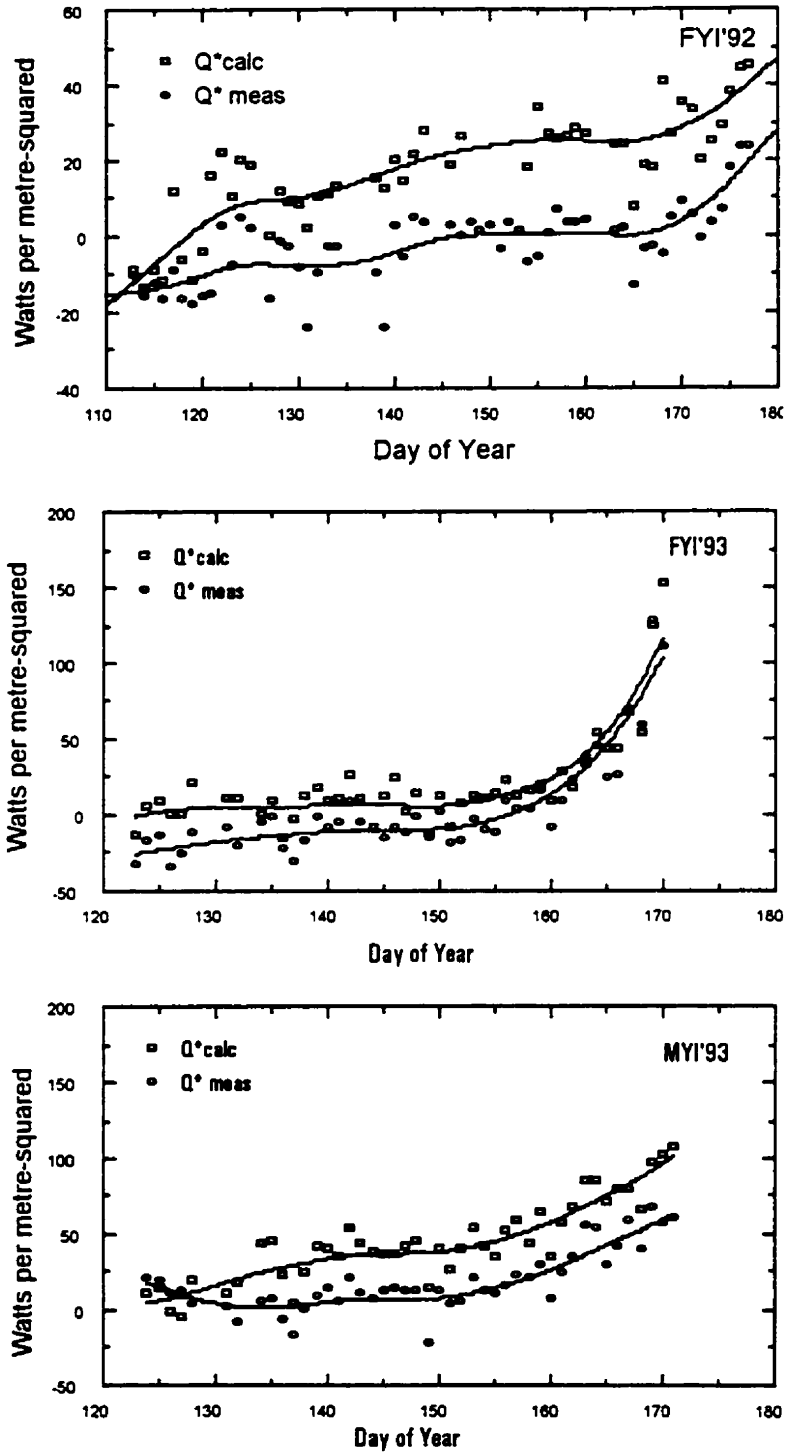


Figure A7.1 Daily average calculated and measured net radiation for the FYI'92, FYI'93 and MYI'93 experiments. The solid line through the daily averages represents a LOWESS fit to the data.

Statistics describing the comparison between $L\downarrow_{meas}$ and $L\downarrow_{resid}$ and between $L\downarrow_{meas}$ and $L\downarrow_{mod}$ during SIMMS'93 appear in Table A7.1, and A7.2, respectively, for hours known as either clear sky, or fully overcast. $L\downarrow_{resid}$ substantially underestimated the flux under clear sky conditions relative to $L\downarrow_{meas}$, and slightly underestimated the flux under overcast conditions. Note, however, that the random error of the comparison remained greater than $25 \text{ W}\cdot\text{m}^{-2}$ regardless of cloud coverage. $L\downarrow_{mod}$ provided an excellent measure of down-welling long-wave radiation relative to the measured flux under the conditions examined. However, the model did not perform as well as reported by Key et al.,(1996a). In that study a mean error of $0.1 \text{ W}\cdot\text{m}^{-2}$ (rmse of $7.8 \text{ W}\cdot\text{m}^{-2}$), and $0.7 \text{ W}\cdot\text{m}^{-2}$ (rmse of $16.9 \text{ W}\cdot\text{m}^{-2}$) was reported when the models of Efimova (1961), and Jacobs (1978) were compared against the long-wave radiation measurements for clear, and all sky conditions, respectively.

Table A7.1 MBE and RMSE describing the relationship between hourly $L\downarrow_{meas}$ and computed $L\downarrow_{calc}$ for hours designated as cloud-free, and complete overcast, during SIMMS'93. Bracketed values represent the percent error. Fluxes are in $\text{W}\cdot\text{m}^{-2}$.

sky	Variable	Average	mbe	rmse	N
clear	L↓	193.58	-27.13 (14)	37.21 (19)	96
cloudy	L↓	302.56	-7.62 (2.5)	25.39 (8.4)	120

Table A7.2 MBE and RMSE describing the relationship between hourly $L\downarrow_{meas}$ and $L\downarrow_{mol}$, using the empirical expression of Jacobs et al., (1978) with the clear sky function of Efimova (1961), for hours designated as cloud-free, and complete overcast, during SIMMS'93. Bracketed values represent the percent error. Fluxes are in $\text{W}\cdot\text{m}^{-2}$.

sky	variable	Average	mbe	rmse	Ta °C	Rh %	N
clear	L↓	193.59	9.78 (5.0)	11.60 (5.9)	-11.47	92.58	96
cloudy	L↓	303.27	3.22 (1.1)	11.12 (3.7)	-0.62	90.55	120

Statistics describing the comparison between $L\downarrow_{resid}$ and $L\downarrow_{mod}$ during SIMMS'95 appear in Table A7.3. The results show that the modeled flux overestimated long-wave radiation relative to $L\downarrow_{resid}$ by over 13% during clear sky conditions, and by approximately 5% under full cloud coverage. Of note is the large random error of the comparison. It approached 10% of the flux under cloudy conditions and represented 25% of the flux under clear skies.

Table A7.3 MBE and RMSE describing the relationship between hourly computed and modeled sky radiation, using the empirical expression of Jacobs (1978) with the clear sky function of Efimova (1961), for hours designated as cloud-free, and complete overcast, during SIMMS'95. Bracketed values represent the percent error.

<i>sky</i>	<i>Variable</i>	<i>Average</i>	<i>mbe</i>	<i>rmse</i>	<i>Ta</i> °C	<i>RH</i>	<i>N</i>
Clear	$L_{\downarrow \text{resid}}$	183.37	25.04 (13.6)	45.94 (25.0)	-10.20	81.36	144
cloudy	$L_{\downarrow \text{resid}}$	275.01	14.90 (5.1)	26.09 (9.4)	-4.11	93.24	120

The pyrradiometer are shown to underestimate the down-welling long-wave flux ($L_{\downarrow \text{resid}}$) for both clear sky and full overcast conditions relative to $L_{\downarrow \text{meas}}$ and $L_{\downarrow \text{mod}}$. The underestimation ranges between $7 \text{ W}\cdot\text{m}^{-2}$ and $27 \text{ W}\cdot\text{m}^{-2}$ which is of the same order as the underestimation of Q^*_{meas} relative to Q^*_{calce} . The similarity between discrepancies leads us to believe that the underestimation in the measure of net radiation by a pyrradiometer during the SIMMS experiments is related to the underestimation of the down-welling long-wave radiation by the pyrradiometer. Further analysis is required to identify the exact reason for the difference in between the measured and computed Q^* .

We assess the variation between measured and modeled L_{\downarrow} using the models of Jacobs (1978) and Efimova (1961) for all-sky conditions using the hourly cloud observations from the AES weather station at Resolute and measured L_{\downarrow} during the 1993 experiment. The results should provide an estimate of the uncertainty we introduce into the 1995 energy balance through the application of modeled L_{\downarrow} . Recall L_{\downarrow} was not directly measured at this site.

Measured L_{\downarrow} is shown to increase with increasing cloud amount (Fig. A7.2a). The maximum discrepancy between measured and modeled L_{\downarrow} is observed for cloud cover fractions between 5 tenths and 8 tenths (Fig. A7.2b). The modeled term underestimated the flux by on average $14 \text{ W}\cdot\text{m}^{-2}$, or approximately 5.6% of the measured flux. Within the course of the diurnal cycle L_{\downarrow} showed only a small average variation (Fig. A7.3a). The average underestimation of the measured flux never exceeded $15 \text{ W}\cdot\text{m}^{-2}$, or approximately 6% of the measured flux (Fig. A7.3b). The largest divergence between the measured and modeled term occurs during the late evening.

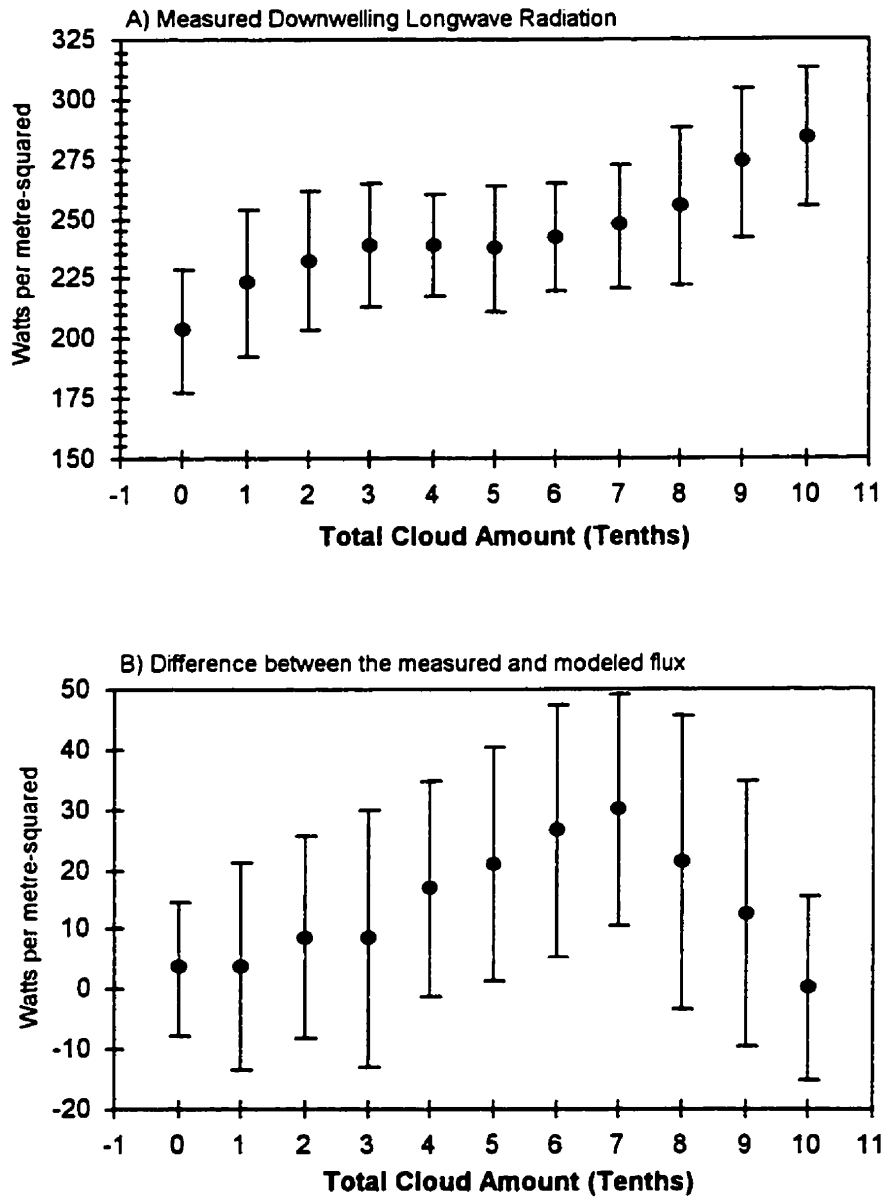


Figure A7.2 a) Measured L_{\downarrow} as a function of total cloud amount as observed at the AES weather station at Resolute. b) The difference between measured and modeled L_{\downarrow} for the various cloud amounts. The error bars denote one standard deviation unit surrounding the mean value.

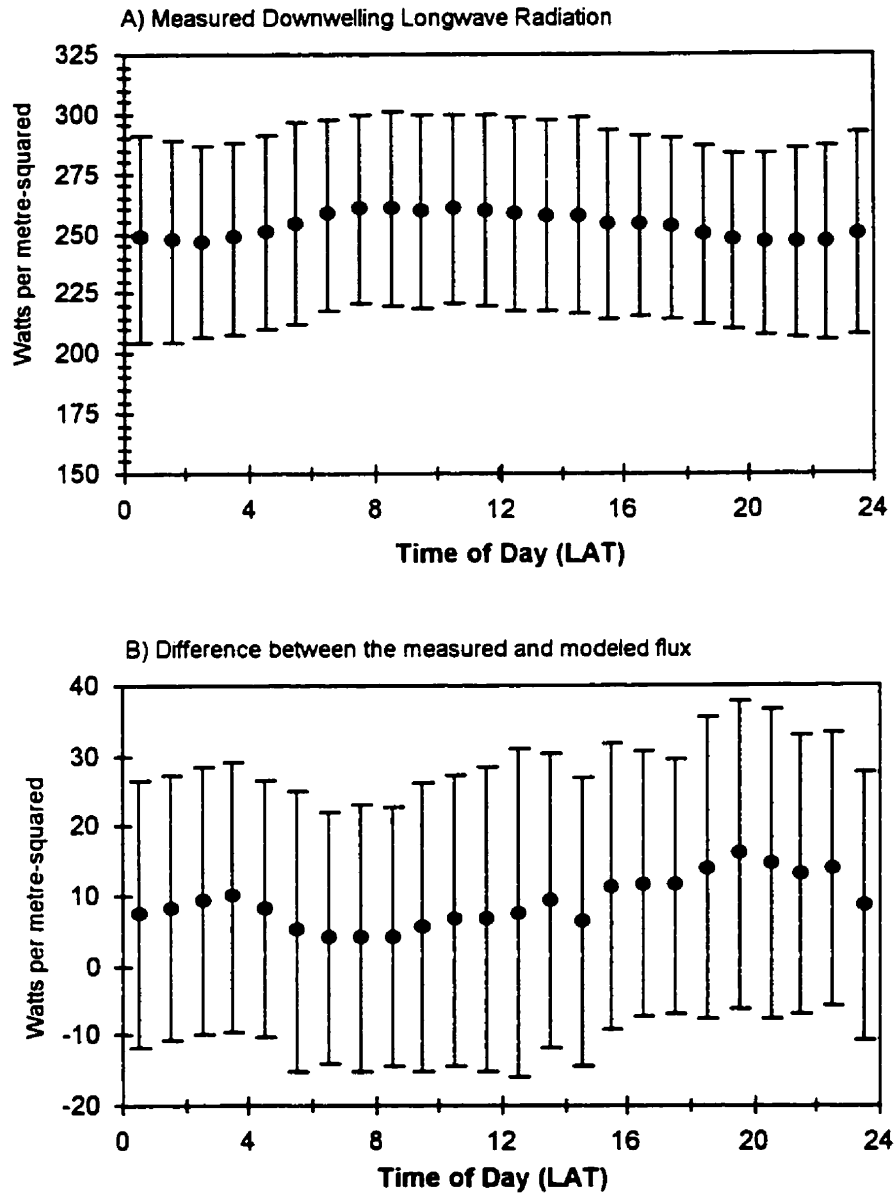


Figure A7.3 A) Diurnal variation in measured L_{\downarrow} . B) The difference between measured and modeled L_{\downarrow} over the diurnal cycle. The error bars denote one standard deviation unit surrounding the mean value.

A7.4 Summary

Several points of interest arise from this analysis. First, the pyrriometer is shown to underestimate the down-welling long-wave flux ($L_{\downarrow_{resid}}$) during both clear sky and full overcast conditions relative to $L_{\downarrow_{meas}}$ and $L_{\downarrow_{mod}}$. The underestimation was approximately $25 \text{ W}\cdot\text{m}^{-2}$, and is of the same order as the underestimation of Q^* by the pyrriometer relative to the component sum estimate. The similarity between discrepancies leads us to believe that the underestimation in the measure of net radiation by a pyrriometer during the SIMMS experiments is related to the underestimation of the pyrriometer measurement of down-welling long-wave radiation. Further analysis is required to identify the exact reason for the difference in between the measured and computed Q^* .

Second, the models of Jacobs (1978) and Efimova (1961) for estimating down-welling long-wave radiation under variable skies and clear skies are shown to perform well under all sky conditions. We have no alternative but to apply these models for the 1995 data set in absence of a functioning sky-facing pyrgeometer at the site. Based on our analysis the underestimation of the measured flux never exceeded $15 \text{ W}\cdot\text{m}^{-2}$, or approximately 6% of the measured flux.

APPENDIX 8: SENSITIVITY OF THE INDIVIDUAL FLUX TERMS TO FORCING VARIABLES

A8.1 Introduction

This Appendix outlines (1) the sensitivity of radiative and non-radiative fluxes to forcing variables and (2) provides a comparison between the aerodynamic determination of the sensible heat flux and direct flux measurements using the eddy correlation technique, with a one-dimensional sonic anemometer.

A8.2 Methods

A8.2.1 Surface Albedo and Extinction

The sensitivity of $K^*(z, \lambda)$ to variations (or uncertainties) in the terms $K \downarrow(o, \lambda)$, κ_λ , and α_λ within or beyond the snow are examined using the following partial derivatives:

$$\frac{\partial K^*(z, \lambda)}{\partial K \downarrow(o, \lambda)} = \exp(-\kappa_\lambda z) - \alpha_\lambda \cdot \exp(-\kappa_\lambda z) \quad (\text{A8.1a})$$

$$\frac{\partial K^*(z, \lambda)}{\partial \kappa_\lambda} = K \downarrow(o, \lambda) \cdot \alpha_\lambda z \exp(-\kappa_\lambda z) - K \downarrow(o, \lambda) \cdot z \exp(-\kappa_\lambda z) \quad (\text{A8.1b})$$

$$\frac{\partial K^*(z, \lambda)}{\partial \alpha_\lambda} = -K \downarrow(o, \lambda) \cdot \exp(-\kappa_\lambda z) . \quad (\text{A8.1c})$$

The sensitivity of the transmitted and absorbed solar flux terms to forcing variables are examined to highlight potential sources of uncertainty²⁴ in the measured and derived fluxes of the energy balance. We can estimate the relative accuracy required for a forcing (or input) variable

²⁴ The use of term *uncertainty* is used in the same context as *error* in this work.

($\frac{\delta\varphi}{\langle\varphi\rangle}$) of a relationship, in order to maintain the flux within a prescribed level of relative error (e.g., $\frac{\delta F}{\langle F \rangle}$ is equal to 0.10). Ebert and Curry (1993) present the expression:

$$\frac{\delta F}{\langle F \rangle} \left[\frac{\langle |\varphi| \rangle}{\langle F \rangle} \left| \frac{\partial F}{\partial \varphi} \right| \right]^{-1} = \frac{\delta \varphi}{\langle \varphi \rangle}, \quad (\text{A8.2})$$

where the angle brackets denotes a time average of the energy flux, F , and input variable φ . δ denotes a measure of uncertainty (here and elsewhere).

A8.2.1 Long-wave Radiation and Surface Temperature

The long-wave measurement is made under the premise that the sensing thermopile is at the same temperature as the instrument body and silicon dome. The effect of a temperature difference between the thermopile and case body is examined using Eq. A8.3.

$$\frac{\partial L}{\partial T_{\text{case}}} = 4\sigma\epsilon T_{\text{case}}^3. \quad (\text{A8.3})$$

The sensitivity of T_s to any variation in ϵ , $L\uparrow$, or $L\downarrow$ is examined by differentiating Eq. 6.2 with respect to each:

$$\frac{\partial T_s}{\partial L\uparrow} = C1 = \frac{(L\uparrow - L\downarrow + L\downarrow \cdot \epsilon)^{\frac{1}{4}}}{4 \cdot \sqrt[4]{\epsilon} \cdot \sqrt[4]{\sigma} \cdot (L\uparrow - L\downarrow + L\downarrow \cdot \epsilon)}, \quad (\text{A8.4a})$$

$$\frac{\partial T_s}{\partial \epsilon} = C1 \cdot L\downarrow - L\uparrow, \quad (\text{A8.4b})$$

$$\frac{\partial T_s}{\partial L\downarrow} = C1 \cdot (\epsilon - 1). \quad (\text{A8.4c})$$

The uncertainties associated with the measure and computation of Q^* is discussed in Appendix 7.

A8.2.2 Non-radiative Fluxes

The propagation of error (or uncertainty) in each component of the atmospheric heating of the snow volume and energy of fusion may be represented following Bevington (1969) as:

$$\frac{\delta dQ_s}{dQ_s} = \left(\frac{\delta Q^*{}^2}{\langle Q^* \rangle^2} + \frac{\delta K_s^*{}^2}{\langle K_s^* \rangle^2} + \frac{\delta Q_H^2}{\langle Q_H \rangle^2} + \frac{\delta Q_E^2}{\langle Q_E \rangle^2} \right)^{0.5}, \text{ and} \quad (\text{A8.5})$$

$$\frac{\delta Q_M}{dQ_M} = \left(\frac{\delta dQ_s^2}{\langle dQ_s \rangle^2} + \frac{\delta Q_{so}^2}{\langle Q_{so} \rangle^2} + \frac{\delta Q_{io}^2}{\langle Q_{io} \rangle^2} \right)^{0.5}, \quad (\text{A8.6})$$

where δ represents a level of uncertainty and the brace brackets denote time averages. The relative error given by Eq. A8.5 and A8.6 represents the probable error, or the 50% probability that the difference between the computation, and the *true* value is within the bounds denoted by the relative error.

The effect of uncertainty associated with the estimates of thermal conductivity (k) and the measured differences in temperature (ΔT) and depth (Δz) on the computed heat flux at a level can be estimated (assuming independence of the error terms), *viz.*:

$$\frac{\delta Q_x}{Q_x} \approx \left[\frac{\delta k_x^2}{\langle k_x \rangle^2} + \frac{\delta \Delta T_x^2}{\langle \Delta T_x \rangle^2} + \frac{\delta \Delta z^2}{\langle \Delta z \rangle^2} \right]^{\frac{1}{2}}. \quad (\text{A8.7})$$

and Δ represents a finite difference.

The literature tends to support an accuracy of $\pm 30\%$ for the computation of the turbulent heat fluxes using aerodynamic approaches (Arya, 1988). Berkowicz and Prahm (1982) observed good association between fluxes computed with the aerodynamic approach and eddy correlation technique. Halliwell and Rouse (1989) found the aerodynamic approach to closely match the Bowen ratio estimate of Q_H . The principal effect of measurement error on the aerodynamic approach was in the determination of the friction velocity in that study. Typically, the temperature difference can be measured to a higher accuracy than differences in wind speed. Bintanja and van den Broeke (1995) showed that the sensible heat flux rapidly increases with increasing temperature difference in an unstable atmosphere. Their analysis showed that that uncertainties in $\Delta\theta$ on the order of 0.3°C could lead to variations in Q_H by $100 \text{ W}\cdot\text{m}^{-2}$ or more in an unstable boundary layer. The sensitivity of the flux to uncertainty in either $\Delta\theta$ or Δu decreased rapidly with increasing stability in the stable boundary layer regime ($\xi > 0$). The sensitivity of the turbulent heat fluxes to measurement error in the temperature, wind speed and specific humidity differences may be assessed using the following partial derivatives:

$$\frac{\partial Q_H}{\partial(\Delta\theta)} = c_p \rho_a \kappa^2 \left(\frac{\Delta u}{\Delta \ln(z)^2} \right) \Phi_H^{-1} \Phi_M^{-1}, \quad (\text{A8.8a})$$

$$\frac{\partial Q_H}{\partial(\Delta u)} = c_p \rho_a \kappa^2 \left(\frac{\Delta \theta}{\Delta \ln(z)^2} \right) \Phi_H^{-1} \Phi_M^{-1}, \quad (\text{A8.8b})$$

$$\frac{\partial Q_E}{\partial(\Delta q)} = L_{s,v} \rho_a \kappa^2 \left(\frac{\Delta u}{\Delta \ln(z)^2} \right) \Phi_E^{-1} \Phi_M^{-1}, \quad (\text{A8.8c})$$

$$\frac{\partial Q_E}{\partial(\Delta u)} = L_{s,v} \rho_a \kappa^2 \left(\frac{\Delta q}{\Delta \ln(z)^2} \right) \Phi_H^{-1} \Phi_M^{-1}. \quad (\text{A8.8d})$$

A8.2.3 Eddy Correlation Determination of Q_H

A8.2.3.1 Theory

The sensible heat flux may be determined directly using the time average of the products of the fluctuating components of the vertical component of wind (w') temperature (T'),

$$Q_H = -\rho_a c_p \langle T' w' \rangle, \quad (\text{A8.9})$$

where ρ_a is the air density and c_p is the heat capacity of air. The sign convention is positive for an upward directed heat flux. During FYI'92 the covariance of temperature and vertical wind was periodically sampled using a one-dimensional sonic anemometer with fine-wire thermocouple (Campbell Scientific, model CA27). The sensor is described by Campbell and Unsworth (1979) and Yen (1995). The temperature signal from the fine-wire thermocouple is not an absolute measure, rather it is a differential measurement referenced to the case body of the anemometer. To minimize non-stationarity in the temperature signal, the manufacturer suggests that the averaging intervals should be less than approximately 20 minutes, and the use of measurement sub-intervals averaged over longer periods should be adopted.

Because the temperature and velocity gradients are steepest near the surface, the eddy fluctuations may be severely underestimated if the sensor is positioned too close to the surface, and if the sensor sampling rate is too course. A relationship between sampling frequency and sensor height is provided by Kristensen and Fitzjarrald (1984):

$$\frac{fz}{U} < \frac{z}{2\pi d}, \quad (\text{A8.10})$$

where f is the turbulent frequency, z is the height above the surface, d is the length of the sonic path, and U is the mean horizontal wind velocity. Kaimal et al.,(1972) relate the atmospheric frequencies important to scalar transport as a function of wind velocity and sensor height with:

$$10^{-3} \leq \frac{fz}{U} = n \leq 10 \quad (\text{A8.11})$$

where n is the non-dimensional frequency. They indicated that the peak value of the cospectrum of w' and T' is near $n=0.1$, and drops rapidly after $n=7$. Eq A8.2 stipulates that the sensor height should be greater than 1.4 m if n is set equal to 7 and d is equal to 0.1 m.

A8.2.3.2 Sensor Implementation and Data Acquisition

The sonic anemometer was mounted at 2.56 m on the principal energy balance tower, oriented in the same direction as the air temperature sensors. Signals were logged by a CR21X using a sampling rate of 10 Hz, and averaging three 10 minute sub-intervals over a 30 minute period. This sampling rate generated 6000 samples per sub-interval, which is sufficient minimize the computational error of algorithms used by the CR21X logger (Yen, 1995). Within each 10-minute sub-interval, the time average of the instantaneous fluctuations from the mean temperature and vertical winds were computed (i.e., T' and w') along with the covariance of the vertical wind, and temperature spectra ($\langle w'T' \rangle$).

A8.2.3.3 Computational Methods and Data Analysis

The sensible heat flux was computed using the eddy correlation technique (hereafter, Q_{Hec}) and the flux-profile technique with stability correction (Q_H).

In this experiment the sonic anemometer was oriented to sample northwest to northeast winds. However, because Yen (1995) showed the sensor to perform well over a fetch limited to less than 10 m over snow, all wind azimuths except those blowing from between south-southeast and south-southwest were considered in the analysis. A southerly air flow placed the sensor in the wake of the instrument tower.

The sonic anemometer was only used during times in which the first-year ice site was attended, or during those periods in which precipitation was highly unlikely. The sonic transducers are highly sensitive to moisture and the fine wire thermocouple is extremely fragile. The eddy correlation estimate of the sensible heat flux was computed and matched in time with the

corresponded 30-minute estimates of $Q_{\text{H Aero}}$ and $Q_{\text{H no-corr}}$. Of this data set, data were excluded from any analysis using the criteria:

- the first 30-minute estimate after the sonic installation;
- reported damage or icing of the fine-wire thermocouple;
- wind direction directly from the south;
- poor solution to the slopes of the temperature and wind speed change with the logarithm of sensor height due to an inability to delineate a straight line through the levels of the respective profiles;
- presence of the surface boundary layer below the height of the sonic anemometer;
- periods during which the average wind speed was less than 2 ms^{-1} and periods of extreme winds during which blowing snow was reported;
- periods of precipitation (clear-sky 'diamond dust' or other).

Alignment of the sensor is critical. Errors in the estimation of the vertical wind may be 8-100% for each degree of misalignment (Dyer and Hicks, 1972), and therefore, in addition to the above mentioned criteria, an entire run was rejected if at its end, the sonic anemometer was observed to be misaligned. Virtually all of the nighttime measurements were eliminated on the basis of sensor misalignment and icing of the sonic transducers and fine-wire thermocouple.

A8.3 Results

A8.3.1 Sensitivity of Absorbed Solar Radiation to Variation in Snow Albedo, Extinction, and Irradiance

The sensitivity of absorbed solar radiation, $K^*(z,\lambda)^{25}$, to variations (or uncertainties) in the terms $K\downarrow(o,\lambda)$, κ_λ , and α_λ within or beyond the snow are examined using Eq. A8.1. These equations are solved over 22 wavelength intervals between 0.3 and 4.0 μm (exact bandwidths are shown in Appendix 6) and summed to produce spectrally-integrated solutions for transmission through:

- thin (1 cm) snow cover of fine-grained snow ($r_{\text{ice}}=0.1 \text{ mm}$),

²⁵ The broadband equivalent to $K^*(z,\lambda)$ is K^*_z , that is $K^*(z,\lambda)$ summed over the 22 wavelength bands. At the snow base the terms Q^*_s and K^*_z are interchangeable.

- thin (1 cm) snow cover of coarse-grained snow ($r_{ice}=1.6$ mm),
- thick (10 cm) snow cover of fine-grained snow ($r_{ice}=0.1$ mm),
- thick (10 cm) snow cover of coarse-grained snow ($r_{ice}=1.6$ mm).

Results appear in Table A8.1a. The effective snow grain radii correspond to the maximum and minimum effective grain radii that are derived for the SIMMS' snow covers (Table 5.2).

The sensitivity of the net radiation to each variable increases with increasing effective grain radii for both snow depths (i.e., during the warm season). Positive variation in both spectral albedo and spectral extinction coefficient act to lower net radiation through a volume, while increasing the spectral flux incident to the snow directly increases net radiation. Net radiation appears generally more sensitive to albedo for a thin snow layer than for the thicker layer for both a fine and coarse snow cover. Sensitivity to κ_λ is greatest for coarse-grained snow for both snow thicknesses, but the differential is larger for a deeper snow cover with a larger optical path length. Sensitivity to $K\downarrow(z,\lambda)$ is likewise stronger in coarse-grained snow, but unlike the relationship involving κ_s , its affect is greater for the thin snow cover.

An examination of Eq. 8.1a and b can explain these results. The albedo of the snow reduces the sensitivity of net radiation to unit changes in κ_s and $K\downarrow(o,\lambda)$ and therefore the response of K^*_z is lessened under the conditions which favor a high albedo, namely for finer-grained (cold) snow characteristic of the early spring. Even though K^*_z is fairly insensitive to a unit change in κ_s and $K\downarrow(o,\lambda)$, large uncertainties in their values (denoted by δ) may lead to significant variations in the net solar flux. The expected uncertainty in K^*_z (termed δK^*_z), which corresponds to variation in each of the forcing variables, is examined using the results of Table 8.1a and by assigning:

- $\delta\alpha$ as one-half the difference in α over the visible wavelengths between albedo computed for fine- and coarse-grained snow within each of the 22 wavebands,
- $\delta\kappa_s$ and one-half the difference in computed κ_s between fine- and coarse-grained snow within each of the 22 wavebands,
- $\delta K\downarrow(o,\lambda)$ as the median difference per waveband between day 120 and day 166 at FYI'93.

In each instance the level of uncertainty in the forcing variable is taken as a function of the seasonal variation. The expected variation in K^*_z (summed over the 22 wavebands) is presented in

Table 8.1b and is expressed in both units of an energy flux ($W \cdot m^{-2}$) and as a percent of the computed flux.

Uncertainty in both optical properties have large ramifications on K^* for both grain sizes and snow depths. The variation in K^*_z can be several times the value of the flux. The uncertainty in α has the largest impact on K^* during the early spring. At this time the resultant variation in K^*_z may range between 74% and 114%. The uncertainty in κ_s has a larger impact on the net flux in the late spring (e.g., variations of between 118% and 512% of the measured flux). The effect of $\delta K \downarrow(z, \lambda)$ is small by comparison. These results demonstrate the danger of prescribing the optical properties of snow in radiative transfer schemes without allowing for a seasonal evolution in the term.

Table 8.1a Sensitivity of computed net radiation at a snow level to a unit variation in the spectrally proportioned global radiation ($W \cdot m^{-2}$), spectral albedo (fraction), and spectral extinction coefficient (m^{-1}). Sensitivity is summed over 22 wavebands between the spectral range 0.36 μm to 4.0 μm .

<i>net radiation within the snow volume to global radiation</i>	<i>snow depth = 0.01 m $r_{ice}=0.1$ mm</i>	<i>snow depth = 0.01 m $r_{ice}=1.6$ mm</i>	<i>snow depth = 0.10 m $r_{ice}=0.1$ mm</i>	<i>snow depth = 0.10 m $r_{ice}=1.6$ mm</i>
$\sum \frac{\partial K^*_{\downarrow}}{\partial K^*_{\downarrow}}$	0.98	6.25	0.05	1.65
<i>net radiation within the snow volume to spectral albedo</i>	<i>snow depth = 0.01 m $r_{ice}=0.1$ mm</i>	<i>snow depth = 0.01 m $r_{ice}=1.7$ mm</i>	<i>snow depth = 0.10 m $r_{ice}=0.1$ mm</i>	<i>snow depth = 0.10 m $r_{ice}=1.7$ mm</i>
$\sum \frac{\partial K^*_{\downarrow}}{\partial \alpha_s}$	-285.07	-509.80	-18.48	-207.98
<i>net radiation within the snow volume to spectral extinction coefficient</i>	<i>snow depth = 0.01 m $r_{ice}=0.1$ mm</i>	<i>snow depth = 0.01 m $r_{ice}=1.7$ mm</i>	<i>snow depth = 0.10 m $r_{ice}=0.1$ mm</i>	<i>snow depth = 0.10 m $r_{ice}=1.7$ mm</i>
$\sum \frac{\partial K^*_{\downarrow}}{\partial \kappa_s}$	-0.30	-2.02	-0.20	-6.55

Table 8.1b The variation in net solar radiation (δK^*_z) expressed in $W \cdot m^{-2}$ and as a percent of the computed flux (bracketed value) at levels 0.01m and 0.1m through snow to estimated levels of uncertainty in albedo, extinction coefficient and global radiation. Each are summed over 22 discrete wavelength intervals between 0.37 μ m and 4 μ m. Also provided in the average computed flux per depth.

<i>Relation</i>	<i>Early Spring</i> snow depth 0.01 m	<i>Early Spring</i> snow depth 0.1 m	<i>Late Spring</i> snow depth 0.01 m	<i>Late Spring</i> snow depth 0.1 m
$\delta\alpha_s \left(\frac{\partial K^*_z}{\partial \alpha_s} \right)$	28.51(74.3)	1.84(113.6)	50.98(51.3)	20.79(120.5)
$\delta\kappa_s \left(\frac{\partial K^*_z}{\partial \kappa_s} \right)$	6.11(15.9)	1.52(93.8)	117.58(118.4)	88.29(511.8)
$\delta K_{\downarrow\lambda} \left(\frac{\partial K^*_z}{\partial \kappa_s} \right)$	3.82(9.9)	0.22(13.5)	18.61(18.7)	7.39(42.8)
$\overline{K^*_z}$	38.37	1.62	99.40	17.25

The maximum relative error in each of, α_s , κ_s , and $K_{\downarrow(o,\lambda)}$, which is required to maintain a relative error of $\pm 10\%$ in net radiation per waveband in the visible portion of the electromagnetic spectrum are estimated using Eq. A8.2 and summarized in Table A8.2. The estimated sensitivity of $K^*(z,\lambda)$ to each variable per wavelength increment is taken from Table 8.1a and the net radiation at 0.01 m and 0.10 m are computed per waveband for day 120 and day 167. Results indicate that an α estimate must be within 1% for the fine-grained snow characteristic of early spring and within approximately 2-3% for coarse-grained snow of the late spring. The allowable relative error in albedo shows a slight increase toward the near infrared because the sensitivity to albedo drops off rapidly with decreasing albedo beyond the visible wavelengths. A slightly coarser estimate of albedo can be used for the coarse-grained snow because of the combined effect of a lower albedo and larger net flux during the late spring on the left-hand side of Eq. A8.2. The uncertainty surrounding our simulated albedo (see above) is very close to the requirements necessary for $\pm 10\%$ in computed K^*_z for shallow snow.

The allowable relative error in κ_s [assuming a $\pm 10\%$ limit on $K^*(z,\lambda)$] remains consistently within 5% over the visible wavelengths for transmission through 10 cm of snow, regardless of effective grain size. The allowable error in κ_s for transmission through 1 cm of snow is much less stringent and ranged between approximately 30 to 44% and 50 to 75% for the sample

days representing early and late spring snow conditions, respectively. $K^*(z,\lambda)$ is relatively insensitive to inaccuracies in κ_s over a small path length (0.01 m) and this insensitivity is attributed to the strong dependency of the flux on albedo for fine-grained snow in the early spring and to the large transmission of solar radiation through coarse-grained snow in the late spring. The partial derivative involving κ_s in Eq. A8.2 is small for coarse-grained snow (refer to Table A8.1a), while in the late spring we observe the combination of a larger net flux and relatively smaller extinction coefficient. These features act to raise $\delta\kappa_s/\kappa_s$ according to Eq. A8.2. The decrease in the allowable relative error in κ_s toward the larger wavelengths occurs because κ_s rises in this portion of the spectrum, while $K^*(z,\lambda)$ tends to zero. Both points act to reduce the left-hand-side of Eq. A8.2. We have no measurements of spectral extinction to place the uncertainty in our simulated term in the context of these accuracy limits. We reiterate comments from Section 5.4 and state that modeled transmission is very close to measured transmission in the 0.4 μm to 0.7 μm until the final days of the experiment, at which time the differences in transmissions may approach 30%. However the results show that $K^*(z,\lambda)$ is less sensitive to κ_s for shallow coarse grained snow, and therefore, the larger discrepancy in the transmitted flux may be more closely associated with errors in $K\downarrow(o,\lambda)$ than with κ_s .

The allowable relative error in $K\downarrow(o,\lambda)$ remained consistently close to 11% over the visible wavelengths in order to maintain the $\pm 10\%$ uncertainty in $K^*(z,\lambda)$ during the early spring. Accuracy of between 3 and 5% in $K\downarrow(o,\lambda)$ is required for the coarse snow of the late spring. A heightened relative accuracy is required during the late season because snow transmissivity is larger, and therefore, the net flux is more sensitive to the incident radiation at this time.

The net radiation at any level within the snow volume is highly sensitive to the seasonal evolution of the snow spectral albedo and spectral extinction coefficient. Albedo has the greatest impact on computed net radiation for dry snow. The potential for variation in the spectral extinction coefficient also has a large effect on the net flux, particularly over a large optical path and for the coarse-grained, warm snow, typically observed in the late spring. The net flux is sensitive to the estimate of the spectral distribution of incident radiation for thin warm snow with coarse snow grains. The results highlight the danger of prescribing the snow optical properties in radiative transfer schemes without making allowances for the seasonal evolution of the terms.

Albedo spectra should be estimated to between 1% and 3% over the visible wavelengths for fine grain and coarse grain snow, respectively, to maintain a $\pm 10\%$ limit on Q^*_{is} . κ_s must be estimated to within approximately 5% over the visible wavelengths for a deep snow. In shallow snow (1 cm), the absorbed solar radiation is less sensitive to the parameterization of κ_s because the flux is more sensitive to variations in snow albedo. The necessary accuracy should be between 30% to 75% over the range in snow conditions from cold and dry to warm and wet. Small errors in the κ_s at wavelengths beyond the visible region of the spectrum are inconsequential because the extinction coefficients are prohibitively large in these wavelengths. Surface irradiance must be represented to within 11% for cold fine-grained snow, but must be parameterized to within 3 to 5% during the late spring, when the transmitted flux can become appreciable.

Table A8.2 The allowable relative error in (a) albedo, (b) extinction coefficient, and (c) incident solar radiation in order to maintain $K^*(z,\lambda)$ to within $\pm 10\%$ within the visible portion of the electromagnetic spectrum.

a) Required Accuracy in α

waveband midpoint (μm)	day 120 (0.01 m depth)	day 120 (0.10 m depth)	day 166 (0.01 m depth)	day 166 (0.10 m depth)
0.36	0.9	0.9	1.8	1.1
0.40	0.9	0.9	1.8	1.1
0.44	0.9	0.9	1.8	1.1
0.48	0.9	0.9	1.8	1.1
0.52	0.9	0.9	1.8	1.1
0.57	0.9	0.9	1.9	1.1
0.64	1.0	1.0	2.0	1.2
0.69	1.0	1.0	2.1	1.2
0.75	1.2	1.2	2.4	1.3

b) Required Accuracy in κ

waveband midpoint (μm)	day 120 (0.01 m depth)	day 120 (0.10 m depth)	day 166 (0.01 m depth)	day 166 (0.10 m depth)
0.36	43.5	4.4	74.5	5.1
0.40	43.7	4.4	74.6	5.1
0.44	43.8	4.4	74.1	5.1
0.48	43.6	4.4	73.1	5.0
0.52	42.8	4.3	71.6	4.8
0.57	41.5	4.2	68.5	4.5
0.64	39.0	3.9	63.8	4.0
0.69	37.1	3.7	59.4	3.6
0.75	33.8	3.4	53.7	3.0

c) Required Accuracy in $K\downarrow_{\alpha}$

waveband midpoint (μm)	day 120 (0.01 m depth)	day 120 (0.10 m depth)	day 166 (0.01 m depth)	day 166 (0.10 m depth)
0.36	11.1	11.1	4.9	3.1
0.40	11.1	11.1	4.9	3.1
0.44	11.1	11.1	4.9	3.0
0.48	11.1	11.1	4.8	3.0
0.52	11.1	11.1	4.8	3.0
0.57	11.1	11.1	4.8	2.9
0.64	11.2	11.2	4.8	2.8
0.69	11.3	11.3	4.7	2.7
0.75	11.4	11.4	4.8	2.6

A8.3.2 Sensitivity Relations Involving Long-wave Radiation and Surface Temperature

The sensitivity of the measured flux per unit deviation in case temperature ranges between $3.67 \text{ W}\cdot\text{m}^{-2}$ at -20°C to $4.61 \text{ W}\cdot\text{m}^{-2}$ at 0°C (Table A8.3). The $\pm 0.2^\circ\text{C}$ tolerance of the case temperature translates into a flux uncertainty of approximately $\pm 0.82 \text{ W}\cdot\text{m}^{-2}$ at -10°C , which represents only a very small percentage of the incident flux.

It is doubtful that heating of the pyrgeometer domes overly biased the $L\downarrow$ measurements during the SIMMS experiments. During May of 1992 the dome was observed to be on average

only $0.089 \pm 0.27^\circ\text{C}$ ($N = 3360$ cases) warmer than the case, with a maximum deviation of 1°C for the sky-facing sensor. Given that the thermistor tolerance is approximately $\pm 0.2^\circ\text{C}$ when logged to the 21X datalogger, the degree of solar heating is on average well within the resolution of the temperature measurement. The maximum temperature difference between the case and dome, on the other hand, increased measured long-wave radiation relative to a true value by approximately $4.12 \text{ W}\cdot\text{m}^{-2}$ (i.e., substituting the dome temperature for the case temperature in Eq. A8.3), or by less than 2% of a typical measured flux of $225 \text{ W}\cdot\text{m}^{-2}$.

Table A8.3 Sensitivity of measured long-wave flux to unit variation in the pyrgeometer case temperature, and sensitivity of the computed surface temperature to up- and downwelling long-wave radiation. Sensitivities were calculated using Eqs. A8.1 and A8.2.

<i>measured long-wave to case temperature¹</i>	<i>Cold ($T_{\text{case}} = -20^\circ\text{C}$)</i>	<i>($T_{\text{case}} = -10^\circ\text{C}$)</i>	<i>Warm ($T_{\text{case}} = 0^\circ\text{C}$)</i>
$\frac{\partial L}{\partial T_{\text{case}}} \text{ (W}\cdot\text{m}^{-2} \cdot ^\circ\text{C}^{-1}\text{)}$	3.67	4.12	4.61
surface temperature to emissivity	clear-sky ($L\downarrow=115\text{-}165$)	($L\downarrow=195\text{-}235$)	cloudy-sky ($L\downarrow=275\text{-}305$)
$\frac{\partial T_s}{\partial \epsilon} \text{ (}^\circ\text{C)}$	-17.91	-11.00	-6.79
surface temperature to upwelling long-wave flux ¹	clear-sky ($L\downarrow=115\text{-}165$)	($L\downarrow=195\text{-}235$)	cloudy-sky ($L\downarrow=275\text{-}305$)
$\frac{\partial T_s}{\partial L\uparrow} \text{ (}^\circ\text{C}\cdot\text{Wm}^{-2}\text{)}$	0.354	0.272	0.224
surface temperature to downwelling long-wave flux ¹	clear-sky ($L\downarrow=115\text{-}165$)	($L\downarrow=195\text{-}235$)	cloudy-sky ($L\downarrow=275\text{-}305$)
$\frac{\partial T_s}{\partial L\downarrow} \text{ (}^\circ\text{C}\cdot\text{Wm}^{-2}\text{)}$	0.003	0.003	0.002

¹ emissivity is held constant at 0.99

The sensitivity of T_s to any uncertainty in ϵ , or any variation in $L\uparrow$, or $L\downarrow$ is assessed using Eq. A8.4. Sensitivity per unit change in forcing variables is also provided in Table A8.3. The bias in the surface temperature related to the accuracy of the pyrgeometer thermistor reference measurement is approximately 0.22°C at -10°C , or, about as accurate as the thermistor reference measurement itself. The surface temperature appears fairly insensitive to the accuracy of the down-welling flux, but it is highly sensitive to the assigned thermal emissivity. Fortunately the expected uncertainty in emissivity is small. The ± 0.01 variation in emissivity provided by Warren (1982) for snow with grain radii between 200 and 1000 μm , translates into a variation in derived

surface kinetic temperature of $\pm 0.11^{\circ}\text{C}$ at -10°C . A positive variation in emissivity diminishes the calculated surface temperature relative to a true value.

In an analysis independent to the SIMMS experiments, the performance of the pyrgeometer was compared against a KT-19 sensor (Himann Optoelectronics, model KT-19) over snow-covered sea ice. The manufacturer specifies that the KT-19 is accurate to within $\pm 0.5^{\circ}\text{C}$ with a 0.1°C resolution (using 0.3 s response time). When both sensors viewed the same snow-covered surface, the MBE and the RMSE of the comparison were 0.091°C , and 0.30°C respectively (N=60 fifteen minute averages). The close association between the two sensors is a testament to the performance of the pyrgeometer under springtime conditions.

A8.3.3 Sensitivity Relations for the Non-Radiative Fluxes

The RMSE for the measurement of $\Delta T_{s, \text{or } i}$, $\Delta\theta$ and Δu is estimated to be 0.17°C , 0.16°C and 0.34 m s^{-1} , respectively using the previously reported calibration results (Appendix 4). The effect of uncertainty associated with the estimates of thermal conductivity and the measured differences in temperature and depth on the computed heat flux, at a level, is estimated using Eq. A8.7. The uncertainty surrounding our computation of the conductive heat flux within the snow ranges between approximately 20% and 60% in the sea ice during the early spring, when the fluxes are strongly positive (Table A8.4). The temperature gradients in the snow and sea ice slacken in the late spring causing the relative uncertainty surrounding the computation of the snow and ice conductive fluxes to increase to approximately 42% and close to 100%, respectively. The measurement errors associated with the snow and ice temperatures contribute the most to the overall flux uncertainty. The fluxes are typically small in the late spring and therefore the ramifications of the large relative errors in terms on the energy balance are not overly damaging.

The sensitivity of Q_H and Q_E to measurement error in the near-surface gradients of potential temperature, wind speed and specific humidity using equations A8.8 a to d. For this analysis, the finite differences (Δu , $\Delta\theta$, Δq) are computed between 0.1 and 2 m. The uncertainty in the estimate of specific humidity (δq) is assumed to be the equivalent of a $\pm 0.5^{\circ}\text{C}$ deviation in dew

Table A8.4 Estimate of uncertainty associated with the computation of Q_{so} , and Q_{io} .

<i>Period</i>	<i>Variable</i>	<i>Average</i>	<i>Estimate of Uncertainty</i>
110-120	K_s ($W \cdot m^{-1} \cdot ^\circ C^{-1}$) [§]	0.33	0.05
	$ \Delta T_s $ ($^\circ C$)	2.27	0.17
	Δz (m)	0.03	0.003
	Q_{so} ($W \cdot m^{-2}$)	15.0	3.40
	K_i ($W \cdot m^{-1} \cdot ^\circ C^{-1}$) [§]	2.05	0.02
	$ \Delta T_i $ ($^\circ C$)	0.48	0.17
	Δz (m)	0.03	0.003
	Q_{io} ($W \cdot m^{-2}$)	17.0	12.02
160-170	K_s ($W \cdot m^{-1} \cdot ^\circ C^{-1}$) [§]	0.39	0.1
	$ \Delta T_s $ ($^\circ C$)	0.92	0.17
	Δz (m)	0.03	0.003
	Q_{so} ($W \cdot m^{-2}$)	4.42	1.85
	K_i ($W \cdot m^{-1} \cdot ^\circ C^{-1}$) [§]	1.63	0.30
	$ \Delta T_i $ ($^\circ C$)	0.31	0.17
	Δz (m)	0.03	0.003
	Q_{io} ($W \cdot m^{-2}$)	10.0	6.03

[§] Assigned as the standard deviation within the 10-day interval from the FYT'92 experiment.

point temperature at the 10 cm level (level 1), and the equivalent of $\pm 5\%$ uncertainty in the relative humidity measurement at level 2 (i.e., at 2 m). Recall that we assume the air at level 1 to be saturated with respect to the air temperature. Andreas (1986) supports this assumption over snow on theoretical grounds and further suggests that the dew point temperature at 10 cm should be typically $\pm 0.1^\circ C$ of the surface temperature.

The variation of specific humidity to fluctuations in saturated vapour pressure is estimated by differentiating Eq. 6.7, with respect to saturated vapour pressure (substituting e_s for e):

$$\frac{\partial q}{\partial e_s} = \frac{(0.622 \cdot P)}{(P^2 + 0.143 \cdot e_s^2 - 0.756 \cdot e_s \cdot P)} \quad (A8.14)$$

The temperature dependency of δq (at both the upper and lower level) and $\delta \Delta q$ is shown in Fig. A8.1. An uncertainty in Δq of $1.5E-5$ $kgkg^{-1}$ corresponds to $\delta \Delta q$ at an air temperature of $-6^\circ C$. This value is used in subsequent sensitivity analysis.

The variation of Q_E and Q_H to Δq and Δu over a stability range is shown in Fig. A8.2 a to d for strong, moderate and weak differences of wind speed, potential temperature

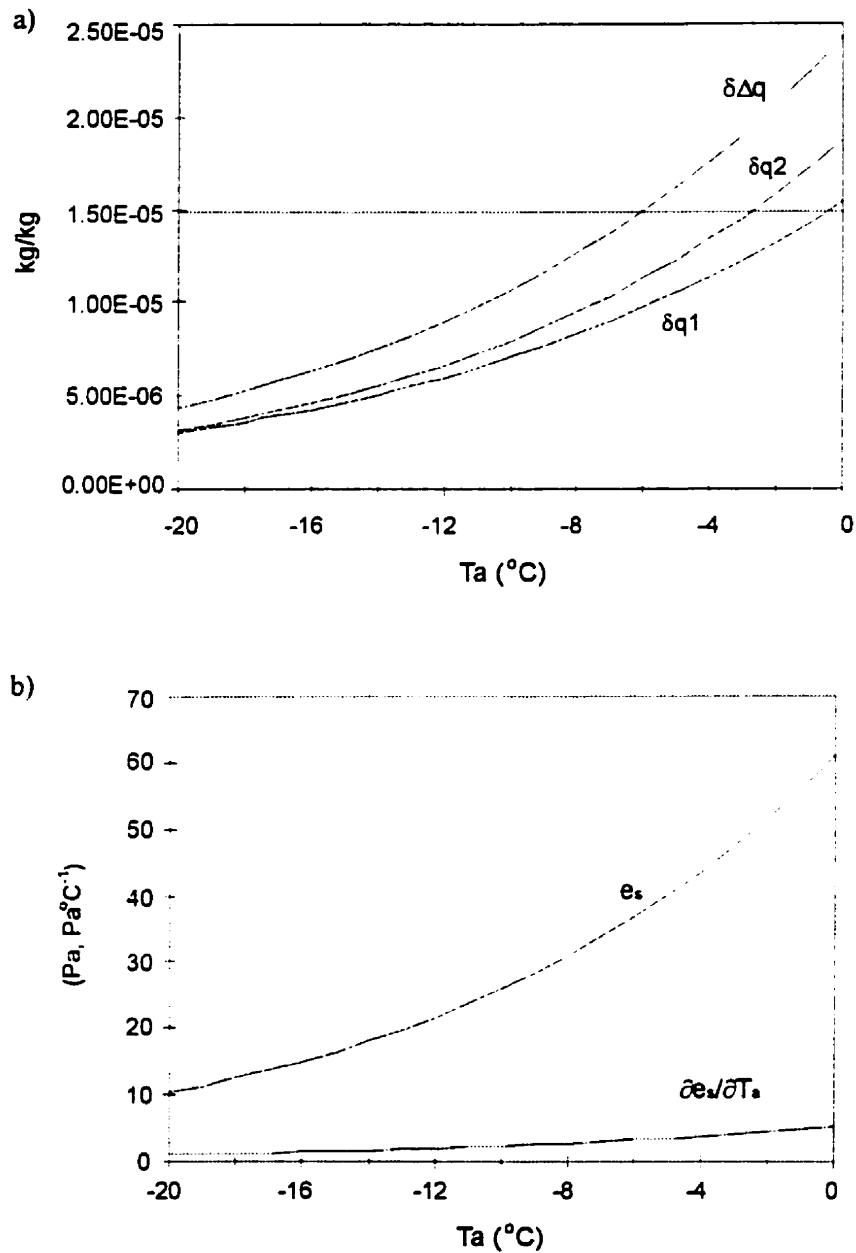


Figure A8.1 The variation in the estimate of: (a) specific humidity at level 2 (δq_2) and level 1 (δq_1), and in the near surface difference in humidity ($\delta\Delta q$), each as a function of air temperature, and (b) the dependency of both the saturated vapour pressure of air over ice (e_s , expressed in Pa) and the slope of the saturation vapour pressure/temperature relationship ($\partial e_s / \partial T_s$, $\text{Pa}\cdot^{\circ}\text{C}^{-1}$) over ice, as a function of temperature.

and specific humidity (Table A8.5). These differences can be compared against elements of the ranked distribution of Δu , $\Delta\theta$, and Δq from the first-year sea ice experiments (also in Table A8.5).

The variation of the heat flux through a unit change in the forcing variable increases with increasing (i) atmospheric instability, (ii) temperature (or specific humidity) difference, and (iii) wind speed difference in the near surface boundary layer (refer to Fig. A8.2). The variation of the latent flux to our estimate of δq (i.e., Equation A8.8c and Fig. 8.2a) can approach $16 \text{ W}\cdot\text{m}^{-2}$ in strongly unstable atmospheres and at high wind speed differences. This level of variation constitutes between 54% and 68% of the maximum daily Q_E losses reported in Table 6.2. At $\xi=0$, the uncertainty is less than $2 \text{ W}\cdot\text{m}^{-2}$, regardless of wind speed difference in the lower 2 m of the atmosphere. The estimate of Q_E appears fairly insensitive to variation in specific humidity during the SIMMS experiments because the atmospheric boundary layer is rarely unstable during the spring season (Table A8.5). This result indicates that a violation to our assumption that the near surface air (i.e., 0.10 m from the surface) is saturated will not appreciably affect the computed flux. The latent heat flux is however quite sensitive to measurement error in wind speed (Eq. A8.8d and Fig. A8.2b). The uncertainty may range between $20 \text{ W}\cdot\text{m}^{-2}$ and $70 \text{ W}\cdot\text{m}^{-2}$ in a highly unstable atmosphere ($\xi=-1$) for specific humidity differences ranging between 0.00011 and $0.00035 \text{ kg}\cdot\text{kg}^{-1}$. These differences represent the 25th and 75th percentile of computed specific humidity difference distribution during the first-year sea ice experiments. The variation in Q_E associated with δu drops below $8 \text{ W}\cdot\text{m}^{-2}$ within a stable boundary layer, regardless of Δq .

The sensible heat flux can be highly sensitive to anticipated measurement errors at both large wind speed (Equation A8.8 b and Fig. A8.2 d) and potential temperature differences (Eq. A8.8 a and Fig. 8.2 c) during unstable boundary layers. Although the variation in Q_H related to the two forcing variables is typically less than $7.5 \text{ W}\cdot\text{m}^{-2}$ under a stable boundary layer, this can be several times larger than the mean flux at any of the sites (Table 6.2).

Table A8.5 Elements of the ranked distribution of the absolute value of the hourly finite difference in u , θ , and q between 2 m and 0.1 m from the first-year sea ice experiments. The vertical bars denote the absolute value. The values of weak, moderate and strong differences, which are used in the analysis, are also shown.

Percentile	$ \Delta u $ (m s ⁻¹)	$ \Delta\theta $ (°C)	$ \Delta q $ (mass ratio)
10 th	0.41	0.06	4.62E-05
25 th	0.80	0.15	1.11E-04
50 th	1.30	0.34	1.92E-04
75 th	1.77	0.96	3.14E-04
90 th	2.34	2.48	5.08E-04
count	4056	4056	4056

Category	$ \Delta u $ (m s ⁻¹)	$ \Delta\theta $ (°C)	$ \Delta q $ (mass ratio)
weak	0.50	0.15	1.10E-04
moderate	1.00	0.50	2.20E-4
strong	2.00	1.50	3.50E-4

Another source of concern in our analysis pertains to the absence of a relative humidity measurement at FYI'92 prior to day 156. The SIMMS'93 experiment provided an opportunity to assess the potential magnitude of the difference between the relative humidity at the AES station and a site on the sea ice in relatively close proximity (Fig. A8.3). A Mann-Whitney U-test at 95% level of confidence shows that the relative humidity is: (i) similar between sites during the early spring (prior to day 130), (ii) greater over land during the transitional spring (days 130 to 142), (iii) greater over the sea ice during the late spring (after day 142). However, a statistically viable difference in air temperature is only observed during the late spring. Both the land and sea ice were cold and snow covered during the early spring. The onset of terrestrial snow melt occurred prior to melt onset over the sea ice. Therefore ample standing water was available to raise near surface humidity over land. Conversely, during the late spring more standing water was observed over sea ice. We used the RH measurement from the AES weather station throughout the equivalent of an early and transitional spring in 1992, but we did have an on sea ice measure during the late spring. The difference in median relative humidity between the AES weather station

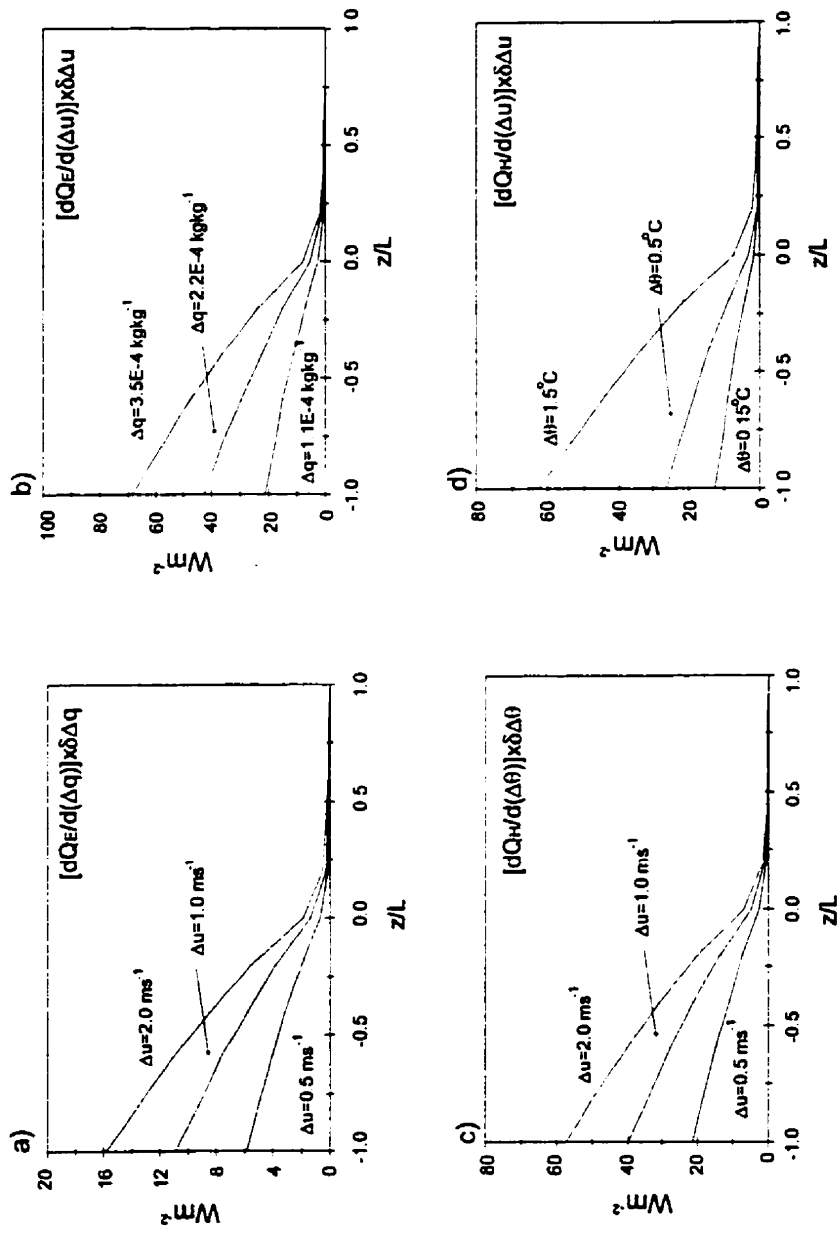


Figure A8.2 Sensitivity of the turbulent heat fluxes (Q_H and Q_E) to uncertainties (prefix δ) in measurement of Δq , Δu and $\Delta \theta$ for small, moderate and large values of Δq , Δu and $\Delta \theta$.

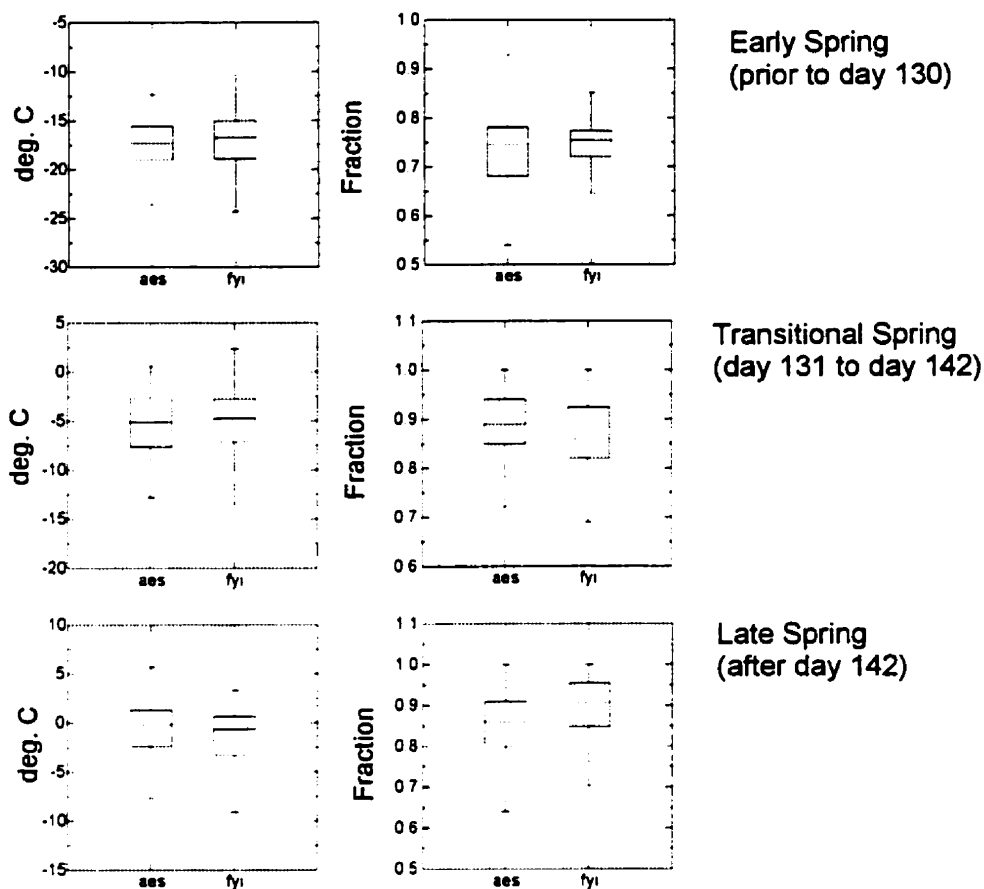


Figure A8.3 A contrast in the distributions of T_a and RH between FYI'93 and the AES weather station at Resolute over the three spring periods.

and FYI'93 is approximately 3% of the relative humidity during the transitional spring, which is within the resolution of the sensor itself. The spring of 1992 experienced a late and protracted melt on both land and sea ice and consequently the difference in relative humidity between stations was probably not greater than observed during the transitional spring of 1993. Consequently, we don't believe that our Q_E estimate at FYI'92 was severely compromised by not having a RH measure on site prior to day 156.

Estimates for the uncertainty surrounding dQ_S and Q_M are made using Eq. A8.5 and A8.6. In theory, the uncertainty surrounding dQ_S ranges from approximately $\pm 40\%$ to $\pm 50\%$ in the early

and late periods, while the uncertainty for Q_M is somewhere between $\pm 60\%$ in the early spring to over $\pm 100\%$ by the end of the experiments. These estimates assume an uncertainty of $\pm 30\%$ for Q_H and Q_E and an uncertainty of $\pm 3.5\%$ for Q^* (Appendix 7). We estimate the uncertainty surrounding our computation of the conductive heat flux within the snow to be approximately $\pm 20\%$ and approximately $\pm 60\%$ in the sea ice during the early spring when the fluxes are strongly positive. In the late spring, the temperature gradients within the snow and ice slacken and the uncertainty surrounding the computation of the snow and ice conductive fluxes are prohibitively large, increasing to approximately $\pm 40\%$ and $\pm 95\%$ for snow and sea ice, respectively (Table A8.4). The error term associated with Q^*_{is} is not considered during the early spring because virtually no net solar radiation is received beyond the snow. A value is assigned as $\pm 30\%$ during the late spring. Each of the error terms are very liberal, but this withstanding, the predicted uncertainty surrounding Q_M can be as large as the flux itself.

A8.3.4 A Comparison of Computational Techniques For Q_H

A8.3.4.1 Analysis

Bivariate plots showing the relationship between Q_{Hec} and Q_{Hacro} are presented for all data pairs (Fig. A8.4). The comparison incorporates a stability range $-2.71 < \xi < 0.03$ (Table A8.6). Wind speeds ranged between $2.6 \text{ m}\cdot\text{s}^{-1}$ and $11.7 \text{ m}\cdot\text{s}^{-1}$, and averaged $5.7 \text{ m}\cdot\text{s}^{-1}$.

The flux estimates from the two techniques are highly correlated in both stability regimes. Pearson's correlation coefficient ranges from 0.96 for the combined data set and the stable boundary layer data set, to 0.80 under unstable atmospheric conditions. The tendency is for Q_{Hacro} to overestimate the flux (for both positive and negative fluxes) when compared to eddy correlation estimates. The extent of the overestimation ranges from 14% of the measured flux during an unstable boundary layer to 10% of the measured flux under stable atmospheric conditions. Mean differences are small, ranging from $1.19 \text{ W}\cdot\text{m}^{-2}$ to $1.51 \text{ W}\cdot\text{m}^{-2}$ for stable and unstable atmospheric boundary layers, respectively. The root-mean square error for each stability category is less than $5 \text{ W}\cdot\text{m}^{-2}$.

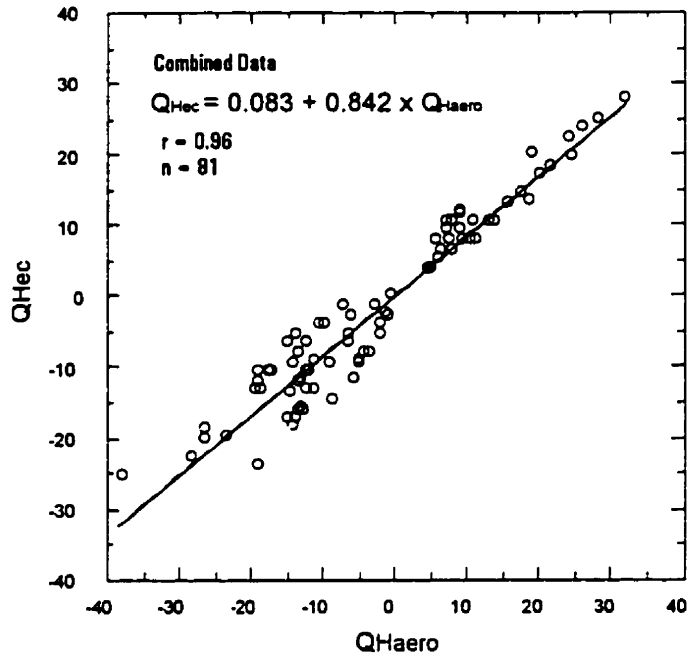


Figure A8.4 Bivariate plot of Q_{Hec} and Q_{Haero} over the full range in atmospheric stability. The standard error about the regression line is $3.45 \text{ W}\cdot\text{m}^{-2}$.

Table A8.6 Statistics describing the relationship between Q_{Hec} , and Q_{Haero} , among the stable, unstable and combined regimes. MBE and RMSE are the mean bias and root mean square error ($\text{W}\cdot\text{m}^{-2}$), while bracketed values represent percent error.

<i>Statistic</i>	<i>unstable</i>	<i>stable</i>	<i>both regimes</i>
Average	-10.83	12.26	-1.99
MBE	-1.51(0.14)	1.19(0.10)	-0.47(0.24)
RMSE	4.86(0.45)	2.63(0.21)	4.15(2.08)
N. of Cases	50	31	81

A8.3.4.2 Summary

We observe small mean differences between the aerodynamic approach and the eddy correlation technique for the computation of Q_H . In light of our results, there is no reason to believe that the uncertainty surrounding a Q_H estimate should be larger than Arya's (1988) estimate of 30%. The over-all relative accuracy is probably well within this range despite potentially large errors in the derivation of the sensible heat flux associated with determination of the temperature and wind speed gradients (refer to Chapter 6).

REFERENCE LIST

- Agnew, T. A. and A. Silis (1994): Spring season climate variability at Resolute Bay, NWT. *Canadian Climate Centre Report No. 94-1*. Unpublished Manuscript, Atmospheric Environment Service, Downsview, ON, 26 pp.
- Agnew, T. A., and A. Silis (1995): Spring season climate variability in the central Canadian Arctic Islands. *Ann. Glaciol.*, 21, 330-336.
- Alados-Arboledas, L., J. Vida, and J. I. Jimenez (1988): Effects of solar radiation on the performance of pyrgeometers with silicon domes. *J. Atmos. Oceanic Technol.*, 5, 666-670.
- Albrecht, B., and S. K. Cox (1977): Procedures for improving pyrgeometer performance. *J. Appl. Meteorol.*, 16, 188-197.
- Alford, D. (1974): Snow. In: *Arctic and Alpine Environments*, edditted by J. Ives and R. Barry, 85-110.
- Alley, R. B., Saltzman, E. S., Cuffey, K. M., and J. J. Fitzpatrick (1990): Summertime formations of depth hoar in central Greenland. *Geophys. Res. Let.*, 17 (12), 2393-2396.
- Ambach, W. (1974): The influence of cloudiness on the net radiation balance of a snow surface with high albedo. *J. Glaciol.*, 13 (67), 73-84.
- Anderson, E. A. (1976): A point energy and mass balance model of a snow cover. *NOAA Technical Report NWS 19*, 150 pp.

- Andreas, E. L., and A. P. Makshtas (1985): Energy exchange over Antarctic sea ice in the spring. *J. Geophys. Res.*, 90(C4), 7199-7212.
- Andreas, E. L. (1986): A new method of measuring snow-surface temperature. *Cold Reg. Sci. Technol.*, 12, 139-156.
- Andreas, E.L., and B. Murphy (1986): Bulk transfer coefficients for heat and momentum over leads and polynyas. *J. Phys. Ocean.*, 16, 1875-1883.
- Andreas, E. L. and S. F. Ackley (1982): On the difference in ablation seasons of the Arctic and Antarctic sea ice. *J. Atmos. Sci.*, 39, 440-447.
- Asrar, G. (1989): *Theory and Application of Optical Remote Sensing*. J. Wiley and Sons. New York. pp. 725.
- Arons, E. M., and S. C. Colbeck (1995): Geometry of heat and mass transfer in dry snow: A review of theory and experiment. *Rev. Geophys.*, 33 (4), 463-493.
- Arya, S. P. (1988): *Introduction to Micrometeorology*. Academic Press, Toronto.
- Barber D. G, A. Thomas, and T. N. Papakyriakou (1997): Role of SAR in surface energy flux measurements over sea ice. In: *Analysis of SAR Data of the Polar Oceans*. Edited by Tsatsoulis, C., and R. Kwok. *Springer-Verlag, Berlin/Heidelberg*, 35-67.
- Barber, D. G., T. N. Papakyriakou, M. E. Shokr, and E. F. LeDrew (1995a): An examination of the relationship between the spring period evolution of the scattering cross section (σ^0) and energy fluxes over landfast sea ice. *Int. J. Rem. Sens.*, 16, 3343-3363.

- Barber, D.G., S.P. Reddan and E.F. LeDrew (1995b): Statistical characterization of the geophysical and electrical properties of snow on landfast first-year sea ice. *J. Geophys. Res.*, 100, 2673-2686.
- Barber D. G., T. N. Papakyriakou, and E. F. LeDrew (1994): On the relationship between energy fluxes, dielectric properties, and microwave scattering over snow covered first-year sea ice during the spring transition period. *J. Geophys. Res.*, 99, 22401-22411.
- Barber, D. G., E. F. LeDrew, D. G. Flett, M. Shokr, and J. Falkingham (1992): Seasonal and diurnal variations in SAR signatures of landfast sea ice, *IEEE Trans. Geosci. and Rem. Sens.*, 30(3), 638-642.
- Barry, R.G. (1989): The present climate of the Arctic Ocean and possible past and future states. In: *The Arctic Seas. Climatology, Oceanography, Geology, and Biology*. Edited by Yvonne Herman. Van Nostrand Reinhold Co. New York, 1-46.
- Barry, R.G., and J. Maslanik (1989): Arctic sea ice characteristics and associated atmosphere-ice interactions in summer inferred from SMMR data and drifting buoys: 1979-1984. *GeoJournal*. 18, 35-44.
- Barry, R.G., M. W. Miles, R. C. Cianflone, G. Scharfen, and R. C. Schnell (1989): Characteristics of Arctic sea ice from remote-sensing data and their relationship to atmospheric processes. *Ann. Glaciol.*, 12, 9-15.
- Barry, R. G., and R. J. Chorley (1987): *Atmosphere Weather and Climate*. Meuthuen, New York, pp. 460.
- Barry, R. G., and A. H. Perry (1973): *Synoptic Climatology Methods and Applications*. Methuen and Co. Ltd, London, 535 pp.

- Barry, R. G. (1978): Seasonal controls of ice melt. In: *Energy Balance Studies in Relation to Fast-Ice Breakup Processes in Davis Strait: Climatological Overview*. Edited by R. G. Barry, J. D. Jacobs, R. R. Crane, R. A. Keen, R. E. Moritz, E. F. LeDrew, and R. L. Weaver. Occ. Pap. 26, Institute of Arctic and Alpine Research, Boulder Colorado. 262-278.
- Berkowicz, R., and L. P. Prahm (1982): Sensible heat flux estimated from routine meteorological data by the resistance method. *J. of Appl. Meteor.*, 21, 1846-1864.
- Bevington, P. R. (1969): *Data reduction and error analysis for the physical sciences*. McGraw-Hill Book Company, Toronto, pp 336.
- Bintanja, R., and M. van den Broeke (1995): The surface energy of Antarctic snow and blue ice. *J. Appl. Meteorol.*, 34, 903-927.
- Brandt, R.E., and S. G. Warren (1993): Solar-heating rates and temperature profiles in Antarctic snow and ice. *J. Glaciol.* 39 (131), 99-110.
- Brutsaert, W. (1982): *Evaporation into the atmosphere: Theory, History, and Applications*. D. Reidel, Boston. 299 pp.
- Bohren, C. F., and D. R. Huff (1983): *Absorption and Scattering of Light by Small Particles*. Wiley and Sons, New York, 530 pp.
- Broecker, W. S. (1991): The great ocean conveyor. *Oceanography*, 4 (2), 79-89.
- Businger, J. A., J. C. Wyngaard, J. C., Y Izumi, and E. F. Bradley (1971): Flux-profile relationships in the atmospheric surface layer. *J. Atmos. Sci.*, 28, 181-189.
- Campbell, G. S. and M. H. Unsworth (1979): An inexpensive sonic anemometer for eddy correlation. *J. Appl. Meteor.*, 18, 1072-1077.

- Campbell Scientific Ltd. (1994): *21X Micrologger Operator's Manual*. Revision 12/94, Campbell Scientific Canada, Corp., Edmonton, AL.
- Carleton, A. M. (1990): *Satellite Remote Sensing In Climatology*. Belhaven Press. London. pp. 291.
- Carlstrom, A, and L. M. H. Ulander (1995): Validation of backscatter models for level and deformed sea ice in ERS-1 SAR images. *Int. J. Rem. Sens.*, 16, 3245-3252.
- Carroll J.J. and B. W. Fitch (1981): Effects of solar elevations and cloudiness on snow albedo at the South Pole. *J. Geophys. Res.* 86(C6), 5271-5276.
- Carson, D. J., and P. J. R. Richards (1978): Modelling surface turbulent fluxes in stable conditions. *Bound.Lay. Meteorol.*, 14, 67-81.
- Carsey, F. (1989): Review and status of remote sensing of sea ice. *IEEE J. Oceanic Eng.* 14, 127-138.
- Chatfield C. (1984): *The Analysis of Time Series*. Chapman and Hall, New York, 250 pp.
- Choudhury, B. J. and A. T. Chang (1981): On the angular variation of solar reflectance of snow. *J. Geophys. Res.*, 86(C1), 465-472.
- Cogley, J.G., and A. Henderson-Sellers (1984): Effects of cloudiness on the high-latitude surface radiation budget. *Mon. Weather Rev.*, 112, 1017-1032.
- Colbeck, S.C. (1991): The layered character of snow covers. *Rev. Geophys.*, 21(1), 81-96.
- Colbeck, S. C. (1988): Snowmelt increase through albedo reduction. U.S. Army Core of Engineers, Cold Regions Research and Engineering Laboratory, Hanover, New Hampshire, *CRREL Report 88-26*.

- Colbeck, S.C. (1987): Snow metamorphism and classification. *In: Seasonal Snowcovers: Physics, Chemistry, Hydrology*. New York: D. Reidel, 1-35.
- Colbeck, S. C. (1983): Theory of metamorphism of dry snow. *J. Geophys. Res.*, 88(C9), 5475-5482.
- Colbeck, S. C. (1982): An overview of seasonal snow metamorphism. *Rev. Geophys. Space Phys.*, 20, 45-61.
- Colbeck, S. C. (1979): Grain clusters in wet snow. *J. Colloid Interf. Sci.*, 72 (3) 371-384.
- Colbeck, S.C. (1974): The capillary effects on water percolation in homogeneous snow. *J. Glaciol.*, 13 (67), 85-97.
- Colbeck, S., Akitaya, E., Armstrong, R., Gubler, H., Lafeuille, J., Lied, K., McClung, D., and A. E. Morris (1990): *The International Classification for Seasonal Snow on the Ground*. Prepared by: The International Commission on Snow and Ice of the International Association of Scientific Hydrology and the International Glaciological Society. 24 pp.
- Conover, W. J. (1971): *Practical Nonparametric Statistics*, John Wiley and Sons Inc., New York, 462 pp.
- Crane, R. G. (1979): Synoptic controls on the energy budget regime of an ablating fast ice surface. *Arch. Met. Geoph. Biokl., Ser. A*, 28, 53-70.
- Crocker, G.B. (1984): Physical model for predicting the thermal conductivity of brine wetted snow. *Cold Reg. Sci. and Technol.*, 10, 69-74.
- Curry J. A., J. L. Schramm, and E. E. Ebert (1993): Impact of clouds on the surface radiation balance of the Arctic Ocean. *Meteor. Atmos. Phys.*, 51, 197-217.

- DeAbreu, R. A., Barber, D. G., Misurak, K., & LeDrew, E. F. (1995): Spectral albedo of snow-covered first year and multiyear sea ice during spring melt. *Ann. Glaciol.*, 21, 337-341.
- den Hartog, G., Smith, S.D., Anderson, R.J., Topham, D.R., Perkin, R.G. (1983): An investigation of a polynya in the Canadian Archipelago, 3, Surface heat flux. *J. Geophys. Res.*, 88(C5), 2911-2916.
- Dickens, D. (1990): Lancaster Sound Region : *A Coastal Atlas for Environmental Protection*. D.F. Dickins Associates Ltd., Vancouver.
- Doronin, Yu. P., and D.E. Kheisin (1977). *Sea Ice*. Amerind Publishing Co. New York, 323 pp.
- Drinkwater, M.R., and G.B. Crocker (1988): Modelling changes in the dielectric and scattering properties of young snow-covered sea ice and GHz frequencies. *J. Glaciol.*, 34(118), 274-282.
- Dyer, A.J. (1974): A review of flux-profile relationships. *Bound.-Layer Meteorol.*, 7, 363-372.
- Dyer, A. J., and B. B. Hicks (1970): Flux gradient relationships in the constant flux layer. *Quart. J. Roy. Met. Soc.*, 96, 715-721.
- Dyer, A. J., and B. B. Hicks (1972): The spatial variability of eddy fluxes in the constant flux layer. *Quart. J. R. Met. Soc.*, 98, 206-212.
- Ebert, E. E., and J.A. Curry (1993): An intermediate one-dimensional thermodynamic sea ice model for investigating ice-atmosphere interactions. *J. Geophys. Res.*, 98 (C6), 10085-10109.
- Ebert, E. E., J. L. Schramm, and J. A. Curry (1995): Disposition of solar radiation in sea ice and the upper ocean. *J. Geophys. Res.*, 100 (C8), 15965-15996.

- Ebisemiju, F. S. (1988): Canonical correlation analysis in geomorphology with particular reference to drainage basin characteristics, *Geomorph.*, 1, 331-342.
- Efimova, N. A. (1961): On methods of calculating monthly values of net long-wave radiation, *Meteorol. Gidrol.*, 10, 28-33.
- Eide, L. I., and S. Martin (1975): The formation of brine drainage features in young sea ice. *J. Glaciol.*, 14 (70), 137-154.
- Field, R. T., L. J. Fritschen, E. T. Kanemasu, E. A. Smith, J. B. Stewart, S. B. Verma and W. P. Kustas (1992): Calibration, comparison, and correction of net radiation instruments used during FIFE, *J. Geophys. Res.*, 97 (D17), 18681-18695.
- Frankenstein, G., and R. Garner (1967): Equations for determining the brine volume of sea ice from -0.5 to -22.9 C. *J. Glaciol.*, 6 (48), 943-944.
- Fritschen, L. J., and C. L. Fritschen (1991): Design and evaluation of net radiometers. Presented at: *The Seventh Symposium on Meteorological Observations and Instrumentation*, January 13-18, 1991, New Orleans, La.
- Fukami, H., Kojima, K., Aburakawa (1985): The extinction and absorption of solar radiation within a snow cover. *Ann. Glaciol.*, 6, 118-122.
- Fukusako, S. (1990): Thermophysical properties of ice, snow and sea ice. *Int. J. Thermophys.*, 11, 353-372.
- Garrity, C. (1992): Characterization of snow on floating ice, and case studies of brightness temperature changes during the onset of melt. In *Microwave Remote Sensing of Sea Ice, Geophysical Monograph 68*. Edited by F.D. Carsey. American Geophysical Union, Washington D.C., 313-328.

- Gates, W. L., A. Henderson-Sellers, G. J. Boer, C. K. Folland, A. Kitoh, B. J. McAvaney, F. Semazzi, N. Smith, A. J. Weaver and Q.-C. Zeng (1996): *Climate Models – Evaluation*. In: *Climate Change 1995: The Science of Climate Change*. Cambridge University Press, pp 228-284.
- Goodrich, L. E. (1976): *A numerical model for assessing the influence of snow cover on the ground thermal regime*. Ph.D. Thesis, Interdisciplinary Programme in Glaciology, McGill University, Montreal, 537 pp.
- Gorman, B. A. (1988): *Sea Ice Characteristics of the Parry Channel*. M.A. Thesis, Geography Dept., Carlton University.
- Granger, R. J. (1977): *Energy exchange during melt of a prairie snowcover*, M.Sc. Thesis. University of Saskatchewan, Saskatoon.
- Granger, R., and D. Male (1978): Melting of a Prairie snowpack. *J. Appl. Meteor.*, 17 (12), 1833-1842.
- Gray J. M. N. T., and L. W. Morland (1994): A dry snow pack model. *Cold Reg. Sci. Technol.*, 22, 135-148.
- Grenfell, T. C., Warren, S. G., and P. C. Mullen (1994): Reflection of solar radiation by the Antarctic snow surface at ultraviolet, visible, and near infrared wavelengths. *J. Geophys. Res.*, 99 (D9), 18669-18684.
- Grenfell, T. C., D. J. Cavalieri, J. O. Comiso, M. R. Drinkwater, R. G. Onstott, I. Rubinstein, K. Steffen, and D. P. Winebrenner (1992): Considerations for microwave remote sensing of thin sea ice. In: *Microwave Remote Sensing of Sea Ice* Edited by F. D. Carsey. Geophysical Monograph 68, American Geophysical Union, Washington, D.C., 291-301.

- Grenfell, T. C., and D. K. Perovich (1984): Spectral albedos of sea ice and incident solar irradiance in the southern Beaufort Sea. *J. Geophys. Res.*, 89 (C3), 3573-3580.
- Grenfell, T. C., Perovich, D. K., and J. A. Ogren (1981): Spectral albedos of an alpine snowpack. *Cold Reg. Sci. Technol.*, 4, 121-127.
- Grenfell, T.C., and G. A. Maykut (1977): The optical properties of ice and snow in the Arctic basin. *J. Glaciol.*, 18 (80), 445-463.
- Guest P. S. and K. L. Davidson (1994): Factors affecting variations of snow surface temperature and air temperature over sea ice in winter. In: *The Polar Oceans and Their Role in Shaping the Global Environment*. Edited by Johannessen O. M., R. D. Muench, and J. E. Overland. Geophysical Monograph 85. American Geophysical Union, Washington, D.C., 435-442.
- Guryanov, I. E. (1985): Thermal-physical characteristics of frozen, thawing and unfrozen grounds. *Fourth International Symposium on Ground Freezing*. Sapporo, Japan, 225-230.
- Haan, C. T. (1977): *Statistical Methods in Hydrology*. The Iowa State University Press, Ames, 378.
- Halldin, S., and A. Lindroth (1992): Errors in net radiometry: comparison and evaluation of six radiometer designs. *J. Atmos. Oceanic Technol.*, 9 (12), 762-783.
- Halliwell, D. H., and W. R. Rouse (1989): A comparison of sensible and latent heat flux calculations using the Bowen ratio and aerodynamic methods. *J. Atm. Ocean. Tech.*, 6, 563-574.
- Hansen, J. E. and L. D. Travis (1974): Light scattering in planetary Atmospheres, *Space Sci. Rev.* 16, 527-610.
- Hare, F. K. and M. K. Thomas (1979): *Climate Canada*, John Wiley and Sons, Toronto, 230 pp.

Hicks, B. B. (1976): Wind profile relationships from the 'Wangara' experiment. *Quart. J. Roy. Met. Soc.*, 102, 535-551.

Holmgren, B. (1971): *Climate and energy exchange on the sub-polar ice cap in summer: Parts A-F*. Meteorol. Inst. Uppsala Univ. Medd. Nox. 107-112, 403 pp.

Illingworth, V. (1991): *Dictionary of Physics*. Penguin Books, New York, 544 pp.

Incropera, F. P., and D. P. DeWitt, (1990): *Introduction to Heat Transfer*, John Wiley and Sons, Toronto.

IPCC, (1996): *Climate Change 1995: The Science of Climate Change*, Cambridge University Press, 572 pp.

Iqbal, M. (1983): *An Introduction to Solar Radiation*. Academic Press, Toronto, 390 pp.

Jacobs, J. D. (1978): Radiation Climate of Broughton Island. In: *Energy Balance Studies in Relation to Fast-Ice Breakup Processes in Davis Strait: Climatological Overview*. Edited by: R. G. Barry, J. D. Jacobs, R. R. Crane, R. A. Keen, R. E. Moritz, E. F. LeDrew, and R. L. Weaver, Occ. Pap. 26, Institute of Arctic and Alpine Research, Boulder Colorado, 105-142.

Jacobs, J.D., Barry, R.G., and R. L. Weaver (1975): Fast ice characteristics, with special reference to the eastern Canadian Arctic. *Polar Record*, 17, 521-536.

Jakubauskas, M. E. (1996): Canonical correlation analysis of coniferous forest spectral and biotic relations, *Int. J. Rem. Sens.*, 17, (12), 2323-2332.

- Jin, Z., K. Stamnes, W. F. Weeks, and S. Tsay (1994): The effect of sea ice on the solar energy budget in the atmosphere-sea ice-ocean system: A model study. *J. Geophys. Res.*, 99(C7), 25281-25294.
- Johannessen, O. M., W. J. Campbell, R. Schuchman, S. Sandven, P. Gloersen, J. A. Johannessen, E. G. Josberger, P. M. Haugan (1992): Microwave study programs of air-ice-ocean interactive processes in the seasonal ice zone of the Greenland and Barents Seas. In: *Microwave Remote Sensing of Sea Ice*. Edited by F. D. Carsey. Geophysical Monograph 68, American Geophysical Union, Washington, D.C., 261-289.
- Johnston, R. J. (1984): *Multivariate Statistical Analysis in Geography*. Longman, New York, 280 pp.
- Johnson, R. A. and D. W. Wichern (1992): *Applied Multivariate Statistical Analysis*. Prentice Hall, Englewood Cliffs, New Jersey, 642 pp.
- Jones, J. M., T. D. Davies, and S. R. Dorling, (1995): Assessment of the use of principal components analysis to relate air pollution and precipitation to climate. *Water, Air Soil Poll.*, 85, 1569-1574.
- Jordan, R. (1991): A one-dimensional temperature model for a snow cover: Technical documentation for SNTHERM89. U.S. Army Core of Engineers, Cold Regions Research and Engineering Laboratory, Hanover, New Hampshire, *CRREL Report No. 91-16*.
- Kahl, J. D., Serreze, M. C., and R. C. Schnell (1992): Tropospheric low level temperature inversions in the Canadian Arctic. *Atmos.-Ocean*, 30 (4), 511-529.
- Kaimal, J. C., J. C. Wyngaard, Y. Izumi and O. R. Cote (1972): Spectral characteristics of surface layer turbulence. *Quart. J. Roy. Meteor. Soc.*, 98, 563-589.

- Kattenberg, A., F. Giorgi, H. Grassl, G. A. Meehl, J. F. B. Mitchell, R. J. Stouffer, T. Tokioka, A. J. Weaver, and T. M. I. Wigley (1996): Climate Models – Projections of Future Climate. In: *Climate Change 1995: The Science of Climate Change*. Cambridge University Press, pp 285-357.
- Key, J. R., R. A. Silcox, and R. S. Stone (1996a): Evaluation of surface radiative flux parameterizations for use in sea ice models. *J. Geophys. Res.*, 101 (C2), 3839-3849.
- Key, J. (1996b): Streamer User's Guide, *Technical Report 96-01*, Department of Geography, Boston University, 72 pp.
- King, J.C. (1990): Some measurements of turbulence over an antarctic ice shelf. *Quart. J. Roy. Meteor. Soc.*, 116, 379-400.
- King J. C. and P. S. Anderson (1994): Heat and water vapour fluxes and scalar roughness lengths over an Antarctic ice shelf. *Bound. Layer Meteorol.*, 69, 101-121.
- Kneizys, F., E. Shettle, L. Abreu, J. Chetwynd, G. Anderson, W. Gallery, J. Selby, and S. Clough, (1988): *User's Guide to LOWTRAN7*. Air Force Geophysics Laboratory. AFGL-TR-88-0177, Environmental Research Papers No. 1010, Bedford, MA. 137 pp.
- Kuhn, M. (1987): Micro-meteorological conditions for snow melt. *J. Glaciol.*, 33(113), 24-26.
- Kristensen, L. and D. R. Fitzjarrald (1984): The effect of line averaging on scalar flux measurement. *J. Atmos. Ocean. Technol.*, 1, 138-146.
- Lang, A. R. G., K. G. McNaughton, Chen Fazu, E. F. Bradley and E. Ohtaki (1983): Inequality of eddy transfer coefficients for vertical transport of sensible and latent heats during advection inversions. *Bound-Layer Meteorol.*, 25, 25-41.

- Lange, N. A., and G. M. Forker (1952): *Handbook of Chemistry*, Ohio, Handbook Publishers, 8th Edition.
- Latimer, J. R. (1972): *Radiation Measurement*. Technical Manual Series NO. 2, International Field Year for the Great Lakes. National Research Council of Canada, 53 pp.
- Launiainen, J., and T. Vihma (1994): On the surface heat fluxes in the Weddell Sea. In: *The Polar Oceans and Their Role in Shaping the Global Environment*. Edited by: O. M. Johannessen, R. D. Muench, and J. E. Overland, The American Geophysical Union, Washington, D.C., 399-419.
- Langham, E. J. (1981): Physics and Properties of Snowcover. In: *Handbook of Snow: Principles, Processes, Management and Use*. Edited by: D. M. Gray and D. H. Male, Pergamon Press, Toronto, 275-337.
- Langleben, M. P. (1966): On the factors affecting the rate of ablation of sea ice. *Can. J. Earth Sci.*, 3, 431-439.
- Leavitt, E., D. Bell, M. Clarke, and A. R. Anderson (1978): Computation of air stress and sensible heat fluxes from surface layer profile data, AIDJEX, 1975. *AIDJEX Bull.*, 36, 157-174.
- Ledley, S. T. (1993): Variations in snow on sea ice: A mechanism for producing climate variations. *J. Geophys. Res.*, 98, 10,401-10,410.
- Ledley, S. T. (1991): Snow on sea ice: competing effects in shaping climate. *J. Geophys. Res.*, 96, 17195-17208.
- LeDrew, E. F. (1995): The role of remote sensing in understanding the effects of sea ice on global change. In: *The Canadian Remote Sensing Contribution to Understanding Global Change*. Edited by: LeDrew, E. F., M. Strome, and F. Hegyi, Department of Geography Publication Series, No. 38, University of Waterloo, pp. 61-92.

- LeDrew, E. F. (1992): Remote sensing of atmosphere-cryosphere interactions in the polar basin. *Canadian Geographer*, Vol.XXXVI, No. 4, 336-350.
- LeDrew, E. F. (1980): Eigenvector analysis of the vertical velocity field over the eastern Canadian Arctic. *Mon. Weath. Rev.*, 108, 1992-2005.
- LeDrew, E. F., and D. G. Barber (1994): The SIMMS program: A study of change and variability within the marine cryosphere. *Arctic*, 47 (3), 256-264.
- Leontyeva, E. N., and K. H. Stamnes (1993): Cloud/albedo effects on the radiation budget in the Arctic. In: *Atmospheric Radiation*. Edited by K. H. Stamnes. The Society of Photo-Optical Instrumentation Engineers (SPIE), 111-119.
- LI-COR Inc. (1991): *LI-COR Radiation Sensors Instruction Manual: Terrestrial Type SA*. LI-COR, Inc. Lincoln, NE, USA.
- Lindroth, A., and S. Halldin (1990): Gradient measurements with fixed and reversing temperature and humidity sensors above a thin forest. *Agr. Forest Meteorol.*, 53, 81-103.
- List, R.J. (1966): *Smithsonian Meteorological Tables*. Sixth revised edition. Published by the Smithsonian Institution, Volume 114, Smithsonian Miscellaneous Collections, pp., 527.
- Lock, G. S. H. (1990): *The Growth and Decay of Ice*. Cambridge University Press, New York, pp., 444
- Lowe, P.R. (1976): An approximating polynomial for computation of saturation vapor pressure. *J. Appl. Meteor.*, 16, 100-103.

- Maeno, N., and T. Kuroda (1986): Structures and Physical Properties of Snow and Ice. *Fundamental Glaciology Series I*, Hokkaido University Press, pp 173-179.
- Makshtas, A. (1991): *The Heat Budget of Arctic Ice in the Winter*. International Glaciological Society, Cambridge, UK., pp., 77.
- Male, D., and R. Granger (1981): Snow surface energy exchange. *Water Res. Res.*, 17(3), 609-627.
- Maxwell J. B. (1980): *The Climate of the Canadian Arctic Islands and Adjacent Waters. Volume I*. Environment Canada, Climatological Studies No. 30, pp., 589.
- Maykut, G., A. (1986): The Surface Heat and Mass Balance. In: *The Geophysics of Sea Ice*. Edited by N. Untersteiner, Plenum Press, New York, 395-464.
- Maykut, G. A. (1978). Energy exchange over young sea ice in the central arctic. *J. Geophys. Res.*, 83 (C7), 3646-3658.
- Maykut, G.A., and D. K. Perovich (1987): The role of shortwave radiation in the summer decay of sea ice cover. *J. Geophys. Res.*, 92 (C7), 7032-7044.
- Maykut, G. A., and T. C. Grenfell (1975): The spectral distribution of light beneath first-year sea ice in the Arctic Ocean. *Limnol. and Oceanog.*, 20 (4), 554-563.
- Maykut, G.A., and N. Untersteiner (1971): Some results from a time-dependent thermodynamic model of sea ice. *J. Geophys. Res.*, 76 (6), 1551-1575.
- Mellor, M. (1977): Engineering properties of snow. *J. Glaciol.*, 19 (81), 15-66.
- McBean, M. G. (1986): The Atmospheric Boundary Layer. In: *The Geophysics of Sea Ice*. Edited by N. Untersteiner, Plenum Press, New York, pp. 283-338.

- McCree, K.J. (1972): Test of current definitions of photosynthetically active radiation against leaf photosynthesis data. *Agric. Meteorol.*, 10, 443-453.
- McGuffie, B., and A. Henderson-Sellers (1985): Hysteresis of snow albedo. *J. Glaciol.*, 31 (108), 188-196.
- McKay, D.C., and G. W. Thurtell (1978): Measurements of the energy fluxes involved in the energy budget of a snow cover. *J. Appl. Meteor.*, 17, 339-349.
- Miller, R. (1985): Multiple comparisons. In: *Encyclopedia of Statistical Sciences*. Edited by Kotz, S., and N. L. Johnson, John Wiley and Sons, Inc., New York, 5, 679-689.
- Minnett, P. J. (1998): On the influence of solar zenith angle and cloud type on cloud radiative forcing at the surface in the Arctic, In press: *J. Clim.*
- Minnett, P. J. (1995): Measurements of the summer surface heat budget of the Northeast Water Polynya in 1992. *J. Geophys. Res.*, 100 (C3), 4309-4322.
- Misurak, K. (1995): Snow Properties, In: *SIMMS'95 Data Report*. Edited by: Misurak K, S., D. G. Barber, and E. F. LeDrew, Earth Observations Laboratory Technical Report, ISTS-EOL-SIMS-TR93-003, University of Waterloo, Waterloo, ON.
- Misurak, K. (1993): Snow Properties, In *SIMMS'93 Data Report*, Edited by: Misurak K, S., D. G. Barber, and E. F. LeDrew, Earth Observations Laboratory, ISTS-EOL-SIMS-TR93-007, University of Waterloo, Waterloo, ON.
- Morassutti, M. P., and E. F. LeDrew (1995): *Melt Pond Dataset for use in Sea-Ice and Climate-Related Studies*. Earth Observations Laboratory Technical Report, ISTS-EOL-TR95-001, Waterloo, ON.

- Moritz, R. E., and D. K. Perovich (editors) (1996): *Surface Heat Budget of the Arctic Ocean Science Plan*, ARCSS/OAII, Report Number 5, University of Washington, Seattle, 64 pp.
- Monin, A. S. and A. M. Obukhov (1954): Dimensionless characteristics of turbulence in the atmospheric surface layer, *Dokl. Akad. Nauk. SSSR*, 93, 223-226.
- Morris, E. M. (1989): Turbulent transfer over snow and ice, *J. Hydrol.*, 105, 205-223.
- Munro, D. S. (1990): Comparison of melt energy computations and ablatometer measurements on melting ice and snow. *Arct. Alp. Res.*, 22, 153-162.
- Nakamura, N., and A. H. Oort (1988): Atmospheric heat budgets of the polar regions. *J. Geophys. Res.*, 92, (D3), 9510-9524.
- Nakawo, M., and N. K. Sinha (1981): Growth rate and salinity profile of first-year sea ice in the high Arctic. *J. Glaciol.*, 27, 315-330.
- Norcliffe, G.B. (1982): *Inferential Statistics for Geographers*, Hutchinson University Library, London, pp. 263.
- Nyberg, A. A., (1965): A study of the evaporation and condensation at a snow surface. *Ark. Geofys.*, 4 (30), 577-590.
- Ohmura, A. (1982): Climate and energy balance on the Arctic tundra. *J. Climatol.*, 2, 65-84.
- Oke, T. R. (1987): *Boundary Layer Climates*. Methuen, New York, pp., 435.
- Ono, N. (1966): Thermal properties of sea ice: III; On the specific heat of sea ice, *Low Temp. Sci.*, A24, 249-258.
- Ono, N., and T. Kasai (1985): Surface layer salinity of young ice. *Ann. Glaciol.*, 6, 298-299.

- Overland, J. E., and P. S. Guest (1991): The Arctic snow and air temperature budget over sea ice during winter. *J. Geophys. Res.*, 96 (C3), 4651-4662.
- Owens W.B, and P.Lemke (1990): Sensitivity studies with a sea ice-mixed layer-pycnocline model in the Weddell Sea. *J. Geophys. Res.*, 95 (C6), 9527-9538.
- Papakryiakou, T. N. and E. F. LeDrew (1999): The effect of physical properties on the snow thermal conductivity of first-year sea ice, Accepted pending revisions, *J. Geophys. Res.*
- Paulson, A., C. (1970): The mathematical representation of wind speed and temperature profiles in the unstable atmospheric surface layer. *J. Appl. Meteorol.*, 9, 857-861.
- Perovich, D.K., and J.A. Richter-Mente (1994): Surface characteristics of lead ice. *J. Geophys. Res.*, 99, 16341-16350.
- Pitman, D., and B. Zuckerman (1967): Effective thermal conductivity of snow at -88, -27, -5 C. *J. Appl. Phys.*, 38, 2698-2699.
- Piwowar, J. M., K.A. McIntyre, and E.F. LeDrew, (1995): Characteristics of pond formation on a melting sea ice surface. *Proceedings, 17th Canadian Symposium on Remote Sensing*, June 13-15, Saskatoon, Canada, 141-146.
- Philipona, R., C. Frohlich, and C. H. Betz (1995): Characterization of pyrgeometers and the accuracy of atmospheric long-wave radiation measurements. *Appl. Optics*, 34 (9), 1598-1605.
- Pritchard, R. S. (editor) (1980): *Sea Ice Processes and Models*. University of Washington Press, Seattle.

- Ratha, D. S. and B. K. Sahu (1993): Multivariate canonical correlation techniques: an economic approach for evaluation of pollutants in soil and sediments of Bombay region, India. *Environ. Geol.*, 21, 201-207.
- Reddan, S. (1992): Snow Properties, In: *SIMMS'92 Data Report*, Edited by Reddan, S., D. G. Barber, and E. F. LeDrew, Earth Observations Laboratory, Technical Report, ISTS-EOL-SIMS-TR92-003, University of Waterloo, Waterloo, ON.
- Robinson, D.A., Scharfen, G., Serreze, M.C., Kukla, G., and R. G. Barry (1986): Snow melt and surface albedo in the arctic basin. *Geophys. Res. Lett.*, 13, 945-948.
- Rouse, W. R. (1987): Examples of enhanced global solar radiation through multiple reflection from an ice-covered arctic sea. *J. Clim. and Appl. Meteor.*, 26, 670-674.
- Rouse, W.R., Hardill, S., and A. Silis, (1989): Energy balance of the intertidal zone of western Hudson Bay II: ice-dominated periods and seasonal patterns. *Atmos.-Ocean*, 27, 346-366.
- Ruffieux, D., Ola, P., Persson, G., Fairall, C. W., and D. E. Wolfe (1995). Ice pack and lead surface energy budgets during LEADDEX 1992. *J. Geophys. Res.*, 100 (C3), 4593-4612.
- Sakazume, S., and N. Seki (1978): On the thermal properties of ice and snow in a low temperature region. *Jap. Soc. Mech. Eng.*, 44 (382), 2059-2069.
- Schlatter, T. W. (1972): The local surface energy balance and subsurface temperature regime in Antarctica. *J. Appl. Meteor.*, 11, 1048-1062.
- Schweiger, A., and J. R. Key (1994): Arctic Ocean radiative fluxes and cloud forcing estimated from ISCCP C2 cloud dataset, 1983-1990. *J. Appl. Meteorol.*, 33 (8), 948-963.

- Schwerdtfeger, P. (1963): Theoretical derivation of the thermal conductivity and diffusivity of snow. In: *International Association of Scientific Hydrology. Commission of Snow and Ice. Assemblée Generale de Berkeley, 75-81.*
- Schwerdtfeger, P. (1962): The thermal properties of sea ice. *J. Glaciol.*, 16, 789-807.
- Serreze, M.C., J.A. Maslanik, and J.R. Key (1993a): Cloud data, albedo transects and multi-year ice floe analysis. In: *SIMMS'93 Data Report*, Earth Observations Laboratory Technical Report, Edited by Misurak, K., D. G. Barber, and E. F. LeDrew, ISTS-EOL-SIMS-TR93-007, University of Waterloo, Waterloo, ON.
- Serreze, M. C., J. E. Box, R. G. Barry, and J. E. Walsh (1993b): Characteristics of Arctic Synoptic Activity, 1952-1989. *Meteor. Atmos. Phys.*, 51, 147-164.
- Serreze, M., Maslanik, J., Scharfen, G., Barry, R., and D. Robinson (1993c): Interannual variations in snow melt over Arctic Ocean and relationships to atmospheric forcings. *Ann. Glaciol.*, 17, 327-331.
- Shine, K. P., and R. G. Crane (1984): The sensitivity of a one-dimensional thermodynamic sea ice model to changes in cloudiness. *J. Geophys. Res.* 89 (C6), 10615-10622.
- Shivola, A., and M. Tiuri (1986): Snow fork determination of the density and wetness profiles of a snow pack. *IEEE Trans. Geosci. Rem. Sens.*, GE-24, 78-86.
- Shokr, M. E., and N. K. Sinha (1995a): Physical, electrical and structural properties of Arctic sea ice observed during SIMMS'92 experiment. *Research Report No., CARD 95-005*, Environment Canada, Downsview, ON.
- Shokr, M. E., and N. K. Sinha (1995b): Physical, dielectrical and microstructural properties of sea ice. In: *SIMMS'95 Data Report*. Edited by: Misurak, K., D. G. Barber, and E. F.

LeDrew, Earth Observations Laboratory Technical Report, ISTS-EOL-SIMS-TR95-003, University of Waterloo, Waterloo, ON.

Shokr, M. E., and N. K. Sinha, (1993): Physical, dielectrical and microstructural properties of sea ice. In: *SIMMS'93 Data Report*. Edited by: Misurak, K., D. G. Barber, and E. F. LeDrew, Earth Observations Laboratory Technical Report, ISTS-EOL-SIMS-TR93-007, University of Waterloo, Waterloo, ON.

Silis, A. (1995): Resolute Weather Station Data, In: *SIMMS'93 Data Report*. Earth Observations Laboratory Technical Report, Edited by Misurak, K., D. G. Barber, and E. F. LeDrew, ISTS-EOL-SIMS-TR93-007, University of Waterloo, Waterloo, ON..

Smith, S. D., Anderson, R. J., Hartog, D., G., Topham, D. R., and R. G. Perkin (1983): An investigation of a polynya in the Canadian Archipelago, 2, Structure of turbulence and sensible heat. *J. Geophys. Res.*, 88 (C5), 2900-2910.

Sokal RR, F.J. Rohlf (1995): *Biometry*. W.H. Freeman and Company, New York, pp., 887.

Steffen, K. (1986): Ice conditions of an arctic polynya: North Water in winter. *J. Glaciol.*, 32, 383-390.

Steffen, K., and T. DeMaria (1996): Surface energy fluxes of Arctic winter sea ice in Barrow Strait. *J. Appl. Meteor.*, 35, 2067-2079.

Sturm, M. (1991): The role of thermal convection in heat and mass transport in the subarctic snow cover. U.S. Army Core of Engineers Cold Regions Research and Engineering Laboratory, Hanover, New Hampshire, *CRREL Report 91-19*, pp., 52.

Sturm, M., and J. B. Johnson (1992), Thermal conductivity measurements of depth hoar. *J. Geophys. Res.*, 97, 2129-2138.

- Sturm, M., and J. B. Johnson (1991): Natural convection in the subarctic snow cover. *J. Geophys. Res.*, 96 (B7), 11657-11671.
- Sverdrup, H.V. (1936): The eddy conductivity of the air over a smooth snow field. Results of the Norwegian-Swedish Spitzhergan expedition in 1934, *Geofys. Publ.*, 11 (7), 1-69.
- Tabachnik, B. G., and L. S. Fidell, (1989): *Using Multivariate Statistics*, Harper Collins Publishers, New York, 746 pp.
- Takizawa, T. (1985): Salination of snow on sea ice and formation of snow ice. *Ann. Glaciol.*, 6, 309-310.
- Thomas, R. H. (1986): Satellite remote sensing over ice. *J. Geophys. Res.*, 91, 2493-2502.
- Thorndike, A. A., D. A. Rothrock, G. A. Maykut, and R. Colony, (1975): The thickness distribution of sea ice. *J. Geophys. Res.* 80, 4501-4513.
- Tucker, W. B. III, D. K. Perovich, A. J. Gow, W. F. Weeks, and M. R. Drinkwater, (1992): Physical properties of sea ice relevant to remote sensing, In: *Microwave Remote Sensing of Sea Ice*. Edited by F. D. Carsey, Geophysical Monograph 68, American Geophysical Union, Washington, D.C., 9-28.
- Twitty, J. T., and J. A. Weinman (1971): Radiative properties of carbonaceous aerosols. *J. Appl. Meteor.*, 10, 725-731.
- Untersteiner, N. (1961): On the mass and heat budget of Arctic sea ice. *Arch. Met. Geoph. Biokl. A.*, 12, 151-182.
- Untersteiner, N. (1966): Natural desalination and equilibrium salinity profile of old sea ice. In: *Physics of Snow and Ice*. Edited by H. Oura, International Conference on Low Temperature

- Science I. Conference on Physics of Snow and Ice. The Institute of Low Temperature Science. Hokkaido University, Sapporo, Japan, 569-577.
- Vant, M. R., R. O. Ramseier, and V. Makios (1978): The complex-dielectric constant of sea ice at frequencies in the range 0.1-40 GHz. *J. Appl. Phys.*, 49 (3), 1264-1280.
- Vowinckle, E. and S. Orvig (1970): The climate of the north polar basin. In: *Climates of the Polar Regions*. Edited by S. Orvig. World Survey of Climatology, 11, 129-141.
- Walsh, J. E., and W. L. Chapman (1998): Arctic cloud-radiation-temperature associations in observational data and atmospheric reanalysis, *J. Clim.*, 11, 3030-3045.
- Walsh, J. E. and R. G. Crane (1992): A comparison of GCM simulations of Arctic Climate. *Geophys. Res. Lett.* 19 (1), 29-32.
- Warren, S. G. (1984): Optical constants of ice from the ultraviolet to the microwave. *Appl. Optics*, 23 (8), 1206-1225.
- Warren, S. G. (1982): Optical properties of snow. *Rev. Geophys. Space Phys.* 20 (1)67-89.
- Warren, S. G., and W. J. Wiscombe (1980): A model for the spectral albedo of snow. II: Snow containing atmospheric aerosols. *J. Atmos. Sci.*, 37, 2735-2745.
- Washington W. M. and C. L. Parkinson (1986): *An Introduction to Three Dimensional Climate Modelling*. University Science Books. Mill Valley California. pp., 422.
- Weaver, R. L., Jacobs, J. D., and R. G. Crane (1978): Micrometeorology of the Fast Ice. In: *Energy Balance Studies in Relation to Fast-Ice Breakup Processes in Davis Strait: Climatological Overview*. Edited by: R. G. Barry, J. D. Jacobs, R. R. Crane, R. A. Keen, R. E. Moritz, E. F. LeDrew, and R. L. Weaver, Institute of Arctic and Alpine Research, University of Colorado, Boulder, Colorado. 177-261.

- Weeks, W.F., and S. F. Ackley (1986): The growth, structure, and properties of sea ice In: *The Geophysics of Sea Ice*. Edited by N. Untersteiner), Plenum Press, New York. 9-164.
- Weeks, W. F. and O. S. Lee (1958): Observations on the physical properties of sea ice at Hopedale, Labrador. *Arctic*, 11, 134-155.
- Welch, H. E., M.A. Bergmann, T.D. Siferd, K.A. Martin, M.F. Curtis, R.E. Crawford, R.J. Conover, and H. Hop (1992): Energy flow through the marine ecosystem of the Lancaster sound region, Arctic Canada. *Arctic*, 45 (4), 343-357.
- Weller, G. (1968): Heat-energy transfer through a four-layer system: air, snow, sea ice and sea water. *J. Geophys. Res.*, 73, 1209-1220.
- Wendler, G., and J. Kelley (1988): On the albedo of snow in Antarctica: A contribution to I.A.G.O. *J. Glaciol.*, 34, 1-7.
- Wendler, G., and F. Eaton (1990): Surface radiation budget at Barrow, Alaska. *Theor. Appl. Climatol.*, 41, 107-115.
- Wilkinson, L., M. A., Hill, J. P., Welna, and G. K., Birkenbeuel, (1992): *Systat for Windows, Vers. 5*. Systat, Inc., Evanston, IL, 750.
- Wiscombe, W. J. (1980): Improved Mie scattering algorithms. *Appl. Optics*, 19 (9), 1505-1509.
- Wiscombe, W. J., and S. G. Warren (1980): A model for the spectral albedo of snow. 1: Pure snow. *J. Atmos. Sci.*, 37, 2712-2733.
- Wolfe, D. E., D. Ruffieux and C. W. Fairall (1993): The 1992 Arctic Leads Experiment: An overview of meteorology. *Arctic Res. U. S.*, 7, 24-28,

- Woodside, W., (1958): Calculation of the thermal conductivity of porous media, *Can. J. Phys.*, 36 (7), 815-821.
- Yamanouchi, T., and J. Borre Orbaek (1995): Comparative study of the surface radiation budget at Ny-Alesund, Svalbard and Syowa Station, Antarctica, 1987. In: *NIPR Symposium of Polar Meteorology and Glaciology*, 9, 118-132.
- Yen, Y. C. (1981): Review of thermal properties of snow, ice and sea ice. U.S. Army Cold Regions Research and Engineering Laboratory, Cold Regions Research and Engineering Laboratory, Hanover, New Hampshire, *CRREL Report 81-10*.
- Yen, Y. C., Cheng, K.C., and S. Fukusako (1991): Review of Intrinsic thermophysical properties of snow, ice, sea ice and frost. In: *Third Conference on Cold Regions Heat Transfer*, 187-218.
- Yen, Y., C. (1993): On the temperature distribution near a cold surface. U.S. Army Cold Regions Research and Engineering Laboratory, Cold Regions Research and Engineering Laboratory, Hanover, New Hampshire *CRREL Report 93-19. 91-19*.
- Yen, Y. C. (1995): Sensible Heat Flux Measurements Near a Cold Surface. U.S. Army Cold Regions Research and Engineering Laboratory, Cold Regions Research and Engineering Laboratory, Hanover, New Hampshire, *CRREL Report 95-22*, 52 pp.
- Yoshida, Z., and others (1955): Physical studies on deposited snow, 1, Thermal properties, *Contrib. Inst. Low Temp. Sci. Hokkaido Univ., Ser. A*, 7, 19-74, 1955.
- Zhang, T., K. Stamnes, and S. A. Bowling (1996): Impact of clouds on surface radiative fluxes and snowmelt in the Arctic and Subarctic. *J. Clim.*, 9, 2110-2123.